

Резюмета на научните трудове на Максим Боянов

1. "Microbial reduction of chlorite and uranium followed by air oxidation", G. Zhang, W. Burgos, J. Senko, M. Bishop, H. Dong, **M. Boyanov**, K. Kemner. *Chemical Geology* 283, 242-250 (2011)

To evaluate the stability of biogenic nanoparticulate U(IV) in the presence of an Fe(II)-rich iron-bearing phyllosilicate, we examined the reduction of structural Fe(III) in chlorite CCa-2 and uranium(VI) by *Shewanella oneidensis* MR-1, and the reoxidation of these minerals (after pasteurization) via the introduction of oxygen. Bioreduction experiments were conducted with combinations of chlorite, U(VI), and anthraquinone-2,6-disulfonate (AQDS). Abiotic experiments were conducted to quantify the reduction of U(VI) by chemically-reduced chlorite-associated Fe(II), the oxidation of nanoparticulate U(IV) by unaltered structural Fe(III) in chlorite, and the sorption of U(VI) to chlorite, to elucidate interactions between U(VI)/U(IV) and Fe(II)/Fe(III)-chlorite. Solids were characterized by X-ray diffraction, scanning electron microscopy, and X-ray absorption spectroscopy to confirm Fe and U reduction and reoxidation. U(VI) enhanced the reduction of structural Fe(III) in chlorite and nanoparticulate U(IV) was oxidized by structural Fe(III) in chlorite, demonstrating that U served as an effective electron shuttle from *S. oneidensis* MR-1 to chlorite-Fe(III). Abiotic reduction of U(VI) by chlorite-associated Fe(II) was very slow compared to biological U(VI) reduction. The rate of nanoparticulate U(IV) oxidation by dissolved oxygen increased in the presence of chlorite-associated Fe(II), but the extent of U(IV) oxidation decreased as compared to no-chlorite controls. In identical experiments conducted with bioreduced suspensions of nanoparticulate U(IV) and nontronite (another iron-bearing phyllosilicate), the rate of U(IV) oxidation by dissolved oxygen increased in the presence of nontronite-associated Fe(II). In summary, we found that structural Fe(III) in chlorite delayed the onset of U(VI) loss from solution, while chlorite-associated Fe(II) enhanced the oxidation rate of U(IV) by dissolved oxygen, indicating that chlorite-associated Fe(II) could not protect nanoparticulate U(IV) from oxygen intrusion but instead increased the oxidation rate of U(IV).

2. "Multiple Mechanisms of Uranium Immobilization by *Cellulomonas* sp. Strain ES6", V. Sivaswamy, **M. Boyanov**, B. M. Payton, S. Viamajala, R. Gerlach, W. A. Apel, R. K. Sani, A. Dohnalkova, K. M. Kemner, T. Borch, *Biotechnology and Bioengineering*, 108, 264-276 (2011)

Removal of hexavalent uranium (U(VI)) from aqueous solution was studied using a Gram-positive facultative anaerobe, *Cellulomonas* sp. strain ES6, under anaerobic, non-growth conditions in bicarbonate and PIPES buffers. Inorganic phosphate was released by cells during the experiments providing ligands for formation of insoluble U(VI) phosphates. Phosphate release was most probably the result of anaerobic hydrolysis of intracellular polyphosphates accumulated by ES6 during aerobic growth and could have served as a detoxification mechanism against U(VI). Microbial reduction of U(VI) to U(IV) was also observed. However, the relative magnitudes of U(VI) removal by abiotic (phosphate-based) precipitation and microbial reduction depended on the buffer chemistry. In bicarbonate buffer, X-ray absorption fine structure (XAFS) spectroscopy (including X-ray Absorption Near Edge Structure (XANES) and extended X-ray absorption fine structure (EXAFS) analyses) analysis showed that the major fraction of U precipitates was present in the reduced form as U(IV), whereas in PIPES buffer, U precipitates consisted primarily of U(VI). In both bicarbonate and PIPES buffer, release of cellular phosphate was measured to be lower than that observed in U-free controls suggesting simultaneous precipitation of U and PO_4^{-3} . In PIPES, it is

very likely that U(VI) phosphates formed a significant portion of U precipitates and mass balance estimates of U and P along with XAFS data corroborate this hypothesis. High-resolution transmission electron microscopy (HR-TEM) and energy dispersive X-ray spectroscopy (EDS) of samples from PIPES treatments indeed showed both extracellular and intracellular accumulation of U solids with nanometer sized lath structures that contained U and P in equimolar concentrations. In bicarbonate, however, more phosphate was removed than required to stoichiometrically balance XAFS-predicted U(VI) precipitates suggesting that U(IV) phosphates also occurred in this system. When anthraquinone-2,6-disulfonate (AQDS), a known electron shuttle, was added to the experimental reactors, U reduction was the dominant removal mechanism in both buffers. Uranium immobilization by abiotic precipitation or microbial reduction has been extensively reported; however, present work suggests that strain ES6 can remove U(VI) from solution simultaneously through precipitation with phosphate ligands and microbial reduction, depending on the environmental conditions. *Cellulomonadaceae* are environmentally relevant subsurface bacteria and here, for the first time, the presence of multiple U immobilization mechanisms within one organism is reported using *Cellulomonas* sp. strain ES6.

3. "One-Pot Aqueous Synthesis of Fe and Ag Core/Shell Nanoparticles", K. Carroll, D. Hudgins, S. Spurgeon, K. Kemner, B. Mishra, **M. Boyanov**, L. Brown, III, M. Taheri, E. Carpenter, *Chemistry of Materials*, 22, 6291–6296 (2010)

This article investigates a facile one-pot method for the synthesis of Fe and Ag core/shell nanoparticles by aqueous reduction under ambient conditions. We have shown that the injection time of silver nitrate into a reaction vessel containing aqueous ferrous salt, sodium borohydride, and sodium citrate is a vital parameter for the precise control of a desired core/shell structure. For example, if silver nitrate is injected one minute after sodium borohydride is added to the reaction vessel, Ag will nucleate first followed by Fe, creating monodisperse Ag/Fe core/shell nanoparticles. In contrast, if the introduction time is prolonged to 5 min, Fe nanoparticles will nucleate followed by Ag producing Fe/Ag nanoparticles. The composition, morphology, and magnetic behavior were investigated by X-ray absorption spectroscopy (XAS), X-ray photoelectron spectroscopy (XPS), X-ray diffraction (XRD), transmission electron microscopy (TEM), and room-temperature vibrating sample magnetometry (VSM). Fe/Ag core/shell nanoparticles with optical and magnetic functionality offer broad opportunities in medicine, catalysis, and chemical detection.

4. "U(VI) Reduction to Mononuclear U(IV) by *Desulfitobacterium* spp.", K. Fletcher, **M. Boyanov**, K. Kemner, S. Thomas, Q. Wu, F. Löffler. *Environ. Sci. Technol.* 44, 4705-4709 (2010).

The bioreduction of U(VI) to U(IV) affects uranium mobility and fate in contaminated subsurface environments and is best understood in gram-negative model organisms such as *Geobacter* and *Shewanella* spp. In this study, we demonstrate that U(VI) reduction is a common trait of gram-positive *Desulfitobacterium* spp. Five different *Desulfitobacterium* isolates reduced 100 μ M U(VI) to U(IV) in less than 10 days while U(VI) remained soluble in abiotic and heat-killed

controls. U(VI) reduction in live cultures was confirmed using X-ray absorption near-edge structure (XANES) analysis. Interestingly, while bioreduction of U(VI) is almost always reported to yield the uraninite mineral (UO₂), extended X-ray absorption fine structure (EXAFS) analysis demonstrated that the U(IV) produced by the *Desulfitobacterium* spp. was not UO₂. The EXAFS data indicated that the U(IV) product was a phase or mineral composed of mononuclear U(IV) atoms closely surrounded by light element shells. This atomic arrangement likely results from inner-sphere bonds between U(IV) and C/N/O or P/S-containing ligands, such as carbonate or phosphate. The formation of a distinct U(IV) phase warrants further study because the characteristics of the reduced material affect uranium stability and fate in the contaminated subsurface.

5. "Effects of Oxyanions, Natural Organic Matter, and Bacterial Cell Numbers on the Bioreduction of Lepidocrocite (γ -FeOOH) and the Formation of Secondary Mineralization Products", E. O'Loughlin, C. Gorski, M. Scherer, **M. Boyanov**, K. Kemner, *Environ. Sci. Technol.* 44, 4570–4576 (2010)

The microbial reduction of Fe(III) oxides results in the production of Fe(II) and may lead to the subsequent formation of Fe(II)-bearing secondary mineralization products (Fe(II)SMPs) including Fe(II) phases such as magnetite, siderite, vivianite, ferrous hydroxy carbonate (FHC) and green rust; however the factors controlling the formation of specific Fe(II)SMPs are often not well defined. This study examines the effects of a range of inorganic oxyanions (arsenate, borate, molybdate, phosphate, silicate, and tungstate), natural organic matter (citrate, oxalate, microbial extracellular polymeric substances (EPS), and humic substances), and the type and number of dissimilatory iron-reducing bacteria on the bioreduction of lepidocrocite and Fe(II)SMP formation. The bioreduction kinetics clustered into two distinct Fe(II) production profiles. "Fast" Fe(II) production kinetics (19 – 24 mM Fe(II) d⁻¹) was accompanied by the formation of magnetite and FHC in the unamended control and in systems amended with borate, oxalate, gellan EPS, or Pony Lake fulvic acid or with "low" cell numbers. Systems amended with arsenate, citrate, molybdate, phosphate, silicate, tungstate, EPS from *Shewanella putrefaciens* CN32, humic substances derived from terrestrial plant material or with "high" cell numbers exhibited comparatively slow Fe(II) production kinetics (1.8 – 4.0 mM Fe(II) d⁻¹) and the formation of green rust. The results are consistent with a conceptual model whereby competitive sorption of more strongly bound anions blocks access of bacterial cells and reduced electron shuttling compounds to surface sites on the iron oxide surface, thereby limiting the rate of bioreduction.

6. "Equations of state and adsorption isotherms of low molecular non-ionic surfactants", I.Ivanov,K.Danov,D.Dimitrova,**M.Boyanov**,K.Ananthapadmanabhan,A.Lips, *Colloids.Surf.A* 354, 118-133 (2010)

After a brief analysis of the three most widely used equations of state and adsorption isotherms, (those of van der Waals, Frumkin and Helfand–Frisch–Lebowitz with second virial coefficient) we analyze the definitions and the values of the main adsorption parameters adsorption constant K_s , minimum area per molecule λ and interaction constant ψ) and derive new expressions for some of them. Since it turned out that all three adsorption isotherms

perform rather poorly, when used to interpret adsorption data, we applied also three more general equations—one was derived for localized adsorption long ago, but we had to derive two new equations for non-localized adsorption. We subject all 6 equations—the simple ones and the three generalized, to rigorous numerical analysis and discussion of the results. Our overall conclusion is that in some cases all equations can describe qualitatively the observed phenomena, but only the new equation of state, proposed by us for non-localized adsorption on fluid interface (and the respective adsorption isotherm), lead to correct quantitative description of the adsorption and the related parameters. In [Appendix A](#) we analyze the shortcomings and the source of errors in the fitting procedures.

7. “High- and low-affinity binding sites for Cd on the bacterial cell walls of *Bacillus subtilis* and *Shewanella oneidensis*” B. Mishra, **M. Boyanov**, B. A. Bunker, S. D. Kelly, K. M. Kemner, J. B. Fein, *Geochimica et Cosmochimica Acta* 74 (2010) 4219–4233

Bulk Cd adsorption isotherm experiments, thermodynamic equilibrium modeling, and Cd K edge EXAFS were used to constrain the mechanisms of proton and Cd adsorption to bacterial cells of the commonly occurring Gram-positive and Gram-negative bacteria, *Bacillus subtilis* and *Shewanella oneidensis*, respectively. Potentiometric titrations were used to characterize the functional group reactivity of the *S. oneidensis* cells, and we model the titration data using the same type of nonelectrostatic surface complexation approach as was applied to titrations of *B. subtilis* suspensions by [Fein et al. \(2005\)](#). Similar to the results for *B. subtilis*, the *S. oneidensis* cells exhibit buffering behavior from approximately pH 3–9 that requires the presence of four distinct sites, with pKa values of 3.3 ± 0.2 , 4.8 ± 0.2 , 6.7 ± 0.4 , and 9.4 ± 0.5 , and site concentrations of $8.9(\pm 2.6) \times 10^{-5}$, $1.3(\pm 0.2) \times 10^{-4}$, $5.9(\pm 3.3) \times 10^{-5}$, and $1.1(\pm 0.6) \times 10^{-4}$ moles/g bacteria (wet mass), respectively. The bulk Cd isotherm adsorption data for both species, conducted at pH 5.9 as a function of Cd concentration at a fixed biomass concentration, were best modeled by reactions with a Cd:site stoichiometry of 1:1. EXAFS data were collected for both bacterial species as a function of Cd concentration at pH 5.9 and 10 g/L bacteria. The EXAFS results show that the same types of binding sites are responsible for Cd sorption to both bacterial species at all Cd loadings tested (1–200 ppm). Carboxyl sites are responsible for the binding at intermediate Cd loadings. Phosphoryl ligands are more important than carboxyl ligands for Cd binding at high Cd loadings. For the lowest Cd loadings studied here, a sulfhydryl site was found to dominate the bound Cd budgets for both species, in addition to the carboxyl and phosphoryl sites that dominate the higher loadings. The EXAFS results suggest that both Gram-positive and Gram-negative bacterial cell walls have a low concentration of very high-affinity sulfhydryl sites which become masked by the more abundant carboxyl and phosphoryl sites at higher metal:bacteria ratios. This study demonstrates that metal loading plays a vital role in determining the important metal-binding reactions that occur on bacterial cell walls, and that high affinity, low-density sites can be revealed by spectroscopy of biomass samples. Such sites may control the fate and transport of metals in realistic geologic settings, where metal concentrations are low.

8. "Iron phase transformations resulting from the respiration of *Shewanella putrefaciens* on a mixed mineral phase", **M. Boyanov**, E. O'Loughlin, K. Kemner, *Journal of Physics: Conference Series* 190 (2009) 012193-012196

The initial Fe(III) minerals and the secondary mineralization products of *Shewanella putrefaciens* CN32 grown in the presence of dissolved phosphate and a commercial Fe(III) oxide, nominally nanoparticulate lepidocrocite, were determined using XRD and XAFS. The starting material was transformed by the bacteria from a reddish brown, rust colour mineral to a dark green phase over 90 days. Acid extraction of the bio-reduced solids with 0.75 M HCl recovered 83% of the total iron as Fe(II), leaving a solid, acid-resistant phase. The latter was identified as nanoparticulate hematite by EXAFS. Subsequently, the starting Fe(III) phase was determined to be a mixture of 60% lepidocrocite, 26% ferrihydrite, and 14% hematite, using linear combination EXAFS analysis. For the acid-extractable phase, XANES and EXAFS indicated a predominantly Fe(II) valence state and a spectrum consistent with a mixture of brucite-type minerals (e.g., green rust or ferrous hydroxide) and siderite. The observed transformations suggest that in this mixed-mineral system, lepidocrocite and ferrihydrite are readily reducible to green rust and siderite, whereas hematite is less amenable to bacterial reduction. This study also demonstrates the utility of XAFS spectroscopy in the quantitative characterization of dissimilatory metal transformations, particularly in complex systems such as nanoparticulate minerals in hydrated mineral-bacteria assemblages.

9. "An X-ray Absorption Spectroscopy Study of Cd Adsorption Onto Bacterial Consortia", B. Mishra, **M. Boyanov**, B. Bunker, S. Kelly, K. Kemner, R. Norenberg, B. Read-Daily, J. Fein, *Geochim. et Cosmochim. Acta* 73, 4311-4325 (2009)

In this study, we use extended X-ray absorption fine structure (EXAFS) spectroscopy measurements to examine the atomic environment of Cd bound onto two experimental bacterial consortia: one grown from river water, and one grown from a manufacturing gas plant site. The experiments were conducted as a function of pH and demonstrate that the complex mixtures of bacteria, containing both Gram-positive and Gram-negative species, yield relatively simple EXAFS spectra, a result which indicates that only a limited number of functional group types contribute to Cd binding for each bacterial consortium. The EXAFS spectra indicate that the average Cd binding environment in the river water consortium varies significantly with pH, but the manufacturing gas plant consortium exhibits a Cd binding environment that remains relatively constant over the pH range examined. The EXAFS data for the river water consortium were modeled using carboxyl, phosphoryl and sulfhydryl sites. However, only carboxyl and phosphoryl sites were required to model the manufacturing gas plant consortium data under similar experimental conditions. This is the first EXAFS study to identify and quantify the relative importance of metal binding sites in bacterial consortia. Although our results indicate differences in the binding environments of the two consortia, the data suggest that there are broad similarities in the binding environments present on a wide range of bacterial cell walls.

10. "Adsorption of iron(II) and uranium(VI) to carboxyl-functionalized microspheres: the influence of speciation on uranyl reduction studied by titration and XAFS", **M. Boyanov**, E.J.O'Loughlin, E.Roden, J.Fein, K.Kemner, *Geochim.Cosmochim.Acta* 1898-1912 (2007)

The chemical reduction of U(VI) by Fe(II) is a potentially important pathway for immobilization of uranium in subsurface environments. Although the presence of surfaces has been shown to catalyze the reaction between Fe(II) and U(VI) aqueous species, the mechanism(s) responsible for the enhanced reactivity remain ambiguous. To gain further insight into the U–Fe redox process at a complexing, non-conducting surface that is relevant to common organic phases in the environment, we studied suspensions containing combinations of 0.1 mM U(VI), 1.0 mM Fe(II), and 4.2 g/L carboxyl-functionalized polystyrene microspheres. Acid-base titrations were used to monitor protolytic reactions, and Fe K-edge and U L-edge X-ray absorption fine structure spectroscopy was used to determine the valence and atomic environment of the adsorbed Fe and U species. In the Fe + surface carboxyl system, a transition from monomeric to oligomeric Fe(II) surface species was observed between pH 7.5 and pH 8.4. In the U + surface carboxyl system, the U(VI) cation was adsorbed as a mononuclear uranyl–carboxyl complex at both pH 7.5 and 8.4. In the ternary U + Fe + surface carboxyl system, U(VI) was not reduced by the solvated or adsorbed Fe(II) at pH 7.5 over a 4-month period, whereas complete and rapid reduction to U(IV) nanoparticles occurred at pH 8.4. The U(IV) product reoxidized rapidly upon exposure to air, but it was stable over a 4-month period under anoxic conditions. Fe atoms were found in the local environment of the reduced U(IV) atoms at a distance of 3.56 Å. The U(IV)–Fe coordination is consistent with an inner-sphere electron transfer mechanism between the redox centers and involvement of Fe(II) atoms in both steps of the reduction from U(VI) to U(IV). The inability of Fe(II) to reduce U(VI) in solution and at pH 7.5 in the U + Fe + carboxyl system is explained by the formation of a transient, "dead-end" U(V)–Fe(III) complex that blocks the U(V) disproportionation pathway after the first electron transfer. The increased reactivity at pH 8.4 relative to pH 7.5 is explained by the reaction of U(VI) with an Fe(II) oligomer, whereby the bonds between Fe atoms facilitate the transfer of a second electron to the hypothetical U(V)–Fe(III) intermediate. We discuss how this mechanism may explain the commonly observed higher efficiency of uranyl reduction by adsorbed or structural Fe(II) relative to aqueous Fe(II).

11. "A pH-Dependent X-Ray Absorption Spectroscopy Study of U Adsorption to Bacterial Cell Walls", B. Ravel, S. Kelly, D.Gorman-Lewis, **M. Boyanov**, J.Fein, K. Kemner, *American Institute of Physics CP 882*, 202-204 (2007)

Metal mobility in subsurface water systems involves the complex interaction of the metal, the fluid, and the mineral surfaces over which the fluid flows. This mobility is further influenced by metal adsorption onto bacteria and other biomass in the subsurface. To better understand the mechanism of this adsorption as well as its dependence on the chemical composition of the fluid, we have performed a series of metal adsorption experiments of aqueous uranyl UO₂²⁺ to the gram-positive bacterium *B. subtilis* in the presence and absence of carbonate along with X-ray Absorption Spectroscopy (XAS) to determine the binding structures at the cell surface. In this paper we demonstrate an approach to the XAS data analysis which allows us to measure

the partitioning of the adsorption of uranium to hydroxyl, carboxyl/carbonato, and phosphoryl active sites at the cell surface.

12. "XAFS and X-Ray and Electron Microscopy Investigations of Radionuclide Transformations at the Mineral-Microbe Interface", K.Kemner, E.O'Loughlin, S.Kelly, B.Ravel, **M.Boyanov**, D.Sholto-Douglas, B.Lai, R.Cook, E.Carpenter, V.Harris, K.Nealson, *American Institute of Physics CP 882*, 250-252 (2007)

The microenvironment at and adjacent to surfaces of actively metabolizing cells, whether in a planktonic state or adhered to mineral surfaces, can be significantly different from the bulk environment. Microbial polymers (polysaccharides, DNA, RNA, and proteins), whether attached to or released from the cell, can contribute to the development of steep chemical gradients over very short distances. It is currently difficult to predict the behavior of contaminant radionuclides and metals in such microenvironments, because the chemistry there has been difficult or impossible to define. The behavior of contaminants in such microenvironments can ultimately affect their macroscopic fates. We have successfully performed a series of U Lm edge x-ray absorption fine structure (XAFS) spectroscopy, hard x-ray fluorescence (XRF) microprobe (150 nm resolution), and electron microscopy (EM) measurements on lepidocrocite thin films (~1 micron thickness) deposited on kapton films that have been inoculated with the dissimilatory metal reducing bacterium *Shewanella oneidensis* MR-1 and exposed to 0.05 mM uranyl acetate under anoxic conditions. Similarly, we have performed a series of U Lm edge EXAFS measurements on lepidocrocite powders exposed to 0.05 mM uranyl acetate and exopolymeric components harvested from *S. oneidensis* MR-1 grown under aerobic conditions. These results demonstrate the utility of combining bulk XAFS with x-ray and electron microscopies.

13. "Comparison of Cd Binding Mechanisms by Gram-Positive, Gram-Negative and Consortia of Bacteria Using XAFS", B.Mishra, J.Fein, **M.Boyanov**, S.Kelly, K.Kemner, B.Bunker, *American Institute of Physics CP 882*, 343-345 (2007)

A quantitative comparison of the Cd binding mechanism to Gram-positive (*Bacillus subtilis*) and Gramnegative bacteria (*Shewanella oneidensis*) is presented. At pH 6.0, EXAFS data for the Gram-positive bacteria were modeled using carboxyl and phosphoryl sites only. However, additional sulfide sites were required to model the spectrum from the Gram-negative bacteria under similar experimental conditions. Cd binding to a bacterial consortium at the same pH value, sampled from natural river water, was modeled using the models developed for the individual Gram-positive and Gram-negative bacterial strains.

14. "Mixed valence cytoplasmic iron granules are linked to anaerobic respiration," S. Glasauer, S. Langley, **M. Boyanov**, B. Lai, K. M. Kemner, T. J. Beveridge, *Appl. Environ. Microb.* 73(3), 993-996 (2007)

Intracellular granules containing ferric and ferrous iron formed in *Shewanella putrefaciens* CN32 during dissimilatory reduction of solid-phase ferric iron. It is the first in situ detection at high

resolution (150 nm) of a mixed-valence metal particle residing within a prokaryotic cell. The relationship of the internal particles to Fe(III) reduction may indicate a respiratory role.

15. "c-Type Cytochrome-Dependent Formation of U(IV) Nanoparticles by *Shewanella oneidensis*", M. Marshall, A. Beliaev, A. Dohnalkova, D. Kennedy, L. Shi, Z. Wang, **M. Boyanov**, B. Lai, K. Kemner, J. McLean, S. Reed, D. Culley, V. Bailey, C. Simonson, D. Saffarini, M. Romine, J. Zachara, J. Fredrickson, PLoS Biology 4(8), 1324-1333 (2006)

Modern approaches for bioremediation of radionuclide contaminated environments are based on the ability of microorganisms to effectively catalyze changes in the oxidation states of metals that in turn influence their solubility. Although microbial metal reduction has been identified as an effective means for immobilizing highly-soluble uranium(VI) complexes in situ, the biomolecular mechanisms of U(VI) reduction are not well understood. Here, we show that c-type cytochromes of a dissimilatory metal-reducing bacterium, *Shewanella oneidensis* MR-1, are essential for the reduction of U(VI) and formation of extracellular UO₂ nanoparticles. In particular, the outer membrane (OM) decaheme cytochrome MtrC (metal reduction), previously implicated in Mn(IV) and Fe(III) reduction, directly transferred electrons to U(VI). Additionally, deletions of *mtrC* and/or *omcA* significantly affected the in vivo U(VI) reduction rate relative to wild-type MR-1. Similar to the wild-type, the mutants accumulated UO₂ nanoparticles extracellularly to high densities in association with an extracellular polymeric substance (EPS). In wild-type cells, this UO₂-EPS matrix exhibited glycocalyx-like properties and contained multiple elements of the OM, polysaccharide, and heme-containing proteins. Using a novel combination of methods including synchrotron-based X-ray fluorescence microscopy and high-resolution immune-electron microscopy, we demonstrate a close association of the extracellular UO₂ nanoparticles with MtrC and OmcA (outer membrane cytochrome). This is the first study to our knowledge to directly localize the OM-associated cytochromes with EPS, which contains biogenic UO₂ nanoparticles. In the environment, such association of UO₂ nanoparticles with biopolymers may exert a strong influence on subsequent behavior including susceptibility to oxidation by O₂ or transport in soils and sediments.

16. "Synchrotron X-ray Investigations of Mineral-Microbe-Metal Interactions", K. Kemner, E. O'Loughlin, S. Kelly, **M. Boyanov**, Elements 1(4), 217-221 (2005)

Interactions between microbes and minerals can play an important role in metal transformations (i.e. changes to an element's valence state, coordination chemistry, or both), which can ultimately affect that element's mobility. Mineralogy affects microbial metabolism and ecology in a system; microbes, in turn, can affect the system's mineralogy. Increasingly, synchrotron-based X-ray experiments are in routine use for determining an element's valence state and coordination chemistry, as well as for examining the role of microbes in metal transformations.

17. "Local structure around Cr³⁺ ions in dilute acetate and perchlorate aqueous solutions", **M.I.Boyanov**, K.M.Kemner, T. Shibata, B.A.Bunker, J. Phys. Chem. A 108, 5131-5138 (2004)

The hydration structure and aqueous acetate complexation of Cr³⁺ ions were studied by X-ray absorption fine structure (XAFS) spectroscopy as a function of pH, concentration, acetate:Cr ratio, and age of the solution. In the perchlorate solutions, we found an octahedral hydration shell around the Cr³⁺ ion at 1.96 Å, confirming previous results through an independent analysis. Distinct Cr-Cr correlation was observed in the Cr acetate solutions, indicating that acetate groups bridge between the metal ions in a polymer structure. Modeling of the data confirmed a cyclic trichromium complex in acetate solutions. Similar spectral features in the Fourier transform were observed at 3.0-3.5 Å for both hydrated and polynuclear Cr. Comparison of the spectral content of such features in the two different cases showed that the origin of the 3.0-3.5 Å structure is multiple scattering within the first O shell alone. Thus, no spectral contribution could be attributed to the outer hydration molecules in data for hydrated Cr³⁺. We also report on differences in first-shell O backscattering (or possible spectral contributions from H atoms) in the aqueous solutions relative to the crystal oxide, determined by systematic analysis of a Cr₂O₃ standard.

18. "Mechanism of aqueous Pb adsorption to fatty acid Langmuir monolayers studied by XAFS spectroscopy", **M.I.Boyanov**, J.Kmetko, T.Shibata, A.Datta, P.Dutta, B.A.Bunker. J. Phys. Chem. B 107, 9780-9788 (2003)

The local atomic environment of lead (Pb) adsorbed to a CH₃(CH₂)₁₉COOH Langmuir monolayer was investigated in situ using grazing-incidence X-ray absorption fine structure (GI-XAFS) spectroscopy at the Pb LIII edge. Measurements were performed at pH 6.5 of the 10⁻⁵ M PbCl₂ solution subphase, a condition under which grazing incidence diffraction (GID) revealed a large-area commensurate superstructure underneath the close-packed organic monolayer. The XAFS results indicate covalent binding of the Pb cations to the carboxyl headgroups, and the observed Pb-Pb coordination suggests that the metal is adsorbed as a hydrolysis polymer, rather than as individual Pb²⁺ ions. The data are consistent with a bidentate chelating mechanism and a one Pb atom to one carboxyl headgroup binding stoichiometry. We discuss how this adsorption model can explain the peculiarities observed with Pb in previous metal-Langmuir monolayer studies. A systematic study of lead perchlorate and lead acetate aqueous solutions is presented and used in the analysis. XAFS multiple scattering effects from alignment of the Pb-C-C atoms in the lead acetate solutions are reported.

19. "Adsorption of cadmium to *B.subtilis* bacterial cell walls — a pH-dependent XAFS spectroscopy study", **M.I.Boyanov**, S.D.Kelly, K.M.Kemner, B.A.Bunker, J.B.Fein, D.A.Fowle. Geochim. et Cosmochim. Acta 67(18), 3299-3311 (2003)

The local atomic environment of Cd bound to the cell wall of the gram-positive bacterium *Bacillus subtilis* was determined by X-ray absorption fine structure (XAFS) spectroscopy.

Samples were prepared at six pH values in the range 3.4 to 7.8, and the bacterial functional groups responsible for the adsorption were identified under each condition. Under the experimental Cd and bacterial concentrations, the spectroscopy results indicate that Cd binds predominantly to phosphoryl ligands below pH 4.4, whereas at higher pH, adsorption to carboxyl groups becomes increasingly important. At pH 7.8, we observe the activation of an additional binding site, which we tentatively ascribe to a phosphoryl site with smaller Cd-P distance than the one that is active at lower pH conditions. XAFS spectra of several cadmium acetate, phosphate, and perchlorate solutions were measured and used as standards for fingerprinting, as well as to assess the ability of FEFF8 and FEFFIT to model carboxyl, phosphoryl, and hydration environments, respectively. The results of this XAFS study in general corroborate existing surface complexation models; however, some binding mechanism details could only be detected with the XAFS technique.

20. "XAFS determination of the bacterial cell wall functional groups responsible for complexation of Cd and U as a function of pH", S.D.Kelly, **M.I.Boyanov**, B.A.Bunker, J.B.Fein, D.A.Fowle, N.Yee, and K.M.Kemner. *J. Synchrot. Radiat.* 8, 946-948 (2001)

Bacteria, which are ubiquitous in near-surface geologic systems, can affect the distribution and fate of metals in these systems through adsorption reactions between the metals and bacterial cell walls. Recently, Fein *et al.* (1997) developed a chemical equilibrium approach to quantify metal adsorption onto cell walls, treating the sorption as a surface complexation phenomenon. However, such models are based on circumstantial bulk adsorption evidence only, and the nature and mechanism of metal binding to cell walls for each metal system have not been determined spectroscopically. The results of XAFS measurements at the Cd K-edge and U L3-edge on *Bacillus subtilis* exposed to these elements show that, at low pH, U binds to phosphoryl groups while Cd binds to carboxyl functional groups.

21. "Non-metabolic reduction of Cr(VI) by bacterial surfaces under nutrient-absent conditions", J.Fein, K.Kemner, D.Fowle, J.Cahill, **M.Boyanov**, B.Bunker. *Geomicrobiology Journal* 19(3), 369-382 (2002)

We have measured the ability of nonmetabolizing cells of the bacterial species *Bacillus subtilis*; *Sporosarcina ureae*, and *Shewanella putrefaciens* to reduce aqueous Cr(VI) to Cr(III) in the absence of externally supplied electron donors. Each species can remove significant amounts of Cr(VI) from solution, and the Cr(VI) reduction rate is strongly dependent on solution pH. The fastest reduction rates occur under acidic conditions, with decreasing rates with increasing pH. XANES data demonstrate that Cr(VI) reduction to Cr(III) occurs within the experimental systems. Control experiments indicate that the Cr removal is not a purely adsorptive process. Reduction appears to occur at the cell wall, and is not coupled to the oxidation of bacterial organic exudates. Detailed kinetic data suggest that the reduction involves at least a two-stage process, involving an initial rapid removal mechanism followed by a slower process that follows first-order reaction kinetics. Due to the prevalence of nonmetabolizing cells and cell wall fragments in soils and deeper geologic environments, our results suggest that the observed nonmetabolic

reduction of Cr(VI) to Cr(III) may significantly affect the environmental distribution of Cr in bacteria-bearing systems.

22. "X-ray-absorption fine-structure determination of pH-dependent cell wall interactions", S.Kelly, K.Kemner, J.Fein, D.Fowle, **M.Boyanov**, B.Bunker, N.Yee. *Geochim. et Cosmochim. Acta*, 66(22), 3855-3871 (2002)

X-ray absorption fine structure (XAFS) measurements was used at the U L3-edge to directly determine the pH dependence of the cell wall functional groups responsible for the absorption of aqueous UO_2^{2+} to *Bacillus subtilis* from pH 1.67 to 4.80. Surface complexation modeling can be used to predict metal distributions in water-rock systems, and it has been used to quantify bacterial adsorption of metal cations. However, successful application of these models requires a detailed knowledge not only of the type of bacterial surface site involved in metal adsorption/desorption, but also of the binding geometry. Previous acid-base titrations of *B. subtilis* cells suggested that three surface functional group types are important on the cell wall; these groups have been postulated to correspond to carboxyl, phosphoryl, and hydroxyl sites. When the U(VI) adsorption to *B. subtilis* is measured, observed is a significant pH-independent absorption at low pH values (≤ 3.0), ascribed to an interaction between the uranyl cation and a neutrally charged phosphoryl group on the cell wall. The present study provides independent quantitative constraints on the types of sites involved in uranyl binding to *B. subtilis* from pH 1.67 to 4.80. The XAFS results indicate that at extremely low pH (pH 1.67) UO_2^{2+} binds exclusively to phosphoryl functional groups on the cell wall, with an average distance between the U atom and the P atom of 3.64 ± 0.01 Å. This U-P distance indicates an inner-sphere complex with an oxygen atom shared between the UO_2^{2+} and the phosphoryl ligand. The P signal at extremely low pH value is consistent with the UO_2^{2+} binding to a protonated phosphoryl group, as previously ascribed. With increasing pH (3.22 and 4.80), UO_2^{2+} binds increasingly to bacterial surface carboxyl functional groups, with an average distance between the U atom and the C atom of 2.89 ± 0.02 Å. This U-C distance indicates an inner-sphere complex with two oxygen atoms shared between the UO_2^{2+} and the carboxyl ligand. The results of this XAFS study confirm the uranyl-bacterial surface speciation model.

23. "XAFS studies of gold and silver-gold nanoparticles in aqueous solutions", T. Shibata, H.Tostmann, B.Bunker, A.Henglein, D.Meisel, S.Cheong, and **M.Boyanov**. *J. Synchrotr. Radiat.* 8, 545-547 (2001)

The x-ray absorption fine structure (XAFS) of colloidal Au and Au/Ag nanoparticles (3.5nm and 20nm mean diameter) in an aqueous solution has been investigated. Size dependent alloying was observed upon deposition of Ag on Au core. Ag forms distinct layers around the 20 nm Au nanoparticles. In contrast, random mixing is found for Ag deposited on 3.5nm Au particles.

24. "Analytical determination of the optical constants of a substrate in the presence of a covering layer by use of ellipsometric data", S.C.Russev, **M.I.Boyanov**, J.P.Drolet, R.M.Lebanc. J. Opt. Soc. Am. A-Opt. Image Sci. Vis. 16(6), 1496-1500 (1999)

An analytical solution for the determination of the substrate refractive index of a single-layered system from ellipsometric measurements is presented. It is shown that the above ellipsometric inverse problem is reduced to the finding of the roots of a third-degree polynomial. A unique approximate solution in the case of a thin covering layer is also presented.

25. "Polynomial Inversion of the Single Transparent Layer Problem in Ellipsometry", J.P.Drolet, S.C.Russev, **M.I.Boyanov**, R.M.Lebanc. J. Opt. Soc. Am. A-Opt. Image Sci. Vis. 1112, 3284-3291 (1994)

It is shown that for a uniform transparent layer over a substrate the layer dielectric constant satisfies a fifth-degree polynomial. The problem of extracting the layer index and thickness from the ellipsometric measurement is then reduced to finding the roots of this polynomial. The coefficients of this polynomial are determined by the angle of incidence, the real incident-medium index, the complex substrate index, and the measured complex ellipsometric ratio p . This approach to the problem gives directly all the possible physical solutions without the need for initial guesses or ranges. Special cases are examined. Numerical analysis and error analysis are provided for the case of a silicon oxide layer over silicon.



Contents lists available at ScienceDirect

Chemical Geology

journal homepage: www.elsevier.com/locate/chemgeo

Microbial reduction of chlorite and uranium followed by air oxidation

Gengxin Zhang^a, William D. Burgos^{b,*}, John M. Senko^c, Michael E. Bishop^d, Hailiang Dong^d, Maxim I. Boyanov^e, Kenneth M. Kemner^e

^a Institute of Tibetan Plateau Research, Chinese Academy of Sciences, Beijing, China

^b Department of Civil and Environmental Engineering, The Pennsylvania State University, University Park, PA, USA

^c Department of Geological and Environmental Sciences, University of Akron, Akron, OH, USA

^d Department of Geology, Miami University, Oxford, OH, USA

^e Biosciences Division, Argonne National Laboratory, Argonne, IL, USA

ARTICLE INFO

Article history:

Received 26 July 2010

Received in revised form 24 January 2011

Accepted 25 January 2011

Available online 3 February 2011

Editor: J. Fein

Keywords:

Smectites

Phyllosilicates

Uraninite

Iron reduction

ABSTRACT

To evaluate the stability of biogenic nanoparticulate U(IV) in the presence of an Fe(II)-rich iron-bearing phyllosilicate, we examined the reduction of structural Fe(III) in chlorite CCa-2 and uranium(VI) by *Shewanella oneidensis* MR-1, and the reoxidation of these minerals (after pasteurization) via the introduction of oxygen. Bioreduction experiments were conducted with combinations of chlorite, U(VI), and anthraquinone-2,6-disulfonate (AQDS). Abiotic experiments were conducted to quantify the reduction of U(VI) by chemically-reduced chlorite-associated Fe(II), the oxidation of nanoparticulate U(IV) by unaltered structural Fe(III) in chlorite, and the sorption of U(VI) to chlorite, to elucidate interactions between U(VI)/U(IV) and Fe(II)/Fe(III)-chlorite. Solids were characterized by X-ray diffraction, scanning electron microscopy, and X-ray absorption spectroscopy to confirm Fe and U reduction and reoxidation. U(VI) enhanced the reduction of structural Fe(III) in chlorite and nanoparticulate U(IV) was oxidized by structural Fe(III) in chlorite, demonstrating that U served as an effective electron shuttle from *S. oneidensis* MR-1 to chlorite-Fe(III). Abiotic reduction of U(VI) by chlorite-associated Fe(II) was very slow compared to biological U(VI) reduction. The rate of nanoparticulate U(IV) oxidation by dissolved oxygen increased in the presence of chlorite-associated Fe(II), but the extent of U(IV) oxidation decreased as compared to no-chlorite controls. In identical experiments conducted with bioreduced suspensions of nanoparticulate U(IV) and nontronite (another iron-bearing phyllosilicate), the rate of U(IV) oxidation by dissolved oxygen increased in the presence of nontronite-associated Fe(II). In summary, we found that structural Fe(III) in chlorite delayed the onset of U(VI) loss from solution, while chlorite-associated Fe(II) enhanced the oxidation rate of U(IV) by dissolved oxygen, indicating that chlorite-associated Fe(II) could not protect nanoparticulate U(IV) from oxygen intrusion but instead increased the oxidation rate of U(IV).

© 2011 Elsevier B.V. All rights reserved.

1. Introduction

Uranium contamination of sediment and groundwater is a problem at many U.S. Department of Energy (DOE) sites and uranium ore-processing sites where soluble U(VI) has migrated into groundwater. In aerobic groundwater, U(VI) carbonate complexes are often the predominant uranium species. These anionic or neutral U species tend to sorb weakly to solid phases and, therefore, can be relatively mobile in the environment (Akca, 1998; Arnold et al., 1998). Under anoxic conditions U(VI) can be reduced to sparingly soluble U(IV) minerals and precipitated from groundwater (Lovley and Phillips, 1992). Bacterially mediated reduction of U(VI) to uraninite may be

exploited for *in situ* remediation of uranium-contaminated sites (Lovley et al., 1991; Fredrickson et al., 2000; Brooks et al., 2003).

The stimulation of indigenous dissimilatory metal-reducing bacteria (DMRB) for uranium remediation is an area of active research at several DOE field sites. Assessment of the efficacy of any one strategy (e.g., ethanol addition) is typically based on changes in aqueous geochemistry measured in monitoring wells. Interpretation of these results is often challenging due to the complex suite of redox reactions potentially operative in these subsurface environments. For example, while the addition of an electron donor will promote reducing conditions, the availability of multiple electron acceptors (e.g., nitrate, Mn(III/IV) oxides, Fe(III) oxides, or sulfate) may enhance or impede U(VI) reduction. In a related manner, the concentration and flux of electron donor addition can also impact U(VI) reduction and U(IV) reoxidation (Tokunaga et al., 2008).

While considerable research has been conducted on uranium interactions with iron (oxyhydr)oxides (e.g., Jeon et al., 2005; Ginder-

* Corresponding author at: Dept. of Civil and Environmental Engineering, The Pennsylvania State University, 212 Sackett Building, University Park, PA 16802-1408, USA. Tel.: +1 814 863 0578; fax: +1 814 863 7304.

E-mail address: wdb3@psu.edu (W.D. Burgos).

Vogel et al., 2006), much less research has focused on uranium interactions with iron-bearing clay minerals (Stucki et al., 2007). Iron-bearing clay minerals are widely distributed in soils and sediments (Stucki et al., 2007) and often account for about half of the Fe mass in soils and sediments (Favre et al., 2006). Specifically, at the Old Rifle and Oak Ridge DOE field sites, the mass of iron associated with clay minerals is higher than the mass of iron associated with oxide minerals (Stucki et al., 2007; Komlos et al., 2008). In addition, chlorite is a common clay mineral at the DOE Hanford site (Schmeide et al., 2000; Baik et al., 2004; McKinley et al., 2007).

Compared to iron oxides which dissolve during reduction, the majority of reduced Fe(II) in iron-bearing clays is retained in the clay structure (Kostka et al., 1999; Dong et al., 2009). Fe(II) sorbed to mineral surfaces may be a more facile reductant compared to structural Fe(II) in clay minerals (Hofstetter et al., 2003, 2006), however, structural Fe(II) will not be flushed from a biostimulated reduction zone by advection. Thus, structural Fe(II) in clay minerals may be an important long-term reactant in maintaining anoxic conditions. The stability of U(IV) is, ultimately, the key criterion for determining success of any reductive immobilization strategy. The intrusion of oxidants such as oxygen or nitrate may be countered by a large reservoir of solid-phase reductants such as Fe(II)-bearing clay minerals.

In a recent, related study we measured the concomitant bioreduction of structural Fe(III) in the clay mineral nontronite and U(VI) by *Shewanella oneidensis* MR-1 (Zhang et al., 2009). From those experiments we found that uranium served as an effective electron shuttle to enhance the reduction of structural Fe(III) in nontronite but that delayed the onset of U(VI) loss from solution. In this current study, we not only report on the bioreduction of structural Fe(III) in the clay mineral chlorite CCa-2 and U(VI) but also measure the stability of bioreduced U(IV) in the presence of chlorite-associated Fe(II) and nontronite-associated Fe(II) upon oxygen intrusion. These two iron-bearing phyllosilicates were selected because they represent mineralogical end-members with respect to Fe(III) and Fe(II) content. Nontronite NAu-2 contains 4.2 mmol Fe/g with the majority of the structural iron as Fe(III) (Jaisi et al., 2007), while chlorite CCa-2 contains 3.4 mmol Fe/g with the majority of the structural iron as Fe(II). The objectives of this research were to study the interactions between U(VI) and the iron-rich ripidolite chlorite CCa-2 during their concomitant biological reduction, and then to further investigate the stability of bioreduced U(IV) and chlorite-associated Fe(II) in the presence of dissolved oxygen.

2. Experimental

2.1. Cell cultivation

S. oneidensis MR-1 was cultured in a chemically defined minimal medium as described previously (Burgos et al., 2008). Cells were harvested by centrifugation (15 min and 20 °C at 3,500 g), washed three times with anoxic 30 mM NaHCO₃ (pH 6.8, prepared under an 80:20% N₂:CO₂ atm) and resuspended in the same buffer.

2.2. Mineral preparation

CCa-2, an iron-bearing ripidolite chlorite from Flagstaff Hill (El Dorado County, CA, USA), was purchased in two separate batches from the Source Clays Repository (West Lafayette, IN). One batch was used for all the laboratory experiments and the second batch was used to produce a chlorite standard for Fe XANES. The chemical formula of this chlorite has been reported as (Mg_{5.5}Al_{2.48}Fe²⁺_{3.02}Fe³⁺_{0.94}Ti_{0.01}Mn_{0.01})(Si_{5.33}Al_{2.66}O₂₀)(OH)₁₆ as determined by electron microprobe analysis (Brandt et al., 2003). Clay fractions (0.5–2.0 μm) were suspended in 1 M NaCl for one week, separated in distilled water by centrifugation, washed repeatedly until no Cl⁻ was detected by

silver nitrate, and then air-dried. The clay fractions were determined by XRD and SEM to be pure chlorite without other iron minerals. The iron content of CCa-2 has been reported to range from 17.6% (Brandt et al., 2003) to 34.5% (Jaisi et al., 2007). As determined by complete dissolution in HF/H₂SO₄, we measured an iron content of 18.8% (3.35 mmol Fe g⁻¹) for the chlorite used in all the experiments, and an iron content of 30.4% (5.42 mmol Fe g⁻¹) for the chlorite used for the Fe XANES standard. The Fe(II) content of CCa-2 has been reported to range from 46% (Fe(II)/total Fe) (Jaisi et al., 2007; Singer et al., 2009a, 2009b) to 76% (Brandt et al., 2003) to 86% (Keeling et al., 2000). As determined by an HF/H₂SO₄-phenanthroline assay (described below), we measured an Fe(II) content of 78% for the unaltered chlorite used in all the experiments, and an Fe(II) content of 55% for the unaltered chlorite used for the Fe XANES standard. CCa-2 is composed of a tetrahedral–octahedral–tetrahedral (TOT) layer attached to a brucite-like sheet (Brandt et al., 2003; Zazzi et al., 2006). According to a proposed structural model for CCa-2 (Brandt et al., 2003), 66% of the total Fe is located in the TOT layer and 34% of the total Fe is located in the brucite sheet, and all of the Fe(III) is located in the TOT layer (specifically in the octahedral sheet). The BET surface area of the air-dried chlorite was determined to be 25.4 m²/g based on N₂ adsorption.

2.3. Bacterial reduction experiments

MR-1 bioreduction experiments were conducted in the presence or absence of U(VI), chlorite, or anthraquinone-2,6-disulfonate (AQDS) in 30 mM NaHCO₃ (pH 6.8) as described previously (Zhang et al., 2009). Chlorite CCa-2 was prepared in anoxic 30 mM NaHCO₃ buffer to produce a stock concentration of 100 g L⁻¹, and was sterilized by a 5-min exposure to microwave radiation (Keller et al., 1988). Chlorite and uranyl acetate were pre-equilibrated for two weeks before inoculation with MR-1. Experiments were conducted in 120 mL glass serum bottles where the chlorite concentration was 5.0 g L⁻¹ (16.8 mM Fe_T, 22% Fe(III)), uranyl acetate concentrations ranged from 0 to 1.5 mM, and AQDS concentrations were either 0 or 0.10 mM depending on the experiment. MR-1 was inoculated at 0.5*10⁸ cells mL⁻¹ (final concentration) with sodium lactate (5 mM) provided as the electron donor. After cells were added, reactors were periodically mixed and samples removed with sterile needle and syringe and HF/H₂SO₄-extractable Fe(II), ferrozine-extractable Fe(II), aqueous Fe(II), NaHCO₃-extractable U(VI), and aqueous U(VI) concentrations were measured as described below. All sample manipulations were performed inside an anoxic chamber (95:5% N₂:H₂ atm).

2.4. Experiments with U(VI) and chemically-reduced chlorite

Chlorite was reduced using the sodium citrate, bicarbonate, and dithionite (CBD) method as described by Stucki et al. (1984), and washed three times with anoxic distilled water (Hofstetter et al., 2003). CBD-reduced chlorite was dispensed into anoxic 30 mM NaHCO₃ buffer (pH 6.8) in 120 mL glass serum bottles (2.5 g L⁻¹ final concentration, 8.4 mM Fe_T, 98% Fe(II)), and equilibrated at least 3 d before uranium addition (0.20 mM). Reactors were periodically mixed and samples removed to measure ferrozine-extractable Fe(II), aqueous Fe(II), NaHCO₃-extractable U(VI), and aqueous U(VI) concentrations.

2.5. Experiments with biogenic nanoparticulate U(IV) and unaltered chlorite

Biogenic nanoparticulate U(IV) precipitates were produced separately by MR-1, pasteurized (70 °C for 30 min), concentrated by centrifugation, and resuspended in anoxic 30 mM NaHCO₃ buffer (pH 6.8). Unaltered chlorite was dispensed into anoxic 30 mM NaHCO₃ buffer in 20 mL glass serum bottles (5.0 g L⁻¹, 16.8 mM Fe_T, 22%

Fe(III)) followed by the addition of 0.11 mM nanoparticulate U(IV). Reactors were periodically mixed and samples removed to measure ferrozine-extractable Fe(II), aqueous Fe(II), NaHCO₃-extractable U(VI), and aqueous U(VI) concentrations.

2.6. Experiments with bioreduced minerals and dissolved oxygen

Bioreduced suspensions containing combinations of U, chlorite, and AQDS were collected after a 21 d incubation period, pasteurized, concentrated by centrifugation, and then resuspended in anoxic 30 mM NaHCO₃ buffer at pH 6.8 in 20 mL glass serum bottles with 0.75 g L⁻¹ bioreduced chlorite (2.5 mM Fe_T, 93% Fe(II)) and 0.15 mM U(IV). Oxygen was provided by flushing the headspace of anoxic NaHCO₃ buffer-containing serum bottles with filter-sterilized air as described previously (Burgos et al., 2008). Identical experiments were conducted with bioreduced suspensions of U, nontronite, and AQDS, except with 0.5 g L⁻¹ bioreduced nontronite (2.1 mM Fe_T, 34% Fe(II)) and 0.15 mM U(IV). Reactors were periodically mixed and samples removed to measure ferrozine-extractable Fe(II), 0.5 N HCl-extractable Fe(II), aqueous Fe(II), NaHCO₃-extractable U(VI), and aqueous U(VI) concentrations.

2.7. Analytical techniques

Aqueous Fe(II) was measured after centrifugation for 10 min at 14,100 g and 20 °C, and analyzed using the ferrozine assay (Stookey, 1970). Ferrozine-extractable Fe(II) was measured after 0.1 mL of well-mixed suspension was added to 0.9 mL of anoxic ferrozine solution for 2 h, centrifuged, and analyzed using the ferrozine assay. HF/H₂SO₄-extractable Fe(II) was measured after samples were completely dissolved with 4.8% HF/2.16 N H₂SO₄ in a boiling water bath for 30 min, centrifuged, and analyzed using the 1,10-phenanthroline assay (Komadel and Stucki, 1988; Amonette and Templeton, 1998).

Aqueous U(VI) was measured after centrifugation for 10 min at 14,100 g and 20 °C. NaHCO₃-extractable U(VI) was measured in samples of well-mixed suspensions that were placed in 1 M anoxic NaHCO₃ (pH 8.4) (all sample collection and manipulations performed in anoxic glovebox) (Elias et al., 2003). After extraction for 1 h, solids were removed by centrifugation and U(VI) was measured in the supernatant. Measurements were done under ambient atmospheric conditions, so they are presumed to represent total U in the supernatant. U(VI) was measured by kinetic phosphorescence analysis on a KPA-11 (ChemChek Instruments, Richland, WA) (Brina and Miller, 1992). Adsorbed U(VI) was operationally defined as the difference between NaHCO₃-extractable and the initial aqueous U(VI) concentrations, divided by the chlorite concentration.

2.8. Mineralogical characterizations

Samples were analyzed by X-ray diffraction (XRD) and scanning electron microscopy (SEM) using previously described procedures (Zhang et al., 2007). Samples were analyzed by X-ray absorption spectroscopy (XAS) as described previously (Boyanov et al., 2007; Kemner and Kelly, 2007; Senko et al., 2007; Zhang et al., 2009). U L_{III}-edge EXAFS, U L_{III}-edge XANES and Fe K-edge XANES measurements were made at the Materials Research Collaborative Access Team (MRCAT/EnviroCAT) sector 10-ID beam line of the Advanced Photon Source at Argonne National Laboratory (ANL) (Segre et al., 2000). The XAS spectra were collected in transmission and fluorescence mode using quick-scanning of the monochromator. Energy calibration was maintained at all times by simultaneous collection of data from hydrogen uranyl phosphate (U edge) or metallic iron foil (Fe edge) using X-rays transmitted through the sample. An aqueous U(VI)-triscarbonato complex and a nanoparticulate U^(IV)O₂ solid were used as U EXAFS standards. Linear combination (LC) analysis of the U XANES spectra was performed using the following end-members:

1) U(VI) in a high carbonate solution at pH 11, speciation ~100% UO₂(CO₃)₃, and 2) a nanoparticulate U^(IV)O₂ standard produced from U(VI) by reduction with green rust (O'Loughlin et al., 2003). Similarly, the Fe XANES spectra were modeled by LC analysis using the following operational end-members: 1) an unaltered chlorite CCa-2 standard (55% Fe(II)), and 2) a fully reduced chlorite CCa-2 (98% Fe(II)). The fully reduced Fe(II)-CCa-2 standard was produced by CBD reduction (Stucki et al., 1984), and the Fe(II) contents of the standards were measured by the HF/H₂SO₄-phenanthroline assay (Komadel and Stucki, 1988).

3. Results

The speciation of Fe in these experiments is difficult to assign because of the multiple possible forms of Fe(II) in chlorite. In its unaltered, initial form, all of the Fe(III) in chlorite is structural Fe(III) located in the octahedral sheet of the TOT layer (Brandt et al., 2003). In its unaltered, initial form, the Fe(II) in chlorite is distributed in both the tetrahedral and octahedral sheets of the TOT layer and in the brucite-like sheet attached to the TOT layer. After chemical or biological reduction, additional Fe(II) should accumulate and be retained in the octahedral sheet of the TOT layer (site of Fe(III) reduction). However, depending on the extent of reduction and possible dissolution, Fe(II) may also exist as surface-complexed Fe(II) or interlayer-exchanged Fe(II). Operational extractions for Fe(II) from reduced phyllosilicates cannot readily distinguish between all these possible forms of Fe(II). In this study we have used centrifugation to measure soluble Fe(II), a ferrozine extraction as an attempt to measure surface-complexed Fe(II) and/or interlayer-exchanged Fe(II), and a HF/H₂SO₄-phenanthroline assay to measure total Fe(II). The difference between HF/H₂SO₄-phenanthroline and ferrozine extractable concentrations could be used to operationally define structural Fe(II) but, as discussed below, this becomes problematic due to analytical precision and the specificity of these extractants. Therefore, we have chosen the terms “structural Fe(III) in chlorite” to define a single, solid Fe(III) species (all in the octahedral sheet of the TOT layer) originally present in the unaltered material, and “chlorite-associated Fe(II)” to include multiple, solid-associated Fe(II) species – structural Fe(II) originally present in the unaltered material, newly formed structural Fe(II) in the octahedral sheet, surface-complexed Fe(II), and interlayer-exchanged Fe(II).

The speciation of reduced U(IV) in these experiments is also challenging to definitively assign because U(IV) may exist as uraninite, amorphous nanoparticulate U(IV), mononuclear U(IV) or some mixture of these phases (Bernier-Latmani et al., 2010; Fletcher et al., 2010). Based on SEM-EDS and XRD (Supplemental Material) of bioreduced suspensions, we found that amorphous uranium-rich nanoparticles were produced and predominated in the presence or absence of chlorite, and consisted predominantly of nanoparticulate uraninite (Fig. 1). The EXAFS and Na HCO₃ extraction data on the bioreduced suspensions also suggested a lack of significant mononuclear U(IV) (discussed below). Therefore, we have chosen the terms “nanoparticulate U(IV)” or simply “U(IV)” to include all possible U(IV) species.

3.1. Bioreduction of U(VI) and structural Fe(III) in chlorite

S. oneidensis MR-1 was able to reduce both U(VI) and structural Fe(III) in chlorite when both of these terminal electron acceptors (TEAs) were present (Fig. 2). AQDS alone did not significantly enhance the reduction of structural Fe(III) in chlorite (Fig. 2a and c). We speculate that, because of the relatively high content of structural Fe(II) in chlorite, AH₂QDS cannot reduce structural Fe(III) in chlorite

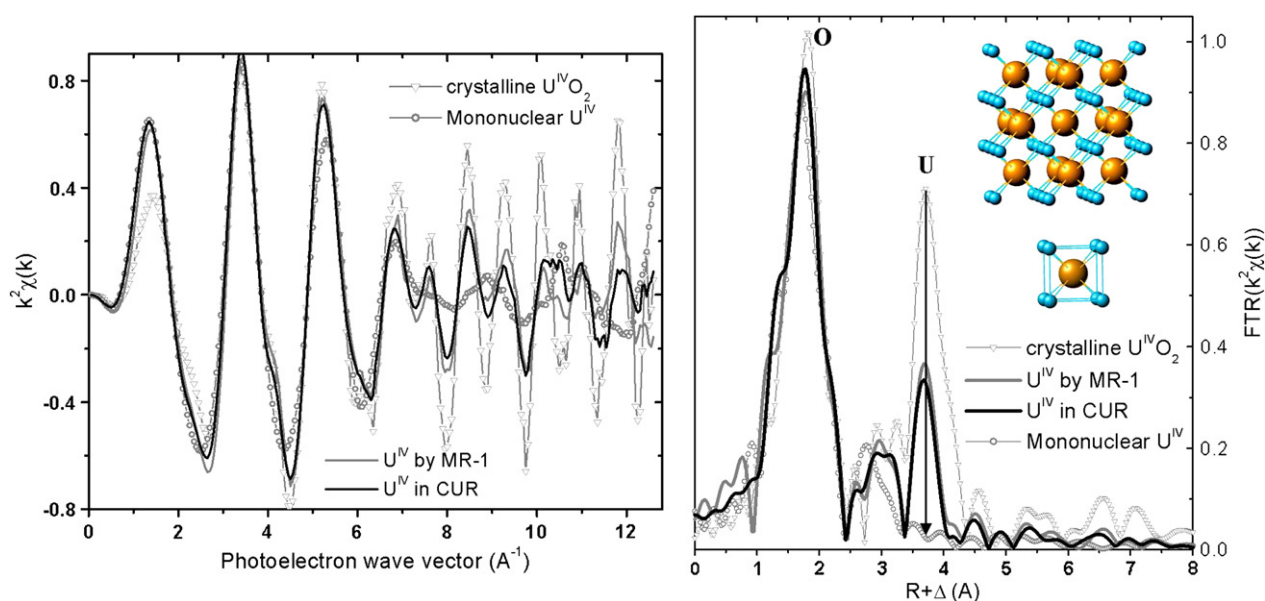


Fig. 1. U L_{III} -edge EXAFS data (left panel: $k^2\chi(k)$, right panel: Fourier transform) from biogenic U(IV) produced in the presence and absence of chlorite CCa-2 (data for the biogenic U(IV) in the absence of CCa-2 are from Burgos et al. (2008)). Data are compared to that from crystalline uraninite and biogenic mononuclear U(IV) (Fletcher et al. 2010). The inset in the right panel shows the molecular structure of a uraninite nanoparticle and the first coordination shell of U(IV). The contribution in the Fourier transformed spectra from the corresponding atoms are noted. The vertical arrow at ca. 3.5 \AA shows the decrease in the U peak amplitude in the different phases.

due to a thermodynamic limitation. We do not believe that AH₂QDS was physically hindered from contacting structural Fe(III) in chlorite because we have previously shown that AQDS can enhance the bioreduction of structural Fe(III) in nontronite (Zhang et al., 2009). Similarly, other studies have shown that AQDS can enhance the rate and extent of reduction of iron oxides (Fredrickson et al., 2000; Zachara et al., 2002), manganese oxides (Fredrickson et al., 2002), smectite (Dong et al., 2003a), and illite (Dong et al., 2003b).

U(VI) alone and the addition of U(VI) + AQDS both enhanced the reduction of structural Fe(III) in chlorite, as evidenced by increased concentrations of aqueous Fe(II), ferrozine-extractable Fe(II), and HF/H₂SO₄-extractable Fe(II) (after 21 d). Measurements of total biogenic Fe(II) production are challenging in this system because of the high concentration of structural Fe(II) in the unaltered chlorite, the sorption of dissolved Fe(II) back onto the chlorite surface, and the oftentimes non-specific nature of some of the operational extractions. For example, we found that 0.5 N HCl did not efficiently extract all chlorite-associated Fe(II) while the HF/H₂SO₄ extraction did completely dissolve chlorite. Stucki et al. (2007) also reported that 0.5 N HCl was not reliable for the quantitative determination of Fe oxidation states in silicate minerals. Because of the high structural Fe(II) content in the unaltered chlorite, only relatively small changes in the large concentrations of HF/H₂SO₄-extractable Fe(II) can be measured in these experiments (Fig. 2d). In no-cell controls, no or very low concentrations of aqueous and ferrozine-extractable Fe(II) were produced and concentrations of HF/H₂SO₄-extractable Fe(II) remained essentially constant.

With respect to U(VI) reduction kinetics, the addition of chlorite increased the lag time before U(VI) was removed from solution and decreased the extent of U(VI) reduction after a 21 d incubation (Fig. 2b). The reduction of structural Fe(III) in chlorite appeared to compete with U(VI) reduction, and this is consistent with several other studies on the bioreduction of U(VI) in the presence of ferrihydrite (Wielinga et al., 2000), manganese oxides (Fredrickson et al., 2002), and nontronite (Zhang et al., 2009). In our recent experiments with U(VI) and nontronite (Zhang et al., 2009), we found that U served as an effective electron shuttle from *S. oneidensis* MR-1 to structural Fe(III) in nontronite, and that the lag phase for the onset

of U(VI) loss from solution increased with increasing nontronite concentrations. The combined addition of chlorite + AQDS caused no lag in U(VI) reduction (compared to U(VI) alone), perhaps because of the stimulatory effect of AQDS on U(VI) reduction. U(VI) was not reduced in no-cell controls.

The sorption of U(VI) onto unaltered chlorite CCa-2 at pH 6.8 in anoxic 30 mM NaHCO₃ buffer was measured to quantify the distribution of U(VI) under the conditions used in the bioreduction experiments (Supplemental Material). With an initial U(VI) concentration of 0.10 to 1.5 mM, 17 to 4.0%, respectively, of the total U(VI) was sorbed onto unaltered chlorite (5.0 g L⁻¹) after 10 d (22 °C), with a maximum surface coverage of 0.54 $\mu\text{mol m}^{-2}$. These results are consistent with Singer et al. (2009a) who reported a U(VI) sorption extent to chlorite CCa-2 of 2.4 $\mu\text{mol m}^{-2}$ at pH 6.5 with 0.1 mM dissolved carbonate (7 d, 23 °C). The higher bicarbonate concentration used in the current study likely suppressed U(VI) sorption to account for the lower value we report. U(VI) was not substantially reduced (<3%) by structural Fe(II) in the unaltered chlorite during our sorption experiments based on NaHCO₃-extractable U(VI) concentrations. This result is also consistent with Singer et al. (2009a) who reported that >95% of the U remained as U(VI) after sorption to chlorite. In U(VI) + chlorite no-cell controls prepared for our bioreduction experiments and analyzed after a 21 d incubation period, U(IV) contents of 3.0 ± 1.1% and 11 ± 10% were detected based on NaHCO₃ extraction and U XANES, respectively (Table 1, sample CUC).

The U L_{III} -edge EXAFS spectrum of the U(VI) + chlorite no-cell control (sample CUC) was similar to an aqueous U(VI)-triscarbonato complex, suggesting outer-sphere complexation of a U(VI)-carbonate anion to the chlorite surface (Supplemental Material). Based on this sorption mechanism, the aqueous tris-carbonato U(VI) complex was chosen as the U(VI) end-member for our XANES analysis. However, U(VI) sorption may cause an edge shift to lower energies, resulting in a XANES determination of 0% U(IV) (±10%) (Supplemental Material). Further evidence for the lack of U(VI) reduction in sample CUC is presented by the amplitude of the axial oxygen peak in the Fourier transformed EXAFS data, which was identical to that of the fully oxidized U(VI) standard (Supplemental Material). We conclude,

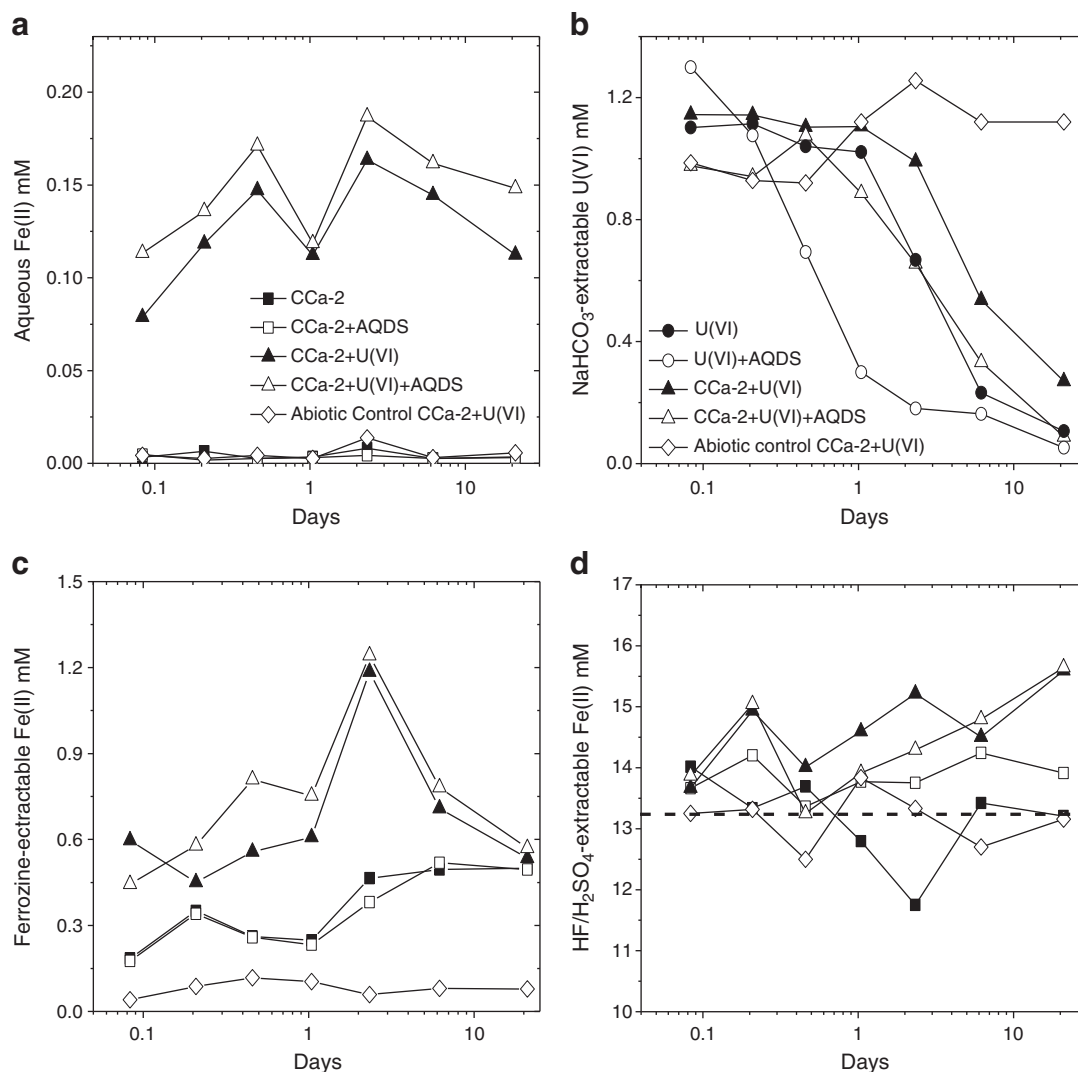


Fig. 2. Biological reduction of U(VI) and structural Fe(III) in chlorite CCa-2 by *S. oneidensis* MR-1 (0.5×10^8 cells mL^{-1}) in the presence or absence of AQDS (0.1 mM). Experiments were conducted with 1.0 mM U(VI), 5.0 g L^{-1} chlorite CCa-2 (16.8 mM Fe_T , 22% Fe(III)), and 5.0 mM lactate in 30 mM NaHCO_3 buffer, pH 6.8. (a) Aqueous Fe(II), (b) NaHCO_3 -extractable U(VI), (c) ferrozine-extractable Fe(II), and (d) $\text{HF}/\text{H}_2\text{SO}_4$ -extractable Fe(II). Dashed line in (d) represents starting concentration of structural Fe(II) in unaltered chlorite CCa-2. Symbols represent means of duplicate measurements.

Table 1

Average valence states of Fe and U within uranium–chlorite samples as determined by wet chemical methods and linear combination analysis of the XANES spectra. Sample names correspond to XANES spectra presented in Fig. 5.

Sample name/description	% Fe(II) in Chlorite		% U(IV) in precipitates	
	HF/H ₂ SO ₄ dissolution	Fe K-edge XANES	NaHCO ₃ extraction	U L _{III} -edge XANES
CUC 5 g L ⁻¹ Chlorite CCa-2 + 1 mM Uranyl(VI) acetate + 0 MR-1 (no-cell control) incubated for 21 d	78.3 ± 5.9	77 ± 10	3.0 ± 1.1	11 ± 10
CUR 5 g L ⁻¹ chlorite CCa-2 + 1 mM Uranyl(VI) acetate + 0.5 × 10 ⁸ cell mL ⁻¹ MR-1 incubated for 21 d	93.1 ± 1.3	99 ± 10	82.4 ± 9.0	99 ± 10
CUO CUR sample reacted with dissolved oxygen for 16 h	79.2 ± 1.0	82 ± 10	20.6 ± 9.6	56 ± 10

therefore, that with the materials and conditions used in these experiments, a very limited amount of U(VI) may be reduced by structural Fe(II) in unaltered chlorite but that this will not likely be an important process.

3.2. Abiotic reactions between U and chlorite

In addition to the biological reduction of U(VI) and structural Fe(III) in chlorite, abiotic reactions between U(VI) and structural Fe(II) in chlorite, between U(VI) and chlorite-associated Fe(II), and between U(IV) and structural Fe(III) in chlorite are all potentially operative. Based on sorption results and no-cell controls discussed above, the reduction of U(VI) by structural Fe(II) in the unaltered chlorite was very limited. Furthermore, in abiotic experiments conducted with chemically reduced chlorite, chlorite-associated Fe(II) displayed a limited ability to reduce U(VI) (Fig. 3a). For example, a significant loss of NaHCO_3 -extractable U(VI) did not occur until after 30 h and decreased from 0.20 mM to 0.16 mM after 88 h of reaction with 2.5 g L^{-1} CBD-reduced chlorite (8.4 mM Fe_T , 98% Fe(II)). Because the aqueous U(VI) concentration remained essentially constant while the NaHCO_3 -extractable U(VI) concentration decreased, we believe U(VI)

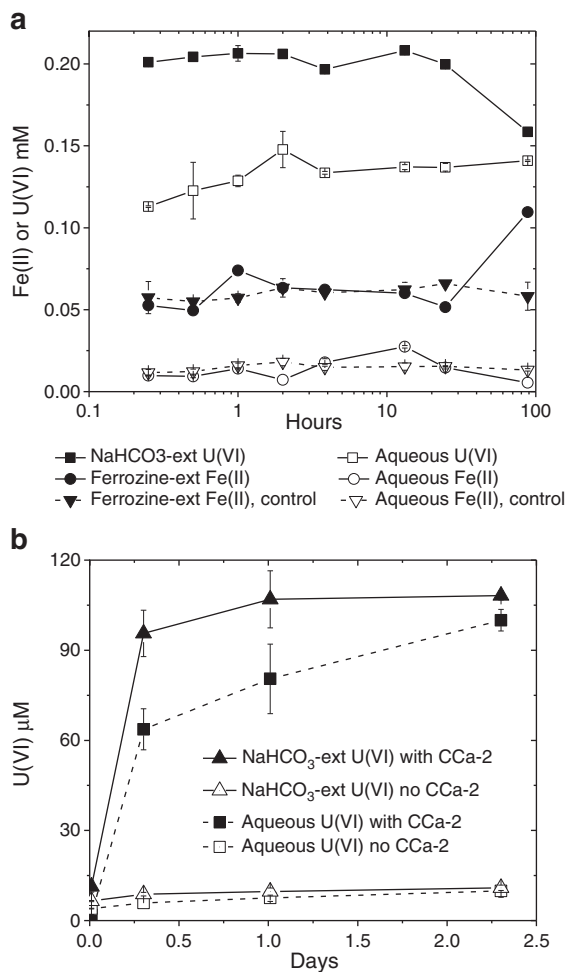


Fig. 3. Abiotic reactions between uranium and chlorite CCa-2. (a) Abiotic reduction of 0.20 mM U(VI) by chemically reduced chlorite CCa-2 (2.5 g L^{-1} , 8.4 mM Fe_T , 98% Fe(II)) in 30 mM NaHCO₃ buffer, pH 6.8. U(VI) was not added to the control. (b) Abiotic oxidation of biogenic nanoparticulate U(IV) (0.11 mM) by structural Fe(III) in unaltered chlorite CCa-2 (5.0 g L^{-1} , 16.8 mM Fe_T , 22% Fe(III)) in 30 mmol/L NaHCO₃, pH 6.8. Symbols and error bars represent means and standard deviations of duplicate measurements.

was first rapidly sorbed and then slowly reduced on the chlorite surface by chlorite-associated Fe(II). Aqueous Fe(II) remained constant in these experiments (Fig. 3a). In previous experiments conducted with 0.25 mM U(VI) and 2.5 g L^{-1} CBD-reduced nontronite (10.5 mM Fe_T , 27% Fe(II)) only a small fraction of U(VI) was reduced over an 83 d period (Zhang et al., 2009). The greater reduction extent of U(VI) by CBD-reduced chlorite as compared to CBD-reduced nontronite was likely due to the lower reduction potential of the fully reduced chlorite (i.e., higher Fe(II) content).

Abiotic experiments were also conducted to measure reaction kinetics between bio-reduced (and pasteurized) nanoparticulate U(IV) and structural Fe(III) in unaltered chlorite. The U L_{III}-edge EXAFS data indicate that the bio-reduced U(IV) phase consisted predominantly of nanoparticulate uraninite prior to pasteurization (Fig. 1). The amplitude of the U–U peak in data from U(VI) reduced by *Shewanella* MR-1 in the presence and absence of chlorite indicated a predominance of nanoparticulate uraninite in these systems. A linear combination fit with data from crystalline uraninite and mononuclear U(IV) did not reproduce our data well. The formation of non-uraninite U(IV) in our systems was unlikely because NaHCO₃ extraction of the bio-reduced solids did not result in additional release of labile U(IV) phases (controls in Fig. 3b). Recent work has shown that biogenic non-uraninite U(IV) is more easily extractable than biogenic nano-

particulate uraninite (Alessi et al., 2010). Extracted U(IV) could then be oxidized to U(VI) prior to or during measurement by KPA. Previous studies found little to no Ostwald ripening of biogenic uraninite when incubated at 90 °C for 2 weeks (Singer et al., 2009b), suggesting that the 30 min pasteurization step did not alter the nanoparticulate U(IV) used in our reoxidation experiments.

Nanoparticulate U(IV) was effectively oxidized by structural Fe(III) in chlorite when reacted in anoxic 30 mM NaHCO₃ buffer (Fig. 2b). The production of U(VI) appeared to be pseudo-first order with respect to the remaining U(IV) concentration and all of the nanoparticulate U(IV) was reoxidized after ca. 2 d. Structural Fe(III) in chlorite oxidized nanoparticulate U(IV) at rates comparable to uraninite oxidation by poorly crystalline Fe(III) oxides (Senko et al., 2005; Ginder-Vogel et al., 2006) and by structural Fe(III) in unaltered nontronite (Zhang et al., 2009). U(IV) reoxidation kinetics were very rapid compared to U(VI) reduction by chlorite-associated Fe(II), demonstrating that the regeneration of U(VI) should enhance chlorite reduction through U valence cycling.

3.3. Reoxidation of nanoparticulate U(IV) and phyllosilicate-Fe(II) by dissolved oxygen

Experiments were conducted in which air was introduced into the headspace of bio-reduced (and pasteurized) suspensions to initiate the reoxidation of U(IV) and chlorite-associated Fe(II). NaHCO₃-extractable U(VI) concentrations in the air-free controls (prepared with and without chlorite) were less than 7% of total U and never increased over the 16 h incubation (Fig. 4). The rate of nanoparticulate U(IV) oxidation (i.e., U(VI) production calculated over first 1–6 h) appeared to be pseudo-first order with respect to the remaining U(IV) concentration. Nanoparticulate U(IV) that was first produced in the presence of chlorite was subsequently oxidized more rapidly (based on first order rate constants) than nanoparticulate U(IV) first produced with U(VI) alone (Fig. 4a, Table 2). Nanoparticulate U(IV) that was first produced in the presence of chlorite was not subsequently completely oxidized, while nanoparticulate U(IV) first produced in the absence of chlorite was subsequently completely oxidized after 16 h (difference between series with square and triangle symbols in Fig. 4a). Only aqueous and ferrozine-extractable Fe(II) concentrations were measured for chlorite-containing suspensions in these experiments and revealed that chlorite-associated Fe(II) was subsequently oxidized simultaneously with U(IV) (data not shown).

When dissolved oxygen was introduced into this system, it could be consumed via the oxidation of nanoparticulate U(IV) or the oxidation of chlorite-associated Fe(II). If these processes were competitive, the rate of U(IV) oxidation would be expected to decrease in the presence of chlorite-associated Fe(II). If these processes were non-competitive, e.g., because of an excess of oxygen, then the rate of U(IV) oxidation would be expected to be unchanged by the presence of chlorite-associated Fe(II). Instead we found that the rate of U(IV) oxidation increased in the presence of chlorite-associated Fe(II) especially within the first hour of the experiment. Since structural Fe(III) in chlorite can rapidly oxidize nanoparticulate U(IV) (Fig. 3b), the “indirect” oxidation of U(IV) via chlorite-Fe(II/III) valence cycling could explain the observed increase in the rate of U(IV) oxidation in the presence of chlorite (Fig. 4a). Alternatively, prolonged solid–solid contact between chlorite and nanoparticulate U(IV) could facilitate solid-state galvanic coupling (Holmes and Crundwell, 1995; Klauber, 2008) which could also have the net effect of increasing the rate of U(IV) oxidation. While the first order rate constants for U(IV) oxidation increased in the presence of chlorite, the 16 h final extent of U(IV) oxidation decreased in the presence of chlorite. For example, 90–101% of the U(IV) produced in the absence of chlorite was reoxidized compared to 76–79% of the U(IV) produced in the presence of chlorite. The presence of chlorite-

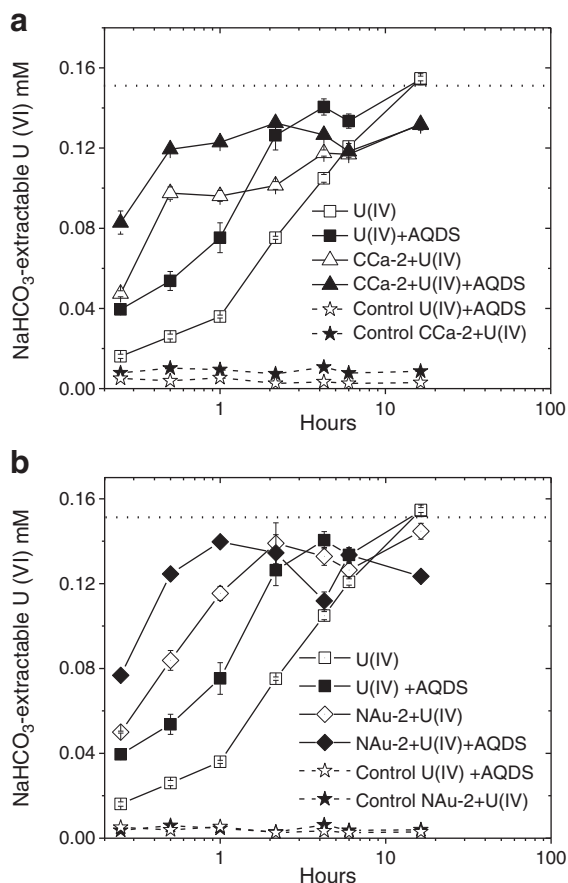


Fig. 4. Abiotic oxidation of biogenic nanoparticulate U(IV) and phyllosilicate-Fe(II) by dissolved oxygen in 30 mmol/L, NaHCO₃, pH 6.8. (a) Experiments initiated with 0.75 g L⁻¹ bioreduced chlorite (2.5 mM Fe_T, 93% Fe(II)) and 0.15 mM U(IV). (b) Experiments initiated with 0.5 g L⁻¹ bioreduced nontronite NAu-2 (2.1 mM Fe_T, 34% Fe(II)) and 0.15 mM U(IV). Air was not added to the controls. Symbols represent means of duplicate measurements. Dashed lines represent total U in suspensions.

associated Fe(II) may have protected U(IV) from complete oxidation.

To further examine the interactions between Fe(II)-bearing phyllosilicates, uraninite, and dissolved oxygen, we repeated these experiments with bioreduced (and pasteurized) suspensions of nontronite NAu-2 and U (Fig. 4b). With nontronite we were also

Table 2

Rates of reoxidation of nanoparticulate U(IV) and chlorite, and reoxidation of nanoparticulate U(IV) and nontronite-associated Fe(II) by the introduction of dissolved oxygen. Rates were modeled as pseudo-first-order with respect to the remaining concentration of the reduced species (i.e., [U(IV)] or [nontronite-Fe(II)]), and are reported as pseudo-first order rate constants. The 16 h extent of oxidation is reported as [reduced species]/[total element]*100%. Chlorite CCa-2 and nontronite NAu-2 were used.

Sample name/ description as shown in Fig. 3	U(IV)		Fe(II)	
	k _U (h ⁻¹)	Reoxidation extent (%)	k _{Fe} (h ⁻¹)	Reoxidation extent (%)
U(VI)	0.26	101 ± 5.0	n.a.	n.a.
U(VI) + AQDS	0.80	90.1 ± 5.1	n.a.	n.a.
CCa-2 + U(VI)	2.5	79.4 ± 9.6	n.d.	n.d.
CCa-2 + U(VI) + AQDS	4.4	75.6 ± 1.6	n.d.	n.d.
NAu-2	n.a.	n.a.	2.5	87.0 ± 0.4
NAu-2 + U(VI)	1.8	84.2 ± 3.6	2.0	86.7 ± 0.2
NAu-2 + U(VI) + AQDS	4.0	75.7 ± 3.1	3.1	88.6 ± 0.2

n.a. – not applicable.

n.d. – not determined due to precision issues with HF/H₂SO₄-phenanthroline assay with chlorite CCa-2.

able to accurately measure the oxidation kinetics of nontronite-associated Fe(II). Because of analytical precision issues associated with the HF/H₂SO₄-phenanthroline assay, this was not feasible with chlorite CCa-2 (e.g., Fig. 2d). As with chlorite, we found that the presence of nontronite increased the first order rate constants for U(IV) oxidation (differences between series with square and triangle symbols in Fig. 4b). The rates of nontronite-associated Fe(II) oxidation were comparable to the rates of U(IV) oxidation and were not strongly influenced by the presence of U (Table 2). As with chlorite, the extent of U(IV) oxidation decreased in the presence of nontronite where 76–84% of the U(IV) was reoxidized.

3.4. Mineralogical characterizations

XRD patterns from chlorite samples showed changes in the relative intensity of peaks (001, 002, 003 and 004) between unaltered and bioreduced chlorite (Supplemental Material), suggesting that bioreduction caused a slight change in the stacking structure (Kameda et al., 2007). SEM images also showed physical alterations and dissolution features in the bioreduced chlorites as compared to abiotic controls (Supplemental Material). Based on XRD patterns and SEM images, biogenic U(IV) was relatively amorphous and nanoparticulate and accumulated extracellularly from MR-1. The U L_{III}-edge EXAFS data from the bioreduced sample indicated that the U(IV) phase consists predominantly of nanoparticulate uraninite (Fig. 1), nearly identical to U(IV) solids produced by *Shewanella* MR-1 in the absence of chlorite (Burgos et al., 2008). SEM-EDS analyses revealed increased uranium content with bioreduced chlorite particles that was not observed after the same samples had been reacted with dissolved oxygen.

The average oxidation state of both U and Fe were determined by XANES for select samples collected during these experiments. XANES spectra were collected from no-cell controls (1.0 mM U(VI), 5.0 g L⁻¹ unaltered chlorite, 78% Fe(II)) that had been incubated for 21 d (referred to as CUC), from a bioreduced suspension containing 0.5*10⁸ cell mL⁻¹ MR-1 that had been incubated for 21 d (referred to as CUR), and from the bioreduced suspension after exposure to dissolved oxygen for 16 h (referred to as CUO). The U L_{III}-edge XANES spectrum for the bioreduced sample closely matched that of a U(IV) standard of nanoparticulate UO₂ (Fig. 5a and b). The U(IV)/U(VI) ratio was determined by LC analysis of the XANES spectra. For the CUR sample, the U reduction extent calculated as ([U(IV)]/[U(IV)] + [U(VI)]) was 99 ± 10%, and in agreement with our estimate of 82 ± 9% based on total U(VI) measured after 1 M NaHCO₃ extraction (Table 1). For the CUO sample, the U reduction extent was 56 ± 10% based on U XANES and 21 ± 10% based on NaHCO₃ extraction. We are uncertain about what caused the discrepancy between these two estimates but note that U reduction extents were consistently higher for U XANES as compared to NaHCO₃ extraction.

The Fe K-edge XANES spectrum for the bioreduced sample (CUR) was similar to the CBD-reduced chlorite standard (Fig. 5c and d). The no-cell control (CUC) and the bioreduced-then-reoxidized sample (CUO) were intermediate between the unaltered chlorite standard (55% Fe(II)) and the CBD-reduced chlorite standard (98% Fe(II)). For the CUR sample, the Fe reduction extent calculated as ([Fe(II)]/[Fe(II)] + [Fe(III)]) was 99 ± 10%, and in agreement with our estimate of 93 ± 1.3% based on total Fe(II) measured after HF/H₂SO₄ extraction. For the CUO sample, the Fe reduction extent was 82 ± 10% based on Fe XANES and 79.2 ± 1.0% based on HF/H₂SO₄ extraction.

4. Discussion

In these experiments with multiple TEAs, i.e., structural Fe(III) in chlorite, U(VI), and AQDS, the apparent utilization of TEAs is complicated by valence cycling of the TEAs themselves. For example, we have recently shown that U valence cycling increased the rate and

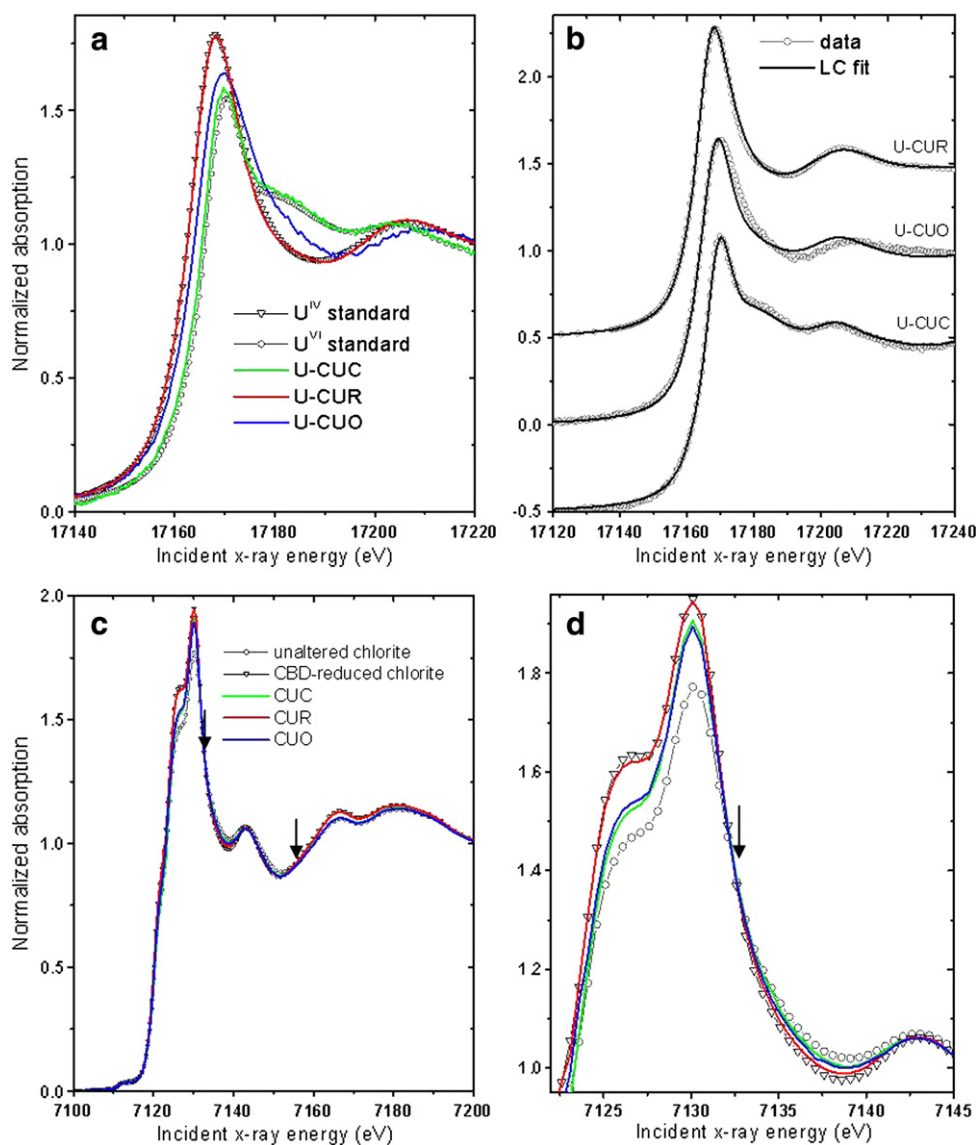


Fig. 5. (a) U L_{III} -edge normalized XANES spectra compared to U standards. U(VI) standard is $UO_2(CO_3)_3(aq)$ and U(IV) standard is nanoparticulate uraninite. (b) Linear combination fit (line) of each U L_{III} -edge spectrum (symbols) where spectra are offset vertically for clarity. Numerical results are presented in Table 1. (c) Normalized Fe K-edge XANES spectra compared to Fe standards. The unaltered chlorite-Fe(II/III) standard is shown with circular symbols, and the CBD-reduced chlorite-Fe(II) standard is shown with triangular symbols. The samples shown are: CUC – 5 g L^{-1} chlorite CCa-2, 1 mM uranyl(VI) acetate, no cells and incubated for 21 days; CUR – 5 g L^{-1} chlorite CCa-2, 1 mM uranyl(VI) acetate, 0.5×10^8 cell mL^{-1} MR-1 and incubated for 21 days; CUO – the CUR sample reacted with dissolved oxygen for 16 h. Isosbestic points are indicated by arrows. (d) Finer detail of the Fe XANES region.

extent of bioreduction of structural Fe(III) in nontronite (Zhang et al., 2009). In those experiments, substantial concentrations of biogenic Fe(II) evolved before any U(VI) was removed from solution even though U(VI) reduction (coupled to $U^{(IV)}O_{2(s)}$ oxidation) was essentially driving the reduction of structural Fe(III) in nontronite. Based on thermodynamic calculations using a reported standard-state reduction potential (E^0) value for nontronite (Jaisi et al., 2007), we showed that the apparent loss of U(VI) from solution would begin when sufficient Fe(II) had accumulated in the system (Zhang et al., 2009). Increasing Fe(II) concentrations decreased the redox potential of the structural Fe(III) in nontronite such that $U^{(IV)}O_{2(s)}$ could not be reoxidized, at which point U valence cycling ceased. Because there are no reported E^0 values for chlorite, analogous thermodynamic calculations cannot yet be performed with the chlorite–uranium system.

The long-term success of *in situ* reductive immobilization of uranium hinges on the stability of U(IV) precipitates when eventually exposed to oxic groundwater. The stability of U(IV) species could be increased in highly reduced sediments if dissolved oxygen preferen-

tially reacted with other reduced species (e.g., Fe(II) and S(-II)) before reacting with U(IV). At several uranium-contaminated DOE sites, iron-bearing phyllosilicates are more abundant than iron oxides and, in their Fe(II) state, could provide a substantial redox buffer to incoming oxidants. However, from these current experiments we have found that structural Fe(III) in chlorite delays the onset of U(VI) loss from solution, and chlorite-associated Fe(II) enhances the oxidation of U(IV) by dissolved oxygen. Although these findings may be a cause for concern, the inhibition of complete U(IV) reoxidation in the presence of chlorite (Fig. 5a) may enhance remediation efforts. Further studies are required to elucidate these processes.

Acknowledgements

This research was supported by the Subsurface Biogeochemical Research (SBR) Program, Office of Science (BER), U.S. Department of Energy (DOE) grant no. DE-SC0005333 to The Pennsylvania State

University, and by the National Science Foundation under grant no. CHE-0431328. ANL contributions were supported, in part, by the ANL Subsurface Science Scientific Focus Area project, which is part of the SBR Program of BER, U.S. DOE under contract DE-AC02-06CH11357. Use of the MRCAT/EnviroCAT sector at the Advanced Photon Source (APS) was supported by the U.S. DOE, Office of Science and the MRCAT/EnviroCAT member institutions. We thank S. D. Kelly, B. Ravel, and the MRCAT/EnviroCAT staff for assistance with XAS data collection at the MRCAT/EnviroCAT. Use of the APS was supported by the U.S. Department of Energy, Office of Science, Office of Basic Energy Sciences, under contract DE-AC02-06CH11357.

Appendix A. Supplementary data

Supplementary data to this article can be found online at doi:10.1016/j.chemgeo.2011.01.021.

References

- Akcaý, H., 1998. Aqueous speciation and pH effect on the sorption behavior of uranium by montmorillonite. *J. Radioanal. Nucl. Chem.* 237 (1–2), 133–137.
- Alessi, D., Uster, B., Veeramani, H., Stubbs, J., Lezama-Pacheco, J., Bargar, J.R., Bernier-Latmani, R., 2010. Method to estimate the contribution of molecular U(IV) to the product of U(VI) reduction. *Geochim. Cosmochim. Acta* 74 (12), A11.
- Amonette, J.E., Templeton, J.C., 1998. Improvements to the quantitative assay of nonrefractory minerals for Fe(II) and total Fe using 1, 10-phenanthroline. *Clays Clay Miner.* 46 (1), 51–62.
- Arnold, T., Zorn, T., Bernhard, G., Nitsche, H., 1998. Sorption of uranium(VI) onto phyllite. *Chem. Geol.* 151 (1–4), 129–141.
- Baik, M.H., Hyun, S.P., Cho, W.J., Hahn, P.S., 2004. Contribution of minerals to the sorption of U(VI) on granite. *Radiochim. Acta* 92 (9–11), 663–669.
- Bernier-Latmani, R., Veeramani, H., Vecchia, E.D., Junier, P., Lezama-Pacheco, J.S., Suvorova, E.I., Sharp, J.O., Wigginton, N.S., Bargar, J.R., 2010. Non-uraninite products of microbial U(VI) reduction. *Environ. Sci. Technol.* 44 (24), 9456–9462.
- Boyanov, M.I., O'Loughlin, E.J., Roden, E.E., Fein, J.B., Kemner, K.M., 2007. Adsorption of Fe(II) and U(VI) to carboxyl-functionalized microspheres: The influence of speciation on uranyl reduction studied by titration and XAFS. *Geochim. Cosmochim. Acta* 71 (8), 1898–1912.
- Brandt, F., Bosbach, D., Krawczyk-Barsch, E., Arnold, T., Bernhard, G., 2003. Chlorite dissolution in the acid pH-range: a combined microscopic and macroscopic approach. *Geochim. Cosmochim. Acta* 67 (8), 1451–1461.
- Brina, R., Miller, A.G., 1992. Direct detection of trace levels of uranium by laser-induced kinetic phosphorimetry. *Anal. Chem.* 64 (13), 1413–1418.
- Brooks, S.C., Fredrickson, J.K., Carroll, S.L., Kennedy, D.W., Zachara, J.M., Plymale, A.E., Kelly, S.D., Kemner, K.M., Fendorf, S., 2003. Inhibition of bacterial U(VI) reduction by calcium. *Environ. Sci. Technol.* 37 (9), 1850–1858.
- Burgos, W.D., McDonough, J.T., Senko, J.M., Zhang, G., Dohnalkova, A.C., Kelly, S.D., Gorby, Y.A., Kemner, K.M., 2008. Characterization of uraninite nanoparticles produced by *Shewanella oneidensis* MR-1. *Geochim. Cosmochim. Acta* 72 (20), 4901–4915.
- Dong, H., Kostka, J.E., Kim, J.W., 2003a. Microscopic evidence for microbial dissolution of smectite. *Clays Clay Miner.* 51 (5), 502–512.
- Dong, H., et al., 2003b. Microbial reduction of structural Fe(III) in illite and goethite by a groundwater bacterium. *Environ. Sci. Technol.* 37 (7), 1268–1276.
- Dong, H., Jaisi, D.P., Kim, J., Zhang, G., 2009. Microbe–clay mineral interactions. *Am. Mineral.* 94, 1505–1519.
- Elias, D.A., Senko, J.M., Krumholz, L.R., 2003. A procedure for quantitation of total oxidized uranium for bioremediation studies. *J. Microbiol. Methods* 53 (3), 343–353.
- Favre, F., Stucki, J.W., Boivin, P., 2006. Redox properties of structural Fe in ferruginous smectite. A discussion of the standard potential and its environmental implications. *Clays Clay Miner.* 54 (4), 466–472.
- Fletcher, K.E., Boyanov, M.I., Thomas, S.H., Wu, Q., Kemner, K.M., Loeffler, F.E., 2010. U(VI) reduction to mononuclear U(IV) by desulfitobacterium species. *Environ. Sci. Technol.* 44 (12), 4705–4709.
- Fredrickson, J.K., Zachara, J.M., Kennedy, D.W., Duff, M.C., Gorby, Y.A., Li, S.M.W., Krupka, K.M., 2000. Reduction of U(VI) in goethite (α -FeOOH) suspensions by a dissimilatory metal-reducing bacterium. *Geochim. Cosmochim. Acta* 64 (18), 3085–3098.
- Fredrickson, J.K., Zachara, J.M., Kennedy, D.W., Liu, C., Duff, M.C., Hunter, D.B., Dohnalkova, A., 2002. Influence of Mn oxides on the reduction of uranium(VI) by the metal-reducing bacterium *Shewanella putrefaciens*. *Geochim. Cosmochim. Acta* 66 (18), 3247–3262.
- Ginder-Vogel, M., Criddle, C.S., Fendorf, S., 2006. Thermodynamic constraints on the oxidation of biogenic UO_2 by Fe(III) (hydr)oxides. *Environ. Sci. Technol.* 40 (11), 3544–3550.
- Hofstetter, T.B., Schwarzenbach, R.P., Haderlein, S.B., 2003. Reactivity of Fe(II) species associated with clay minerals. *Environ. Sci. Technol.* 37 (3), 519–528.
- Hofstetter, T.B., Neumann, A., Schwarzenbach, R.P., 2006. Reduction of nitroaromatic compounds by Fe(II) species associated with iron-rich smectites. *Environ. Sci. Technol.* 40 (1), 235–242.
- Holmes, P.R., Crundwell, F.K., 1995. Kinetic aspects of galvanic interactions between minerals during dissolution. *Hydrometallurgy* 39, 353–375.
- Jaisi, D.P., Dong, H.L., Liu, C.X., 2007. Influence of biogenic Fe(II) on the extent of microbial reduction of Fe(III) in clay minerals nontronite, illite, and chlorite. *Geochim. Cosmochim. Acta* 71 (5), 1145–1158.
- Jeon, B.H., Dempsey, B.A., Burgos, W.D., Barnett, M.O., Roden, E.E., 2005. Chemical reduction of U(VI) by Fe(II) at the solid–water interface using natural and synthetic Fe(III) oxides. *Environ. Sci. Technol.* 39 (15), 5642–5649.
- Kameda, J., Miyawaki, R., Kitagawa, R., Kogure, T., 2007. XRD and HRTEM analyses of stacking structures in sudoite, di-trioctahedral chlorite. *Am. Mineral.* 92 (10), 1586–1592.
- Keeling, J.L., Raven, M.D., Gates, W.P., 2000. Geology and characterization of two hydrothermal nontronites from weathered metamorphic rocks at the Uley Graphite Mine, South Australia. *Clays Clay Miner.* 48 (5), 537–548.
- Keller, M.D., Bellows, W.K., Guillard, R.R.L., 1988. Microwave treatment for sterilization of phytoplankton culture media. *J. Exp. Mar. Biol. Ecol.* 117 (3), 279–283.
- Kemner, K.M., Kelly, S.D., 2007. In: Hurst, C.J. (Ed.), *Synchrotron-based Techniques for Monitoring Metal Transformations, Third Edition. Manual of Environmental Microbiology*. ASM Press, pp. 1183–1194.
- Klauber, C., 2008. A critical review of the surface chemistry of acidic ferric sulphate dissolution of chalcopyrite with regards to hindered dissolution. *Int. J. Miner. Process.* 86 (1–4), 1–17.
- Komadel, P., Stucki, J.W., 1988. Quantitative assay of minerals for Fe-2+ and Fe-3+ using 1, 10-phenanthroline. 3. A rapid photochemical method. *Clays Clay Miner.* 36 (4), 379–381.
- Komlos, J., Peacock, A., Kukkadapu, R.K., Jaffe, P.R., 2008. Long-term dynamics of uranium reduction/reoxidation under low sulfate conditions. *Geochim. Cosmochim. Acta* 72 (15), 3603–3615.
- Kostka, J.E., Haefele, E., Viehweger, R., Stucki, J.W., 1999. Respiration and dissolution of iron(III)-containing clay minerals by bacteria. *Environ. Sci. Technol.* 33, 3127–3133.
- Lovley, D.R., Phillips, E.J.P., 1992. Bioremediation of uranium contamination with enzymatic uranium reduction. *Environ. Sci. Technol.* 26, 2228–2234.
- Lovley, D.R., Phillips, E.J.P., Gorby, Y.A., Landa, E.R., 1991. Microbial reduction of uranium. *Nature* 350, 413–416.
- McKinley, J.P., Zachara, J.M., Smith, S.C., Liu, C., 2007. Cation exchange reactions controlling desorption of Sr-90(2+) from coarse-grained contaminated sediments at the Hanford site, Washington. *Geochim. Cosmochim. Acta* 71 (2), 305–325.
- O'Loughlin, E.J., Kelly, S.D., Cook, R.E., Csencsits, R., Kemner, K.M., 2003. Reduction of uranium(VI) by mixed iron(II/iron(III) hydroxide (green rust): formation of UO₂ nanoparticles. *Environ. Sci. Technol.* 37 (4), 721–727.
- Schmeide, K., Pompe, S., Bubner, M., Heise, K.H., Bernhard, G., Nitsche, H., 2000. Uranium(VI) sorption onto phyllite and selected minerals in the presence of humic acid. *Radiochim. Acta* 88 (9–11), 723–728.
- Segre, C.U., Leyarovska, N.E., Chapman, L.D., Lavender, W.W., Plag, P.W., King, A.S., Kropf, A.J., Bunker, B.A., Kemner, K.M., Dutta, P., Duran, R.S., Kaduk, J., 2000. In: Pianetta, P. (Ed.), *The MRCAT insertion device beamline at the Advanced Photon Source. Synchrotron Radiation Instrumentation: Eleventh U. S. National Conference Vol. CP521*. American Institute of Physics, New York, pp. 419–422.
- Senko, J.M., Mohamed, Y., Dewers, T.A., Krumholz, L.R., 2005. Role for Fe(III) minerals in nitrate-dependent microbial U(IV) oxidation. *Environ. Sci. Technol.* 39 (8), 2529–2536.
- Senko, J.M., Kelly, S.D., Dohnalkova, A.C., McDonough, J.T., Kemner, K.M., Burgos, W.D., 2007. The effect of U(VI) bioreduction kinetics on subsequent reoxidation of biogenic U(IV). *Geochim. Cosmochim. Acta* 71 (19), 4644–4654.
- Singer, D.M., Farges, F., Brown Jr., G.E., 2009a. Biogenic nanoparticulate UO₂: synthesis, characterization, and factors affecting surface reactivity. *Geochim. Cosmochim. Acta* 73 (12), 3593–3611.
- Singer, D.M., Mahera, K., Brown Jr., G.E., 2009b. Uranyl–chlorite sorption/desorption: evaluation of different U(VI) sequestration processes. *Geochim. Cosmochim. Acta* 73 (20), 5989–6007.
- Stookey, L.L., 1970. Ferrozine—a new spectrophotometric reagent for iron. *Anal. Chem.* 42, 779–781.
- Stucki, J.W., Golden, D.C., Roth, C.B., 1984. Effects of reduction and reoxidation of structural iron on the surface-charge and dissolution of dioctahedral smectites. *Clays Clay Miner.* 32 (5), 350–356.
- Stucki, J.W., Lee, K., Goodman, B.A., Kostka, J.E., 2007. Effects of in situ biostimulation on iron mineral speciation in a sub-surface soil. *Geochim. Cosmochim. Acta* 71 (4), 835–843.
- Tokunaga, T.K., Wan, J., Kim, Y., Daly, R.A., Brodie, E.L., Hazen, T.C., Herman, D., Firestone, M.K., 2008. Influences of organic carbon supply rate on uranium bioreduction in initially oxidizing, contaminated sediment. *Environ. Sci. Technol.* 42 (23), 8901–8907.
- Wielinga, B., Bostick, B., Hansel, C.M., Rosenzweig, R.F., Fendorf, S., 2000. Inhibition of Bacterially Promoted Uranium Reduction: Ferric (Hydr)oxides as Competitive Electron Acceptors. *Environ. Sci. Technol.* 34 (11), 2190–2195.
- Zachara, J.M., Kukkadapu, R.K., Fredrickson, J.K., Gorby, Y.A., Smith, S.C., 2002. Biomineralization of poorly crystalline Fe(III) oxides by dissimilatory metal reducing bacteria (DMRB). *Geomicrobiol. J.* 19 (2), 179–207.
- Zazzi, A., Hirsch, T.K., Leonova, E., Kaikkonen, A., Grins, J., Annersten, H., Eden, M., 2006. Structural investigations of natural and synthetic chlorite minerals by X-ray diffraction, Mossbauer spectroscopy and solid-state nuclear magnetic resonance. *Clays Clay Miner.* 54 (2), 252–265.
- Zhang, G., Dong, H., Kim, J., Eberl, D.D., 2007. Microbial reduction of structural Fe³⁺ in nontronite by a thermophilic bacterium and its roles in promoting the smectite to illite reaction. *Am. Mineral.* 92, 1411–1419.
- Zhang, G., Senko, J.M., Kelly, S.D., Tan, H., Kemner, K.M., Burgos, W.D., 2009. Microbial reduction of iron(III)-rich nontronite and uranium(VI). *Geochim. Cosmochim. Acta* 73, 3523–3538.

Multiple Mechanisms of Uranium Immobilization by *Cellulomonas* sp. Strain ES6

Vaideswaran Sivaswamy,^{1,2} Maxim I. Boyanov,³ Brent M. Peyton,^{1,4}
Sridhar Viamajala,^{1,5} Robin Gerlach,⁴ William A. Apel,⁶ Rajesh K. Sani,^{1,7}
Alice Dohnalkova,⁸ Kenneth M. Kemner,³ Thomas Borch⁹

¹Center for Multiphase Environmental Research and Department of Chemical Engineering, Washington State University, Pullman, Washington

²Research and Development, NLC Nalco India Ltd, Pune, India

³Biosciences Division, Argonne National Laboratory, Argonne, Illinois

⁴Center for Biofilm Engineering, Chemical and Biological Engineering, Montana State University, Bozeman, Montana

⁵Department of Chemical and Environmental Engineering, The University of Toledo, Toledo, Ohio; telephone: +1-419-530-8094; fax: +1-419-530-8086; e-mail: sridhar.viamajala@utoledo.edu

⁶Biological Systems Department, Idaho National Laboratory, Idaho Falls, Idaho

⁷Chemical and Biological Engineering Department, South Dakota School of Mines & Technology, Rapid City, South Dakota

⁸Fundamental Sciences Department, Pacific Northwest National Laboratory, Richland, Washington

⁹Department of Soil and Crop Sciences, Colorado State University, Fort Collins, Colorado

Received 5 April 2010; revision received 4 September 2010; accepted 7 September 2010

Published online 24 September 2010 in Wiley Online Library (wileyonlinelibrary.com). DOI 10.1002/bit.22956

ABSTRACT: Removal of hexavalent uranium (U(VI)) from aqueous solution was studied using a Gram-positive facultative anaerobe, *Cellulomonas* sp. strain ES6, under anaerobic, non-growth conditions in bicarbonate and PIPES buffers. Inorganic phosphate was released by cells during the experiments providing ligands for formation of insoluble U(VI) phosphates. Phosphate release was most probably the result of anaerobic hydrolysis of intracellular polyphosphates accumulated by ES6 during aerobic growth. Microbial reduction of U(VI) to U(IV) was also observed. However, the relative magnitudes of U(VI) removal by abiotic (phosphate-based) precipitation and microbial reduction depended on the buffer chemistry. In bicarbonate buffer, X-ray absorption fine structure (XAFS) spectroscopy showed that U in the solid phase was present primarily as a non-uraninite U(IV) phase, whereas in PIPES buffer, U precipitates consisted primarily of U(VI)-phosphate. In both bicarbonate and PIPES buffer, net release of cellular phosphate was measured to be lower than that observed in

U-free controls suggesting simultaneous precipitation of U and PO_4^{3-} . In PIPES, U(VI) phosphates formed a significant portion of U precipitates and mass balance estimates of U and P along with XAFS data corroborate this hypothesis. High-resolution transmission electron microscopy (HR-TEM) and energy dispersive X-ray spectroscopy (EDS) of samples from PIPES treatments indeed showed both extracellular and intracellular accumulation of U solids with nanometer sized lath structures that contained U and P. In bicarbonate, however, more phosphate was removed than required to stoichiometrically balance the U(VI)/U(IV) fraction determined by XAFS, suggesting that U(IV) precipitated together with phosphate in this system. When anthraquinone-2,6-disulfonate (AQDS), a known electron shuttle, was added to the experimental reactors, the dominant removal mechanism in both buffers was reduction to a non-uraninite U(IV) phase. Uranium immobilization by abiotic precipitation or microbial reduction has been extensively reported; however, the present work suggests that strain ES6 can remove U(VI) from solution simultaneously

Correspondence to: S. Viamajala

Contract grant sponsor: U.S. Department of Energy, Office of Science, Environmental Management Science Program

Contract grant number: DE-FG02-03ER63582

Contract grant sponsor: DOE-NE Idaho Operations Office

Contract grant number: DE-AC07-05ID14517

Contract grant sponsor: Inland Northwest Research Alliance

Contract grant number: WSU 005

Contract grant sponsor: National Science Foundation (NSF) (CAREER Award)

Contract grant number: EAR 0847683

Contract grant sponsor: National Science Foundation—Earth Sciences

Contract grant number: EAR-0622171

Contract grant sponsor: Department of Energy—Geosciences

Contract grant number: DE-FG02-94ER14466

Additional supporting information may be found in the online version of this article.

through precipitation with phosphate ligands and microbial reduction, depending on the environmental conditions. *Cellulomonadaceae* are environmentally relevant subsurface bacteria and here, for the first time, the presence of multiple U immobilization mechanisms within one organism is reported using *Cellulomonas* sp. strain ES6.

Biotechnol. Bioeng. 2011;108: 264–276.

© 2010 Wiley Periodicals, Inc.

KEYWORDS: U(VI) reduction; *Cellulomonas*; U(VI)-phosphate; bioremediation; XAFS; U(IV)-phosphate

Introduction

Contamination of groundwater, soils and sediments by uranium (U) is a significant environmental problem (Borch et al., 2010). Sources of U include natural deposits and cold war-era extraction and processing of U ore (Anderson et al., 2003; Spear et al., 1999). A survey by Riley et al. (1992) showed that 11 of 18 U.S. Department of Energy (DOE) sites had U contaminated soil and groundwater. Uranium at contaminated sites exists predominantly in two forms—U(VI) and U(IV) (Bertsch et al., 1994). U(VI) is the most oxidized valence state (Emsley 1989), and in natural environments often forms aqueous complexes with high solubility and mobility in water. Reduction of U(VI) to U(IV) greatly decreases U solubility and mobility in groundwater (Lovley et al., 1991).

Subsurface environments contaminated with radionuclides pose difficult remediation challenges. According to the National Research Council (2000), cleanup across the DOE complex is expected to cost at least \$200 billion and will take decades to complete. Physical/chemical methods to treat U-contaminated groundwater, including anion exchange, lime softening, conventional and activated alumina coagulation, and pump-and-treat, are expensive (Spear et al., 1999). An alternative to these technologies is the use of indigenous subsurface bacteria for immobilizing U in contaminated groundwater and soil (Borch et al., 2010; Merroun and Selenska-Pobell, 2008). Four basic mechanisms by which bacteria can immobilize U are (1) microbially mediated reductive precipitation of U(VI) to U(IV), (2) U uptake and accumulation by cells, (3) adsorption onto cell surfaces, and (4) precipitation of U(VI) with inorganic phosphate released or produced by cells from the hydrolysis of phosphate containing compounds.

Cultures of *Desulfovibrio desulfuricans*, *Desulfovibrio vulgaris*, *Geobacter metallireducens*, *Shewanella putrefaciens* MR1, and *Deinococcus radiodurans*, among others have been demonstrated to reduce U(VI) to U(IV) (Fredrickson et al., 2000a,b; Gorby and Lovley, 1992; Lloyd et al., 2005; Lovley and Phillips, 1992; Spear et al., 2000; Suzuki and Banfield, 2004). Reduction of U(VI) can occur both directly by enzymatic action in the presence of an electron donor and indirectly by humic acid-mediated electron transfer (Gu et al., 2005). Cultures of *Pseudomonas aeruginosa*

(Strandberg et al., 1981), *Bacillus subtilis* (Fowle et al., 2000), and *Chryseomonas* MGF48 (Malekzadeh et al., 1998) can immobilize U by cellular uptake. In some cases, U chelates with intracellular polyphosphates and remains immobilized (Merroun et al., 2003, 2005). A third mechanism of U immobilization is by adsorption onto cell surfaces. It has also been shown that *Bacillus subtilis* can immobilize U through formation of uranyl-hydroxide, uranyl-carbonate, and calcium-uranyl-carbonate species with functional groups present on cell surfaces (Fowle et al., 2000; Gorman-Lewis et al., 2005). Finally, U immobilization can occur by precipitation with inorganic phosphate released by cells. Cultures of *Citrobacter* sp. (Yong and Macaskie, 1998), *Acidithiobacillus ferrooxidans* (Merroun et al., 2002), *Bacillus sphaericus* (Knopp et al., 2003), and *Acinetobacter johnsonii* (Boswell et al., 1999) have been demonstrated to remove uranium from water using a phosphate release mechanism. Under aerobic growth conditions, these microorganisms can accumulate phosphorus intracellularly in the form of polyphosphate (polyP) granules (Groenestijn et al., 1988; Tandoi et al., 1998). Under subsequent anaerobic conditions, the polyP granules are hydrolyzed to produce ATP while simultaneously releasing inorganic phosphate (PO_4^{3-}) from the cells (Groenestijn et al., 1987; Zafiri et al., 1999). In addition to hydrolysis of intracellular polyP, PO_4^{3-} can also be released by microbial metabolism of P-containing substrates such as glycerol-3-phosphate. It has recently been demonstrated that naturally occurring bacterial isolates from the DOE Oak Ridge Field Research Center were capable of generating sufficient PO_4^{3-} through phosphatase activity to abiotically precipitate up to 95% of U(VI) in laboratory tests. This approach has been shown to be successful in removing U(VI) through formation of autunite-like U-phosphate minerals under both aerobic and anaerobic, denitrifying conditions as well as at pH values as low as 5.0 (Beazley et al., 2007, 2009; Martinez et al., 2007).

Microbial release of PO_4^{3-} has been coupled to biologically induced precipitation of heavy metals or radionuclides (Boswell et al., 1998; Nakajima and Sakaguchi, 1986). Often, metal phosphates are highly insoluble and will precipitate on surfaces including cell walls (Macaskie et al., 1994; Montgomery et al., 1995). Solubility products of U(VI) phosphates as compiled by Palie (1970) range between 4.73×10^{-47} and 2.14×10^{-11} . Natural immobilization of U as U(VI) phosphates occurs extensively at the Kongarra deposit in Australia (Duerden, 1990) and addition of phosphate minerals (e.g., hydroxyapatite) is reported to have reduced the solubility and bioavailability of U in contaminated soils from the DOE Savannah River Site (Arey et al., 1999). The potential effectiveness of phosphate-bearing, reactive barrier systems for U removal from groundwater has also been demonstrated (Fuller et al., 2002; Naftz et al., 2000). Jerden and Sinha (2003) reported that the low solubility of stable U(VI) phosphate minerals can limit U concentrations to less than 15 $\mu\text{g/L}$ and phosphate-based strategies for in situ stabilization of U in oxidizing, fluid

rich environments may be effective for long-term containment.

Strain ES6 is a Gram-positive isolate from subsurface cores obtained from the DOE Hanford site in Washington State. Sani et al. (2002) reported that *Cellulomonas* sp. removed Cr(VI) and U(VI) from solution under non-growth conditions in the presence and absence of electron donor, and Borch et al. (2005) showed strain ES6 reduced nitroaromatics and ferrihydrite. Viamajala et al. (2007) showed that a majority of isolates enriched from Hanford cores contaminated with Cr and U, and from uncontaminated overlying sediments, were Gram-positive facultative anaerobes in, or closely related to, the genus *Cellulomonas*. In addition, Viamajala et al. (2008) demonstrated the ability of ES6 to reduce Cr(VI) in continuous flow soil columns for prolonged periods without a continuous nutrient supply, indicating that *Cellulomonas*-like subsurface organisms could be stimulated to form stable biobarriers for long-term contaminant removal in the subsurface. Compared to Gram-negative bacteria, only a few Gram-positive organisms have been examined for remediation strategies through bio-immobilization. Thus, the study of metal transformations by *Cellulomonas* is environmentally relevant, particularly to the DOE Hanford site, and provides needed information on metal biotransformations by Gram-positive organisms. Results presented here show for the first time that a subsurface *Cellulomonas* sp. can simultaneously precipitate U by release of cellular inorganic phosphate and by enzymatic reduction in the presence and absence of anthraquinone-2,6-disulfonate (AQDS).

Materials and Methods

Culture Conditions

Frozen stock cultures of *Cellulomonas* sp. ES6 (-80°C in 20% glycerol) were streaked on tryptic soy agar (TSA) and incubated aerobically at 30°C for 3 days. Sterile flasks containing tryptic soy broth (30 g/L; Difco, Sparks, MD) were inoculated with a single colony from the plate and were incubated at 30°C at 100 rpm for 3 days to aerobically grow the cultures. These flasks provided the inocula for subsequent experiments.

Preparation of Cells and Experimental Design

All experiments were carried out with washed cells of a culture that had been grown as described above. Either bicarbonate buffer (30 mM, pH 7; 1.3 mM KCl) or Piperazine-1,4-bis(2-ethanesulfonic acid) (PIPES) buffer (30 mM, pH 7; 1.3 mM KCl) was used for washing and re-suspension. Cultures were centrifuged at $10,000g$ for 20 min. The supernatant was discarded and the cell pellets were re-suspended in anaerobic bicarbonate or PIPES buffer with all transfers occurring in an anaerobic glove box ($\text{N}_2/\text{H}_2/\text{CO}_2$,

90:5:5). This process was performed three times and the cells were then re-suspended under non-growth conditions (defined here as the absence of exogenous nitrogen, phosphorus, vitamins, and other micronutrients) in sterile KCl (1.3 mM), with bicarbonate or PIPES buffer, and used for U precipitation experiments.

Anoxic conditions were obtained in the experimental medium containing bicarbonate and in the stock solution (1,000 mg/L) of U by bubbling with N_2/CO_2 (80:20) for 30 min. The medium containing PIPES buffer was bubbled with ultrapure N_2 for 30 min. The final pH values of the media were 7.0. Aliquots of washed-cell suspensions were added to the buffered medium to give a total liquid volume of 20 mL (including cells, buffer, and U) contained in 25 mL serum bottles. Final cell concentrations in PIPES buffer experiments were 0.52 mg/mL, while experiments in bicarbonate had either 1.15 or 2.3 mg-cells/mL. Cultures were incubated at room temperature (25°C) and shaken at 75 rpm. Sodium bicarbonate, potassium chloride, and PIPES were obtained from Fisher (Pittsburgh, PA). Water for all experiments had a resistivity of $18.2\ \text{M}\Omega\text{-cm}$ supplied from a Barnstead/Nanopure water system. For studies with AQDS, cells were re-suspended in autoclaved buffer solution containing 0.1 mM AQDS (Fisher). Uranium was added as $\text{UO}_2\text{Cl}_2\cdot 3\text{H}_2\text{O}$ (Bodman, Aston, PA) to reach either 0.1 mM or 0.25 mM U, depending upon the experiment. In addition to cell- and uranium-free controls, heat-killed cell controls were included. For heat-killed cell controls, aliquots of washed cell suspensions were transferred to anaerobic serum bottles in the glove box, sealed with butyl rubber septa, capped, crimped with aluminium seals and autoclaved. Anaerobic conditions in all treatments were verified by a resazurin indicator (0.5 mg/L) changing from pink to clear indicating an $E_h \leq -51\ \text{mV}$ (Twigg, 1945). Abiotic controls served as indicators that aseptic conditions were maintained during the experiments. Culture purity was also checked by bright field microscopy (Model Leica DMLB, Leica Microsystems, Wetzlar, Germany) and by plating aliquots from individual treatment units on TSA. Samples were collected using disposable syringes, which were purged with N_2 to avoid introducing O_2 into the serum bottles.

Each set of experiments was carried out in duplicate and all critical treatments were repeated as separate experiments to ensure reproducibility. Data presented here are the average values and error bars represent the computed standard deviation between duplicates.

Analytical Methods

Dry cell weight analyses were performed at the start of the experiments by filtering 0.5 mL of sample through a preweighed $0.2\ \mu\text{m}$ Supor[®] membrane syringe filter (Gelman Acrodisc, Pall Corporation, Port Washington, NY). Samples from cell free controls were also filtered to ensure no change in weight due to the buffer itself. The filters were dried at 60°C for 3 days, until a constant weight was

observed (Gerhardt et al., 1981). Removal of U(VI) from solution was evaluated by monitoring U(VI) concentration in filtered samples (0.22 μm) withdrawn by syringe and needle and measured immediately as described previously (Sani et al., 2002). Filtered samples (0.2 mL) were diluted 1,000 or 4,000 times based on initial U(VI) concentration. Anoxic nanopure water was used to dilute the samples, and 1 mL of the diluted sample was mixed with 1.5 mL (according to instrument vendor recommendations) of UraplexTM complexing agent (Chemchek, Richland, WA). Samples were analyzed with a kinetic phosphorescence analyzer (Chemchek), which uses a pulsed nitrogen dye laser to specifically measure U(VI) concentrations in solution (Brina and Miller, 1992). Calibrations were performed using uranyl chloride solutions from 0 to 0.23 μM , yielding a U(VI) detection limit of 0.04 μM with a precision of $\pm 5\%$. Samples for inorganic phosphate analysis were withdrawn by syringe and needle and centrifuged at 10,000g for 8 min. Inorganic phosphate concentrations were determined on the supernatant spectrophotometrically using Phosver[®] 3 Phosphate reagent (Hach, Loveland, CO) at 880 nm on a UV-vis spectrophotometer (Milton Roy Company Spectronic[®] GENESYS 5TM, Rochester, NY). The minimum detectable phosphate concentration by this method is 0.2 μM .

Transmission Electron Microscopy (TEM)

The embedding procedure, as well as thin sectioning, was conducted in an anaerobic glove box (Ar/H₂, 95:5; Coy Laboratory Products, Inc., Grass Lakes, MI). Centrifuged *Cellulomonas* cells were briefly fixed (1 h) in 2.5% glutaraldehyde, and washed in anoxic nanopure water followed by a gradual ethanol dehydration series and infiltration in LR White embedding resin (London Resin Company, London, UK). Cured blocks were sectioned to 70 nm on an ultramicrotome (Leica Ultracut UCT), and sections were mounted on 200 mesh copper grids coated with formvar support film sputtered with carbon. Sections were examined using a JEOL 2010 high resolution transmission electron microscope (HR-TEM) equipped with a LaB₆ filament operating at 200 kV with a resolution of 0.19 nm. Elemental analysis was performed using an Oxford Energy Dispersive Spectroscopy (EDS) system equipped with a SiLi detector coupled to the TEM, and spectra were analyzed with ISIS software (Oxford Instruments, Abingdon, UK). Images were digitally collected and analyzed using Digital Micrograph software (Gatan, Inc., Pleasanton, CA).

X-Ray Absorption Spectroscopy

X-ray absorption near-edge structure (XANES) and extended X-ray absorption fine structure (EXAFS) analyses were performed to determine the valence state and the average local environment of uranium in the solid phase. Filter paper with filtered residues (including cells and insoluble U) were dried in an anaerobic glovebox and sealed

between two pieces of Kapton[®] polyimide film to prevent oxidation while minimizing X-ray absorption (Borch et al., 2007). Samples were stored in the glovebox until analysis. XAFS data were collected on beamline 13-BM-C (GSECARS) at the Advanced Photon Source (APS). Energy selection was accomplished with a water-cooled Si(111) monochromator. Higher-order harmonics were eliminated by detuning the monochromator $\sim 10\%$. The energy range studied was -150 to $+370$ eV (up to 9.8 \AA^{-1}) about the L_{III} edge of U (17.166 keV). Incident and transmitted intensities were measured with in-line ionization chambers. Fluorescence spectra were recorded by monitoring the U L_{III α} fluorescence with a 13-element Ge detector. The integrated peak intensities from 9 to 11 detector elements were averaged for 3–4 scans on each sample. Spectra from a uraninite and a uranyl nitrate standard were collected periodically in transmission. All spectra were collected at ambient temperature and pressure. Data were compared to spectra collected from well characterized samples at sector 10-ID (MR/Enviro-CAT) for previous projects (Burgos et al., 2008; Fletcher et al., 2010). The sector 10-ID beamline undulator was tapered, and the incident energy was scanned using the Si(111) reflection of a liquid nitrogen cooled double-crystal monochromator in quick-scanning mode (approximately 3 min per scan for the extended region and 40 s per scan for the near-edge region) (Segre et al., 2000). Energy calibration for sector 10-D measurements was maintained at all times by simultaneously collecting a spectrum from a hydrogen uranyl phosphate mineral using X-rays transmitted through the samples.

The spectra obtained from the uranyl nitrate standards at both beamlines were compared to account for energy resolution and energy calibration differences. The spectrum from beamline 10-ID was broadened and translated in energy until it coincided with the spectrum collected at beamline 13-BM-C. The same amount of broadening and translation was applied to all other data collected at sector 10-ID. Background subtraction for the spectra was performed using AUTOBK (Newville et al., 1993). The relative amounts of reduced and oxidized uranium were determined by linear combination analysis with the ATHENA software (Ravel and Newville, 2005). The uncertainty of the linear combination analysis is conservatively estimated at 10–15%.

Geochemical Modeling

Geochemical Modeling was performed using Visual Minteq (Ver 2.61).

Results and Discussion

U(VI) Precipitation Experiments in PIPES Buffer

Figure 1a shows measured soluble inorganic phosphate concentrations over time in experiments performed with PIPES buffer at a cell concentration of 0.52 mg/mL. Initially,

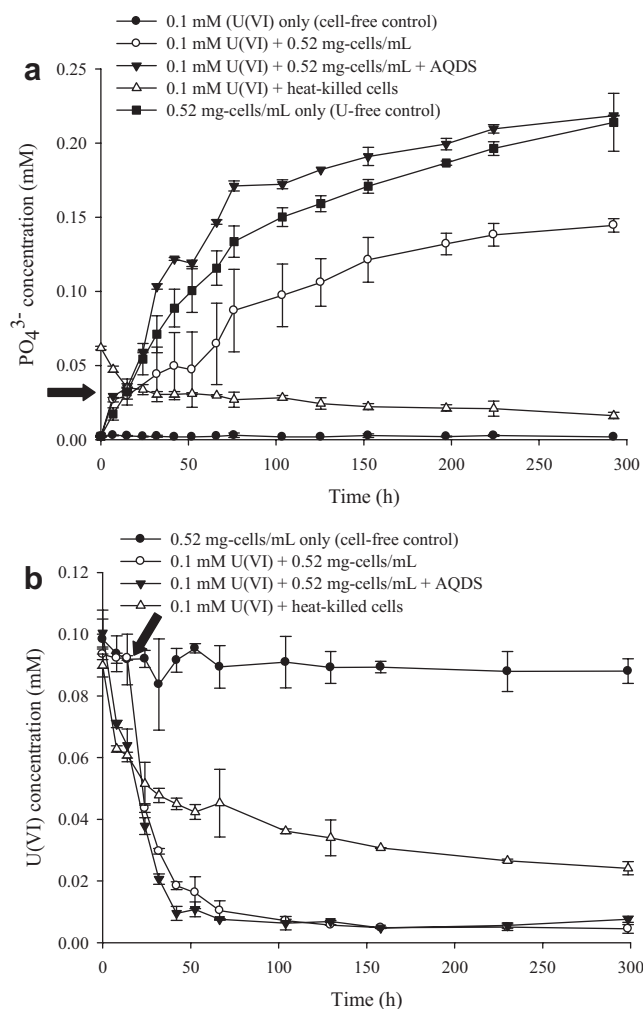


Figure 1. Measured concentrations of (a) soluble inorganic phosphate, and (b) soluble U(VI) over time for experiments performed with ES6 cultures (0.52 mg-cells/mL) re-suspended in PIPES buffer (pH 7). Data for cell-free, U-free, and heat-killed cell controls are also shown. Error bars represent one standard deviation from mean values. Arrow on (a) points to the phosphate concentration above which U(VI) precipitation started in treatments containing U(VI) and active ES6 cultures. Arrow on (b) indicates the corresponding data point on the U(VI) curve.

the phosphate concentration was below detection limits in all treatments except the heat-killed cell control. The phosphate concentration in the cell-free control was approximately zero throughout the experiment indicating that the buffer itself contained no measurable phosphate. Treatments containing U(VI) and cells showed an increase in phosphate concentration over time. In the absence of AQDS, the increase in phosphate was less than in the corresponding treatments that did not contain U(VI). In the presence of AQDS, added as a humic acid analog, approximately the same amount of phosphate was released in the U(VI)-containing treatments as in the U(VI)-free treatments (statistically verified at $P=0.05$). With heat-killed cells there was a measurable initial phosphate concentration, which decreased with time as U precipitated.

Like most other Gram-positive bacteria, the cell walls of *Cellulomonas* consist of secondary polymers, which often include teichoic acids and teichuronic acids, and contain phosphate and carboxylate residues, respectively (Panak et al., 2000). The initial amount of phosphate observed in heat-killed cells is likely from these polymers, nucleic acids, and other phosphate rich cellular components that may have been released during autoclaving.

Figure 1b shows soluble U(VI) concentrations measured during the anaerobic, non-growth experiments in PIPES buffer with cell suspensions and cell-free controls. Since spontaneous precipitation of U(VI), as metaschoepite, occurs in PIPES buffer for U(VI) concentrations greater than 0.125 mM (Fredrickson et al., 2000b), only 0.1 mM U(VI) was used in these studies. In all treatments containing cells, including the heat-killed cell control, soluble U(VI) concentrations decreased over time. No change in soluble U(VI) concentration was observed in cell-free controls. In the treatment with heat-killed cells, the decrease in U(VI) concentration occurred immediately after inoculation, while with viable cells there was a lag period preceding soluble U(VI) removal in AQDS-free treatments (approximately 14 h, shown by arrow in Fig. 1b). AQDS-containing treatments showed a fairly rapid decrease in U(VI) concentrations. The immediate onset of U(VI)-precipitation with heat-killed cells was likely caused by readily available dissolved phosphate released from cells due to heat-induced lysis, although adsorption to lysed cell surfaces is also possible (Gorman-Lewis et al., 2005). As there are likely no active enzymes in autoclaved cells, phosphate concentration did not increase above the initial value and U(VI) precipitation started immediately after addition into solution. In treatments with viable cells, phosphate concentrations were initially below measurable values, but increased with time (Fig. 1a). However, the onset of U(VI) precipitation in these treatments appears to have been delayed for at least 14 h (data point indicated by arrow in Fig. 1b). The phosphate concentration at 14 h in all tests with viable cells was 0.029 ± 0.002 mM (arrow on Fig. 1a). Experiments performed at lower cell concentrations (0.26 mg-ES6/mL) as well as other abiotic tests (data not shown) showed that precipitation of 0.1 mM U(VI) in PIPES did not occur below a phosphate concentration of 0.03 ± 0.01 mM. Similar results were observed with *Citrobacter* sp. and the delay in onset of phosphate-mediated uranyl removal was attributed to the solubility product and the time required for the formation of nucleation sites (Yong and Macaskie, 1995).

U(VI) Precipitation Experiments in Bicarbonate Buffer

Similar to tests in PIPES buffer, experiments were also performed under non-growth conditions in bicarbonate buffer. To keep the duration of study similar to the experiments in PIPES buffer, higher cell concentrations (1.15 and 2.3 mg-cells/mL) were used since preliminary

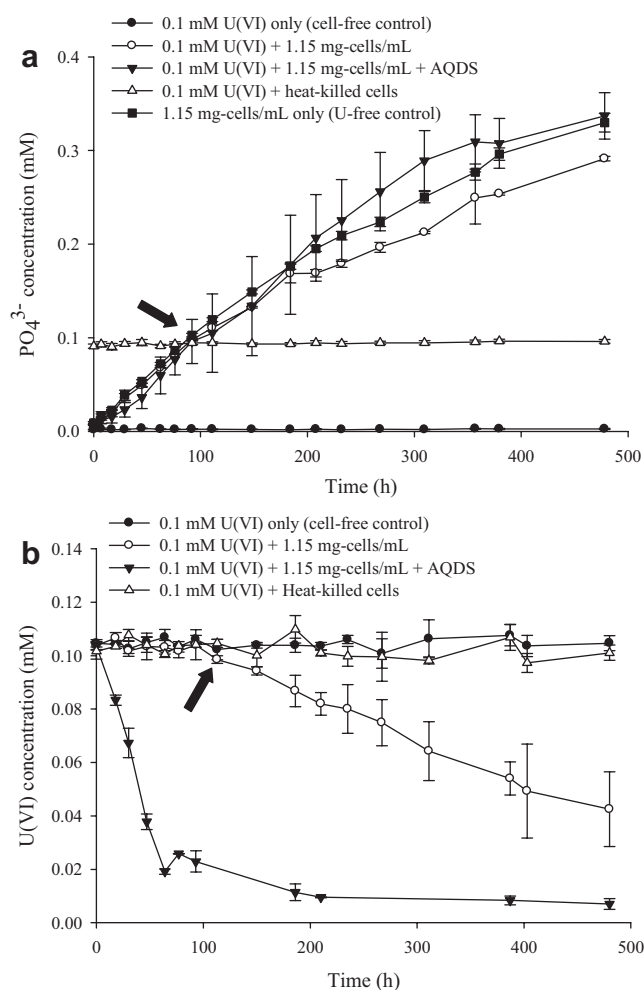


Figure 2. Measured concentrations of (a) soluble inorganic phosphate, and (b) soluble U(VI) over time for experiments performed with ES6 cultures (1.15 mg-cells/mL) re-suspended in bicarbonate buffer (pH 7). Data for cell-free, U-free, and heat-killed cell controls are also shown. Error bars represent one standard deviation from mean values. Arrows on (a and b) indicate the first sample showing measurable U(VI) removal in treatments containing active ES6 cultures.

results showed that U(VI) removal occurred at a much slower rate in the bicarbonate buffered systems compared to PIPES. Figures 2a and 3a show phosphate release by ES6 at the two cell concentrations in the presence and absence of U(VI). As observed during experiments in PIPES buffer, phosphate concentrations increased over time in all bicarbonate buffer experiments containing viable cells. Heat-killed controls, while containing measurable phosphate at the start of the experiments, did not show an increase in phosphate over time (Fig. 2a).

Similar to treatments in PIPES buffer, viable cells in bicarbonate buffer continuously removed U(VI) from solution after sufficient release of phosphate. Figures 2b and 3b show the observed changes in concentrations of soluble U(VI) over time for cell suspensions and cell-free controls under non-growth anaerobic conditions in

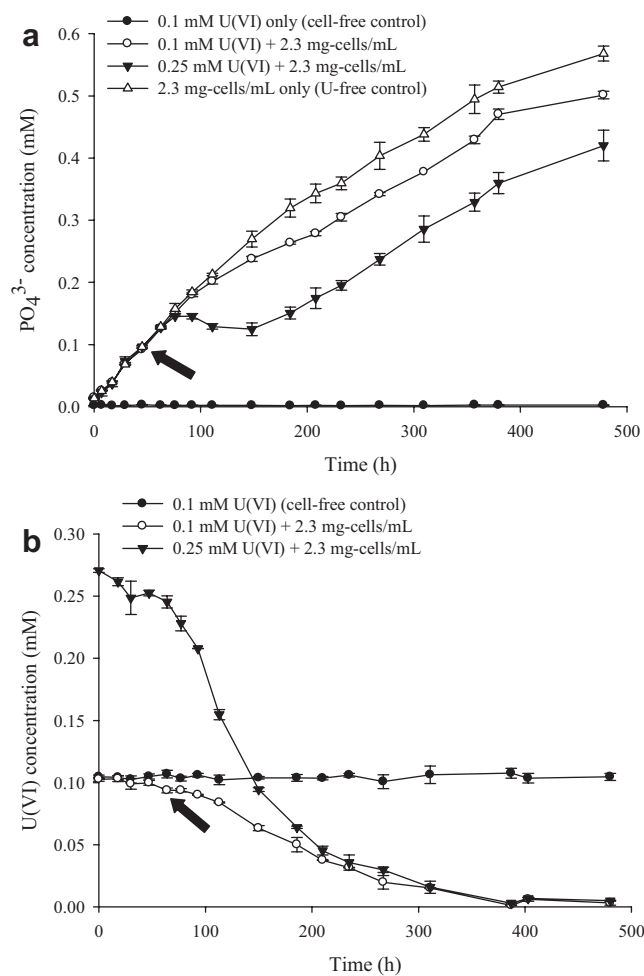


Figure 3. Measured concentrations of (a) soluble inorganic phosphate, and (b) soluble U(VI) over time for experiments performed with ES6 cultures (2.3 mg-cells/mL) re-suspended in bicarbonate buffer (pH 7). Data for cell-free and U-free controls are also shown. Error bars represent one standard deviation from mean values. Arrows on (a and b) indicate the first sample showing measurable U(VI) removal in treatments containing active ES6 cultures.

bicarbonate buffer. No change in soluble U(VI) concentration was observed in cell-free controls or in the heat-killed cell control. In heat-killed controls, active enzymes responsible for phosphate release were likely denatured and the initial phosphate concentration was insufficient to initiate U precipitation. Adsorption was also likely more difficult due to formation of stable uranyl-carbonato complexes; so no decrease in soluble U(VI) concentration was measured.

U(VI) removal from solution occurred more slowly in the bicarbonate buffer experiments compared to the PIPES buffer experiments despite the higher cell and phosphate concentrations. These results are consistent with previous observations of slower precipitation or adsorption of U(VI) in systems containing bicarbonate due to formation of uranyl-carbonato complexes (Kim et al., 2009; Stewart et al.,

2010). It is interesting to note that at high cell loadings the onset of rapid removal of U(VI) corresponds closely with the lowering of the measured rate of increase in soluble PO_4^{3-} ; both phenomena occur between 100 and 250 h (Fig. 3). This behavior is consistent with the formation of U(VI)-phosphates during this period, resulting in lower soluble phosphate concentrations in treatments containing U(VI), relative to U-free controls. However, these results would also not be inconsistent with reduction of U(VI) to U(IV) and precipitation of U(IV)-phosphate as suggested by Khijniak et al. (2005) and Fletcher et al. (2010) in studies with Gram-positive *Thermoterrabacterium ferrireducens* and *Desulfotobacterium* spp., respectively that were also performed in bicarbonate buffered media. In AQDS-free treatments, U(VI) concentrations did not decrease until approximately 0.1 mM of PO_4^{3-} were detected in solution (as indicated by arrows in Figs. 2 and 3). U(VI) removal was not observed in heat killed controls although phosphate was present at a concentration of just below 0.1 mM (Fig. 2). The AQDS containing treatments while showing the fastest U(VI) removal from solution in bicarbonate buffered treatments (Fig. 2) removed U(VI) more slowly than the PIPES buffer treatments (Fig. 1) despite an approximately two-fold higher cell concentration.

Visual Minteq-based equilibrium speciation modeling indicated that the presence of 30 mM carbonate results in the formation of uranyl-carbonate complexes such as $\text{UO}_2(\text{CO}_3)_{2(\text{aq})}^{2-}$ and $\text{UO}_2(\text{CO}_3)_{3(\text{aq})}^{4-}$, and $\text{UO}_2\text{CO}_3^{0(\text{aq})}$ while uranyl-hydroxo and -phosphate species dominated the PIPES buffered systems. Similar predictions were made by Fredrickson et al. (2000b). Even at the phosphate concentrations observed in the heat-killed cell treatments (0.1 mM PO_4^{3-}), Minteq did not predict any uranyl-phosphate species, which agrees with the constant phosphate and U(VI) concentration observed in the heat-killed control treatments (Fig. 2).

Effects of AQDS on Phosphate Release and U(VI) Removal

A soil component that can significantly influence the mobility of metals is naturally occurring organic matter, such as humic materials. Humic substances are heterogeneous high-molecular-weight organic materials, widely distributed on the earth's surface (Benz et al., 1998) and often thermodynamically stable in the subsurface (Watts, 1997). In addition, humic materials can function as catalysts for bacterial metal reduction. Lovley et al. (1996, 1998) reported that microorganisms can donate electrons to humic acids, which can shuttle electrons between microbes and Fe(III) oxide, and that relatively low concentrations of humic substances are sufficient to facilitate Fe(III) reduction. AQDS (2,6-antraquinone disulfonate) has been proposed as a model compound for quinone moieties in humics that can catalyze microbial reduction of Cr(VI), U(VI), Fe(III), and Mn(IV) (Fredrickson et al., 2000a,b;

Gounot, 1994; Lovley et al., 1996). Previous studies showed that ES6 can enzymatically reduce AQDS and can facilitate reduction of Cr(VI), Fe(III) (Viamajala et al., 2008) and nitroaromatics such as 2,4,6-trinitrotoluene (Borch et al., 2005). Because of the ubiquitous nature of humic substances in the subsurface, it is important to understand the relative contributions of both, direct microbial processes and indirect mechanisms, through electron shuttling compounds on soluble U(VI) removal.

Experiments with viable ES6 cells were performed in PIPES and bicarbonate buffer in the presence of 0.1 mM AQDS and 0.1 mM U(VI). During these experiments, the media turned yellow indicating the reduction of AQDS by ES6, and a continuous decrease in soluble U(VI) concentration was observed (Figs. 1b and 2b). The phosphate concentrations measured at the end of the experiments in AQDS containing treatments were nearly equal to the measured values in U-free controls ($t=295$ h in Fig. 1a and $t=480$ h in Fig. 2a). These observations suggest that phosphate-mediated precipitation was likely not a major mechanism contributing to U(VI) removal in treatments containing AQDS and that U(VI) reduction to U(IV) was probably responsible for a significant fraction of the observed decrease in soluble U(VI).

In both buffers, the presence of AQDS enhanced rates of U(VI) removal in comparison with experiments performed in its absence—an effect that was slightly more pronounced in bicarbonate (Fig. 2b) than in PIPES (Fig. 1b). However, the overall specific U(VI) removal rates (when normalized to biomass concentrations) in the presence of AQDS were much higher in PIPES (average initial rate = 0.005 mmol/h/mg-cells) than in bicarbonate (average initial rate = 0.001 mmol/h/mg-cells). As discussed earlier, $\text{UO}_2^{2+(\text{aq})}$ forms a series of stable aqueous complexes [$\text{UO}_2(\text{CO}_3)_{3(\text{aq})}^{4-}$, $\text{UO}_2(\text{CO}_3)_{2(\text{aq})}^{2-}$, and $\text{UO}_2\text{CO}_3^{0(\text{aq})}$] in bicarbonate buffer, whereas speciation in PIPES buffer is dominated by hydroxo complexes such as $\text{UO}_2\text{OH}^{+(\text{aq})}$ or $\text{UO}_2(\text{OH})_{2(\text{aq})}^0$ (Fredrickson et al., 2000b). $\text{UO}_2(\text{OH})_{2(\text{aq})}^0$ reduction is accompanied by a greater change in free energy than reduction of uranyl-carbonate complexes and is therefore favored (Fredrickson et al., 2000b; Scott and Morgan, 1990; Zehnder and Stumm, 1988).

Characterization of ES6 Mediated U Precipitates

XANES spectra

Figure 4 shows XANES spectra from samples of ES6 reacted with U(VI) under four different conditions (PIPES or bicarbonate buffer, \pm AQDS). The samples were collected at the end of the experimental run. Spectra are compared to U(IV) and U(VI) endmembers. For U(VI), an autunite precipitate verified by X-ray diffraction was used; for U(IV), a previously characterized, fully-reduced mononuclear U(IV) phase was used (Fletcher et al., 2010). The comparisons show that in the absence of AQDS, U is

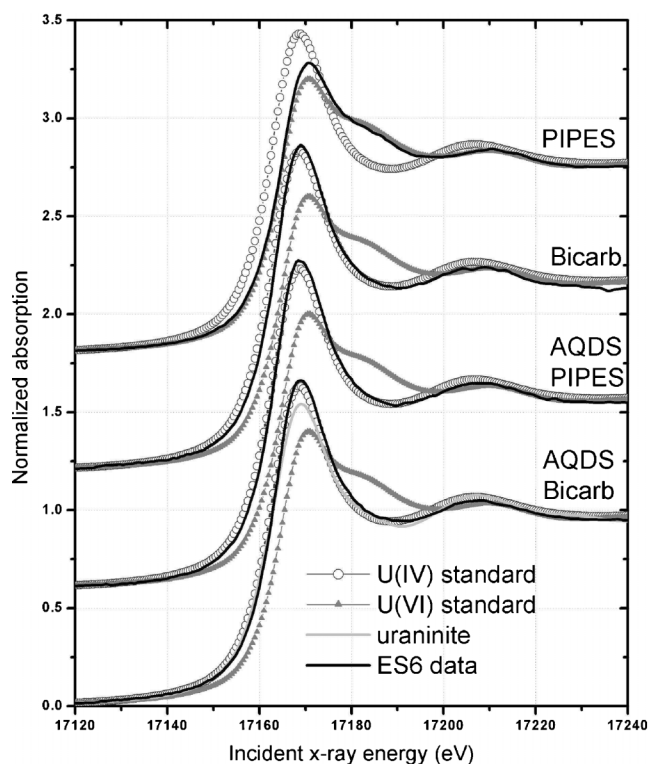


Figure 4. XANES data from U(VI) reacted with ES6 under different solution conditions (lines), compared to the U(VI) and U(IV) standards (symbols). The light gray line in the bottom graph shows the XANES spectrum of polycrystalline uraninite.

predominantly oxidized U(VI) in the PIPES buffer ES6 sample, whereas U is predominantly reduced in the bicarbonate buffer ES6 sample. In the presence of AQDS, U is predominantly reduced to U(IV) in both bicarbonate and PIPES systems. Linear combination analysis to quantify U(IV)/U(VI) ratios was not performed for the XANES data because possible small monochromator shifts during the measurement could not be excluded (spectra from standards were not collected simultaneously with the data). The U(IV)/U(VI) ratios were estimated instead from fits of the EXAFS data, which are less susceptible to energy axis shifts.

EXAFS spectra

Figures 5A and 6A demonstrate significant similarity between the EXAFS data from the ES6-PIPES buffer sample and an abiotic autunite precipitate (U(VI)-phosphate), indicating that U was sequestered predominantly as uranyl phosphate in this system. The smaller amplitude of the EXAFS signal in the ES6-PIPES system relative to the standard is likely due to the presence of small amounts of reduced U(IV), which was estimated at about 15% of total U by linear combination (LC) analysis. The EXAFS spectrum from the ES6-bicarbonate buffer sample appears very similar to the reduced U(IV) endmember (black line on

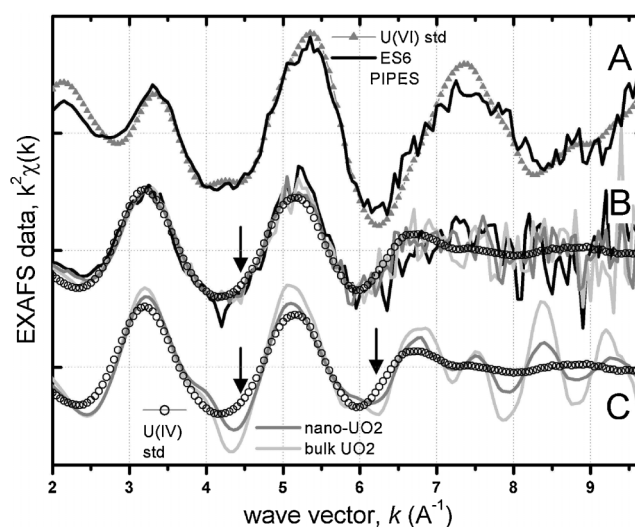


Figure 5. U L(III)-edge EXAFS data from *Cellulomonas* ES6 samples, compared to U(VI) and U(IV) standards. **A:** ES6 in PIPES/no AQDS buffer (line) compared to an autunite (U(VI)-PO₄) precipitate (symbols). **B:** ES6 in bicarbonate/no AQDS buffer (black line) and in bicarbonate or PIPES buffer with AQDS (gray lines). Symbols: mononuclear U(IV) phase from Fletcher et al. (2010). **C:** U(IV) standards: bulk uraninite (light gray), nanoparticulate uraninite from Burgos et al. (2008) (dark gray), and mononuclear U(IV) from Fletcher et al. (2010) (symbols).

Figs. 5B and 6B). The Fourier transform of the data reveals the presence of a uranyl component in the spectrum, suggested by the intermediate position of the 1–2 Å peak between the U(IV) and U(VI) endmember on Figure 5B. The U(IV)/U(VI) ratio in this sample was quantified as approximately 70:30 in this sample by LC analysis of the EXAFS data.

In the presence of AQDS, the EXAFS spectra from samples in both PIPES and bicarbonate buffer resemble significantly the mononuclear U(IV) phase obtained in a previous study (Fletcher et al., 2010) (gray lines and symbols on Fig. 5B). Although the noise level in the spectra is high at larger k values, the spectra are of good quality below 7 \AA^{-1} and do not show features characteristic of the nanoparticulate or polycrystalline uraninite standards (arrows on Fig. 5C). The Fourier transform (FT) of the ES6 + AQDS spectra are compared to mononuclear U(IV), nanoparticulate uraninite, and bulk uraninite on Figure 6C. The FT peak around $R + \Delta = 1.6 \text{ \AA}$ (U–O) is nearly identical in position and amplitude to that of the fully reduced, mononuclear U(IV) standard, confirming complete reduction to U(IV) in the ES6 + AQDS samples. The FT peak around $R + \Delta = 3.6 \text{ \AA}$ (vertical line) is due to the bidentate bond between two U atoms in uraninite. A 40–50% decrease in its amplitude relative to uraninite suggests the presence of nanoparticulate uraninite with average particle size of 2–5 nm (e.g., Boyanov et al., 2007; Burgos et al., 2008; Suzuki et al., 2002). The spectra from U(IV) reduced by ES6 in the presence of AQDS show a very small amplitude of the U–U peak, much smaller than the spectrum of nanoparticulate

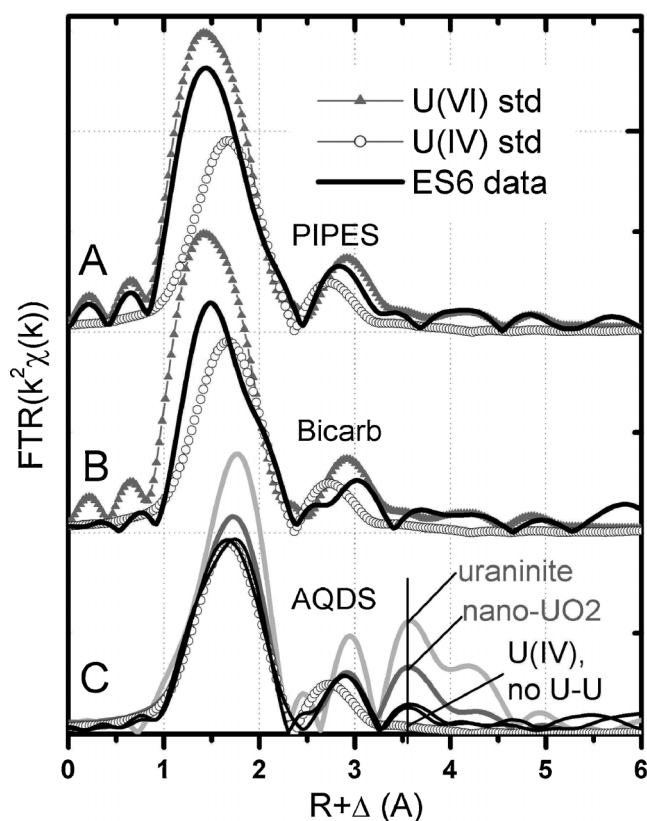


Figure 6. Fourier transformed EXAFS data from *Cellulomonas* ES6 samples (black lines), compared to standards: U(VI)-phosphate (triangles) and mononuclear U(IV) from Fletcher et al. (2010) (open circles). Fourier transform is over 2.0–9.7 Å⁻¹. **A:** ES6 in PIPES, no AQDS. **B:** ES6 in bicarbonate, no AQDS. **C:** ES6 with AQDS, in PIPES and bicarbonate (black lines), compared to U(IV) standards: bulk uraniumite (light gray), nanoparticulate uraniumite from Burgos et al. (2008) (dark gray), and mononuclear U(IV) from Fletcher et al. (2010) (symbols).

uraninite produced by *Shewanella* in Burgos et al. (2008), which is used here as a reference. The spectra in the systems with AQDS are very similar to the spectrum from the mononuclear U(IV) product produced by *Desulfotobacterium* in the presence of phosphate (Fletcher et al., 2010). The EXAFS data are of insufficient quality for a detailed shell-by-shell analysis of this U(IV) phase. Linear combination fits with the U(IV) and U(VI) endmembers determined a U(IV)/U(VI) ratio of about 90:10.

The results above suggest that the presence of AQDS facilitates a more complete reduction of U(VI) to U(IV), whereas in the absence of AQDS partial or very little U(VI) reduction by ES6 occurs, depending on the buffer condition. The formation of the mononuclear U(IV) reduction product with AQDS is likely controlled by the presence of aqueous phosphate, as observed by Fletcher et al. (2010).

In addition to EXAFS-based estimates, relative contributions of U removal from solution by precipitation with phosphate and precipitation by reduction to U(IV) were estimated through mass balance calculations based on final concentrations of soluble species (Table I). For these

calculations, lower soluble phosphate concentrations in treatments containing U relative to U-free controls was assumed to have occurred due to the formation of U(VI)-phosphate precipitates with a 1:1 stoichiometry of uranium and phosphate. Equilibrium speciation modeling using Visual Minteq indicated Na-autunite (NaUO₂PO₄) to be the most likely precipitate and thus equimolar amounts of uranium and phosphate were assumed to have precipitated (Table I, Column 4). The balance of U removed from solution was attributed to the production of U(IV) (Table I, Column 5). The calculated fraction of U(IV) in the precipitated U is shown in Column 6 of Table I. Although standard deviations associated with these calculations are larger than desired due to propagation of errors through mathematical operations, these calculations provide a basis for comparison across different treatments.

In PIPES buffer, the average U(IV) content of precipitates in the absence of AQDS was calculated to be 22%. These values are close to those predicted by EXAFS (last column of Table I and supplementary material). In bicarbonate buffer without AQDS, mass balance estimates predicted that 34–44% of U removed was due to reduction of U(VI) to U(IV) or due to adsorption. These values are significantly different from EXAFS estimates (last column of Table I and supplementary material) which also determined that solids in the bicarbonate system were present primarily as a non-uraninite U(IV) phase, most likely as U(IV)-phosphates. Since precipitation of phosphate with U(IV) cannot be accounted for through our mass balance approach, our mass balance-based estimates of relative U(VI)/U(IV) content are likely erroneous. In the presence of AQDS, mass balance calculations suggest that almost all the U removed from solution in both PIPES and bicarbonate buffer was due to reduction to U(IV) and are consistent with our EXAFS estimates (last column of Table I and supplementary material).

TEM, HR-TEM and EDS analysis

In addition to XAS analysis, TEM, and EDS data were obtained to support the proposed immobilization mechanisms. Figure 7 shows electron dense granules in whole cells that had not been exposed to U. Such metachromatic granules are often masses of volutin, a polymetaphosphate (Liu et al., 1996; Nester et al., 2004; Nielsen et al., 1998). Inorganic polyphosphates are usually linear polymers of phosphate residues linked by phosphoanhydride bonds (Merroun et al., 2002) with chain lengths varying between 3 and 1,000 monomeric units, depending on the organism, its growth, and other physiological conditions (van Veen et al., 1993). Polyphosphate has many biochemical functions, and can be used as an energy source and a chelator of bivalent metals ions (Keasling and Hupf, 1996). The presence of electron dense granules in ES6 and release of excessive phosphate indicates that polyphosphate is very likely the source of phosphate released by ES6.

Table 1. Estimates of U(IV) in precipitated U based on EXAFS and mass balance calculations.

Experimental conditions	Calculations based on mass balance of soluble U(VI) and PO ₄ ³⁻					Calculations from EXAFS measurements; % U(IV) of total U removed
	U(VI) removed (mM) ^a	PO ₄ ³⁻ remaining in solution (mM) ^b	Calculated U(VI) removal assuming precipitation with PO ₄ ³⁻ or by reduction to U(IV)		% U(IV) of total U removed	
			Precipitation (mM) ^c	Reduction (mM) ^d		
CO₃²⁻ buffer—2.3 mg-cells/mL						
ES6 + 0.1 mM U(VI)	0.102 ± 0.003	0.501 ± 0.00	0.035 ± 0.014	0.035 ± 0.014	34.3 ± 15.2	Not measured
ES6 + 0.25 mM U(VI)	0.266 ± 0.005	0.420 ± 0.025	0.148 ± 0.028	0.118 ± 0.028	44.4 ± 12.4	Not measured
ES6 only (U-free control)	n.a.	0.568 ± 0.012	n.a.	n.a.	n.a.	n.a.
HCO₃⁻ buffer—1.15 mg-cells/mL						
ES6 + 0.1 mM U(VI)	0.061 ± 0.019	0.291 ± 0.002	0.038 ± 0.010	0.023 ± 0.021	37.7 ± 37.3	69
ES6 + 0.1 mM U(VI) + AQDS	0.097 ± 0.003	0.337 ± 0.025	Not significant	0.097 ± 0.003	100	88
ES6 only (U-free control)	n.a.	0.330 ± 0.010	n.a.	n.a.	n.a.	n.a.
PIPES buffer—0.52 mg-cells/mL						
ES6 + 0.1 mM U(VI)	0.089 ± 0.002	0.145 ± 0.005	0.069 ± 0.020	0.020 ± 0.02	22.4 ± 23.5	16
ES6 + 0.1 mM U(VI) + AQDS	0.093 ± 0.005	0.219 ± 0.002	Not significant	0.093 ± 0.005	100	90
ES6 only (U-free control)	n.a.	0.214 ± 0.019	n.a.	n.a.	n.a.	n.a.

Mass balance calculations for U and P were used to determine relative amounts of uranyl phosphate and U(IV). These calculations assumed that a difference in PO₄³⁻ concentrations between treatments containing U(VI) and U-free controls was the result of U(VI)-phosphate formation. Estimates were based on measured final concentrations of soluble species ($t=295$ h and $t=480$ h for experiments in PIPES and bicarbonate, respectively). EXAFS calculations are based on relative content of the endmember U(VI) and U(IV) spectra in each sample's spectrum. Errors on mass balance calculations represent one standard deviation from mean values. The uncertainty in the EXAFS determinations is estimated at 10–15%.

^aEqual to the difference between initial and final U(VI) concentrations in the experiment.

^bEqual to the concentration of PO₄³⁻ measured in solution at the end of the experiment

^cCalculated as equal to PO₄³⁻ removed relative to U-free control.

^dCalculated as balance of U removed after accounting for losses due to precipitation with PO₄³⁻.

Figure 8a shows intracellular U-phosphate precipitates when ES6 was exposed to U(VI) in PIPES although extracellular precipitates formed as well (Fig. 9a and b). Extracellular association of U with bacterial cell surfaces is likely due to physical and chemical interactions involving adsorption and ion exchange (Francis et al., 2004). Bacterial cell walls, exopolymers, and lipids contain carboxyl, hydroxyl, amino, and phosphate groups capable of extracellular U binding (Fowle et al., 2000; Gorman-Lewis

et al., 2005). However, since some U precipitation also occurred within cells, it is likely that U was transported into cells and precipitated either as a result of enzymatic reduction or by reaction with intracellular phosphate. Andres et al. (1993, 1994) observed both intra- and extracellular U association in *Mycobacterium smegmatis*. *Pseudomonas fluorescens* accumulates U as fine-grained crystals in the periplasm along its plasma and outer membranes (Krueger et al., 1993). Francis et al. (2004) observed extracellular association with *Bacillus subtilis*, *Pseudomonas fluorescens*, *Haloanaerobium praevalens*, and *Halobacterium halobium* while studies with *Halomonas* sp. showed both extracellular and intracellular association. Figure 8b shows that U(VI)-phosphate precipitates formed laths ~40–70 nm long, but only 2–5 nm in width, while Figure 8c shows the corresponding EDS spectrum. Such laths have also been reported by Marques et al. (1991) with a *Pseudomonas* sp. Copper peaks are the result of the copper grid used for mounting thin sections. EDS analysis confirmed the presence of U and P in these precipitates (Fig. 8c).

In addition to cell associated U precipitates, we observed precipitates that did not appear to be cell-associated (Fig. 9a and b). These precipitates appeared to be larger than cell-associated precipitates, but generally retained their nanometer size lath nature. The EDS spectrum also indicates the presence of both U and P (Fig. 9c). The general formula of uranylphosphate precipitates is $M(UO_2PO_4)_n \cdot mH_2O$ in

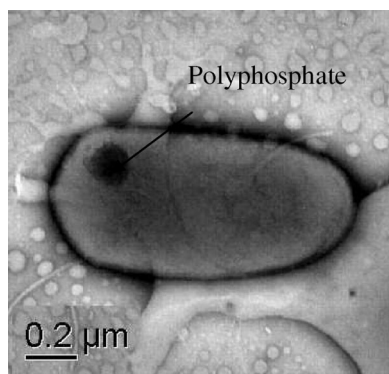


Figure 7. Transmission electron micrographs of whole cell mounts of strain ES6 showing electron-dense polyphosphate-like intracellular granules. Samples for imaging were obtained from ES6 treatments in bicarbonate buffer in the absence of AQDS.

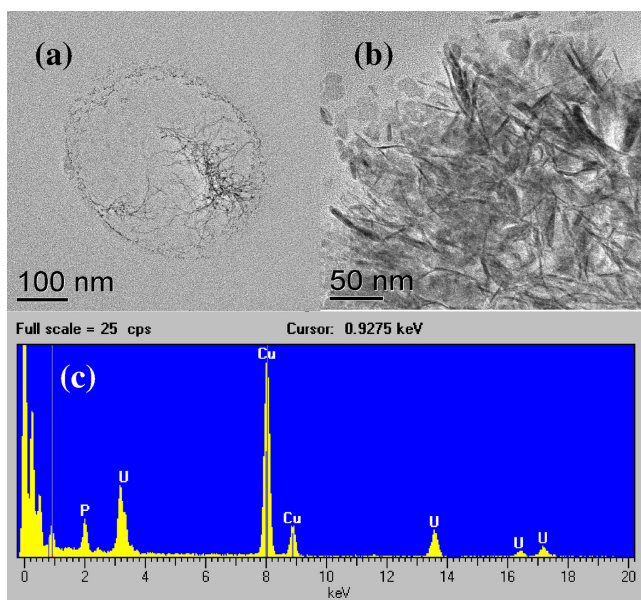


Figure 8. Transmission electron micrograph of thin section of strain ES6 cells challenged with uranium in PIPES buffer without AQDS (a). b: Nanometer size, lath like uranylphosphate precipitates. c: EDS spectrum of cell associated precipitates. Copper peak is from the grid. [Color figure can be seen in the online version of this article, available at wileyonlinelibrary.com.]

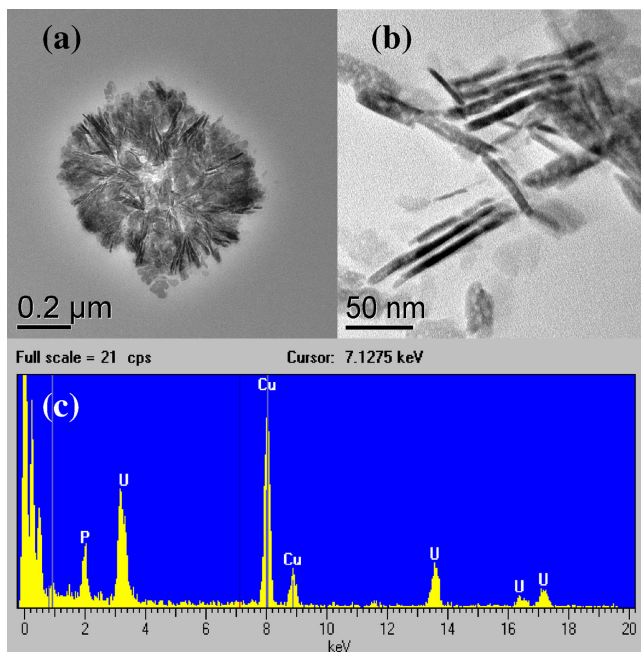


Figure 9. a and b: Transmission electron micrograph of uranylphosphate precipitates. c: EDS spectrum of uranylphosphate precipitates. Copper peak is from the grid. Samples for imaging were obtained from ES6 treatments with U(VI) in PIPES buffer in the absence of AQDS. [Color figure can be seen in the online version of this article, available at wileyonlinelibrary.com.]

which M may be mono or divalent cations and n may be 1 or 2 depending on the valence state of the metal cation. Based on the Minteq modeling, Na-autunite is the most likely mineral phase to precipitate. Autunites have been described to have a typical structure of negatively charged layers of $(\text{UO}_2\text{PO}_4)_n$ separated by staggered layers of water molecules and compensating cations (Yong and Macaskie, 1995).

The results presented here are the first report of an environmentally relevant subsurface microorganism capable of U immobilization by two different mechanisms (reductive precipitation or precipitation with biogenic phosphate ligands) depending on the environmental conditions. Polyphosphate accumulation and release is generally related to cellular energetics for survival and growth. In ES6, it may be also serving as a detoxification mechanism, as proposed recently for the hydrolysis of exogenous organophosphate compounds with other microorganisms (Beazley et al., 2007, 2009). Adsorption of U(VI) to cell surfaces might have also occurred, but was not independently verified in this study. Overall, our results offer a first step toward understanding and quantifying the phosphate release and U removal by *Cellulomonas* sp. strain ES6. This work demonstrates a potential role for Gram-positive fermentative organisms, represented here by the genus *Cellulomonas*, in metals biotransformation in the environment. The ability of *Cellulomonas* sp. to reduce Cr(VI) to Cr(III) (Sani et al., 2002; Viamajala et al., 2007, 2008) and to precipitate U as U(IV) and U(VI)-phosphate indicates a potential long-term application of in situ heavy metal and radionuclide removal.

We thank Chris Davitt, Valerie Lynch of the Electron Microscopy Center, Washington State University for TEM images. We also thank Pacific Northwest National Laboratory—Environmental Molecular Sciences Laboratory for HR-TEM analyses. Research was supported by the U.S. Department of Energy, Office of Science, Environmental Management Science Program under Grant No. DE-FG02-03ER63582 and DOE-NE Idaho Operations Office Contract DE-AC07-05ID14517. Research was also supported by the Inland Northwest Research Alliance under contract WSU 005 and a National Science Foundation (NSF) CAREER Award (EAR 0847683 to Thomas Borch). Funding for Ken Kemner and Maxim Boyanov was provided under the Argonne Subsurface Science Focus Area grant by the U.S. Department of Energy's Office of Science (DOE-SC), Office of Biological and Environmental Research, Subsurface Biogeochemical Research Program. Portions of this work were performed at GeoSoilEnviroCARS (Sector 13), Advanced Photon Source (APS), Argonne National Laboratory. GeoSoilEnviroCARS is supported by the National Science Foundation—Earth Sciences (EAR-0622171) and Department of Energy—Geosciences (DE-FG02-94ER14466). Use of the Advanced Photon Source was supported by the U.S. Department of Energy, Office of Science, Office of Basic Energy Sciences, under Contract No. DE-AC02-06CH11357.

References

- Anderson RT, Vrionis HA, Ortiz-Bernad I, Resch CT, Long PE, Dayvault R, Karp K, Marutzky S, Metzler DR, Peacock A, White DC, Lowe M, Lovley DR. 2003. Stimulating the *in situ* activity of Geobacter species to

- remove uranium from the groundwater of a uranium-contaminated aquifer. *Appl Environ Microbiol* 69:5884–5891.
- Andres Y, MacCordick J, Hubert JC. 1993. Adsorption of several actinides (TH, U) and lanthanide (LA, EU, YB) ions by *Mycobacterium smegmatis*. *Appl Microbiol Biotechnol* 39:413–417.
- Andres Y, MacCordick J, Hubert JC. 1994. Binding sites of sorbed uranyl ion in the cell wall of *Mycobacterium smegmatis*. *FEMS Microbiol Lett* 115:27–32.
- Arey JS, Seaman JC, Bertsch PM. 1999. Immobilization of uranium in contaminated sediments by hydroxyapatite addition. *Environ Sci Technol* 33:337–342.
- Beazley MJ, Martinez RJ, Sobecky PA, Webb SM, Taillefert M. 2007. Uranium biomineralization as a result of bacterial phosphatase activity: Insights from bacterial isolates from a contaminated subsurface. *Environ Sci Technol* 41:5701–5707.
- Beazley MJ, Martinez RJ, Sobecky PA, Webb SM, Taillefert M. 2009. Nonreductive biomineralization of uranium(VI) phosphate via microbial phosphatase activity in anaerobic conditions. *Geomicrobiol J* 26: 431–441.
- Benz M, Schink B, Brune A. 1998. Humic acid reduction by Propiionibacterium freudenreichii and other fermenting bacteria. *Appl Environ Microbiol* 64:4507–4512.
- Bertsch PM, Hunter DB, Sutton SR, Bajt S, Rivers ML. 1994. In situ chemical speciation of uranium in soils and sediments by micro x-ray adsorption spectroscopy. *Environ Sci Technol* 28:980–984.
- Borch T, Inskip WP, Harwood JA, Gerlach R. 2005. Impact of ferrihydrite and anthraquinone-2,6-disulfonate on the reductive transformation of 2,4,6-trinitrotoluene by a Gram-positive fermenting bacterium. *Environ Sci Technol* 39:7126–7133.
- Borch T, Masue Y, Kukkadapu RK, Fendorf S. 2007. Phosphate imposed limitations on biological reduction and alteration of ferrihydrite. *Environ Sci Technol* 41:166–172.
- Borch T, Kretzschmar R, Kappler A, Cappellen PV, Ginder-Vogel M, Voegelin A, Campbell K. 2010. Biogeochemical redox processes and their impact on contaminant dynamics. *Environ Sci Technol* 44:15–23.
- Boswell CD, Hewitt CJ, Macaskie LE. 1998. An application of bacterial flow cytometry—Evaluation of the toxic effects of four heavy metals on *Acinetobacter* sp. with potential for bioremediation of contaminated waste waters. *Biotechnol Lett* 20:857–863.
- Boswell CD, Dick RE, Macaskie LE. 1999. The effect of heavy metals and other environmental conditions on anaerobic phosphate metabolism of *Acinetobacter johnsonii*. *Microbiology* 145:1711–1720.
- Boyantov MI, O'Loughlin EJ, Roden EE, Fein JB, Kemner KM. 2007. Adsorption of Fe(II) and U(VI) to carboxyl-functionalized microspheres: The influence of speciation on uranyl reduction studied by titration and XAFS. *Geochim Cosmochim Acta* 71(8):1898–1912.
- Brina R, Miller AG. 1992. Direct detection of trace levels of uranium by laser induced kinetic phosphoremeter. *Anal Chem* 64:1415–1418.
- Burgos WD, McDonough JT, Senko JM, Zhang GX, Dohnalkova AC, Kelly SD, Gorby Y, Kemner KM. 2008. Characterization of uraninite nanoparticles produced by *Shewanella oneidensis* MR-1. *Geochim Cosmochim Acta* 72(20):4901–4915.
- Duerden P. 1990. Alligator river analogue project, 1st Annual Report 1988–89, Australian Nuclear Science and Technology Organization (ANSTO).
- Emsley J. 1989. *The elements*. New York, NY: Oxford University Press. p. 202.
- Fletcher K, Boyantov MI, Kemner KK, Thomas SH, Wu Q, Loeffler F. 2010. U(VI) reduction to mononuclear U(IV) by *Desulfotobacterium* spp. *Environ Sci Technol* 44:4705–4709.
- Fowle DA, Fein JB, Martin AM. 2000. Experimental study of uranyl adsorption onto *Bacillus subtilis*. *Environ Sci Technol* 34:3737–3741.
- Francis AJ, Gillow JB, Dodge CJ, Harris R, Beveridge TJ, Papenguth HW. 2004. Uranium association with halophilic and non-halophilic bacteria and archaea. *Radiochim Acta* 98:1–8.
- Fredrickson JK, Kostandarites HM, Li SW, Plymale AE, Daly MJ. 2000a. Reduction of Fe(III), Cr(VI), U(VI) and Tc(VII) by *Deinococcus radiodurans* R1. *Appl Environ Microbiol* 66:2006–2011.
- Fredrickson JK, Zachara JM, Kennedy DW, Duff MC, Gorby YA, Li SW, Krupka KM. 2000b. Reduction of U(VI) in goethite (α -FeOOH) suspensions by a dissimilatory metal-reducing bacterium. *Geochim Cosmochim Acta* 64:3085–3098.
- Fuller CC, Bargar JR, Davis JA, Piana MJ. 2002. Mechanisms of uranium interactions with hydroxyapatite: Implications for ground water remediation. *Environ Sci Technol* 36:58–65.
- Gerhardt P, Murray RGE, Costilow RN, Nester EW, Wood WA, Krieg NR, Phillips GB. 1981. *Manual of methods for general bacteriology*. Am Soc Microbiol 505.
- Gorby YA, Lovley DR. 1992. Enzymatic uranium precipitation. *Environ Sci Technol* 26:205–207.
- Gorman-Lewis D, Elias PE, Fein JB. 2005. Adsorption of aqueous uranyl complexes onto *Bacillus subtilis* cells. *Environ Sci Technol* 39:4906–4912.
- Gounot AM. 1994. Microbial oxidation and reduction of manganese: Consequences in groundwater and applications. *FEMS Microbiol Rev* 14:339–349.
- Groenestijn JW, Deinema MH, Zehnder AJB. 1987. ATP production from polyphosphate in *Acinetobacter* strain 210A. *Arch Microbiol* 148:14–19.
- Groenestijn JW, Bentvelsen MMA, Deinema MH, Zehnder AJB. 1988. Polyphosphate-degrading enzymes in *Acinetobacter* spp. And activated sludge. *Appl Environ Microbiol* 55:219–223.
- Gu B, Yan H, Zhou P, Watson DB, Park M, Istok J. 2005. Natural humics impact uranium bioreduction and oxidation. *Environ Sci Technol* 39:5268–5275.
- Jerden JL, Sinha AK. 2003. Phosphate based immobilization of uranium in an oxidizing bedrock aquifer. *Appl Geochem* 18:823–843.
- Keasling JD, Hupf GA. 1996. Genetic manipulation of polyphosphate metabolism affects cadmium tolerance in *Escherichia coli*. *Appl Environ Microbiol* 62:743–746.
- Khijniak TV, Slobodkin AI, Coker V, Renshaw JC, Livens FR, Bonch-Osmolovskaya EA, Birkeland NK, Medvedeva-Lyalikova NN, Lloyd JR. 2005. Reduction of uranium(VI) phosphate during growth of the thermophilic bacterium *Thermoterrabacterium ferrireducens*. *Appl Environ Microbiol* 71(10): 6423–6426.
- Kim KW, Kim YH, Lee SY, Lee JW, Joe KS, Lee EH, Kim JS, Song K, Song KC. 2009. Precipitation characteristics of uranyl ions at different pHs depending on the presence of carbonate ions and hydrogen peroxide. *Environ Sci Technol* 43:2355–2361.
- Knopp R, Panak PJ, Wray LA, Renninger NS, Keasling JD, Nitsche H. 2003. Laser spectroscopic studies of interactions of UVI with bacterial phosphate species. *Chem Eur J* 9:2812–2818.
- Krueger S, Olsen GJ, Johnsonbaugh D, Beveridge TJ. 1993. Characterization of the binding of gallium, platinum, and uranium to pseudomonas fluorescens by small-angle X-ray scattering and transmission electron microscopy. *Appl Environ Microbiol* 59:4056–4064.
- Liu W, Nakamura K, Matsuo T, Mino T. 1996. Internal energy-based competition between polyphosphate- and glycogen-accumulating bacteria in biological phosphorus removal reactors—Effect of P/C feeding ration. *Water Res* 31:1430–1438.
- Lloyd JR, Renshaw JC, May I, Livens FR, Burke IT, Mortimerc RJG, Morris K. 2005. Biotransformation of radioactive waste: Microbial reduction of actinides and fission products. *J Nucl Radiochem Sci* 6:17–20.
- Lovley DR, Phillips JP. 1992. Reduction of uranium by *Desulfovibrio desulfuricans*. *Appl Environ Microbiol* 58:850–856.
- Lovley DR, Phillips EJP, Gorby YA, Landa ER. 1991. Microbial reduction of uranium. *Nature* 350:413–416.
- Lovley DR, Coates JD, Blunt-Harris EL, Phillips EJ, Woodward JC. 1996. Humic substances as electron acceptors for microbial respiration. *Nature* 382:445–448.
- Lovley DR, Fraga JL, Blunt-Harris EL, Hayes LA, Phillips EJP, Coates JD. 1998. Humic substances as a mediator for microbially catalyzed metal reduction. *Acta Hydrochim Hydrobiol* 26:152–157.
- Macaskie L, Bonthron KM, Rouch DA. 1994. Phosphatase-mediated heavy metal accumulation by a *Citrobacter* sp. and related enterobacteria. *FEMS Microbiol Lett* 121:141–146.

- Malekzadeh F, Farazmand A, Ghafmrian H, Shahamat M, Levin M, Colwell RR. 2002. Uranium accumulation by a bacterium isolated from electroplating effluent. *World J Microbiol Biotechnol* 18:295–302.
- Marques AM, Roca X, Simon-Pujol MD, Fuste MC, Congregado F. 1991. Uranium accumulation by *Pseudomonas* sp. EPS-5028. *Appl Microbiol Biotechnol* 35:406–410.
- Martinez RJ, Beazley MJ, Taillefert M, Arakaki AK, Skolnick J, Sobczyk PA. 2007. Aerobic uranium (VI) bioprecipitation by metal-resistant bacteria isolated from radionuclide- and metal-contaminated subsurface soils. *Environ Microbiol* 9:3122–3133.
- Merroun ML, Selenska-Pobell S. 2008. Bacterial interactions with uranium: An environmental perspective. *J Cont Hydrol* 102:285–295.
- Merroun ML, Hennig C, Rossberg A, Geipel G, Reich T, Selenska-Pobell S. 2002. Molecular and atomic analysis of uranium complexes formed by three eco-types of *Acidithiobacillus ferrooxidans*. *Proceedings in Biometals 2002: Bioremediation, Biochemical Society Transactions* 30: 669–672.
- Merroun ML, Hennig C, Rossberg A, Reich T, Selenska-Pobell S. 2003. Characterization of U (VI)-*Acidithiobacillus ferrooxidans* complexes by using EXAFS, transmission electron microscopy and energy-dispersive X-ray analysis. *Radiochim Acta* 91:583–591.
- Merroun ML, Raff J, Rossberg A, Hennig C, Reich T, Selenska-Pobell S. 2005. Complexation of uranium by cells and S-layer sheets of *Bacillus sphaericus* JG-A12. *Appl Environ Microbiol* 71:5542–5553.
- Montgomery DM, Dean ACR, Wiffen P, Macaskie LE. 1995. Phosphatase production and activity in *Citrobacter freundii* and a naturally occurring, heavy-metal-accumulating *Citrobacter* sp. *Microbiology* 141:2433–2441.
- Naftz DL, Morrison SJ, Felcorn EM, Freethy GW, Fuller CC, Piana MJ, Wilhelm RG, Rowland RC, Davis JA, Blue JE. 2000. Field demonstration of permeable reactive barriers to remove dissolved uranium from groundwater, Fry Canyon, Utah. Interim Report, EPA, USGS, EPA 402-C-00–001, published on web: www.epa.gov.
- Nakajima A, Sakaguchi T. 1986. Selective accumulation of heavy metals by microorganisms. *Appl Microbiol Biotechnol* 24:59–64.
- National Research Council. 2000. Research needs in subsurface science. National Academy Press. Washington, DC.
- Nester EW, Anderson DG, Roberts CE, Jr., Pearsall NN, Nester MT. 2004. *Microbiology: A human perspective*. 4th edition. New York, NY: McGraw Hill. p. 67.
- Newville M, Livins P, Yacoby Y, Rehr JJ, Stern EA. 1993. Near-edge X-ray absorption fine structure of Pb—A comparison of theory and experiment. *Phys Rev B* 47(21): 14126–14131.
- Nielsen AT, Liu W, Filipe C, Grady L, Jr., Molin S, Stahl D. 1998. Identification of a novel group of bacteria in sludge from a deteriorated biological phosphorus removal reactor. *Appl Environ Microbiol* 65: 1251–1258.
- Palie PN. 1970. Analytical chemistry of uranium. Ann Arbor: Humphrey Science Publishers, Inc. (Translated by Kaner N).
- Panak PJ, Raff J, Selenska-Pobell S, Geipel G, Bernhard G, Nitsche H. 2000. Complex formation of U(VI) with *Bacillus*-isolates from a uranium mining waste pile. *Radiochem Acta* 88:71–76.
- Ravel B, Newville M. 2005. Athena, artemis, hephaestus: Data analysis for X-ray absorption spectroscopy using IFEFFIT. *J Synchrotron Radiat* 12:537–541.
- Riley RG, Zachara JM, Wobber FJ. 1992. Chemical contaminants on DOE lands and selection of contaminant mixtures for subsurface research. DOE/ER-0547T, United State Department of Energy, Washington, DC.
- Sani RK, Peyton BM, Smith WA, Apel WA, Petersen JN. 2002. Dissimilatory reduction of Cr(VI), Fe(III), and U(VI) by *Cellulomonas* isolates. *Appl Microbiol Biotechnol* 60:192–199.
- Scott MJ, Morgan JJ. 1990. Energetics and conservative properties of redox systems. *Chem Modeling of Aqueous Systems II*. Chap. 29:368–378 (Am Chem Soc).
- Segre CU, Leyarovska NE, Chapman LD, Lavender WM, Plag PW, King AS, Kropf AJ, Bunker BA, Kemner KM, Dutta P, Duran RS, Kaduk J. 2000. The MRCAT insertion device beamline at the advanced photon source. In: Pianetta P, editor. *Synchrotron radiation instrumentation: Eleventh U.S. National Conference*. New York: American Institute of Physics. pp. 419–422.
- Spear JR, Figueroa LA, Honeyman BD. 1999. Modeling the removal of uranium U(VI) from aqueous solutions in the presence of sulfate reducing bacteria. *Environ Sci Technol* 33:2667–2675.
- Spear JR, Figueroa LA, Honeyman BD. 2000. Modeling reduction of uranium U(VI) under variable sulfate concentrations by sulfate-reducing bacteria. *Appl Environ Microbiol* 66:3711–3721.
- Stewart BD, Mayes MA, Fendorf S. 2010. Impact of uranyl-calcium-carbonato complexes on uranium(VI) adsorption to synthetic and natural sediments. *Environ Sci Technol* 44:928–934.
- Strandberg GW, Shumate SE II, Parrott JR, Jr. 1981. Microbial cells as biosorbents for heavy metals: Accumulation of uranium by *Saccharomyces cerevisiae* and *Pseudomonas aeruginosa*. *Appl Environ Microbiol* 41:237–245.
- Suzuki Y, Banfield J. 2004. Resistance to, and accumulation of, uranium by bacteria from a uranium-contaminated site. *Geomicrobiol J* 21:113–121.
- Suzuki Y, Kelly SD, Kemner KM, Banfield JF. 2002. Radionuclide contamination—Nanometre-size products of uranium bioreduction. *Nature* 419(6903):134–134.
- Tandoi V, Majone M, May J, Ramadori R. 1998. The behavior of polyphosphate accumulating *Acinetobacter* isolates in an anaerobic-aerobic chemostat. *Water Res* 32:2903–2912.
- Twigg RS. 1945. Oxidation-reduction aspects of resazurin. *Nature* 155:401–402.
- Van Veen HW, Abee T, Kortstee GJJ, Konings WN, Zehnder AJB. 1993. Characterization of two phosphate transport systems in *Acinetobacter johnsonii* 210A. *J Bacteriol* 175:200–206.
- Viamajala S, Smith WA, Sani RK, Apel WA, Petersen JN, Neal AL, Roberto FF, Newby DT, Peyton BM. 2007. Isolation and characterization of Cr(VI) reducing *Cellulomonas* spp. from subsurface soils: Implications for long term chromate reduction. *Bioresource Technol* 98: 612–622.
- Viamajala S, Peyton BM, Gerlach R, Sivaswamy V, Apel WA, Petersen JN. 2008. Permeable reactive biobarriers for in situ Cr(VI) reduction: Bench scale tests using *Cellulomonas* sp. strain ES6. *Biotech Bioeng* 101:1150–1162.
- Watts RJ. 1997. Hazardous wastes: Sources, pathways, receptors. Hoboken, NJ: John Wiley & Sons, Inc., p. 265.
- Yong P, Macaskie LE. 1995. Enhancement of uranium bioaccumulation by a *Citrobacter* sp. via enzymatically-mediated growth of polycrystalline $\text{NH}_4\text{UO}_2\text{PO}_4$. *J Chem Tech Biotechnol* 63:101–108.
- Yong P, Macaskie LE. 1998. Bioaccumulation of lanthanum, uranium and thorium, and use of a model system to develop a method for the biologically-mediated removal of plutonium from solution. *J Chem Technol Biotechnol* 71:15–26.
- Zafiri C, Kornaros K, Lyberatos G. 1999. Kinetic modeling of biological phosphorus removal with a pure culture of *Acinetobacter* sp. under aerobic, anaerobic and transient operating conditions. *Water Res* 33: 2769–2788.
- Zehnder AJB, Stumm W. 1988. Geochemistry and biogeochemistry of anaerobic habitats. *Biology of anaerobic microorganisms*. Hoboken, NJ: John Wiley and Sons. pp. 1–38.

One-Pot Aqueous Synthesis of Fe and Ag Core/Shell Nanoparticles

Kyler J. Carroll,[†] Daniel M. Hudgins,[†] Steven Spurgeon,[‡] Kenneth M. Kemner,[§]
Bhoopesh Mishra,[§] Maxim I. Boyanov,[§] Lester W. Brown III,[†] Mitra L. Taheri,[‡] and
Everett E. Carpenter^{*†}

[†]Department of Chemistry, Virginia Commonwealth University, Richmond, Virginia 23284, United States,

[‡]Department of Materials Science and Engineering, Drexel University, Philadelphia, Pennsylvania 19104,
United States, and [§]Biosciences Division Argonne National Laboratory, Argonne, Illinois 60439, United States

Received July 18, 2010. Revised Manuscript Received October 1, 2010

This article investigates a facile one-pot method for the synthesis of Fe and Ag core/shell nanoparticles by aqueous reduction under ambient conditions. We have shown that the injection time of silver nitrate into a reaction vessel containing aqueous ferrous salt, sodium borohydride, and sodium citrate is a vital parameter for the precise control of a desired core/shell structure. For example, if silver nitrate is injected one minute after sodium borohydride is added to the reaction vessel, Ag will nucleate first followed by Fe, creating monodisperse Ag/Fe core/shell nanoparticles. In contrast, if the introduction time is prolonged to 5 min, Fe nanoparticles will nucleate followed by Ag producing Fe/Ag nanoparticles. The composition, morphology, and magnetic behavior were investigated by X-ray absorption spectroscopy (XAS), X-ray photoelectron spectroscopy (XPS), X-ray diffraction (XRD), transmission electron microscopy (TEM), and room-temperature vibrating sample magnetometry (VSM). Fe/Ag core/shell nanoparticles with optical and magnetic functionality offer broad opportunities in medicine, catalysis, and chemical detection.

1. Introduction

Bimetallic nanoparticles with a core/shell morphology offer greater flexibility with enhanced properties as compared to their monometallic and bulk counterparts. The fabrication of bimetallic core/shell nanoparticles has thus attracted both fundamental and practical interest due to their potential applications in areas such as biosensing, catalysis, cancer therapy, and drug delivery.^{1–4} Various types of core/shell structures have been fabricated where the core or shell consists of metals, semiconductors, and dielectric materials.^{5–7} In addition, core/shell nanoparticles with both magnetic and optical properties offer a

range of applications from magnetic separators to optical probes and recoverable catalysts.^{8–11}

Several multistep synthetic methods have been reported to prepare bimetallic nanoparticles, including chemical reduction, microemulsion techniques, sonochemical reactions, γ -ray irradiation, and laser ablation.^{1,12–20} These methods to create core/shell nanoparticles are typically done by using presynthesized Ag or Au particles which are then deposited onto presynthesized iron oxide nanoparticles by the use of functional groups such as amines and thiols.²¹ Although these techniques have shown viability in synthesizing core/shell nanoparticles, the precise control of morphological properties is essential for many applications.

*To whom correspondence should be address. E-mail: ecarpenter2@vcu.edu. Tel: (804) 828-7508.

- (1) Park, H.-Y.; Schadt, M. J.; Wang, Lim, I. I. S.; Njoki, P. N.; Kim, S. H.; Jang, M.-Y.; Luo, J.; Zhong, C.-J. *Langmuir* **2007**, *23*, 9050.
- (2) Lee, I. S.; Lee, N.; Park, J.; Kim, B. H.; Yi, Y.-W.; Kim, T.; Kim, T. K.; Lee, I. H.; Paik, S. R.; Hyeon, T. *J. Am. Chem. Soc.* **2006**, *128*, 10658.
- (3) Lu, P.; Teranishi, T.; Asakura, K.; Miyake, M.; Toshima, N. *J. Phys. Chem. B* **1999**, *103*, 9673.
- (4) Gupta, A. K.; Gupta, M. *Biomaterials* **2005**, *26*, 3995.
- (5) Sobal, N. S.; Ebels, U.; Möhwald, H.; Giersig, M. *J. Phys. Chem. B* **2003**, *107*, 7351.
- (6) Gerion, D.; Pinaud, F.; Williams, S. C.; Parak, W. J.; Zanchet, D.; Weiss, S.; Alivisatos, A. P. *J. Phys. Chem. B* **2001**, *105*, 8861.
- (7) Sao-Joao, S.; Giorgio, S.; Penisson, J. M.; Chapon, C.; Bourgeois, S.; Henry, C. *J. Phys. Chem. B* **2004**, *109*, 342.
- (8) Jun, B.-H.; Noh, M. S.; Kim, J.; Kim, G.; Kang, H.; Kim, M.-S.; Seo, Y.-T.; Baek, J.; Kim, J.-H.; Park, J.; Kim, S.; Kim, Y.-K.; Hyeon, T.; Cho, M.-H.; Jeong, D. H.; Lee, Y.-S. *Small* **2009**, *9999*, NA.
- (9) Kim, K.; Jing Jan, H.; Shin Soo, K. *Analyst* **2009**, *134*, 208.
- (10) Noh, M. S.; Jun, B.-H.; Kim, S.; Kang, H.; Woo, M.-A.; Minai-Tehrani, A.; Kim, J.-E.; Kim, J.; Park, J.; Lim, H.-T.; Park, S.-C.; Hyeon, T.; Kim, Y.-K.; Jeong, D. H.; Lee, Y.-S.; Cho, M.-H. *Biomaterials* **2009**, *30*, 3915.

- (11) Radwan, F. N.; Carroll, K. J.; Carpenter, E. E. *J. Appl. Phys.* **2010**, *107*, 09B515.
- (12) Lu, L.; Zhang, W.; Wang, D.; Xu, X.; Miao, J.; Jiang, Y. *Mater. Lett.* **2010**, *64*, 1732.
- (13) Bala, T.; Bhame, S. D.; Joy, P. A.; Prasad, B. L. V.; Sastry, M. *J. Mater. Chem.* **2004**, *14*, 2941.
- (14) Lin, J.; Zhou, W.; Kumbhar, A.; Wiemann, J.; Fang, J.; Carpenter, E. E.; O'Connor, C. J. *J. Solid State Chem.* **2001**, *159*, 26.
- (15) Kim, K.; Jang, H. J.; Shin, K. S. *Analyst* **2009**, *134*, 308.
- (16) Kinoshita, T.; Seino, S.; Mizukoshi, Y.; Otome, Y.; Nakagawa, T.; Okitsu, K.; Yamamoto, T. A. *J. Magn. Magn. Mater.* **2005**, *293*, 106.
- (17) Zhang, J.; Post, M.; Veres, T.; Jakubek, Z. J.; Guan, J.; Wang, D.; Normandin, F.; Deslandes, Y.; Simard, B. *J. Phys. Chem. B* **2006**, *110*, 7122.
- (18) Mandal, M.; Kundu, S.; Ghosh, S. K.; Panigrahi, S.; Sau, T. K.; Yusuf, S. M.; Pal, T. *J. Colloid Interface Sci.* **2005**, *286*, 187.
- (19) Stoeva, S. I.; Huo, F.; Lee, J.-S.; Mirkin, C. A. *J. Am. Chem. Soc.* **2005**, *127*, 15362.
- (20) Wang, L.; Luo, J.; Fan, Q.; Suzuki, M.; Suzuki, I. S.; Engelhard, M. H.; Lin, Y.; Kim, N.; Wang, J. Q.; Zhong, C.-J. *J. Phys. Chem. B* **2005**, *109*, 21593.
- (21) Levin, C. S.; Hofmann, C.; Ali, T. A.; Kelly, A. T.; Morosan, E.; Nordlander, P.; Whitmire, K. H.; Halas, N. J. *ACS Nano* **2009**, *3*, 1379.

In this study, we utilize a simplistic one-pot aqueous synthesis of Fe and Ag core/shell nanoparticles using sodium borohydride and sodium citrate under ambient conditions. Although Fe/Au nanoparticles have been the subject of intense research,^{22–30} recently there has been increasing interest in the design of Fe/Ag core/shell nanoparticles due to a much larger extinction coefficient of the surface plasmon band relative to Au.^{8–10,31} In addition, Ag nanoparticles exhibit a plasmon band between 390 and 420 nm, whereas Au nanoparticles exhibit a plasmon band between 520 and 580 nm.³² Therefore, Ag nanoparticles have the ability to offer new application opportunities that can rely on the differences in the position and intensity of the surface plasmon band, relative to Au.

Recently, Lu et al. reported a two-step process to create monodisperse Fe/Ag core–shell nanoparticles to achieve higher saturation magnetization relative to the conventional iron oxide cores.¹² However, we report on the formation of Fe/Ag core/shell nanoparticles by a one-pot method. We have shown that by changing the time in which the AgNO₃ solution is added to the reduction of Fe nanoparticles, we are able to create either Ag/Fe or Fe/Ag core–shell nanoparticles. For example, if silver nitrate is injected 1 min after sodium borohydride is added to the reaction vessel, Ag will nucleate first followed by Fe, creating monodisperse Ag/Fe core/shell structures. In contrast, if the introduction time is prolonged to 5 min, Fe nanoparticles will nucleate followed by Ag growth producing Fe/Ag nanoparticles. This work offers not only a facile one-pot method for creating various types of core/shell structures by controlling one parameter, but it also has the ability to be easily scalable for industrial synthesis due to the inexpensive materials, short reaction times, and ambient conditions. Because of their potentially useful optical activity and magnetic properties, we have focused on the Ag–Fe system, although we believe the general approach described below may be applicable to other important materials systems as well.

2. Experimental Section

Iron(II) sulfate heptahydrate (FeSO₄·7H₂O), silver nitrate (AgNO₃), and sodium borohydride (NaBH₄) were purchased

from ACROS Organics. Trisodium citrate dihydrate was purchased from Mallinckrodt chemicals. All chemicals were used as received and without further purification.

Stock 0.5 M AgNO₃ aqueous solutions were made and kept under dark conditions in an amber bottle to maintain uniformity between experiments. AgNO₃ stock solutions were discarded after 1 week to ensure minimal photodegradation. In each case, the synthesis was carried out under ambient conditions.

Preparation of Fe nanoparticles. Fe nanoparticles were synthesized as previously reported.^{33,34} Briefly, to produce consistent spherical Fe nanoparticles, a borohydride to Fe ratio, and an Fe to citrate ratio were kept at 2:1 and 10:1, respectively. First, a 2.0 L solution containing 4.6 mM FeSO₄ and 0.46 mM trisodium citrate dihydrate was mixed using magnetic stirring. NaBH₄ (8.8 mM) was added to the mixture and allowed to react for 10 min. The solution was quenched with ethanol several times and magnetically separated using a rare earth magnet. After washing was complete, the remaining ethanol was decanted and the particles were placed in a vacuum oven at room temperature to dry.

Preparation of Fe/Ag and Ag/Fe Core/Shell Nanoparticles. By varying the injection time of AgNO₃ to the reaction vessel containing sodium citrate, FeSO₄, water, and NaBH₄, we were able to manipulate which metal resided in the core and the shell.

Several ratios of Ag/Fe were analyzed as well as times between the addition of NaBH₄ and AgNO₃. The Ag precursor addition time is an important parameter for creating the desired core/shell structures and will be discussed in detail below. In the reaction, sodium citrate and iron sulfate are added to 2.0 L of DI-H₂O followed by the addition of NaBH₄. The solution turns from clear to a gray/black color after the addition of NaBH₄.

Characterization. The dried powders were characterized by X-ray diffraction (XRD), transmission electron microscopy (TEM), X-ray photoelectron spectroscopy (XPS), X-ray absorption spectroscopy (XAS), and vibrating sample magnetometry (VSM) for the determination of phase, morphology, and magnetic properties. XRD measurements were performed using a PANalytical X'pert pro diffractometer at a scanning step of 0.05° with a 2θ range from 20 to 120° using a graphite monochromated Cu–K_α radiation source. Samples were ground and pressed onto a no background, low volume holder. Room-temperature magnetometry was performed on a Lakeshore Cryotronics Inc. model 7300 VSM with an applied field between –10 000 and 10 000 Oe. The powders were characterized using a JEOL JEM2100 transmission electron microscope and imaged in bright field at an accelerating voltage of 200 keV. Samples were mounted on a 300 mesh lacey carbon TEM grid. The particles were first ultrasonicated in solution for about 9 min. During this time, lacey carbon grids were immersed in chloroform for 30 s to dissolve their Formvar-backing layer. After sonication, a pipet was used to transfer a drop of each nanoparticle solution onto a grid. The grids were then placed on a hot plate at 50 °C and allowed to dry for an hour. After drying, each sample was mounted in the instrument. UV–vis absorption analysis was carried out using a Hewlett-Packard 8453 photodiode spectrophotometer. Solutions were prepared in an aqueous environment using a quartz cuvette with a 1 cm path length. X-ray photoelectron spectroscopy (XPS) was performed on a Thermo Scientific ESCALAB 250 microprobe with a focused monochromatic Al K_α X-ray (1486.6 eV) source and a 180°

- (22) Cho, S. J.; Idrobo, J. C.; Olamit, J.; Liu, K.; Browning, N. D.; Kauzlarich, S. M. *Chem. Mater.* **2005**, *17*, 3181.
 (23) Cho, S. J.; Jarrett, B. R.; Louie, A. Y.; Kauzlarich, S. M. *Nanotechnology* **2006**, *17*, 640.
 (24) Cho, S. J.; Kauzlarich, S. M.; Olamit, J.; Liu, K.; Grandjean, F.; Rebbouh, L.; Long, G. J. *J. Appl. Phys.* **2004**, *95*, 6804.
 (25) Cho, S. J.; Shahin, A. M.; Long, G. J.; Davies, J. E.; Liu, K.; Grandjean, F.; Kauzlarich, S. M. *Chem. Mater.* **2006**, *18*, 960.
 (26) Lin, J.; Zhou, W. L.; Kumbhar, A.; Wiemann, J.; Fang, J. Y.; Carpenter, E. E.; O'Connor, C. J. *J. Solid State Chem.* **2001**, *159*, 26.
 (27) Srikanth, H.; Carpenter, E. E.; Spinu, L.; Wiggins, J.; Zhou, W. L.; O'Connor, C. J. *Mater. Sci. Eng., A* **2001**, *304*, 901.
 (28) Wiggins, J.; Carpenter, E. E.; O'Connor, C. J. *J. Appl. Phys.* **2000**, *87*, 5651.
 (29) Zhou, W. L.; Carpenter, E. E.; Lin, J.; Kumbhar, A.; Sims, J.; O'Connor, C. J. *Eur. Phys. J. D* **2001**, *16*, 289.
 (30) Gole, A.; Stone, J. W.; Gemmill, W. R.; zur Loye, H.-C.; Murphy, C. J. *Langmuir* **2008**, *24*, 6232.
 (31) Lee, K. J.; Nallathamby, P. D.; Browning, L. M.; Osgood, C. J.; Xu, X.-H. N. *ACS Nano* **2007**, *1*, 133.
 (32) Cao, Jin, R.; Mirkin, C. A. *J. Am. Chem. Soc.* **2001**, *123*, 7961.

- (33) Carroll, K. J.; Hudgins, D. M.; Brown, L. W.; Iii; Yoon, S. D.; Heiman, D.; Harris, V. G.; Carpenter, E. E. *J. Appl. Phys.* **2010**, *107*, 09A303.
 (34) Carroll, K. J.; Pitts, J. A.; Zhang, K.; Pradhan, A. K.; Carpenter, E. E. *J. Appl. Phys.* **2010**, *107*, 09A302.

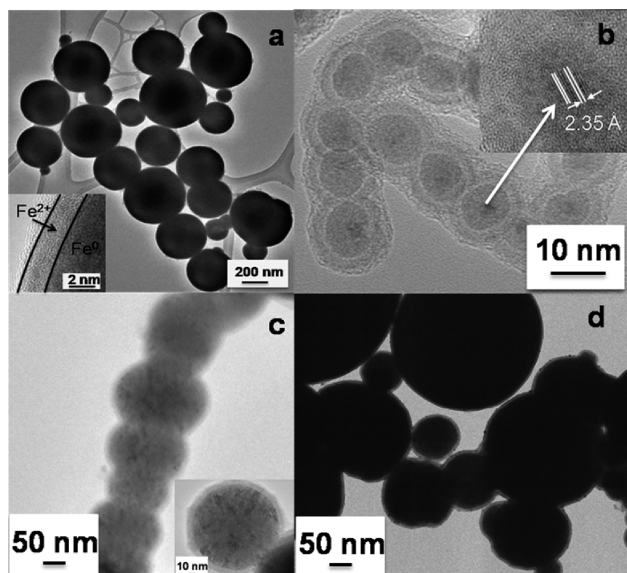


Figure 1. High-resolution TEM images of (a) as-synthesized Fe nanoparticles, (b) Ag/Fe nanoparticles showing a clear distinction between the core (Ag) and shell (FeB/Fe₂B), (c) Fe/Ag nanoparticles, and (d) Fe nanoparticles with islanding of Ag.

hemispherical analyzer with a 6-element multichannel detector. The incident X-ray beam was 45° off normal to the sample while the X-ray photoelectron detector was normal to the sample. Charge compensation was employed during data collection using an internal flood gun (2 eV electrons) and a low-energy Ar⁺ external flood gun. Binding energies of the photoelectron are corrected to the aliphatic hydrocarbon C 1s peak at 284.6 eV. A Large area XL magnetic lens with a 500 μm spot size in constant analyzer energy (CAE) mode was utilized with a pass energy of 20 eV. Thirty scans per region were taken with a step size of 0.100 eV. The powdered samples were pressed onto a strip of indium foil and mounted on a sample holder using double-sided carbon tape. Fe K edge (7112 eV) XAFS measurements (encompassing both XANES and EXAFS) were performed at the MRCAT beamline 10-BM at the Advanced Photon Source (APS). Samples were measured in transmission mode. The data quality is represented in the k-weighted spectra (see S1 in the Supporting Information). The energy of the incident X-rays was scanned using a Si(111) reflection plane of a cryogenically cooled double-crystal monochromator. Detailed XAFS analysis can be found in the Supporting Information.

3. Results and Discussion

Figure 1A–D depicts high-resolution transmission electron microscopy images. TEM observations indicates that if the reaction is left to react for 15 min, the resulting particles are approximately 5 nm Fe nanoparticles encased in 200 nm bundles (Figure 1a), as reported by others.³⁴ Typically, in an aqueous reaction where sodium borohydride is used as the reducing agent, the resulting Fe nanoparticles are in the form of borides (FeB/Fe₂B).^{35–37} However, Ekirt et al. have recently found that by adding

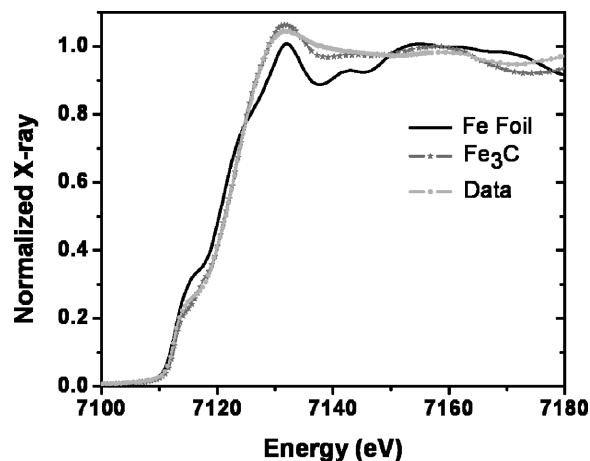


Figure 2. XANES spectra of the Fe/Ag core/shell nanoparticles plotted with spectra collected from Fe metal foil and Fe₃C standards.

a capping agent, such as sodium citrate, the resulting Fe nanoparticles are in the form of 5 nm body-centered cubic (bcc) Fe with a protective citrate layer encapsulating the particles and preventing oxidation.³⁸ This has been observed and confirmed in our work by both XRD and VSM data, which show diffraction lines of bcc-Fe and magnetization saturation values of ~175 emu/g (see Figures S4 and S5 in the Supporting Information).

Alternatively, an injection of aqueous AgNO₃ 1 min past the addition of NaBH₄ into the reaction vessel results in the formation of monodisperse Ag core and Fe shell nanoparticles with a total diameter of 12 nm (4 nm Ag core and an 8 nm Fe shell) (Figure 1b). The *d*-spacing of the core was found to be 2.350 Å, which was measured from the HR-TEM image. This spacing is consistent with that of the (111) reflection of face-centered cubic (fcc) Ag.³⁹ Figure 1c represents an injection of aqueous AgNO₃ 5 min past the addition of NaBH₄ into the reaction vessel and shows the formation of Fe/Ag core/shell nanoparticles. Lastly, if the injection of aqueous AgNO₃ is prolonged to 15 min, the formation of 200 nm Fe clusters (as in 1a) with a discontinuous shell (islanding) of Ag is shown (Figure 1d).

To gain a better understanding of the structural nature of the formed core/shell nanoparticles XAFS measurements were conducted. Figure 2 shows the Fe K-edge XANES data of the as-synthesized Ag/Fe core/shell nanoparticles plotted with spectra collected from Fe₃C and from Fe metal foil. The pre-edge and edge features of the Fe nanoparticles are clearly different from bcc Fe and match well with the Fe₃C standard. Postedge features are susceptible to longer-range structure and appear different from both the Fe₃C standard and Fe foil. Given the 8 nm thickness of the Fe shell of the core/shell nanoparticles as shown by TEM, the postedge features could not be unambiguously assigned from XANES. EXAFS analysis rules out a bcc Fe coordination environment. However, inclusion of carbon or boron atoms in addition to Fe atoms in the first shell resulted in statistically significant improvement in the fitting results of the sample.

(35) Glavee, G. N.; Klabunde, K. J.; Sorensen, C. M.; Hadjipanayis, G. C. *Langmuir* **1994**, *10*, 4726.
 (36) Glavee, G. N.; Klabunde, K. J.; Sorensen, C. M.; Hadjipanayis, G. C. *Langmuir* **1993**, *9*, 162.
 (37) Glavee, G. N.; Klabunde, K. J.; Sorensen, C. M.; Hadjipanayis, G. C. *Langmuir* **1992**, *8*, 771.

(38) Ekeirt, T. F., University of Delaware, 2010.
 (39) Mishra, Y. K.; Mohapatra, S.; Kabiraj, D.; Mohanta, B.; Lalla, N. P.; Pivin, J. C.; Avasthi, D. K. *Ser. Mater.* **2007**, *56*, 629.

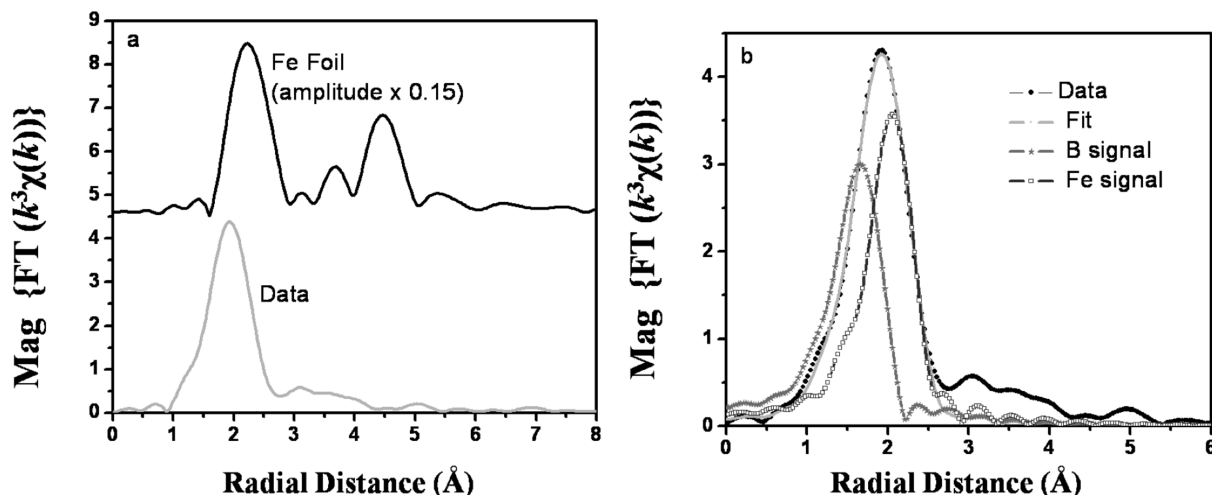


Figure 3. (a) Comparison of Fourier Transform EXAFS spectra of Fe foil and Ag/Fe; (b) Fourier Transform magnitude of the data and the fit plotted with the contributions of Fe and B signals.

Table 1. Fitting with Fe and B Paths

path	N	R (Å)	σ^2 ($\times 10^{-3}$ Å $^{-2}$)	χ^2_{ν}	R factor	E_0 (eV)
Fe–B	2.82 ± 0.14	2.18 ± 0.01	15.5^a	67	0.0014	-5.9 ± 1.8
Fe–Fe	3.52 ± 0.21	2.63 ± 0.01	11.8^a			

^aFixed to best fit value.

Hence, the two most reasonable models (i.e., carbide and boride) will be discussed further.

Comparisons of the FT EXAFS data (Figure 3a) of the Fe nanoparticles to that of bcc Fe metal show that the first FT peak is of much smaller amplitude and shifted to shorter distances, similar to what is observed by Qadri et al. with Fe-boride nanoparticles.⁴⁰ Since FeSO₄ was reduced with borohydride as the starting material, formation of Fe-boride is consistent with the chemical composition of the system. An Fe-boride standard spectrum was not available for comparison. The Ag/Fe spectrum also showed similarity to the Fe-carbide standard. However, Fe-carbide can be excluded on the basis of the chemical composition of the material. Below we discuss a fitting model based on the observed spectral similarity between the unknown sample and Fe-boride.

A single Fe shell does not reproduce well with the main FT peak in a fitting procedure. The inclusion of B atoms in addition to Fe atoms in the first shell resulted in statistically significant improvement in the fitting results of the sample. Fitting parameters for Fe-boride are given in Table 1. Magnitudes of the Fourier transform data and fit with the contribution of Fe and B signals are shown in Figure 3b. Fitting with Fe and B signals result in an average coordination numbers of ~ 3.5 Fe atoms and ~ 2.8 B atoms around Fe at an average distance of 2.63 and 2.18 Å, respectively. These distances match well both with the previously reported crystallography as well as EXAFS analysis of Fe-boride compounds.^{40,41} However,

the coordination number reported in our study is smaller than the typical Fe and B coordination number in FeB/Fe₂B nanoparticles. This can possibly arise from a thin coating of FeB/Fe₂B over a Ag core, consistent with the TEM results. The lack of second and higher shell structure in the Fourier transform of the sample (Figure 3a) is also consistent with a thin disordered Fe-boride coating over a Ag core. Since the Fe–Fe distance reported in this study (2.63 Å) falls in the distance range seen for both FeB (2.62–2.95 Å) and Fe₂B (2.40–2.72 Å), the EXAFS analysis cannot unequivocally distinguish between the formation of FeB from Fe₂B coating over the Ag core.⁴¹

Figure 4a presents the XPS survey scan of freshly prepared Fe/Ag core/shell nanoparticles. The photoelectron peaks reveal that the nanoparticle surface consists of mainly Ag, O, C and Fe, as well as trace amounts of B. C1s and O1s regions scans suggest that the nanoparticle surface contains some adsorbed citrate, which is consistent with literature.³⁸ Two peaks at ~ 192 and ~ 188 eV in the B1s region spectra could be due to a oxidized boron (borate) adsorbed on the surface or B from FeB/Fe₂B, respectively. Both of which are common with borohydride reduction.⁴² Detailed XPS region scans for Fe2p are shown in the Supporting Information (Figures S2 and S3). Shakeup and satellite peaks can be seen at 712 and 716 eV.^{43,44} Literature suggests that the smaller peak at 706.82 eV, which typically corresponds to elemental Fe

(40) Qadri, S. B.; Dinderman, M. A.; Dressick, W. J.; Schoen, P. E.; Lubitz, P.; He, J. H.; Tonucci, R. J.; Cross, J. *Appl. Phys. A: Mater. Sci. Process* **2007**, *89*, 493.

(41) Kapfenberger, C.; Albert, B.; Pottgen, R.; Huppertz, H. Z. *Kristallogr.* **2006**, *221*, 477.

(42) Nurmi, J. T.; Tratnyek, P. G.; Sarathy, V.; Baer, D. R.; Amonette, J. E.; Pecher, K.; Wang, C. M.; Linehan, J. C.; Matson, D. W.; Penn, R. L.; Driessen, M. D. *Environ. Sci. Technol.* **2005**, *39*, 1221.

(43) Joyner, D. J.; Johnson, O.; Hercules, D. M. *J. Am. Chem. Soc.* **1980**, *102*, 1910.

(44) Grosvenor, A. P.; Kobe, B. A.; Biesinger, M. C.; McIntyre, N. S. *Surf. Interface Anal.* **2004**, *36*, 1564.

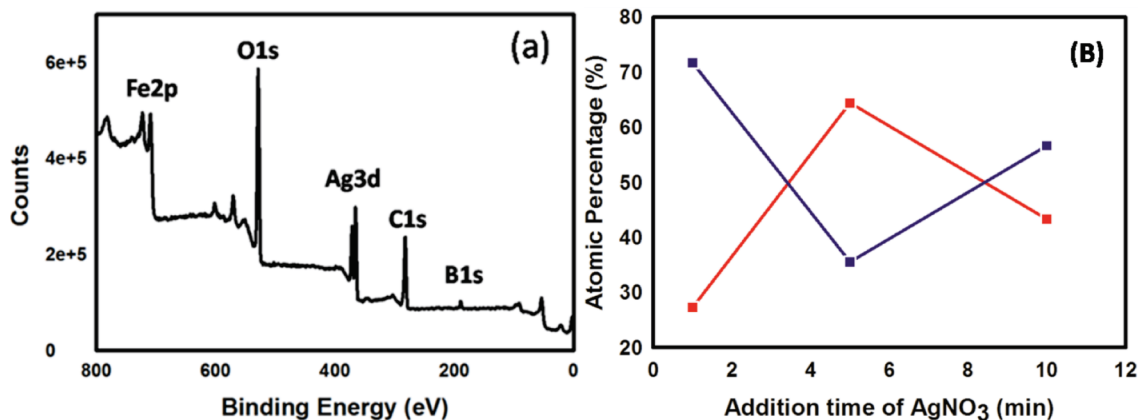


Figure 4. (a) XPS survey scan of a representative Fe/Ag core/shell nanoparticle. (b) Atomic percentage of Fe2p (blue) and Ag3d (red) as a function of AgNO₃ addition time determined by survey scans and standard sensitivity factors. The plotted solid lines are intended as a guide to the eye.

Table 2. XPS Binding Energies of FeB, Fe₂B, and Elemental Fe Core Levels

	literature			observed		
	Fe2p		B1s	Fe2p		B1s
	1/2	3/2		1/2	3/2	
Fe	720	706.9–707.4	1 min	719.5	706.9	187.77
FeB	720.3	707.2	5 min	719.98	707	187.84
Fe ₂ B	720.2	707.1	10 min	719.77	706.98	187.92

could also be also associated with FeB/Fe₂B.^{45–50} Table 2 lists the binding energies of the Fe and B core levels observed at various AgNO₃ introduction times and is compared to the literature core level values. Binding energy shifts for the corresponding elemental Fe and boride core levels are very small (within 0.3 eV) and the B1s level binding energies are very similar, making the identification of elemental Fe and FeB/Fe₂B very difficult, especially because the literature values for elemental Fe shift from 706.9 to 707.4 eV. Photoelectron peaks at ~710 and ~721 eV correspond to the binding energies of Fe 2p_{3/2} and 2p_{1/2} for Fe²⁺, respectively. Figure S5 in the Supporting Information describes how the amount of Fe²⁺ decreases depending on the introduction time of AgNO₃. For example, the particles that were formed after one minute AgNO₃ introduction formed Ag/Fe core/shell structures. Using the information from the TEM data, which suggests an 8 nm shell, it can be hypothesized that the reactivity of the Fe is increased, resulting in the surface of the nanoparticle to become easily oxidized, thus having a larger intensity of Fe²⁺. However, the particles that were formed after 5 min of AgNO₃ introduction formed Fe/Ag core/shell structures, whereas in this case, the Ag would prevent the surface of the Fe from being oxidized.

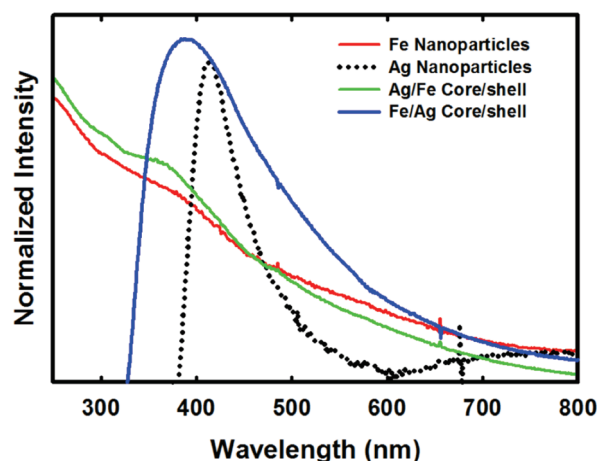


Figure 5. UV-vis absorption spectra of the Fe/Ag (solid blue line), Ag/Fe (solid green line), pure Ag (dotted black line), and pure Fe (solid red line) nanoparticles.

In addition, an increase in the intensity of the ~707 eV peak is seen at various AgNO₃ introduction times. This increase is due to the different core/shell formations. Figure 4b is a representative atomic percentage of the core level Ag3d and the Fe2p regions associated with either elemental Fe or FeB/Fe₂B as a function of different introduction times of AgNO₃. The atomic percentage was derived from integrated peak areas using standard sensitivity factors and is corrected for the differences in the photoelectron escape depth for both Ag3d and Fe2p. What this suggests is that the surface composition of Fe2p is changing because of the formation and growth of Ag nanoparticles on the surface. These results, along with the other characterization techniques, suggest the formation of Fe/Ag core/shell nanoparticles.

Figure 5 shows UV-vis absorption data of the synthesized Fe/Ag, Ag/Fe, Fe nanoparticles, and Ag nanoparticles showing various plasmon absorption properties. The absorption band of the pure Ag nanoparticles synthesized by the citrate/borohydride method is centered at 410 nm, and is consistent with the literature values.^{51–54} A plasmon shift in the absorption band to 380 nm is seen along with a broadening of the band for Fe/Ag core/shell nanoparticles and is due to the small surface layer of Ag.⁵⁵ Similar absorption properties are seen when comparing

(45) Johnson, O.; Joyner, D. J.; Hercules, D. M. *J. Phys. Chem.* **1980**, *84*, 542.

(46) Joyner, D. J.; Hercules, D. M. *J. Chem. Phys.* **1980**, *72*, 1095.

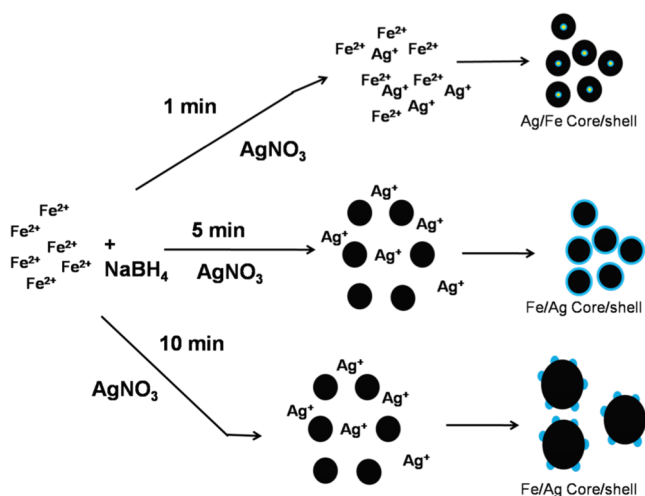
(47) Joyner, D. J.; Johnson, O.; Hercules, D. M. *J. Am. Chem. Soc.* **1980**, *102*, 1910.

(48) Joyner, D. J.; Johnson, O.; Hercules, D. M. *J. Phys. F: Met. Phys.* **1980**, *10*, 169.

(49) Joyner, D. J.; Johnson, O.; Hercules, D. M.; Bullett, D. W.; Weaver, J. H. *Phys. Rev. B* **1981**, *24*, 3122.

(50) Joyner, D. J.; Willis, R. F. *Philos. Mag., A* **1981**, *43*, 815.

Scheme 1. Proposed Reaction Scheme for the Reduction of Sodium Citrate, FeCl₂·7H₂O and NaBH₄; Addition of AgNO₃ at Various Times after the Addition of NaBH₄ Produced Various Core/Shell Morphologies



the synthesized pure Fe nanoparticles with the Ag/Fe nanoparticles, consistent with the formation of a Ag core. In addition, the absorption spectra of the synthesized pure Fe nanoparticles are similar to literature data and consists of two small bands at 200 and 360 nm.⁵⁶ The band at 200 nm corresponds to the citrate ion while the band at 360 nm corresponds to the small Fe nanoparticles.⁵⁷

4. General Discussion

The above results suggest that the formation of different core/shell structures are determined by the various introduction times of AgNO₃ to the reaction vessel after the NaBH₄ addition. Scheme 1 depicts how the introduction of AgNO₃ at different times after the addition of NaBH₄ creates various core/shell structures.

These results can be explained by the differences in the reduction potentials for Fe²⁺ and Ag⁺ in an aqueous solution ($E^{\circ}_{\text{Fe}^{2+}/\text{Fe}^0} = -0.41$ V vs SHE; $E^{\circ}_{\text{Ag}^{2+}/\text{Ag}^0} = +0.80$ V vs SHE).^{58,59} In this sense, for the 1 min introduction time after NaBH₄ addition, the Ag is formed by classical homogeneous nucleation and growth resulting in 4–5 nm spherical nanoparticles. These Ag nanoparticles serve as nucleation sites for the Fe nanoparticles to grow, which simulates a heterogeneous nucleation and

growth process.^{52,53,57,60–62} For the 5 min reaction, the Fe nanoparticles have already formed and therefore act as nucleation sites for the Ag nanoparticles to form and grow, creating an Fe/Ag core/shell nanoparticles. Lastly, the 10 min introduction of AgNO₃ produces ~150 nm Fe clusters, as previously reported.³⁴ These Fe clusters again act as nucleation sites for the Ag to form. This scenario creates islands of Ag nanoparticles on the larger Fe clusters.

Although we were unable to definitively determine if the Fe nanoparticles formed were that of elemental Fe, FeB, or Fe₂B, the room temperature VSM data shows that the particles do in fact have a high magnetization saturation (M_s) over 150 emu/g for the 10 min addition of Ag (see Figure S5 in the Supporting Information). This is a higher value than any previously reported FeO_x/Ag or iron boride nanoparticles. For the purpose of this study a saturation magnetization (M_s) was determined by plotting a magnetization versus 1/H and extrapolating to the point where 1/H is equal to zero. The samples prepared with silver nitrate injection times of one minute and five minutes after NaBH₄ addition show a saturation magnetization of 105 and 126 emu/g, respectively. The changes in the magnetization can be explained by the formation of various core/shell morphologies.

5. Conclusion

We reported on a one-pot aqueous synthesis of Fe/Ag and Ag/Fe core/shell nanoparticles synthesized using sodium borohydride and sodium citrate under ambient conditions. Fe/Ag core/shell nanoparticles with optical and magnetic functionality offer broad opportunities in medicine, catalysis and chemical detection. On the basis of TEM, XAS, and XPS characterization, we demonstrated that varying the addition times of silver nitrate we were able to form various core/shell morphologies consisting of Fe and Ag. For example, if silver nitrate is injected 1 min after sodium borohydride is added to the reaction vessel, Ag will nucleate first followed by Fe, creating monodisperse Ag/Fe core/shell nanoparticles. In contrast, if the introduction time is prolonged to 5 min, Fe nanoparticles will nucleate followed by Ag producing Fe/Ag nanoparticles. This work demonstrates a facile route to chemically manipulating the formation of core/shell nanoparticles and can be tailored to other core/shell systems with relative ease.

Acknowledgment. The authors acknowledge the use of the Centralized Research Facilities in Drexel University's College of Engineering and the MRCAT at the Advanced Photon Source, which are supported by the United States Department of Energy, Office of Science, Basic Energy Sciences Division, and the MRCAT member institutions. This research was also supported in part by the VCU Nanomaterials Core Characterization Facility, School of Engineering Foundation, and a Grant from NSF CHE-0820945 MRI (XPS).

Supporting Information Available: Experimental procedures and additional figures (PDF). This material is available free of charge via the Internet at <http://pubs.acs.org>.

- (51) Medina-Ramirez, I.; Bashir, S.; Luo, Z. P.; Liu, J. L. *Colloids Surf., B* **2009**, *73*, 185.
- (52) Prema, P.; Raju, R. *Biotechnol. Bioprocess Eng.* **2009**, *14*, 842.
- (53) Ratyakshi; Chauhan, R. P. *Asian J. Chem.* **2009**, *21*, 113.
- (54) Sato-Berru, R.; Redon, R.; Vaquez-Olmos, A.; Saniger, J. M. *J. Raman Spectrosc.* **2009**, *40*, 376.
- (55) Alvarez-Puebla, R. A.; Aroca, R. F. *Anal. Chem.* **2009**, *81*, 2280.
- (56) Blanco, M. C.; Meira, A.; Baldomir, D.; Rivas, J.; Lopezquintela, M. A. *IEEE Trans. Magn.* **1994**, *30*, 739.
- (57) Dong, X. Y.; Ji, X. H.; Wu, H. L.; Zhao, L. L.; Li, J.; Yang, W. S. *J. Phys. Chem. C* **2009**, *113*, 6573.
- (58) Wiley, B.; Sun, Y.; Xia, Y. *Acc. Chem. Res.* **2007**, *40*, 1067.
- (59) Machulek Junior, A.; de Oliveira, H. P.; Gehlen, M. H. *Photochem. Photobiol. Sci.* **2003**, *2*, 921.
- (60) Van Hynning, D. L.; Zukoski, C. F. *Langmuir* **1998**, *14*, 7034.
- (61) Calvin, S.; Carpenter, E. E.; Harris, V. G. *Phys. Rev. B: Condens. Matter Mater. Phys.* **2003**, *68*, 033411/1.
- (62) Carpenter, E. E.; Calvin, S.; Stroud, R. M.; Harris, V. G. *Chem. Mater.* **2003**, *15*, 3245.

U(VI) Reduction to Mononuclear U(IV) by *Desulfitobacterium* Species

KELLY E. FLETCHER,[†]
 MAXIM I. BOYANOV,[§] SARA H. THOMAS,[†]
 QINGZHONG WU,[†]
 KENNETH M. KEMNER,[§] AND
 FRANK E. LÖFFLER^{*,†,‡,||}

School of Civil and Environmental Engineering and School of Biology, Georgia Institute of Technology, 311 Ferst Drive, Atlanta, Georgia 30332, and Biosciences Division, Argonne National Laboratory, Argonne, Illinois 60439

Received December 1, 2009. Revised manuscript received April 4, 2010. Accepted April 22, 2010.

The bioreduction of U(VI) to U(IV) affects uranium mobility and fate in contaminated subsurface environments and is best understood in Gram-negative model organisms such as *Geobacter* and *Shewanella* spp. This study demonstrates that U(VI) reduction is a common trait of Gram-positive *Desulfitobacterium* spp. Five different *Desulfitobacterium* isolates reduced 100 μ M U(VI) to U(IV) in <10 days, whereas U(VI) remained soluble in abiotic and heat-killed controls. U(VI) reduction in live cultures was confirmed using X-ray absorption near-edge structure (XANES) analysis. Interestingly, although bioreduction of U(VI) is almost always reported to yield the uraninite mineral (UO₂), extended X-ray absorption fine structure (EXAFS) analysis demonstrated that the U(IV) produced in the *Desulfitobacterium* cultures was not UO₂. The EXAFS data indicated that the U(IV) product was a phase or mineral composed of mononuclear U(IV) atoms closely surrounded by light element shells. This atomic arrangement likely results from inner-sphere bonds between U(IV) and C/N/O- or P/S-containing ligands, such as carbonate or phosphate. The formation of a distinct U(IV) phase warrants further study because the characteristics of the reduced material affect uranium stability and fate in the contaminated subsurface.

Introduction

Uranium processing has resulted in widespread environmental contamination, particularly at U.S. Department of Energy (DOE) sites. Oxidized hexavalent uranium, U(VI), is generally soluble and mobile, but forms sparingly soluble uraninite (UO₂) upon reduction to tetravalent uranium, U(IV) (1). Therefore, bioreduction of U(VI) to U(IV) is a promising approach to immobilize uranium in subsurface environments

and prevent plume migration (2). Research on U(VI) reduction has focused on Gram-negative model organisms that reduce U(VI) to UO₂ even though the ability to reduce U(VI) is distributed among numerous bacterial phyla and recent observations suggest that not all bacteria produce UO₂ (1, 3–5). The mobility and long-term stability of uranium are influenced by the form of the reduced product; therefore, identifying and characterizing microbial U(VI) reduction products are vital for predicting U(IV) behavior in situ (3, 6–11).

At the uranium-contaminated DOE Integrated Field-Scale Subsurface Research Challenge (IFC) site in Oak Ridge, TN, organisms closely related to characterized metal reducers affiliated with both the Gram-negative delta-Proteobacteria and the Gram-positive Clostridia classes have been detected (12–14). Within the class Clostridia, *Clostridium*, *Desulfitobacterium*, and *Desulfosporosinus* populations are present at the Oak Ridge IFC site (12–14), and members of the *Clostridium* and *Desulfosporosinus* groups have been shown to reduce U(VI) to U(IV) (15, 16). *Desulfitobacterium* spp. are not recognized as U(VI) reducers, and only one strain has been implicated in U(VI) reduction (17). *Desulfitobacterium* spp. are members of soil and subsurface microbial communities, but the commonality of U(VI) reduction among members of the *Desulfitobacterium* genus is unknown. The goal of this study was to determine if U(VI) reduction is a shared trait of *Desulfitobacterium* spp. and to characterize the reduced product.

Experimental Section

Bacterial Strains and Experimental Conditions. The isolates used in this study were *Desulfitobacterium chlororespirans* strain Co23 (18), *D. dehalogenans* strain JW/IU-DC1 (19), *D. hafniense* strain JH1 (20), *Desulfitobacterium* sp. strain PCE1 (21), and *Desulfitobacterium* sp. strain Viet1 (22). These strains were isolated in different laboratories from soil, sludge, and freshwater sediments obtained from geographically distinct locations. Defined, anaerobic, 30 mM bicarbonate-buffered mineral salts medium was prepared with a N₂/CO₂ (80%/20%, vol/vol) headspace as described (23), except that the phosphate concentration was reduced from 1.5 to 0.3 mM and sodium sulfide was omitted. Medium was amended with a vitamin solution (24) and 5 or 10 mM pyruvate. Pyruvate supported fermentative growth and served as the carbon source. Glass serum bottles with 60 or 160 mL nominal capacity contained approximately 30 or 100 mL of medium, respectively, and received 3% (v/v) inocula. When cultures became visibly turbid, the vessels were amended with 100 μ M soluble U(VI) from a 30 mM uranyl carbonate stock prepared as described (23) and also received 2 mL of H₂ (strains JH1 and Viet1) or 10 mM pyruvate (strains Co23, JW/IU-DC1, and PCE1) as electron donor. Following U(VI) amendment, cultures were incubated at room temperature in the dark without shaking. Strain Viet1 cultures grown with pyruvate and then incubated at 80 °C for 15 min (which resulted in complete loss of viability) served as killed controls. After cooling to room temperature in an ice bath, the cultures were amended with 100 μ M U(VI) and electron donor. Uninoculated (i.e., abiotic) controls consisted of mineral salts medium amended with vitamins, 10 mM pyruvate, and 100 μ M uranyl carbonate.

Uranium Quantification. All manipulations were performed using anoxic techniques or inside an anoxic chamber (Coy Laboratory Products, Ann Arbor, MI). Aqueous samples (1 mL) were removed from the bottles 1 h after U(VI) amendment and periodically thereafter. Immediately after

* Corresponding author mail: Department of Microbiology, University of Tennessee, Knoxville, TN 37996-0845; phone: (865) 974-3441; fax: (865) 974-4007; e-mail: frank.loeffler@utk.edu.

[†] School of Civil and Environmental Engineering, Georgia Institute of Technology.

[‡] School of Biology, Georgia Institute of Technology.

[§] Argonne National Laboratory.

^{||} Current address: Departments of Microbiology and Civil and Environmental Engineering, University of Tennessee, Knoxville, Tennessee 37996 and Biosciences Division, Oak Ridge National Laboratory, Oak Ridge, Tennessee, 37831.

TABLE 1. U(VI) Reduction by *Desulfitobacterium* Isolates

	incubation time (days)	% uranium detected ^a		
		U(VI)	total U	U(IV)
Controls				
medium only (abiotic)	15	109.1 ± 10.7	97.4 ± 3.8	3.9 ± 3.4
strain Viet1 (heat-inactivated)	9	88.9 ± 10.6	84.1 ± 21.0	6.2 ± 14.9
Live Cultures				
strain Co23	3	BDL ^b	103.5 ± 10.8	111.7 ± 16.4
strain JH1	7	9.6 ± 8.6	127.1 ± 15.4	135.5 ± 26.1
strain JW/IU-DC1	3	BDL	90.5 ± 5.5	118.4 ± 6.6
strain PCE1	6	5.3 ± 7.4	118.5 ± 29.0	121.2 ± 9.2
strain Viet1	9	BDL	104.6 ± 19.7	108.4 ± 9.5

^a Reported values represent averages from duplicate (strain JW/IU-DC1 and strain PCE1) or triplicate vessels (strain Co23, strain JH1, strain Viet1, and controls). The percent uranium detected was determined by dividing the amount of uranium measured at the incubation time (second column) by the amount of total uranium measured initially. ^b BDL indicates that concentrations were below the detection limit of 5 μ M.

sample removal, 0.5 mL from each 1 mL sample was filtered through a 0.2 μ m membrane syringe filter (Pall Corp., East Hills, NY) or was centrifuged inside an anoxic chamber for 15 min at 10000 rpm. Concentrations of U(VI) measured in the filtrate and supernatant were similar and, in some cases, below the detection limit of 5 μ M, suggesting that both procedures removed insoluble uranium. Hence, the U(VI) concentrations measured in these samples correspond to the concentration of soluble U(VI). To verify the formation of U(IV), the remaining 0.5 mL sample volumes were transferred to sterile 2 mL plastic tubes under oxic conditions (i.e., ambient air) and placed on a shaker at 150 rpm for a minimum of 1 h to oxidize U(IV) to U(VI) (23, 25, 26). After shaking, these samples were filtered through 0.2 μ m membrane syringe filters. Exposure of the samples to air resulted in U(IV) oxidation, and subsequent U(VI) measurements yielded total uranium concentrations. Soluble U(VI) was quantified by laser excitation spectrofluorescence with a luminescence spectrometer as previously described (27). Briefly, 0.1 mL aliquots from samples were diluted with 0.9 mL of filtered, deionized water and amended with 30 μ L of a 40 mM sodium hypophosphite and 80 mM sodium pyrophosphate solution. Nominal U(IV) concentrations were calculated by subtracting the concentration of soluble U(VI) from the nominal concentration of total uranium.

Characterization of Uranium Precipitates Using X-ray Absorption Spectroscopy. Uranium L_{III} edge X-ray absorption near-edge structure (XANES) and extended X-ray absorption fine structure (EXAFS) analyses were performed to determine the valence state and the average local environment of uranium in the hydrated solid phase. Measurements were carried out at the MRCAT/EnviroCAT sector 10-ID (28), Advanced Photon Source (APS), Argonne National Laboratory, Argonne, IL. Samples for XAFS analysis were mounted by filtering the suspensions through 0.22 μ m membranes in an anoxic glovebox. The membrane and solids were sealed in Kapton film (DuPont, Circleville, OH). Samples prepared in this manner have shown no oxidation changes under ambient atmosphere for at least 8 h (29). The sealed sample holders were exposed to air for only about 30 s while being transferred from an O₂-free transport container to the N₂-purged detector housing. Beamline parameters have been published previously (30, 31). Briefly, the beamline undulator was tapered, and the incident energy was scanned by using the Si(111) reflection of the double-crystal monochromator in quick-scanning mode (approximately 3 min per scan for the extended region and 40 s per scan for the near-edge region). Sample heterogeneity and beam-induced chemical changes were closely monitored and were not observed. The linearity of the experimental setup resulted in <0.1% change in the EXAFS signal when the incident intensity was attenu-

ated by 50% (32). Data reduction and analysis were performed using the programs Autobk and Feffit (33, 34).

An alkaline (pH 10.7) solution of U/carbonate (1:30, mol/mol) was used as a standard for carbonate-complexed U(VI) (speciation ~100% UO₂(CO₃)₃). U(IV) standards included a crystalline UO₂ (Alfa Aesar, Ward Hill, MA) diluted 1:100 in SiO₂ (35) and previously characterized U(IV) nanoparticles, produced either biogenically by *Shewanella oneidensis* MR-1 (26) or abiotically by green rust (29).

Results

U(VI) Reduction Is a Common Trait of *Desulfitobacterium* Species. In live strain Viet1 cultures, the concentration of soluble U(VI) decreased with incubation time and was below the detection limit of 5 μ M 9 days after U(VI) amendment (Table 1; Figure 1A). The amount of insoluble U(IV) increased concomitantly with the decrease in soluble U(VI) (Figure 1A), indicating that the cells had reduced U(VI) to an insoluble form of U(IV). Similar observations were made in cultures of *Desulfitobacterium* sp. strains Co23, JH1, JW/IU-DC1, and PCE1. Within 7 days of U(VI) amendment, 90% of the initial U(VI) was removed from solution, whereas the nominal concentration of total uranium remained approximately constant (Table 1), indicating that soluble U(VI) was reduced to an insoluble U(IV) precipitate. In abiotic medium and heat-inactivated strain Viet1 controls, soluble U(VI) decreased negligibly, thus demonstrating that U(VI) reduction is a biotic process (Table 1; Figure 1B).

XANES and EXAFS Analyses Confirm U(VI) Reduction and Demonstrate the Formation of Mononuclear U(IV). XANES and EXAFS analyses performed on samples from all five live *Desulfitobacterium* cultures directly determined the average valence state and atomic environments of the solid phase uranium. The XANES spectra obtained from samples prepared from live *Desulfitobacterium* cultures demonstrated that at least 95% of all solid phase uranium was present as U(IV) (Figure 2), confirming the spectrofluorescence measurements and U(VI) reduction. Figure 3B shows that indistinguishable EXAFS spectra were obtained from all strains, indicating that all of the cultures generated the same U(IV) product. To further characterize the reduced product, the spectrum of the biogenic U(IV) produced in the *Desulfitobacterium* cultures was compared to U(IV) standards of known structure (Figure 3A). The Fourier transformed (FT) EXAFS spectra of a crystalline UO₂ standard and a previously characterized nanoparticulate U(IV) phase (26) show a doublet between 3 and 4.2 Å (Figure 3A). This spectral feature results from the edge-sharing U–U coordination in UO₂ at approximately 3.87 Å (details of spectral fitting parameters are provided as Supporting Information). The U(IV) produced in the *Desulfitobacterium* cultures does not show this doublet

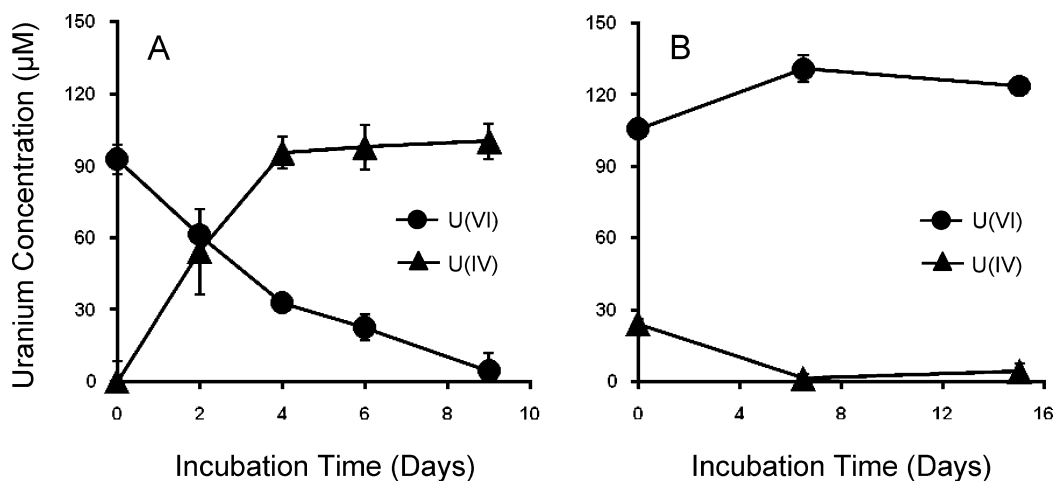


FIGURE 1. Soluble U(VI) and nominal U(IV) concentrations in live *Desulfitobacterium* sp. strain Viet1 cultures (A) and in abiotic controls (B). Data were averaged from triplicate cultures, and error bars depict one standard deviation. In some cases, error bars are not visible because standard deviations are small.

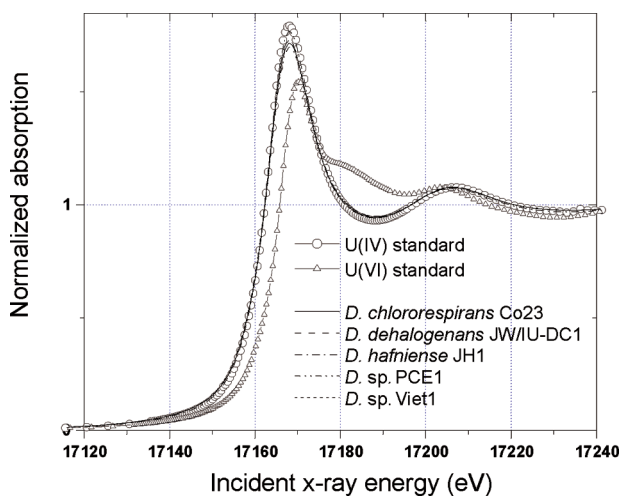


FIGURE 2. Uranium L_{III} edge XANES data obtained from the solid phase uranium in *Desulfitobacterium* cultures compared to completely reduced and oxidized standards. The data from the *Desulfitobacterium* cultures overlay each other and the U(IV) standard spectrum.

(Figure 3), and fits of the U(IV) spectra with the uraninite EXAFS model demonstrate the lack of a defined bidentate U(IV)–O₂–U(IV) coordination, which is found in uraninite or coffinite [U(SiO₄)₉(OH)₄] (see the Supporting Information). Consequently, the reduced U(IV) atoms are either individually bound to solid phase ligands or exist as molecular U(IV) minerals such as CaU(PO₄)₂ (36). The FT spectral feature observed between 2.4 and 3.6 Å in spectra obtained with the material generated in the *Desulfitobacterium* cultures is not part of the main peak contribution at 1.8 Å from the near-neighbor O atoms. Modeling indicates consistency of the additional spectral feature with the presence of at least two light atom shells (such as C/N/O or S/P) at U(IV) atom distances between 3.0 and 3.8 Å. Due to the small amplitude and overlapping peaks, the exact identity of the shells could not be unambiguously assigned. Nevertheless, the presence of the additional spectral structure, the ability to model the spectra with light atom shells, and the close distance of these shells suggest inner-sphere complexes of the U(IV) atoms with light element oxyanion ligands (e.g., carbonate, carboxyl, phosphoryl).

Discussion

Desulfitobacterium spp. are metabolically versatile anaerobic bacteria commonly present in soil, sediment, and subsurface

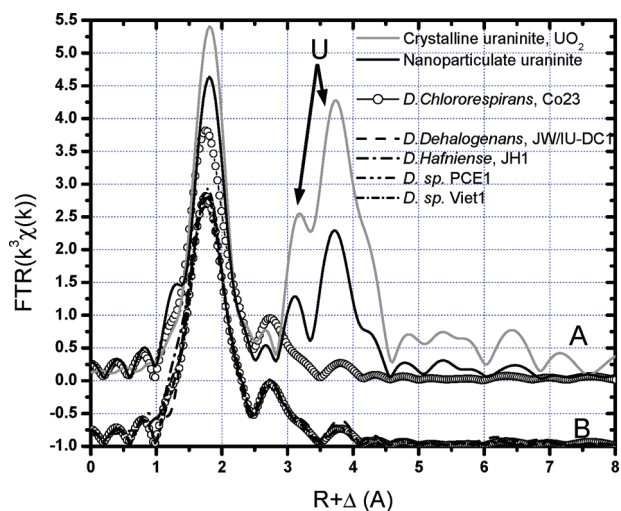


FIGURE 3. Uranium L_{III} edge EXAFS data of the U(IV) phase produced by strain Co23 (symbols) compared to (A) crystalline UO₂ and nanoparticulate UO₂ and (B) the U(IV) phases produced by four other *Desulfitobacterium* cultures. The spectral doublet resulting from U–U coordination in the UO₂ structure is indicated by the arrows (fitting details are provided in the Supporting Information). Data are k^3 weighted and FT over the range $\Delta k = 2.0\text{--}10.4 \text{ \AA}^{-1}$ using a 1.0 Å Hanning window (34).

environments and contribute to the reduction of oxidized metals and metalloids including arsenic, iron, manganese, and selenium (37, 38). The ability of members of this bacterial genus to reduce radionuclides such as U(VI) has not been established. Our findings show that U(VI) reduction is a feature shared among *Desulfitobacterium* spp. and suggest that *Desulfitobacterium* spp. play important roles in controlling subsurface uranium mobility and fate. This is of particular importance as *Desulfitobacterium* species have been detected at several uranium-impacted DOE sites (13, 14, 39).

The product of microbial U(VI) reduction is almost always reported to be nanoparticulate UO₂ (7–11, 26, 40, 41). Only in a few cases has U(VI) bioreduction resulted in the formation of products other than UO₂. Specifically, Khijniak et al. (5) demonstrated that *Thermoterrabacterium ferriducens* produces ningyoite [CaU(PO₄)₂·H₂O], Francis and Dodge (3) reported that *Clostridium* spp. produce a U(IV)–citrate complex, and Junier et al. (4) reported that UO₂ is likely not the dominant product of U(VI) reduction by spores of *Desulfotomaculum reducens* strain MI-1. Experiments assessing U(VI) microbial reduction typically use uranyl acetate

or uranyl carbonate (7–9, 25–27, 41–43), but in the experiments performed with *T. ferriducens* and the *Clostridium* spp., U(VI) was provided as uramphite [(NH₄)(UO₂)(PO₄)·3H₂O] and U(VI)–citrate, respectively (3, 5), which likely affected the form of the produced U(IV). Although some *Desulfitobacterium* spp. were reported to produce spores, strains JH1, Viet1, and PCE1 are not spore formers, indicating that vegetative cells were responsible for U(VI) reduction.

In contrast to most U(VI)-reducing organisms, including Gram-negative model organisms such as *Anaeromyxobacter*, *Geobacter*, *Desulfovibrio*, and *Shewanella* (8, 11, 25, 42, 44), *Desulfitobacterium* spp. did not produce UO₂ but generated mononuclear U(IV). Biotic factors (e.g., electron transport machineries, cellular components, extracellular features) and abiotic factors (e.g., solution composition) can influence the nature of the reduced product. For example, a U(IV) phase different from UO₂ is produced by the chemical reduction of U(VI) by Fe(II) (30). Microbial U(VI) reduction yielding UO₂ has been observed in a variety of media with diverse solution compositions including bicarbonate-buffered groundwater (25), piperazine-*N,N'*-bis(2-ethanesulfonic acid)-buffered artificial groundwater (26), 30 mM bicarbonate buffer (7, 8, 26, 41, 43), and unbuffered water (16). The medium used in our *Desulfitobacterium* experiments was similar in composition to aqueous systems used in previous work that determined UO₂ as the reduced product, suggesting biological factors are involved; however, mononuclear U(IV) formation may be controlled by a complex interplay between biotic and abiotic (e.g., medium composition) factors, which future studies should explore in more detail.

Similarly to UO₂, the mononuclear U(IV) phase produced in *Desulfitobacterium* cultures is readily oxidized upon oxygen exposure (Table 1), but further characterization is needed to describe the stability and mobility of mononuclear U(IV) (e.g., the potential for complexation with organic ligands and colloidal transport). Comprehensive knowledge of the different processes and mechanisms involved in U(VI) reduction is crucial for making meaningful predictions about the mobility and fate of uranium in the contaminated subsurface and for achieving lasting uranium immobilization in situ. Future studies assessing the biomolecular mechanisms of U(VI) reduction and identifying and characterizing the properties of the reduced product(s) are required to understand the contributions of *Desulfitobacterium* spp. to U(VI) immobilization.

Acknowledgments

We thank M. J. Beazley for helpful discussions and Tomohiro Shibata at the MRCAT/EnviroCAT beamline and Snow Rui from the University of Notre Dame for assistance in collection of the XAFS data. This research was supported by the U.S. DOE Office of Science (OS), Biological and Environmental Research Division (BER), Environmental Remediation Sciences Program (ERSP, Grant ER64782, and the ANL Subsurface Science Focus Area Program). MRCAT/EnviroCAT operations are supported by the U.S. Department of Energy and the MRCAT/EnviroCAT member institutions. Use of the Advanced Photon Source is supported by the U.S. DOE Basic Energy Sciences (BES) Division under Contract DE-AC02-06CH11357. K.E.F. acknowledges financial support through NSF IGERT and NSF graduate research fellowships.

Supporting Information Available

Additional information on EXAFS data analysis, EXAFS data quality and useable range, and fits of the EXAFS spectra. This material is available free of charge via the Internet at <http://pubs.acs.org>.

Literature Cited

- Wall, J. D.; Krumholz, L. R. Uranium reduction. *Annu. Rev. Microbiol.* **2006**, *60*, 149–166.
- Wu, W. M.; Carley, J.; Gentry, T.; Ginder-Vogel, M. A.; Fienen, M.; Mehlhorn, T.; Yan, H.; Carroll, S.; Pace, M. N.; Nyman, J.; Luo, J.; Gentile, M. E.; Fields, M. W.; Hickey, R. F.; Gu, B. H.; Watson, D.; Cirpka, O. A.; Zhou, J. Z.; Fendorf, S.; Kitanidis, P. K.; Jardine, P. M.; Criddle, C. S. Pilot-scale in situ bioremediation of uranium in a highly contaminated aquifer. 2. Reduction of U(VI) and geochemical control of U(VI) bioavailability. *Environ. Sci. Technol.* **2006**, *40*, 3986–3995.
- Francis, A. J.; Dodge, C. J. Bioreduction of uranium(VI) complexed with citric acid by *Clostridia* affects its structure and solubility. *Environ. Sci. Technol.* **2008**, *42*, 8277–8282.
- Junier, P.; Frutschi, M.; Wigginton, N. S.; Vecchia, E. D.; Sharp, J. O.; Suvorova, E.; Schofield, E.; Bargar, J. R.; Bernier-Latmani, R. U(VI) reduction by *Desulfotomaculum reducens* MI-1. *Geochim. Cosmochim. Acta* **2009**, *73*, A610–A610.
- Khijniak, T. V.; Slobodkin, A. I.; Coker, V.; Renshaw, J. C.; Livens, F. R.; Bonch-Osmolovskaya, E. A.; Birkeland, N. K.; Medvedeva-Lyalikova, N. N.; Lloyd, J. R. Reduction of uranium(VI) phosphate during growth of the thermophilic bacterium *Thermoterrabacterium ferrireducens*. *Appl. Environ. Microbiol.* **2005**, *71*, 6423–6426.
- Bargar, J. R.; Bernier-Latmani, R.; Giammar, D. E.; Tebo, B. M. Biogenic uraninite nanoparticles and their importance for uranium remediation. *Elements* **2008**, *4*, 407–412.
- Marshall, M. J.; Beliaev, A. S.; Dohnalkova, A. C.; Kennedy, D. W.; Shi, L.; Wang, Z. M.; Boyanov, M. I.; Lai, B.; Kemner, K. M.; McLean, J. S.; Reed, S. B.; Culley, D. E.; Bailey, V. L.; Simonson, C. J.; Saffarini, D. A.; Romine, M. F.; Zachara, J. M.; Fredrickson, J. K. c-Type cytochrome-dependent formation of U(IV) nanoparticles by *Shewanella oneidensis*. *PLoS Biol.* **2006**, *4*, 1324–1333.
- Marshall, M. J.; Dohnalkova, A. C.; Kennedy, D. W.; Plymale, A. E.; Thomas, S. H.; Löffler, F. E.; Sanford, R. A.; Zachara, J. M.; Fredrickson, J. K.; Beliaev, A. S. Electron donor-dependent radionuclide reduction and nanoparticle formation by *Anaeromyxobacter dehalogenans* strain 2CP-C. *Environ. Microbiol.* **2009**, *11*, 534–543.
- Singer, D. M.; Farges, F.; Brown, G. E. Biogenic nanoparticulate UO₂: synthesis, characterization, and factors affecting surface reactivity. *Geochim. Cosmochim. Acta* **2009**, *73*, 3593–3611.
- Suzuki, Y.; Kelly, S. D.; Kemner, K. M.; Banfield, J. F. Radionuclide contamination—nanometre-size products of uranium bioreduction. *Nature* **2002**, *419*, 134–134.
- Sharp, J. O.; Schofield, E. J.; Veeramani, H.; Suvorova, E. I.; Kennedy, D. W.; Marshall, M. J.; Mehta, A.; Bargar, J. R.; Bernier-Latmani, R. Structural similarities between biogenic uraninites produced by phylogenetically and metabolically diverse bacteria. *Environ. Sci. Technol.* **2009**, *43*, 8295–8301.
- Cardenas, E.; Wu, W. M.; Leigh, M. B.; Carley, J.; Carroll, S.; Gentry, T.; Luo, J.; Watson, D.; Gu, B.; Ginder-Vogel, M.; Kitanidis, P. K.; Jardine, P. M.; Zhou, J.; Criddle, C. S.; Marsh, T. L.; Tiedje, J. A. Microbial communities in contaminated sediments, associated with bioremediation of uranium to submicromolar levels. *Appl. Environ. Microbiol.* **2008**, *74*, 3718–3729.
- North, N. N.; Dollhopf, S. L.; Petrie, L.; Istok, J. D.; Balkwill, D. L.; Kostka, J. E. Change in bacterial community structure during in situ biostimulation of subsurface sediment cocontaminated with uranium and nitrate. *Appl. Environ. Microbiol.* **2004**, *70*, 4911–4920.
- Petrie, L.; North, N. N.; Dollhopf, S. L.; Balkwill, D. L.; Kostka, J. E. Enumeration and characterization of iron(III)-reducing microbial communities from acidic subsurface sediments contaminated with uranium(VI). *Appl. Environ. Microbiol.* **2003**, *69*, 7467–7479.
- Gao, W. M.; Francis, A. J. Reduction of uranium(VI) to uranium(IV) by *Clostridia*. *Appl. Environ. Microbiol.* **2008**, *74*, 4580–4584.
- Suzuki, Y.; Kelly, S. D.; Kemner, K. M.; Banfield, J. F. Enzymatic U(VI) reduction by *Desulfosporosinus* species. *Radiochim. Acta* **2004**, *92*, 11–16.
- Shelobolina, E. S.; Vanpraagh, C. G.; Lovley, D. R. Use of ferric and ferrous iron containing minerals for respiration by *Desulfitobacterium frappieri*. *Geomicrobiol. J.* **2003**, *20*, 143–156.
- Sanford, R. A.; Cole, J. R.; Löffler, F. E.; Tiedje, J. N. Characterization of *Desulfitobacterium chlororespirans* sp. nov., which grows by coupling the oxidation of lactate to the reductive dechlorination of 3-chloro-4-hydroxybenzoate. *Appl. Environ. Microbiol.* **1996**, *62*, 3800–3808.

- (19) Utkin, I.; Woese, C.; Wiegel, J. Isolation and characterization of *Desulfitobacterium dehalogenans* gen. nov., sp. nov., an anaerobic bacterium which reductively dechlorinates chlorophenolic compounds. *Int. J. Syst. Bacteriol.* **1994**, *44*, 612–619.
- (20) Fletcher, K. E.; Ritalahti, K. M.; Pennell, K. D.; Takamizawa, K.; Löffler, F. E. Resolution of culture *Clostridium bifermentans* DPH-1 into two populations, a *Clostridium* sp. and tetrachloroethene-dechlorinating *Desulfitobacterium hafniense* strain JH1. *Appl. Environ. Microbiol.* **2008**, *74*, 6141–6143.
- (21) Gerritse, J.; Renard, V.; Gomes, T. M. P.; Lawson, P. A.; Collins, M. D.; Gottschal, J. C. *Desulfitobacterium* sp. strain PCE1, an anaerobic bacterium that can grow by reductive dechlorination of tetrachloroethene or ortho-chlorinated phenols. *Arch. Microbiol.* **1996**, *165*, 132–140.
- (22) Tront, J. M.; Amos, B. K.; Löffler, F. E.; Saunders, F. M. Activity of *Desulfitobacterium* sp. strain Viet1 demonstrates bioavailability of 2,4-dichlorophenol previously sequestered by the aquatic plant *Lemna minor*. *Environ. Sci. Technol.* **2006**, *40*, 529–535.
- (23) Sanford, R. A.; Wu, Q.; Sung, Y.; Thomas, S. H.; Amos, B. K.; Prince, E. K.; Löffler, F. E. Hexavalent uranium supports growth of *Anaeromyxobacter dehalogenans* and *Geobacter* spp. with lower than predicted biomass yields. *Environ. Microbiol.* **2007**, *9*, 2885–2893.
- (24) Wolin, E. A.; Wolin, M. J.; Wolfe, R. S. Formation of methane by bacterial extracts. *J. Biol. Chem.* **1963**, *238*, 2882–2886.
- (25) Gorby, Y.; Lovley, D. R. Enzymatic uranium precipitation. *Environ. Sci. Technol.* **1992**, *26*, 205–207.
- (26) Burgos, W. D.; McDonough, J. T.; Senko, J. M.; Zhang, G. X.; Dohnalkova, A. C.; Kelly, S. D.; Gorby, Y.; Kemner, K. M. Characterization of uraninite nanoparticles produced by *Shewanella oneidensis* MR-1. *Geochim. Cosmochim. Acta* **2008**, *72*, 4901–4915.
- (27) Wu, Q.; Sanford, R. A.; Löffler, F. E. Uranium(VI) reduction by *Anaeromyxobacter dehalogenans* strain 2CP-C. *Appl. Environ. Microbiol.* **2006**, *72*, 3608–3614.
- (28) Segre, C. U.; Leyarovska, N. E.; Chapman, L. D.; Lavender, W. W.; Plag, P. W.; King, A. S.; Kropf, A. J.; Bunker, B. A.; Kemner, K. M.; Dutta, P.; Duran, R. S.; Kaduk, J. The MRCAT insertion device beamline at the Advanced Photon Source In *Synchrotron Radiation Instrumentation: Eleventh U. S. National Conference*; Pianetta, P., Ed.; American Institute of Physics: New York, 2000; Vol. CP521, pp 419–422.
- (29) O'Loughlin, E. J.; Kelly, S. D.; Cook, R. E.; Csencsits, R.; Kemner, K. M. Reduction of uranium(VI) by mixed iron(II)/iron(III) hydroxide (green rust): formation of UO₂ nanoparticles. *Environ. Sci. Technol.* **2003**, *37*, 721–727.
- (30) Boyanov, M. I.; O'Loughlin, E. J.; Roden, E. E.; Fein, J. B.; Kemner, K. M. Adsorption of Fe(II) and U(VI) to carboxyl-functionalized microspheres: the influence of speciation on uranyl reduction studied by titration and XAFS. *Geochim. Cosmochim. Acta* **2007**, *71*, 1898–1912.
- (31) Kemner, K. M.; Kelly, S. D. Synchrotron-based techniques for monitoring metal transformations In *Manual of Environmental Microbiology*, 3rd ed.; Hurst, C. J., Ed.; ASM Press: Washington, DC, 2007; pp 1183–1194.
- (32) Kemner, K. M.; Kropf, J.; Bunker, B. A. A low-temperature total electron yield detector for X-ray absorption fine-structure spectra. *Rev. Sci. Instrum.* **1994**, *65*, 3667–3669.
- (33) Newville, M.; Livins, P.; Yacoby, Y.; Rehr, J. J.; Stern, E. A. Near-edge X-ray absorption fine structure of Pb—a comparison of theory and experiment. *Phys. Rev. B* **1993**, *47*, 14126–14131.
- (34) Newville, M.; Ravel, B.; Haskel, D.; Rehr, J. J.; Stern, E. A.; Yacoby, Y. Analysis of multiple-scattering XAFS data using theoretical standards. *Physica B* **1995**, *208–209*, 154–156.
- (35) Kelly, S. D.; Kemner, K. M.; Fein, J. B.; Fowle, D. A.; Boyanov, M. I.; Bunker, B. A.; Yee, N. X-ray absorption fine structure determination of pH-dependent U-bacterial cell wall interactions. *Geochim. Cosmochim. Acta* **2002**, *66*, 3855–3871.
- (36) Dusauroy, Y.; Ghermani, N. E.; Podor, R.; Cuney, M. Low-temperature ordered phase of CaU(PO₄)₂: synthesis and crystal structure. *Eur. J. Mineral.* **1996**, *8*, 667–673.
- (37) Lanthier, M.; Villemur, R.; Lépine, F.; Bisailon, J. G.; Beaudet, R. Geographic distribution of *Desulfitobacterium frappieri* PCP-1 and *Desulfitobacterium* spp. in soils from the province of Quebec, Canada. *FEMS Microbiol. Ecol.* **2001**, *36*, 185–191.
- (38) Villemur, R.; Lanthier, M.; Beaudet, R.; Lépine, F. The *Desulfitobacterium* genus. *FEMS Microbiol. Rev.* **2006**, *30*, 706–733.
- (39) Finneran, K. T.; Forbush, H. M.; VanPraagh, C. V. G.; Lovley, D. R. *Desulfitobacterium metallireducens* sp. nov., an anaerobic bacterium that couples growth to the reduction of metals and humic acids as well as chlorinated compounds. *Int. J. Syst. Evol. Microbiol.* **2002**, *52*, 1929–1935.
- (40) Schofield, E. J.; Veeramani, H.; Sharp, J. O.; Suvorova, E.; Bernier-Latmani, R.; Mehta, A.; Stahlman, J.; Webb, S. M.; Clark, D. L.; Conradson, S. D.; Ilton, E. S.; Bargar, J. R. Structure of biogenic uraninite produced by *Shewanella oneidensis* strain MR-1. *Environ. Sci. Technol.* **2008**, *42*, 7898–7904.
- (41) Senko, J. M.; Kelly, S. D.; Dohnalkova, A. C.; McDonough, J. T.; Kemner, K. M.; Burgos, W. D. The effect of U(VI) bioreduction kinetics on subsequent reoxidation of biogenic U(IV). *Geochim. Cosmochim. Acta* **2007**, *71*, 4644–4654.
- (42) Fredrickson, J. K.; Zachara, J. M.; Kennedy, D. W.; Liu, C. X.; Duff, M. C.; Hunter, D. B.; Dohnalkova, A. Influence of Mn oxides on the reduction of uranium(VI) by the metal-reducing bacterium *Shewanella putrefaciens*. *Geochim. Cosmochim. Acta* **2002**, *66*, 3247–3262.
- (43) Lovley, D. R.; Phillips, E. J. P. Bioremediation of uranium contamination with enzymatic uranium reduction. *Environ. Sci. Technol.* **1992**, *26*, 2228–2234.
- (44) Lovley, D. R.; Phillips, E. J. P. Reduction of uranium by *Desulfobrevibrio desulfuricans*. *Appl. Environ. Microbiol.* **1992**, *58*, 850–856.

ES903636C

Effects of Oxyanions, Natural Organic Matter, and Bacterial Cell Numbers on the Bioreduction of Lepidocrocite (γ -FeOOH) and the Formation of Secondary Mineralization Products

EDWARD J. O'LOUGHLIN,^{*,†}
CHRISTOPHER A. GORSKI,[‡]
MICHELLE M. SCHERER,[‡]
MAXIM I. BOYANOV,[†] AND
KENNETH M. KEMNER[†]

Biosciences Division, Argonne National Laboratory,
Argonne, Illinois 60439-4843, and Department of Civil and
Environmental Engineering, University of Iowa, Iowa City,
Iowa 52242-1527

Received January 27, 2010. Revised manuscript received
May 5, 2010. Accepted May 7, 2010.

Microbial reduction of Fe(III) oxides results in the production of Fe(II) and may lead to the subsequent formation of Fe(II)-bearing secondary mineralization products including magnetite, siderite, vivianite, chukanovite (ferrous hydroxy carbonate (FHC)), and green rust; however, the factors controlling the formation of specific Fe(II) phases are often not well-defined. This study examined effects of (i) a range of inorganic oxyanions (arsenate, borate, molybdate, phosphate, silicate, and tungstate), (ii) natural organic matter (citrate, oxalate, microbial extracellular polymeric substances [EPS], and humic substances), and (iii) the type and number of dissimilatory iron-reducing bacteria on the bioreduction of lepidocrocite and formation of Fe(II)-bearing secondary mineralization products. The bioreduction kinetics clustered into two distinct Fe(II) production profiles. "Fast" Fe(II) production kinetics [19–24 mM Fe(II) d⁻¹] were accompanied by formation of magnetite and FHC in the unamended control and in systems amended with borate, oxalate, gellan EPS, or Pony Lake fulvic acid or having "low" cell numbers. Systems amended with arsenate, citrate, molybdate, phosphate, silicate, tungstate, EPS from *Shewanella putrefaciens* CN32, or humic substances derived from terrestrial plant material or with "high" cell numbers exhibited comparatively slow Fe(II) production kinetics [1.8–4.0 mM Fe(II) d⁻¹] and the formation of green rust. The results are consistent with a conceptual model whereby competitive sorption of more strongly bound anions blocks access of bacterial cells and reduced electron-shuttling compounds to sites on the iron oxide surface, thereby limiting the rate of bioreduction.

Introduction

The biogeochemical cycling of Fe in aquatic and terrestrial environments is complex, involving a suite of highly inter-

dependent biotic and abiotic processes. For example, microbial reduction of Fe(III) oxides results in the production of Fe(II) and may lead to formation of Fe(II)-bearing secondary mineralization products including magnetite, siderite, vivianite, chukanovite (ferrous hydroxy carbonate (FHC)), and green rust. Green rusts—mixed Fe(II)/Fe(III) layered double hydroxides—have been reported as products of the bioreduction of Fe(III) oxides in laboratory-based studies (1–13), as well as in Fe(III)/Fe(II) transition zones in natural systems (14–18).

The factors controlling formation of specific Fe(II) phases as a consequence of microbial Fe(III) reduction are complex and not fully understood; however, the rate and magnitude of Fe(II) production and its reaction with residual Fe(III) phases and other ligands (e.g., phosphate, carbonate) are often cited as primary factors (2, 19–23). In laboratory experiments with single Fe(III) oxide phases, the formation of green rust as a secondary mineralization product is typically linked to phosphate concentration or the number of dissimilatory iron-reducing bacteria (IRB) present (1, 2, 5, 11, 13). In natural systems, the factors contributing to green rust formation have yet to be identified. Soils and sediments contain a range of organic and inorganic ligands (e.g., inorganic oxyanions such as phosphate and silicate, as well as natural organic matter [NOM] ranging from low-molecular-mass aliphatic acids to high-molecular-mass biopolymers and humic substances) that are known to affect Fe(II)/Fe(III) redox transformations and accompanying changes in Fe speciation (24); however, their potential role in the formation of green rusts in these environments is uncertain. For example, a green rust phase was identified by X-ray absorption spectroscopy analysis of Fe-rich lacustrine sediments containing high As levels (18), although what role, if any, As played in formation of green rust in these sediments remains unclear.

To better understand the factors contributing to the formation of green rust as a secondary mineralization product of the bioreduction of Fe(III) oxides, we examined the effects of (i) the oxyanions arsenate, borate, molybdate, phosphate, silicate, and tungstate; (ii) NOM including aliphatic acids (citrate and oxalate), humic substances (Elliott soil humic acid [ESHA], leonardite humic acid [LHA], Pony Lake fulvic acid [PLFA], Suwannee River fulvic acid [SRFA], and Suwannee River humic acid [SRHA]), and microbially produced extracellular polymeric substances (EPS); and (iii) the type and number of bacterial cells on the bioreduction of lepidocrocite (γ -FeOOH) and the accompanying formation of Fe(II)-bearing secondary mineralization products.

Experimental Section

Details on the sources of chemicals, synthesis and characterization of lepidocrocite, and isolation of EPS produced by *Shewanella putrefaciens* CN32 (hereafter designated CN32 EPS) are in the Supporting Information. The experimental systems consisted of sterile 160 mL serum vials containing 100 mL of sterile defined mineral medium (DMM) (6) with Fe(III) as lepidocrocite (80 mM), formate (75 mM), and anthraquinone-2,6-disulfonate (AQDS) (100 μ M); the levels of lepidocrocite and formate were chosen to provide sufficient material for frequent sampling over the course of the experiments and to ensure that electron donor limiting conditions did not develop. DMM was prepared by combining all components except formate, AQDS, and oxyanions/NOM. The pH was adjusted to 7.5, and the medium was autoclaved. After the medium cooled to ambient temperature,

* Corresponding author phone: 630-252-9902; fax: 630-252-9793; e-mail: oloughlin@anl.gov.

[†] Argonne National Laboratory.

[‡] University of Iowa.

TABLE 1. Fe(II) Production Rates^a and Identification of Secondary Mineralization Products Based on XRD, ⁵⁷Fe Mössbauer Spectroscopy, and SEM Imaging

system	Fe(II) production rate		identification of secondary mineralization products ^b		
	mM Fe(II) d ⁻¹	kinetic profile ^c	XRD	Mössbauer	SEM ^d
no amendment	21.66 ± 0.87	fast	Mag ^e , FHC ^f (trace)	Mag, FHC	Mag, FHC (minor)
Oxyanions					
arsenate (500 μM)	2.19 ± 0.096	slow	GR ^g	GR	GR
borate (500 μM)	21.09 ± 3.36	fast	Mag, FHC (trace)	Mag, FHC	Mag, FHC (minor)
borate (5 mM)	21.39 ± 3.13	fast	Mag, FHC (trace)	ND ^h	Mag, FHC (minor)
molybdate (500 μM)	2.44 ± 0.102	slow	GR	GR	GR
phosphate (500 μM)	2.85 ± 0.154	slow	GR	GR	GR
silicate (500 μM)	2.63 ± 0.122	slow	GR	GR	GR
tungstate (500 μM)	2.56 ± 0.132	slow	GR	GR	GR
Natural Organic Matter					
citrate (500 μM)	2.41 ± 0.180	slow	GR	GR	GR
oxalate (500 μM)	21.55 ± 1.37	fast	Mag, FHC (trace)	Mag, FHC	Mag, FHC (minor)
oxalate (5 mM)	20.74 ± 1.33	fast	Mag, FHC (trace)	ND	Mag, FHC (minor)
Elliott soil humic acid (20 mg L ⁻¹)	2.21 ± 0.117	slow	GR	ND	GR
leonardite humic acid (20 mg L ⁻¹)	2.42 ± 0.144	slow	GR	ND	GR
Pony Lake fulvic acid (20 mg L ⁻¹)	25.14 ± 3.93	fast	Mag, FHC (trace)	ND	Mag, FHC (minor)
Suwannee River fulvic acid (20 mg L ⁻¹)	1.81 ± 0.043	slow	GR	ND	GR
Suwannee River humic acid (20 mg L ⁻¹)	2.61 ± 0.237	slow	GR	GR	GR
EPS from <i>S. putrefaciens</i> CN32 (100 mg L ⁻¹)	2.54 ± 0.265	slow	GR	ND	GR
gellan (100 mg L ⁻¹)	26.23 ± 1.14	fast	Mag, FHC (trace)	ND	Mag, FHC (minor)
Biomass					
<i>S. putrefaciens</i> ATCC 8071 (5 × 10 ⁹ cells mL ⁻¹)	19.84 ± 2.56	fast	Mag, FHC (trace)	ND	ND
<i>S. putrefaciens</i> ATCC 8071 (1 × 10 ¹⁰ cells mL ⁻¹)	4.00 ± 0.255	fast	GR	ND	ND
<i>S. putrefaciens</i> CN32 (5 × 10 ⁹ cells mL ⁻¹)	21.66 ± 0.87	fast	Mag, FHC (trace)	Mag, FHC	Mag, FHC (minor)
<i>S. putrefaciens</i> CN32 (1 × 10 ¹⁰ cells mL ⁻¹)	24.26 ± 6.35	fast	Mag, FHC (trace)	ND	ND
<i>S. putrefaciens</i> CN32 (2 × 10 ¹⁰ cells mL ⁻¹)	3.66 ± 0.400	slow	GR	ND	ND

^a Fe(II) production rates calculated by linear regression using least-squares regression of the data during the period of maximum sustained Fe(II) production. ^b Additional information on the results of XRD (Figures S3–S6), Mössbauer spectroscopy (Table S3) and SEM imaging (Figures S7–S12) is in Supporting Information. ^c Fe(II) production profiles designated as “fast” or “slow” as described in the Results section. ^d Identification based on particle morphology. ^e Magnetite (Mag). ^f Ferrous hydroxy carbonate (FHC). ^g Green rust (GR). ^h Not determined (ND).

formate and AQDS were added from filter-sterilized stock solutions. The medium was then portioned into sterile serum bottles, and NOM or oxyanions were added to achieve the concentrations indicated in Table 1. The bottles were sealed with Teflon-lined rubber septa and aluminum crimp caps and sparged with sterile Ar to remove molecular oxygen. All systems were prepared in duplicate.

The inoculum was prepared from late-log-phase cultures of *S. putrefaciens* strain CN32 (ATCC BAA-543) or *S. putrefaciens* strain 8071 (ATCC 8071) as described by O’Loughlin et al. (7). Experiments were initiated by spiking each vial with the volume of inoculum needed to achieve the desired cell density (5 × 10⁹ cells mL⁻¹ of *S. putrefaciens* CN32 unless otherwise indicated). The effect of metabolically inactive cells on the abiotic reduction of lepidocrocite was determined with H₂ as the reductant in the presence of Pd catalyst as described by O’Loughlin (6), with the addition of pasteurized (70 °C for 1 h) *S. putrefaciens* CN32 cells. The suspensions were placed on a roller drum and incubated at 30 °C in the dark. Samples of the suspensions-for monitoring pH and Fe(II), as well as for identification of secondary mineralization products by X-ray diffraction (XRD), scanning electron microscopy (SEM), and ⁵⁷Fe Mössbauer spectroscopy (see Supporting Information for details)-were collected with sterile syringes. Unless otherwise indicated, sample collection and processing were conducted in a glovebox containing an anoxic atmosphere (95% N₂ with 5% H₂).

Results

Bioreduction of Lepidocrocite. Lepidocrocite was readily bioreduced by *S. putrefaciens* CN32 in unamended DMM. After inoculation, Fe(II) production commenced without a significant lag, reaching a concentration of 25 mM within

24 h and remaining at 25–30 mM for the duration of the experiment (Figure 1A). XRD analysis of the solids remaining 50 d after inoculation indicated complete removal of lepidocrocite, with formation of magnetite and traces of FHC (Figure 2). Analysis of the solids by Mössbauer spectroscopy (Figure 3) also indicated complete removal of lepidocrocite and the formation of magnetite (86% of total Fe) and FHC (14% of total Fe); the corresponding Mössbauer hyperfine parameters are listed in Table S3 (Supporting Information). SEM imaging of the solids (Figures 4A and 4B) showed the presence of rounded, cubic crystallites (~50 nm), consistent with fine-grained magnetite commonly observed as a secondary mineralization product of Fe(III) oxide bioreduction (2, 5, 25–28), as well as platy, micrometer-sized crystallites with a morphology consistent with FHC formed by bioreduction of a ferrihydrite-akaganéite mixture (26).

Phosphate binds strongly to Fe(III) oxides through formation of inner-sphere complexes (24) known to affect the stability and subsequent transformations of Fe(III) oxides (including biotic and abiotic reduction) (13, 29, 30). The addition of phosphate (500 μM) significantly affected lepidocrocite bioreduction (Figure 1A). Initially, Fe(II) production was suppressed; only 3 mM of Fe(II) was produced within the first 24 h (compared to 25 mM of Fe(II) in the absence of P), and significant additional Fe(II) production was not observed until day 5. The concentration of Fe(II) increased through day 32, then remained at 56–61 mM. The bioreduction of lepidocrocite in the presence of 500 μM phosphate resulted in the formation of green rust, as indicated by XRD and Mössbauer analysis of the solids (Figures 2 and 3); neither magnetite nor FHC was observed. The solids consisted primarily of platy hexagonal particles nominally 0.2 μm thick and up to 3 μm across (Figure 4C), having an overall

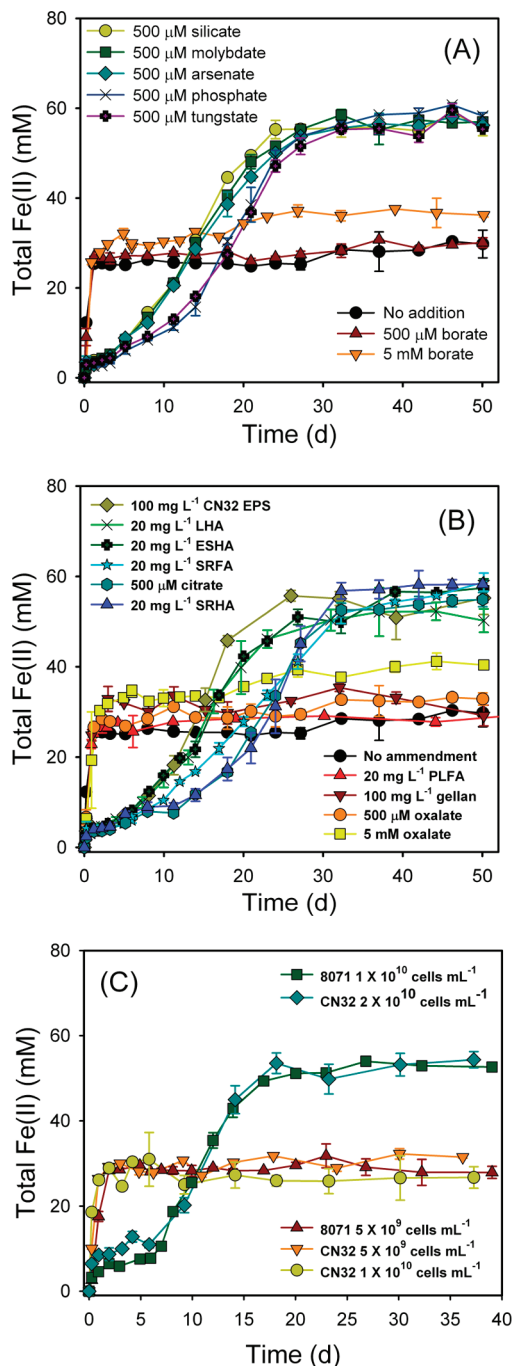


FIGURE 1. Production of Fe(II) during the bioreduction of 80 mM lepidocrocite by *S. putrefaciens* CN32 in the presence and absence of oxyanions (A) and NOM (B) and in the presence of various cell numbers of *S. putrefaciens* strains CN32 and ATCC 8071 (C). Lines are a visual aid only. Error bars indicate the average deviation.

morphology consistent with biogenic green rust (2, 5, 7, 8, 10). The addition of 500 μM of arsenate, molybdate, silicate, or tungstate had similar effects on the kinetics and overall extent of Fe(II) production, and (as with phosphate) resulted in green rust formation (Table 1). In contrast, with either 500 μM or 5 mM borate added, Fe(II) production kinetics were similar to those for the unamended system—but with slightly higher Fe(II) production with 5 mM borate (Figure 1A)—with formation of magnetite and FHC (Table 1).

Lepidocrocite bioreduction was also examined in systems containing organic ligands representing different components of NOM, including aliphatic acids, humic substances,

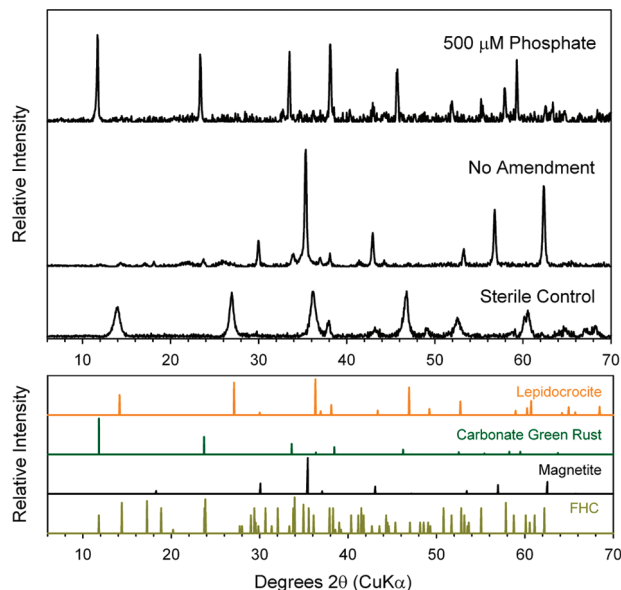


FIGURE 2. XRD patterns of solids in the sterile control and biomineralization products resulting from the reduction of lepidocrocite in the unamended and 500 μM phosphate-amended experimental systems, compared with reference patterns of lepidocrocite, carbonate green rust, magnetite, and FHC.

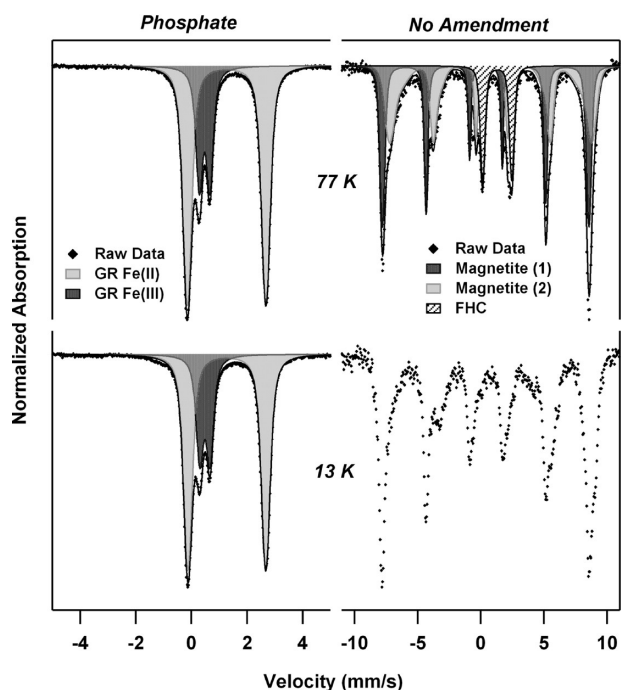


FIGURE 3. ^{57}Fe Mössbauer spectra of the biomineralization products resulting from the reduction of lepidocrocite in the unamended (right) and 500 μM phosphate-amended (left) experimental systems. The raw data (\blacklozenge) are presented with the least-squares fit overlaid (shaded areas) and total fit (—). The 13 K spectrum for the unamended system could not be fitted because of magnetic ordering of the FHC doublet to an octet. The presented spectra are representative of the other amended systems.

and microbially produced EPS. As with the inorganic oxyanions, the kinetics of Fe(II) production clustered into two distinct profiles (Figure 1B). Fe(II) production in the systems containing oxalate (either 500 μM or 5 mM), gellan, or PLFA tracked with the unamended control, exhibiting a rapid increase in Fe(II) concentration that quickly leveled off at

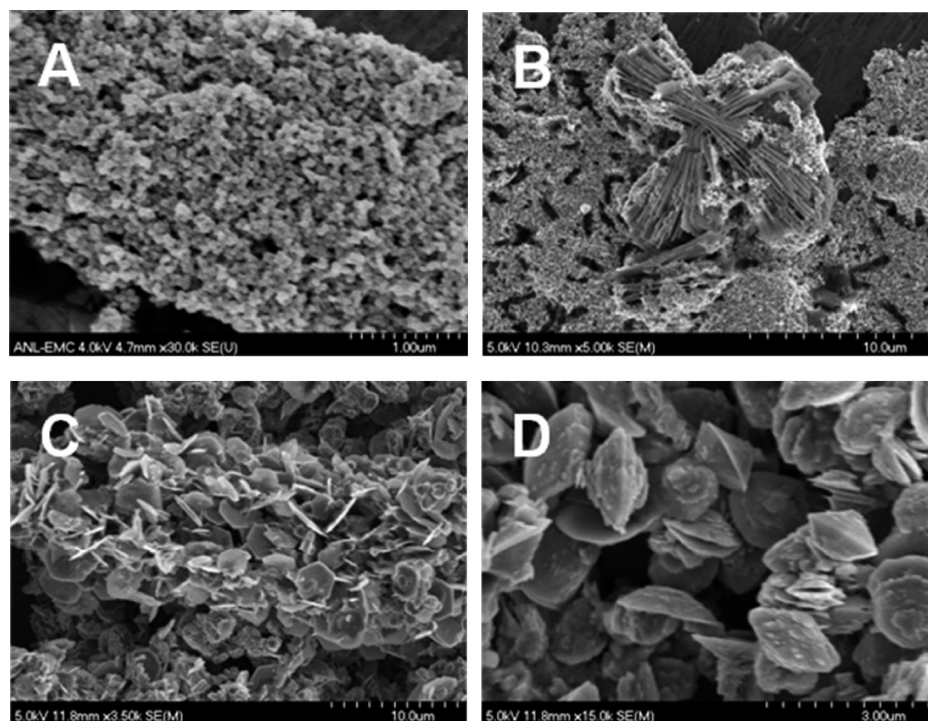


FIGURE 4. SEM images of magnetite (A) and magnetite/FHC (B) formed in the unamended system and of green rust formed in the systems containing 500 μM phosphate (C) and 20 mg L^{-1} ESHA (D).

25–30 mM (~ 40 mM for 5 mM oxalate; which may have been due, in part, to oxalate-enhanced lepidocrocite dissolution). Magnetite and FHC were the only secondary mineralization products observed in these systems (Table 1). The addition of citrate, ESHA, LHA, SRFA, SRHA, or CN32 EPS resulted in Fe(II) production profiles similar to those for the arsenate, molybdate, phosphate, silicate, and tungstate systems. An initial pulse of 3–4.6 mM Fe(II) within the first 24 h was followed by a 3–5 d pause, then increasing Fe(II) concentrations through days 6–31; after this, Fe(II) concentrations remained relatively constant at 52–58 mM. Green rust was the only identified secondary mineralization product in each of these systems (Table 1). In contrast to the platy habit typically reported for green rust, and evident in the green rusts formed in the arsenate, molybdate, phosphate, silicate, tungstate, citrate, and CN32 EPS-amended systems (Figure 4C and Figures S8–10, and S12, Supporting Information), the green rusts in the LHA-, SHA-, SRFA-, and SRHA-amended systems exhibited pyramidal and prismatic habits (Figure 4D and Figure S11, Supporting Information), similar to that of several related, layered double hydroxides of the hydroxalite group (31).

Altering the number and type of bacterial cells resulted in the same two types of Fe(II) production profiles as observed with the inorganic oxyanions and NOM. Initial cell loadings of 5×10^9 cells mL^{-1} for *S. putrefaciens* strains 8071 or CN32 resulted in rapid Fe(II) production (Figure 1C) and formation of magnetite and FHC (Table 1). Cell loadings of 1×10^{10} cells mL^{-1} of *S. putrefaciens* CN32 also exhibited rapid Fe(II) production and magnetite/FHC formation, while the same loading of *S. putrefaciens* 8071 resulted in slower Fe(II) production, higher final Fe(II) concentration, and the formation of green rust. Increasing *S. putrefaciens* CN32 to 2×10^{10} cells mL^{-1} resulted in “slow” Fe(II) production kinetics and green rust formation. The effects of *S. putrefaciens* CN32 cell density were the same regardless of the metabolic state of the cells. We examined the effects of metabolically inactive (dead) cells on lepidocrocite reduction of by H_2/Pd catalyst in the presence of AQDS. As in the experiments with live cells, the addition of 5×10^9 or 1×10^{10} cells mL^{-1} of

pasteurized *S. putrefaciens* CN32 resulted in formation of magnetite, and green rust formed with 2×10^{10} cells mL^{-1} (Figure S6, Supporting Information). These results demonstrate that the levels of biomass (whether metabolically active or dead) or cell products (such as EPS) can have a significant effect on Fe(III) oxide reduction and subsequent secondary mineralization product formation and that cell density effects may be species specific. Our results are generally consistent with a previous study by Zegeye et al. (11), which showed similar cell number effects on secondary mineralization product formation during lepidocrocite bioreduction by *S. putrefaciens* CIP 8040 (equivalent to ATCC 8071).

Lepidocrocite bioreduction was complete in all of the experimental systems to the extent that no lepidocrocite was detected at the end of the experiments. However, substantial Fe(III) remained after Fe(II) production ceased; ~ 37 –75% of Fe(III) was reduced to Fe(II), of which $>98\%$ was present in the solids. The overall extent of Fe(III) reduction appears to be constrained by the incorporation of Fe(III) into specific secondary mineralization products. The lower overall extent of Fe(II) production [~ 30 –41 mM Fe(II)] observed in the systems with “rapid” Fe(II) production profiles (Figure 1) is consistent with formation of magnetite as the major product, as magnetite nominally has an Fe(III):Fe(II) ratio of 2. Systems with “slow” Fe(II) production profiles had higher overall Fe(II) levels [~ 52 –60 mM Fe(II)], consistent with the formation of green rust, which, although variable, has a nominal Fe(III):Fe(II) ratio of 0.5. Under the appropriate conditions or given sufficient time, the Fe(III) in magnetite and green rust can be bioreduced (9, 32); however, incorporation of Fe(III) into these phases effectively rendered it unavailable for use by *S. putrefaciens* as a terminal electron acceptor for anaerobic respiration in our experiments.

Discussion

Although this study was primarily a phenomenological investigation of the effects of various organic and inorganic ligands on lepidocrocite bioreduction and secondary mineralization product formation rather than an in-depth

mechanistic treatment, our results do offer new insight that provides a basis for discussion of possible controls on Fe(III) oxide bioreduction and product formation. In particular, the distinct clustering of the Fe(II) production kinetics into a “fast” profile leading to magnetite/FHC or a “slow” profile leading to green rust is suggestive of a common underlying mechanism. Many studies have identified green rust as a product of Fe(III) oxide bioreduction (1–13); however, few have explicitly identified the factor(s) leading to green rust formation at the expense of other products such as magnetite. The presence of phosphate (2), or more directly, the extent of phosphate sorption to Fe(III) oxides (1, 13), has been identified as the key factor in the formation of green rust (instead of magnetite) following the bioreduction of ferrihydrite by *S. putrefaciens* CN32; however, the mechanism by which phosphate leads to green rust formation is not clear (i.e., whether phosphate explicitly *suppresses* magnetite formation or *promotes* green rust formation). Zegeye et al. (11) proposed that the formation of green rust versus magnetite is controlled by the rate of Fe(III) oxide bioreduction, with faster rates promoting the formation of magnetite; which is consistent with magnetite formation in our experimental systems exhibiting “fast” Fe(II) production profiles versus green rust formation in systems with “slow” Fe(II) production profiles. However, it is still unclear whether the Fe(II) production rate really is the controlling factor or merely a consequence of other processes having more direct control on secondary mineralization product formation.

Given the relatively low solubility of Fe(III) oxides, lepidocrocite bioreduction in our experimental system is driven by transfer of electrons from components of the respiratory chain in *S. putrefaciens* CN32 to the oxide surface—both directly, via contact of the cell surface with the oxide, and indirectly by microbial reduction of AQDS to anthrahydroquinone-2,6-disulfonate (AH₂QDS) and subsequent reduction of the oxide by AH₂QDS. Indeed, *S. oneidensis* MR-1, a species closely related to *S. putrefaciens* CN32 (7), binds to hematite via inner-sphere complexation of phosphoryl groups to Fe centers on the oxide surface (33). Moreover, MtrC and OmcA, outer membrane cytochromes that are key components in the transfer of electrons from the interior of the cell to external electron acceptors like Fe(III) oxides, bind to hematite (34) and, as shown for OmcA, remain catalytically active (i.e., can transfer electrons from an electron donor like NADH to the oxide) (35). Both direct and indirect reduction processes require access to surface sites on the oxide; therefore, binding of competing ligands to Fe(III) oxides can potentially decrease the rate of Fe(II) production by limiting access of bacterial cells and AH₂QDS to surface sites on Fe(III) oxides where electron transfer occurs. For example, the competitive binding of phosphate limits the reduction of hematite by AH₂QDS (30).

An in-depth discussion of the multiple factors controlling the sorption of the various ligands examined in this study to Fe(III) oxides is beyond the scope of this paper; however, an overview of the topic indicates substantial variability in the extent and mechanisms of ligand binding to Fe(III) oxides (24). A comparison of the Fe(II) production rates and corresponding secondary mineralization product formation (Table 1) with the uptake of 500 μM of arsenate, borate, citrate, molybdate, oxalate, phosphate, silicate, and tungstate by lepidocrocite (Figure S13, Supporting Information) is consistent with the premise that the extent of anion sorption constrains Fe(III) oxide bioreduction (13). However, the uptake of 5 mM borate or oxalate was comparable to that of the other anions at 500 μM, and yet Fe(II) production kinetics and secondary mineralization product formation were nominally the same as for the unamended system. These results may be a consequence of relative differences in the strength of anion binding and/or binding to different sites

on lepidocrocite. An overview of the literature regarding the sorption of arsenate, borate, citrate, molybdate, oxalate, phosphate, silicate, and tungstate to Fe(III) oxides indicates that all typically form inner-sphere complexes (Table S2, Supporting Information); however, the relative strength of binding among these anions is highly variable. Although few studies have explicitly examined the competitive binding of the anions examined in this study to iron oxides, reported data indicate that borate and oxalate bind less strongly than arsenate, citrate, phosphate, and silicate (29, 36–38) and therefore might be more easily displaced by bacteria or AH₂QDS—consistent with the lack of inhibition of lepidocrocite bioreduction, even when levels of sorbed borate and oxalate were greater than levels of adsorbed arsenate, citrate, molybdate, phosphate, silicate, and tungstate.

Similar considerations may contribute to the differences in Fe(II) production kinetics and secondary mineralization product formation among the various NOM fractions. The general trend for the binding of NOM by iron oxides is for preferential sorption of aromatic over aliphatic, hydrophobic over hydrophilic, and larger over smaller molecules (24). Therefore, given the relative differences in aromaticity and molecular mass among the humic substances examined in this study (Table S1, Supporting Information), it is perhaps not surprising that the more aromatic and larger humics, derived primarily from the degradation of terrestrial plants and thus containing a significant fraction of lignin residues, exhibited the same kinetic profile and secondary mineralization product formation as the strongly adsorbing anions, while the less aromatic and lower-molecular-mass PLFA, derived from microbial biomass consisting primarily of polypeptides and polysaccharides, exhibited Fe(II) production kinetics and product formation similar to borate- and oxalate-amended systems. Likewise, the different effects observed with CN32 EPS and gellan likely reflect differences in their compositions. The CN32 EPS used in this study was not fractionated and thus contained a heterogeneous mixture of polysaccharides, proteins, lipids, and nucleic acids. The proteins and nucleic acids in EPS can bind strongly to iron oxides via phosphoryl groups (33, 39); therefore, strong preferential binding to lepidocrocite by multiple components of CN32 EPS is likely. Conversely, gellan is a highly purified EPS consisting primarily of a high-molecular-mass (~500 kDa) polysaccharide (additional details are provided in Supporting Information). Despite gellan’s high molecular mass, which should favor sorption, the overall charge density is relatively low, with only one carboxylate group per tetrasaccharide structural unit (~658 Da), which is likely to limit its competitive binding.

Our results offer new insight into factors that can contribute to green rust formation during iron oxide bioreduction; however, key questions remain. Although there are data for many of the anions examined in this study that indicate sorption to Fe(III) oxides occurs via formation of inner-sphere complexes (Table S2, Supporting Information); there is little known about the specific binding site(s) involved, particularly in the case of lepidocrocite. Likewise, the specific site(s) on lepidocrocite where electron transfer can occur are also not known. We are currently engaged in focused investigations probing the molecular-scale mechanism(s) of anion-specific controls on Fe(II) production kinetics and secondary mineralization product formation.

Environmental Implications. Iron biogeochemistry is complex and is coupled with the biogeochemical cycling of many major (C, S, N, O) and minor (e.g., P, As, and Se) elements. This, in turn, affects other biogeochemical processes, including contaminant fate and transport. Fe(II) is an effective reductant for a range of contaminants including chlorinated hydrocarbons, nitroaromatics, nitrate, Cr(VI), U(VI), Tc(VII), Np(V), and Pu(V). However, the redox reactivity

of Fe(II) depends strongly on its speciation. Among common Fe(II) phases, green rust is a particularly effective reductant for several contaminants of concern (40–43); therefore, an improved understanding of the processes leading to the formation of green rust in natural and engineered environments (e.g., in situ biostimulation of native populations of IRB for contaminant bioremediation) may lead to better management of contaminant fate and transport. Although our experimental conditions are not typical of natural environments (i.e., relatively high levels of electron donor (formate), Fe(III), and IRB), the formation of the green rust mineral fougérite in reductomorphic soils correlates well with the activity of native IRB populations (44). Although the factors controlling the formation of fougérite are not well-defined, our results suggest that oxyanions and various forms of NOM commonly found in soils and sediments, as well as the types and numbers bacterial cells and their exudates, may all play a role in the formation of fougérite as a product of the bioreduction of Fe(III) oxides.

Acknowledgments

We thank Russell Cook for his assistance with SEM imaging; Michael McCormick for determining the surface area of the lepidocrocite used in this study; and Karen Haugen and three anonymous reviewers for their thoughtful reviews of the manuscript. Funding was provided by the U.S. Department of Energy's Office of Science (DOE-SC), Office of Biological and Environmental Research, Subsurface Biogeochemical Research Program, under contract DE-AC02-06CH11357. Use of the APS and the Electron Microscopy Center for Materials Research at Argonne National Laboratory was supported by the DOE-SC Office of Basic Energy Sciences, under contract DE-AC02-06CH11357. The submitted manuscript has been created by UChicago Argonne, LLC, Operator of Argonne National Laboratory ("Argonne"). Argonne, a U.S. Department of Energy Office of Science laboratory, is operated under Contract No. DE-AC02-06CH11357. The U.S. government retains for itself and others acting on its behalf, a paid-up, non-exclusive, irrevocable worldwide license in said article to reproduce, prepare derivative works, distribute copies to the public and perform publicly and display publicly, by or on behalf of the Government.

Supporting Information Available

Details on sources of chemicals; preparation of reagents; synthesis and characterization of lepidocrocite; measurement of Fe(II) concentrations; and characterization of secondary mineralization products by XRD, ⁵⁷Fe Mössbauer, and SEM. This material is available free of charge via the Internet at <http://pubs.acs.org>.

Literature Cited

- (1) Kukkadapu, R. K.; Zachara, J. M.; Fredrickson, J. K.; Kennedy, D. W. Biotransformation of two-line silica-ferrihydrite by a dissimilatory Fe(III)-reducing bacterium: Formation of carbonate green rust in the presence of phosphate. *Geochim. Cosmochim. Acta* **2004**, *68* (13), 2799–2814.
- (2) Fredrickson, J. K.; Zachara, J. M.; Kennedy, D. W.; Dong, H.; Onstott, T. C.; Hinman, N. W.; Li, S.-M. Biogenic iron mineralization accompanying the dissimilatory reduction of hydrous ferric oxide by a groundwater bacterium. *Geochim. Cosmochim. Acta* **1998**, *62* (19/20), 3239–3257.
- (3) Parmar, N.; Gorby, Y. A.; Beveridge, T. J.; Ferris, F. G. Formation of green rust and immobilization of nickel in response to bacterial reduction of hydrous ferric oxide. *Geomicrobiol. J.* **2001**, *18*, 375–385.
- (4) Salas, E. C.; Berelson, W. M.; Hammond, D. E.; Kampf, A. R.; Nealson, K. H. The influence of carbon source on the products of dissimilatory iron reduction. *Geomicrobiol. J.* **2009**, *26*, 451–462.
- (5) Glasauer, S.; Weidler, P. G.; Langley, S.; Beveridge, T. J. Controls on Fe reduction and mineral formation by a subsurface bacterium. *Geochim. Cosmochim. Acta* **2003**, *67* (7), 1277–1288.

- (6) O'Loughlin, E. J. Effects of electron transfer mediators on the biodegradation of lepidocrocite (γ -FeOOH) by *Shewanella putrefaciens* CN32. *Environ. Sci. Technol.* **2008**, *42* (18), 6876–6882.
- (7) O'Loughlin, E. J.; Larese-Casanova, P.; Scherer, M. M.; Cook, R. E. Green rust formation from the bioreduction of γ -FeOOH (lepidocrocite): Comparison of several *Shewanella* species. *Geomicrobiol. J.* **2007**, *24*, 211–230.
- (8) Ona-Nguema, G.; Abdelmoula, M.; Jorand, F.; Benali, O.; Géhin, A.; Block, J.-C.; Génin, J.-M. R. Iron(II, III) hydroxycarbonate green rust formation and stabilization from lepidocrocite bioreduction. *Environ. Sci. Technol.* **2002**, *36* (1), 16–20.
- (9) Ona-Nguema, G.; Morin, G.; Wang, Y.; Menguy, N.; Juillot, F.; Olovi, L.; Aquilanti, G.; Abdelmoula, M.; Ruby, C.; Bargar, J. R.; Guyot, F.; Calas, G.; Brown, G. E., Jr. Arsenite sequestration at the surface of nano-Fe(OH)₂, ferrous-carbonate hydroxide, and green-rust after bioreduction of arsenic-sorbed lepidocrocite by *Shewanella putrefaciens*. *Geochim. Cosmochim. Acta* **2009**, *73*, 1359–1381.
- (10) Jorand, F.; Zegeye, A.; Landry, F.; Ruby, C. Reduction of ferric green rust by *Shewanella putrefaciens*. *Lett. Appl. Microbiol.* **2007**, *45*, 515–521.
- (11) Zegeye, A.; Ruby, C.; Jorand, F. Kinetic and thermodynamic analysis during dissimilatory γ -FeOOH reduction: Formation of green rust 1 and magnetite. *Geomicrobiol. J.* **2007**, *24*, 51–64.
- (12) Hansel, C. M.; Benner, S. G.; Neiss, J.; Dohnalkova, A.; Kukkadapu, R. K.; Fendorf, S. Secondary mineralization pathways induced by dissimilatory iron reduction of ferrihydrite under advective flow. *Geochim. Cosmochim. Acta* **2003**, *67* (16), 2977–2992.
- (13) Borch, T.; Masue, Y.; Kukkadapu, R. K.; Fendorf, S. Phosphate imposed limitations on biological reduction and alteration of ferrihydrite. *Environ. Sci. Technol.* **2007**, *41* (1), 166–172.
- (14) Bearcock, J. M.; Perkins, W. T.; Dinelli, E.; Wade, S. C. Fe(II)/Fe(III) 'green rust' developed within ocherous coal mine drainage sediment in South Wales, U.K. *Mineral. Mag.* **2006**, *70* (6), 731–741.
- (15) Christiansen, B. C.; Balic-Zunic, T.; Dideriksen, K.; Stipp, S. L. S. Identification of green rust in groundwater. *Environ. Sci. Technol.* **2009**, *43* (10), 3436–3441.
- (16) Feder, F.; Trolard, F.; Klingelhöfer, G.; Bourrié, G. In situ Mössbauer spectroscopy: Evidence for green rust (fougérite) in a gleysol and its mineralogical transformations with time and depth. *Geochim. Cosmochim. Acta* **2005**, *69* (18), 4463–4483.
- (17) Génin, J.-M. R.; Bourrié, G.; Trolard, F.; Abdelmoula, M.; Jaffrezic, A.; Refait, P.; Maitre, V.; Humbert, B.; Herbillon, A. Thermodynamic equilibria in aqueous suspensions of synthetic and natural Fe(II)-Fe(III) green rusts: Occurrences of the mineral in hydromorphic soils. *Environ. Sci. Technol.* **1998**, *32* (8), 1058–1068.
- (18) Root, R. A.; Dixit, S.; Campbell, K. M.; Jew, A. D.; Hering, J. G.; O'Day, P. A. Arsenic sequestration by sorption processes in high-iron sediments. *Geochim. Cosmochim. Acta* **2007**, *71*, 5782–5803.
- (19) Dong, H.; Fredrickson, J. K.; Kennedy, D. W.; Zachara, J. M.; Kukkadapu, R. K.; Onstott, T. C. Mineral transformation associated with the microbial reduction of magnetite. *Chem. Geol.* **2000**, *169*, 299–318.
- (20) Fredrickson, J. K.; Kota, S.; Kukkadapu, R. K.; Liu, C.; Zachara, J. M. Influence of electron donor/acceptor concentrations on hydrous ferric oxide (HFO) bioreduction. *Biodegradation* **2003**, *14*, 91–103.
- (21) Johnson, C. M.; Roden, E. E.; Welch, S. A.; Beard, B. L. Experimental constraints on Fe isotope fractionation during magnetite and Fe carbonate formation coupled to dissimilatory hydrous ferric oxide reduction. *Geochim. Cosmochim. Acta* **2005**, *69* (4), 963–993.
- (22) Zachara, J. M.; Fredrickson, J. K.; Li, S.-M.; Kennedy, D. W.; Smith, S. C.; Gassman, P. L. Bacterial reduction of crystalline Fe³⁺ oxides in single phase suspension and subsurface materials. *Am. Mineral.* **1998**, *83*, 1426–1443.
- (23) Zachara, J. M.; Kukkadapu, R. K.; Frederickson, J. K.; Gorby, Y. A.; Smith, S. C. Biomineralization of poorly crystalline Fe(III) oxides by dissimilatory metal reducing bacteria (DMRB). *Geomicrobiol. J.* **2002**, *19*, 179–207.
- (24) Cornell, R. M.; Schwertmann, U. *The Iron Oxides: Structure, Properties, Reactions, Occurrence and Uses*, 2nd ed.; Wiley-VCH: New York, 2003; p 664.
- (25) Behrends, T.; Van Cappellen, P. Transformation of hematite into magnetite during dissimilatory iron reduction—Conditions and mechanisms. *Geomicrobiol. J.* **2007**, *24*, 403–416.

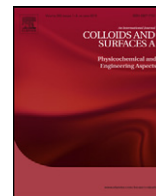
- (26) Kukkadapu, R. K.; Zachara, J. M.; Fredrickson, J. K.; Kennedy, D. W.; Dohnalkova, A. C.; Mccready, D. E. Ferrous hydroxy carbonate is a stable transformation product of biogenic magnetite. *Am. Mineral.* **2005**, *90*, 510–515.
- (27) Roh, Y.; Zhang, C.-L.; Vali, H.; Lauf, R. J.; Zhou, J.; Phelps, T. J. Biogeochemical and environmental factors in Fe biomineralization: Magnetite and siderite formation. *Clays Clay Miner.* **2003**, *51* (1), 83–95.
- (28) Sparks, N. H. C.; Mann, S.; Bazylinski, D. A.; Lovley, D. R.; Jannasch, H. W.; Frankel, R. B. Structure and morphology of magnetite anaerobically-produced by a marine magnetotactic bacterium and a dissimilatory iron-reducing bacterium. *Earth Planet. Sci. Lett.* **1990**, *98*, 14–22.
- (29) Biber, M.; dos Santos Afonso, M.; Stumm, W. The coordination chemistry of weathering: IV. Inhibition of the dissolution of oxide minerals. *Geochim. Cosmochim. Acta* **1994**, *58* (9), 1999–2010.
- (30) Liu, C.; Zachara, J. M.; Foster, N. S.; Strickland, J. Kinetics of reductive dissolution of hematite by bio-reduced anthraquinone-2,6-disulfonate. *Environ. Sci. Technol.* **2007**, *41* (22), 7730–7735.
- (31) Drits, V. A.; Sokolova, T. N.; Sokolova, G. V.; Cherkashin, V. I. New members of the hydrotalcite-manasseite group. *Clays Clay Miner.* **1987**, *35* (6), 401–417.
- (32) Kostka, J. E.; Nealson, K. H. Dissolution and reduction of magnetite by bacteria. *Environ. Sci. Technol.* **1995**, *29* (10), 2535–2540.
- (33) Parikh, S. J.; Chorover, J. ATR-FTIR spectroscopy reveals bond formation during bacterial adhesion to iron oxide. *Langmuir* **2006**, *22*, 8492–8500.
- (34) Lower, B. H.; Shi, L.; Youngsuntorn, R.; Droubay, T. C.; McCready, D. E.; Lower, S. K. Specific bonds between an iron oxide surface and outer membrane cytochromes MtrC and OmcA from *Shewanella oneidensis* MR-1. *J. Bacteriol.* **2007**, *189* (13), 4944–4952.
- (35) Xiong, Y.; Shi, L.; Chen, B.; Mayer, M. U.; Lower, B. H.; Londer, Y.; Bose, S.; Hochella, M. F.; Fredrickson, J. K.; Squier, T. C. High-affinity binding and direct electron transfer to solid metals by the *Shewanella oneidensis* MR-1 outer membrane *c*-type cytochrome OmcA. *J. Am. Chem. Soc.* **2006**, *128*, 13978–13979.
- (36) Goldberg, S. Reactions of boron with soils. *Plant Soil* **1997**, *193*, 35–48.
- (37) Johnson, S. E.; Loeppert, R. H. Role of organic acids in phosphate mobilization from iron oxide. *Soil Sci. Soc. Am. J.* **2006**, *70*, 222–234.
- (38) Mohapatra, D.; Singh, P.; Zhang, W.; Pullammanappallil, P. The effect of citrate, oxalate, acetate, silicate and phosphate on stability of synthetic arsenic-loaded ferrihydrite and Al-ferrihydrite. *J. Hazard. Mater.* **2005**, *B124*, 95–100.
- (39) Omoike, A.; Chorover, J. Adsorption to goethite of extracellular polymeric substances from *Bacillus subtilis*. *Geochim. Cosmochim. Acta* **2006**, *70*, 827–838.
- (40) Elsner, M.; Schwarzenbach, R. P.; Haderlein, S. B. Reactivity of Fe(II)-bearing minerals toward reductive transformation of organic contaminants. *Environ. Sci. Technol.* **2004**, *38* (3), 799–807.
- (41) Lee, W.; Batchelor, B. Reductive capacity of natural reductants. *Environ. Sci. Technol.* **2003**, *37* (3), 535–541.
- (42) O’Loughlin, E. J.; Kelly, S. D.; Kemner, K. M. XAFS investigation of the interactions of U^{VI} with secondary mineralization products from the bioreduction of Fe^{III} oxides. *Environ. Sci. Technol.* **2010**, *44* (5), 1656–1661.
- (43) Williams, A. G. B.; Scherer, M. M. Kinetics of Cr(VI) reduction by carbonate green rust. *Environ. Sci. Technol.* **2001**, *35*, 3488–3494.
- (44) Berthelin, J.; Ona-Nguema, G.; Stemmler, S.; Quantin, C.; Abdelmoula, M.; Jorand, F. Bioreduction of ferric species and biogenesis of green rusts in soils. *C. R. Geosci.* **2006**, *338*, 447–455.

ES100294W



Contents lists available at ScienceDirect

Colloids and Surfaces A: Physicochemical and Engineering Aspects

journal homepage: www.elsevier.com/locate/colsurfa

Equations of state and adsorption isotherms of low molecular non-ionic surfactants

Ivan B. Ivanov^{a,*}, Krassimir D. Danov^a, Dora Dimitrova^a, Maxim Boyanov^a, Kavssery P. Ananthpadmanabhan^b, Alex Lips^b

^a Laboratory of Chemical Physics & Engineering, Faculty of Chemistry, University of Sofia, Bulgaria

^b Unilever Global Research Center, Trumbull, CT 06611, USA

ARTICLE INFO

Article history:

Received 5 September 2009

Received in revised form

13 November 2009

Accepted 16 November 2009

Available online 22 November 2009

Dedicated to the 70th birthday of Professor Dieter Vollhardt.

Keywords:

Surface tension

Adsorption constant

Area per molecule

Interaction constant

Dimethyl alkyl phosphine oxides (DMPO)

Aliphatic acids

ABSTRACT

After a brief analysis of the three most widely used equations of state and adsorption isotherms, (those of van der Waals, Frumkin and Helfand–Frisch–Lebowitz with second virial coefficient) we analyze the definitions and the values of the main adsorption parameters (adsorption constant K_s , minimum area per molecule α and interaction constant β) and derive new expressions for some of them. Since it turned out that all three adsorption isotherms perform rather poorly, when used to interpret adsorption data, we applied also three more general equations—one was derived for localized adsorption long ago, but we had to derive two new equations for non-localized adsorption. We subject all 6 equations—the simple ones and the three generalized, to rigorous numerical analysis and discussion of the results. Our overall conclusion is that in some cases all equations can describe qualitatively the observed phenomena, but only the new equation of state, proposed by us for non-localized adsorption on fluid interface (and the respective adsorption isotherm), lead to correct quantitative description of the adsorption and the related parameters. In [Appendix A](#) we analyze the shortcomings and the source of errors in the fitting procedures.

© 2009 Elsevier B.V. All rights reserved.

1. Introduction

The non-ionic surfactants are important ingredients in many industrial products—the most trivial example are soaps, but they play important role also in many other technological and biological processes. Besides, depending on the conditions, they can acquire charge and then they become ionic/non-ionic mixtures, very complicated and difficult for analysis. On the other hand, they serve also as raw products for synthesis of important ionic surfactants and it is difficult sometimes to understand the behavior of the latter without good understanding of their non-ionic skeleton. Last, but not least, because of the low repulsion between their hydrophilic heads, the simple non-ionic surfactants had strong tendency to aggregate not only as micelles, but also to form several bulk and surface phases and various surface aggregates, which are interesting not only because they change the surface behavior but often simply from esthetic view point like in the Vollhardt articles related to chirality (see e.g. [1]). Of course, the experts in the

area are not only admiring the beautiful pictures, but are applying sophisticated experimental and theoretical tools to explain and use them. D. Vollhardt has also published numerous theories of such complicated phenomena. As examples we will cite only two subjects, to some extent related to the present article: phase transition between condensed phases of different compressibility [2] and mixed monolayers of fatty acids [3]. (An extensive review of complex phenomena, involving surfactants can be found in [4].) However, very often some theories are based on or are modifications of several simple adsorption equations, the most widely used being those of Langmuir [5] (and its modification by Frumkin [6]) and that of Volmer [7], which has been extended by adding an attractive term to become two-dimensional (2D) analog of the 3D equation of van der Waals. For reasons, which will become clear later, we will consider also another, less popular equation, that of Helfand, Frisch and Lebowitz (HFL)—in order to be able to compare it with the equations of van der Waals and Frumkin we added also an attraction term similar to that in Eq. (6), see Eq. (15) below. All these equations suppose that the adsorbed layer consists of rigid circular discs (possibly interacting through van der Waals forces) lying in a plane coinciding with or parallel to the interface, i.e. they are 2D analogs of the 3D equations of state of a fluid of spherical molecules. About the effect of the thermal motion normal to the interface see Section 3.1.

* Corresponding author. Tel.: +359 2 9625310; fax: +359 2 9625643.

E-mail addresses: ii@lcpe.uni-sofia.bg (I.B. Ivanov), KP.Ananth@unilever.com (K.P. Ananthpadmanabhan), Alex.Lips@unilever.com (A. Lips).

Table 1

Parameters from the fit with three equations of the data for adsorption of sodium dodecyl sulfate at interfaces Air/Water and Oil/Water.

Boundary	Air/water			Oil/water			Oil/water, $\beta=0$	
	K	$\alpha, \text{\AA}^2$	β	K	$\alpha, \text{\AA}^2$	β	K	$\alpha, \text{\AA}^2$
Frumkin	147	31.2	0.4	321	36.6	-1.8	186	45.2
van der Waals	137	22.9	1.2	299	26.8	-1.7	206	30.8
HFL	131	15.8	2.9	284	18.5	-1.4	237	20.3

These models have physical basis and describe and/or explain the basic features of the studied phenomena. However, they contain usually at least three free parameters and in more complicated systems it is sometimes hard to imagine from the obtained data how are the adsorption parameters related and how they depend on the other properties of the system. Another problem with the multi-parameter fits, which we will demonstrate below, is that the adsorption parameters may combine in such a way that the experimental data are fitted perfectly, but the calculated values of the parameters may change significantly, depending on the theoretical model used. We are not the only ones to point out on these problems (see e.g. [8]). In a paper, devoted to ionic surfactants [9], we analyzed some of these problems, but at that time could often find solution only to part of them. In the present paper we continue and extend our previous analysis, but deal only with non-ionic surfactants with the hope that they are simpler and easier for thorough understanding. With respect to the previous paper [9] we hope to have succeeded to find explanations of a few more unclear issues.

Our goal is not to look for explanation of complicated phenomena. We realize that when somebody is working on a complicated subject, very often it is impossible to carry out deep analysis and one is forced often to use intuition, rather than rigorous approaches. We believe however that more rigorous understanding of the simple processes and systems can help work on complicated subject at least by showing to the respective researchers which hypothesis and speculations are permissible and which ones are not. That is why we are looking mainly for qualitative physical insight on the adsorption process and the structure of the adsorbed layer. Toward this aim we selected very simple experimental systems and considerably simplified the theory in the hope that this will permit more thorough analysis of the theory and the experimental data and will shed more light on the meaning of the adsorption parameters and the factors affecting them.

To make our point, we will begin by experimental verification and comparison of the above cited equations of van der Waals, Frumkin and Helfand–Frisch–Lebowitz (HFL). We obtained at that some surprising results. Although in this article we will be dealing only with non-ionic surfactants, we will demonstrate some of them on the example of an ionic surfactant, the sodium dodecyl sulfate (SDS). The reason is that the non-ionic surfactants are soluble in oils, but the presence of the oil phase allows shedding additional light on some effects, which are also important for non-ionic surfactants. We will treat the data for SDS by using the ionic counterparts of the above equations, derived in [9]—see the respective Eqs. (2.22) and (2.23) therein. In fact the relation between the isotherms for the two types of surfactant is rather direct. The appropriate variables for the fit in the case of ionic surfactants are the adsorption Γ and $C_s^{2/3}$, where C_s is the surfactant concentration. The adsorption constant K and K_s for ionics and non-ionics are related: $K \propto K_s^{1/3}$. The results for SDS are presented in Fig. 1 and Table 1 (for the interface air/water we used the results of Hines [10] and for hexadecane/water we determined experimentally the adsorption isotherm). It is noteworthy that the fits were perfect, with the exception of the Langmuir fit with $\beta=0$, and they had regression coefficients 0.999. Nonetheless the determined adsorption parameters vary very much from model to model, but

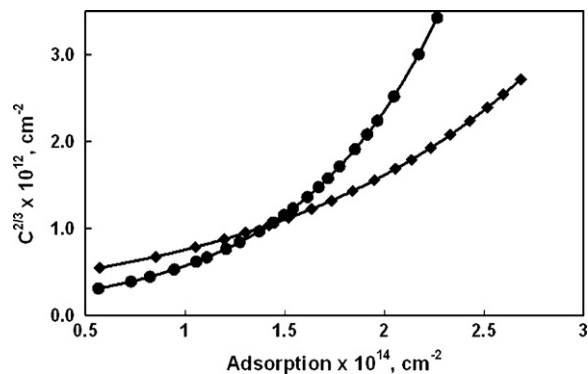


Fig. 1. Adsorption isotherms of SDS (sodium dodecyl sulfate) at the interface air/water [10] (●) and hexadecane/water (◆).

systematically—for example the values of the minimum areas per molecule α are always in the order Langmuir > Volmer > HFL and those for the interaction constant β follow the opposite trend. This dependence of the parameter's values confirms our opinion in [9] that the good fit is by no means a criterion for correct results.

Another strange result is the large negative values of β for O/W, which should be in fact zero, because of the similarity between the hydrophobic surfactant tails and the oil [11]. As a matter of fact at least for HFL model we obtained for O/W perfect fits by setting $\beta=0$ and the value of α so obtained (last column) is close to the one, which we will show in our subsequent article by using more refined equations. Another surprise was that the extended HFL equation (with account for the attraction), which we believed to be the best, gave the worst results for the interface air/water.

The overall conclusion we reached from this analysis is that the three models, presented above, lead to inconsistent results for the adsorption parameters. This confirms L. D. Landau opinion that “*The experimental data can be fitted by any not too wild theory, provided that it contains enough undetermined constants*”. In order to find the reason for this we decided to analyze as thoroughly as possible both the structure of the equations and the meaning and the role of the parameters. In fact, attempt for such analysis was already done in [9], but it was not always complete. Hence, we will present briefly again part of this analysis (in some cases extended) for convenience of the reader, the more so that we will need the results for the present analysis as well. We will present also some new results, which we hope explain some of these paradoxes and help removing them.

The paper is organized as follows. In Section 2 we present and briefly analyze the equations of state and adsorption isotherms of van der Waals, Frumkin and Helfand–Frisch–Lebowitz. Since detailed analysis is impossible without deeper understanding of the theoretical expressions and the values of the main adsorption parameters (adsorption constant K_s , minimum area per molecule α and interaction constant β), Section 3 is devoted to their analysis and derivation of some new expressions for them. It turned out that the poor performance of all three adsorption isotherms, when applied to adsorption data could not be explained only by defects of the adsorption parameters. Hence, in Section 4 we decided to deal with more general equations—one was derived for localized adsorption long ago, but we had to derive two new equations for non-localized adsorption. After describing shortly the method of data processing in Section 5, in Section 6 we subject all 6 equations—the three simple and the three generalized, to rigorous numerical analysis and discussion of the results. The article terminates by conclusion and Appendix A, analyzing the shortcomings and the source of errors in the fitting procedures.

2. Simple equations of state and adsorption isotherms

We will begin by presenting and analyzing the two most widely used surface equation of state (EOS), which are often used as basis for generalizations or extensions: the equations of Frumkin and van der Waals. Since they differ only by their hard core parts, which were suggested by Langmuir and Volmer respectively, we will often call them equations (or models) of Langmuir or Volmer.

2.1. Equation of van der Waals

To make our viewpoint more clear, we will modify for a 2D-system the derivation of Landau and Lifshits (Chapter 7 in [12]) of the original 3D van der Waals equation, which is the most transparent physically. Let us take the virial expansion for the free energy F of a 2D fluid of area A consisting of N_a circular discs each of diameter d :

$$F = N_a F_0(T) + N_a kT \ln \left(\frac{N_a}{A} \right) + kTB_2 \frac{N_a^2}{A};$$

$$B_2 = \pi \int_0^\infty \left[1 - \exp \left(-\frac{u}{kT} \right) \right] r dr \quad (1)$$

where kT is the thermal energy, B_2 is the second virial coefficient and $u(r)$ is the interaction energy between two discs at a distance r . It is assumed further that at $r < d$ the molecules interact like rigid bodies with energy $+\infty$ and at $r > d$ the energy is small, $|u/(kT)| \ll 1$. Then

$$B_2 = \alpha_V - b; \quad \alpha_V = \frac{\pi d^2}{2} = 2\alpha; \quad b = -\frac{\pi}{kT} \int_d^\infty u(r)r dr \approx \frac{\alpha_V w}{2 kT} \quad (2)$$

where α is the true area of the disc, w is the interaction energy at contact and by α_V we have denoted the contribution to B_2 from the repulsive energy (the subscript “V” denotes that the respective values pertain to the Volmer model). If one assumes that $u < 0$ for any $r > d$, the constant b will be positive. If $u(r)$ is described by London’s equation, the integral can be solved with the result shown in Eq. (2). The ratio $w/(kT)$ will be denoted hereafter by β . If the surface layer is not dense, $N_a \alpha_V / A \ll 1$, one can use the relation

$$\ln(A - N_a \alpha_V) \approx \ln A - \frac{N_a \alpha_V}{A} \quad (3)$$

to eliminate $\ln A$ from Eq. (1) and to obtain

$$F = N_a F_0(T) - N_a kT \ln \left(\frac{A - N_a \alpha_V}{N_a} \right) - kT \beta \frac{N_a^2 \alpha_V}{2A} \quad (4)$$

By using the fundamental equation for an isothermal one-component 2D system with chemical potential μ and surface pressure $\Delta\sigma$:

$$dF = -\Delta\sigma dA + \mu dN_a \quad (5)$$

one obtains with Eq. (4) the 2D equation of state (EOS):

$$\frac{\Delta\sigma}{kT} = \frac{\Gamma}{1 - \alpha_V \Gamma} - \frac{\alpha_V \beta}{2} \Gamma^2 \quad (6)$$

where $\Gamma = N_a/A$ is the adsorption.

The above derivation shows the limitations of the van der Waals EOS: it is valid only for small interaction energy (small β) and low surface coverage $\alpha_V \Gamma \ll 1$, when only double collisions play a role (only B_2 was accounted for). Landau and Lifshits [12] warned that “the constant b (in the 3D van der Waals equation) can by no means be regarded as fourfold “volume of the molecule” even for one-molecular gas”. Similar conclusion should be true of course for the constant α_V in the 2D van der Waals equation, Eq. (6).

The adsorption isotherm can be obtained by integrating Gibbs equation, which for isothermal one-component adsorbed layer with surfactant bulk concentration (or activity) C_s reads:

$$d(\Delta\sigma) = kT\Gamma d(\ln C_s) \quad (7)$$

By substituting here $\Delta\sigma$ from Eq. (6) and integrating one finds:

$$K_s C_s = \frac{\Gamma}{1 - \alpha_V \Gamma} \exp \left(\frac{\alpha_V \Gamma}{1 - \alpha_V \Gamma} - \beta \alpha_V \Gamma \right) \quad (8)$$

where

$$K_s = \delta_s \exp \left(\frac{E_A}{kT} \right) \quad (9)$$

is the adsorption constant, E_A is the free adsorption energy (i.e. the free energy for bringing the surfactant molecule from the bulk solution into the adsorbed layer) and δ_s has the meaning of “thickness of the adsorbed layer”. These quantities are discussed later.

Another useful equation is related to the Gibbs elasticity, E_G , which is defined as

$$E_G = \frac{d(\Delta\sigma)}{d \ln \Gamma} \quad (10)$$

In dimensionless form, with $\theta = \alpha_V \Gamma$, Eqs. (6) and (10) yield

$$\frac{\alpha_V E_G}{kT} = \frac{\theta}{(1 - \theta)^2} - \beta \theta^2 \quad (11)$$

There are several experimental methods for measurement of E_G , providing possibility for additional checking the adsorption model and parameters but this is beyond the scope of this study.

2.2. Equation of Frumkin

It is based on the Langmuir EOS. The latter is a rigorous equation for adsorption on a 2D lattice of adsorption centers if the following conditions hold [13]: (i) each center can be occupied only by one molecule; (ii) the adsorbed molecules cannot interact with each other neither by attractive nor by repulsive forces – this means that the area occupied by the adsorbed molecule must be equal or smaller than the area pertaining to the center; (iii) the combinatorial formula the derivation is based upon describes the distribution of N_a undistinguishable molecules over M numbered centers – this means that the molecules cannot exchange positions over the surface and jump from center to center even if there are non-occupied centers. The combination of these conditions cannot be realized with a fluid adsorbed layer. Belton and Evans [14] succeeded to derive Langmuir EOS for liquid mixtures but only on the condition that the solvent and the solute have exactly the same size—in this case removing one solvent molecule from the interface in fact creates a center for adsorption of a solute molecule and *vice versa*. They showed that small difference in sizes leads to considerable errors.

Nonetheless from its very derivation the EOS of Langmuir has been widely applied to adsorbed fluid layers. One possible reason is the fact that its integration by means of Gibbs adsorption isotherm to eliminate Γ leads exactly to the empirical Szyszkowski equation, which was shown to describe well the dependence of the surface tension σ on the surfactant concentration C_s for low molecular surfactants. This is not so surprising since the size of the hydrophilic groups of these substances is not much different from that of water.

However, attempts to treat the adsorption of other molecules by using Langmuir equation failed. Frumkin [6] attributed it to the intermolecular interaction and suggested, by analogy with van der Waals equation of fluids, to add a term accounting for this effect through β (the first term in the right is Langmuir’s equation):

$$\frac{\Delta\sigma}{kT} = -\frac{1}{\alpha_L} \ln(1 - \alpha_L \Gamma) - \alpha_L \beta \Gamma^2; \quad \beta = \frac{w_L}{kT} \quad (12)$$

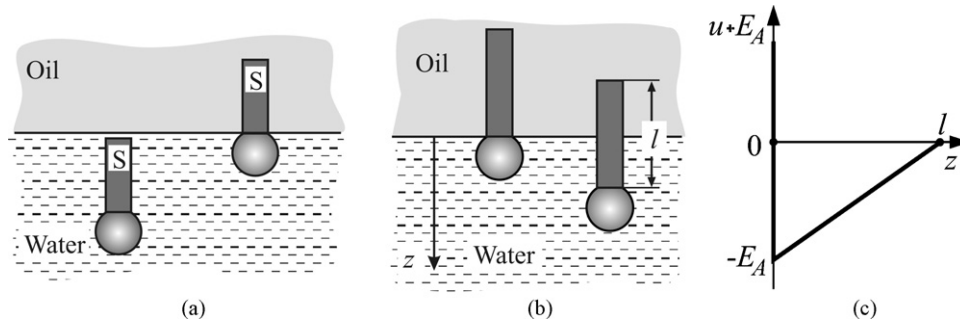


Fig. 2. Schematic presentation of the process of adsorption and the related energy u . (a) Molecules in the water phase and in adsorbed state. (b) Adsorbed and partially immersed molecule. (c) Energy u of a molecule immersed at a distance z from the interface.

In fact, the equation of Frumkin is analogous to the equation of Bragg and Williams [see e.g. reference [13], Chapter 14], who introduced in the model of Langmuir interaction between closest neighbors. Their equation differs from that of Frumkin only by the attractive term which they found to be $z_n \alpha_L \beta \Gamma^2 / 2$, where z_n is the number of closest neighbors (usually 4 or 6) and w_1 in β is replaced by the interaction energy w_1 with one neighbor only. Frumkin equation is obtained by setting $z_n = 2$, which corresponds to adsorption on a line. However, Frumkin equation does not coincide with the exact EOS for adsorption on a line (see Eq. 14.16 in [13]).

The respective adsorption isotherm is obtained again by integrating Gibbs equation along with the EOS:

$$K_s C_s = \frac{\Gamma}{1 - \alpha_L \Gamma} \exp(-2\beta \alpha_L \Gamma) \quad (13)$$

and the relation for the Gibbs elasticity is (with $\theta = \alpha_L \Gamma$)

$$\frac{\alpha_L E_G}{kT} = \frac{\theta}{1 - \theta} - 2\beta \theta^2 \quad (14)$$

2.3. Equation of Helfand–Frisch–Lebowitz (HFL)

Reiss et al. [15] developed a very astute procedure, (which they called “Scaled Particle Theory”) for treating systems of hard core particles. Unfortunately nobody has succeeded to apply it to particles with attraction. They solved exactly several problems, related to hard particles, but it turned out that the 2D case (hard discs at interfaces) has in principle no exact solution. Nevertheless, Helfand et al. [16] succeeded to derive an almost exact simple 2D EOS. It is impossible to present in a concise manner their theory and we refer the interested reader to the original paper. In order to be able to compare the theory with the equations of van der Waals and Frumkin we added to their (hard core) result an attraction term as in Eq. (6) but in order to keep the definition of $\beta = w/(kT)$ unchanged, we substituted there 2α for α_V , see Eq. (2). Thus the modified HFL equation became:

$$\frac{\Delta\sigma}{kT} = \frac{\Gamma}{(1 - \alpha\Gamma)^2} - \alpha\beta\Gamma^2 \quad (15)$$

The respective adsorption isotherm is:

$$K_s C_s = \frac{\Gamma}{1 - \alpha\Gamma} \exp \left[\frac{\alpha\Gamma(3 - 2\alpha\Gamma)}{(1 - \alpha\Gamma)^2} - 2\beta\alpha\Gamma \right] \quad (16)$$

and the Gibbs elasticity (with $\theta = \alpha\Gamma$)

$$\frac{\alpha E_G}{kT} = \frac{\theta(1 + \theta)}{(1 - \theta)^3} - 2\beta\theta^2 \quad (17)$$

3. Analysis of the adsorption parameters

3.1. Adsorption constant and thickness of the adsorbed layer

According to Eq. (9) the adsorption energy, E_A , is the major factor determining the value of the adsorption constant, K_s . It can be calculated by finding the change in free energy involved in the transfer of a molecule from the water phase to the upper hydrophobic phase (oil, in Fig. 2). We will consider a surfactant with a paraffinic chain with n_c carbon atoms, length per $-\text{CH}_2-$ group $l_1 \approx 0.126$ nm, cross-sectional area $\alpha_c \approx 0.20$ nm², and lateral area (along the chain) pertaining to one $-\text{CH}_2-$ group $\alpha_1 \approx 0.21$ nm² (all data are based on the geometrical parameters of the paraffinic chain as determined by Tanford [17]). Let w_c be the energy of transfer of one $-\text{CH}_2-$ group. The energy of transfer of the top $-\text{CH}_3$ group, is larger than w_c because of its larger area, but since there are no precise data for this energy for the interface air/water we will account for this approximately by adding an additional term w_c as for one more methyl group.

An effect, usually neglected (and we added it), is the displacement of an area α_c from the interface when the surfactant tail is adsorbed. The polar head remains immersed in the water phase and it should not contribute much to the adsorption energy when only short range interactions are effective. The situation could be different with the electrostatic interaction of the head with the interface for ionic surfactants or if there is change of hydration of the polar head. Hence, we will add a term E_h to account for this effect.

On the other side, one must account also for the partial immersion of the hydrophobic chain, due to the fact that the adsorption energy of a $-\text{CH}_2-$ unit is of the order of kT . If one assumes that the surfactant molecules is perpendicular to the interface as shown in Fig. 2b, its energy $u(z)$ will vary with the immersion depth as depicted in Fig. 2c and can be written as

$$u = -E_A + w_1 z \quad (18)$$

where w_1 is the immersion energy per unit length and E_A is the adsorption energy. Then the average immersion depth z_{imm} of the aliphatic chain will be:

$$z_{\text{imm}} = \int_0^{l_1} \exp(-bz) dz \approx \frac{1}{b} = \frac{kT}{w_c} l_1 \quad (19)$$

where $b = w_1/(kT) = w_c/(kTl_1)$. And since $kT \approx w_c$, one must conclude that $z_{\text{imm}} \approx l_1$, i.e. that the first $-\text{CH}_2-$ group will be entirely in the water phase and its contribution to the adsorption energy E_A will be negligible. This effect will cancel the additional contribution of the terminal $-\text{CH}_3$ group, which was assumed above equal to w_c .

Thus, the overall balance of energy leads to:

$$E_A = E_h + w_c n_c + \sigma_{\text{OW}} \alpha_c = E_0 + w_c n_c \quad (20)$$

where $E_0 \equiv E_h + \sigma_{ow}\alpha_c$ is that part of the adsorption energy, which is independent of the chain length. Equation similar to the second Eq. (20) was postulated by Davies and Rideal [19] based on experimental data. However, unlike us, they ascribed E_0 only to the adsorption energy of the polar head.

The result, Eq. (20), was used by us to derive an explicit equation for the “thickness of the adsorbed layer” [9] and the adsorption constant K_s . From Eq. (18), Boltzmann equation and Gibbs definition of Γ one can write:

$$\Gamma = \int_0^l [C_s(z) - C_s] dz \approx \frac{kT}{w_1} \exp\left(\frac{E_A}{kT}\right) C_s = K_s C_s \quad (21)$$

The comparison with Eq. (9) shows that $\delta_s = kT/w_1$. For air/water interface $\delta_s = 1.16 \text{ \AA}$ [9]. This result will be checked below. The effect of the term $\sigma_{ow}\alpha_c$ will be checked separately in a subsequent paper by using adsorption data obtained with several oil phases with different interfacial tension.

When deriving Eqs. (19) and (21) it was tacitly assumed that all surfactant molecules are fluctuating synchronically, that is they all remain in the same plane which is moving up and down. In reality, their motion is not coordinated so that the collision between the molecules might occur when the immersion of the colliding molecules is different which should affect the minimum area α . This effect was investigated in [18], where a general theory was developed and it was shown that in most cases it is small. The situation might be different if the transfer energy w_1 is small, which will be so if there are double bonds close to the hydrophilic head.

3.2. Minimum (proper) area of a molecule α

We used a simple method to find the dependence of α on Γ for Langmuir and Volmer equations, based on the fact, that α in the HFL equation of state, Eq. (15), is the true area per molecule $\alpha = \pi d^2/4$. To avoid confusion we will denote here the latter by α_H and $\alpha_H \Gamma_H$ by θ_H , and will use the notations θ_L and α_L , θ_V and α_V for the equations of state of Langmuir and Volmer, respectively. All three EOS (with $\beta=0$) can be written as [see Eqs. (6), (12) and (15)]:

$$\frac{\Delta\sigma}{kT\Gamma} = f_M(\theta_M) \quad (22)$$

where f_M is a function of θ_M different for the models of Langmuir, Volmer or HFL (hence the subscript M , indicating that the function is model dependent). Since the left hand sides of these equations do not depend on the model, the right hand sides must be equal. This leads to the equations:

$$-\frac{1}{\theta_L} \ln(1 - \theta_L) = \frac{1}{1 - \theta_V} = \frac{1}{(1 - \theta_H)^2} \quad (23)$$

For small θ one can expand the above expressions in series and by keeping only the linear terms in the expansions one finds

$$\alpha_L = 2\alpha_V = 4\alpha_H; \quad \text{at } \theta \rightarrow 0 \quad (24)$$

The second equation in Eq. (23) can be solved easily and leads to the exact relationship for the Volmer model:

$$\frac{\alpha_V}{\alpha_H} = 2 - \theta_H \quad (25)$$

The exact relation between θ_L and θ_H from Eq. (23) can be found only numerically and the obtained dependence of α_L/α_H vs. θ_H is shown in Fig. 3. Its asymptotic behavior at $\theta_H \rightarrow 0$ or $\theta_H \rightarrow 1$ is respectively

$$\frac{\alpha_L}{\alpha_H} = 4 - \frac{14}{3}\theta_H \quad \text{at } \theta_H \rightarrow 0 \quad \text{and} \quad \frac{\alpha_L}{\alpha_H} = 2 - \theta_H \quad \text{at } \theta_H \rightarrow 1 \quad (26)$$

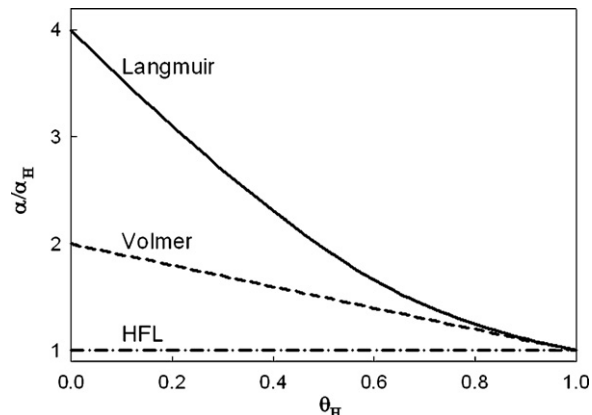


Fig. 3. Theoretical dependence of the minimum area per molecule α/α_H (relative to the value α_H of the isotherm HFL) for three models as a function of the degree of surface coverage $\theta_H = \alpha_H \Gamma$.

The second equation coincides with Eq. (25). This fact explains why the exact solutions for α_V/α_H and α_L/α_H in Fig. 3 merge already around $\theta_H = 0.7-0.8$.

Russanov [20] had ideas similar to ours about the dependence of the minimum area per molecule α on the adsorption Γ . By using a different approach from ours he also found for Langmuir model the limiting values 4 and 1 at $\theta_H \rightarrow 0$ and $\theta_H \rightarrow 1$, respectively. For the initial slope at $\theta_H \rightarrow 0$ he obtained however -6.616 instead of our value $-14/3$, see Eq. (26).

To check the reliability and applicability of the results for α for the three models we performed numerical comparison between the results they lead to. The hard core part of HFL equation has been checked numerically by Monte Carlo and dynamical calculations (see Fig. 4, adapted by us from [16] by adding the data for Volmer and Langmuir models) and showed excellent agreement with these data almost up to complete coverage. At the same figure are plotted the data, obtained from the models of Langmuir and Volmer [the hard core parts of Eqs. (6) and (12), respectively]—the differences are obvious.

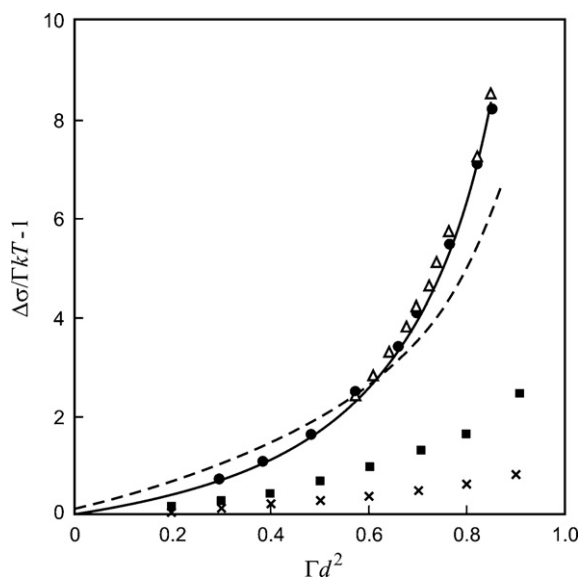


Fig. 4. Comparison of the hard core parts of three two-dimensional equations of state: solid line—Eq. (15) of HFL; ●: Monte Carlo calculations of Wood; Δ: dynamical calculations of Alder and Wainwright; - - - -: Lennard–Jones–Devonshire cell theory; ■: Volmer Eq. (6); ×: Langmuir Eq. (12).

Such differences are revealed also by the virial expansions of the hard core parts of the three equations. The expansion of the hard core part of the HFL Eq. (15) is:

$$\frac{\Delta\sigma}{kTT} = 1 + 2\theta + 3\theta^2 + 4\theta^3 + 5\theta^4 + \dots \quad (27)$$

to be compared with the exact result [16]:

$$\frac{\Delta\sigma}{kTT} = 1 + 2\theta + 3.128\theta^2 + 4.262\theta^3 + 4.95\theta^4 + \dots \quad (28)$$

The respective expansions for Langmuir and Volmer models are:

$$\frac{\Delta\sigma}{kTT} = 1 + \frac{\theta}{2} + \frac{\theta^2}{3} + \frac{\theta^3}{4} + \frac{\theta^4}{5} + \dots \quad (29)$$

$$\frac{\Delta\sigma}{kTT} = 1 + \theta + \theta^2 + \theta^3 + \theta^4 + \dots \quad (30)$$

The large discrepancy with the exact result for HFL should not be surprising for the model of Langmuir, which was developed for a very different (localized) monolayer, but the Volmer model is supposed to work just as HFL model for a fluid monolayer. The results from this section lead to the important conclusion that the area per molecule, determined by using a model isotherm (not based on HFL), may not be a true physical constant, but may depend on the model used and the adsorption, Γ . The other, even more important, conclusion is that it is not enough to use the correct hard core part (that of HFL) to obtain correct EOS. Indeed, the results shown in Table 1, obtained by the modified HFL Eq. (15), are by no means better than the ones obtained by Frumkin and van der Waals equations. On the other hand, when the same data are treated for O/W by setting $\beta=0$, the result for HFL is quite reasonable. This shows that the blame must be put also on β and one must find a more correct way to account for the intermolecular interaction.

As already pointed out all three considered models are based on the assumption that the surfactant molecules are hard interacting discs, analogously to most of the bulk model EOS, where the molecules are considered as hard interacting spheres. We accounted in part for the role of the surfactant tails (which we considered as solid rods) in the adsorption constant, K_s , both by the adsorption energy and the immersion of the tails, determining the thickness of the adsorbed layer δ_s . However, the tails are by no means rigid rods, because even simple tails, like the aliphatic chains, can perform (hindered) rotation around the C–C bonds and can therefore change conformation. As a result if the chain is long enough it will behave like a polymer and form coils, which might be larger than the hydrophilic group and will determine the minimum area per molecule, α . The shorter chains may remain approximately linear, but have the freedom to be inclined or even to lie flat on the interface. Which one of these possibilities will take place depends on the relative contribution of the respective process to the free energy of the system. Many researchers account in one way or another for some of these complications in order to explain some experimental observations. However, we formulated as our goal the understanding of the very basic effects and dealing with these complications is beyond the scope of this article, the more so that their rigorous treatment usually requires special techniques—the interested reader can find detailed discussion of some of these effects in ref. [4]. We will return to the discussion of the simplest case—rigid rods perpendicular to the interface later, in Sections 3.3 and 6.

3.3. The interaction constant, β

This is the most controversial and the most difficult for determination constant. The error of its determination is very rarely as small as 10%. It is usually 20–25% but can be even higher than 100% (for more detailed discussion see Appendix A). That is why

we decided to derive an approximate expression for β just to have some benchmark for comparison of the results of the different fits.

In fact constant β is part of the second virial coefficients B_2 and enters in it always as a product with α , see Eqs. (6), (12) and (15).

The interaction part of the second virial coefficient, $B_{2,\text{int}}$, is defined as [13]

$$B_{2,\text{int}} = \pi \int_d^\infty \left[1 - \exp\left(-\frac{u_{\text{int}}}{kT}\right) r \, dr \right] \quad (31)$$

where u_{int} is the interaction energy between two surfactant molecules, r is the separation between them and $d = (4\alpha/\pi)^{1/2}$ is the closest distance. We will suppose that the molecules are perpendicular to the interface. The integral accounts for the contribution from the long range (usually attractive) interactions.

We will assume that $|u_{\text{int}}| \ll kT$ so that the integrand in the right-hand side of Eq. (31) can be expanded in series with respect of $u_{\text{int}}/(kT)$. The most common case is the attractive London interaction. In this case one can model the tails of the surfactant molecules as a line with uniform linear molecular density, $\rho_t = 1/l_1$ each with constant of interaction with another $-\text{CH}_2$ -group $L = 3\alpha_p I_0/4$ where α_p is polarizability and I_0 is the ionization potential [11]. In this case the interaction energy is calculated as

$$u_{\text{int}}(r) = -\rho_t^2 L \int_0^l \int_0^l [r^2 + (z_2 - z_1)^2]^{-3} \, dz_1 \, dz_2 \quad (32)$$

where z_1 and z_2 are the vertical coordinates of the interacting $-\text{CH}_2$ -groups.

Performing the integration of Eq. (32), substituting the result in Eq. (31) and having in mind Eq. (15) one finds:

$$B_{2,\text{int}} = -\frac{\pi\rho_t^2 L}{4d^2 kT} \frac{l}{d} \arctan\left(\frac{l}{d}\right) = -\alpha\beta \quad (33)$$

Therefore, one can use the second virial coefficient for the calculation of β if α is known. In the case $l \gg d$ one can write:

$$B_{2,\text{int}} = -\frac{\pi\rho_t^2 L}{4d^2 kT} \left[\frac{\pi l}{2d} - 1 + \frac{1}{3}\left(\frac{d}{l}\right)^2 - \frac{1}{5}\left(\frac{d}{l}\right)^4 + \dots \right] \quad (34)$$

Then one can use the following asymptotic expression for estimation of β :

$$B_{2,\text{int}} \approx -\frac{\pi^2 \rho_t^2 L l}{8d^3 kT} = -\alpha\beta \quad (35)$$

4. Generalized equations for interacting surfactants

4.1. Localized adsorption (Langmuir model)

We will try now to use more general analogs of the equations of Frumkin, Eq. (12), van der Waals, Eq. (6), and the extended equation of HFL, Eq. (15), by accounting more correctly for the effect of the intermolecular interaction. We will begin by Langmuir model, since a generalized equation, much more precise than Frumkin equation, is known. It was derived first by Bethe and later by Guggenheim (see [13], Chapter 14) who called it *quasi-chemical approximation*. The reason for this title is that the basic equation is in fact the equilibrium constant between the pairs 0–0, 0–1 and 1–1 (0 stands for an empty and 1 stands for an occupied center) with free energy w . The resulting EOS is (see also [9]):

$$\frac{\alpha_L \Delta\sigma}{kT} = -\ln(1 - \theta) - \frac{z_n}{2} \ln \left[\frac{\beta_n + 1 - 2\theta}{(\beta_n + 1)(1 - \theta)} \right]; \quad (36)$$

$$\beta_n \equiv [1 + 4\beta\theta(1 - \theta)]^{1/2}$$

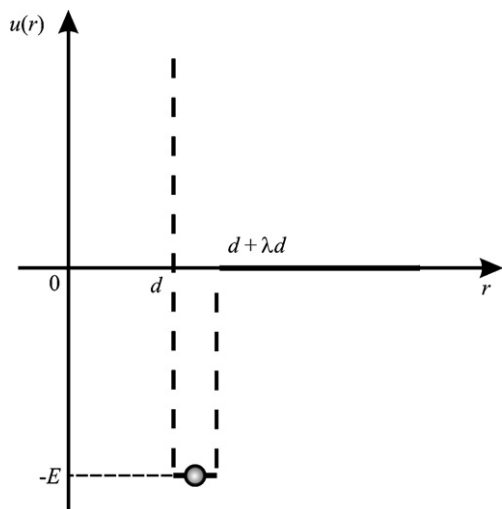


Fig. 5. Sketch of “sticky potential” of width λd and depth E for a molecule of length (or diameter) d .

The adsorption isotherm is

$$K_s C_s = \frac{\Gamma}{1-\theta} \left[\frac{1}{1+\beta} \frac{1+\beta_n+2\beta(1-\theta)}{1+\beta_n+2\beta\theta} \right]^{z_n/2} \quad (37)$$

and the Gibbs elasticity:

$$\frac{\alpha_L E_G}{kT} = \frac{\theta}{1-\theta} - \frac{2z_n \beta \theta^2}{\beta_n(\beta_n+1)} \quad (38)$$

In order to compare Eqs. (36) and (12), we expanded the interaction term, that is the second term in the right-hand side in Eq. (36), in series:

$$\frac{\alpha_L \Delta\sigma}{kT} = -\ln(1-\theta) - \frac{z_n \beta}{2} \theta^2 + z_n \beta^2 \theta^3 - \frac{3+10\beta}{4} z_n \beta^2 \theta^4 + \dots \quad (39)$$

This result suggests three important conclusions: (i) the hard core part of the Langmuir equation (the first term in the right) is correct; (ii) the Frumkin equation, Eq. (12), accounts accurately for the interaction up to the second virial coefficient (the term with θ^2); (iii) more importantly, only in the second virial coefficient the interaction contribution is proportional to β , whereas in the third virial coefficient it is proportional to β^2 , and so on. This means that if $\beta \ll 1$, it is legitimate even for large θ to keep only the term with the second virial coefficient (proportional to β) from the interaction contributions. Hence, the Langmuir–Frumkin equation is exact if $\beta \ll 1$, provided that the adsorption is really localized.

4.2. Non-localized 1D adsorption (Volmer model)

This problem can be solved exactly if one uses the approach of the “sticky potential” developed by Baxter [21]. It is based on the fact that in many cases the width of the interaction well is very small and the attraction between the particles becomes sizable only when they almost touch each other. The assumed potential distribution is sketched in Fig. 5 by dashed line. Up to the minimum distance d between the particles the potential energy u is $+\infty$, then in the potential well between d and $d + \lambda d$ it remains constant and equal to $-E$, after which it becomes zero. When the particles are approaching each other, $\lambda \rightarrow 0$, but $E \rightarrow -\infty$ in such a way that the product λE remains equal to the interaction energy at contact w . Briefly, this means that the interaction energy is represented by a δ -function of Dirac.

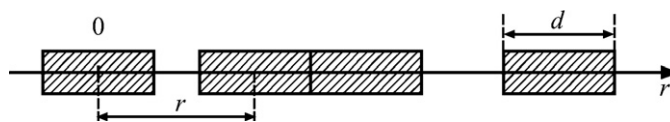


Fig. 6. Scheme of one-dimensional adsorption: sticks of zero thickness and length d strung on a thread.

The system we will consider (see Fig. 6) represents a set of N_a sticks each of length d strung on a thread of total length L_1 which is analog for this case to the area A of 2D systems. The moving particles in direction r exert a 1D pressure $\Delta\sigma$.

The convenient thermodynamic potential for this problem is the isothermic-isobaric potential $N_a \mu$ ([13], Chapter 1):

$$N_a \mu = F + L_1 \Delta\sigma; \quad d(N_a \mu) = L_1 d(\Delta\sigma) + \mu dN_a \quad (40)$$

with partition function Δ_p :

$$N_a \mu = -kT \ln \Delta_p \quad (41)$$

$$\Delta_p = \int_0^\infty Z \exp\left(-\frac{L_1 \Delta\sigma}{kT}\right) d\left(\frac{L_1 \Delta\sigma}{kT}\right); \quad Z = Z_{hc} \exp\left(-\frac{u}{kT}\right) \quad (42)$$

where Z is the configurational integral. Its hard core part Z_{hc} can be found by substituting the first term in the right-hand side of Eq. (6) in Eq. (5) (both written for one dimension with $N_a = \text{constant}$) and integrating. The result is:

$$F_{hc} = -kT \ln Z_{hc} = -kT \ln(L_1 - N_a d) \quad (43)$$

The adsorption isotherm is obtained from the second Eq. (40) along with Eq. (41):

$$\frac{1}{\Gamma} = -\frac{kT}{N_a} \left[\frac{\partial \ln \Delta_p}{\partial(\Delta\sigma)} \right]_{N_a}; \quad \Gamma \equiv \frac{N_a}{L_1} \quad (44)$$

By introducing the dimensionless variables

$$x \equiv r \frac{N_a \Delta\sigma}{kT}; \quad x_0 \equiv d \frac{N_a \Delta\sigma}{kT} \quad (45)$$

we can put Eq. (42) in a simpler form:

$$\Delta_p = \frac{kT}{\Delta\sigma} \int_{x_0}^\infty (x - x_0) \exp\left[-x - \frac{u(x)}{kT}\right] dx \quad (46)$$

The integral splits into two parts, which are easily solvable: (i) $x_0 < x < (1 + \lambda)x_0$, where u is constant ($u = -E$) and (ii) $(1 + \lambda)x_0 < x < \infty$ where $u = 0$. In the result one must use the sticky approximation, which means to set $\exp[E/(kT)] = w/(\lambda kT) = \beta/\lambda$. Upon inserting the result in Eq. (46) and expanding the appearing exponential function of $\lambda \rightarrow 0$ in series up to the linear term, one obtains a quadratic equation with respect of $\Delta\sigma/(kT\Gamma)$, whose solution is the sought for 1D EOS¹:

$$\frac{\Delta\sigma}{kT} = \frac{\Gamma}{2\alpha\beta} \left[-1 + \left(1 + 4\beta \frac{\alpha\Gamma}{1-\alpha\Gamma}\right)^{1/2} \right] \quad (47)$$

where $\alpha \equiv d$. This result can be rationalized to acquire more convenient and transparent form:

$$\frac{\Delta\sigma}{kT} = \frac{\Gamma}{1-\alpha\Gamma} \frac{2}{1+R_\beta^1}; \quad R_\beta^1 \equiv \left(1 + 4\beta \frac{\alpha\Gamma}{1-\alpha\Gamma}\right)^{1/2}; \quad \beta = \frac{w}{kT} \quad (48)$$

¹ This result was first obtained in [22] by using a somewhat different approach.

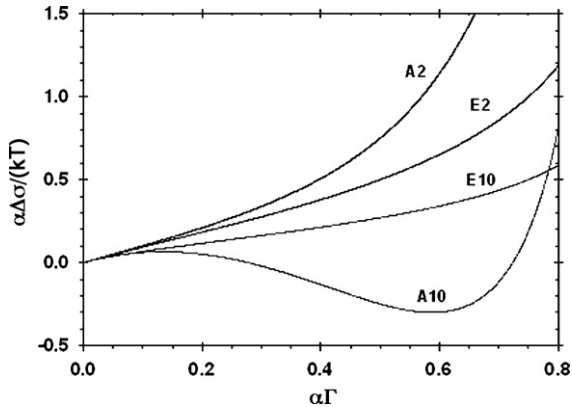


Fig. 7. Comparison of the exact E (Eq. (48)) and approximate A (Eq. (6)) equations of Volmer. The numbers indicate the values of $\beta=2$ and $\beta=10$, respectively.

In view of further discussions we will expand the result in series with respect to β :

$$\frac{\Delta\sigma}{kT} = \frac{\Gamma}{1-\alpha\Gamma} \frac{2}{1+R_\beta^1} \approx \frac{\Gamma}{1-\alpha\Gamma} \times \left[1 - \beta \frac{\alpha\Gamma}{1-\alpha\Gamma} + 2\beta^2 \left(\frac{\alpha\Gamma}{1-\alpha\Gamma} \right)^2 - \dots \right] \quad (49)$$

The respective adsorption isotherm is obtained as usual by integrating Gibbs equation along with Eq. (48):

$$K_s C_s = \frac{\Gamma}{1-\theta} \left(\frac{2}{1+R_\beta^1} \right)^2 \exp \left[\frac{2\theta}{(1+R_\beta^1)(1-\theta)} \right] \quad (50)$$

Some obvious conclusions follow from this result: (i) the comparison with Eq. (6) (with $\beta=0$) reveals that Volmer equation for hard particles is rigorous only in one dimension; (ii) the van der Waals term $\alpha\beta\Gamma^2$ is obtained if in Eq. (49) one sets β^2 , β^3 etc. equal to zero and if in the denominator of the term, linear in β , one neglects $\alpha\Gamma$ —but then, why should one keep $\alpha\Gamma$ in the main term, multiplying the square brackets? The expansion in series of the attractive terms leads to the same conclusion:

$$\frac{\Delta\sigma}{kT} = \frac{\Gamma}{1-\alpha\Gamma} \frac{2}{1+R_\beta^1} \approx \frac{\Gamma}{1-\alpha\Gamma} \times \left[1 - \beta\theta - (\beta - 2\beta^2)\theta^2 - (\beta - 4\beta^2 + 5\beta^3)\theta^3 + \dots \right] \quad (51)$$

One sees that unlike the case of localized adsorption, see Eq. (39), all virial coefficients contain terms linear in β , so that it is not obvious if one can keep only the term $\beta\theta$ as it is done in van der Waals equation, Eq. (6).

In Fig. 7 we carried out numerical comparison for two values of β of van der Waals equation, Eq. (6), and the exact Eq. (48). One sees that for small values of $\beta=2$ and θ the van der Waals equation is reasonably close to the exact solution. They diverge however strongly for large $\beta=10$ even when θ is small. Worst of all, at large values of β van der Waals equation exhibits phase transition, although phase transitions in one-dimensional systems are forbidden [12].

4.3. Non-localized 2D adsorption (HFL model)

It has been rigorously shown [21] that exact solution for the 2D case is impossible even for hard particles. The exact solution with sticky potential of Baxter is difficult even in the 3D case and the result is very complicated and not very convenient for use. That is why we decided to use a heuristic approach in the hope that it will

lead to an EOS more rigorous than the equations for non-localized adsorption presented in Section 2.

The starting point for us was a procedure developed by Hemmer and Stell [23] for deriving equations for 3D systems, which are exact up to terms linear in β . We modified their basic equation to make it applicable to 2D systems:

$$\Delta\sigma = (\Delta\sigma)_{hc} - \left(\frac{B}{B_{hc}} - 1 \right) \left[(\Delta\sigma)_{hc} - \theta \frac{\partial(\Delta\sigma)_{hc}}{\partial\theta} \right] \quad (52)$$

where the subscript “hc” denotes “hard core” both for the second virial coefficient B and the surface pressure $(\Delta\sigma)_{hc} = (kT/\alpha)\theta/(1-\theta)^2$, see Eq. (15). For hard discs $B/B_{hc} - 1 = -\beta$. By inserting this and the expression for $(\Delta\sigma)_{hc}$ in the right-hand side of Eq. (52), we obtain a more general form of the HFL equation:

$$\frac{\Delta\sigma}{kT} = \frac{\Gamma}{(1-\alpha\Gamma)^2} \left(1 - 4\beta \frac{\alpha\Gamma}{1-\alpha\Gamma} \right) \quad (53)$$

A comparison with Eq. (49) reveals that the two equations have the same structure: the respective hard core factor is multiplied by expressions differing only by the numerical coefficient. It is not difficult to realize that if instead of Eq. (48) one uses

$$\frac{\Delta\sigma}{kT} = \frac{\Gamma}{(1-\alpha\Gamma)^2} \frac{2}{1+R_\beta^1}; \quad R_\beta^1 \equiv \left(1 + 16\beta \frac{\alpha\Gamma}{1-\alpha\Gamma} \right)^{1/2} \quad (54)$$

we will obtain an expansion in series of β which is identical to Eq. (53) up to the linear term in β and looks like Eq. (49) (with different numerical coefficients):

$$\frac{\Delta\sigma}{kT} \approx \frac{\Gamma}{(1-\alpha\Gamma)^2} \left[1 - 4\beta \frac{\alpha\Gamma}{1-\alpha\Gamma} + 32\beta^2 \left(\frac{\alpha\Gamma}{1-\alpha\Gamma} \right)^2 - \dots \right] \quad (55)$$

The adsorption isotherm, following from Eq. (54), is:

$$K_s C_s = \frac{\Gamma}{1-\theta} \left(\frac{2}{1+R_\beta^1} \right)^{(1+8\beta/4\beta)} \exp \left[\frac{2\theta(4-3\theta)}{(1+R_\beta^1)(1-\theta)^2} \right] \quad (56)$$

and the Gibbs elasticity:

$$\frac{\alpha E_G}{kT} = \frac{\theta}{(1+R_\beta^1)(1-\theta)^3} \left(1 + 2\theta + \frac{1}{R_\beta^1} \right) \quad (57)$$

We tried to check at least approximately the reliability of Eq. (55) by two methods: (i) calculation of the third virial coefficient B_3 by the method of Kihara [24] and (ii) by solving Kirkwood integral equation (see e.g. [25]). Both methods involve very complicated and lengthy calculations, which will be published in a separate paper. Here we will give only an idea how they were done and will present the final results.

The virial expansion is

$$\frac{\Delta\sigma}{kT\Gamma} = 1 + B_2\Gamma + B_3\Gamma^2 + B_4\Gamma^3 + \dots \quad (58)$$

The method of Kihara for B_3 for spheres represent integration over the overlapping volumes of three spheres weighted by the respective energies of interaction, represented by square well. We modified it for three discs on a surface and applied to the final results the sticky approximation instead of square well. The expansion of Eq. (54) in terms of Γ gives $B_3 = 3\alpha^2(1-4\beta+3\beta^2)$ and the obtained theoretical value by the method of Kihara was $B_3 = 3\alpha^2(1-4\beta+1.33\beta^2-0.62\beta^3)$. Therefore, Eq. (54) gives for B_3 exactly the linear term in β , reasonably well β^2 , but β^3 comes only from the next term of the expansion. These differences will be important at rather large values of β and θ , but as we will see later such values are rarely encountered with most simple surfactants. Besides, Kihara himself pointed out that the third virial coefficient is very sensitive to the shape of the potential, so that one can hardly

expect exact results from approximate potentials like “square well” or “sticky potential”.

The 2D analog of the integral equation of Kirkwood

$$-kT \ln[g(r_{12})] = u(r_{12}) + \Gamma \int_{(A)} u(r_{13})g(r_{13})[g(r_{13}) - 1] dA_3 \quad (59)$$

accounts through the correlation function g for the fluid structure, multiple collisions and interaction energy and can be used to derive the EOS. As it is usual when solving such problems we used several approximations, the most important ones being the use of the sticky potential and expansion of the correlation function in series up to linear terms in β (in ref. [25] the same approximation was used):

$$g(r) = g_{hc}(r) + \frac{w}{kT}g_1(r) + \dots \quad (60)$$

We succeeded to obtain an EOS which confirmed the coefficients 4β and $32\beta^2$ in Eq. (55) for small and moderate θ 's.

5. Data processing

The experimental data for $\sigma = \sigma(C_s)$ were processed by numerical simultaneous solution of the equations of the adsorption isotherm and the equation of state. They are obtained experimentally as a set of values $\sigma^{\text{exp}}(c_k)$ for $k=1, 2, \dots, N$, where N is the number of experimental points. The value of the interfacial tension of pure solvent, σ_p , is known and therefore, the input data for the numerical procedure are the values of the surface pressure $\Delta\sigma^{\text{exp}}(c_k)$ for $k=1, 2, \dots, N$. If we choose some trial values for the model parameters (α, β and K_s), then for each concentration, c_k , we can calculate the adsorption, $\Gamma^{\text{th}}(c_k)$, predicted from the adsorption isotherm. The adsorption isotherms are represented by monotonic functions (except for the cases of phase transition). For that reason we use the simplest bisection method for numerical solution of the transcendental equations describing the adsorption isotherms. Substituting the calculated value of $\Gamma^{\text{th}}(c_k)$ into the equation of state we calculate the prediction for the surface pressure $\Delta\sigma^{\text{th}}(c_k)$. Such procedures has a useful “bi-product”—it gives as intermediate result the dependence $\Gamma(C_s)$, which can be used for calculation of the EOS $\Delta\sigma$ vs Γ and the Gibbs elasticity.

The adjustable parameters (α, β and K_s) are determined by means of the least-squares method, that is, by numerical minimization of the merit function

$$\chi^2(\alpha, \beta, K_s) = \frac{1}{N} \sum_{k=1}^N [\Delta\sigma^{\text{exp}}(c_k) - \Delta\sigma^{\text{th}}(c_k; \alpha, \beta, K_s)]^2 \quad (61)$$

assuming that all experimental points have equal errors. The minimization algorithm is simple. We define relative steps ($s_\alpha, s_\beta, s_{K_s}$) of model parameters. Starting from a given point (α, β, K_s) we define all points in the $3 \times 3 \times 3$ local grid around (α, β, K_s) with absolute steps ($s_\alpha\alpha, s_\beta\beta, s_{K_s}K_s$) and calculate the values of the merit function. We compare all 27 values in order to find the position of the local minimum, change the initial guess with the obtained position, and repeat the procedure again. The algorithm stops when the initial guess and the obtained position of the local minimum coincide. This simple procedure gives possibility to calculate the position of the global minimum χ_{min} of the merit function.

One problem we encountered with the generalized HFL isotherm, Eq. (56), was that it contains a power $(1+8\beta)/(4\beta)$, which diverges for $\beta=0$ and makes the fit uncertain for small β . To avoid or at least to decrease this problem we transformed the logarithm

of the singularity term as follows:

$$\frac{1}{4\beta} \ln \left(\frac{2}{1+R_\beta} \right) = -\frac{1}{4\beta} \ln \left(1 + \frac{R_\beta - 1}{2} \right) = -\frac{1}{4\beta} \ln(1 + \xi)$$

$$\text{with } \xi \equiv \frac{8\beta}{1+R_\beta} \frac{\theta}{1-\theta} \quad (62)$$

leading to

$$\frac{1}{4\beta} \ln \left(\frac{2}{1+R_\beta} \right) = -\frac{2}{1+R_\beta} \frac{\theta}{1-\theta} \left(1 - \frac{\xi}{2} + \frac{\xi^2}{3} - \frac{\xi^3}{4} + \dots \right) \quad (63)$$

In the new expression β appears in the nominators and there is no divergence.

6. Numerical results and discussion

We decided to check and compare all adsorption equations discussed above with two types of surfactant: (i) several homologues of the dimethyl alkyl phosphine oxide DMPO: C8, C10, C12 and C14 from ref. [26] and C8, C9, C10, C11, C12 and C13 from ref. [27]; and (ii) aliphatic acids: C7, C8 and C9 from ref. [28] and C10 from ref. [29]. The reason for this choice was our desire to investigate the role of different factors. The DMPO's are typical surfactants with large hydrophilic groups, which are supposed to interact between themselves only by steric repulsion, whereas the acids are known to form strong hydrogen bonds and to remain dimerized even in gas phase. For the sake of brevity we will use the following abbreviations for the names of the models: the first capital letter indicates the model equations are based upon (H for HFL, V for Volmer and L for Langmuir). If it is followed by G, it means that we are using the generalized isotherm or EOS for the respective model. When it is followed by a number, it indicates the number of free parameters involved (2 or 3), e.g. H-G means generalized HFL, Eq. (56), and V-3 means Volmer model with 3 parameters, Eq. (8). We must point out that all fits were practically perfect—most had regression coefficients $R^2=0.999$ or 0.9999 and only a few were with 0.997 or alike. In spite of the good fits couple of substances gave somewhat strange results and we discarded them from the numerical calculations, although we kept them in the table—this refers to the C8 and C10 DMPO from both series. The reason for this could be purely mathematical (see Appendix A), although we suspect also some physical reasons, but could not prove them beyond doubt.

Because of the numerous data, we did not present all results graphically, especially when they were similar. Although all groups of data lead to similar or even identical results, in most numerical calculations with DMPO we used the data of ref. [27] simply because they were more numerous. Typical fits of the adsorption isotherms $\sigma = \sigma(C_s)$ and the equations of state $\Delta\sigma = \Delta\sigma(\Gamma)$ are presented in Figs. 8 and 9 (for clarity the fitting curves in Fig. 9 are not shown). The numerical results obtained from the fits of the adsorption isotherms for all considered above six models are presented in Table 2 (for DMPO) and 3 (for acids). We processed also all EOS, which gave practically identical data with the adsorption isotherms for the parameters α and β . Only for illustration of this statement in Table 2 we presented the results obtained with the EOS from the model H-G with DMPO, which can be compared with the results in the adjacent column H-G, obtained by the adsorption isotherm.

Even superficial inspection of the data in Tables 2 and 3 allows some interesting conclusions.

- (i) Practically all 6 models lead to identical (although slightly scattered) values of the adsorption constant K_s . This should not be surprising since K_s is present only in the left hand side of the adsorption isotherms. Indeed, if in all adsorption isotherms

Table 2

Parameters from the fit with seven equations of the data for adsorption of alkyl di-methyl phosphine oxides (DMPO) at Air/Water interface (K_s : adsorption constant; α : minimum area per molecule; β : interaction constant); H-G: EOS Eq. (54); H-G Eq. (56); V-G Eq. (48); H-3 Eq. (16); V-3 Eq. (8); L-3 Eq. (13).

Surfactant	Parameters	EOS-G	H-G	V-G	L-G	H-3	V-3	L-3
C8-DMPO [26]	$K_s \times 10^4$, (cm)	–	8.30	8.56	7.85	9.23	8.58	7.84
	α (\AA^2)	24.0	26.70	36.17	47.92	18.61	31.20	47.92
	β	0.14	0.28	0.18	0.01	0.14	0.09	0.01
C8-DMPO [27]	$K_s \times 10^4$, (cm)	–	11.41	10.71	9.33	11.86	10.77	9.32
	α (\AA^2)	24.5	23.91	35.09	48.80	19.84	32.55	48.80
	β	0.13	0.12	0.08	0.00	0.03	0.00	0.01
C9-DMPO [27]	$K_s \times 10^4$, (cm)	–	20.46	23.78	23.94	20.56	23.12	23.92
	α (\AA^2)	31.0	31.33	41.91	45.95	24.40	34.21	45.95
	β	0.52	0.61	0.55	0.08	4.16	1.25	0.08
C10-DMPO [26]	$K_s \times 10^4$, (cm)	–	83.50	88.44	73.93	91.32	83.65	74.46
	α (\AA^2)	18.9	25.80	31.50	43.17	19.56	30.78	43.23
	β	0.01	0.29	0.06	0.01	1.03	0.42	0.01
C10-DMPO [27]	$K_s \times 10^4$, (cm)	–	81.90	81.30	71.77	79.37	85.03	71.83
	α (\AA^2)	24.49	25.04	35.29	42.71	20.44	29.39	42.71
	β	0.20	0.27	0.25	0.01	2.05	0.06	0.01
C11-DMPO [27]	$K_s \times 10^4$, (cm)	–	116.4	165.7	172.0	133.0	144.0	171.7
	α (\AA^2)	30.02	30.04	38.65	40.59	22.62	31.96	40.69
	β	1.15	1.25	1.05	0.78	6.13	2.81	0.74
C12-DMPO [26]	$K_s \times 10^4$, (cm)	–	429.0	583.0	634.5	500.9	548.1	639.5
	α (\AA^2)	29.8	30.30	39.66	41.01	22.61	31.89	40.96
	β	1.02	1.23	1.14	0.73	5.92	2.61	0.67
C12-DMPO [27]	$K_s \times 10^4$, (cm)	–	300.0	475.0	508.4	402.0	440.3	524.4
	α (\AA^2)	33.34	33.45	42.77	44.15	24.52	34.55	44.06
	β	1.76	1.97	1.74	1.59	7.24	3.55	1.34
C13-DMPO [27]	$K_s \times 10^4$, (cm)	–	612.2	982.0	1066	842.1	927.4	1061
	α (\AA^2)	27.90	27.90	35.68	36.73	20.38	28.69	36.98
	β	1.93	2.07	1.82	1.63	7.33	3.59	1.48
C14-DMPO [26]	$K_s \times 10^4$, (cm)	–	3740	5972	6273	4629	5142	6048
	α (\AA^2)	30.7	31.00	38.64	40.38	23.02	32.15	40.81
	β	1.31	1.51	1.10	0.80	6.52	2.95	0.88

we set $\alpha = \beta = 0$, they will all give the same result-Henry's law $K_s C_s = \Gamma$, which is of course model independent.

- (ii) The two models, based on Langmuir isotherm L-G and L-3, lead for DMPO practically to the same values of the adsorption parameters. This confirms our theoretical considerations in Section 4.1 that for small values of β the Frumkin equation becomes exact for localized adsorption. The situation is however somewhat different with the acids in Table 3, where β can be as large as 6.
- (iii) The area per molecule, α , determined by the generalized equations H-G, V-G and L-G increases in this order, as anticipated in Section 3.2. However, their ratio is not 1/2/4 as it must be for $\theta \rightarrow 0$ according to the theory, because the fit gives some aver-

aged value for all concentrations—for the lower homologues the ratio is approximately 1/1.3/2, but for the higher homologues it becomes 1/1.3/1.3, which is in agreement with the behavior of the curves at $\theta \rightarrow 1$ in Fig. 3.

- (iv) The simplified equations, Eqs. (8), (13) and (16), lead to smaller values of α and larger values of β (in a correlated manner) with respect to the values from the generalized equations. For example, the values of α , obtained by the approximate van der Waals equation V-3 are lower than the values obtained with the respective exact equation V-G, which in turn are much larger than the values, obtained with the 2D equation H-G. As a result the values of α obtained by V-3 become closer (but still remain larger by 10–25%) to the presumably true values,

Table 3

Parameters from the fit with seven equations of the data for adsorption of aliphatic acids at Air/Water interface (K_s : adsorption constant, α : minimum area per molecule, β : interaction constant); H-G EOS Eq. (54); H-G Eq. (56); V-G Eq. (48); H-3 Eq. (16); V-3 Eq. (8); L-3 Eq. (13).

Surfactant, [ref.]	Parameters	EOS-G	H-G	V-G	L-G	H-3	V-3	L-3
C7-acid [28]	$K_s \times 10^4$, (cm)	–	0.906	1.46	1.68	1.53	1.58	1.82
	α (\AA^2)	22.9	23.1	30.0	30.5	16.5	23.6	30.5
	β	2.97	3.38	3.55	3.44	8.54	4.67	2.51
C8-acid [28]	$K_s \times 10^4$, (cm)	–	1.76	2.20	3.16	3.63	3.73	3.90
	α (\AA^2)	15.1	18.1	27.9	29.3	14.5	21.5	29.8
	β	3.26	6.26	10.3	6.91	10.4	6.02	3.58
C9-acid [28]	$K_s \times 10^4$, (cm)	–	9.52	15.5	18.4	16.9	18.4	20.7
	α (\AA^2)	20.9	21.8	28.6	29.1	15.7	22.3	29.1
	β	3.04	4.18	4.65	4.27	9.31	5.03	2.66
C10-acid [29]	$K_s \times 10^4$, (cm)	–	16.8	30.0	42.3	41.8	45.7	51.2
	α (\AA^2)	20.2	21.9	28.5	28.8	15.6	22.1	28.8
	β	4.28	7.55	8.58	6.07	10.5	5.86	3.30

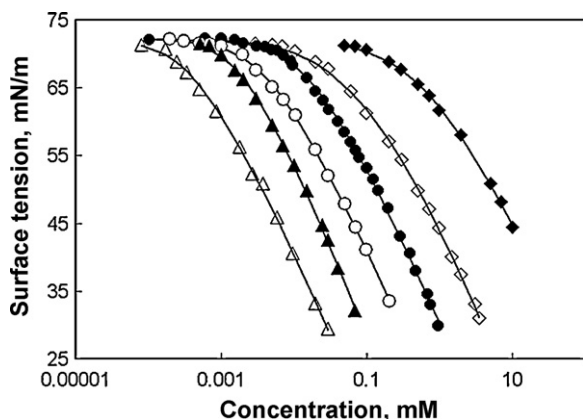


Fig. 8. Fit by model H–G of the curves surface tension vs. surfactant concentration for the DMPO surfactants—◆: C8; ◇: C10; ●: C11; ○: C12; ▲: C13; △: C14.

obtained from H–G (see Tables 2 and 3) thus creating the wrong impression that V–3 might be a correct equation. However, this decrease is not uniform for all DMPO's and it is not clear how large the error is. The reason for this behavior can be understood by comparing curves E2 (for the exact equation V–G) and A2 (for the approximate V–3). For example, value of the abscissa $\alpha\Gamma \approx 0.5$ corresponds to ordinate 0.5 for E2, but to 0.75 for A2. In order to obtain the correct value of the ordinate 0.5 from A2 one must choose $\alpha\Gamma \approx 0.4$, which can be achieved only by decreasing α by 25%. The coordination between α and β is analyzed in Appendix A. The same effects are observed with all approximate models. For instance, α drops for the approximate model H–3 even below 20 \AA^2 , while β reaches the incredible values of 6–7.

Truthful to our philosophy, presented in Introduction, we did everything possible to check at least some results of the fits by independent methods or data. We are not aware of a method allowing direct determination of the most important parameter α . However, this information can be extracted from the EOS of C18–DMPO measured by Noskov et al. [30]. From their curves one can deduce that the collapse point of the monolayer corresponds to area 34 \AA^2 . Assuming that at this area the packing was closed hexagonal and knowing that the area of the inscribed circle is 0.906 of that of the hexagon, one finds $\alpha = 30.8 \text{ \AA}^2$, which is practically equal to the values obtained by us by the method H–G for the DMPO's above C10. It is very probable that the other few DMPO have the same area. As for the acids, the values obtained (except for C8) between 20 \AA^2 and 20.9 \AA^2 hardly need verification, since this is the cross-sectional area of the paraffinic chain.

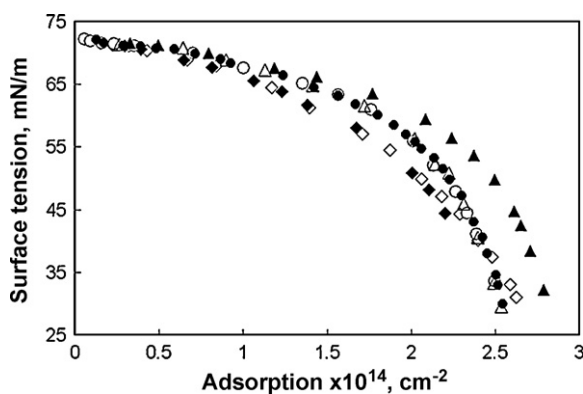


Fig. 9. Equation of state of DMPO surfactants from model H–G (same symbols as in Fig. 8).

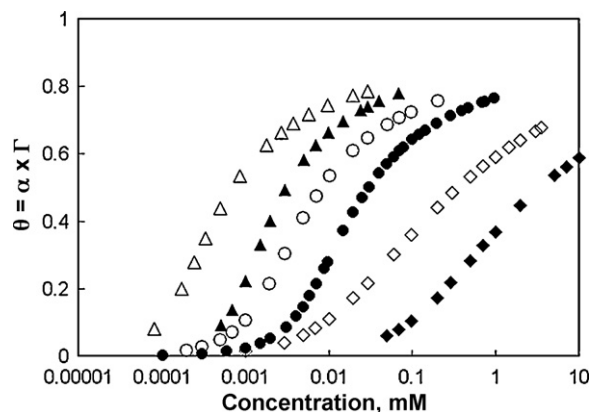


Fig. 10. Degree of coverage θ vs. DMPO concentration from model H–G (same symbols as in Fig. 8).

We used the H–G data for α to calculate the degree of coverage of the surface. The data are shown in Figs. 10 and 11. As one sees, the degree of coverage $\theta = \alpha\Gamma$ is significantly lower than unity even at the highest concentrations. This result cast doubt on the common belief that before and close to the critical micelle concentration CMC the degree of coverage is complete. We believe that this finding may have some technological significance.

The values of the adsorption constants K_s can be checked from the slope of the initial portions of the plots of σ vs. C_s . This procedure is extremely difficult since the concentrations are very small and the data for σ are not very reliable (the authors of [27] also mentioned this problem). To decrease the possible errors we were drawing a line through the point $(C_s = 0, \sigma_p)$, where σ_p is the surface tension of the pure solvent and were trying to find several data points lying on this or close to this line. Examples of this procedure are given in Figs. 12 and 13. The adsorption constant is calculated by combining Gibbs' equation and Henry's law $\Gamma = K_{s,c}C_s$, where the subscript c indicates that the constant is calculated in this way. The result is

$$K_{s,c} = -\frac{kT}{(\partial\sigma/\partial C_s)_{in}} \quad (64)$$

where "in" stands for "initial". In Figs. 14 and 15 the respective results for K_s of DMPO's and acids are plotted vs. the number of carbon atom in the chain n_c along with the results in columns H–G, V–3 and L–3 of Table 2 obtained by fits with the respective equations. As already mentioned, although not coinciding, the results are reasonably close and follow rather well straight lines, see Eq.

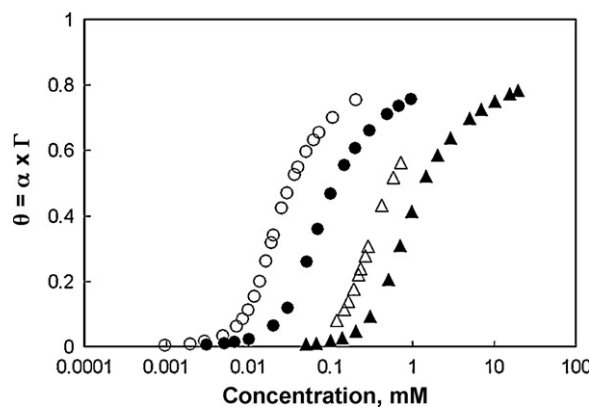


Fig. 11. Degree of coverage θ vs. acid concentration from model H–G—▲: C7; △: C8; ●: C9; ○: C10.

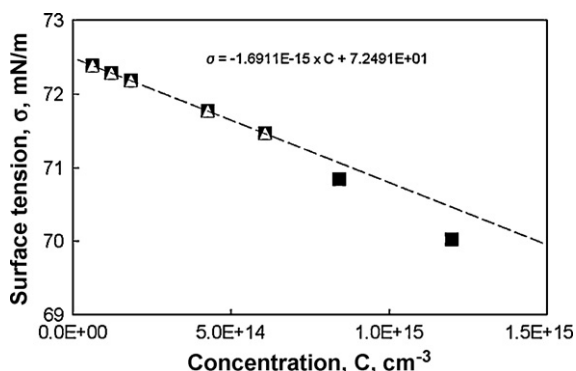


Fig. 12. Initial portion of the curve surface tension vs. C12 DMPO concentration. The equation is shown in the figure.

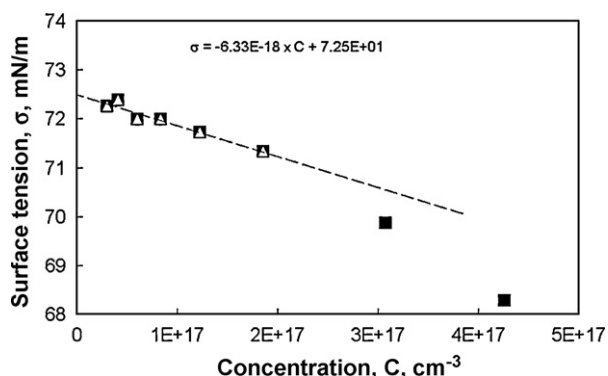


Fig. 13. Initial portion of the curve surface tension, σ , vs. heptanoic acid concentration, C . The equation is shown in the figure.

(9):

$$\ln K_s = \frac{w_c}{kT} n_c + Q \quad (65)$$

The points are so close, that it was impossible to draw separate lines. Hence, we summarized the values of the slopes $w_c/(kT)$, the intercepts Q and the regression coefficients r^2 of the lines in Table 4. We assumed that the most probable slope is 0.96 although the average value is 0.951. The slope of this dependence was determined also by Davies and Rideal [19], who found slightly larger value: $w_c/(kT) = 1.02$.

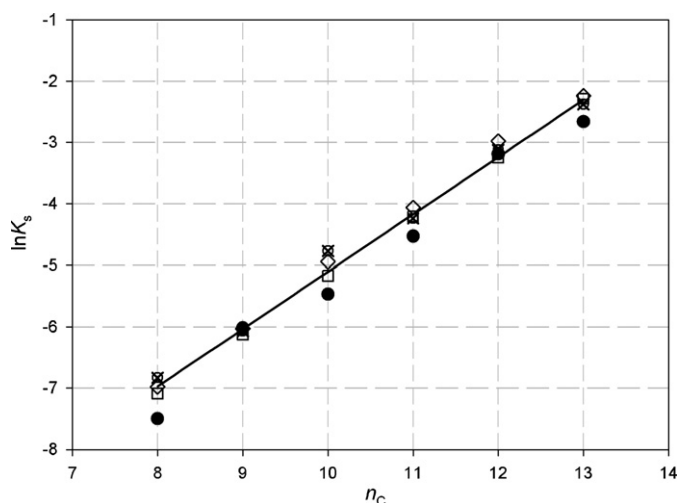


Fig. 14. $\ln K_s$ (adsorption constant) vs. number of carbon atoms n_c for DMPO surfactants. The average line has the following parameters: slope 0.933, intercept -14.43 and $r^2 = 0.9862$. The numerical data and the symbols are given in Table 4.

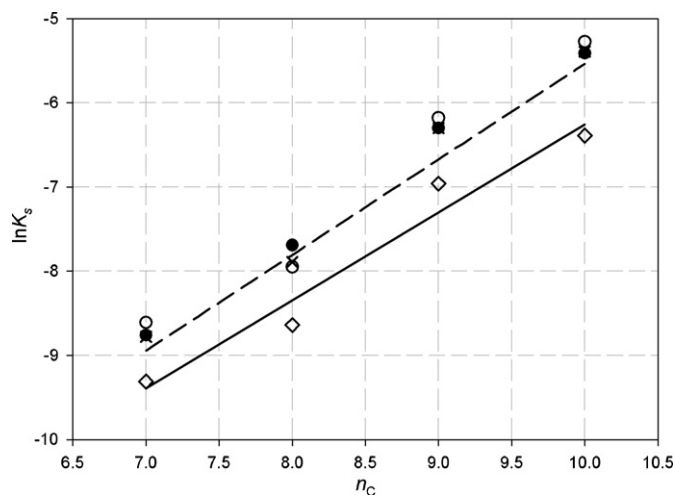


Fig. 15. Plot of $\ln K_s$ for aliphatic acids vs. the number of carbon atoms n_c . The symbols are the same as in Table 4. For the parameters of the linear fits see the text.

The data for acids are slightly worse and more scattered than those for DMPO. The average slope of all data in Fig. 15 (the dashed line) is $w_c/(kT) = 1.135$ (slightly larger than that for DMPO) and the intercept is -16.89 . There is no reason however that the adsorption energy of the methyl groups in both types of compounds be different. We attribute this difference to the lower precision of the data, the more so that the data obtained with the model H-G (the solid line) gives a lower slope, 1.044 with intercept -16.70 .

We decided to use these data to check the correctness of our theoretical Eq. (9) for K_s . Besides the slope $w_c/(kT) = 0.96$ we used the following data: $\sigma_p = 72.2$ mN/m, $\alpha_c = 20 \text{ \AA}^2$ and $\delta_s = 1.16 \times 10^{-8}$ cm [9]. In fact, the theoretical results were already plotted in Fig. 14 as $\ln K_s$ vs. n_c (see also Table 4). The agreement with the other data in Fig. 14 is very good. Another way to check Eq. (9) is to calculate theoretically the intercept $Q = \ln \delta_s + \sigma_p \alpha_c / (kT)$. The result is -14.76 , which is almost equal to the value -14.66 obtained from the fit by the H-G method. The final check of the reliability of our Eq. (9) was the direct comparison of the results it leads to with the data, obtained by fitting the experimental isotherms by the method H-G. Fig. 16 demonstrates almost perfect agreement between the theoretically calculated values K_s^{th} and the ones obtained from the experimental data, $K_s^{\text{H-G}}$.

The last constant to be checked is β . We have assumed during the derivation of Eq. (33) that the chains are perpendicular to the interface, but at the same time showed in Eq. (19) that the first methyl group is immersed in the solution. Therefore, these groups can interact only through the water, which significantly weakens the interaction [11] and we will neglect them as we did when deriving Eq. (20). However, in the present case the top cover on the molecule does not take part in the interaction, so that the number of interacting methyl groups will be $n_c - 1$. The situation with the acids is even more complicated. The first carbon atom is in fact that of the carboxyl group and it is certainly immersed. The second one should

Table 4

Parameters of the linear fits of the data for the dependence of the adsorption constants K_s of DMPO compounds on the number of carbon atoms n_c , obtained by five methods (see table).

Symbol	Model/(Eq.)	$w_c/(kT)$	Intercept Q	r^2
●	$\sigma(C_s)$ (64)	0.961	-14.98	0.9841
◆	Theory (9) and (20)	0.960	-14.77	1.0000
◇	Fit H-G (56)	0.964	-14.66	0.9979
×	Fit V-3 (8)	0.904	-14.06	0.9922
○	Fit L-3 (13)	0.967	-14.69	0.9974

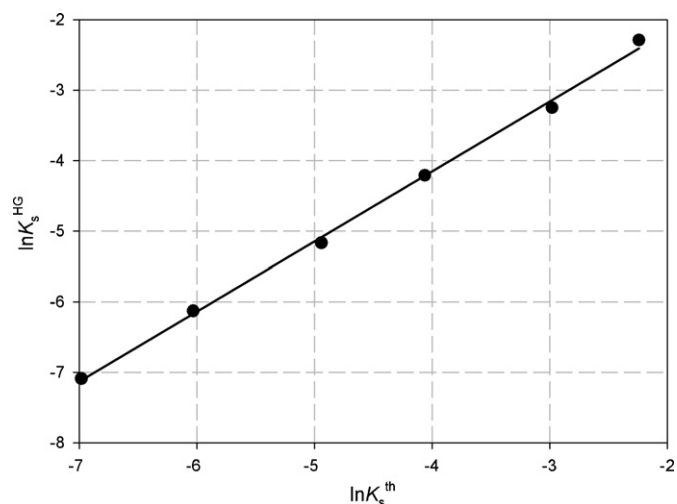


Fig. 16. Linear dependence between the logarithms of the theoretical K_s^{th} and the experimentally obtained by the model H–G value K_s^{HG} of the adsorption constants or DPMO surfactants. The parameters of the fits are: slope 1.004 and intercept -0.170 .

be also immersed (as the first one of the DMPO) not only because of Eq. (20), but because of the mere fact that the acetic acid is infinitely soluble in water. Therefore, for acids the interacting methyl groups must be $n_c - 2$. We will denote the number of interacting groups by n_{int} .

Since some of the molecules have short chains and large area α of the polar head, it is possible that the length l and the diameter d have close values. That is why we will not use the simple Eq. (35), but the exact one, Eq. (33), which we will rewrite in slightly different form:

$$\beta = \frac{0.75\pi\rho_t^2\alpha_p l}{4d^2\alpha kT} \frac{1}{d} \arctan\left(\frac{l}{d}\right) \quad (66)$$

We determined the values of the parameters of a methyl group from the properties of the paraffinic compounds [18,32]: $l = l_1 n_{\text{int}}$; $l_1 = 1.27 \text{ \AA}$; $\rho_t = 1/l_1$; $\alpha_p = 2 \text{ \AA}^3$; $I = 10.5 \text{ eV}$. After some calculations we thus found:

$$\beta = 510 \frac{n_{\text{int}}}{\alpha^{5/2}} \arctan\left(\frac{1.12n_{\text{int}}}{\alpha^{1/2}}\right) \quad (67)$$

where $n_{\text{int}} = n_c - 1$ for DMPO and $n_c - 2$ for acids.

As we already mentioned, with the exception of $\ln K_s$, the data for the DMPO compounds C8, C10 (and to some extent C13) exhibit some deviations from the trend followed by the other data (for additional discussion see Appendix A)—the values of α are with 10–15% lower than for the other compounds and the values of β also deviate considerably from the general trend (see Table 2). That is why we performed calculations of β only for the other compounds. In Fig. 17 the results for β obtained from the fit of the experimental data by the method H–G (we call them “experimental”) are compared with the respective theoretical calculations of β by Eq. (67). The scattering of the data points for the H–G isotherm with respect to the theoretical curve β vs. n_c , calculated from Eq. (67) do not exceed 15–25%, which is very close to the usual error of determination of β . Note that again this is result of direct calculation without using any adjustable parameter. The (moderate) success of this procedure is rather surprising, in view of the crudeness of the theoretical model and the lack of relevant data.

Parallel comparison of results between several models is performed in Fig. 18, where the “experimental” and the theoretical values of β vs. n_c are plotted together for the three models: H–G, V–3 and L–3. The coincidence between theory and experiment for the model L–3 in Fig. 18 is pretty good, but this result might be

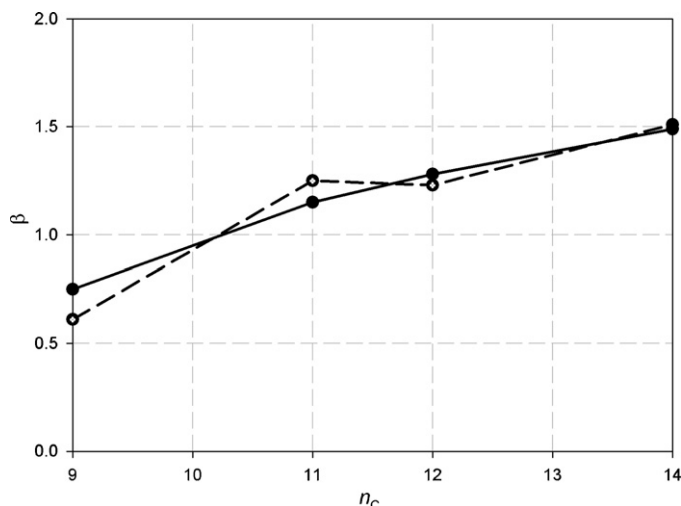


Fig. 17. Values of the interaction constant, β , vs. the number of carbon atoms n_c , for DMPO surfactants. The dashed line is only for guiding the eye. The theoretical values, calculated from Eq. (67) are with solid line. The experimental values (with dashed lines and empty symbols) are calculated from the fit of the experimental data by the model H–G.

misleading. The values of β for this model are very small (<0.5) and the values of α (which in Eq. (67) is in the denominator as $\alpha^{5/2}$) are very large (see Table 2), which might be the reason for this coincidence. If one calculates the theoretical values for L–3 of β by using the presumed true values of $\alpha \approx 30 \text{ \AA}^2$, they will become larger than 1 and the coincidence between theory and experiment for L–3 will vanish. As for the model of Volmer V–3, the difference between experimental and theoretical values is enormous—up to 5–6 times, which confirms the data from Table 2, showing that this model exaggerates the values of β .

Although the results for β are not excellent, we will dare some speculations. The fact that Eq. (67), which works rather well, was derived from the second virial coefficient, accounting only for binary interactions between molecules, perpendicular to the interface, seems to suggest that this is the dominant orientation of interacting molecules even at low surface

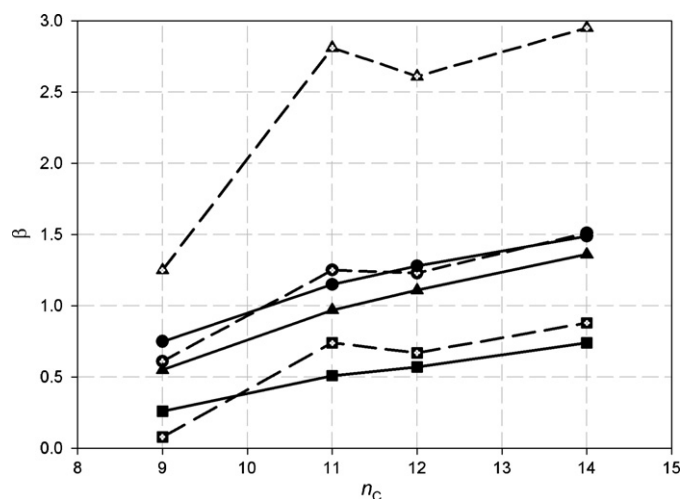


Fig. 18. Values of the interaction constant, β , vs. the number of carbon atoms n_c , for 4 DMPO surfactants (see the text). The dashed lines are only for guiding the eye. The theoretical values, calculated from Eq. (67) are with solid lines with values of α , corresponding to do respective model, indicated on the right. The experimental values (with dashed lines and empty symbols) are calculated from the fit of the experimental data by the models H–G [circles; Eq. (16)], L–3 [squares, Eq. (13)] and V–3 [triangles, Eq. (6)].

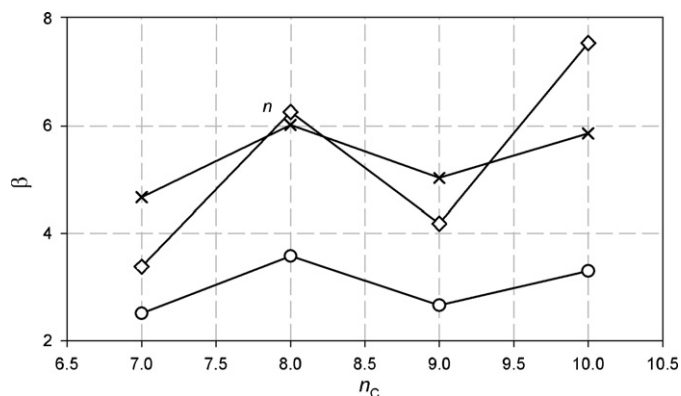


Fig. 19. Experimental results for the parameter, β , vs. number of carbon atoms n_c for aliphatic acids, obtained by fitting the data with three models; H-G, V-3 and L-3 (see symbols in Table 4). The dashed lines are only for guiding eye. See text for discussion.

concentrations—probably the attraction between the hydrocarbon tails is the dominant effect trying to decrease the free energy of the surfactant molecules by forcing them to stay as close as possible to each other. This is also in agreement with the fact that the area per molecule α , determined by the fit of the model H-G leads to values of α very close to those determined from the collapse pressure of DMPO (see above). Such effect is possible however only if the molecular length l exceeds considerably the distance of closest approach d . For example for C12 the ratio is $l/d \approx 2.5$. On the contrary, for short molecules like C8 this ratio is close to 1 and since l is small the attraction is too weak to orient the molecules vertically. This might be one of the reasons for the small values of β for short molecules.

The experimental results for β vs. n_c in Fig. 19 for acids look very differently from those for DMPO. First, the values of β are much larger, which is probably due to the strong hydrogen bonding. More important is the observed saw-shape of the curves. It looks a little bit as the well known dependence of the melting point of alkanes and the reason might be the same. With alkanes the substances with even number of carbon atoms are supposed to be more able to acquire in the solid phase conformations with higher attractive energy, which leads to higher melting point. Some similar, but probably more complicated effect is possible in the adsorbed layer. Indeed, the very small values of $\alpha \approx 21 \text{ \AA}^2$, which is very close to the cross-sectional area of the paraffinic chain, may lead to interpenetration of the chains, making their structure similar to that in solid phase with alkanes more strongly attracting for even number carbon atoms which manifests itself here by larger values of β . Another possible effect is the change of acidity of the carboxylic groups with the chain length, which may lead to vertical displacement and change of density of the adsorbed layer—similar effect of ions on alkanes was investigated in [31]. This is of course a speculation, which can hardly be proven.

Unfortunately, no comparison between the models by direct fit of the experimental data for σ vs C_s is possible, because as already mentioned, all models fit perfectly the experimental data but lead to different system parameters. The different behavior of the models can be however demonstrated by plotting the Gibbs elasticity E_G and the degree of surface coverage $\theta = \alpha \Gamma$ vs. the surfactant concentration C_s . This is done in Figs. 20 and 21 for the generalized versions of the three models. As one might expect, the fact that the model H-G corresponds to the smallest values of α leads to considerably smaller values of E_G and θ .

We consider the results, presented in this section, especially those with DMPO (which are also due to the excellent experimental data from refs. [26,27]), as confirmation not only of our new

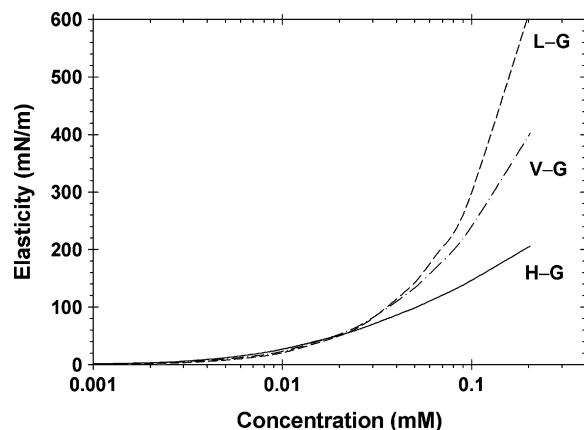


Fig. 20. Gibbs elasticity as a function of surfactant concentration for DMPO-C12 calculated from models L-G, V-G, and H-G.

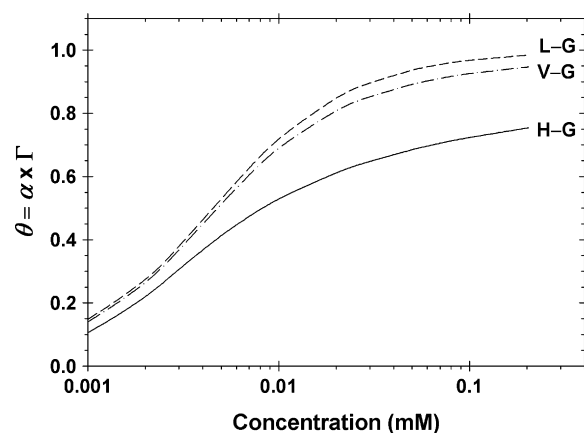


Fig. 21. Degree of surface coverage, θ , as a function of surfactant concentration for DMPO-C12 calculated from models L-G, V-G, and H-G.

adsorption isotherm, Eq. (56) and the EOS Eq. (54), whose fit gave the above values, but also as confirmation of our equations for the adsorption energy E_A , Eq. (20), thickness of the adsorbed layer δ_s , Eq. (21), and the adsorption constant K_s , Eq. (9). It is noteworthy that we obtained these results without using during the calculation any adjustable parameters.

7. Conclusion

We carried out analysis, based on the three most popular simple equations with three free parameters (adsorption constant K_s , minimum area per molecule α and interaction constant β) of surface tension isotherms of DMPO and aliphatic acids. It revealed more or less the same problems which we met in [9] with ionic surfactants. This stimulated us to look again on the expressions and the values of α , K_s and β . In [9] we have shown that correct results can be obtained only if the hard core part of the EOS is based on the model of HFL (see Section 3.b). We had also significantly modified the expression for K_s by introducing new terms in the expression for the adsorption energy E_A , Eq. (20), and derived a new expression for the thickness of the adsorbed layer, δ_s . The new modification we introduced now are the calculations of the average immersion depth z_{imm} of the paraffinic chain due to thermal fluctuations, Eq. (19), which affects E_A and β , and of the parameter β by integrating the interaction energy between two paraffinic chains, Eqs. (33) and (66). In this way we prepared the ground for independent verification of the parameters determined by the fit of the experimental data surface tension σ vs. surfactant concentrations C_s . However,

our results from such fits, (see Tables 2 and 3), showed that again the values of the parameters determined were not only strongly dependent on the model used, but were in most cases different from the independent theoretical estimates.

The conclusion we reached was that the poor results are due to the models used (the EOS and the adsorption isotherm). That is why we tried to use also or to derive equations as precise as possible. An almost exact generalization of the Langmuir–Frumkin equation was available, see Eqs. (36) and (37) and [13]. However, nothing was available for fluid monolayers. We succeeded to derive an exact EOS, Eq. (48), for 1D adsorption of sticks on a thread by using the so-called “sticky approximation” of Baxter [21] assuming that attraction between the molecules appears only when they touch each other. Our result turned out to be a generalization of Volmer equation, since its hard core part exactly coincides with that of Eq. (6). Since we have proven that the Volmer equation leads to values of α larger than the true ones (see Fig. 3), the new equation must have the same defect. On the other hand, it has been rigorously proven [21] that it is impossible to derive a 2D EOS even for hard discs, let alone for attracting each other disks. Hence, we used a heuristic approach: we derived rigorously a 2D generalization of the HFL equation with correction up to linear in β terms, see Eq. (53), and changed suitably the hard core part and the numerical coefficients in the 1D equation to make it compatible with the new 2D result. The numerical checks of the new equation, Eq. (54), and the respective adsorption isotherm, Eq. (56), were performed by calculating the third virial coefficient and by deriving an analogous equation by expansion of the correlation function in series of β and solving Kirkwood's integral equation. Both checks gave satisfactory results.

We subject the three simple equations (more precisely the respective adsorption isotherms) from Section 2, Eqs. (8), (13) and (16), and their respective generalized analogs Eqs. (37), (50) and (56) to experimental checks by fitting the data of Makievski and Grigoriev [26] and Warszynski and Lunkenheimer [27] for DMPO and of Malysa et al. [28] and Lunkenheimer and Hirte [29] for acids. The results are summarized in Tables 2 and 3. They show that practically all 6 models lead to close (although slightly scattered) values of the adsorption constant K_s . This should not be surprising since K_s is present only in the left hand (model independent) side of the adsorption isotherm. The two models, based on Langmuir isotherm, lead for DMPO practically to the same values of the adsorption parameters. This is so because only the second virial coefficient contains a term linear in β and in all other terms β is at higher power. For small β (which is the case with DMPO) these terms can be neglected and Frumkin equation becomes from this view point exact (see Section 5a)—however, the problems with the exaggerated values of α remain. The situation is however different with the acids, where β can be as large as 4 and the two equations lead to different results.

The area per molecule α , determined by the generalized equations increases from HFL to Volmer to Langmuir, as anticipated in Fig. 3. The simple equations leads to smaller α and larger β (in a correlated manner) with respect to the values from the generalized equations. We showed, by using the data of Noskov et al. [30] that the values of $\alpha \approx 30 \text{ \AA}^2$ given in Table 1 by the generalized HFL model are very close to the geometrical area of the DMPO heads.

We performed several independent calculations of the three adsorption parameters in order to compare the results with those obtained by the fits and to check in this way our theoretical developments and the reliability of our fitting procedures. The first one was to calculate K_s directly from the initial slope of the experimental curves $\sigma(C_s)$ (see Figs. 12 and 13). The data were rather scattered but the result, shown in Table 4 was in agreement with the other data. The other test was direct calculation by the method H–G of the adsorption constant K_s from Eq. (9) without use of any adjustable

parameter. Finally, we calculated the constant β from Eq. (67) again without using adjustable parameters. The best results were again obtained by the method H–G (see Figs. 16 and 17). The experimental results with acids for β vs. n_c in Fig. 19 look very differently from those for DMPO. First, the values of β are much larger, which is probably due to the strong hydrogen bonding. More important is the observed saw-shape of the curves. We have no explanation for this, but we suspect that similarly to the dependence of the melting point of paraffins on n_c , it is due to the better capability of the substances with even number of carbon atoms to acquire conformations with higher attractive energy.

In conclusion, we believe to have shown that the new EOS, Eq. (54), and adsorption isotherm, Eq. (56), derived by us have given very reliable results. However, we are aware that no definite conclusion is yet possible without check with other suitable systems and without more rigorous derivation and possibly improvement of our equations. At the same time our analysis has demonstrated that the other equation tested, those of Frumkin and van der Waals qualitatively correctly describe the adsorption phenomena. Moreover, they are simpler and more easy for applications, so that if one is interested mainly in qualitative comparison of surfactants or in the general features of the phenomena observed, they might be preferable. If however one wants to obtain more information for the value of some parameter, one must be cautious in the selection of the method to be used.

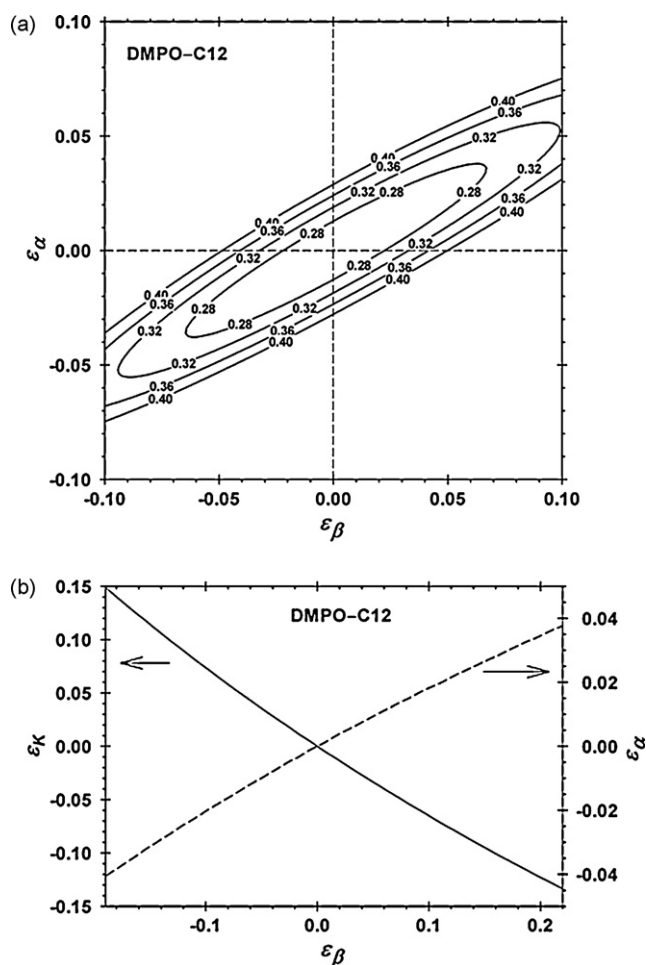


Fig. A.1. Results from processing of experimental data for DMPO–C12 using H–G model. (a) Contour plot of the merit function for fixed $K_{s,min}$; (b) change of ϵ_K and ϵ_α as a function of $\epsilon\beta$.

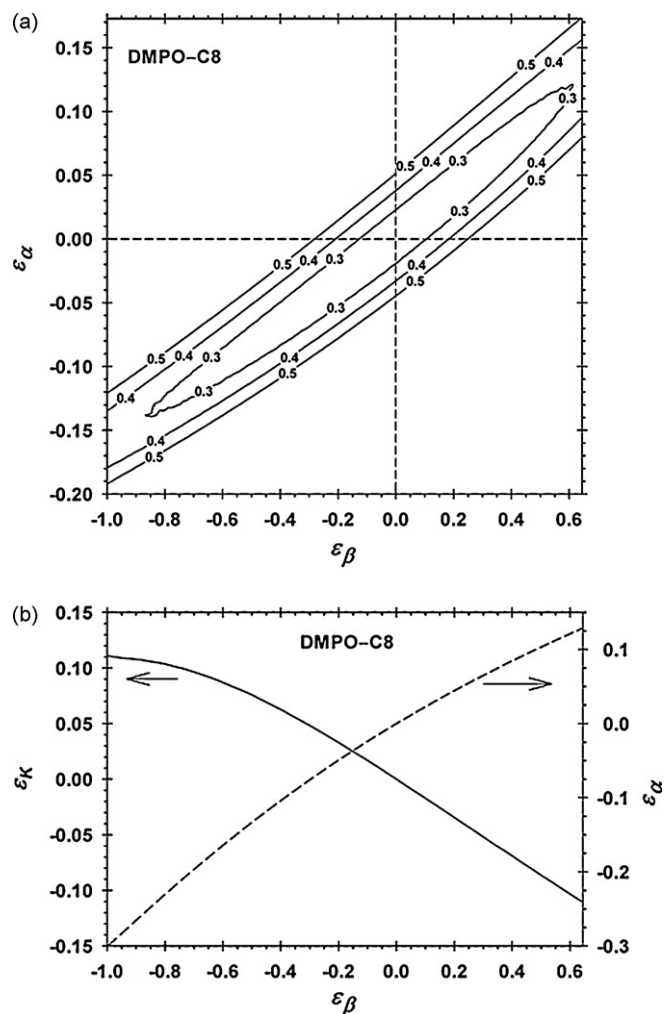


Fig. A.2. Results from processing of experimental data for DMPO-C8 using H-G model: (a) contour plot of the merit function for fixed $K_{s,\min}$; (b) change of ε_K and ε_α as a function of ε_β .

Acknowledgement

We are indebted to Miss M. Paraskova for the qualified help in preparing the artwork.

Appendix A. Relative errors of the adjustable parameters

In order to understand the accuracy of the parameters, α_{\min} , β_{\min} , and $K_{s,\min}$, minimizing the merit function, we define their relative errors as follows:

$$\varepsilon_\alpha \equiv \left| \frac{\alpha - \alpha_{\min}}{\alpha_{\min}} \right|, \quad \varepsilon_\beta \equiv \left| \frac{\beta - \beta_{\min}}{\beta_{\min}} \right|, \quad \varepsilon_K \equiv \left| \frac{K_s - K_{s,\min}}{K_{s,\min}} \right| \quad (\text{A.1})$$

We studied the two dimensional contour plot diagrams of the merit function at fixed third parameter. In all cases we found that the relative errors ε_α and ε_K are smaller at fixed value of the interaction parameter, β .

Fig. A.1.a shows the contour plot of the merit function cross-sections at fixed value of $K_{s,\min}$ calculated from the experimental data for DMPO-C12 using H-G model. One sees that the minimum is well pronounced and the relative errors of the parameters are of the order of 5%. For deeper understanding of the behavior we fixed the value of β and minimized the merit function with respect to K_s and α . Thus we calculate the functions $K_{s,\min}(\beta)$, $\alpha_{\min}(\beta)$, and $\chi_{\min}(\beta)$. Fig. A.1.b shows the respective relative errors ε_α and ε_K as a function of ε_β for DMPO-C12. In Fig. A.1.b the increase of the calculated merit function from its minimum value is only 0.01 mN/m. The main conclusions are: (i) the area α is calculated with a good precision (error smaller than 4%); (ii) the parameters K_s and β are correlated and their relative errors are of the order of 10%.

When applying the H-G model to the experimental data for DMPO-C8 the conclusions are different. Fig. A.2.a illustrates that the contour 0.3 mN/m covers relative errors of area 10% but the relative errors of the interaction parameter β is from -100% to 60% . Fig. A.2.b has the analogous meaning as Fig. A.1.b but drawn for DMPO-C8. The main conclusions are: (i) the area α and the parameter K_s can be estimated with precision of about 20%; (ii) the interaction parameter β is determined with very large relative error. The same behavior of the merit function was observed for the experimental data for DMPO-C10.

References

- [1] N. Nandi, D. Vollhardt, *Curr. Opin. Coll. Interface Sci.* 13 (2008) 40.
- [2] V. Fainerman, D. Vollhardt, *J. Phys. Chem. B* 113 (2009) 6311.
- [3] G. Brezesinski, D. Vollhardt, K. Iimura, H. Colfen, *J. Phys. Chem. C* 112 (2008) 15777.
- [4] V. Fainerman, D. Mobius, R. Miller (Eds.), *Surfactant Chemistry, Interfacial Properties, Applications*, Elsevier, 2001.
- [5] I. Langmuir, *J. Am. Chem. Soc.* 40 (1918) 1361.
- [6] A. Frumkin, *Z. Phys. Chem. (Munich)* 16 (1925) 466.
- [7] M. Volmer, *Z. Phys. Chem.* 115 (1925) 253.
- [8] M. Mulqueen, D. Balnkshtein, *Langmuir* 16 (2000) 7640.
- [9] I.B. Ivanov, K.P. Ananthapadmanabhan, A. Lips, *Adv. Colloid Interface Sci.* 123–126 (2006) 189.
- [10] J.D. Hines, *J. Colloid Interface Sci.* 180 (1996) 488.
- [11] J.N. Israelachvili, *Intermolecular and Surface Forces*, Academic Press, London, 1992.
- [12] L.D. Landau, E.M. Lifshits, *Statistical physics*, "Naouka", Moscow 1964, in Russian.
- [13] T.L. Hill, *An Introduction to Statistical Thermodynamics*, Addison-Wesley, Reading, MA, 1962.
- [14] J. Belton, M. Evans, *Trans. Faraday Soc.* 41 (1945) 1.
- [15] H. Reiss, H. Frisch, J. Lebowitz, *J. Chem. Phys.* 31 (1959) 369.
- [16] E. Helfand, H. Fisch, J. Lebowitz, *J. Chem. Phys.* 34 (1961) 1037.
- [17] C. Tanford, *The Hydrophobic Effect. The Formation of Micelles and Biological Membranes*, Wiley, New York, 1980.
- [18] K. Danov, I.B. Ivanov, K.P. Ananthapadmanabhan, A. Lips, *Adv. Colloid Interface Sci.* 128–130 (2006) 185.
- [19] J. Davies, E. Rideal, *Interfacial Phenomena*, Academic Press, New York, 1963.
- [20] A.I. Russanov, *Colloids Surf. A: Physicochem. Eng. Aspects* 239 (2004) 105.
- [21] R.J. Baxter, *J. Chem. Phys.* 49 (1968) 2770.
- [22] T. Gurkov, I.B. Ivanov, *Proceedings of the 4th World Congress on Emulsions*, Paper No. 2.1–509, Lyon, France, 2006.
- [23] P.C. Hemmer, G. Stell, *J. Chem. Phys.* 93 (1990) 8220.
- [24] T. Kihara, *Rev. Modern Phys.* 25 (1953) 831.
- [25] J. Kirkwood, V. Lewinson, B. Alder, *J. Chem. Phys.* 20 (1952) 929.
- [26] A.V. Makievski, D.O. Grigoriev, *Colloids Surf. A: Physicochem. Eng. Aspects* 143 (1998) 233.
- [27] P. Warszynski, K. Lunkenheimer, *J. Phys. Chem. B* 103 (1999) 4404.
- [28] K. Malysa, R. Miller, K. Lunkenheimer, *Colloids Surf.* 53 (1991) 47.
- [29] K. Lunkenheimer, R. Hirte, *J. Phys. Chem.* 96 (1992) 8683.
- [30] B. Noskov, D. Grigoriev, R. Miller, *Langmuir* 13 (1997) 295.
- [31] R. Viswanathan, J. Garnæs, D.K. Schwartz, J.A.N. Zasadzinski, *Proceedings Annual Meeting Microscopy Society of America*, 1993.
- [32] *Handbook of Chemistry*, "Himia", Moscow, 1964.

High- and low-affinity binding sites for Cd on the bacterial cell walls of *Bacillus subtilis* and *Shewanella oneidensis*

Bhoopesh Mishra^{a,*}, Maxim Boyanov^c, Bruce A. Bunker^a, Shelly D. Kelly^c,
Kenneth M. Kemner^c, Jeremy B. Fein^b

^a Department of Physics, University of Notre Dame, Notre Dame, IN 46556, USA

^b Department of Civil Engineering and Geological Sciences, University of Notre Dame, Notre Dame, IN 46556, USA

^c Molecular Environmental Science Group, Biosciences Division, Argonne National Laboratory, Argonne, IL 60439, USA

Received 31 August 2009; accepted in revised form 17 February 2010; available online 23 February 2010

Abstract

Bulk Cd adsorption isotherm experiments, thermodynamic equilibrium modeling, and Cd K edge EXAFS were used to constrain the mechanisms of proton and Cd adsorption to bacterial cells of the commonly occurring Gram-positive and Gram-negative bacteria, *Bacillus subtilis* and *Shewanella oneidensis*, respectively. Potentiometric titrations were used to characterize the functional group reactivity of the *S. oneidensis* cells, and we model the titration data using the same type of non-electrostatic surface complexation approach as was applied to titrations of *B. subtilis* suspensions by Fein et al. (2005). Similar to the results for *B. subtilis*, the *S. oneidensis* cells exhibit buffering behavior from approximately pH 3–9 that requires the presence of four distinct sites, with pK_a values of 3.3 ± 0.2 , 4.8 ± 0.2 , 6.7 ± 0.4 , and 9.4 ± 0.5 , and site concentrations of $8.9(\pm 2.6) \times 10^{-5}$, $1.3(\pm 0.2) \times 10^{-4}$, $5.9(\pm 3.3) \times 10^{-5}$, and $1.1(\pm 0.6) \times 10^{-4}$ moles/g bacteria (wet mass), respectively. The bulk Cd isotherm adsorption data for both species, conducted at pH 5.9 as a function of Cd concentration at a fixed biomass concentration, were best modeled by reactions with a Cd:site stoichiometry of 1:1. EXAFS data were collected for both bacterial species as a function of Cd concentration at pH 5.9 and 10 g/L bacteria. The EXAFS results show that the same types of binding sites are responsible for Cd sorption to both bacterial species at all Cd loadings tested (1–200 ppm). Carboxyl sites are responsible for the binding at intermediate Cd loadings. Phosphoryl ligands are more important than carboxyl ligands for Cd binding at high Cd loadings. For the lowest Cd loadings studied here, a sulfhydryl site was found to dominate the bound Cd budgets for both species, in addition to the carboxyl and phosphoryl sites that dominate the higher loadings. The EXAFS results suggest that both Gram-positive and Gram-negative bacterial cell walls have a low concentration of very high-affinity sulfhydryl sites which become masked by the more abundant carboxyl and phosphoryl sites at higher metal:bacteria ratios. This study demonstrates that metal loading plays a vital role in determining the important metal-binding reactions that occur on bacterial cell walls, and that high affinity, low-density sites can be revealed by spectroscopy of biomass samples. Such sites may control the fate and transport of metals in realistic geologic settings, where metal concentrations are low.

© 2010 Elsevier Ltd. All rights reserved.

1. INTRODUCTION

Bacteria are ubiquitous in a wide range of low temperature aqueous systems, and aqueous metal adsorption onto

bacterial cell wall functional groups can influence metal speciation, bioavailability, and transport (Ledin et al., 1996, 1999; Ledin, 2000; Ohnuki et al., 2007). Metal adsorption onto bacterial cell walls can be viewed as a surface complexation reaction, and the thermodynamic stabilities of a wide range of metal-bacterial surface complexes have been determined using bulk adsorption measurements (e.g., Fein et al., 1997; Small et al., 1999; Yee and Fein, 2001; Daughney et al., 2002; Yee and Fein, 2003; Borrok

* Corresponding author. Present address: Biosciences Division, Argonne National Laboratory, Argonne, IL 60439, USA.

E-mail address: bmishra@anl.gov (B. Mishra).

et al., 2004b; Wightman and Fein, 2005; Kulczycki et al., 2005; Burnett et al., 2006; Leone et al., 2007; Ngwenya, 2007; Pokrovsky et al., 2008a). In addition, X-ray absorption spectroscopy studies have identified cell wall carboxyl, phosphoryl, and sulfhydryl groups as important sites of metal binding (Hennig et al., 2001; Kelly et al., 2002; Panak et al., 2002; Boyanov et al., 2003; Toner et al., 2005; Guiné et al., 2006; Mishra et al., 2007; Pokrovsky et al., 2008b; Mishra et al., 2009). Most of these previous studies examined metal–bacterial adsorption under conditions with relatively high metal:bacterial site concentration ratios, and many of these studies focused on the pH dependence of adsorption rather than on the concentration dependence. While measurements of the pH dependence of metal adsorption onto bacteria place constraints on the cell wall sites responsible for the binding, measurements conducted as a function of metal:ligand ratio better constrain the metal:site stoichiometry of the adsorption reactions than do standard pH edge adsorption experiments. Furthermore, the important binding mechanisms can change as a function of metal:ligand concentration ratio, and studies at relatively high and fixed metal concentrations may mask the presence and importance of low concentration, high affinity metal binding sites on surfaces (Sarret et al., 1998).

Extended X-ray absorption fine structure (EXAFS) spectroscopy has demonstrated that only a limited number of binding sites are responsible for metal binding onto cell walls from a range of bacterial species. Phosphoryl and carboxyl functional groups are responsible for metal complexation by both Gram-positive bacteria (Kelly et al., 2002; Boyanov et al., 2003) and Gram-negative bacteria (Toner et al., 2005; Hennig et al., 2001; Panak et al., 2002) despite fundamental differences in molecular structure of their exterior surfaces. These two functional groups have also been found responsible for metal binding in both natural and contaminated consortia of bacteria obtained from river water and a manufactured gas plant site, respectively (Mishra et al., 2009). However a Cd-sulfhydryl binding site was also identified in the river water consortium (Mishra et al., 2009). Using infrared spectroscopy, Wei et al. (2004) studied both Gram-positive and Gram-negative bacterial surface functional groups and determined that phosphoryl and carboxyl groups are the primary contributors to the negative charge, and hence the reactivity of the bacterial cell wall.

Relatively few studies have investigated the mechanisms of metal complexation with bacterial cell walls as a function of metal loading. Sarret et al. (1998) examined Zn and Pb sorption to fungal cell walls of *Penicillium chrysogenum* at pH 6 as a function of Zn and Pb loading, and the phosphoryl group was found to be the predominant complexing ligand. Carboxyl binding was significant only under the highest Zn loading and the lowest Pb loading conditions. Burnett et al. (2006) studied Cd adsorption onto the thermophilic species *A. flavithermus*, and found that at high bacteria:Cd ratios Cd adsorption occurs by formation of a 1:1 complex with deprotonated cell wall carboxyl functional groups. At lower bacteria:Cd ratios, a second adsorption mechanism occurs at pH > 7, which may correspond to the formation of a Cd-phosphoryl, CdOH-carboxyl, or CdOH-phosphoryl surface complex. Guiné et al.

(2006) reported the importance of sulfhydryl ligands in addition to phosphoryl and carboxyl ligands in the adsorption of Zn onto three Gram-negative bacterial strains (*Cupriavidus metallidurans* CH34, *Pseudomonas putida* ATCC12633, and *Escherichia coli* K12DH5 α) at low loadings of Zn. Mishra et al. (2007) reported that sulfhydryl ligands, in addition to carboxyl and phosphoryl sites, were required for EXAFS modeling of Cd binding with the Gram-negative bacteria *Shewanella oneidensis* and an aquatic consortium of bacteria at 30 ppm Cd loading and 10 g/L (wet mass) biomass. However, sulfhydryl ligands were not required for EXAFS modeling of the Gram-positive bacteria *Bacillus subtilis* under the same conditions, consistent with previous finding by Boyanov et al. (2003). Similarly, Pokrovsky et al. (2008b) observed Cd complexation with sulfhydryl functional groups on the marine anoxygenic bacteria *R. palustris* in systems with 3 ppm Cd and 4 g/L biomass. While the Cd-sulfhydryl binding by Mishra et al. (2007) and Pokrovsky et al. (2008b) was observed in systems near pH 6, Mishra et al. (2009) demonstrated that aquatic consortia of bacteria exhibit sulfhydryl binding of Cd across a wide pH range and even at relatively elevated Cd concentrations.

The objective of this study is to explore metal–bacterial adsorption reactions using both bulk adsorption measurements and X-ray absorption spectroscopy over a wide range of metal:ligand ratios, and to compare these results for the Gram-positive bacterial species *B. subtilis* and the Gram-negative bacterial species *S. oneidensis*. Cell wall functional group reactivity for *B. subtilis* has been characterized by Fein et al. (2005), and we collect new potentiometric titration data in this study using *S. oneidensis* in order to determine the site concentrations and acidity constants for the important binding sites on the *S. oneidensis* cell wall. Thermodynamic equilibrium modeling of the bulk adsorption data was used to constrain the stoichiometries of the important proton and Cd adsorption reactions. EXAFS measurements were conducted at pH 5.9, over a wide range of Cd concentrations (1–200 ppm for *B. subtilis* and 3–200 ppm for *S. oneidensis*) at a fixed bacterial concentration of 10 g/L (wet mass), and we use these data to constrain the molecular-scale Cd adsorption mechanisms and to determine whether the adsorption mechanisms change as a function of Cd loading onto the bacterial cell walls.

Although Cd binding onto *B. subtilis* cells has already been studied using EXAFS by members of our group previously (Boyanov et al., 2003), the goals of this study are fundamentally different. While Boyanov et al. (2003) studied the adsorption behavior of *B. subtilis* over a pH range of 3.4–7.8 at a fixed Cd:biomass ratio, this study attempts to determine the site stoichiometry, and the sequence of reactions occurring on bacterial cell walls as a function of Cd loading at a fixed pH.

2. METHODS AND MATERIALS

2.1. Bacterial growth and harvest

S. oneidensis str., formerly classified as *S. putrefaciens* MR-1 (Venkateswaren et al., 1999), is a Gram-negative

dissimilatory metal-reducing bacterium found in soils, sediments, surface waters, and ground waters (e.g., Sorenson, 1982; Nealson and Myers, 1992). *B. subtilis* is an aerobic Gram-positive soil microorganism with well-characterized surface charge and reactivity (Harden and Harris, 1952; Beveridge and Murray, 1980; Fein et al., 1997, 2005). The bacterial growth and wash procedures used in this study were identical for both bacterial species and similar to those described in Fein et al. (2005). A plated colony was transferred from an agar plate to a test tube containing 7 mL of sterilized trypticase soy broth (TSB) + 0.5% yeast extract. Each broth tube was then incubated for 24 h at 32 °C in an incubator/shaker. The subsequent bacterial suspension was then transferred to 1 L of TSB + 0.5% yeast extract and incubated for another 24 h at 32 °C in the incubator/shaker. The cells were removed from the nutrient medium by centrifugation and rinsed five times with 0.1 M NaClO₄ (the electrolyte used in the experiments). The cells were not acid washed in order to avoid disruption of the cell wall structure (Borrok et al., 2004a). Biomass is cited in terms of wet mass, determined by centrifugation at 5800g for 60 min, and corresponds to approximately eight times the dry mass of the cells (Borrok et al., 2005).

2.2. Potentiometric titrations

Three replicate potentiometric titrations were performed, each using 100 g/L (wet mass) suspensions of *S. oneidensis* in 0.1 M NaClO₄. The electrolyte solution was bubbled with N₂ gas for 1 h prior to use, and the titration cell containing the bacterial suspension was kept under a N₂ atmosphere during the experiment. The sample was continuously stirred with a small magnetic stir bar during the titration. The titrations were first run down-pH from an initial pH of approximately 4 with aliquots of 1.0005 N HCl to approximately pH 2.7, then up-pH with aliquots of 1.005 N NaOH to approximately pH 9.5. Each addition of acid or base occurred only after a stability of 0.01 °mV/s was attained. Although it is likely that the buffering capacity of the bacterial cell wall extended to extremely low pH conditions (e.g., Fein et al., 2005), we limited the potentiometric titrations to a low pH value of 2.7 in order to avoid excessive disruption of the Gram-negative cell wall structure (Borrok et al., 2004a).

2.3. Cd adsorption experiments

Washed bacteria were suspended in high density polyethylene test tubes containing 0.1 M NaClO₄ electrolyte to form a suspension of 10 g/L of bacteria (wet mass). A 500 ppm parent solution of Cd in 0.1 M NaClO₄ was prepared from a commercially-supplied 1000 ppm Cd reference solution. The pH of this parent solution was adjusted to 5.9 by adding small aliquots of 1 M NaOH. Appropriate amounts of the parent solution were added to the bacterial suspensions, and these suspensions were topped off with additional 0.1 M NaClO₄ to achieve the desired Cd and bacterial concentrations. The pH of each system was adjusted using small aliquots of 1 M HNO₃ or NaOH, and the systems were allowed to react for 2 h on a shaker.

The concentrations of total Cd in the experimental systems ranged from 0.25 to 200 ppm. Previous studies involving *B. subtilis* have demonstrated that equilibrium of Cd adsorption reactions occurs in less than 1 h, and that the adsorption reactions are fully reversible (e.g., Fowle and Fein, 2000). pH was monitored every 30 min, and adjusted as required using minute aliquots of 1 M HNO₃ or NaOH. The final pH was measured after two hours, and the solution was then centrifuged. The final pH of each experimental system was 5.9 ± 0.1, and the pH of the solutions never varied by more than 0.3 during the course of the experiments. The bacterial pellet was retained for X-ray absorption spectroscopy analysis, and the resultant supernatant was filtered (0.45 µm) and analyzed for dissolved Cd using an inductively coupled plasma-optical emission spectroscopy technique with matrix-matched standards. The concentration of metal adsorbed to bacteria in each vessel was calculated by subtracting the concentration of metal that remained in solution from the original Cd concentration in the experiment.

2.4. EXAFS measurements and data reduction

EXAFS is a powerful structural probe that provides information on the short-range coordination environment of the atom under study (Stern, 1974). Fluorescence mode Cd K edge (26,711 eV) EXAFS measurements were performed at MRCAT, sector 10-ID beamline of the Advanced Photon Source at Argonne National Laboratory (Segre et al., 2000). The energy of the incident X-rays was scanned by using a Si(1 1 1) reflection plane of a cryogenically-cooled double-crystal monochromator. The third harmonic of the undulator was utilized, with an undulator tapering of about 3.5 keV to reduce the variation in the incident intensity to less than 15% over the scanned energy range. X-rays of higher harmonic energies were removed using grazing incidence reflection from a Pt-coated mirror. The incident ionization chamber was filled with 100% N₂ gas. The transmitted and reference ion chambers were filled with 100% Ar gas. The fluorescence detector in the Stern–Heald geometry (Stern and Heald, 1983) was filled with Kr gas, and a Pd filter of six absorption lengths was used to reduce the background signal. The incident X-ray beam profile was 1 mm square. Linearity tests (Kemner et al., 1994) indicated less than 0.1% nonlinearity for a 50% decrease in incident X-ray intensity. Several energy scans were collected from each sample. All scans were aligned by using the simultaneously collected absorption spectrum of a Cd foil, by setting the first inflection point of the spectrum at 26,711 eV.

The homogeneous bacterial pellet that formed at the base of each experimental test tube was loaded into a slotted Plexiglas holder, covered with Kapton film, and transported immediately to the beamline for EXAFS measurements. All the EXAFS measurements were performed within 30 h of the adsorption experiment, and the samples were refrigerated during the entire time between adsorption experiment and EXAFS measurements. Quick scans (continuous-scanning mode of the monochromator), with signal sampling every 0.5 eV and an integration time of 0.1 s per

point were used. The advantage of using quick-scans is that it reduces the radiation exposure during a single scan. Consecutive spectra were monitored for possible radiation-induced changes; no changes were observed. To further reduce the possibility of radiation-induced changes or of sample inhomogeneity, the X-ray beam was moved to a fresh spot every 5 scans. A total of 30–150 consecutive scans from each sample were collected and averaged, depending on the Cd concentration in the sample.

Data were analyzed using the UWXAFS package (Stern et al., 1995). Processing of the raw data, including alignment of datasets and background removal, were implemented by using ATHENA (Ravel and Newville, 2005), IFEFFIT (Newville, 2001) and AUTOBK (Newville et al., 1993). The input parameter to ATHENA that determines the maximum frequency of the background, R_{bkg} , was set to 1.1 Å (Newville et al., 1993). The data range used for Fourier transforming the EXAFS $\chi(k)$ data was 2.3–9.8 Å⁻¹ with a Hanning window function and a dk value of 1.0 Å⁻¹ (Newville et al., 1993). Simultaneous fitting of each dataset with multiple k -weighting (k^1 , k^2 , k^3) of each spectrum was performed using the Fourier transformed $\chi(R)$ spectra. The fitting range for all of the datasets was 1.2–3.4 Å. The simultaneous fitting approach reduces the possibility of obtaining erroneous parameters due to correlations at any single k -weighting (Kelly et al., 2002; Mishra et al., 2009).

2.5. EXAFS standards

Powder and aqueous Cd standards were used to determine the spectral features of Cd in carboxyl, phosphoryl and sulfhydryl binding environments. A CdS powder standard was prepared from commercially available chemicals (Sigma–Aldrich), after grinding and sieving (~400 mesh). The aqueous Cd standards included Cd-acetate, and Cd-phosphate solutions. All aqueous Cd standards were prepared by dissolving Cd(NO₃)₂·4H₂O in the appropriate acid/electrolyte. The Cd-acetate and Cd-phosphate standards were prepared with a Cd:ligand ratio of 1:100 (acetate or phosphate), by adding appropriate amounts of acetic and phosphoric acids. The pH of the Cd-acetate solution was adjusted using NaOH to 4.5, where the aqueous Cd-acetate aqueous complexes dominate the Cd speciation in solution. The pH of the Cd-phosphate solution was kept at 3.0 to avoid precipitation of a cadmium phosphate solid phase. Although the choice of standards is of paramount importance when applying a linear combination fitting approach to X-ray absorption near edge structure (XANES) data, EXAFS analysis is model independent. The main use of experimental standards is to fine-tune the fitting parameters for a given signal against a theoretical EXAFS signal generated by simulating a known crystal structure (as explained below). Therefore, the choice of aqueous versus crystalline standards for EXAFS analyses is not critical, and the use of a crystalline CdS powder as a standard for the biomass Cd–S EXAFS signal, when all other standards are aqueous, is acceptable.

EXAFS data analysis is based on refining theoretical EXAFS spectra against the experimental data. Models are

constrained by use of crystalline model compounds with well-characterized local structures. The crystallographic information of the standard compounds were first transformed into a cluster of atoms by using the program ATOMS (Ravel, 2001). Then FEFF8 (Ankudinov et al., 1998) was used to carry out self-consistent quantum mechanical calculations to simulate theoretical EXAFS spectra based on the cluster of atoms thus obtained. Experimentally obtained EXAFS data on the standard compounds were fit to these theoretically generated EXAFS spectra using the program FEFFIT (Newville et al., 1995). We refined *ab initio* calculations on clusters of atoms derived from known crystal structures (Caminiti, 1982; Caminiti et al., 1984) against the EXAFS data from powdered CdS and aqueous Cd-acetate and Cd-phosphate standards.

The value obtained for the EXAFS amplitude reduction factor for all standards was $S_0^2 = 1.00 \pm 0.03$, and this value was used in modeling the spectra from the bacterial samples. Statistically significantly lower R factor and χ_r^2 values were used as criteria for improvement in the fit to justify the addition of an atomic shell to the model (Kelly et al., 2002).

3. RESULTS AND DISCUSSION

3.1. Potentiometric titrations

The three replicate titration curves are similar and are depicted in Fig. 1 as the mass normalized net molality of H⁺ added versus pH. The mass normalized net molality of H⁺ added is equal to the concentration of acid added to the system minus the concentration of base added, divided by the mass of the bacteria (in g/L; wet mass) used in the titration. Similar to other bacterial titrations (e.g., Plette et al., 1995; Fein et al., 1997; Daughney et al., 1998; Cox et al., 1999; Yee and Fein, 2003; Yee et al., 2004; Haas et al., 2001; Sokolov et al., 2001; Martinez et al., 2002; Ngwenya et al., 2003; Smith and Ferris, 2003; Claessens et al., 2004; Fein et al., 2005), our potentiometric titration data indicate that *S. oneidensis* exhibits significant proton buffering over the entire pH range studied. This finding indicates that the bacterial cell wall was not fully protonated, even under the lowest pH conditions attained (~2.7), and it is possible that proton-active functional groups are important contributors to the buffering at even lower pH values. The potentiometric titration data obtained by Haas et al. (2001), Sokolov et al. (2001), and Smith and Ferris (2003) for *S. putrefaciens* exhibit positive values for the mass normalized net molality of H⁺ added to solution below pH values of approximately 7, with negative values at higher pH. Similar to those previous studies, the mass normalized net molality of H⁺ added in this study is positive below a pH of approximately 7.5–8.0, and exhibits negative values at higher pH conditions. Although some previous studies have done so, the sign of this parameter should not be interpreted to indicate the sign of the surface charge of the bacterial surface at a particular pH value. Rather, the excess or deficit of this parameter relative to its value for a bacteria-free blank at the same pH indicates only that protons have been taken up or released by the

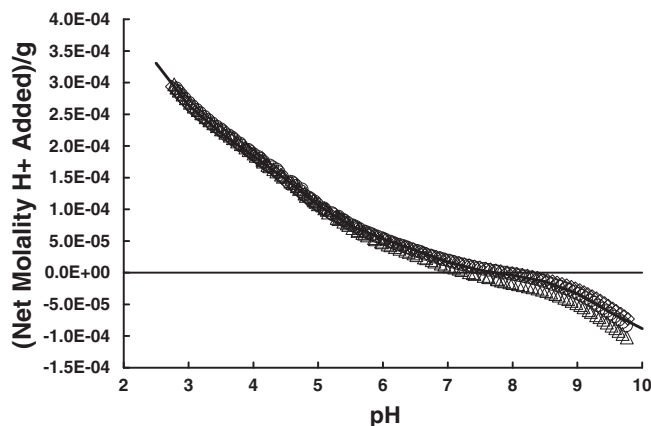


Fig. 1. Three replicate titration curves of *S. oneidensis* (50 g/L, wet wt.) in 0.1 M NaClO₄. Open diamonds, circles, and triangles represent experimental data points for individual titrations. Solid curve represents the average model fit.

bacteria. Electrophoretic mobility measurements indicate an overall negative charge associated with the *S. oneidensis* cell wall (Claessens et al., 2004). Therefore, we model the charging behavior of *S. oneidensis* with a series of organic acid functional group sites. We use a surface complexation approach to model the potentiometric titration and Cd adsorption data in order to relate pH and sorbent:sorbate ratio effects on adsorption to the speciation of the bacterial surface. Our first step is to model the potentiometric titration data to determine site concentrations and stability constants for the important surface reactive sites. A generalized deprotonation reaction for bacterial surface sites is represented as:



where $R - A_i$ represents a bacterial surface functional group type and i is an integer ≥ 1 . A generalized mass action equation for the above reaction is:

$$K_{a(i)} = \frac{[R - A_i^-] a_{H^+}}{[R - A_i H^0]} \quad (2)$$

where K_a and a represent the equilibrium (acidity) constant and activity of the subscripted reaction or species, respectively, and the brackets represent the concentration of surface sites in moles/L of solution. Each bacterial site $R - A_i$ represents a discrete site with its own site concentration and acidity constant. FITEQL (Westall, 1982) was used as the computational tool to determine the number of discrete sites necessary to account for the observed buffering behavior and to solve for the site concentrations and acidity constants for each type of site. We used a non-electrostatic surface complexation model to describe proton and Cd adsorption onto the bacterial cell wall functional groups (e.g., Fein et al., 2005).

For each model tested, FITEQL calculates a variance function, $V(Y)$, that describes the goodness-of-fit of the model to the experimental measurements. The best-fitting model was determined to be the one that yields the lowest $V(Y)$ value to the experimental data. Each titration was modeled separately. A 4-site model with four deprotonation reactions associated with each site provides the best fit to the experimental data of all three bacterial titrations, with

an average $V(Y) = 0.52$. Models utilizing less than 4-sites yield significantly higher $V(Y)$ values and exhibit a worse visual fit to the experimental data. Models utilizing more than 4-sites fail to converge, indicating that the experimental data do not support more than four discrete sites. The average model fit to all three bacterial titrations is illustrated as a solid curve in Fig. 1. The best-fitting reaction stoichiometries with corresponding averaged deprotonation constants and averaged site concentrations for the *S. oneidensis* bacterial surface are given in Table 1.

Borrok et al. (2005) reviewed and compiled the available potentiometric titration datasets for individual bacterial species, bacterial consortia, and bacterial cell wall components, and derived an internally consistent thermodynamic model, similar to the model used in this study, for all the datasets. Borrok et al. (2005) found that, if one assumed a 4-site model for each titration dataset with pK_a values fixed to 3.1, 4.7, 6.6, and 9.0, the calculated site concentrations for the individual datasets were remarkably similar, yielding best-fit values of 1.13×10^{-4} , 9.08×10^{-5} , 5.32×10^{-5} , and 6.63×10^{-5} moles/g bacteria (wet mass) for the site concentrations for the lowest to the highest pK_a sites, respectively. The site concentrations and deprotonation constants that we determined for *S. oneidensis* (Table 1) are within uncertainties of the averages obtained by Borrok et al. (2005).

3.2. Cd adsorption

The results of the bulk adsorption measurements for *B. subtilis* and *S. oneidensis* are shown in Fig. 2a and b, respectively. The observed extents of Cd adsorption for the two

Table 1
Log K and site concentration values of *S. oneidensis* surface sites.

[Site] ^a	Reaction	Log K
$8.9 (\pm 2.6) \times 10^{-5}$	$R - A_{(1)} H^0 \rightleftharpoons R - A_{(1)}^- + H^+$	-3.3 ± 0.2
$1.3 (\pm 0.2) \times 10^{-4}$	$R - A_{(2)} H^0 \rightleftharpoons R - A_{(2)}^- + H^+$	-4.8 ± 0.2
$5.9 (\pm 3.3) \times 10^{-5}$	$R - A_{(3)} H^0 \rightleftharpoons R - A_{(3)}^- + H^+$	-6.7 ± 0.4
$1.1 (\pm 0.6) \times 10^{-4}$	$R - A_{(4)} H^0 \rightleftharpoons R - A_{(4)}^- + H^+$	-9.4 ± 0.5

^a Site concentrations in moles/g.

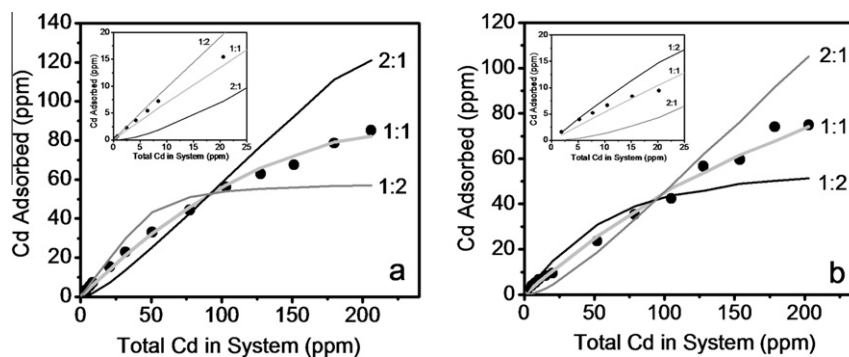
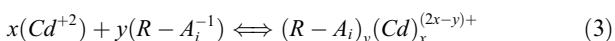


Fig. 2. Experimental data and models for different Cd:Site stoichiometries for (a) *B. subtilis*, and (b) *S. oneidensis*. These experiments were conducted at $\text{pH } 5.9 \pm 0.2$, and the 10 g/L bacterial solution was prepared in a 0.1 M NaClO_4 electrolyte. The low Cd concentration range of the experimental data has been expanded for clarity and shown as insets in Figs. 2a and b.

bacterial species are similar. For each species, the concentration of adsorbed Cd increases with increasing total Cd in the experimental systems, but the slope decreases at higher Cd concentrations. Under the lowest Cd concentrations studied, Cd is predominantly adsorbed to the solid phase, while at higher total Cd concentrations a higher proportion remains in solution. Such adsorption behavior is typical for a system with a limited number of binding sites, in which sites are undersaturated at low metal concentrations and become increasingly saturated with increasing metal loading.

3.3. Thermodynamic modeling of the adsorption isotherms

Adsorption experiments that are conducted as a function of solute:sorbent concentration ratio at a fixed pH do not uniquely define which sorbing site or sites of a multi-site sorbent are responsible for the uptake, but the results do place rigorous constraints on the average stoichiometry of the adsorption reactions. A generic Cd adsorption reaction can be represented as an interaction between the aqueous Cd cation (Cd^{+2}) and deprotonated surface sites on the bacterial cell wall to create a bacterial surface complex:



where x and y represent stoichiometric coefficients that must be determined experimentally. We use the discrete 4-site non-electrostatic model of Fein et al. (2005) to describe the protonation state of the cell wall functional groups for *B. subtilis*; and we use the similar model for *S. oneidensis* from this study. The pK_a values for the four sites on *B. subtilis* are 3.3, 4.8, 6.8, and 9.1, respectively, and the corresponding site concentrations are 8.1×10^{-5} , 1.1×10^{-4} , 4.4×10^{-5} , and 7.4×10^{-5} moles of sites/gm wet mass bacteria, respectively (Fein et al., 2005). We refer to these sites as Sites 1–4, respectively.

Because the adsorption experiments were conducted under fixed pH conditions, the data can be equally well modeled by ascribing Cd adsorption onto any of the four site types on the bacterial cell wall, and more than one site may be involved in Cd binding under the experimental conditions. However, because the experiments were conducted

at pH 5.9, we choose to model the Cd adsorption data for each bacterial species as an interaction between Cd^{2+} and the deprotonated form of Site 2 (the site with a pK_a value of 4.8 for both *B. subtilis*, and *S. oneidensis*). This exercise is intended only to constrain the average site stoichiometry of the important Cd–bacterial complexes at pH 5.9, and does not provide a molecular-scale understanding of the Cd binding environment. We attempted to model the Cd adsorption data using Cd:Site stoichiometries of 1:1, 1:2 and 2:1, using the $V(Y)$ fit parameter from FITEQL to distinguish the best-fitting stoichiometry. The value of $V(Y)$ depends on estimates for standard deviation in the experimental data, but in general $V(Y)$ values between 0.1 and 20 represent reasonable fits, and models with lower $V(Y)$ values represent better fits of the model to the data (Westall, 1982). Even if the reaction mechanism changes as a function of Cd loading, that is if different binding sites are important under different Cd loading conditions, this approach determines the average reaction stoichiometry for each binding mechanism.

The best-fitting models for each reaction stoichiometry are shown in Fig. 2a and b. The low Cd concentration range of the experimental data has been expanded for clarity and shown as insets in Fig. 2a and b. The $V(Y)$ values associated with the best-fitting 1:1, 1:2, and 2:1 Cd:Site stoichiometry models for *B. subtilis* are 10.6, 320.1, and 174.9, respectively, indicating that the 1:1 model yields the best overall fit to the experimental data over the entire Cd concentration range. Fig. 2a illustrates that the 1:1 model fit to the data, with a calculated best-fit $\log K$ value for reaction (3) of 3.4 ± 0.2 , provides a better fit than do the 1:2 or the 2:1 models when considering the entire Cd concentration range. The inset figure shows that the data cannot distinguish between the 1:1 and the 1:2 models under low Cd concentration conditions, so under these conditions, as the Cd concentration decreases and as the site:Cd molal ratio increases, it is possible that a surface complex with a 1:2 Cd:site stoichiometry becomes important. Similarly for *S. oneidensis*, the $V(Y)$ values associated with the best-fitting 1:1, 1:2, and 2:1 Cd:Site stoichiometry models over the entire Cd concentration range studied are 20.9, 238.3, and 351.5, respectively. Fig. 2b demonstrates that the 1:1 model fit to the *S. oneidensis* data, also with a calculated best-fit

log K value for reaction (3) of 3.4 ± 0.3 , provides a good fit to the experimental Cd adsorption data over the entire range of Cd concentrations. As is the case for the *B. subtilis* data in Fig. 2a, the data cannot distinguish between the 1:1 and the 1:2 models under low Cd concentration conditions, so it is possible that under these conditions a surface complex with a 1:2 Cd:site stoichiometry becomes important. It should be noted that Cd may be bound to more than one site under the experimental conditions, so the best-fit log K values reported here represent averages of the stability constant values for all of the important Cd–bacterial surface complexes.

The modeling results for *B. subtilis* and *S. oneidensis* are remarkably similar. The two bacterial species exhibit similar extents of adsorption over the entire range of Cd concentrations studied, and because of their similar proton reactivities and site concentrations, the calculated log K values for reaction (3) are within error of each other. Although these data do not constrain which site is involved in Cd binding, the 1:1 model yields the best fit to the entire Cd concentration range dataset regardless of which site we use in the model. If more than one site is involved in the Cd binding over this range of Cd loadings, the modeling suggests that any mechanism involves a 1:1 metal:site binding ratio, except perhaps under the lowest Cd concentration conditions studied here where a 1:2 complex is also possible.

3.4. Analysis of XAFS data from standard compounds

The fitting results for the Cd standards are shown in Table 2. The coordination environment of Cd in the acetate-bearing standard was modeled with O and C shells, corresponding to a bound acetate group. Data were fit with $5.5 (\pm 0.3)$ O atoms in the first shell and 3C (fixed to this value based on speciation calculation) atoms in the second shell, consistent with the bidentate bonding mechanism observed by Caminiti et al. (1984). The Cd–C distance in the Cd-acetate standard was found to be $2.70 (\pm 0.02)$ Å. The aqueous Cd-phosphate standard data were fit with $5.8 (\pm 0.3)$ O atoms in the first shell, and $1.5 (\pm 0.3)$ P atoms in the second shell. The Cd–O bond length was found to be $2.28 (\pm 0.02)$ Å, the same distance as in the Cd-acetate standard, and the Cd–P bond distance was found to be $3.41 (\pm 0.03)$ Å. The Cd sulfide standard was fit with 4 S

atoms in the first shell at a distance of $2.53 (\pm 0.02)$ Å. The sulfide standard displays characteristic spectral features that can be seen in Fig. 3a. The second and third oscillations of the Cd sulfide spectrum are out of phase relative to all the other standards. The phase shift arises from Cd bonding to sulfur in the first shell, as opposed to bonding to oxygen in all of the other standards. This phase shift (and change in frequency) in the chi data is manifested in a shift in the first peak of the Fourier transformed data for the Cd–S spectrum in Fig. 4a relative to the other standard spectra. In the Cd-acetate data, note the reduction in amplitude of the first shell peak in Cd-acetate compared to the Cd-phosphate spectrum (Fig. 4a). Detailed modeling reveals that the reduction in amplitude is due to the signal from the carbon atom interfering destructively with that from the oxygen atom. The subtle features in the second shell of the Cd-phosphate and Cd-acetate spectra are not seen clearly from the full view of the magnitude of the Fourier transformed data, because C and P are both light elements that do not backscatter the photoelectrons strongly. The enlarged real part of the Fourier transformed data, however, illustrates the relatively small changes in the second shell of the Cd-acetate and Cd-phosphate spectra (Fig. 4b). As can be seen from Fig. 4b, the Cd-phosphate standard exhibits a feature (line shape) at about 2.7 Å, indicative of the P atom in a bound phosphate group. The position of the S peak overlaps the position of the C feature at 2.2 Å in the Cd-acetate spectrum, but is shifted to larger distances. From the above analysis it is clear that the characteristic spectral features of a Cd-carboxyl and a Cd-phosphoryl local environment are: (1) for Cd-carboxyl binding, a smaller first shell peak amplitude exists, associated with an increase in the second shell peak at about 2.2 Å (Fig. 4b), and (2) for Cd-phosphoryl binding, a larger first shell amplitude is evident, along with a feature at 2.7 Å. The characteristic feature of Cd-sulfhydryl binding is a shifted first shell peak to larger distances relative to a Cd–O environment, and this shift is associated with an increase in the peak to a position just over 2.2 Å (Fig. 4b).

The collection of high quality EXAFS data allowed assignment of the subtle features in the EXAFS spectra to the corresponding ligands, as well as the quantitative modeling described above. The structural parameters of the Cd–O, Cd–S, Cd–C and Cd–P contributions (paths) used in fitting the Cd sulfide, Cd-acetate and Cd-phosphate standards are the same as listed in Table 3 of Mishra et al., 2009. The presence of these contributions in the spectrum of an unknown sample can be taken as indicative of sulfhydryl-, carboxyl-, and phosphoryl- binding environments, respectively. Our approach was to use these well-calibrated paths in the analysis of the spectra for the bacterial samples. A Cd–Cd contribution (path) obtained from the fit of the CdS spectrum was used to test for the presence of Cd precipitation in each sample.

3.5. Qualitative analysis of spectra from the bacterial samples

The magnitude and real part of the Fourier transform data for the *B. subtilis* samples at various Cd loadings are

Table 2
Structural parameters obtained from fits of the standard compounds spectra.

Standard	Path	N	$R(\text{Å})$	$\sigma^2 (10^{-3} \text{Å}^2)$
CdAc	Cd–O	5.5 ± 0.3	2.28 ± 0.02	10.9 ± 0.9
	Cd–C	3.0^b	2.70 ± 0.02	12.8 ± 4.0
CdPO ₄	Cd–O	5.8 ± 0.3	2.28 ± 0.02	10.5 ± 1.2
	Cd–P	1.5 ± 0.3	3.41 ± 0.03	15.0 ± 3.0
CdS	Cd–S	4.0^a	2.53 ± 0.02	9.0 ± 1.0
	Cd–Cd	12.0^a	4.2 ± 0.01	25.0 ± 4.0

^a Fixed to this value based on crystallographic data.

^b Fixed to this value based on speciation calculations.

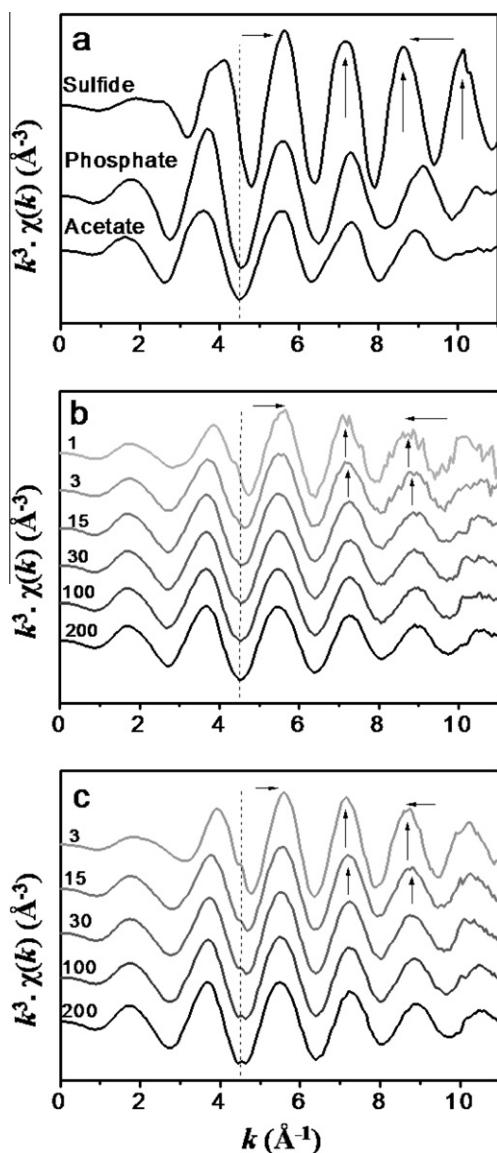


Fig. 3. (a) k^3 weighted $\chi(k)$ data for (a) the Cd standards, (b) *B. subtilis* isotherm, and (c) *S. oneidensis* isotherm data. Data range used for Fourier transform was $2.3\text{--}9.8 k (\text{\AA}^{-1})$.

shown in Fig. 4c and Fig. 4d, respectively. The data can be compared to the standards spectra that are depicted in Fig. 4a and b. An increase in the amplitude of the oscillation at 2.2\AA with decreasing Cd loading in the system can be clearly seen in Fig. 4d. Based on the analysis in the previous paragraph, this increase can be attributed to either increasing carboxyl or sulfhydryl binding to Cd. The choice between these two possibilities is based on the shift of the main peak position towards higher r values in Fig. 4c. As discussed above, this shift is characteristic of sulfhydryl binding, and suggests that in the two lowest concentration samples, 3.0 and 1.0 ppm, the adsorbed Cd is predominantly bound to sulfhydryl groups.

The magnitude and the real part of the Fourier transform data for the *S. oneidensis* samples are shown in Fig. 4e and Fig. 4f, respectively. A consistent increase in

the amplitude oscillation and phase shift towards higher r value at about 2.2\AA occurs in the real part of the Fourier transform data (Fig. 4f) with decreasing Cd loading on the bacterial cell wall. By the same arguments as those applied to the *B. subtilis* spectra, we conclude that an increase in the relative amount of Cd atoms bound to sulfhydryl groups on the *S. oneidensis* cell wall occurs with decreasing Cd loading.

3.6. Quantitative EXAFS modeling

The six spectra from the samples taken along the *B. subtilis* isotherm were first fit independently, using the Cd–O, Cd–S, Cd–C and Cd–P paths that were used to model the Cd standards (Table 2). The numerical results from these fits are not shown because the final model, based on simultaneous fitting of data from all six Cd concentrations, yielded identical results but with smaller uncertainties. Below we discuss the individual fits separately only to show that the observed binding behavior with Cd concentration is not the result of the global fitting constraint.

We attempted to model the 200 ppm Cd *B. subtilis* spectrum with a single binding site and found that Cd-phosphoryl binding yields the best fit to the data. However, the addition of a Cd-carboxyl binding site to the Cd-phosphoryl model significantly improves the fit. There is no evidence for Cd-sulfhydryl binding in the 200 ppm Cd spectrum. Best-fit values of the path parameters (σ^2 and ΔR) for this sample were the same (within uncertainties) as those obtained for the Cd standards reported above. Modeling of the 100 ppm Cd *B. subtilis* spectrum yields results similar to those from the 200 ppm Cd spectrum, with phosphoryl and carboxyl binding able to yield an excellent fit to the data and with no evidence for Cd-sulfhydryl binding. Conversely, modeling of the individual spectra for the 30, 15, 3 and 1 ppm Cd samples requires an additional Cd-sulfhydryl binding site, and indicates an increase in the sulfhydryl coordination numbers with decreasing Cd concentration. While the carboxyl contribution to Cd binding remains constant (within error) over this concentration range, the phosphoryl contribution remains constant (within error) up to 15 ppm, decreases for 3 ppm, and was not required at all in order to successfully model the 1 ppm data. A steep increase in the sulfhydryl coordination number was found at 1 ppm, indicating the predominance of Cd-sulfhydryl binding under these conditions.

The Cd-sulfhydryl binding that we observed in the 30 ppm *B. subtilis* experiment, although only a small portion of the bound Cd budget, is in contrast with the findings of Boyanov et al. (2003) and Mishra et al. (2007) who did not report any sulfhydryl binding for the same bacterial species at similar Cd concentrations and pH values. However, the S coordination number that we report here for these conditions (0.08 ± 0.04) is extremely small, and could easily be masked by carboxyl and phosphoryl functional groups with small changes in experimental conditions.

Although independent modeling of the six *B. subtilis* samples provides an approximation of the contributions of Cd-carboxyl, -phosphoryl and -sulfhydryl binding in each spectrum, the average binding environment is complex

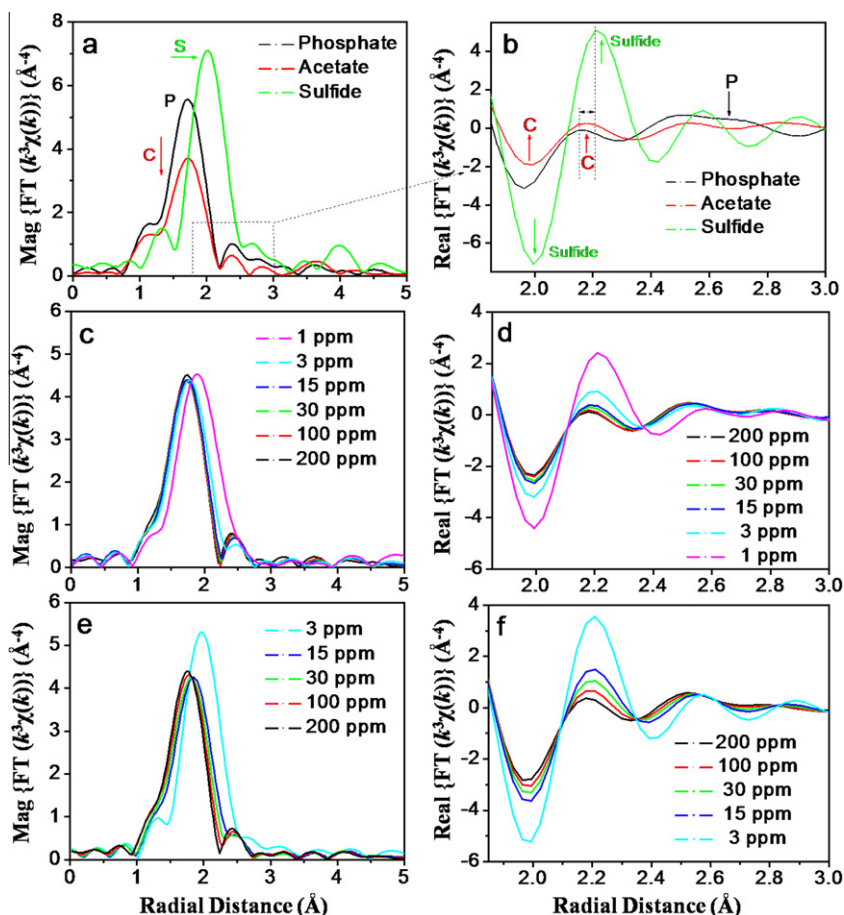


Fig. 4. (a) Fourier Transform magnitude of the Cd Standard data, (b) real part of the Fourier transform data of the Cd standard data, (c) Fourier Transform magnitude of the *B. subtilis* isotherm data, (d) real part of the Fourier Transform data of the *B. subtilis* isotherm, (e) Fourier Transform magnitude of the *S. oneidensis* isotherm data, and (f) real part of the Fourier Transform data of the *S. oneidensis* isotherm.

in nature and there are overlapping contributions of relatively small amplitude in the spectra. Correlations within each individual fit between coordination numbers and sigma-square values, as well as between ΔE_0 (energy shift) and bond distances, can mask trends in the structural parameters in the series of samples. To deal with the problem, all six spectra were fit simultaneously, each at three k -weights, resulting in a simultaneous fit of eighteen datasets. The energy shift, ΔE_0 , the radial distance (R) and the distance variation (σ^2 -value) to each ligand were refined, but were constrained to be the same in all samples. This approach carries in it the implicit assumption of identical molecular binding geometry to the corresponding ligands in all samples, and attributes the variation in amplitude to variations in the relative coordination numbers. In other words, it is assumed that the Cd–ligand distance and variation in average radial distance (σ^2 -values) are the same whether Cd is bound to that ligand alone or is in a mixed environment of Cd-carboxyl, Cd-phosphoryl and/or Cd-sulfhydryl binding. This simultaneous fitting approach yields best-fit values of the path parameters (σ^2 and ΔR) for all paths that are the same (within uncertainties) as those obtained for the Cd standards (Table 2). These variables were therefore fixed to be equal to the values obtained

for them from the Cd standards. The increased number of independent data points for the fit and the reduced number of variables resulted in smaller correlations between the fitting parameters, allowing their determination with smaller uncertainties and revealing the trends in average binding environment with changes in Cd loading.

Further confidence in the fitting approach adopted in this study was gained by a simple test to determine the robustness of the model. The variables (distances, and Debye–Waller factors) which have been fixed in this fitting approach to the values obtained by standard compounds were set to the upper and lower limits of their uncertainties and the fits were performed again (Table 2). This results in less than a 15% change in the final coordination numbers of the corresponding ligands reported in Table 3a. Although a rigorous qualitative modeling of the data has been attempted, and a robust fitting of the EXAFS spectra has been achieved, the determination of the absolute number of ligands bound to a metal in a complex natural system is difficult. However, the technique is much more precise in determining relative changes in the coordination environment of the metal, so the observed changes in the coordination numbers that we report in Table 3 are significant and real.

Table 3
EXAFS fitting parameters for (a) *B. subtilis* and (b) *S. oneidensis* samples.

[Cd] (in ppm)	1.0	3.0	15	30	100	200
(a) <i>Bacillus subtilis</i>						
<i>Paths</i>						
No	1.95 ± 0.16	3.93 ± 0.28	4.67 ± 0.16	4.78 ± 0.12	4.98 ± 0.16	4.93 ± 0.14
Nc	1.22 ± 0.52	1.23 ± 0.62	0.97 ± 0.48	0.89 ± 0.46	0.99 ± 0.60	0.98 ± 0.48
Ns	2.87 ± 0.14	0.98 ± 0.22	0.17 ± 0.14	0.08 ± 0.04		
Np		0.48 ± 0.24	0.82 ± 0.36	0.82 ± 0.32	1.12 ± 0.40	1.03 ± 0.40
Ro = 2.28 Å, $\sigma_o^2 = 0.009 \text{ \AA}^{-2}$						
Rc = 2.70 Å, $\sigma_c^2 = 0.012 \text{ \AA}^{-2}$						
Rs = 2.53 Å, $\sigma_s^2 = 0.009 \text{ \AA}^{-2}$						
Rp = 3.41 Å, $\sigma_p^2 = 0.015 \text{ \AA}^{-2}$						
$\Delta E_0 = -2.2 \pm 0.8 \text{ eV}$						
(b) <i>Shewanella oneidensis</i>						
<i>Paths</i>						
No			3.18 ± 0.28	3.72 ± 0.22	4.28 ± 0.20	4.98 ± 0.14
Nc			1.17 ± 0.42	1.30 ± 0.56	1.46 ± 0.60	1.40 ± 0.54
Ns		4.10 ± 0.65	1.42 ± 0.14	0.90 ± 0.16	0.45 ± 0.16	
Np			0.35 ± 0.26	0.58 ± 0.30	0.83 ± 0.30	0.95 ± 0.34
Ro = 2.28 Å, $\sigma_o^2 = 0.009 \text{ \AA}^{-2}$						
Rc = 2.70 Å, $\sigma_c^2 = 0.012 \text{ \AA}^{-2}$						
Rs = 2.53 Å, $\sigma_s^2 = 0.009 \text{ \AA}^{-2}$						
Rp = 3.41 Å, $\sigma_p^2 = 0.015 \text{ \AA}^{-2}$						
$\Delta E_0 = -1.4 \pm 0.6 \text{ eV}$						

The number of variables used to fit the EXAFS data in this study is less than one-third the number of independent data points in the data as obtained using Nyquist's theorem (Nyquist, 1928). Hence, the goodness-of-fit of the model to the data is not the result of excessive flexibility in the model and each refined parameter represents meaningful information about the binding environments.

Final fitting parameters for the *B. subtilis* system are tabulated in Table 3a, and the magnitude and real part of the Fourier transform of the data and fits are shown in Fig. 5a and b, respectively. Table 3a shows that the number of oxygen atoms bound to each Cd atom consistently decreases with decreasing Cd concentration from 4.93 ± 0.14 for the 200 ppm sample to 1.95 ± 0.16 for the 1.0 ppm sample. This is concurrent with an increase in the average number of sulfur atoms bound to each Cd atom from 0.8 ± 0.04 for 30 ppm to 2.87 ± 0.14 for the 1.0 ppm *B. subtilis* sample. The two highest Cd loading samples (200 and 100 ppm Cd) do not exhibit any sulfhydryl contribution to the Cd binding. The coordination numbers of the carboxyl group ($\sim 1.0 \pm 0.5$) remain the same within the uncertainty of the measurement over the entire concentration range measured. The coordination number of the phosphoryl group remains the same ($\sim 1.0 \pm 0.3$) within the uncertainty of the measurement for the 200, 100, 30 and 15 ppm Cd samples, but decreases to 0.48 ± 0.24 for the 3.0 ppm sample. The 1.0 ppm *B. subtilis* data do not require the inclusion of Cd-phosphoryl binding to account for the experimental spectra.

We used a similar approach to model the *S. oneidensis* data as we did for the *B. subtilis* data. That is, we first attempted to model each spectrum individually with as few site types as possible. We then compared these results with

simultaneous fits of all of the spectra together. In general, we observed similar Cd binding environments and trends in the *S. oneidensis* samples as we did for the *B. subtilis* samples. Modeling of the 200 ppm Cd *S. oneidensis* spectrum with a single binding site provided the best fit with Cd-phosphoryl binding. However, as was the case for the 200 ppm Cd *B. subtilis* sample, the addition of Cd-carboxyl binding to the Cd-phosphoryl model significantly improved the fit. Best-fit values of the parameters (σ^2 and ΔR) for this sample are the same (within uncertainties) as those obtained for the Cd standards reported above. Modeling of the individual spectra for the 100, 30, and 15 ppm Cd samples shows an increase in the sulfhydryl coordination numbers with decreasing Cd concentration. While the carboxyl contribution to Cd binding remains constant (within error) over this concentration range, the phosphoryl contribution decreases with decreasing Cd concentration in the samples. A steep increase in sulfhydryl coordination number to 4.10 ± 0.65 occurs for the 3 ppm Cd sample, where carboxyl and phosphoryl contributions to Cd binding are not required to fit the data. This spectrum was fit solely with a Cd-S path, indicating the complete dominance of Cd-sulfhydryl binding under these conditions.

Final fitting parameters for the *S. oneidensis* system, using the same simultaneous fitting approach as we applied to the *B. subtilis* spectra, are listed in Table 3b, and the magnitude and real part of the Fourier transform of the measured spectra and the model fits are shown in Fig. 5c and d, respectively. Table 3b shows that the number of oxygen atoms bound to each Cd atom consistently decreases with decreasing Cd concentration from 4.98 ± 0.14 for the 200 ppm sample to 3.18 ± 0.28 for the 15 ppm sample. This is concurrent with an increase in the average number of S

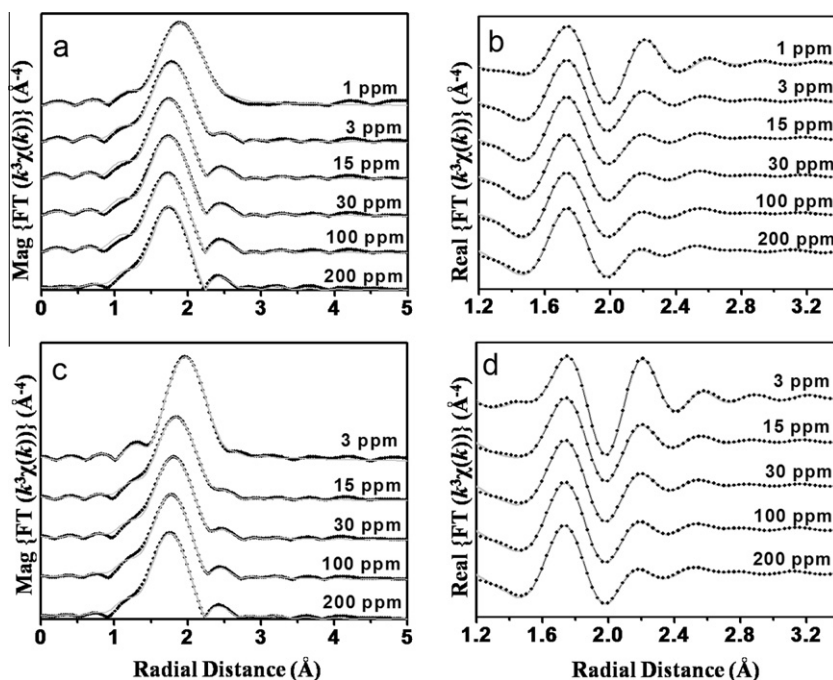


Fig. 5. Fourier Transform (a) magnitude and (b) real part of the EXAFS data and fits for the *B. subtilis* isotherm, and Fourier transform (c) magnitude and (d) real part of the EXAFS data and fits for the *S. oneidensis* isotherm.

atoms bound to each Cd atom from 0.45 ± 0.16 for the 100 ppm Cd sample to 1.42 ± 0.14 for the 15.0 ppm Cd-*S. oneidensis* sample. The highest Cd loading sample (200 Cd) does not exhibit any Cd-sulfhydryl contribution. The coordination numbers of the carboxyl group remain the same (1.30 ± 0.15) as a function of Cd loading within the uncertainty of the measurement. The coordination number of the phosphoryl group decreases from 0.95 ± 0.34 for the 200 ppm Cd sample to 0.35 ± 0.26 for the 15 ppm Cd-*S. oneidensis* sample. The 3 ppm Cd-*S. oneidensis* data were modeled with Cd-sulfhydryl binding only. Carboxyl and phosphoryl contributions to the Cd binding were not required for modeling the 3 ppm Cd data.

3.7. Discussion of Cd adsorption on bacterial cell walls as a function of Cd loading

The EXAFS fitting results are consistent with the modeling of the bulk adsorption data, and indicate that *B. subtilis* and the *S. oneidensis* cells exhibit broadly similar binding mechanisms for Cd as a function of metal loading under the conditions of this study. Phosphoryl and carboxyl binding are primarily responsible for Cd binding to *B. subtilis* cells at higher and intermediate Cd loading conditions (200, 100, 30 and 15). Carboxyl and sulfhydryl binding become much more important at 3 ppm and sulfhydryl sites become the most important binding sites at 1 ppm Cd loading for *B. subtilis*. On the other hand, phosphoryl binding dominates Cd binding to *S. oneidensis* cells under high Cd loading conditions (the 200 and 100 ppm Cd samples). The importance of carboxyl functional groups is highest at intermediate Cd loading conditions (the 30 and 15 ppm Cd samples) for *S. oneidensis*, due to the decreasing importance of the phosphoryl group. Sulfhydryl sites completely

dominate the Cd binding for the *S. oneidensis* samples with the lowest Cd loading (3 ppm Cd). Sulfhydryl binding likely does not disappear with increasing Cd loading onto the bacterial cell wall. Rather, carboxyl and phosphoryl binding dominate the bound Cd budget under these conditions, swamping the signal of the relatively low abundance Cd-sulfhydryl sites. The EXAFS fitting parameters indicate that more than one site is involved simultaneously in Cd binding under most of the conditions studied, and except for the lowest Cd concentrations studied, the dominant adsorption stoichiometry for each site type is a 1:1 Cd:Site ratio. These results are consistent with the surface complexation modeling of the bulk Cd adsorption data, which also indicates an average Cd:Site stoichiometry of 1:1 and 1:2 at the high and low Cd concentration ranges of this study. The increase in average coordination number under the lowest Cd loading conditions is evident from the steepening of the Cd adsorption isotherms (Fig. 2a and b) under these conditions. In addition, if we determine the average adsorption stoichiometry that is consistent with only the data points with the lowest three Cd concentrations for each bacterial species, then we obtain best-fitting Cd:Site stoichiometries of 1:3 and 1:4 for the *B. subtilis* and the *S. oneidensis* data, respectively. These results are consistent with the increase in S coordination number to 2.87 ± 0.14 and 4.10 ± 0.65 for the lowest Cd concentrations studied for *B. subtilis* and *S. oneidensis*.

The lowest concentration *S. oneidensis* sample exhibits sulfhydryl binding only, and therefore can be used to estimate the concentration of sulfhydryl sites on the bacterial cell wall. Cd forms stable tetrahedral bonds with S, so our observed coordination number of 4.10 ± 0.65 for S is consistent with the absence of any carboxyl and/or phosphoryl binding of Cd in this sample. It would, therefore,

be reasonable to assume that for the 3 ppm Cd *S. oneidensis* sample, the concentration of sulfhydryl functional groups on the cell wall can be approximated as four times the concentration of adsorbed Cd atoms. This approximation is likely an underestimation, as not all sulfhydryl sites on the cell wall are involved in Cd binding under these conditions. However, these are the first estimates of the sulfhydryl site concentration and are valuable as preliminary constraints at least. Under these conditions, the concentration of adsorbed Cd is 2.2×10^{-6} moles of Cd per gram (wet mass) of bacteria, yielding an estimate of the sulfhydryl site concentration of 8.8×10^{-6} moles of sites per gram (wet mass) of bacteria. This site concentration represents only approximately 2% of the total number of sites on the cell wall, as determined by the potentiometric titrations.

The observation and characterization of the low abundance, high-affinity sulfhydryl sites in this study was made possible by using very low metal-to-surface loading conditions. This avoided masking of the sulfhydryl spectral signal by larger signals from the more abundant, lower-affinity sites that become occupied under higher metal loading conditions. A possible reason why purely sulfhydryl bonding has not been observed in previous spectroscopy studies was the use of high metal loadings in order to obtain good signal-to-noise ratio during data collection. We were able to collect high quality spectra from low concentration samples by utilizing a high-flux undulator beamline and a Stern–Heald fluorescence detector (Stern and Heald, 1983). The more intuitive approach of using a 13-element energy-dispersive Ge detector provided inferior data quality above $k \sim 8 \text{ \AA}^{-1}$. We explain this by the fact that our system is composed predominantly of low-Z elements, resulting in a low fluorescence background. Therefore, the advantage of removing the small background using energy-dispersive detectors is outweighed by the limited count rate compared to ionization chambers. In addition, by optimizing the gasses, voltages, and the sensitivity regimes of the incident and fluorescence ionization detectors we were able to achieve a better linear response between the *I_o* and *I_f* detectors. This resulted in low-noise data from samples as dilute as 1 ppm Cd in the original solution phase.

4. CONCLUSIONS

This study highlights the strengths and limitations of both bulk adsorption and EXAFS measurements of metal–bacterial complexation. Bulk metal adsorption measurements conducted as a function of metal loading provide constraints on the average adsorption reaction stoichiometry, and enable quantification of the stability constants for the important metal–bacterial complexes. However, these measurements do not provide for direct identification of the important site or sites involved in metal binding. Conversely, EXAFS measurements can rigorously identify the important adsorption sites, but are less precise for determining reaction stoichiometry and stability constant values.

We use these complementary techniques to elucidate the nature and extent of Cd adsorption onto typical Gram-positive and Gram-negative bacterial cell walls. The bulk Cd adsorption measurements indicate that adsorption can be

reasonably explained by a 1:1 metal:site reaction stoichiometry over the range of metal loading conditions studied here. The EXAFS results are consistent with the bulk adsorption measurements, indicating monodentate binding of Cd onto both the carboxyl and the phosphoryl sites. The only conditions where multi-dentate binding was observed in the EXAFS data were for the lowest Cd loading samples for both species (1 ppm for *B. subtilis* and 3 ppm for *S. oneidensis*), where the coordination number for the sulfhydryl binding site becomes significantly greater than one.

The EXAFS measurements, collected over two orders of magnitude of Cd:site loading conditions, indicate similar binding environments for the two bacterial species studied. In addition, the EXAFS modeling indicates that three different sites are responsible for Cd binding to these two bacterial cell walls. Fig. 6 depicts the general predominance regions for the three different types of sites as a function of Cd loading for the *S. oneidensis* samples, and a similar picture would apply to the *B. subtilis* samples as well. Phosphoryl and carboxyl binding play important roles at high (100–200 ppm) and mid (15–30 ppm) Cd loadings, respectively, for the *S. oneidensis* samples. For the *B. subtilis* samples, phosphoryl and carboxyl sites exhibit overlapping and equal contributions for the samples with Cd concentrations of 15 ppm and higher. Carboxyl binding becomes more important than phosphoryl binding at 3 ppm Cd loading for *B. subtilis* samples. However, at the lowest Cd loadings for both of the species studied here, sulfhydryl surface complexes dominate the adsorbed Cd budgets. Because the sulfhydryl binding sites out-compete other deprotonated sites for Cd at low Cd concentrations, these sites must have a higher binding affinity for Cd than the other sites that are deprotonated at pH 5.9. However, the EXAFS data in this study do not constrain the location or identity of the sulfhydryl groups that bind Cd onto the biomass. The sulfhydryl sites may be a component of cell wall-bound metal regulator proteins, or they may represent a component of a toxicity response mechanism located on the cell walls, initiated by the non-metabolizing cells with the small amount of stored energy that remains after washing. Our EXAFS

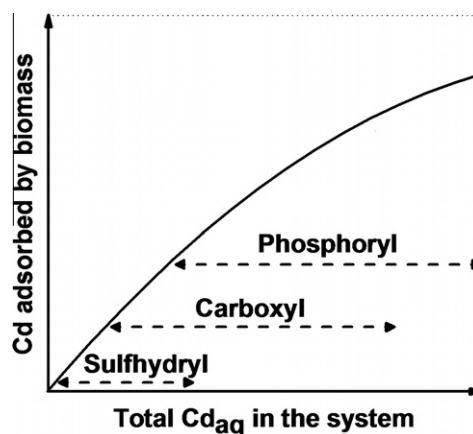


Fig. 6. A schematic representation of the regions of predominance of the three different Cd binding environments as a function of Cd loading onto biomass as determined by EXAFS.

analysis indicates that the sulfhydryl sites are limited in abundance relative to other cell wall site types, their binding stoichiometries with Cd are much higher than those found for the other functional groups, and these multi-dentate bonds bind Cd tightly. However, a precise determination of the location and more general molecular structure of the sulfhydryl sites require additional experimental and analytical constraints.

Because of the overlapping ranges of the phosphoryl, carboxyl, and sulfhydryl binding, we could not explicitly determine the stability constant for each Cd–bacterial surface complex for each species studied here. However, because a single stability constant yielded an excellent fit to the bulk Cd adsorption data over a wide range of Cd loading conditions, the value of this stability constant represents the average of the individual stability constants of the Cd-sulfhydryl, the Cd-carboxyl, and the Cd-phosphoryl bacterial surface complexes. Potentiometric titrations and Cd adsorption measurements that explicitly probe conditions under which these sites each dominate are needed in order to explicitly determine the speciation and thermodynamic stability of each complex.

The EXAFS results presented in this study demonstrate the following: (1) there is a broad similarity between the Cd binding environments of these two species over a wide range of Cd concentrations at circumneutral pH conditions, and (2) Cd-sulfhydryl binding dominates the adsorbed Cd budget under low Cd loading conditions. The similarity in the extent of bulk Cd adsorption of these two bacterial species over a wide range of Cd loadings complements the recent finding that diverse bacterial consortia exhibit broadly similar binding environments over a wide pH range at a fixed Cd loading (Mishra et al., 2009; Johnson et al., 2007; Borrok et al., 2004b). Metal-sulfhydryl binding likely occurs under the higher Cd loading conditions studied here, but its presence is masked to EXAFS probing by the relatively high-abundance of carboxyl and phosphoryl binding sites when metal:site molal concentration ratios are high. However, our data indicate the important role of these sites in Cd binding to both Gram-positive and Gram-negative bacterial cells under the circumneutral pH conditions of many natural systems. Since Cd represents typical trace metal binding (e.g., Fein, 2000), sulfhydryl binding is likely to control metal binding under low loading conditions for a wide range of metals of environmental and geologic interest. Our finding that sulfhydryl is the dominant binding ligand at lower Cd loadings suggests that these sites may also dominate metal binding by bacteria in realistic geologic settings where metals are typically present in trace concentrations.

ACKNOWLEDGMENTS

Research funding was provided by a National Science Foundation through an Environmental Molecular Science Institute Grant to the University of Notre Dame (EAR02-21966), and from a Bayer Corporation Predoctoral Fellowship. S.D.K. and K.M.K. were supported by the US Department of Energy office of Science Biological and Environmental Research Division Environmental Remediation Science Program. MRCAT is supported by the US Department of Energy under contract DE-FG02-94-ER-45525

and the member institutions. Use of the Advanced Photon Source was supported by the US Department of Energy under contract W-31-109-Eng-38. Some analyses were conducted using instruments in the Center for Environmental Science and Technology at University of Notre Dame. Help in sample preparation from Jennifer Szymanowski, and beamline setup help from Tomohiro Shibata and Soma Chattopadhyay of MRCAT are greatly appreciated. Two anonymous journal reviewers and Associate Editor Michael Machesky made helpful suggestions and significantly improved the clarity of this paper.

REFERENCES

- Ankudinov A. L., Ravel B., Rehr J. J. and Conradson S. D. (1998) Real-space multiple-scattering calculation and interpretation of X-ray-absorption near-edge structure. *Phys. Rev. B* **58**, 7565–7576.
- Beveridge T. J. and Murray R. G. E. (1980) Sites of metal deposition in the cell wall of *Bacillus subtilis*. *J. Bacteriol.* **141**, 876–887.
- Borrok D., Fein J. B. and Kulpa C. F. (2004a) Proton and Cd adsorption onto natural bacterial consortia: testing universal adsorption behavior. *Geochim. Cosmochim. Acta* **68**, 3231–3238.
- Borrok D. M., Fein J. B. and Kulpa C. F. (2004b) Cd and proton adsorption onto bacterial consortia grown from industrial wastes and contaminated geologic settings. *Environ. Sci. Technol.* **38**, 5656–5664.
- Borrok D., Fein J. B. and Turner B. F. (2005) A universal surface complexation framework for modeling proton binding onto bacterial surfaces in geologic settings. *Am. J. Sci.* **305**, 826–853.
- Boyanov M. I., Kelly S. D., Kemner K. M., Bunker B. A., Fein J. B. and Fowle D. A. (2003) Adsorption of cadmium to *Bacillus subtilis* bacterial cell walls: a pH-dependent X-ray absorption fine structure spectroscopy study. *Geochim. Cosmochim. Acta* **67**, 3299–3311.
- Burnett P. G. G., Daughney C. J. and Peak D. (2006) Cd adsorption onto *Anoxybacillus flavithermus*: Surface complexation modeling and spectroscopic investigations. *Geochim. Cosmochim. Acta* **70**, 5253–5269.
- Claessens J., Behrends T. and Van Cappellen P. (2004) What do acid–base titrations of live bacteria tell us? A preliminary assessment. *Aqua Sci* **66**, 19–26.
- Caminiti R. (1982) Nickel and cadmium phosphates in aqueous-solution – cation anion complex-formation and phosphate–H₂O interactions. *J. Chem. Phys.* **77**, 5682–5686.
- Caminiti R., Cucca P., Monduzzi M., Saba G. and Crisponi G. (1984) Divalent metal–acetate complexes in concentrated aqueous-solutions – an X-ray-diffraction and NMR-spectroscopy study. *J. Chem. Phys.* **81**, 543–551.
- Cox J. S., Smith D. S., Warren L. A. and Ferris F. G. (1999) Characterizing heterogeneous bacterial surface functional groups using discrete affinity spectra for proton binding. *Environ. Sci. Technol.* **33**, 4515–4521.
- Daughney C. J., Fein J. B. and Yee N. (1998) A comparison of the thermodynamics of metal adsorption onto two common bacteria. *Chem. Geol.* **144**, 161–176.
- Daughney C. J., Siciliano S. D., Rencz A. N., Lean D. and Fortin D. (2002) Hg(II) adsorption by bacteria: a surface complexation model and its application to shallow acidic lakes and wetlands in Kejimikujik National Park, Nova Scotia, Canada. *Environ. Sci. Technol.* **36**, 1546–1553.
- Fein J. B. (2000) Quantifying the effects of bacteria on adsorption reactions in water–rock systems. *Chem. Geol.* **169**, 265–280.

- Fein J. B., Daughney C. J., Yee N. and Davis T. A. (1997) A chemical equilibrium model for metal adsorption onto bacterial surfaces. *Geochim. Cosmochim. Acta* **61**, 3319–3328.
- Fein J. B., Boily J. F., Yee N., Gorman-Lewis D. and Turner B. F. (2005) Potentiometric titration of *Bacillus subtilis* cells to low pH and a comparison of modeling approaches. *Geochim. Cosmochim. Acta* **69**, 1123–1132.
- Fowle D. A. and Fein J. B. (2000) Experimental measurements of the reversibility of metal–bacteria adsorption reactions. *Chem. Geol.* **168**, 27–36.
- Guiné V., Spadini L., Sarret G., Muris M., Delolme C., Gaudet J. P. and Martins J. M. F. (2006) Zinc sorption to three Gram-negative bacteria: combined titration, modeling, and EXAFS study. *Environ. Sci. Technol.* **40**, 1806–1813.
- Harden V. and Harris J. O. (1952) The isoelectric point of bacterial cells. *J. Bacteriol.* **65**, 198–202.
- Haas J. R., Dichristina T. J. and Wade, Jr., R. (2001) Thermodynamic of U(VI) sorption onto *Shewanella putrefaciens*. *Chem. Geol.* **180**, 33–54.
- Hennig C., Panak P. J., Reich T., Rossberg A., Raff J., Selenska-Pobell S., Matz W., Bucher J. J., Bernhard G. and Nitsche H. (2001) EXAFS investigation of uranium(VI) complexes formed at *Bacillus cereus* and *Bacillus sphaericus* surfaces. *Radiochim. Acta* **89**, 625–631.
- Kelly S. D., Kemner K. M., Fein J. B., Fowle D. A., Boyanov M. I., Bunker B. A. and Yee N. (2002) X-ray absorption fine structure determination of pH-dependent U-bacterial cell wall interactions. *Geochim. Cosmochim. Acta* **66**, 3855–3871.
- Kemner K. M., Kropf A. J. and Bunker B. A. (1994) A low-temperature total electron yield detector for X-ray absorption fine structure spectra. *Rev. Sci. Instrum.* **65**, 3667–3669.
- Kulczycki E., Fowle D. A., Fortin D. and Ferris F. G. (2005) Sorption of cadmium and lead by bacteria–ferrihydrite composites. *Geomicrobiol. J.* **22**, 299–310.
- Ledin M., Krantz-Rulcker C. and Allard B. (1996) Zn, Cd and Hg accumulation by microorganisms, organic and inorganic soil components in multi-compartment systems. *Soil Biol. Biochem.* **28**, 791–799.
- Ledin M., Krantz-Rulcker C. and Allard B. (1999) Microorganisms as metal sorbents: comparison with other soil constituents in multi-compartment systems. *Soil Biol. Biochem.* **31**, 1639–1648.
- Ledin M. (2000) Accumulation of metals by microorganisms–processes and importance for soil systems. *Earth-Sci. Rev.* **51**, 1–31.
- Leone L., Ferri D., Manfredi C., Persson P., Shchukarev A., Sjöberg S. and Loring J. (2007) Modeling the acid–base properties of bacterial surfaces: a combined spectroscopic and potentiometric study of the Gram-positive bacterium *Bacillus subtilis*. *Environ. Sci. Technol.* **41**, 6465–6471.
- Martinez R. E., Smith D. S., Kulczycki E. and Ferris F. G. (2002) Determination of intrinsic bacterial surface acidity constants using a donnan shell model and a continuous pK(a) distribution method. *J. Colloid Interface Sci.* **253**, 130–139.
- Mishra B., Fein J. B., Boyanov M. I., Kelly S. D., Kemner K. M. and Bunker B. A. (2007) Comparison of Cd binding mechanisms by Gram-positive, Gram-negative and consortia of bacteria using XAFS. *AIP Conf. Proc.* **882**, 343–345.
- Mishra B., Boyanov M. I., Bunker B. A., Kelly S. D., Kemner K. M., Nerenberg R., Read-Daily B. L. and Fein J. B. (2009) An X-ray absorption spectroscopy study of cd binding onto bacterial consortia. *Geochim. Cosmochim. Acta* **73**, 4311–4325.
- Nealson K. H. and Myers C. R. (1992) Microbial reduction of manganese and iron: new approaches to carbon cycling. *Appl. Environ. Microbiol.* **58**, 439–443.
- Newville M. (2001) IFEFFIT: interactive XAFS analysis and FEFF fitting. *J. Synch. Rad.* **8**, 322–324.
- Newville M., Ravel B., Haskel D., Rehr J. J., Stern E. A. and Yacoby Y. (1995) Analysis of multiple-scattering Xafs data using theoretical standards. *Physica B* **209**, 154–156.
- Newville M., Livins P., Yacoby Y., Rehr J. J. and Stern E. A. (1993) Near-edge X-ray-absorption fine-structure of Pb – a comparison of theory and experiment. *Phys. Rev. B* **47**, 14126–14131.
- Ngwenya B. T., Sutherland I. W. and Kennedy L. (2003) Comparison of the acid–base behaviour and metal adsorption characteristics of a Gram-negative bacterium with other strains. *Appl. Geochem.* **18**, 527–538.
- Ngwenya B. T. (2007) Enhanced adsorption of zinc is associated with aging and lysis of bacterial cells in batch incubations. *Chemosphere* **67**, 1982–1992.
- Nyquist H. (1928) Certain topics in telegraph transmission theory. *Trans. AIEE* **47**, 617–644.
- Ohnuki T., Yoshida T., Ozaki T., Kozai N., sakamoto F., Nankawa T., Suzuki Y. and Francis A. J. (2007) Chemical Speciation and association of plutonium with bacteria, kaolinite clay, and their mixture. *Environ. Sci. Technol.* **41**, 3134–3139.
- Panak P. J., Booth C. H., Caulder D. L., Bucher J. J., Shuh D. K. and Nitsche H. (2002) X-ray absorption fine structure spectroscopy of plutonium complexes with *Bacillus sphaericus*. *Radiochim. Acta* **90**, 315–321.
- Pokrovsky O. S., Martinez R. E., Golubev S. V., Kompantseva E. I. and Shirokova L. S. (2008a) Adsorption of metals and protons on *Gloeocapsa* sp. cyanobacteria: a surface speciation approach. *Appl. Geochem.* **23**, 2574–2588.
- Pokrovsky O. S., Pokrovsky G. S. and Feurtet-Mazel A. (2008b) A structural study of Cd interaction with aquatic microorganisms. *Environ. Sci. Technol.* **42**, 5527–5533.
- Plette A. C. C., Vanriemsdijk W. H., Benedetti M. F. and Vanderwal A. (1995) pH dependent charging behavior of isolated cell-walls of a Gram-positive soil bacterium. *J. Colloid Interface Sci.* **173**, 354–363.
- Ravel B. (2001) ATOMS: crystallography for the X-ray absorption spectroscopist. *J. Synch. Rad.* **8**, 314–316.
- Ravel B. and Newville M. (2005) Athena, artemis, hephaestus: data analysis for X-ray absorption spectroscopy using IFEFFIT. *J. Synch. Rad.* **12**, 537–541.
- Sarret G., Manceau A., Spadini L., Roux J. C., Hazemann J. L., Soldo Y., Eybert-Berard L. and Menthonnex J. J. (1998) Structural determination of Zn and Pb binding sites in *Penicillium chrysogenum* cell walls by EXAFS spectroscopy. *Environ. Sci. Technol.* **32**, 1648–1655.
- Segre C. U., Leyarovska N. E., Chapman L. D., Lavender W. M., Plag P. W., King A. S., Kropf A. J., Bunker B. A., Kemner K. M., Dutta P., Duran R. S. and Kaduk J. (2000) The MRCAT insertion device beamline at the advanced photon source. *Synch. Rad. Instrum.: 11th US Conf.* **CP521**, 419–422.
- Small T. D., Warren L. A., Roden E. E. and Ferris F. G. (1999) Sorption of strontium by bacteria, Fe(III) oxide, and bacteria–Fe(III) oxide composites. *Environ. Sci. Technol.* **33**, 4465–4470.
- Smith D. S. and Ferris F. G. (2003) Specific surface chemical interactions between hydrous ferric oxide and iron-reducing bacteria determined using pK_a spectra. *J. Colloid Interface Sci.* **266**, 60–67.
- Sokolov I., Smith D. S., Henderson G. S., Gorby Y. A. and Ferris F. G. (2001) Cell surface electrochemical heterogeneity of the Fe(III)-reducing bacteria *Shewanella putrefaciens*. *Environ. Sci. Technol.* **35**, 341–347.
- Sorenson J. (1982) Reduction of ferric iron in anaerobic, marine sediment, and interaction with reduction of nitrate and sulphate. *Appl. Environ. Microbiol.* **43**, 319–324.

- Stern E. A. (1974) Theory of extended X-ray absorption fine structure. *Phys. Rev. B* **10**, 3027–3037.
- Stern E. A. and Heald S. M. (1983) Basic principles and applications of EXAFS. *Handbook Sync. Rad.* **10**, 995–1014.
- Stern E. A., Newville M., Ravel B., Yacoby Y. and Haskel D. (1995) The Uwxafs analysis package – philosophy and details. *Physica B* **209**, 117–120.
- Toner B., Manceau A., Marcus M. A., Millet D. B. and Sposito G. (2005) Zinc sorption by a bacterial biofilm. *Environ. Sci. Technol.* **39**, 8288–8294.
- Venkateswaren K., Moser D. P., Dollhopf M. E., Lies D. P., Saffarini D. A., MacGregor B. J., Ringelberg D. B., White D. C., Nishijima M., Sano H., Burghardt J., Stackebrandt E. and Nealon K. H. (1999) Polyphasic taxonomy of the genus *Shewanella* and description of *Shewanella oneidensis* sp. nov. *Int. J. Sys. Bacteriol.* **49**, 705–724.
- Wei J., Saxena A., Song B., Ward B. B., Beveridge T. J. and Myneni S. C. B. (2004) Elucidation of functional groups on Gram-positive and Gram-negative bacterial surfaces using infrared spectroscopy. *Langmuir* **20**, 11433–11442.
- Westall, J. C. (1982) FITEQL, a computer program for determination for chemical equilibrium constants from experimental data. Version 2.0. Report 82-02 Dept. Chem., Oregon St. Univ., Corvallis, OR, USA.
- Wightman P. G. and Fein J. B. (2005) Iron adsorption by *Bacillus subtilis* bacterial cell walls. *Chem. Geol.* **216**, 177–189.
- Yee N. and Fein J. (2001) Cd adsorption onto bacterial surfaces: a universal adsorption edge? *Geochim. Cosmochim. Acta* **65**, 2037–2042.
- Yee N. and Fein J. B. (2003) Quantifying metal adsorption onto bacteria mixtures: a test and application of the surface complexation model. *Geomicrobiol. J.* **20**, 43–60.
- Yee N., Fowle D. A. and Ferris F. G. (2004) A donnan potential model for sorption onto *Bacillus subtilis*. *Geochim. Cosmochim. Acta* **68**, 3657–3664.

Associate editor: Michael L. Machesky

Iron phase transformations resulting from the respiration of *Shewanella putrefaciens* on a mixed mineral phase

M.I. Boyanov, E.J. O'Loughlin, K.M. Kemner

Molecular Environmental Science Group

Biosciences Division, Argonne National Laboratory, Argonne, IL 60439, U.S.A.

E-mail: mboyanov@anl.gov

Abstract. The initial Fe(III) minerals and the secondary mineralization products of *Shewanella putrefaciens* CN32 grown in the presence of dissolved phosphate and a commercial Fe(III) oxide, nominally nanoparticulate lepidocrocite, were determined using XRD and XAFS. The starting material was transformed by the bacteria from a reddish brown, rust colour mineral to a dark green phase over 90 days. Acid extraction of the bioreduced solids with 0.75 M HCl recovered 83% of the total iron as Fe(II), leaving a solid, acid-resistant phase. The latter was identified as nanoparticulate hematite by EXAFS. Subsequently, the starting Fe(III) phase was determined to be a mixture of 60% lepidocrocite, 26% ferrihydrite, and 14% hematite, using linear combination EXAFS analysis. For the acid-extractable phase, XANES and EXAFS indicated a predominantly Fe(II) valence state and a spectrum consistent with a mixture of brucite-type minerals (e.g., green rust or ferrous hydroxide) and siderite. The observed transformations suggest that in this mixed-mineral system, lepidocrocite and ferrihydrite are readily reducible to green rust and siderite, whereas hematite is less amenable to bacterial reduction. This study also demonstrates the utility of XAFS spectroscopy in the quantitative characterization of dissimilatory metal transformations, particularly in complex systems such as nanoparticulate minerals in hydrated mineral-bacteria assemblages.

1. Introduction

Dissimilatory iron reducing bacteria (DIRB) are a group of microorganisms that can utilize Fe(III) minerals as terminal electron acceptors for anaerobic respiration [1]. The resulting Fe(II)/Fe(III) transformations are studied extensively to understand bacterial metabolism, but there is also significant interest in using reduced bacterial products for *in situ* bioremediation. For instance, the reduction of soluble U(VI) to the relatively insoluble U(IV) is considered a promising immobilization strategy for subsurface uranium plumes. The reactivity of Fe(II) with respect to U(VI) reduction can depend strongly on Fe(II) speciation [2], and studies have shown that different Fe(II) minerals exhibit varying redox reactivity [3]. Therefore, it is important to be able to identify the secondary mineralization products resulting from DIRB respiring on Fe(III) oxides and the factors that lead to the formation of reactive Fe(II) phases. Although there are many reports characterizing the products of DIRB respiration on single phase iron oxides (e.g., [4] and references inside), there are limited reports on the differential ability of DIRB to utilize a defined mixture of Fe(III) mineral phases or on the biomineralization products in the presence of phosphate.

Environmental systems consist of multiple mineral phases that are often nanoparticulate, making characterization by laboratory x-ray diffraction (XRD) or electron microscopy difficult. In addition, some dominant Fe(III) phases such as ferrihydrite have only broad XRD features that cannot be used

for identification, especially in cases where particle size is small. In this study, we have used Fe K-edge x-ray absorption spectroscopy (XANES and EXAFS) to characterize the initial minerals and the biomineralization products during the growth of *Shewanella putrefaciens* strain CN32 in the presence of a commercial Fe(III) oxide, nominally a nanoparticulate lepidocrocite. The preliminary stages of this work identified the presence of additional Fe(III) phases in the parent material, which allowed us to draw conclusions about the dynamics of Fe during anaerobic respiration of *S. putrefaciens* CN32 using a nanoparticulate, mixed Fe(III) oxide phase as the terminal electron acceptor.

2. Materials and methods

2.1.1. System composition, experimental conditions, and solution phase characterization

The iron oxide—nominally a nanoparticulate lepidocrocite (γ -FeOOH)—used in this study was generously provided by Rockwood Pigments in the form of an aqueous slurry. Defined mineral medium[5]—containing 80 mM Fe(III) and 5 mM phosphate—was placed in serum bottles. The serum bottles were sealed with aluminum crimp caps and deoxygenated by sparging with sterile Ar. The suspensions were inoculated with *S. putrefaciens* CN32, (cultured in tryptic soy broth for 24 hr, harvested, and rinsed twice in sterile medium without Fe(III) or *e*- donor) at an initial cell density of 5×10^9 cells mL⁻¹. The suspensions were placed on a roller drum and incubated at 30 °C in the dark. Samples of the suspensions were collected over time using sterile syringes. The reduction of the Fe(III) oxides was monitored by using the ferrozine assay to measure the total Fe(II) content of 0.75 M HCl extractions of the suspensions [5]. Whenever possible, sample collection and processing were conducted in a glove box containing an anoxic atmosphere (95% N₂ with 5% H₂).

2.1.2. X-ray absorption spectroscopy characterization (XANES and EXAFS)

The solid and solution fractions of the suspensions were separated by filtration and the hydrated filter cakes were sealed in polycarbonate film. Strict anoxic conditions were maintained during sample manipulations, transport, and x-ray measurements. X-ray absorption fine structure spectroscopy (XAFS) spectra were collected at the MRCAT bending magnet station, sector 10-BM at the Advanced Photon Source near Chicago, IL. Measurements on well-characterized crystalline Fe(II) and Fe(III) oxyhydroxide minerals were used as standards in the analysis. Data reduction was performed using the program Autobk[6]. Linear combination (LC) EXAFS analysis was performed using the program SIXpack [7].

3. Results and discussion

3.1. Observed evolution of the system

Over the course of 90 days following inoculation, the starting material changed from a reddish brown rust colour to a dark green phase, concomitant with total Fe(II) concentration reaching steady state. Acid extraction of the final phase recovered 83% of the total iron added as Fe(II), leaving a solid, acid-resistant phase. No colour transformation or Fe(II) production was observed in an abiotic (sterile) control. The rapid dissolution kinetics of the green coloured phase (<30 sec) suggests the presence of a pure ferrous phase (e.g., ferrous hydroxide, carbonate, or phosphate) or a green rust phase (a mixed Fe(II)/Fe(III) brucite mineral), but not magnetite. The remaining acid-resistant phase was bright red.

3.2. Characterization of the reduced solid phase

The Fourier transformed EXAFS data from the bright-red fraction remaining after acid extraction of the bioreduced phase is shown on Fig. 1A. Comparison to spectra taken from single phase Fe minerals identified it as nanoparticulate hematite, as evidenced by the smaller amplitude of the peaks around 3.5 Å, resulting from the reduced average Fe-Fe coordination of the surface Fe atoms.

The Fourier transformed EXAFS data from the green-coloured bioreduced phase is shown on Fig. 1B. The spectrum indicates a local atomic environment similar to that of Fe in green rust; however, the

XANES spectrum (not shown) and the Fe(II) content analysis were consistent with a more reduced Fe phase. Linear combination (LC) analysis (Fig. 2A) produced a best fit with 63% green rust, 18% Fe(OH)₂, and 24% siderite (ferrous carbonate). Ferrous phosphate (vivianite) was not consistent with the observed spectrum. It should be noted that the spectral mixture of Fe(OH)₂ and siderite could be indicative of the presence of ferrous hydroxycarbonate. The local atomic environment of Fe atoms in ferrous hydroxycarbonate is that of Cu in malachite (Cu₂(OH)₂CO₃), consisting of edge sharing Me octahedra (as found in Fe(OH)₂ or green rust) which are bound at the corners to carbonate groups (as found in siderite); however, we lacked a spectrum of the crystalline mineral to compare.

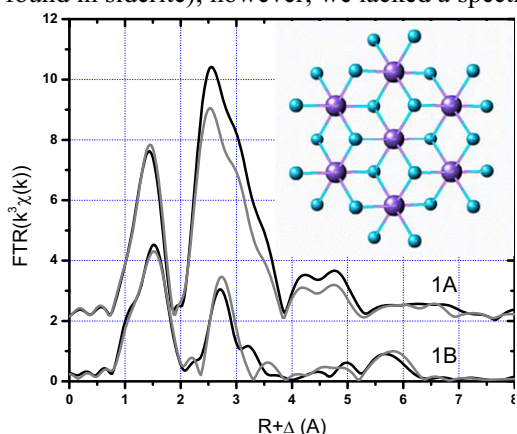


Fig. 1: Fourier transformed EXAFS data: A) phase recalcitrant to acid extraction (gray) compared to crystalline hematite (black); B) bio-reduced phase (gray) compared to green rust (black). Inset: intralayer structure of a brucite type mineral such as green rust or Fe(OH)₂ viewed along the 001 direction.

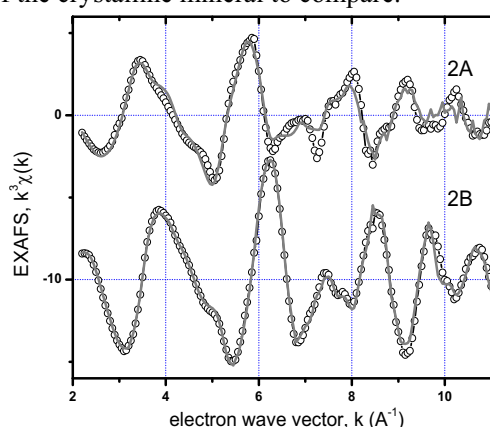


Fig. 2: Linear combination analysis of k³-weighted EXAFS data. Data (symbols), fit (gray line). A) Bio-reduced green-coloured phase; B) parent Fe(III) material before bio-reduction.

3.3. Characterization of the parent Fe(III) material

The parent Fe(III) material was characterized at the beginning of the experiment using a Rigaku MiniFlex x-ray diffractometer (Ni-filtered Cu K α radiation, scanned between 5° and 80° 2 θ at a speed of 2.5° 2 θ min⁻¹). The diffractogram on Fig. 3 shows three broad, very low intensity peaks, that can be attributed to lepidocrocite; however, assignment of such broad features is ambiguous. Hematite peaks could not be observed. The ambiguity of the XRD data and the unexpected results from the analysis of the bio-reduced products prompted a more detailed characterization of the parent material. Figure 2B shows the result of the LC analysis of the EXAFS spectrum from the parent material. The best fit (as judged by the addition of all fractions to 1 and the lowest *R*-factor) was obtained by a spectral mixture of 60% lepidocrocite, 26% ferrihydrite, and 14% hematite (Fig. 2B).

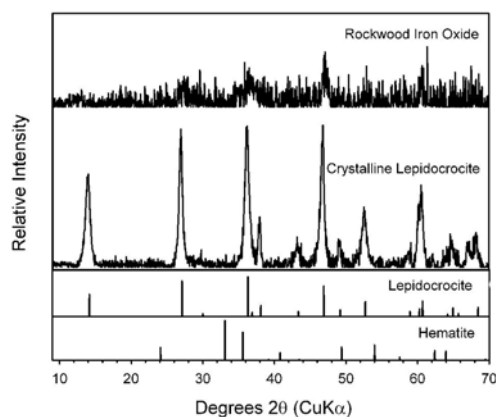


Fig. 3: X-ray diffraction pattern of the parent Fe(III) material compared to that of crystalline lepidocrocite.

3.4. Discussion

It is generally accepted that the reactivity of a mineral increases with decreasing particle size, both because of the larger surface area on a mass basis and because of the increased strain at the surface. It is therefore important to accurately identify small-sized reactive phases and their transformations. In this study, we show that laboratory-based XRD analysis may not be effective in detecting nanoparticulate iron minerals in multi-phase hydrated systems. On the other hand, it is possible to use linear combination EXAFS analysis to identify *and* quantify Fe nanoparticulate minerals that are

utilized or formed during iron reduction. In combination, EXAFS, XRD, and Fe(II)/Fe(total) content analyses can be powerful tools in tracking dissimilatory iron transformations.

The multiple Fe(III) phases detected in the parent material allowed us to study bacterial respiration in the presence of several minerals. Preferential utilization of lepidocrocite and ferrihydrite is observed, whereas hematite appears recalcitrant over the time period of the experiment. This result is consistent with the relative rates of Fe(III) reduction observed in systems with single phase minerals [4, 8]. The usually observed biomineralization product with lepidocrocite or ferrihydrite as the electron acceptor is magnetite (e.g., [9]). However, in the presence of phosphate green rust has been observed [8]. Recent work by our group shows that increasing the concentration of phosphate or other oxyanions beyond a “tipping point” causes a change in the biomineralization products from magnetite to green rust [10]. The transformation mechanism of lepidocrocite or ferrihydrite during DIR is considered to be reductive dissolution of the parent material and reprecipitation of the end product. The reason for the observation of green rust in our systems vs. magnetite in phosphate-free systems could be different reduction and dissolution kinetics of the nanoparticulate phase relative to the bulk phases; in addition, adsorption of the reduced Fe(II) to the more slowly dissolving iron phases could also lead to different reprecipitation dynamics. Alternatively, the presence or absence of dissolved phosphate may be the determining factor. The mechanisms by which oxyanions such as phosphate influence the formation of green rust instead of magnetite remain unclear and will be studied in future work.

4. Conclusions

We have shown that linear combination EXAFS analysis can enable the identification and quantification of mixed-phase, nanoparticulate Fe minerals during dissimilatory iron reduction. The application of such analysis to the parent material and the secondary mineralization products formed as a consequence of *S. putrefaciens* CN32 respiring on a mineral mixture of lepidocrocite, ferrihydrite, and hematite allowed us to discern differences in the reduction kinetics of the different phases. Lepidocrocite and ferrihydrite showed faster reduction kinetics in this mixed system, whereas hematite was recalcitrant and remained in the system after steady state Fe(II) production was reached. The primary secondary mineralization product in our experimental system was green rust rather than magnetite, the latter being commonly observed in phosphate-free systems. The mechanisms of these transformations will be investigated in future work.

This work was supported by the Environmental Remediation Science Program, United States Department of Energy (DOE), Office of Science (OS). Use of the APS is supported by the DOE OS, Office of Basic Energy Sciences (BES) under contract DE-AC02-06CH11357. MRCAT operations are supported by its member institutions and the DOE OS BES.

5. References

- [1] D. R. Lovley, D. E. Holmes, and K. P. Nevin, in *Advances in Microbial Physiology*, Vol. 49, Vol. 49, Academic Press Ltd, London, 2004, p. 219.
- [2] M. I. Boyanov, E. J. O'Loughlin, E. E. Roden, J. B. Fein, and K. M. Kemner, *Geochimica Et Cosmochimica Acta* 71 (2007) 1898.
- [3] M. Elsner, R. P. Schwarzenbach, and S. B. Haderlein, *Environmental Science & Technology* 38 (2004) 799.
- [4] C. M. Hansel, S. G. Benner, P. Nico, and S. Fendorf, *Geochimica Et Cosmochimica Acta* 68 (2004) 3217.
- [5] E. J. O'Loughlin, *Environmental Science & Technology* 42 (2008) 6876.
- [6] M. Newville, P. Livins, Y. Yacoby, J. J. Rehr, and E. A. Stern, *Physical Review B* 47 (1993) 14126.
- [7] S. M. Webb, *Physica Scripta T115* (2005) 1011.
- [8] J. K. Fredrickson, J. M. Zachara, D. W. Kennedy, H. L. Dong, T. C. Onstott, N. W. Hinman, and S. M. Li, *Geochimica Et Cosmochimica Acta* 62 (1998) 3239.
- [9] R. S. Cutting, V. S. Coker, J. W. Fellowes, J. R. Lloyd, and D. J. Vaughan, *Geochimica et Cosmochimica Acta* 73 (2009) 4004.
- [10] E. J. O'Loughlin, C. Gorski, M. M. Scherer, M. I. Boyanov, R. E. Cook, and K. M. Kemner, *Environmental Science and Technology* (in review)

An X-ray absorption spectroscopy study of Cd binding onto bacterial consortia

Bhoopesh Mishra^{a,*}, Maxim I. Boyanov^c, Bruce A. Bunker^a, Shelly D. Kelly^c, Kenneth M. Kemner^c, Robert Nerenberg^b, Brenda L. Read-Daily^b, Jeremy B. Fein^b

^a Department of Physics, University of Notre Dame, Notre Dame, IN 46556, USA

^b Department of Civil Engineering and Geological Sciences, University of Notre Dame, Notre Dame, IN 46556, USA

^c Molecular Environmental Science Group, Biosciences Division, Argonne National Laboratory, Argonne, IL 60439, USA

Received 27 May 2008; accepted in revised form 25 November 2008; available online 7 December 2008

Abstract

In this study, we use extended X-ray absorption fine structure (EXAFS) spectroscopy measurements to examine the atomic environment of Cd bound onto two experimental bacterial consortia: one grown from river water, and one grown from a manufacturing gas plant site. The experiments were conducted as a function of pH and demonstrate that the complex mixtures of bacteria, containing both Gram-positive and Gram-negative species, yield relatively simple EXAFS spectra, a result which indicates that only a limited number of functional group types contribute to Cd binding for each bacterial consortium. The EXAFS spectra indicate that the average Cd binding environment in the river water consortium varies significantly with pH, but the manufacturing gas plant consortium exhibits a Cd binding environment that remains relatively constant over the pH range examined. The EXAFS data for the river water consortium were modeled using carboxyl, phosphoryl and sulfhydryl sites. However, only carboxyl and phosphoryl sites were required to model the manufacturing gas plant consortium data under similar experimental conditions. This is the first EXAFS study to identify and quantify the relative importance of metal binding sites in bacterial consortia. Although our results indicate differences in the binding environments of the two consortia, the data suggest that there are broad similarities in the binding environments present on a wide range of bacterial cell walls. © 2008 Elsevier Ltd. All rights reserved.

1. INTRODUCTION

The speciation, distribution, and fate of metals in many aquatic and near-surface systems can be affected by metal adsorption onto bacterial surfaces (Ledin et al., 1996; Barnes and Nierzwicki-Bauer, 1997; Ledin et al., 1999). Despite the importance of these reactions, the chemical reactivity of bacterial surfaces is not well understood. Thermodynamic surface complexation models (SCMs), originally developed to describe the adsorption of metal ions onto mineral

surfaces, have recently been applied to describe the adsorption of metals onto bacterial surfaces (Xue et al., 1988; Plette et al., 1995; Plette et al., 1996; Fein et al., 1997; He and Tebo, 1998; Fein, 2000). However, an obstacle in modeling realistic bacteria-bearing systems with SCMs is that each natural system of interest contains a unique consortium, potentially consisting of a large number of bacterial species. If the cell wall functional group sites of each bacterial species exhibit unique adsorption properties, then it would be necessary to determine site densities and binding constants for each site on each bacterial species of interest.

There are some indications of commonalities in adsorption behavior between bacterial species. For example, recent studies have shown that individual pure strains of bacteria (Daughney et al., 1998; Yee and Fein, 2001; Kulczycki et al., 2002; Ngwenya et al., 2003; Borrok

* Corresponding author. Present address: Department of Geosciences, B 73 Guyot Hall, Washington Road, Princeton University, Princeton, NJ 08544, USA. Fax: +1 609 258 0796.

E-mail address: bmishra@princeton.edu (B. Mishra).

et al., 2005), and artificial mixtures of pure strains of bacteria (Yee and Fein, 2003), exhibit similar adsorptive behavior. Similarly, Borrok et al. (2004a) found that consortia of bacteria grown from a range of uncontaminated soil and aquatic environments exhibit similar affinities for protons and Cd. In contrast, however, Borrok et al. (2004b) demonstrated that bacterial consortia grown from hydrocarbon-contaminated environments do not exhibit the same relatively narrow range of proton and Cd adsorption behavior that characterizes bacterial consortia from uncontaminated environments. The studies by Borrok et al. (2004a,b) are based on bulk adsorption experiments only, and do not provide a mechanistic underpinning to explain the observed adsorption commonalities within bacterial consortia grown from natural environments and pure laboratory cultures; nor do the studies offer a mechanistic understanding of why the commonalities of metal binding onto bacterial consortia do not apply when the bacterial consortia are grown from contaminated environments. Clearly, successful application of the surface complexation approach for quantifying bacterial adsorption of aqueous metal cations onto bacterial consortia requires a detailed understanding of the binding mechanisms and a determination if common mechanisms exist between diverse consortia. That information can be provided directly by using extended X-ray absorption fine structure (EXAFS) spectroscopy to identify the surface adsorption sites and to quantify the relative amounts of metal bound to each site.

There are a number of EXAFS studies of metal adsorption onto bacterial and fungal cell walls. However, all of the previous EXAFS studies focused on a single strain of microbes, and identified only a few important binding mechanisms. For example, EXAFS of fungal cell walls (Sarret et al., 1998), Gram-positive bacteria (Kelly et al., 2002; Boyanov et al., 2003), and Gram-negative bacteria (Hennig et al., 2001; Panak et al., 2002; Toner et al., 2005) indicate that phosphoryl and carboxyl functional groups are responsible for metal complexation by these three types of microorganisms despite the differences in molecular structure of their exterior surfaces. Sarret et al. (1998) examined Zn and Pb sorption to fungal cell walls of *Penicillium chrysogenum* at pH 6 as a function of Zn and Pb loading, and the phosphoryl group was shown to be the predominant complexing ligand. The carboxyl group was found to contribute to binding only under the highest Zn loading and the lowest Pb loading. Kelly et al. (2002) determined the pH dependence of the cell wall functional groups responsible for the adsorption of aqueous UO_2^{2+} to the Gram-positive bacteria *Bacillus subtilis* from pH 1.67 to 4.80. While UO_2^{2+} was found to bind exclusively to phosphoryl functional groups at extremely low pH, an increase in the contribution of the carboxyl functional groups was observed with increasing pH. Hennig et al. (2001) found that UO_2^{2+} was predominantly bound to vegetative cells and spores of *Bacillus cereus* and *Bacillus sphaericus* as phosphoryl residues. Similarly Panak et al. (2002) found Pu to be primarily bound to phosphate groups on the cell surface of the aerobic soil bacteria, *Bacillus sphaericus*. Boyanov et al. (2003) reported that Cd binds to the Gram-positive bacteria *Bacillus subtilis* predominantly due

to phosphoryl binding below pH 4.4, whereas with increasing pH (4.4–6.5), adsorption to carboxyl groups becomes increasingly important. However, at pH 7.8, Boyanov et al. (2003) observed the activation of an additional binding site, which was tentatively ascribed as a phosphoryl site with shorter Cd–P distance than the one reported to be active under lower pH conditions. Toner et al. (2005) investigated Zn sorption by a bacterial biofilm of Gram-negative bacteria *Pseudomonas putida* at pH 6.9, and attributed Zn sorption to the biofilm predominantly to Zn-phosphoryl complexes, with a relatively small contribution from carboxyl-type complexes. Burnett et al. (2006) studied Cd adsorption onto the thermophilic species *A. flavithermus*, and found that at high bacteria:Cd ratios Cd adsorption occurs by formation of a 1:1 complex with deprotonated cell wall carboxyl functional groups. At lower bacteria:Cd ratios, a second adsorption mechanism occurs at $\text{pH} > 7$, which may correspond to the formation of a Cd-phosphoryl, CdOH-carboxyl, or CdOH–phosphoryl surface complex. Guiné et al. (2006) reported sulfhydryl ligands in addition to phosphoryl and carboxyl ligands responsible for Zn adsorption to three Gram-negative bacterial strains (*Cupriavidus metallidurans* CH34, *Pseudomonas putida* ATCC12633, and *Escherichia coli* K12DH5 α) at low loadings of Zn.

The studies discussed above demonstrate that there is spectroscopic evidence that Cd, Zn, Pb, Pu and UO_2^{2+} sorption onto microbial biomass is controlled by phosphoryl, carboxyl, and perhaps sulfhydryl functional groups on cell walls. The possibility that there are only a few types of cell wall binding environments may explain the similar adsorption behaviors observed for natural bacterial consortia by Borrok et al. (2004a). In this study, we test this hypothesis by using EXAFS to directly determine the binding environments for Cd using one of the natural consortia tested by Borrok et al. (2004a). Additionally, by determining the binding mechanisms responsible for Cd adsorption in one of the contaminated systems studied by Borrok et al. (2004b), we attempt to explain the differences in adsorption behavior between contaminated and natural bacterial consortia. We characterize the bacterial diversity of each sample by preparing and analyzing a clone library based on 16S rRNA genes from each consortium. The current study is the first to examine the molecular scale mechanisms of metal binding onto complex bacterial consortia.

2. METHODS AND MATERIALS

2.1. Sampling and growth of bacterial consortia

Two bacterial consortia are used in this study, a river water consortium and a contaminated soil consortium. The river water consortium was collected from the St. Joseph River in South Bend, IN, USA. The contaminated soil consortium was collected from a manufactured gas plant (MGP) site in Iowa, USA. We will refer to the river water consortium and manufacturing gas plant consortium as RWC and MGPC, respectively. The clay-rich soils from the MGP site were severely impacted by polycyclic aromatic hydrocarbons that had co-mingled with gasoline

range hydrocarbons from a nearby leaky underground storage tank site. The contamination is characterized by visible coal tar and elevated concentrations of benzene, toluene, ethylbenzene, and xylene. All materials used for sample collection of both samples, including glass jars and lids, and digging scoops, were sterilized and sealed in plastic bags before use. The sampling protocol for the RWC was identical to that described by Borrok et al. (2004a). The MGP site soil material used in this study is the same material used in the previous study by Borrok et al. (2004b). The consortium of bacteria obtained from the MGP site was re-cultured for EXAFS measurements from the frozen stock that was cultured by Borrok et al. (2004b).

Approximately 1 mL of frozen MGP soil culture or 10 mL of St. Joseph River (SJR) water samples were used to inoculate a 2 L broth solution. Bacteria were cultured using a Luria–Bertani (LB) broth, containing 10 g/L tryptone, 10 g/L NaCl, and 5 g/L yeast extract at pH 7. Inoculated broth solutions were shaken at 100 rpm at room temperature for 6 days before they were harvested. Preliminary experiments indicated that 6 days was the minimum growth period for the cultures to yield the same bacterial diversity in terms of number of species present as the original samples, as determined by denaturing gradient gel electrophoresis (DGGE) analysis. After harvest, 1 mL aliquots of the samples were collected in autoclaved 2 mL microcentrifuge tubes, spiked with 20% sterile glycerol, rapidly frozen using liquid nitrogen, and then placed into a -80°C freezer for storage until genomic characterization could be performed.

2.2. Genomic characterization of the consortia

2.2.1. Characterization approach

Because a particular set of growth conditions supports growth of only particular types of bacterial species, the bacteria cultured for our experiments (or the ‘experimental consortia’) likely included only a subset of the total bacterial population present in each environment sampled (or the ‘environmental consortia’). However, many individual bacterial species within natural consortia cannot survive repeated inoculations in laboratory growth media (Kaeblerlein et al., 2002). Therefore, by growing the bacteria directly in broth solutions and limiting the number of re-inoculations, we produced experimental consortia that are at least representative of the diversity of organisms which exist in the sampled locations. Previous analyzes of bacterial diversity on consortia grown from these locations using denaturing gradient gel electrophoresis and Gram-staining suggested that the RWC and the MGPC contained at least six and four bacterial species, respectively, with both exhibiting a mix of Gram-positive and Gram-negative species (Borrok et al., 2004a,b). We conducted a more rigorous determination of the genetic diversity present in each sample by generating PCR-based 16S rRNA gene clone libraries from each experimental consortium.

2.2.2. DNA extraction

Genomic DNA was extracted from the two frozen samples using a Mo Bio Power Soil DNA Extraction Kit

(Carlsbad, CA), following the manufacturer’s protocol. The DNA quality was checked using gel electrophoresis with a 0.8% agarose gel stained with GelStar nucleic acid dye (Cambrex, International).

2.2.3. PCR amplification

For each sample, portions of the bacterial 16S rRNA genes were amplified from the extracted DNA using polymerase chain reaction (PCR). Each 50 μL PCR mix contained 25 μL 2 \times PCR mix (Quiagen, Valencia, CA), 2 μL 25 mM MgCl_2 (Sigma–Aldrich, St. Louis, MO), 2.5 μL bovine serum albumin (BSA) (Roche Diagnostics, Mannheim, Germany), 0.25 μL forward primer 341F-GC, 0.25 μL reverse primer 907R, and 20 μL nuclease-free water. The PCR reaction included an initial step of denaturation at 95°C for 5 min, and 30 cycles of the following three steps: denaturation (94°C ; 30 s); annealing (62°C ; 35 s); and elongation (72°C ; 35 s). A final 7 min incubation at 72°C was included. PCR products were checked for size and yield by gel electrophoresis on 1.5% agarose gels stained with GelStar nucleic acid dye. The general bacterial primers (Invitrogen Corporation, Carlsbad, CA) have been extensively used for bacterial community analysis (Muyzer et al., 1993).

2.2.4. Cloning and sequencing

Bacterial 16S rRNA gene amplicons were cleaned using the UltraClean PCR clean-up kit (Mo Bio Laboratories, Carlsbad, CA) and subsequently cloned using the TOPO TA cloning kit (Invitrogen Corporation, Carlsbad, CA) according to the manufacturer’s instructions. Randomly selected clones were sequenced by Sequetech Corporation (Mountain View, CA) and analyzed using CLC Gene Workbench (CLC Gene Workbench version 2.2). Bacterial sequences recovered from the sequencing of the clones were classified with the ribosomal database project (RDB) classifier (Cole et al., 2007) and with the basic local alignment search tool BLAST (National Center for Biotechnology Information; Altschul et al., 1997).

2.3. Cd Adsorption experiments

Bacteria were harvested from the growth media by centrifugation, transferred to test tubes, and washed five times in 0.1 M NaClO_4 . Sodium perchlorate was chosen as the experimental electrolyte because perchlorate does not form complexes to an appreciable extent with Cd under the experimental conditions. During each wash, the bacteria were suspended in fresh electrolyte solution using a vortex machine and stir rod. Bacteria were centrifuged for 5 min at 8000 rpm to form a pellet at the base of the test tube and the electrolyte was discarded. After the final wash, the bacteria were placed in weighed test tubes and centrifuged (8000 rpm at 25°C) for 1 h, stopping two times to decant all supernatant. After 1 h, the weight of the moist bacterial pellet was determined. The weight recorded at this stage is reported throughout this paper and termed the wet weight of the biomass.

In each metal adsorption experiment, 10 g/L of an experimental bacterial consortium was suspended in a pH-neutralized stock solution of 0.1 M NaClO_4 and

30 ppm Cd. After an initial 10 min equilibration time, the bacterial stock solution was divided into individual reaction vessels. The pH of each reaction vessel was adjusted by adding minute aliquots of 1.0 M or 0.1 M HNO₃ or NaOH. After adjustment of the pH, and an additional 2 h of reaction time on a rotating rack, the final (equilibrium) pH of each vessel was measured. Previous studies using these same procedures have demonstrated that equilibrium of the adsorption reaction generally occurs in less than 1 h and that the adsorption reaction is fully reversible (Fowle and Fein, 2000). The individual vessels were then centrifuged, and the resulting supernatant was filtered (0.45 μm nylon filter membranes) and acidified. The filtered supernatant was analyzed for dissolved Cd using an inductively coupled plasma-optical emission spectroscopy technique with matrix-matched standards. The concentration of metal adsorbed to bacteria in each vessel was calculated by subtracting the concentration of metal that remained in solution (supernatant) from the original 30 ppm in the stock solution. There were slight variations in the final pH values of the two consortia. Experiments for the RWC exhibited equilibrium pH at 3.7, 4.7, 5.7, 6.2, 6.5 and 7.6; the equilibrium pH values of the MGPC samples were 3.4, 4.4, 5.4, 5.9, 6.4 and 7.6. The biomass pellet formed at the base of each vessel after centrifugation was loaded into slotted Plexiglas holders and covered with Kapton film for EXAFS measurements (see description below). All EXAFS measurements were performed within 30 h of the adsorption experiment, and the samples were refrigerated during the time leading up to the measurement.

2.4. EXAFS standards

Powder and aqueous Cd standards were used to determine the EXAFS signature of carboxyl, phosphoryl, sulfide and sulfate binding environments. CdS and CdSO₄ powder standards were prepared from commercially available chemicals (Sigma–Aldrich), after grinding and sieving (~400 mesh). The aqueous Cd standards included hydrated Cd (CdClO₄), Cd–acetate (CdAc) and Cd–phosphate (CdPO₄) solutions. All aqueous Cd standards were prepared by dissolving Cd(NO₃)₂·4H₂O in the appropriate acid/electrolyte. The hydrated Cd standard was 0.1 M CdClO₄ at pH ~1.5. The CdAc and CdPO₄ standards were prepared with a Cd:ligand ratio of 1:100 (acetate or phosphate), by adding appropriate amounts of acetic and phosphoric acids. The pH of the CdAc solution was adjusted using NaOH to 4.5, where the aqueous Cd–acetate aqueous complexes were calculated using PHREEQC (Parkhurst and Appelo 1999) to dominate the Cd speciation in solution. Similarly, the pH of the CdPO₄ solution was kept at 3.0 to avoid precipitation of solid cadmium phosphate.

2.5. EXAFS measurements

Extended X-ray absorption fine structure spectroscopy (EXAFS) measurements at the Cd K edge (26.711 eV) were performed at the MRCAT sector 10-ID beamline (Segre et al., 2000), Advanced Photon Source, Argonne National Laboratory. The energy of the incident X-rays was scanned

by using a Si (111) reflection plane of a cryogenically-cooled double-crystal monochromator. The 3rd harmonic of the undulator was utilized, with undulator tapering of about 3.5 keV to reduce the variation in the incident intensity to less than 15% over the scanned energy range. X-rays of higher harmonic energies were minimized using grazing incidence reflection from a Pt-coated mirror. The incident ionization chamber was filled with 100% N₂ gas. The transmitted and reference ion chambers were filled with 100% Ar gas. The fluorescence detector in the Stern–Heald geometry (Stern and Heald, 1983) was filled with Kr gas, and a Pd filter of six absorption lengths was used to reduce the background signal. The incident X-ray beam profile was 1 mm square. Although use of 100% N₂ in the incident ion chamber gas allowed for only 2% absorption of incident beam in this ion chamber, the combination of gases described above gave the best linearity between incidence and fluorescence detectors. Linearity tests (Kemner et al., 1994) indicated less than 0.1% nonlinearity of the experimental setup for a 50% decrease in incident X-ray intensity. Several energy scans were collected from each sample. The scans were aligned by using the simultaneously collected Cd foil data, setting the first inflection point of the spectrum at 26.711 eV.

Quick scans (continuous-scanning mode of the monochromator), with signal sampling every 0.5 eV over the entire scanning range and integration time of 0.1 s per point were used. The advantage of using quick-scans is that it reduces the radiation exposure during a single scan. Consecutive spectra were monitored for possible radiation-induced changes; no changes were observed. To further reduce the possibility of radiation-induced changes, the sample was moved to a fresh spot every 5 scans. A total of 30–50 consecutive scans from each sample were collected and averaged, depending on the Cd uptake in the sample.

2.6. EXAFS data reduction

The data were analyzed using the methods described within the UWXAFS package (Stern et al., 1995). The processing of the raw data including alignment of data sets and background removal were implemented by using ATHENA (Ravel and Newville, 2005), which is an interface to IFEFIT (Newville, 2001). In ATHENA the background removal procedure is based on the AUTOBK method (Newville et al., 1993). The input parameter to ATHENA that determines the maximum frequency of the background, R_{bkg} , was set to 1.1 Å (Newville et al., 1993). The data range used for Fourier transforming the EXAFS $\chi(k)$ data was 2.3–9.8 Å⁻¹ with a Hanning window function and a dk value of 1.0 Å⁻¹ (Newville et al., 1993).

To generate theoretical EXAFS models, the crystallographic information were first transformed into a cluster of atoms by using the program ATOMS (Ravel, 2001). Based on the cluster of atoms thus obtained, the theoretical EXAFS models were built by using FEFF8 (Ankudinov et al., 1998). The theoretical models were optimized to the measured spectra using the program FEFFIT (Newville et al., 1995). Statistically significant lower R factor and χ^2_{v} values were used as criteria for improvement in the fit to justify the addition of an atomic shell to the model. Simultaneous fitting of several

Table 1
Results from Clone Library Preparations.

Genus	Percentage of all clones	Typical physiology
Manufactured gas plant experimental consortium		
<i>Total number of clones</i> = 22		
<i>Clostridium</i>	9	Gram-positive, obligate anaerobes, rod-shaped, endospore-forming, fermentative
<i>Flavimonas</i>	4	Gram-negative, aerobic, rod-shaped, non spore-forming
<i>Pseudomonas</i>	86	Gram-negative, aerobic, rod-shaped, non spore-forming
River water experimental consortium		
<i>Total number of clones</i> = 53		
<i>Clostridium</i>	15.1	Gram-positive, obligate anaerobes, endospore-forming, fermentative
Unclassified Clostridiaceae	3.8	Gram-positive, endospore-forming
<i>Bacteroides</i>	17.0	Gram-negative, obligate anaerobes, rod-shaped, spore-forming, fermentative
<i>Dysgonomonas</i>	3.8	Gram-negative, facultatively anaerobic, coccobacillus-shaped
<i>Parabacteroides</i>	15.1	Gram-negative, obligate anaerobes, rod-shaped non spore-forming,
<i>Aeromonas</i>	1.9	Gram-negative, facultative anaerobes, rod-shaped
<i>Providencia</i>	39.6	Gram-negative, facultative anaerobes
Unclassified	3.8	Gram-negative, facultative anaerobes, rod-shaped
Enterobacteriaceae		

data sets with multiple k -weighting (k^1 , k^2 , k^3) of each spectrum was performed using the Fourier transformed $\chi(R)$ spectra. Fitting range for all the data sets was 1.2–3.4 Å. The simultaneous fitting approach reduces the possibility of obtaining erroneous parameters due to correlations at any single k -weighting (Kelly et al., 2002).

3. RESULTS AND DISCUSSION

3.1. Community diversity

A clone library was created for each of the two experimental communities, the RWC and the MGPC. A total of 22 sequences were recovered from the MGPC sample, while 53 sequences were recovered from the RWC sample (Table 1). The MGPC clone library was comprised of sequences belonging to three genera within two phyla. The genus *Pseudomonas* (Gamma proteobacteria) dominated the MGPC library, comprising approximately 86% (19 of 22) of the total clones. The RWC clone library was more diverse, with eight genera (two unclassified) within three phyla. The dominant genera in the RWC sample were *Providencia* (39%), *Bacteroides* (17%), *Parabacteroides* (15%), and *Clostridium* (15%), and almost half of the clones belonged to the phylum Proteobacteria. Although cultured under aerobic conditions in this study, the bacteria in these genera typically are anaerobic and are most commonly found in mammalian intestinal tracts. It is likely that the stirred, but un-aerated, culture bottles became at least partially anaerobic during the 6 day incubation, promoting the growth of the strict anaerobic species. The river from which the RWC was collected receives outflow from municipal water treatment plants, as well as from combined sewer overflows, perhaps explaining the presence of species not typically found in pristine aerobic environments. In contrast, most of the bacteria in the MGPC sample were aerobic heterotrophic species, commonly found in soil or water. Both Gram-positive and Gram-negative species were found in both consortia samples.

Although biases associated with PCR- and cloning-based analyses have been well established (Snaird et al., 1997), such analyses can nonetheless serve to differentiate mixed microbial communities. We note that our enrichment conditions were selective for fast-growing heterotrophic bacteria, and would be expected to decrease the observed differences between the native environmental communities. Nonetheless, based on the cloning results presented above, we observe substantial differences in community composition between the MGPC and the RWC consortia samples, and find little overlap in the members of the two samples.

3.2. Cd Adsorption experiment

Cd adsorption experiments involving both types of bacterial consortia are shown in Fig. 1. The MGPC exhibits

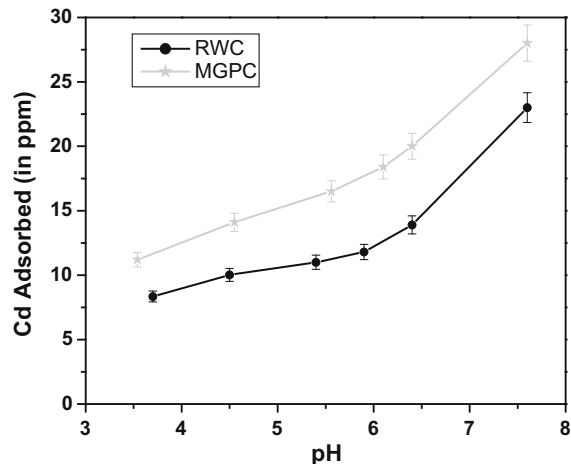


Fig. 1. Extent of Cd adsorption onto the river water consortium (RWC) and the manufactured gas plant consortium (MGPC) as a function of pH. Experimental conditions: Total Cd concentration of 30 ppm; ionic strength of 0.1 M NaClO₄; biomass concentration of 10 g/L.

significantly higher Cd uptake at all experimental pH conditions. Our measured extents of Cd adsorption are in agreement with the observations by Borrok et al. (2004b), who demonstrated that bacterial consortia from hydrocarbon-contaminated environments do not exhibit the same relatively narrow range of proton and Cd adsorption behavior that characterizes bacterial consortia from natural environments. However, we observed a smaller difference (in terms of the percentage of Cd adsorbed) between these two experimental consortia than was observed by Borrok et al. (2004a,b). The smaller difference may be due to population differences between the consortia samples used in this study compared to those used by Borrok et al. (2004a,b), especially the MGP samples. The MGP sample used for this study was a consortia grown from a frozen sample prepared in the Borrok et al. (2004b) study, and sampling bias may have been introduced during regrowth of this consortia.

3.3. Analysis of EXAFS data from standard compounds

The theoretical EXAFS spectra for the powder (CdS) and aqueous Cd standards (CdAc and CdPO₄) were based on a cluster of atoms derived from known crystal structures (Caminiti, 1982; Caminiti et al., 1984). For CdClO₄, a simple octahedral geometry of water molecules (6 oxygen atoms with 2 hydrogen atoms associated with each oxygen atom) was simulated. The theoretical Cd–H signal for the hydrated Cd spectra was based on the crystal structure of Cd(H₂PO₂)₂ (Naumov et al., 2005). A hydrated Cd cluster was not used as the basis for the FEFF calculation because the procedures within FEFF can cause the outer most shell of atom of a unique atom type to be incorrectly calculated, as is the case for the H atoms at the edge of the hydrated Cd cluster.

The EXAFS fitting results for the Cd standards are listed in Table 2. The averaged EXAFS $\chi(k) \cdot k^3$ spectra are shown in Fig. 2. The value obtained for the EXAFS amplitude reduction factor for all standards is $S_0^2 = 1.00 \pm 0.03$. This value was therefore used in modeling the spectra from the bacterial consortia samples. The CdClO₄ data were modeled with six nearest neighbor oxygen in the first shell at 2.28 (± 0.02) Å. The measures of the goodness of fit, *R* factor and χ^2_r , significantly improved by considering 12 hydrogen

atoms in the first hydration shell at 2.94 (± 0.08) Å, so this shell was used in the model of a hydrated Cd ion. The coordination environment of the CdAc standard was modeled with O and C shells, corresponding to a bound acetate group. Data were fit with 5.5 (± 0.3) O atoms in the first shell and 3.0 C atoms in the second shell which is consistent with a bidentate binding mechanism, as is observed in crystalline Cd–acetate (Caminiti et al., 1984). The Cd–O bond length and mean square displacements of the atomic pairs were similar for CdAc and CdClO₄. The Cd–C distance in CdAc was found

Table 2
Structural parameters obtained from fits of the standard compounds spectra. *N_x* gives the coordination number in the X-shell.

Standard	Path	<i>N</i>	<i>R</i> (Å)	σ^2 (10^{-3} Å ²)
CdClO ₄	Cd–O	6.0 \pm 0.18	2.28 \pm 0.02	8.8 \pm 0.2
	Cd–H	(2 <i>N</i> _{Cd–O}) ^a	2.94 \pm 0.08	13.7 \pm 0.5
CdAc	Cd–O	5.5 \pm 0.3	2.28 \pm 0.02	10.9 \pm 0.9
	Cd–C	3.0 ^c	2.70 \pm 0.02	12.8 \pm 4.0
CdPO ₄	Cd–O	5.8 \pm 0.3	2.28 \pm 0.02	10.5 \pm 1.2
	Cd–P	1.5 \pm 0.3	3.41 \pm 0.03	15.0 \pm 3.0
CdS	Cd–S	4.0 ^b	2.53 \pm 0.02	9.0 \pm 1.0
	Cd–Cd	12.0 ^b	4.2 \pm 0.01	25.0 \pm 4.0

^a Fixed to twice the coordination number of O atoms in the hydration sphere around aqueous Cd. ion.

^b Fixed to this value based on, crystallographic coordination.

^c Fixed to this value based on stability calculations.

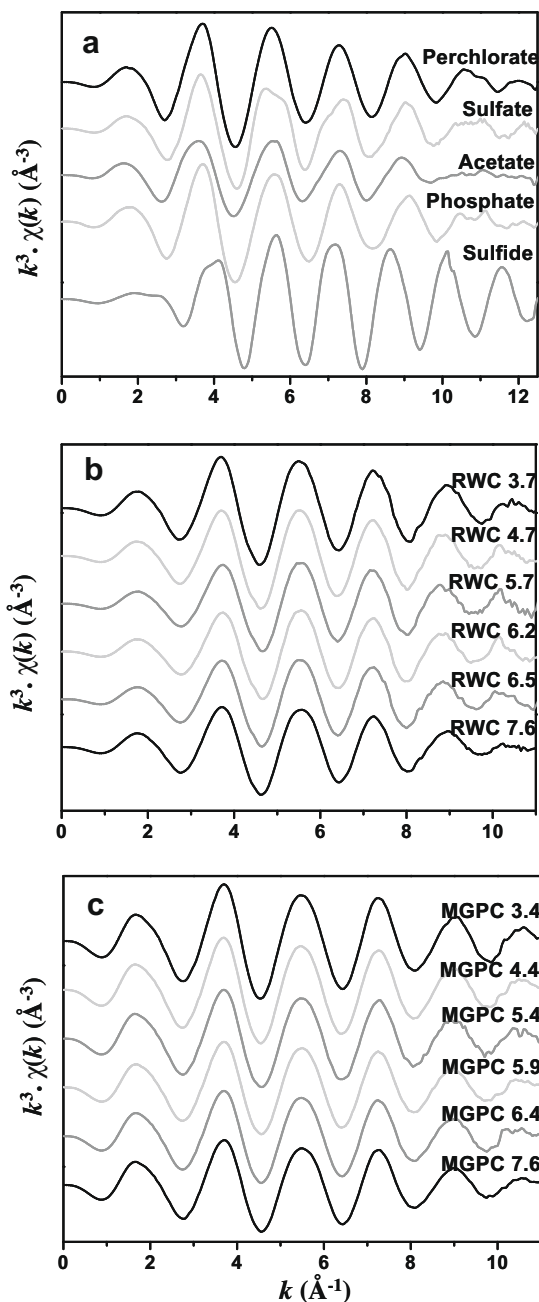


Fig. 2. k^3 Weighted $\chi(k)$ data for (a) the Cd standards, (b) the river water consortium (RWC), and (c) the manufactured gas plant soil consortium (MGPC). Data range used for Fourier transform was 2.3–9.8 k (Å^{-1}).

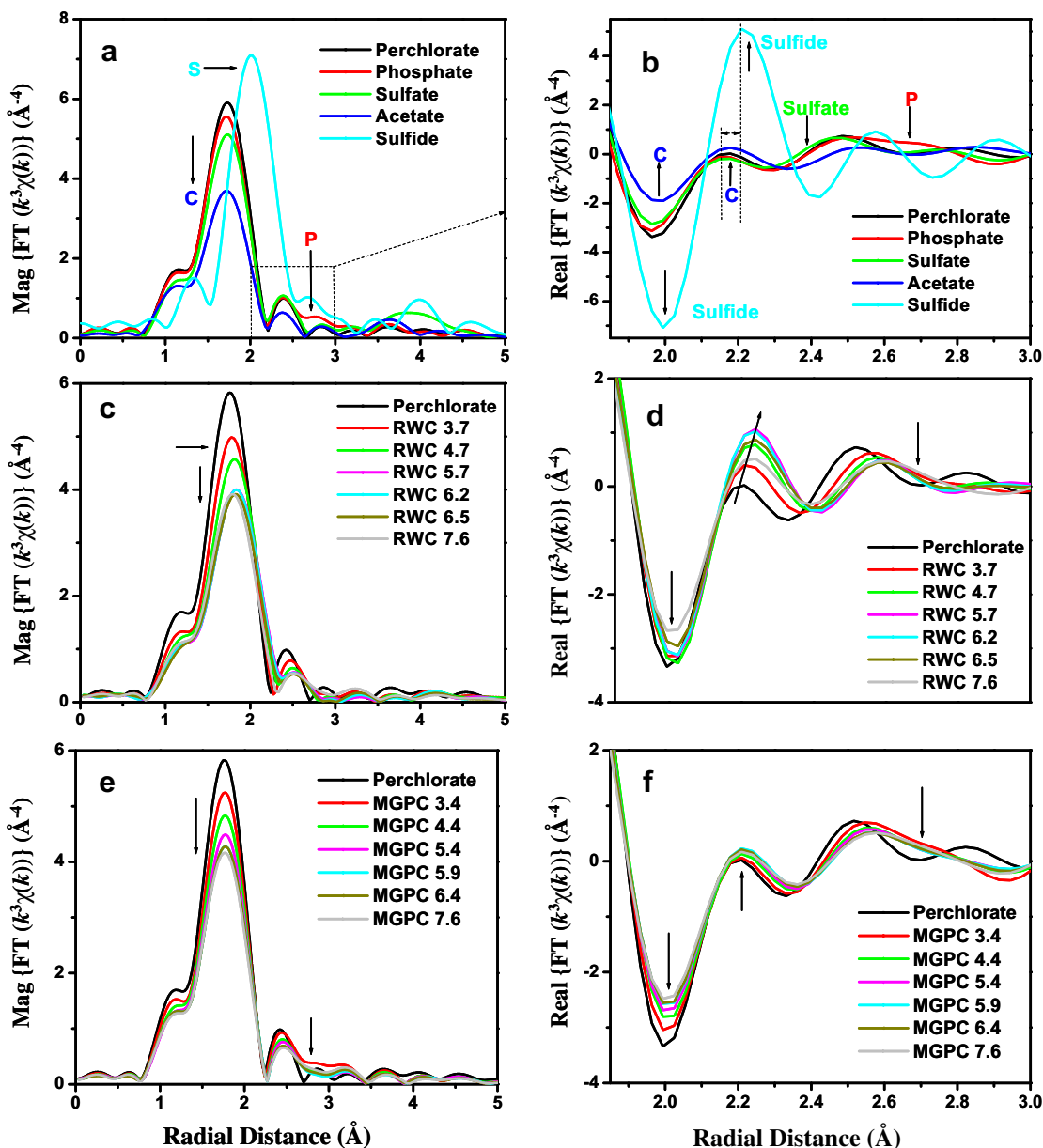


Fig. 3. Magnitude of the Fourier transformed data (FT; range 2.3–9.8 k (\AA^{-1})) for a) the Cd standard compounds; (c) the river water consortium (RWC). (e) the manufactured gas plant soil consortium (MGPC). Characteristic features, reduction in peak amplitude, and shifts of the peaks are noted with arrows; Real part of the Fourier transformed data plotted in the range 1.85–3.0 \AA for (b) the Cd standards; (d) the RWC samples (f) MGPC samples. Spectral features in the standards resulting from the atoms present in the different binding environments are noted with arrows, as well as trends in the spectra of the RWC and MGPC samples.

to be $2.70 (\pm 0.02)$ \AA . CdPO_4 aqueous standard data were fit with $5.8 (\pm 0.3)$ O atoms in the first shell and $1.5 (\pm 0.3)$ P atoms in the second shell. The Cd–O bond length was the same as in the CdPO_4 and CdClO_4 standards, $2.28 (\pm 0.02)$ \AA , and the Cd–P bond distance was found to be $3.41 (\pm 0.03)$ \AA . The coordination number, average radial distances, and their mean square displacement values for all the solution standards in this study are consistent with previously reported values (Boyanov et al., 2003). The CdS powdered standard was fit with 4 S atoms in the first shell at a distance of $2.53 (\pm 0.02)$ \AA . This distance of Cd–S binding in inorganic CdS standard is the same as reported for organic

Cd–S complexes (Pickering et al., 1999). As can be seen from Fig. 2a, the second and third oscillations of the CdS spectrum are clearly phase shifted in $\chi(k) \cdot k^{-3}$ relative to all the other standards. The phase shift comes from Cd bonding to S in the first shell, as opposed to bonding to oxygen in all of the other standards presented here. This phase shift is shown by the first peak shift in the Fourier transformed data for the Cd–S spectrum in Fig. 3a relative to the other standard spectra. Note the reduction in amplitude of the first shell peak in CdAc compared to the hydrated Cd spectrum (Fig. 3a). Detailed modeling reveals that in CdAc the signal from the oxygen atom interferes destructively with that of the carbon

atom, leading to this reduction. The subtle features in the second shell of the CdPO₄, CdAc and CdSO₄ spectra are not seen clearly from the full view of the magnitude of the Fourier transformed data, because C, P, and S are all light elements that do not scatter strongly. The enlarged real part of the Fourier transformed data, however, brings out the relatively small changes in the second shell of the CdAc, CdPO₄ and CdSO₄ spectra, relative to the hydrated Cd spectrum (Fig. 3b). As can be seen from Fig. 3b, CdPO₄ has a distinct feature (line shape) at about 2.7 Å, indicative of the P atom in a bound PO₄ group. CdSO₄ has a small phase shift towards lower *r* values (left) at about 2.4 Å, relative to the hydrated Cd spectrum (Fig. 3b). Because phosphate and sulfate are similar backscatterers, and because sulfate forms only weak complexes with Cd, it would be hard to distinguish the contribution of the sulfate signal from the contribution of the phosphate signal in an unknown sample. Despite that, it is useful to compare sulfate and phosphate standards, at least qualitatively, in order to test for the existence of sulfate-type sites. Additionally, the sulfate standard enables us to unequivocally distinguish sulfate-type binding from sulfide-type binding. The characteristic feature of the CdAc standard relative to the hydrated Cd spectrum is a significant reduction in the first shell peak at about 2.0 Å, associated with an increase in the second shell peak at about 2.2 Å (Fig. 3b). The signal from the CdAc and CdS standards overlap at about 2.2 Å, but the CdS signal has a shift towards higher *r* values (right) at 2.2 Å (Fig. 3b).

Through careful and consistent analysis procedures and through the collection of high quality spectra from a variety of standards, the subtle differences in the EXAFS spectra between hydrated Cd and Cd bound to different ligands are noticeable and can be modeled quantitatively as described above. The Cd–O, Cd–S, Cd–C and Cd–P paths listed in Table 3 were determined to be the four important signals (single scattering paths) in fitting the CdClO₄, CdS, CdAc and CdPO₄ standards and their presence in the spectrum of an unknown sample can be taken as indicative of sulfhydryl-, carboxyl-, and phosphate- binding environments, respectively. We will attempt to use only these four signals in the analysis of the bacterial consortia samples. A Cd–Cd signal was also used to fit the CdS spectrum, which can be helpful in identifying Cd precipitation in the unknown samples.

3.4. Qualitative analysis of EXAFS data from the bacterial systems

3.4.1. River water consortium (RWC)

We used the analysis of EXAFS spectra from the Cd standards described above as a basis for identifying the binding

environment of Cd in the experimental bacterial consortia samples. The magnitude and real part of the Fourier transformed data from the RWC samples are shown in Fig. 3c and d, respectively. The spectrum from the RWC sample at pH 3.7 exhibits a line shape around 2.7 Å (Fig. 3d) that is similar to the CdPO₄ binding signal (Fig. 3b), suggesting phosphoryl binding in the RWC sample at pH 3.7. The EXAFS spectrum at pH 4.7 has a significant increase in the peak at 2.2 Å compared to the spectrum at pH 3.7 (Fig. 3d). This could indicate an increase of carboxyl and/or sulfhydryl binding with increasing pH from 3.7 to 4.7. The drop and shift to higher *r* values in the first shell amplitude of the spectrum measured at pH 4.7 compared to pH 3.7 (Fig. 3c) also suggest the presence of carboxyl and sulfhydryl binding. The real part of the Fourier transform shows a small shift towards higher *r* value in the peak at 2.2 Å for the spectrum at pH 4.7 relative to the spectrum at pH 3.7. The same trend is observed for the CdS spectrum shown in Fig. 3b compared to the CdAc spectrum, and this trend is also more characteristic of sulfhydryl binding relative to carboxyl binding. Spectra of the sample exposed to Cd at pH 5.7 and 6.2 are quite similar to the spectrum of the pH 4.7 sample (Fig. 3c), and a further increase in the peak in the real part of the spectra at about 2.2 Å (Fig. 3d) for these two spectra suggests an increasing relative contribution of sulfhydryl binding at the pH values of 5.7 and 6.2 compared to that observed at pH 4.7. With further increase in pH to 6.5 and 7.6, these trends are reversed. The real part of the Fourier transform shows a reduction in the peaks at 2.0 and 2.2 Å for pH values 6.5 and 7.6 compared to that observed at pH 6.2, implying a decrease in the relative sulfhydryl contribution with increasing pH beyond pH 6.2 (Fig. 3d). The real part of the Fourier transform of the spectrum collected from the sample at pH 7.6 has a smooth line shape at 2.7 Å (Fig. 3d), and is similar to the CdPO₄ signal at 2.7 Å (Fig. 3b). The similar spectra at 2.7 Å indicate a relative increase in phosphoryl binding at pH 7.6 relative to that observed under lower pH conditions. An increase in the phosphoryl contribution at this pH value is consistent with the analysis of Cd binding onto pure bacterial strains observed by Boyanov et al. (2003) who found a shorter Cd–P distance at pH 7.8 compared to Cd–P distance at lower pH values and ascribed the shorter Cd–P distance at higher pH value to be coming from Cd binding with deprotonated phosphoryl sites. Overall, the qualitative analysis of the RWC indicates that phosphoryl binding dominates at pH 3.7, with an increase in the carboxyl and sulfhydryl contribution at pH values 4.7, 5.7 and 6.2. This trend, however, changes at pH 6.5 and 7.6, where a decrease in the sulfhydryl and an increase in the phosphoryl contribution is suggested by the EXAFS spectra.

3.4.2. Manufacturing gas plant consortium (MGPC)

The magnitudes of the Fourier transformed (FT) MGPC data are shown in Fig. 3e. Comparisons of the FT of RWC spectra (Fig. 3c) with the FT of the MGPC spectra (Fig. 3e) shows that the amplitudes of the main peaks in the Fourier transformed data of the MGPC are greater than the amplitudes of the similar peaks in the Fourier transformed data of the RWC at corresponding pH values. The higher amplitudes of the MGPC samples could

Table 3

Paths used for fitting the unknown samples, showing their distances and σ^2 values.

Path	Distance (Å)	σ^2 (Å ⁻²)
Cd–O	2.28 ± 0.02	0.0090 ± 0.002
Cd–C	2.70 ± 0.03	0.0120 ± 0.003
Cd–S	2.53 ± 0.02	0.0090 ± 0.001
Cd–P	3.41 ± 0.03	0.0150 ± 0.003

suggest that the carboxyl contribution to the Cd binding is less important in these samples than for the RWC samples. This is because the Cd–C signal causes the first shell peak height to be diminished by destructive interference as determined from the modeling of the CdAc standard. Another possible explanation for the change in the amplitude of the first shell signal could be due to more disorder in the samples with smaller signals. This effect can be probed through the σ^2 -value for the Cd–O and Cd–C signals. The spectra from the MGPC samples (Fig. 3e) demonstrates that the magnitude of the Fourier transformed spectra have similar shapes in the region between 2.0 and 3.5 Å, an observation that is also seen in the real part of the Fourier transformed spectra (Fig. 3f shows only up to 3.0 Å for clarity). In contrast to the RWC spectra, which show dramatic differences in the peak shape at 2.2 Å with increasing pH (Fig. 3d), the real part of the Fourier transformed spectra of the MGPC (Fig. 3f) are strikingly similar under all of the pH conditions studied. Because the height of the peak at 2.2 Å in the real part of the Fourier transformed data of the MGPC is much lower than the corresponding peak heights of the RWC samples, the possibility of significant sulfhydryl binding is less likely. Even a small sulfhydryl component would increase the height of the peak in this region, as seen in Fig. 3b and as shown in our discussion of the low pH samples of the RWC spectra shown in Fig. 3d. However, the real part of the Fourier transform around 2.7 Å (Fig. 3f) for all of the spectra of the MGPC strongly resembles the phosphate signature in this range (Fig. 3b). This qualitative observation indicates that it is highly likely that a phosphoryl group is the dominant binding ligand in the entire pH range examined for the MGPC.

It is worth emphasizing here that the qualitative analyses of EXAFS spectra can only serve as a guide to which models need to be tested using a quantitative model. Interference of EXAFS signals from overlapping shells is difficult to interpret visually, and may affect the resulting EXAFS spectrum. Therefore, rigorous quantitative modeling was carried out for a precise characterization of the binding environments present in the consortia samples.

3.5. Quantitative analysis of EXAFS data from the bacterial systems

3.5.1. River water consortium (RWC)

The six RWC samples were first fit independently of each other, each spectrum being fit simultaneously at k weights of 1–3. The four paths listed in Table 3 (indicative of sulfhydryl, carboxyl, and phosphoryl binding environments) that were used to model the Cd standards were used for fitting the biomass samples.

The pH 3.7 RWC data were initially modeled with only Cd-phosphoryl binding. However, modeling the spectrum for this sample required inclusion of Cd-carboxyl and Cd-sulfhydryl binding in addition to the phosphoryl binding to obtain a reasonable fit to the data. Best-fit values of the path parameters (σ^2 and ΔR) for this sample were the same (within uncertainties) as obtained for the Cd standards reported above. These independent fitting results for this sample are not shown,

because the final model based on simultaneous fitting of the data from the pH series gave the same results but with smaller uncertainties.

The independent modeling of the spectra at pH 3.7, 4.7, and 5.7 RWC samples showed an increase in the C and S coordination numbers with pH, concurrent with a decrease in the coordination number of P atoms. RWC spectra at pH 5.7 and 6.2 were very similar indicating the same binding environment at these two pH conditions. However the trend observed for the three lowest pH samples (pH 3.7, 4.7, and 5.7) was reversed at pH 6.5 and 7.6. The C and S coordination numbers decreased at these pH conditions. Although independent modeling of all the six consortium samples gave us an idea of the contributions in each spectrum, the average binding environment is complex in nature and there are overlapping contributions of relatively small amplitude in the spectra. Thus, coordination numbers obtained from independent modeling of each sample cannot be compared due to correlations with σ^2 . Similarly, differences in ΔE_0 (energy shift) values in the independent fits could lead to variations in the resulting bond distances.

To deal with these parameter correlations, all spectra except the pH 7.6 one were fit simultaneously. This approach constrains the energy shift, ΔE_0 , to be the same in all samples, and assumes the same radial distance (R) and variation in average radial distance (σ^2 -values) to a certain ligand in all samples, attributing the variation in amplitude to variations in the relative coordination numbers. In such a way, the correlations between different fitting parameters are reduced, resulting in smaller uncertainties in the fitting parameters. Since the best fit values of the path parameters (σ^2 and ΔR) for all the samples except the highest pH sample i.e. pH 7.6 sample obtained during their independent modeling were the same (within uncertainties) as obtained for the Cd standards, these path parameters (σ^2 and ΔR) of the O, S, C and P signals (single scattering paths) were constrained to the ones obtained for the Cd standards reported in Table 3.

The underlying assumption behind constraining these path parameters (σ^2 and ΔR) to the corresponding standards is that the Cd-ligand distance and variation in average radial distance (σ^2 -values) will be the same whether Cd is bound to that ligand alone or is in a mixed environment of CdAc, CdPO₄ and/or Cd–S. A single ΔE_0 was optimized for all 5 spectra, leaving only 21 parameters to determine (ΔE_0 , and coordination number of the four binding sites for five samples). It was verified using information theory (Nyquist, 1928) that the number of variables used to fit the EXAFS data in this study is far below the number of variables that could be used for extracting meaningful information from the data used for this study. Final fitting parameters thus obtained are tabulated in Table 4, and the magnitude and real part of the Fourier transform of the data and fits are shown in Figs. 4a and 4b, respectively.

Further confidence in the fitting approach adopted in this study was gained by a simple test to determine the robustness of the model. The variables which have been fixed in this fitting approach to the values obtained by standard compounds were varied to the upper and lower limit values of their uncertainties (Table 3). This results in less than a 15% change in the final coordination numbers of the corresponding ligands

Table 4

Values obtained for the fitting parameters from simultaneous fits of the five river water consortium (RWC) samples, pH 3.7–6.5. A common E_0 , shell distance and shell disorder for each shell were refined for all spectra. Coordination numbers were varied individually for each sample.

pH	3.7	4.7	5.7	6.2	6.5
<i>River water consortium (RWC)</i>					
No	4.83 ± 0.18	4.12 ± 0.15	3.23 ± 0.18	3.25 ± 0.16	3.41 ± 0.15
Nc	0.54 ± 0.40	0.65 ± 0.38	0.74 ± 0.40	0.81 ± 0.42	0.67 ± 0.36
Ns	0.51 ± 0.10	0.86 ± 0.10	1.27 ± 0.11	1.26 ± 0.10	0.98 ± 0.09
Np	1.45 ± 0.30	0.77 ± 0.28	0.54 ± 0.32	0.62 ± 0.30	0.57 ± 0.28
$R_o = 2.28 \text{ \AA}$, $\sigma_o^2 = 0.009 \text{ \AA}^{-2}$					
$R_c = 2.70 \text{ \AA}$, $\sigma_c^2 = 0.012 \text{ \AA}^{-2}$					
$R_s = 2.53 \text{ \AA}$, $\sigma_s^2 = 0.009 \text{ \AA}^{-2}$					
$R_p = 3.41 \text{ \AA}$, $\sigma_p^2 = 0.015 \text{ \AA}^{-2}$					
$\Delta E_0 = -2.15 \pm 0.10 \text{ eV}$					

reported in Table 3 and 5. The magnitude and real part of the Fourier transform of the RWC data and the contribution of the four signals (O, C, P and S) used to model the data are shown for one of the samples, at pH 5.7, in Fig. 5a and b, respectively. The contribution of the sulfhydryl signal can be better seen in Fig. 5b.

The pH 7.6 sample could not be fit with the model developed for the other samples. An unusually low (0.002

$\pm 0.002 \text{ \AA}^{-1}$) σ^2 -value was found for the Cd–P bond for this sample. This suggests a more rigid Cd–phosphoryl bond at this pH, which could indicate the presence of a different kind of phosphoryl binding. Since the pK_A value for the second deprotonation constant of phosphoric acid is 7.2, we propose that this more rigid binding is caused by interaction between the Cd and a deprotonated phosphoryl group. Boyanov et al. (2003) also reported a deprotonated

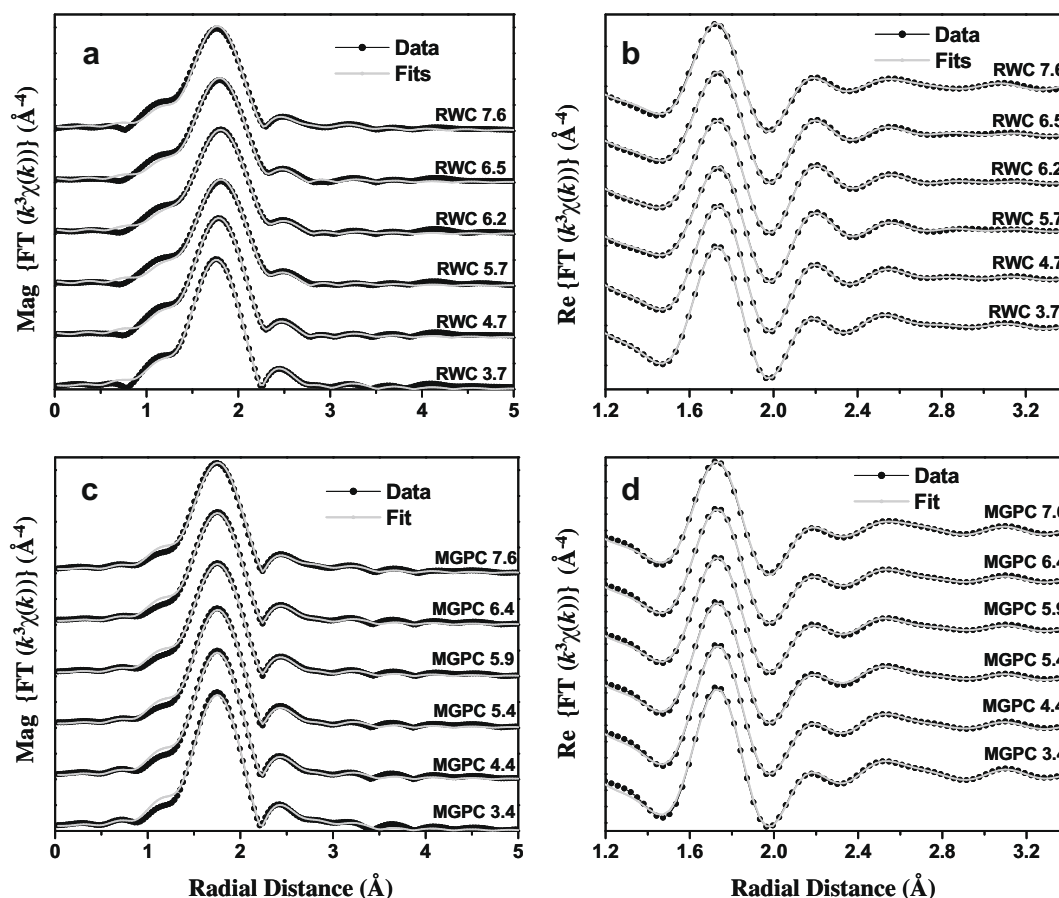


Fig. 4. Data and fits of (a) the magnitude of the Fourier transform of the river water consortium (RWC) data; (b) the real part of the Fourier transform of the RWC data plotted over the fitting range of 1.2–3.4 Å; (c) the magnitude of the Fourier transform of the manufactured gas plant soil consortium (MGPC) data; and (d) real part of the Fourier transform of the MGPC data plotted over the fitting range of 1.2–3.4 Å.

Table 5

Values obtained for the fitting parameters from simultaneous fits of the five manufactured gas plant consortium (MGPC) samples, pH 3.4–6.4. A common E_0 , shell distance and shell disorder for each shell were refined for all spectra. Coordination numbers were varied individually for each sample.

pH	3.4	4.4	5.4	5.9	6.4
<i>Manufactured gas plant consortium (MGPC)</i>					
No	5.53 ± 0.15	5.17 ± 0.18	4.76 ± 0.22	4.58 ± 0.14	4.57 ± 0.15
Nc	0.64 ± 0.33	0.52 ± 0.30	0.45 ± 0.32	0.46 ± 0.28	0.53 ± 0.32
Np	2.05 ± 0.50	1.46 ± 0.45	1.30 ± 0.48	1.22 ± 0.42	1.28 ± 0.45
$R_o = 2.28 \text{ \AA}, \sigma_o^2 = 0.009 \text{ \AA}^{-2}$					
$R_c = 2.70 \text{ \AA}, \sigma_c^2 = 0.012 \text{ \AA}^{-2}$					
$R_p = 3.41 \text{ \AA}, \sigma_p^2 = 0.015 \text{ \AA}^{-2}$					
$\Delta E_0 = -1.67 \pm 0.10 \text{ eV}$					

phosphoryl binding at pH 7.8 for Cd binding to individual bacterial strain. However they found a shorter Cd–P bond distance at this pH, while the RWC data at pH 7.6 could be modeled using the same Cd–P distance with which the RWC data at lower pH values have been modeled.

Although a rigorous qualitative modeling has been attempted and a robust fitting of the EXAFS spectra achieved, it is important to understand that the determination of the absolute value for the number of ligands bound to a metal in a complex natural system is difficult using EXAFS but the technique is uniquely precise in determining the relative changes in the coordination environment of ligands bound to the metal.

3.5.2. Manufacturing gas plant consortium (MGPC)

The approach described in the previous section was also applied to the EXAFS modeling of the MGPC samples. The best-fit values of the simultaneous fitting procedure are listed in Table 5 and the magnitude and real part of the Fourier transform of the measured spectra and the model fit are shown in Figs. 4c and 4d, respectively. The samples within the pH range from 3.4 to 6.4 were simultaneously refined with a single model.

The pH 7.6 sample was modeled independently. The lowest pH sample, pH 3.4, was modeled initially using only Cd-phosphoryl binding, but inclusion of Cd-carboxyl binding was necessary to obtain a reasonably good fit. The pH 3.4 sample was modeled with 2.05 ± 0.50 P atoms involved in the binding of each Cd atom, a value that is higher than expected for phosphoryl binding to bacterial systems assuming a Cd-phosphate type binding environment onto bacterial cells. However, the high value of P atoms could possibly result from the EXAFS data not having high enough resolution to distinguish between phosphate and sulfate groups. The typical bond length for Cd–S in a sulfate group is 3.5 \AA , only 0.08 \AA higher than the typical Cd–P bond length (Caminiti, 1982; Caminiti and Johansson 1981). In addition, the effective scattering amplitude by these two groups would also be similar. Hence, we are unable to resolve the contribution of sulfate from phosphate in these types of samples. Another possible reason for higher value of P atoms than expected could be due to a difference in Cd–P binding mechanism from the one observed in CdPO₄ standard. An elaborate discussion about such a possibility is given in the following section (see Section 3.5).

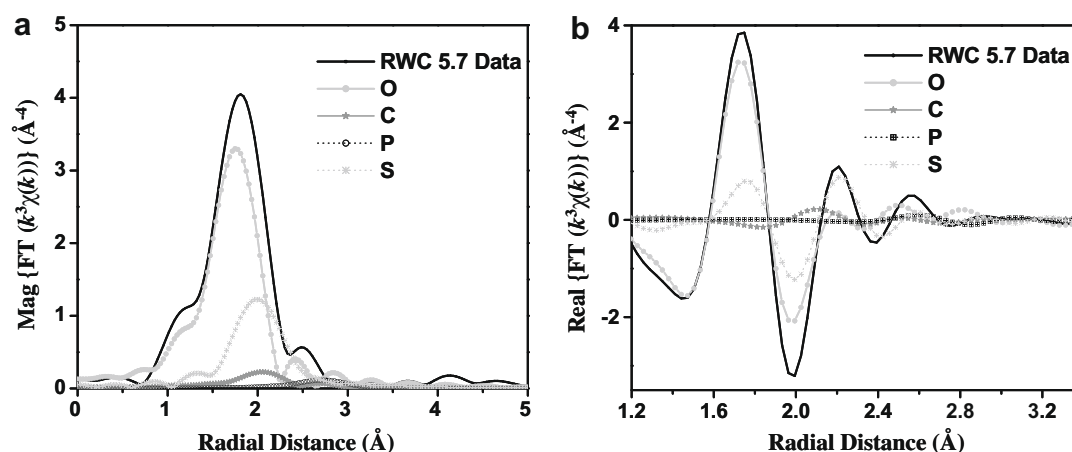


Fig. 5. (a) Magnitude of the Fourier transform of the river water consortium (RWC) data at pH 5.7 and the contribution of the four paths (Cd–O, Cd–C, Cd–P and Cd–S) used in the EXAFS modeling of these data, and (b) the real part of the Fourier transform of the pH 5.7 RWC data plotted over the fitting range of 1.2–3.4 Å and the contribution of the four paths (Cd–O, Cd–C, Cd–P and Cd–S) used in the EXAFS modeling of these data.

The number of oxygen atoms consistently decreases with increasing pH from 5.53 ± 0.15 for the pH 3.4 sample to 4.57 ± 0.15 for the pH 6.4 sample. The coordination numbers of the carboxyl group show a slight decrease but remain roughly the same within the uncertainty of the measurement ($\sim 0.50 \pm 0.30$). The coordination number of the phosphoryl group also remains constant ($\sim 1.50 \pm 0.50$) within uncertainty for the samples at pH 4.4, 5.4, 5.9, and 6.4. Although first shell S-ligands were not required to fit the data, the first shell Cd–O coordination numbers in Table 5 are well below the expected value of 6. There is no physical explanation of this observation but this trend is consistent with that observed by Boyanov et al. (2003).

Unlike what was found for the RWC samples, the MGPC sample at pH 7.6 could be successfully modeled using the same model as was applied to the five samples at lower pH values, with a slightly lower σ^2 -value of 0.010 ± 0.004 instead of 0.015 \AA^{-2} . The RWC sample at pH 7.6 was found to have some contribution from the sulfhydryl signal which is missing in the MGPC sample at the same pH condition. In addition, the MGPC sample does not exhibit the more rigid Cd–phosphoryl binding that we observed for the RWC sample at pH 7.6. The fitting parameters for the pH 7.6 RWC and pH 7.6 MGPC samples are shown in Table 6.

3.6. Discussion of Cd adsorption onto bacterial consortia

Perhaps the most striking result from this study is that the wide ranges of bacterial species present in the two experimental consortia samples exhibit only a limited range of Cd binding environments over a wide pH range. Clearly for this to be true, bacterial surfaces must exhibit commonalities in binding sites, consistent with the observations made by Yee and Fein (2001). Mineral surfaces exhibit dramatically different adsorption properties from each other (e.g., Stumm and Morgan, 1996), reflecting the unique underlying crystallographic features of each mineral. Conversely, bacteria to a large extent exhibit broadly similar cell wall binding sites. There are differences from one species to another in binding site concentrations and relative importance of each binding site type. However, only a few types of binding sites are important on bacterial cell walls, so Cd adsorption onto a complex mixture of bacterial species can be reasonably modeled using a relatively simple model that involves these few binding site types. Our results suggest that, despite the fundamental differences in the composition and structure of the cell walls of the bacteria within our experimental consortia samples, the same families of functional groups are responsible for the reactivity of the bacterial surfaces. Because our study examines two bacterial consortia obtained from markedly different geologic settings with significant differences in their phyla, it is likely that the similarities in binding environments apply to bacterial surfaces from a wide range of settings.

The EXAFS spectra from the RWC samples can be modeled using only three functional group sites: phosphoryl, carboxyl and sulfhydryl. The EXAFS spectra from the MGPC data were modeled successfully using phosphoryl and carboxyl sites only. A sulfhydryl-type ligand

Table 6

Refined parameters of the river water (RWC) and manufactured gas plant consortium (MGPC) data at pH 7.6.

	RWC 7.6	MGPC 7.6
ΔE_0	-0.90 ± 0.30	-1.30 ± 0.25
No	4.05 ± 0.22	4.55 ± 0.20
Nc	0.84 ± 0.40	0.62 ± 0.40
Ns	0.30 ± 0.10	–
Np	0.42 ± 0.24	1.12 ± 0.44
Ro	2.29 ± 0.01	2.29 ± 0.01
Rc	2.70 ± 0.03	2.70 ± 0.03
Rp	3.41 ± 0.03	3.41 ± 0.03
Rs	2.53 ± 0.02	–
σ_o^2	0.009*	0.009*
σ_c^2	0.012*	0.012*
σ_p^2	0.002 ± 0.002	0.010 ± 0.004
σ_s^2	0.009	–

Rx is in \AA , σ_x^2 is in \AA^{-2} and ΔE_0 is in eV.

* Fixed to the values in table 3.

was also reported by Guiné et al. (2006) for Zn adsorption to Gram-negative bacterial cell walls. Our study is the first to present a quantitative determination of this binding site for Cd adsorption, providing coordination numbers and distances for the binding of Cd to S- sites on bacterial cell walls.

The MGPC exhibits little change in Cd binding mechanisms over the pH range examined (pH 3.4–7.6), a result that contrasts markedly to what we observed for the RWC samples, which show dramatic changes in the relative contributions of the three functional groups at each pH value measured. In the MGPC samples, Cd is bound predominantly to phosphoryl groups under all pH conditions studied. The coordination number of P atoms is also slightly higher than we observed for the RWC samples. One explanation for the higher coordination number of P atoms could be the presence of sulfate-type groups. Although it is difficult to distinguish Cd–phosphate binding from Cd–sulfate binding using EXAFS, the increase in the coordination number of P atoms is not likely to be caused by the presence of sulfate-type groups because the MGPC data do not show the signature of Cd–sulfate binding seen in the CdSO₄ standard. Alternatively, binding between Cd and extracellular polymeric substances (EPS) may explain the observed predominant phosphoryl binding over the entire pH range examined, and the associated increase in the coordination number of P atoms could be explained by a different Cd–P binding mechanism from that in the standards. The production of EPS (both quantity and quality) is genetically controlled and influenced by environmental conditions. Bacteria produce EPS under nutrient limiting conditions, during surface-adhesion, flocculation, biofilm formation, and under environmental conditions considered hostile to them (Costerton et al., 1987). Phospholipids and phosphorylated polysaccharides are constituents of EPS (Makin and Beveridge, 1996; Shashkov et al., 1997; Madigan et al., 2002), and metal-phosphoryl interactions have been identified near surface-adhered cells that produce EPS (Kemner et al., 2004). Further, the production of copious amounts of P-rich EPS may provide a defense

against the hostile environment at the MGPC site and a competitive advantage over other microbial species. It is also possible that the cell membrane physiology of the bacterial species change in response to the hostile environments at MGPC site. Thus, the environmental conditions of the contaminated site may preferentially select for those species' presence in the MGPC inoculum used in the experiments for this study. Hence, it is possible that the observed differences in binding mechanisms between the MGPC and the RWC samples stem either from enhanced EPS production or changes in the chemical properties of the cell membrane or both, leading to consequent enrichment of phosphoryl sites, by the bacteria from the MGPC site relative to the RWC site.

4. CONCLUSIONS

Cd K edge EXAFS measurements of two different experimental bacterial consortia indicate that complex mixtures of bacteria, containing both Gram-positive and Gram-negative species, yield relatively simple EXAFS spectra. The EXAFS spectra indicate that the Cd binding environments within the samples vary as a function of pH, as the important functional groups undergo deprotonation reactions. However, only a limited number of functional group types were identified for each bacterial consortium. Our results suggest that there are broad similarities in the binding environments present on a wide range of bacterial cell walls, a conclusion consistent with the findings of Yee and Fein (2001). Our results are also in agreement with the bulk adsorption experiments reported by Borrok et al. (2004a), who showed that consortia of bacteria grown from a wide range of uncontaminated soil and water environments exhibit similar affinities for protons and Cd.

The Cd EXAFS data for the RWC were modeled using only three types of Cd binding sites: phosphoryl, carboxyl and sulfhydryl. The lowest pH sample, pH 3.7, exhibited predominantly Cd-phosphoryl binding, with a small contribution from the Cd-carboxyl and -sulfhydryl group. We observed a steep increase in the sulfhydryl contribution and a corresponding decrease in the phosphoryl contribution to the Cd binding with increasing pH, up to pH 5.7. The carboxyl contribution modestly increased with increasing pH over this pH range. This trend reversed at higher pH values, i.e. at pH 6.5 and 7.6 where the sulfhydryl contribution went down. The pH 7.6 RWC sample, however, could not be fit with the model used for the lower pH samples. At pH 7.6, the RWC was dominated by phosphoryl and carboxyl binding with a smaller σ^2 -value for the phosphoryl ligand, indicating a more rigid Cd-phosphoryl bond, likely due to deprotonated phosphoryl binding.

The MGPC sample exhibited enhanced Cd adsorption relative to that found for the RWC. Cd EXAFS data for the MGPC were modeled using phosphoryl and carboxyl groups only. Cd-phosphoryl binding was the dominant adsorption mechanism over the entire pH range investigated, i.e., from pH 3.4 to 7.6. Although we observed differences in the binding environments of the MGPC relative to that of the RWC, it is not clear why these differences lead to enhanced Cd adsorption.

This study suggests that, despite the complex physiology of each bacterial strain, adsorption mechanisms do not vary greatly from one species to another, and that metal binding within complex bacterial consortia can be explained using the same number of binding site types as is typically found in samples of a single bacterial species. The main difference between the two experimental consortia studied here and between the single bacterial species studied to date, lies in the relative site concentrations of the two or three important binding site types. Our results suggest that bacterial consortia from a range of geological settings exhibit relatively simple metal binding environments, and that models of metal adsorption onto bacteria within these complex consortia may be correspondingly simple as well.

ACKNOWLEDGMENTS

B.M. thanks the Environmental Molecular Science Institute at University of Notre Dame and the Bayer Corporation for their support through an EMSI Scholarship and a Bayer Predoctoral Fellowship, respectively. Help in sample preparation from Jennifer Szymanowski, and beamline setup help from the staff of MRCAT are greatly appreciated.

We would also like to thank Stefan Green for helpful discussions on the approaches to measure genomic diversity. A journal review by Bryne Ngwenya, and comments by AE Roy Wogelius, significantly improved the presentation of the research. This work was supported by the funding provided by the National Science Foundation through an Environmental Molecular Science Institute grant (EAR02-21966) to the University of Notre Dame. S.D.K. and K.M.K. were supported by the US Department of Energy Biological and Environmental Research Division Environmental Remediation Science Program. MRCAT is supported by the US Department of Energy under contract DE-FG02-94-ER-45525 and the member institutions. Use of the Advanced Photon Source was supported by the US Department of Energy under contract W-31-109-Eng-38.

REFERENCES

- Altschul S. F., Madden T. L., Schaffer A. A., Zhang J. H., Zhang Z., Miller W. and Lipman D. J. (1997) Gapped BLAST and PSI-BLAST: a new generation of protein database search programs. *Nucleic Acids Res.* **25**, 3389–3402.
- Ankudinov A. L., Ravel B., Rehr J. J. and Conradson S. D. (1998) Real-space multiple-scattering calculation and interpretation of X-ray-absorption near-edge structure. *Phys. Rev. B* **58**, 7565–7576.
- Barnes S. M. and Nierzwicki-Bauer S. A. (1997) Microbial diversity in ocean, surface and subsurface environments. In *Geomicrobiology: Interactions Between Microbes and Minerals. Reviews in Mineralogy*, vol. 35 (eds. J. F. Banfield and K. H. Nealson). Mineralogical Society of America, Washington, DC.
- Borrok D., Fein J. B. and Kulpa C. F. (2004a) Proton and Cd adsorption onto natural bacterial consortia: testing universal adsorption behavior. *Geochim. Cosmochim. Acta* **68**, 3231–3238.
- Borrok D. M., Fein J. B. and Kulpa C. F. (2004b) Cd and proton adsorption onto bacterial consortia grown from industrial wastes and contaminated geologic settings. *Environ. Sci. Technol.* **38**, 5656–5664.
- Borrok D., Fein J. B. and Turner B. F. (2005) A universal surface complexation framework for modeling proton binding

- onto bacterial surfaces in geologic settings. *Am. J. Sci.* **305**, 826–853.
- Boyanov M. I., Kelly S. D., Kemner K. M., Bunker B. A., Fein J. B. and Fowle D. A. (2003) Adsorption of cadmium to *Bacillus subtilis* bacterial cell walls: a pH-dependent X-ray absorption fine structure spectroscopy study. *Geochim. Cosmochim. Acta* **67**, 3299–3311.
- Burnett P. G. G., Daughney C. J. and Peak D. (2006) Cd adsorption onto *Anoxybacillus flavithermus*: surface complexation modeling and spectroscopic investigations. *Geochim. Cosmochim. Acta* **70**, 5253–5269.
- Caminiti R. (1982) Nickel and cadmium phosphates in aqueous-solutions - cation anion complex-formation and phosphate-H₂O interactions. *J. Chem. Phys.* **77**, 5682–5686.
- Caminiti R. and Johansson G. (1981) On the structures of cadmium sulfate complexes in aqueous-solutions. *Acta Chem. Scand. Ser. A* **35**, 373–381.
- Caminiti R., Cucca P., Monduzzi M., Saba G. and Crisponi G. (1984) Divalent metal-acetate complexes in concentrated aqueous-solutions – an X-Ray-diffraction and NMR-Spectroscopy Study. *J. Chem. Phys.* **81**, 543–551.
- Cole J. R., Chai B., Farris R. J., Wang Q., Kulam-Syed-Mohideen A. S., McGarrell D. M., Bandela A. M., Cardenas E., Garrity G. M., and Tiedje J. M. (2007) The ribosomal database project (RDP-II). *Nucleic Acids Research* **35** (Database issue):D169–D172; doi:10.1094/nar/gk1889.
- Costerton J. W., Cheng K. J., Geesay G. G., Ladd T. I., Nickel J. C., Dasgupta M. and Marrie T. J. (1987) Bacterial biofilm in nature and disease. *Annu. Rev. Microbiol.* **41**, 435–464.
- Daughney C. J., Fein J. B. and Yee N. (1998) A comparison of the thermodynamics of metal adsorption onto two common bacteria. *Chem. Geol.* **144**, 161–176.
- Fein J. B. (2000) Quantifying the effects of bacteria on adsorption reactions in water–rock systems. *Chem. Geol.* **169**, 265–280.
- Fein J. B., Daughney C. J., Yee N. and Davis T. A. (1997) A chemical equilibrium model for metal adsorption onto bacterial surfaces. *Geochim. Cosmochim. Acta* **61**, 3319–3328.
- Fowle D. A. and Fein J. B. (2000) Experimental measurements of the reversibility of metal-bacteria adsorption reactions. *Chem. Geol.* **168**, 27–36.
- Guiné V., Spadini L., Sarret G., Muris M., Delolme C., Gaudet J. P. and Martins J. M. F. (2006) Zinc sorption to three Gram-negative bacteria: combined titration, modeling, and EXAFS study. *Environ. Sci. Technol.* **40**, 1806–1813.
- He L. M. and Tebo B. M. (1998) Surface charge properties of and Cu(II) adsorption by spores of the marine *Bacillus* sp. strain SG-1. *Appl. Environ. Microbiol.* **64**, 1123–1129.
- Hennig C., Panak P. J., Reich T., Rossberg A., Raff J., Selenska-Pobell S., Matz W., Bucher J. J., Bernhard G. and Nitsche H. (2001) EXAFS investigation of uranium(VI) complexes formed at *Bacillus cereus* and *Bacillus sphaericus* surfaces. *Radiochim. Acta* **89**, 625–631.
- Kaeberlein T., Lewis K. and Epstein S. S. (2002) Isolating “uncultivable” microorganisms in pure culture in a simulated natural environment. *Science* **296**, 1127–1129.
- Kelly S. D., Kemner K. M., Fein J. B., Fowle D. A., Boyanov M. I., Bunker B. A. and Yee N. (2002) X-ray absorption fine structure determination of pH-dependent U-bacterial cell wall interactions. *Geochim. Cosmochim. Acta* **66**, 3855–3871.
- Kemner K. M., Kropf A. J. and Bunker B. A. (1994) A low-temperature total electron yield detector for X-ray absorption fine structure spectra. *Rev. Sci. Instrum.* **65**, 3667–3669.
- Kemner K. M., Kelly S. D., Lai B., Maser J., O’Loughlin E. J., Sholto-Douglas D., Cai Z., Schneegurt M. A., Kulpa, Jr., C. F. and Neelson K. H. (2004) Elemental and redox analysis of single bacterial cells by X-ray microbeam analysis. *Science* **306**, 686–687.
- Kulczycki E., Ferris F. G. and Fortin D. (2002) Impact of cell wall structure on the behavior of the bacterial cells as sorbents of cadmium and lead. *Geomicrobiol. J.* **19**, 553–565.
- Ledin M., Krantz-Rulcker C. and Allard B. (1996) Zn, Cd and Hg accumulation by microorganisms, organic and inorganic soil components in multi-compartment systems. *Soil Biol. Biochem.* **28**, 791–799.
- Ledin M., Krantz-Rulcker C. and Allard B. (1999) Microorganisms as metal sorbents: comparison with other soil constituents in multi-compartment systems. *Soil Biol. Biochem.* **31**, 1639–1648.
- Madigan M. T., Martinko J. M. and Parker J. (2002) *Biology of Microorganisms*, tenth ed. Prentice Hall Inc.
- Makin S. A. and Beveridge T. J. (1996) The influence of A-band and B-band lipopolysaccharide on the surface characteristics and adhesion of *Pseudomonas aeruginosa* to Surfaces. *Microbiology* **142**, 299–307.
- Muyzer G., De Waal E. C. and Uitterlinder A. G. (1993) Profiling of complex microbial populations by denaturing gradient gel electrophoresis analysis of polymerase chain reaction - amplified genes coding for 16S rRNA. *Appl. Environ. Microbiol.* **59**, 695–700.
- Naumov D. Y., Naumova M. I. and Kuratieva N. V. (2005) Cadmium bis dihydrogenphosphate(I). *Acta Crystallogr. Sect. E-Structure Rep. Online* **61**, 1251–1252.
- Newville M. (2001) IFEFFIT: interactive XAFS analysis and FEFF fitting. *J. Sync. Rad.* **8**, 322–324.
- Newville M., Ravel B., Haskel D., Rehr J. J., Stern E. A. and Yacoby Y. (1995) Analysis of multiple-scattering Xafs data using theoretical standards. *Physica B* **209**, 154–156.
- Newville M., Livins P., Yacoby Y., Rehr J. J. and Stern E. A. (1993) Near-edge X-Ray-absorption fine structure of Pb – a comparison of theory and experiment. *Phys. Rev. B* **47**, 14126–14131.
- Ngwenya B. T., Sutherland I. W. and Kennedy L. (2003) Comparison of the acid-base behaviour and metal adsorption characteristics of a Gram-negative bacterium with other strains. *Appl. Geochem.* **18**, 527–538.
- Nyquist H. (1928) Certain topics in telegraph transmission theory. *Trans. AIEE* **47**, 617–644.
- Panak P. J., Booth C. H., Caulder D. L., Bucher J. J., Shuh D. K. and Nitsche H. (2002) X-ray absorption fine structure spectroscopy of plutonium complexes with *Bacillus sphaericus*. *Radiochim. Acta* **90**, 315–321.
- Parkhurst, D. L., and Appelo, C. (1999) A. J. User’s guide to PHREEQC (version 2) – A computer program for speciation, batch-reaction, one-dimensional transport, and inverse geochemical calculations. *USGS Water-Resources Investigations Report* 99–4259.
- Pickering I. J., Prince R. C., George G. N., Rauser W. E., Wickramasinghe W. A., Watson A. A., Dameron C. T., Dance I. G., Fairlie D. P. and Salt D. E. (1999) X-ray Absorption spectroscopy of cadmium phytochelatin and model systems. *Biochim et Biophys Acta* **1429**, 351–364.
- Plette A. C. C., Benedetti M. F. and vanRiemsdijk W. H. (1996) Competitive binding of protons, calcium, cadmium, and zinc to isolated cell walls of a gram-positive soil bacterium. *Environ. Sci. Technol.* **30**, 1902–1910.
- Plette A. C. C., Vanriemsdijk W. H., Benedetti M. F. and Vanderwal A. (1995) Ph Dependent charging behavior of isolated cell walls of a gram-positive soil bacterium. *J. Colloid Interface Sci.* **173**, 354–363.
- Ravel B. (2001) ATOMS: crystallography for the X-ray absorption spectroscopist. *J. Sync. Rad.* **8**, 314–316.

- Ravel B. and Newville M. (2005) Athena, artemis, hephaestus: data analysis for X-ray absorption spectroscopy using IFEFFIT. *J. Sync. Rad.* **12**, 537–541.
- Sarret G., Manceau A., Spadini L., Roux J. C., Hazemann J. L., Soldo Y., Eybert-Berard L. and Menthonnex J. J. (1998) Structural determination of Zn and Pb binding sites in *Penicillium chrysogenum* cell walls by EXAFS spectroscopy. *Environ. Sci. Technol.* **32**, 1648–1655.
- Shashkov A. S., Senchenkova S. N., Nazarenko E. L., Zubkov V. A., Gorshkova N. M., Knirel Y. A. and Gorshkova R. P. (1997) Structure of a phosphorylated polysaccharide from *Shewanella putrefaciens* strain S29. *Carbohydr. Res.* **303**, 333.
- Segre, C. U., Leyarovska, N. E., Chapman, L. D., Lavender, W. M., Plag, P. W., King, A. S., Kropf, A. J., Bunker, B. A., Kemner, K. M., Dutta, P., Duran, R. S., and Kaduk, J. (2000) The MRCAT insertion device beamline at the advanced photon source, *In: Sync. Rad. Instrum: Eleven US Conference CP521*, 419–422.
- Snaidr J., Amann R., Huber I., Ludwig W. and Schleifer K. H. (1997) Phylogenetic analysis and in situ identification of bacteria in activated sludge. *Appl. Environ. Microbiol.* **63**, 2884–2896.
- Stern E. A. and Heald S. M. (1983) Basic principles and applications of EXAFS. In *Handbook of Sync. Rad.*, vol. 10. North Holland, pp. 995–1014.
- Stern E. A., Newville M., Ravel B., Yacoby Y. and Haskel D. (1995) The uwxafs analysis package – philosophy and details. *Physica B* **209**, 117–120.
- Stumm W. and Morgan J. J. (1996). *Aquatic Chemistry, Chemical Equilibria and Rates in Natural Waters*, third ed. JohnWiley and Sons.
- Toner B., Manceau A., Marcus M. A., Millet D. B. and Sposito G. (2005) Zinc sorption by a bacterial biofilm. *Environ. Sci. Technol.* **39**, 8288–8294.
- Xue H. B., Stumm W. and Sigg L. (1988) The binding of heavy metals to algal surfaces. *Water Res.* **22**, 917–926.
- Yee N. and Fein J. (2001) Cd adsorption onto bacterial surfaces: a universal adsorption edge? *Geochim. Cosmochim. Acta* **65**, 2037–2042.
- Yee N. and Fein J. B. (2003) Quantifying metal adsorption onto bacteria mixtures: a test and application of the surface complexation model. *Geomicrobiol. J.* **20**, 43–60.

Associate editor: Roy A. Wogelius

Adsorption of Fe(II) and U(VI) to carboxyl-functionalized microspheres: The influence of speciation on uranyl reduction studied by titration and XAFS

Maxim I. Boyanov^{a,b,*}, Edward J. O’Loughlin^a, Eric E. Roden^c,
Jeremy B. Fein^b, Kenneth M. Kemner^a

^a Biosciences Division, Argonne National Laboratory, Argonne, IL 60439, USA

^b Department of Civil Engineering and Geological Sciences, University of Notre Dame, Notre Dame, IN 46556, USA

^c Department of Geology and Geophysics, University of Wisconsin-Madison, Madison, WI 53706, USA

Received 10 July 2006; accepted in revised form 29 January 2007; available online 6 February 2007

Abstract

The chemical reduction of U(VI) by Fe(II) is a potentially important pathway for immobilization of uranium in subsurface environments. Although the presence of surfaces has been shown to catalyze the reaction between Fe(II) and U(VI) aqueous species, the mechanism(s) responsible for the enhanced reactivity remain ambiguous. To gain further insight into the U–Fe redox process at a complexing, non-conducting surface that is relevant to common organic phases in the environment, we studied suspensions containing combinations of 0.1 mM U(VI), 1.0 mM Fe(II), and 4.2 g/L carboxyl-functionalized polystyrene microspheres. Acid-base titrations were used to monitor protolytic reactions, and Fe K-edge and U L-edge X-ray absorption fine structure spectroscopy was used to determine the valence and atomic environment of the adsorbed Fe and U species. In the Fe + surface carboxyl system, a transition from monomeric to oligomeric Fe(II) surface species was observed between pH 7.5 and pH 8.4. In the U + surface carboxyl system, the U(VI) cation was adsorbed as a mononuclear uranyl–carboxyl complex at both pH 7.5 and 8.4. In the ternary U + Fe + surface carboxyl system, U(VI) was not reduced by the solvated or adsorbed Fe(II) at pH 7.5 over a 4-month period, whereas complete and rapid reduction to U(IV) nanoparticles occurred at pH 8.4. The U(IV) product reoxidized rapidly upon exposure to air, but it was stable over a 4-month period under anoxic conditions. Fe atoms were found in the local environment of the reduced U(IV) atoms at a distance of 3.56 Å. The U(IV)–Fe coordination is consistent with an inner-sphere electron transfer mechanism between the redox centers and involvement of Fe(II) atoms in both steps of the reduction from U(VI) to U(IV). The inability of Fe(II) to reduce U(VI) in solution and at pH 7.5 in the U + Fe + carboxyl system is explained by the formation of a transient, “dead-end” U(V)–Fe(III) complex that blocks the U(V) disproportionation pathway after the first electron transfer. The increased reactivity at pH 8.4 relative to pH 7.5 is explained by the reaction of U(VI) with an Fe(II) oligomer, whereby the bonds between Fe atoms facilitate the transfer of a second electron to the hypothetical U(V)–Fe(III) intermediate. We discuss how this mechanism may explain the commonly observed higher efficiency of uranyl reduction by adsorbed or structural Fe(II) relative to aqueous Fe(II).

© 2007 Elsevier Ltd. All rights reserved.

1. INTRODUCTION

Uranium has become an environmental concern as a contaminant from power generation and defense-related

activities (Riley et al., 1992; Batson et al., 1996), as well as from weathering of uranium minerals near mine tailings (Landa and Gray, 1995). To predict contaminant fate and develop remediation strategies, the factors controlling uranium speciation and reactivity must be identified and their effects evaluated for diverse environmental conditions. Aqueous ion transport in water-rock systems is usually

* Corresponding author.

E-mail address: mboyanov@nd.edu (M.I. Boyanov).

controlled by adsorption and/or precipitation reactions, which can be manipulated to contain a propagating contaminant plume. For aqueous uranium, in particular, a promising immobilization strategy is reduction and mineral formation (e.g., Langmuir, 1978). Oxidized uranium, U^{VI} , is relatively soluble and mobile, but when uranium is reduced to U^{IV} , it forms sparingly soluble minerals, and mass transport is, in general, retarded. Dissimilatory metal-reducing bacteria (DMRB) can affect the redox conditions present in the subsurface, either by enzymatically reducing U^{VI} to U^{IV} (Gorby and Lovley, 1992; Lovley and Phillips, 1992a,b; Fredrickson et al., 2000), or by producing significant amounts of Fe^{II} during dissimilatory Fe^{III} reduction (DIR) (Bell et al., 1987; Lovley et al., 1987; Kostka and Nealson, 1995; Fredrickson et al., 1998). The Fe^{II} phases resulting from DIR provide reducing capacity in natural systems (Stumm and Sulzberger, 1992), and some of the phases, such as adsorbed Fe^{II} and mixed-valence Fe^{II}/Fe^{III} minerals, are known reductants of U^{VI} (see below). The relative importance of the microbial (enzymatic) reduction vs. the abiotic (chemical) reduction of U^{VI} in natural environments is still in question, partly due to insufficient information on the mechanisms of both processes. It is therefore important to understand the controls on U^{VI} reduction by Fe^{II} .

Reduction of U^{VI} by Fe^{II} is thermodynamically favorable under a range of environmental conditions and has been the subject of recent investigations. The homogeneous reaction between hydrated U^{VI} and Fe^{II} species is kinetically inhibited and fails to occur over at least 3 days at neutral pH under anoxic conditions; however, the addition of particulate minerals under identical experimental conditions causes complete uranium removal within hours, presumably through heterogeneous reduction by adsorbed $Fe^{II}OH^+$ species (Liger et al., 1999; Fredrickson et al., 2000; Jeon et al., 2005). Structural Fe^{II} (i.e., Fe^{II} in crystalline compounds) is also capable of reducing U^{VI} . Mixed-valence $Fe^{II,III}$ oxides and hydroxides (magnetite and green rusts), Fe^{II} sulfide (pyrite), and Fe^{II} -bearing phyllosilicates (micas) have been shown to reduce aqueous U^{VI} (Wersin et al., 1994; O'Loughlin et al., 2003; Ilton et al., 2004; Scott et al., 2005). The catalytic effect of surfaces is most often attributed to decreased redox potential due to complexation of the reduced species to an electron donor ligand (i.e., a ligand effect). This interpretation is based on a body of work studying the reduction of Cr^{VI} and organic contaminants by adsorbed/complexed Fe^{II} (e.g., Stumm, 1992; Schwarzenbach et al., 1997; Buerge and Hug, 1999; Strathmann and Stone, 2002; Sposito, 2004). However, recent findings indicate that electrons from adsorbed Fe^{II} can migrate inside the adsorbing ferric oxide lattice (Williams and Scherer, 2004) and that non-local redox interactions can be mediated by semiconductor surfaces, such as those of galena and pyrite (Becker et al., 2001). These results suggest that what is thought to be adsorbed Fe^{II} may actually be structural Fe^{II} , and that electron transfer may be occurring between spatially separated redox centers through a lattice conduction/hopping mechanism. Because the reduction of U^{VI} to U^{IV} requires two electrons, whereas the oxidation of Fe^{II} to Fe^{III} provides only one, the higher U^{VI} reduction

rate in the presence of a surface may also be due to the enhanced ability of two separate Fe^{II} atoms to transfer electrons to an adsorbed U^{VI} atom at the same binding site. In summary, although it is well established that Fe^{II} atoms are more efficient reducers of U^{VI} in the presence of minerals than as aqueous species, the mechanism of enhanced reactivity and the reactive species in the presence of a surface remain ambiguous. Ligand effects, atomic proximity of reducing centers, and electron lattice conduction all remain possible reduction-enhancing mechanisms at a surface.

In this work, we investigated the U^{VI} - Fe^{II} redox reactivity as a function of Fe^{II} speciation in the presence of a carboxyl-functionalized surface. Although the carboxyl functionality was chosen for its relevance to cation sorption/complexation in biotic environments (Beveridge and Murray, 1980; Fein et al., 1997; Boyanov et al., 2003), our primary focus was to determine the controls and mechanisms of U^{VI} reduction by Fe^{II} . The use of a non-conducting polystyrene matrix avoided the issue of electron tunneling in the substrate that may be present in crystal oxides, and ensured the direct electron transfer between Fe and U atoms. The complexing surface provided control over the partitioning of Fe^{II} between solvated, adsorbed, and oligomerized species. Our specific goals were to (i) identify conditions under which U^{VI} reduction occurs, (ii) identify the U^{VI} and Fe^{II} species present under non-reactive conditions, (iii) identify the U^{VI} and Fe^{II} species present in Fe-only and U-only systems under reactive conditions, and (iv) analyze the reaction products and infer details about the electron transfer mechanism. We used titration experiments to provide information on H^+ release from the surface and on OH^- consumption in precipitation reactions. X-ray absorption fine structure (XAFS) spectroscopy was used to determine the average valence and molecular environment of U and Fe atoms in the hydrated solid phase. The combination of these approaches allowed us to relate speciation to reactivity in the studied system and to deduce a mechanism for the electron transfer.

2. MATERIALS AND METHODS

2.1. Latex particles, suspensions, and reagents

Carboxyl-modified polystyrene microspheres were obtained from Bangs Laboratories, Inc. The colloids are produced by co-polymerization of polystyrene and acrylic acid, resulting in uniform spherical particles (diameter deviation of several percent) with carboxyl functional groups on the surface. The size and the carboxyl functionality were chosen to emulate the cation-binding characteristics of bacterial cells. Transmission electron microscopy (TEM) confirmed the shape and narrow size distribution of the particles (Fig. EA-1 in the electronic annex). Some properties provided by the manufacturer are summarized in Table 1. The latex particles were washed 3 times in 0.5 M HCl and 2 times in distilled deionized water, then suspended in 0.03 M $NaClO_4$ or NaCl electrolyte to buffer the ionic strength. Control experiments showed that the redox properties of the system were not affected by the type of

Table 1
Properties of the carboxyl-modified colloid (catalog number PC03N), as provided by Bangs Laboratories, Inc.

Property	Value	Units
Diameter	0.92	μm
Surface area	6.153	m^2/g
Surface titration data	94.6	$\mu\text{eq}/\text{g}$
Surface density of COOH	10.8	$\text{\AA}^2/\text{site}$
Density of polymer core	1.06	g/cm^3

electrolyte used. The amounts of adsorbent in the suspensions were monitored by following optical density at 600 nm, using the manufacturer's suspensions as standards. Samples for the experiments were produced from a stock suspension and then separated into crimp-sealed glass bottles. Dissolved O_2 and CO_2 were removed by bubbling N_2 through the solutions and suspensions for 40 min. The purge gas was purified by removing O_2 with an O_2 trap (model 1000, from Chromatography Research Supplies, Inc.), followed by consecutive passage through a 5% HCl solution, a 5% NaOH solution, and the 0.03 M electrolyte solution, to remove potential acid- or base-soluble impurities and introduce humidity. The mass of the purged sample bottles, measured before and after purging, showed no change. After sparging, the bottles were immediately placed in an anoxic chamber. All further operations were carried out under an O_2 -free atmosphere.

The 0.3 M stock Fe^{2+} solution was prepared by using $\text{FeCl}_2 \cdot 4\text{H}_2\text{O}$ obtained from Aldrich Chemical, Inc. To maintain the dissolved Fe as Fe^{II} , metallic Fe powder and HCl was added, the bottle was crimp-sealed, and the solution was boiled for 1 h during purging with purified N_2 gas. An aliquot for the experiment was filtered through a 0.22- μm filter in the anoxic chamber and analyzed for Fe^{II} content (final pH 3.0, $[\text{Fe}] = 0.3 \text{ M}$). Dissolved oxygen, total Fe, and possible Fe^{3+} content in the solution were monitored by using methods described below. These procedures were used before each set of experiments to refresh the stock solution, which was kept in the dark and used under anoxic conditions within 2 days. Aqueous U^{VI} was added from an acidified uranyl chloride stock solution (pH 2.0, $[\text{U}] = 0.01 \text{ M}$), prepared by dissolving UO_3 (obtained from STREM Chemicals, Newburyport, MA) in HCl and diluting to known volume.

2.2. Oxygen and carbon dioxide exclusion

Great care was taken to ensure complete O_2 removal from the samples. The atmosphere inside the anoxic chamber (Coy Laboratories, Inc.) used in the study was maintained at a 96:4 mixture of $\text{N}_2:\text{H}_2$ gases that was continuously cycled through a Pd catalyst to remove traces of oxygen. A Model 10 gas monitor (Coy Laboratories, Inc.) indicated $0 \pm 1 \text{ ppm}$ O_2 content in the chamber atmosphere at all times. All vessels, bottles, pipette tips, flasks, etc., were equilibrated for several days inside the anoxic atmosphere before use. The dissolved O_2 content in the samples and titrants was checked before and after all experiments by using a CHEMets[®] colorimetric analysis kit R-

7540 (2.5 ppb sensitivity). Solutions were used only if they tested negative for O_2 . Others have demonstrated decreased Fe^{II} concentration with time in solutions left open in the anoxic chamber (Jeon et al., 2004). Removal of Fe^{II} was attributed to oxidation by residual O_2 in the chamber atmosphere (i.e., O_2 not removed by the Pd scrubber), with an estimated half-time of 10 days. In our study, the experiments were completed within 2 h after opening of the purged bottles in the anoxic chamber and placement of the suspensions in a closed reaction vessel.

Complexation of U^{VI} by dissolved carbonate ligands significantly affects U speciation. To exclude this competing process from our experiments, dissolved CO_2 was removed from the solutions by bubbling with purified N_2 gas. After the sealed bottles were opened in the anoxic chamber, the samples were quickly transferred to the reaction vessel. The headspace was purged with gas from the anoxic chamber that had been passed through an Ascarite[®] column to remove CO_2 . Cyclic acid-base titrations of blank water samples treated the same way as the samples showed no evidence of dissolved carbonate for at least 4 h after the bottles were opened.

2.3. Acid-base titration and metal uptake

Titrations were carried out inside the anoxic chamber, using a computer-controlled TitraLab 90 titrator from Radiometer-Copenhagen. More information on the titrants, electrode, procedures, etc., can be found in the electronic annex. Samples for the XAFS experiments were brought to the desired pH by slow titration, transferred to 50-mL tubes (<1 mL headspace), and placed on an end-over-end rotator inside the anoxic chamber. A reaction time of 3 days was chosen on the basis of previous kinetic studies (Liger et al., 1999; Fredrickson et al., 2000; Jeon et al., 2005) and to allow time for possible mineral formation and particle ripening. Identical results were obtained in control samples after 4-months of reaction time. The solid and solution phases were separated in the anoxic atmosphere by filtration through a 0.22- μm membrane. The supernatants were acidified and brought out of the chamber for total Fe and U analysis with a Perkin-Elmer inductively coupled plasma-atomic emission spectrometer (ICP-AES) calibrated with matrix-matched standards. The estimated detection limits are 2 ppb for Fe and 15 ppb for U. To minimize experimental artifacts, 0.1 mM Y was added as an internal standard to all samples and standards. Measurements were made in triplicate, and the average and standard deviation were used. The Fe^{II} concentration was measured by using the ferrozine method (Sørensen, 1982).

2.4. X-ray absorption experiments/standards

The Fe K-edge and U L_{III} -edge XAFS experiments were carried out at the Materials Research Collaborative Access Team (MRCAT) beamline, sector 10 at the Advanced Photon Source (Segre et al., 2000). The beamline undulator was tapered, and the incident energy was scanned by using the Si(111) reflection of the double-crystal monochromator in quick-scanning mode (approximately 2 min per scan for

the extended region and 30 s per scan for the near-edge region). More details on the XAFS data collection and analysis procedures can be found in the electronic annex.

The filtered wet paste samples were mounted in drilled Plexiglas slides and sealed with Kapton film windows inside the anoxic chamber. Separate tests showed that sealed slides left in the air kept the sample inside anoxic for at least 8 h. In our experiments, the sealed slides were exposed to air for about 1 min while being transferred from an O₂-free container to the N₂-purged detector housing. All samples were handled identically.

Several solution and polycrystalline samples were used as XAFS standards in the analysis. Acidic (pH 2–3) solutions of ferrous and uranyl chloride were used as standards for the structure of hydrated Fe^{II} and U^{VI}. The structure of aqueous Me–acetate complexes (Me = Fe^{II}, U^{VI}) were used as analogues of the Me–carboxyl complex at the surface. For an aqueous Fe^{II}–acetate (Fe^{II}–Ac) complex, a solution of composition [Fe^{II}] = 60 mM, [Na–Ac] = 2 M, pH 6.1 [speciation: 90% FeAc₂, 8% FeAc, 2% Fe(aq)] was used. For an aqueous U^{VI}–Ac complex, a solution of composition [U^{VI}] = 1 mM, [Na–Ac] = 100 mM, pH 5.5 (speciation: 100% UAc₃) was used. The EXAFS amplitudes and phases calculated by FEFF were calibrated by using data from fine-powder standards of known Fe and U crystal structures, mounted on tape and measured in transmission mode or diluted in SiO₂ and measured in fluorescence mode. The powder uraninite (U^{IV}O₂) standard was purchased from Alfa Aesar and diluted 1:100 in SiO₂. X-ray diffraction indicated ~95% purity (Kelly et al., 2002).

3. RESULTS

3.1. Acid-base titrations

Fig. 1 shows added [OH⁻] vs. pH obtained by titration of the experimental systems with NaOH. Vertical differences between the unbuffered electrolyte curve (open up-triangles) and all other curves are indicative of OH⁻ consumption in reactions such as hydrolysis or precipitation of solvated metals, or in the formation of water with the H⁺ released from proton-active surface groups. The behavior of the isolated components (colloid, Fe, U) will be discussed first, followed by the binary (colloid + Fe, colloid + U), and ternary (colloid + Fe + U) systems.

For the carboxyl-modified colloid suspension, the release of adsorbed H⁺ starts at about pH 5.0 and continues throughout the pH range (solid triangles). The titration curve is significantly different from that of a monofunctional carboxylic acid in solution. Deprotonation starts at higher pH values in the colloid and is completed over a broader pH range. Such pH shift and broadening can be simulated for carboxyl groups (pK_a ~ 4) by surface electrostatic effects and by heterogeneity in the carboxyl ionization constant, both resulting from the carboxyl groups being confined to the surface. Indeed, titration curves showed a dependence on the background electrolyte concentration that indicates the presence of surface electrostatic effects. Analysis of the extended data set through use of double-layer models will be the subject of an upcoming report;

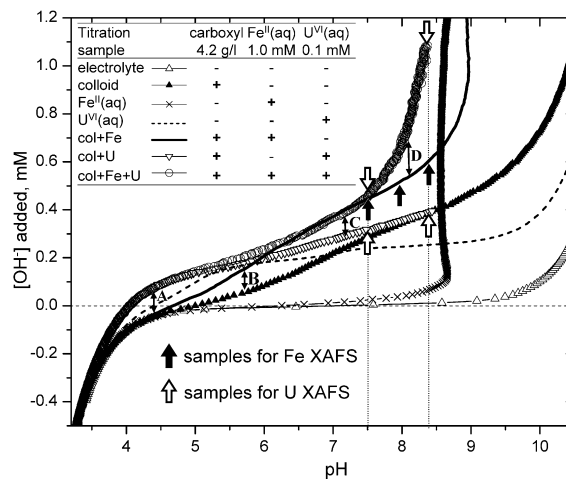


Fig. 1. Titration of acidified samples with 0.02 M NaOH. Double arrows (labeled A–D) point to differences in buffering capacity between samples that are discussed in the text. Block arrows show pH values at which filtered samples were prepared for XAFS analysis. The vertical dashed lines indicate the pH values at which XAFS spectra are compared. The table on the inset shows the composition of the titrated systems.

for the purposes of this study, only titrations at 0.03 M ionic strength will be considered. The H⁺ sorption capacity of the 4.2 g/L suspensions was calculated as 0.4 mM. For the homogeneous 1 mM FeCl₂ solution (Fig. 1, diagonal cross), the titration curve is consistent with that observed previously for Fe^{II} solutions (Arden, 1950; Doelsch et al., 2002). An interval of little or no OH⁻ consumption up to about pH 8.6 is followed by a vertical section with no pH change until the dissolved Fe^{II} pool is consumed, presumably in Fe(OH)₂ precipitate formation. No significant Fe^{III} appears to be present in the solution, in view of the absence of an additional step in the titration curve in the pH 5–7 range that would result from mixed Fe^{II}–Fe^{III} mineral formation (Arden, 1950). For 0.1 mM solutions of U^{VI}, the titration curve follows the electrolyte curve up to about pH 4.5, indicating the presence of only UO₂²⁺(aq) species. Subsequent steps were observed at higher pH, consistent with the formation of the U^{VI} hydrolysis complexes, such as UO₂OH⁺, UO₂(OH)₂⁰, (UO₂)₃(OH)₅⁺, and (UO₂)₄(OH)₇⁺, and precipitates (Grenthe et al., 1992).

Titration of the binary system colloid + Fe show increased OH⁻ consumption with pH relative to the colloid-only system (arrow B in Fig. 1). The OH⁻ consumption ratio between the two systems decreases from 3 at pH 5.5 until it levels off to 1.5 at pH 8.0, above which it increases again. Below a pH of approximately 7.5, the solvated Fe^{II} does not hydrolyze to a significant extent, so the additional buffering capacity observed in the binary colloid + Fe system is likely due to interactions between Fe^{II} and the colloid surface, such as proton release from the surface caused by Fe^{II} adsorption and/or hydroxylation of the adsorbed Fe^{II} (i.e., the formation of surface-Fe^{II}(OH)_n species). Both adsorption and hydroxylation are consistent with specific (inner-sphere) binding of Fe^{II} to the carboxyl. Non-specific binding is unlikely to result in such a large

increase in proton release, and hydroxylation of the otherwise hydroxylation-inert $\text{Fe}^{\text{II}}(\text{aq})$ at low pH is unlikely to occur unless a bound ligand from adsorption facilitates the loss of H^+ on the opposite side of the metal (a *trans* ligand effect). For the binary system colloid + U (down-triangles in Fig. 1), increased OH^- consumption relative to the colloid-only and U^{VI} -only systems begins in the pH range 3.5–5.0 (arrow A). The enhanced OH^- consumption suggests surface H^+ release caused by specific U^{VI} sorption onto the colloid surface. Because this pH range is mostly below that of aqueous U^{VI} hydrolysis, the sorbed species are likely non-hydrolyzed $\text{PS} - \text{COO}^- - \text{UO}_2^{2+} \cdot n\text{H}_2\text{O}$, where PS is the polystyrene group to which the surface COOH is attached. No hydrolysis steps are seen at higher pH in the titration curve, in contrast to titrations of aqueous U^{VI} , suggesting that the adsorbed U^{VI} ions do not hydrolyze or form oligomers as they do in the absence of the surface.

The titration curve of the ternary system, colloid + Fe + U, displays features from both the colloid + U and the colloid + Fe systems (open circles in Fig. 1). For pH values between 3.5 and 5.3 the curve follows that of the colloid + U system, indicating U sorption to the surface. At higher pH the slope of the curve increases relative to that of the colloid + U system, and for pH values between 6.2 and 7.5 the curve follows that of the colloid + Fe system (arrow C). The additional OH^- consumption relative to the colloid + U system in this pH region can be interpreted as resulting from proton release due to Fe^{II} sorption. The convergence of the colloid + Fe + U titration curve first with the colloid + U curve and then with the colloid + Fe curve is consistent with competitive adsorption of U, Fe, and H to a limited number of discrete sites, implying specific binding rather than non-specific electrostatic adsorption to a distributed surface charge. Between pH 7.5 and pH 8.4, the slope of the titration curve increases dramatically relative to that of the colloid + Fe (arrow D). The slope is much larger than that of the sum of the colloid + U and the colloid + Fe systems, and therefore the increased OH^- consumption is the result of some interaction between Fe and U at the surface. A likely cause for the steep increase is the onset of a mineral-forming reaction, in addition to the surface-proton release and hydrolysis reactions that may be going on. Speculating at this point that a $\text{U}^{\text{VI}} - \text{Fe}^{\text{II}}$ redox reaction is taking place, the forma-

tion of U^{IV} and Fe^{III} species will almost immediately exceed the solubility limit of U^{IV} - and Fe^{III} -containing minerals at this pH. We note that the reaction taking place above pH 7.5 occurs on the time scale of minutes, as the entire titration is completed within an hour.

3.2. XAFS spectroscopy

Suspensions of the binary (colloid + Fe and colloid + U) and the ternary (colloid + Fe + U) systems were prepared at pH values shown by block arrows in Fig. 1. All colloid + U and colloid + Fe samples, as well as the colloid + Fe + U sample at pH 7.5, had the same white color as did the acidified suspensions. Some flocculation of the suspension was observed in the colloid + Fe sample at pH 8.4. In contrast, the colloid + Fe + U suspension at pH 8.4 settled quickly and had a distinct gray-brown color (Fig. EA-2 in the electronic annex). The suspensions were filtered, and the supernatants were analyzed for total Fe and U content. The results are summarized in Table 2. The 0.1 mM uranium was removed from solution in all samples, whereas the 1.0 mM iron was partitioned between the solid and solution phases. The amounts of both adsorbed and solvated Fe^{II} were sufficient for stoichiometric reduction of 0.1 mM U^{VI} in all 4.2 g/L samples (i.e., >0.2 mM). Two control samples, colloid + Fe + U at pH 7.5 and pH 8.4, were sealed and filtered after 4 months in the anoxic atmosphere.

The hydrated solid phases were analyzed by Fe K-edge and U L_{III}-edge XAFS spectroscopy, which probed the valence and atomic structure of the adsorbed species. Control measurements showed that a 1 mM Fe^{II} solution produced a negligible absorption signal relative to the one measured in the wet pastes, so spectral contributions from Fe^{II} remaining in the pore water of the pastes can be neglected. The quality of the measured EXAFS data is illustrated in Fig. EA-3 in the electronic annex.

3.2.1. Fe K-edge XANES and EXAFS analysis

XANES measurements on the colloid + Fe pastes confirmed that the adsorbed Fe atoms were in the +2 valence state (Fig. EA-4 in the electronic annex). Fourier transforms (FT) of the EXAFS data are compared to standards in Fig. 2. Interpretation of the spectra is based on the coordination environment of Fe^{II} in crystal oxides/hydroxides

Table 2

Total Fe and U concentrations in the supernatants of the samples filtered for the XAFS experiments, $[\text{Me}]_{\text{sol}}$, determined by ICP-AES

Sample	pH	[colloid] (g/L)	$[\text{U}]_{\text{sol}}$ (mM)	$[\text{U}]_{\text{ads}}$ (mM)	$[\text{Fe}]_{\text{sol}}$ (mM)	$[\text{Fe}]_{\text{ads}}$ (mM)	U ($\text{\AA}^2/\text{atom}$)	Fe ($\text{\AA}^2/\text{atom}$)
Colloid + Fe	7.5	4.2	—	—	0.71	0.29	—	14.8
Colloid + Fe	8.4	4.2	—	—	0.55	0.45	—	9.5
Colloid + U	7.5	4.2	0.00	0.10	—	—	42.9	—
Colloid + U	8.4	4.2	0.00	0.10	—	—	42.9	—
Colloid + Fe + U	7.5	4.2	0.00	0.10	0.72	0.28	42.9	15.3
Colloid + Fe + U	8.4	4.2	0.00	0.10	0.31	0.69	42.9	6.2
Colloid + Fe + U	7.5	20.0	0.00	0.10	0.19	0.81	204.3	25.2
Colloid + Fe + U	8.4	20.0	0.00	0.10	0.09	0.91	204.3	22.5

Metal uptake, $[\text{Me}]_{\text{ads}}$, and calculated area per adsorbed metal atom are determined from $[\text{Me}]_{\text{sol}}$. The calculated H^+ sorption capacity of 4.2 g/L colloid suspensions is 0.4 mM. Standard deviations in concentration values are less than the accuracy shown.

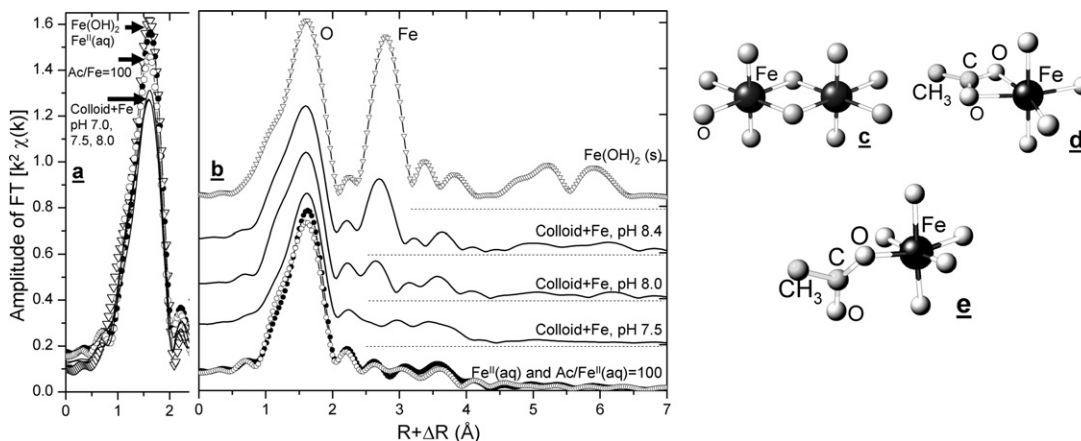


Fig. 2. Fourier transform of Fe K-edge EXAFS data (k^2 -weighted, $\Delta k = 2.4\text{--}10.5 \text{ \AA}^{-1}$ with a 1 \AA^{-1} Hanning window). (a) Comparison of O-shell peak amplitude. The line convention is the same as in (b). Arrows indicate the peak heights of the samples listed to the left of the arrows. (b) Comparison between colloid + Fe samples and standards. Spectra are offset vertically for clarity. (c) Bond geometry between Fe atoms in $\text{Fe}(\text{OH})_2$. (d) Bidentate binding mode of an acetate group to a metal atom. Both O atoms of the carboxyl group are involved in the bond. (e) Monodentate binding mode of an acetate group to a metal atom. Only one of the carboxyl O atoms participates in the bond.

and in solution. In crystalline $\text{Fe}(\text{OH})_2$, $\text{Fe}^{\text{II}}\text{--O}_6$ octahedra (six O atoms at 2.15 \AA) share edges (Fig. 2c) and form layered sheets, resulting in sixfold Fe–Fe coordination at 3.26 \AA in each layer (Lutz et al., 1994; Doelsch et al., 2002). The O shell is reflected in the single FT peak at around 1.6 \AA , and the sixfold Fe–Fe coordination is reflected in the single FT peak around 2.8 \AA in the $\text{Fe}(\text{OH})_2$ standard spectrum. The three data sets for Fe^{II} sorbed to the carboxyl colloid have the smallest amplitude of the 1.6 \AA peak (Fig. 2a). Modeling of the Fe EXAFS data is given in Fig. EA-5 in the electronic annex. It indicates a broader distribution of Fe–O distances (larger Debye–Waller factor) relative to that in the solution standards and is consistent with replacement of hydration water molecule(s) by ligand oxygen atom(s). Comparisons of the FT structure at $1.9\text{--}2.3 \text{ \AA}$ between the colloid + Fe, the Fe^{II} –acetate standard, and the hydrated Fe^{II} standard show no evidence of a C atom signal in any of the spectra. A bidentate metal–carboxyl complex (Fig. 2d) typically produces a feature in that region due to coherent backscattering from the C atom, as in the cases of Cd^{II} and U^{VI} (Kelly et al., 2002; Boyanov et al., 2003). Conversely, no C atom feature is seen in spectra from a monodentate (Fig. 2e) Cu^{II} –acetate complex (Boyanov, 2003), likely because of loss of C backscattering coherence due to vibrations in this more flexible complex type. In the case of the colloid + Fe system, the lack of C signal, together with the indication of inner-sphere complexation from both the titration and the first-shell EXAFS data, strongly suggest a monodentate Fe^{II} –carboxyl complex as the adsorption mechanism. The FT data at 2.8 \AA in the colloid + Fe spectra show no evidence of Fe–Fe coordination at pH 7.5, whereas increasing Fe–Fe coordination is seen at pH 8.0 and 8.4. The average Fe^{II} – Fe^{II} coordination of 3 ± 1 atoms obtained by fitting the pH 8.4 spectrum is lower than in bulk $\text{Fe}(\text{OH})_2$; this can be explained either if about 50% of the Fe atoms in the sample are in a bulk precipitate and the rest are adsorbed as monomeric atoms, or by undercoordination of the surface

Fe atoms in nanometer-sized $\text{Fe}(\text{OH})_2$ particles that are attached to the polystyrene microspheres. Fits of the EXAFS data indicate strain in the Fe–O bonds, which suggests that a bulk $\text{Fe}(\text{OH})_2$ precipitate is not formed (Fig. EA-5 in the electronic annex shows contraction of the distances and larger Debye–Waller factors in the pH 8.4 system relative to the $\text{Fe}(\text{OH})_2$ standard). Regardless of the form of the phase with Fe–Fe coordination, the EXAFS data establish the presence of oligomeric edge-sharing Fe^{II} octahedra in the solid phase at pH 8.4 (schematic bond structure shown on Fig. 2c), whereas only monomeric species are present at pH 7.5. “Oligomeric” here is used in the sense of “having local Fe^{II} – Fe^{II} coordination”, which can include Fe dimers, polymers, or bulk precipitate.

3.2.2. U L_{III} -edge XANES analysis

Fig. 3 compares U XANES data from the colloid + U and colloid + Fe + U systems to standards. A higher energy position of the absorption edge and a shoulder at $17,190 \text{ eV}$ are indicative of U in the +6 valence state and the UO_2^{2+} (uranyl) coordination geometry (Hudson et al., 1995; O’Loughlin et al., 2003). A lower energy position of the edge, lack of the shoulder at $17,190 \text{ eV}$, and higher amplitude of the peak immediately after the edge indicate U in the +4 valence state. The XANES data verify the predominantly U^{VI} state and uranyl geometry in the colloid + U system (within the experimental uncertainty). In the ternary colloid + Fe + U system, U is present predominantly as U^{VI} at pH 7.5 and predominantly as U^{IV} at pH 8.4. The same results were obtained for the pH 7.5 and pH 8.4 samples that were left for 4 months in the anoxic atmosphere. Typical accuracy of valence state determinations from XANES data is about 10–15%.

3.2.3. U^{VI} EXAFS analysis

Fig. 4 compares EXAFS data from the three U^{VI} samples to data from two aqueous standards: a hydrated and an acetate bound U^{VI} . The magnitude of the FT between

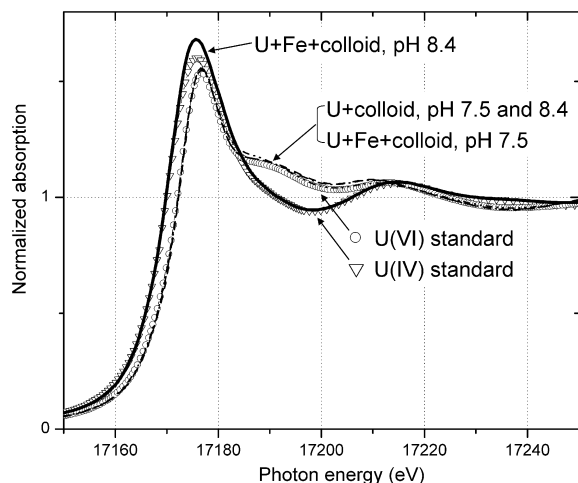


Fig. 3. Normalized uranium L_{III}-edge XANES spectra from the colloid + U (+Fe) samples compared to a U^{VI} and U^{IV} standard. An edge position at higher energy and a shoulder at 17,190 eV indicates U^{VI}, whereas an edge position at lower energy and lack of the shoulder indicate U^{IV}.

1.0 and 2.2 Å displays the splitting of the O near-neighbors in an axial and an equatorial shell, characteristic of the uranyl geometry. Two axial O atoms at about 1.75 Å and 4–6 equatorial O atoms at larger distance, usually 2.3–2.5 Å, are seen in many U^{VI} compounds (Morosin, 1978; Templeton et al., 1985; Fischer, 2003; Kubatko and Burns, 2004). The axial atoms are inert to chemical substitution, so complexation occurs in the equatorial plane. A comparison between the hydrated and acetate-bound U^{VI} standards shows the effect of substituting equatorial water molecules with a carboxyl ligand (vertical lines on Fig. 4). The feature of interest is better seen in the real part of the FT (inset).

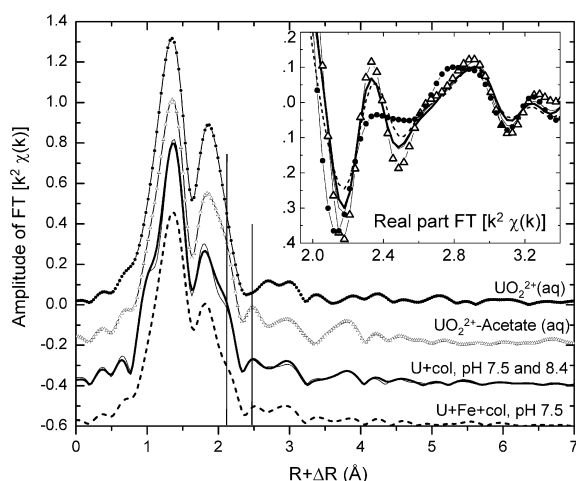


Fig. 4. Fourier transform of U L-edge EXAFS data from U^{VI} samples and standards (k^2 -weighted, $\Delta k = 2.8$ – 13.5 \AA^{-1} with a 1 \AA^{-1} Hanning window). Vertical lines indicate the positions of features resulting from the C shell contribution in the EXAFS data. Inset: Real part of the FT in a smaller R -range. The line convention is the same as for the magnitude of FT.

The acetate-bound U^{VI} standard (triangles) shows an oscillation centered at around 2.4 Å relative to the hydrated U^{VI} (circles). Modeling shows that this feature is due to C atom(s) in a bidentate geometry (Fig. EA-6 in the electronic annex), consistent with previous work (Kelly et al., 2002). Therefore, U^{VI} is adsorbed to the carboxyl colloid as a bidentate carboxyl complex. The C signal amplitude in the adsorbed U spectra is smaller than that in the U^{VI}-acetate standard (speciation 100% [UO₂Ac₃]), suggesting a 1:1 or 1:2 U^{VI}:acetate stoichiometry. Exact stoichiometry assignment is problematic, given the dependence of EXAFS amplitudes on both coordination number and Debye–Waller factor (related to the bond strength), and the unknown, likely inverse relation between bond strength and bond number. No evidence of a U near-neighbor is observed in any of the three spectra, indicating lack of significant U oligomerization between the adsorbed U^{VI} atoms. There is also no evidence of an Fe backscatterer in the colloid + Fe + U spectrum at pH 7.5, indicating lack of bonds between the adsorbed Fe^{II} and U^{VI} atoms in the ternary system. The colloid + U samples at both pH 7.5 and pH 8.4 have nearly identical spectra, indicating that no change in adsorbed U^{VI} speciation occurs over this pH range.

3.2.4. U^{IV} EXAFS analysis

Fig. 5 compares data for the colloid + Fe + U system at pH 8.4 to data for a U^{IV} standard, a UO₂ (uraninite) mineral. The features of the FT magnitude are similar to those of the uraninite standard, but the amplitudes of the peaks in the colloid + Fe + U spectrum are significantly smaller. The peak at 1.8 Å is due to the cubical O shell in UO₂, whereas the double peak between 2.9 and 4.5 Å is mostly due to the 12-member U shell at $R = 3.87 \text{ \AA}$ in UO₂, the splitting coming from the characteristic backscattering amplitude of U. Modeling of the data shows that the

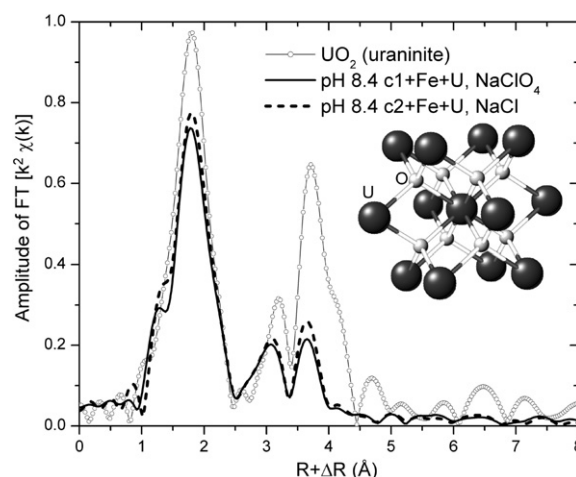


Fig. 5. Fourier transform of U L-edge EXAFS data for U^{IV} samples and standards (k^2 -weighted, $\Delta k = 2.2$ – 10.4 \AA^{-1} with a 1 \AA^{-1} Hanning window). The dashed line shows the repeatability of the spectrum with a different electrolyte and a different batch of adsorbent, measured during a different beamline experiment. The crystal structure of uraninite, UO₂, is illustrated in the inset.

smaller amplitude of the 1.8 Å peak is due to a larger Debye–Waller factor (Table 3A and B), indicating a broader U–O bond length distribution in the colloid + Fe + U sample than in the UO₂ standard. When modeled with a single U shell, the smaller doublet amplitude in the colloid + Fe + U data at pH 8.4 can be attributed to smaller average U–U coordination and larger disorder in that shell relative to the standard (Table 3A and B). The drop in average coordination number from 12 in crystalline UO₂ to 6.9 ± 2.7 in the colloid + Fe + U pH 8.4 system can be attributed to either partitioning of the U^{IV} between a monomeric phase and a precipitate, or formation of nanometer-sized uraninite particles. In the latter, more likely case, we estimate the average particle size to be less than 3.5 nm in diameter (Fig. EA-7 in the electronic annex).

The presence of U^{IV} in nanoparticulate form may also be the reason why the structure between 3 and 4.5 Å (Fig. 5) appears simpler in the pH 8.4 sample than in the uraninite standard. Disorder caused by strain in a small particle is likely to reduce the spectral contribution of multiple-scattering and outer-shell paths significantly more than that of single-scattering paths, resulting in mostly single-scattering content in the pH 8.4 spectrum.

Further analysis of the doublet between 3 and 4 Å in Fig. 5 reveals that the peak amplitudes are in about 1:2 ratio for the UO₂ standard, whereas that ratio is about 1:1 in the pH 8.4 sample. Equal ratios are expected in the two spectra if the amplitude difference between the sample and standard is due to the difference in U–U coordination only. The reason for this different amplitude ratio was

Table 3
Results from modeling of the U^{IV} EXAFS data^a

Shell	<i>N</i>	<i>R</i> (Å)	σ^2 (10^{-3} Å ²) ^b	ΔE_0 (eV)	Fit quality ^c
(A) UO ₂ standard					
O→	8.0	2.37 ± 0.01	6.7 ± 2.1	−2.1 ± 0.8	208
MS→	8.0	4.73 ± 0.02	13.4 ± 4.2	−2.1 ± 0.8	0.037
O2→	24.0	4.54 ± 0.04	16.6 ± 8.6	−2.1 ± 0.8	9
U→	12.0	3.88 ± 0.01	4.4 ± 1.2	−2.1 ± 0.8	
(B) U + Fe + colloid, pH 8.4, full <i>R</i> -range					
O→	7.9 ± 0.6	2.36 ± 0.01	10.9 ± 1.7	−0.7 ± 0.6	241
MS→	7.9 ± 0.6	4.73 ± 0.02	21.8 ± 3.4	−0.7 ± 0.6	0.016
O2→	24.0	4.43 ± 0.09	48.9 ± 16.6	−0.7 ± 0.6	8
U→	6.9 ± 2.7	3.84 ± 0.02	9.1 ± 3.3	−0.7 ± 0.6	
(C) U + Fe + colloid, pH 8.4, limited <i>R</i> -range					
O→	7.9	2.36	10.9	−0.7	190
MS→	7.9	4.73	21.8	−0.7	0.047
O2→	24.0	4.42 ± 0.07	51 ± 13	−0.7	5
U→	6.5 ± 2.3	3.85 ± 0.02	8.7 ± 3.0	−0.7	
(D) U + Fe + colloid, pH 8.4, limited <i>R</i> -range, unconstrained Fe					
O→	7.9	2.36	10.9	−0.7	60
MS→	7.9	4.73	21.8	−0.7	0.006
O2→	24.0	4.47 ± 0.04	39.8 ± 10.0	−0.7	2
U→	8.5 ± 2.1	3.85 ± 0.01	10.7 ± 1.9	−0.7	
Fe→	4.2 ± 4.5	3.56 ± 0.03	21.4 ± 13.3	−0.7	
(E) U + Fe + colloid, pH 8.4, limited <i>R</i> -range, constrained Fe					
O→	7.9	2.36	10.9	−0.7	61
MS→	7.9	4.73	21.8	−0.7	0.009
O2→	24.0	4.46 ± 0.04	45.5 ± 7.2	−0.7	3
U→	8.1 ± 1.8	3.85 ± 0.01	11.1 ± 2.0	−0.7	
Fe→	1.5 ± 0.4	3.56 ± 0.02	10.0	−0.7	

(A) Fit of the uraninite (UO₂) standard data in the range $R + \Delta R = 1.41\text{--}4.35$ Å.

(B) Fit of the U + Fe + colloid data in the range $R + \Delta R = 1.41\text{--}4.35$ Å using the uraninite model.

(C) Fit of the U + Fe + colloid data in the range $R + \Delta R = 2.82\text{--}4.35$ Å using the uraninite model with fixed first-shell parameters.

(D) Fit of the U + Fe + colloid data in the range $R + \Delta R = 2.82\text{--}4.35$ Å using the uraninite model with an added Fe shell.

(E) Fit of the U + Fe + colloid data in the range $R + \Delta R = 2.82\text{--}4.35$ Å using the UO₂ + Fe shell model with constrained Debye–Waller factor.

^a Parameters for which uncertainties are not given are held constant during the fit. Uncertainties are estimated by the FEFFIT program. A single ΔE_0 parameter was refined for all shells. Multiple-scattering (MS) parameters for the O shell were constrained to those for the single-scattering paths, assuming uncorrelated thermal motion in the O shell ($N_{MS} = N_O$, $R_{MS} = 2R_O$, and $\sigma_{MS}^2 = 2\sigma_O^2$).

^b Disorder parameter (EXAFS Debye–Waller factor).

^c Given from top to bottom for each fit are χ^2_ν (goodness-of-fit indicator taking into account the number of data points and variables used), *R*-factor (the fractional misfit: difference between data and model relative to the absolute value of the data), and degrees of freedom in the fit (number of independent points minus number of variables). More information on these parameters is given in the FEFFIT documentation (see Section 2.2).

determined by simultaneously fitting the k^1 , k^2 , and k^3 weighted EXAFS spectra with the same set of parameters (Kelly et al., 2002; Haskell et al., 2004). The detailed analytical procedure is given in the electronic annex. Modeling of the uraninite standard data at k^1 , k^2 , and k^3 weights is shown at the top of Fig. 6a. The uraninite model reproduces well the features of the data simultaneously at all k^n weights with parameters given in Table 3A. The same model, when applied to the reduced uranium data from the colloid + Fe + U system at pH 8.4, is unable to reproduce the amplitude ratio and features in the U doublet at all three k^n -weights (Fig. 6b and Table 3B). The addition of a third or fourth cumulant disorder parameter to the U shell also did not improve the fit. All of the above suggests the presence of a spectral contribution around 3.1 Å in the pH 8.4 system that is not present in the uraninite standard.

The best fit of the data was obtained by adding an Fe shell at 3.56 Å to the model used for the uraninite standard. Details on why this model was chosen and how it compensates the misfit at all three k^n FT weights are given in the

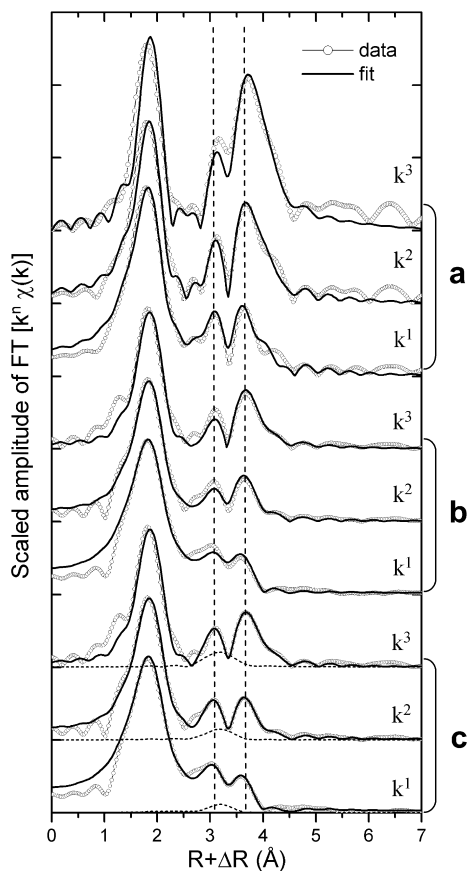


Fig. 6. FEFF8/FEFFIT modeling of data from U^{IV} samples. Fourier-transformed $k^n\chi(k)$ data are scaled as follows: $k^3 \times 1$, $k^2 \times 5$, $k^1 \times 23$. Fit parameters are given in Table 3. Vertical dashed lines indicate the peak positions of the U doublet. (a) UO_2 data modeled with the O + U shell model, (b) colloid + Fe + U sample at pH 8.4 modeled with the O + U shell model, (c) colloid + Fe + U sample at pH 8.4 modeled with the O + U + Fe shell model. The contribution from the Fe atoms is given by the dashed peaks.

electronic annex. The quality of the fit is shown in Fig. 6c, and the parameters from an unconstrained Fe-shell fit are given in Table 3D. The strong correlation between the coordination number and Debye–Waller (σ^2) of the Fe shell was removed by assuming a σ^2 of 0.010 \AA^2 for the Fe shell (similar to that obtained for the O shell), and a constrained fit produced the parameters in Table 3E. Applying a range of reasonable constraints for the Debye–Waller factor ($0.005\text{--}0.015 \text{ \AA}^2$) yielded a coordination number between 1 and 2 Fe atoms around each U^{IV} atom.

An edge-sharing U^{IV} –Fe complex geometry is compared to the uraninite U^{IV} – U^{IV} coordination geometry in Fig. 7. Assuming that the U–O bond geometry is not affected by the Fe atom, we calculated an Fe–O distance of 2.12 Å and an O–Fe–O angle of 80 deg from the observed U–Fe distance. Some adjustment of the bond angles can be expected in a U–Fe complex, leading to slightly shorter or longer Fe–O distances. The geometrically derived Fe–O distance and O–Fe–O angle are consistent with Fe octahedra found in Fe^{II} compounds [2.15 Å in FeO , $Fe(OH)_2$, and $FeCO_3$], Fe^{III} oxides/hydroxides [1.95–2.09 Å in hematite, goethite, lepidocrocite], and magnetite [2.06 Å for octahedral Fe^{II} or Fe^{III}] (Wyckoff, 1960; Blake et al., 1966; Forsyth et al., 1968; Christensen et al., 1982; Wechsler et al., 1984; Lutz et al., 1994).

The spectrum of the colloid + Fe + U pH 8.4 sample, showing smaller U^{IV} – U^{IV} coordination and Fe in the local U^{IV} environment, could be the result of two possible scenarios. If all U^{IV} is in a single phase, the observed average local environment can be achieved in the structure shown in Fig. EA-8 in the electronic annex. This structure can be described as an Fe-coated uraninite plate, in which an interface between oligomeric U^{IV} and Fe species produces the U–Fe and U–U coordination observed by EXAFS. Alternatively, U^{IV} may be partitioned between two phases: U^{IV} in uraninite particles and monomeric U^{IV} adsorbed in an edge-sharing geometry to the $Fe^{II,III}$ oxide/hydroxide produced from Fe^{II} oxidation. This scenario seems less likely, because the amount of uranium in each of the latter phases needs to be comparable to produce the observed spectrum.

3.2.5. Fe XAFS analysis of the Colloid + Fe + U system

The colloid + Fe + U pH 8.4 sample was also analyzed by Fe XAFS to correlate U^{VI} reduction with Fe^{II} oxidation

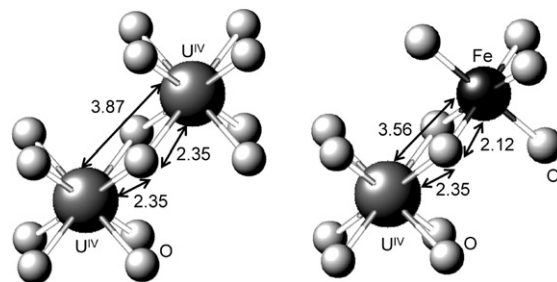


Fig. 7. Geometry of the U–U bond in uraninite (left), compared to the U–Fe coordination obtained in the colloid + Fe + U sample at pH 8.4 (right). The Fe–O bond distance and the O–Fe–O bond angle of 80 deg were calculated from the U–Fe bond distance.

and to characterize the resulting Fe phase. Interpretation of the data is problematic, because less than 30% of the Fe atoms present in the sample are expected to be oxidized. Table 2 shows that the 0.1 mM U was completely removed from solution and that total Fe in the solid phase was about 0.7 mM. Assuming that the oxidized Fe^{III} produced by stoichiometric reduction of U^{VI} was all present in the solid phase, the Fe^{III}/Fe^{II} ratio should be less than 30% (0.2/0.7). Fig. 8a compares the XANES data to Fe standards of valence state between +2 and +3. The edge position and shape of the pH 8.4 spectrum are consistent with an Fe^{III}/Fe^{II} ratio of 30% or less, and they show a higher Fe^{III}/Fe^{II} ratio at pH 8.4 than at pH 7.5. The higher Fe^{III} content, concurrent with U^{VI} reduction in the pH 8.4 sample, is evidence of the electron transfer from Fe^{II} to U^{VI} atoms.

Fig. 8b shows the Fe EXAFS data. Spectra from the colloid + Fe ± U samples at pH 7.5 are identical, indicating the same monomeric Fe^{II} species regardless of the presence

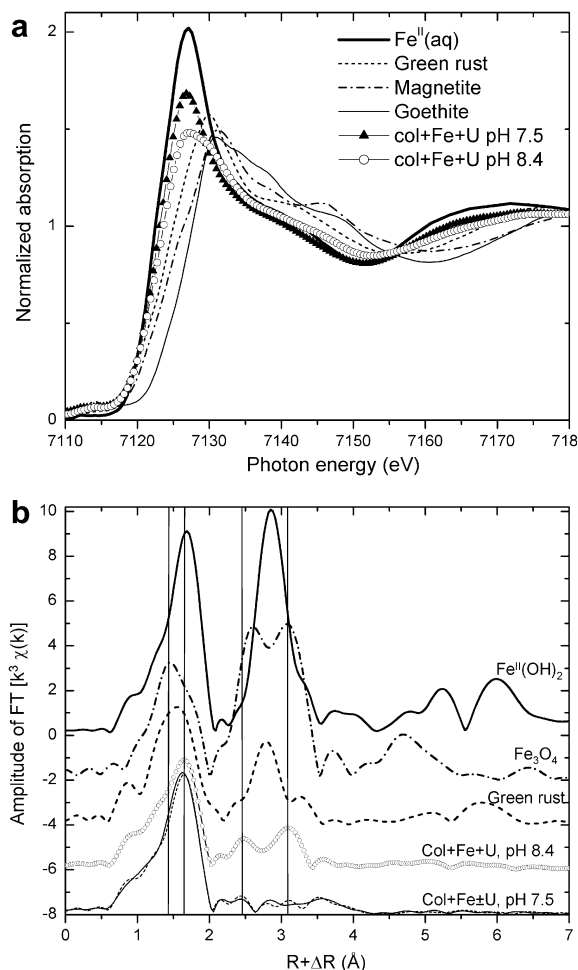


Fig. 8. Fe K-edge data from colloid + Fe + U samples compared to standards. (a) XANES, (b) FT of EXAFS. The similar FT magnitudes of spectra from samples with and without U at pH 7.5 are shown at the bottom. Vertical lines indicate the similarity of EXAFS features between the Fe + U + col sample at pH 8.4 and magnetite.

of adsorbed U^{VI}. In contrast, the spectrum of the colloid + Fe + U pH 8.4 sample shows peaks between 2.3 and 3.5 Å that are likely due to adjacent Fe atoms in an iron mineral structure or structures. As already discussed, interpretation of data from this sample is complicated by the presence of mixed Fe^{II}/Fe^{III} species. Comparison to the spectra of standards that are representative of the possible end phases (Fe^{II}, Fe^{III}, and mixed-valence minerals, e.g., Fe(OH)₂, green rust, magnetite, goethite, hematite, etc.) shows that the second-shell structure is most similar to that of magnetite. Magnetite is a common product of Fe^{II} oxidation in bacterial and abiotic systems at circum-neutral pH (Cornell and Schwertman, 1996; Chaudhuri et al., 2001) and can therefore be anticipated in the pH 8.4 system as well. The reduced O and Fe peak amplitudes relative to the standard are consistent with partitioning of the Fe between magnetite and adsorbed Fe^{II}.

3.2.6. Effect of surface area and Fe^{II} concentration on U^{VI} reduction

Increasing the suspension concentration in the colloid + Fe + U system from 4.2 to 20 g/L while keeping the concentrations of U and Fe constant resulted in the removal of more Fe from the solution at both pH 7.5 and 8.4 (Table 2). The U XANES spectra of the samples at both pH 7.5 and 8.4 were identical to those of the colloid + U only system at 4.2 g/L loading (Fig. 3), indicating that U^{VI} reduction was not occurring in any of the 20-g/L samples after 3 days. The spectra of 4.2-g/L colloid + Fe + U samples at pH 8.4 in which the Fe^{II} concentration was reduced from 1.0 to 0.4 mM were also identical to those of the colloid + U system, indicating no significant U^{VI} reduction after 3 days. Fe K-edge EXAFS on the samples described above (increased surface area and decreased Fe concentration) showed no Fe–Fe coordination peaks in the spectra, indicating no Fe^{II} oligomerization under these conditions.

3.2.7. Reoxidation of the reduced U particles in air

Following a U XANES measurement of an anoxic colloid + Fe + U sample at pH 8.4 (~100% U^{IV}), the surface of the wet sample was exposed to air. No significant oxidation was seen within 15 min. After that, the U^{VI}/U^{IV} ratio increased at approximately 10% h⁻¹ for the first 7 h. The next XANES measurement after 21 h of exposure to air showed 100% reoxidation to U^{VI}. These measurements show that the reduced U^{IV} product in the pH 8.4 colloid + Fe + U system is unstable to oxidation in air and provide an estimate of the rate of oxidation. They also serve as control experiments, showing that the anoxically sealed samples are not susceptible to possible oxidation during the measurement in a way that can be noticed in the XAFS spectra or analysis.

4. DISCUSSION

The combination of pH titrations, uptake measurements, and XAFS spectroscopy allows us to look for correlations between the reactivity and the speciation of the same system. Such correlations provide important insight and

constrain our mechanistic interpretation of both adsorption and redox processes. When molecular information about speciation at a surface is unavailable, the tendency is to extrapolate bulk speciation to the surface. This may not be accurate if the electrostatic and steric contributions to the surface binding energy are significant, and may result in inaccurate interpretation of observed reactivity. The following results in our work underscore this point.

In studying the adsorption of Fe^{II} to the carboxyl surface, we observed additional OH^- consumption in the colloid + Fe system relative to the colloid by itself (Fig. 1, arrow B). Without knowledge of the molecular structure of the adsorbate, the OH^- balance can be explained by (1) carboxyl deprotonation due to changes in surface electrostatics caused by outer-sphere Fe^{II} adsorption, (2) deprotonation (H^+ displacement) caused by inner-sphere Fe^{II} adsorption, or (3) hydrolysis of the adsorbed Fe^{II} species. However, the relatively disordered O shell of the adsorbed Fe^{II} atoms observed by EXAFS, together with the significant OH^- consumption in titration experiments, suggests an inner-sphere complexation mechanism. This result is unexpected in view of the small binding affinity of Fe^{II} to carboxyl ligands [$\text{Log} K = 0.54$, (Martell et al., 2001)]. Unfortunately, EXAFS cannot determine unequivocally whether the adsorbed Fe^{II} species are hydrolyzed. We speculate that the adsorbed Fe^{II} species are probably not hydrolyzed, because substitution of hydration molecule(s) for OH^- ligand(s), with the resulting charge neutralization of the adsorbed cation, is likely to lead to changes in the O shell larger than those observed by EXAFS. The reactivity implication of inner-sphere-adsorbed Fe^{II} is higher redox reactivity than a fully hydrated adsorbed species.

Another example of unexpected speciation is the observed Fe^{II} oligomerization in the colloid + Fe system at pH 8.0 and pH 8.4. The titration curve shows no significant change in slope between pH 7.5 and pH 8.4 (Fig. 1) and precipitation of the aqueous Fe^{II} phase in the system presumably occurs around pH 8.8 (vertical section). Fe^{II} uptake also does not conclusively establish precipitation, because uptake at pH 8.4 is about the same as the total surface site concentration (Table 2). Because of the large spread of $\text{Fe}(\text{OH})_2(\text{s})$ solubility constants in the literature ($\text{Log} K_{\text{sp}}$ range from -13.1 to -15.3 , Leussing and Koltzoff, 1953), we could not determine whether the $\text{Fe}^{\text{II}}\text{-Fe}^{\text{II}}$ coordination is predicted from supersaturation of the solution phase at pH 8.4 or is the result of oligomerization of surface species at undersaturated conditions. The EXAFS results however provide unequivocal evidence of $\text{Fe}^{\text{II}}\text{-Fe}^{\text{II}}$ coordination (i.e., Fe^{II} oligomerization) in the solid phase. Oligomerization implies the presence of hydrolyzed Fe^{II} species that combine to form oligomers. The reactivity implication from the presence of hydrolyzed/oligomerized Fe^{II} species is higher redox reactivity above pH 8.0.

Similarly for U^{VI} adsorbed to the carboxyl surface, the speciation observed in the colloid + U system appears different from that expected in bulk solution. A calculation for a solution containing no carbonate, 0.1 mM uranium, and 0.6 mM acetate, considering only hydrolysis and acetate-complexation reactions, showed that U^{VI} hydrolysis polymers should dominate the speciation at circumneutral

pH and that $\text{U}^{\text{VI}}\text{-carboxyl}$ complexes should exist only as a minor component between pH 4 and 5 (Fig. EA-9 in the electronic annex) (Grenthe et al., 1992; Martell et al., 2001). However, no hydrolysis steps were seen in pH titrations of the colloid + U system. The EXAFS data show that U hydrolysis oligomers are not present in the samples and that surface carboxyl complexation is responsible for the U uptake. The observations above suggest that surface complexation is responsible for the uptake throughout the pH range and that $\text{U}^{\text{VI}}\text{-carboxyl}$ stability constants in the presence of a surface are significantly higher than those determined in bulk solution under the same conditions.

Our redox reactivity results show that monomeric adsorption of U^{VI} and Fe^{II} to the carboxyl surface (pH 7.5) does not lead to U^{VI} reduction over at least 4 months, despite sufficient surface and aqueous Fe^{II} concentrations for a stoichiometric reaction. These results suggest that both aqueous and carboxyl-adsorbed monomeric Fe^{II} species are not redox reactive toward U^{VI} under these conditions. Conversely, under conditions where Fe^{II} oligomers form in the colloid + Fe system (pH 8.4), complete and rapid reduction of U^{VI} occurs in the colloid + Fe + U system. EXAFS shows that speciation of the inner-sphere-adsorbed U^{VI} atoms does not change from pH 7.5 to pH 8.4 in the colloid + U system. Therefore, the increased reactivity at pH 8.4 relative to pH 7.5 is attributed to the difference in Fe^{II} speciation.

One possible mechanism for the increased Fe^{II} reactivity is a ligand effect. Binding to electron donor ligands (e.g., OH^- or CH_3COO^-) generally lowers the redox potential of reductant metals, presumably by increasing the electron density at the metal and facilitating the loss of electrons on the opposite side of the metal (Stumm, 1992; Sposito, 2004). Higher stability (i.e., lower energy) of an oxidized $\text{Fe}^{\text{III}}\text{-ligand}$ complex relative to the reduced $\text{Fe}^{\text{II}}\text{-ligand}$ complex may also provide a driving force for the electron transfer. Evidence for such effects are found in previous work: addition of carboxyl ligands increased the rate of Cr^{VI} and oxamyl reduction by Fe^{II} (Buerge and Hug, 1998; Strathmann and Stone, 2002); hydroxyl ligands were found to increase Fe^{II} reactivity towards O_2 , Cr^{VI} , and organic pollutants (Sposito, 2004) (p.100 and references within). In the colloid + Fe + U system at pH 7.5, U^{VI} reduction is not enhanced by Fe^{II} complexation to the surface carboxyl, implying that a ligand effect is not sufficient to overcome the barrier to U^{VI} reduction. This implication does not preclude a ligand effect from hydroxylation, as the hydroxyl ligand might be a better electron donor than the carboxyl, or it might bridge between the Fe and U atoms. In kinetic measurements, the increased rate of U^{VI} removal in the presence of Fe^{II} and hematite was correlated to the amount of hydroxylated surface-adsorbed Fe^{II} species, $>\text{Fe}^{\text{III}}\text{O-Fe}^{\text{II}}\text{OH}^0$ (Liger et al., 1999). The surface hydroxylation hypothesis is also frequently used to explain increased reactivity of Fe^{II} in suspensions of metal oxides (e.g., Wehrli et al., 1989; Buerge and Hug, 1999; Strathmann and Stone, 2003; Elsner et al., 2004). However, the inherent uncertainty associated with surface speciation from titration data and the possibility of electron transfer through the oxide interface (Williams and Scherer, 2004) leaves other possibil-

ities open. Our results from the increased-surface-area system at pH 8.4 (see Section 3.2.6) do not support surface species hydroxylation as the reason for enhanced reactivity in our system. The increase in the amount of adsorbed Fe^{II} at pH 8.4 with surface area (Table 2) should increase the amount of hydroxylated surface species present. The fact that we see complete U^{VI} reduction at low surface area and no reduction at high surface area suggests that (1) hydroxylated surface Fe^{II} species are not the species responsible for enhanced U^{VI} reduction, and (2) the actual reactive species are formed from the dissolved Fe^{II} species pool, which is decreased when the surface area is increased.

Exclusion of aqueous, carboxyl-adsorbed, and hydroxylated-adsorbed Fe^{II} species as the reactive species at pH 8.4 leaves aqueous FeOH⁺ and oligomerized Fe(OH)₂-like species as possibilities (see Fig. 2c for the structure of the Fe–Fe bond in Fe(OH)₂). The Fe–Fe coordination observed at pH 8.4 in the low-surface-area system confirms the presence of the latter, but the former cannot be excluded. Although reactivity enhancement by OH[−] ligands in FeOH⁺ and Fe(OH)₂-like species appears to be a well-established mechanism (Sposito, 2004), the observed Fe–Fe coordination and the U^{VI} reduction occurring under the same conditions suggest another possible mechanism for increased Fe^{II} reactivity specifically toward U^{VI}: facilitation of the two-electron transfer by Fe^{II} oligomerization. Monomeric Fe^{II} can reduce oxidants that go through one-electron reduction steps (e.g., Cr^{VI}), so no obstacle for electron transfer from Fe^{II} to U^{VI} is apparent. Uranium is peculiar in that aqueous U^V rapidly disproportionates to U^{VI} and U^{IV} (Ekstrom, 1974). Thus, if aqueous U^V is the result of the one-electron transfer, then the reduction to U^{IV} should be completed through disproportionation. In the systems where reduction to U^{IV} does not occur, a bound U^V species must be formed. If the bound U^V species are stable, they will accumulate over time and be observable. We detected no U^V atoms by XAFS in the systems where reduction did not occur (colloid + Fe + U system at pH 7.5 or with increased surface area at pH 8.4), either by the edge position or by elongation of the axial U–O bond (Docrat et al., 1999). This result suggests that the hypothesized U^V–Fe^{III} intermediate is short-lived and experiences a quick electron back transfer to return to the original Fe^{II} and U^{VI} species. Such a non-productive pathway is known as a dead-end intermediate pathway (Haim, 1983). To complete the reduction to U^{IV}, a second electron needs to be transferred during the lifetime of the U^V intermediate. In aqueous solution with monomeric species, a three-body correlation between a U^{VI} and two Fe^{II} atoms is essentially required. The probability for this is exceedingly small; it likely provides the kinetic limitation to the U^{VI}–Fe^{II} reaction in solution. Conversely, if the Fe^{II} oligomer is already formed, a net two-electron transfer can occur more efficiently through the bonds between Fe^{II} atoms during the lifetime of the intermediate. Facilitation of a second electron transfer to a bound U^V species may also be the reason for the commonly observed high efficiency of U^{VI} reduction by Fe^{II} in the presence of oxide surfaces (Wersin et al., 1994; Liger et al., 1999; O’Loughlin et al., 2003; Ilton et al., 2004; Jeon et al., 2005). Adsorbed U^V species have

been observed on dried mica surfaces by X-ray photoelectron spectroscopy (Ilton et al., 2005). Moderate stabilization of the U^V moiety by the surface is likely to provide greater opportunity for complete reduction to U^{IV}. Combined with possible electron transfer through the oxide (Williams and Scherer, 2004), the overall catalytic role of oxides may be to provide a second electron non-locally from adsorbed or structural Fe^{II} atoms to a stabilized U^V intermediate.

The proposed two-electron (non-disproportionation) mechanism for abiotic reduction of U^{VI} by Fe^{II} is in contrast to recent studies of enzymatic U^{VI} reduction by *Geobacter sulfurreducens* (Renshaw et al., 2005). The authors conclude that disproportionation of U^V is responsible for the second electron transfer step and that reduction goes through a stable (i.e., measurable by EXAFS) U^V intermediate. It is possible that the complexation and redox properties of enzymes are different than those of Fe^{II} and cause a different mechanism to occur in biological systems, one in which the transition from U^V to U^{IV} is the rate-limiting step. Conversely, because of the possibility for a quick two-electron transfer when Fe^{II} atoms are connected through bonds or a crystal, the rate-limiting step in these systems may be the initial complexation between the redox centers or the U^{VI} to U^V reduction. Observation of U^V species in this case will require a technique with better time resolution than XAFS.

As discussed in Section 3.2.4, we observed U^{IV}–Fe coordination in the colloid + Fe + U system at pH 8.4. This result provides support for the involvement of Fe^{II} in both reduction steps (as opposed to a disproportionation step from U^V to U^{IV}): if aqueous U^V disproportionation was responsible for the second reduction step, the resulting “free” U^{IV} atoms would likely bind to other U^{IV} atoms (because of the extremely low solubility of U^{IV} minerals), and the U^{IV}–Fe coordination would not be observed. The U^{IV}–Fe coordination suggests that the U and Fe atoms remain together in an inner-sphere complex after the first or both electron transfer steps.

The arguments presented above may provide insight into controls on the efficacy of abiotic U^{VI} reduction by surface-associated Fe^{II} in natural soil and sediment materials. Previous studies with a variety of synthetic and natural Fe^{III}–oxide-bearing solids have shown that Fe^{II} associated with mineralogically complex natural solids is much less efficient in catalyzing U^{VI} reduction than are pure-phase Fe^{III} oxides or natural materials rich in Fe^{III} oxide (Fredrickson et al., 2000; Finneran et al., 2002; Jeon et al., 2005). Jeon et al. (2005) suggested that heterogeneity in Fe^{II} binding sites, leading to lower average Fe^{II} sorption densities (e.g., in terms of the number of Fe^{II} atoms per square nanometer of solid surface) than in pure-phase oxide systems, was responsible for the observed inefficient abiotic reduction of U^{VI} in Fe^{II}-rich, mineralogically complex natural materials. The authors speculated that significantly lower Fe^{II} sorption density on natural materials could limit the ability of Fe^{II} and U^{VI} to achieve the surface coordination and subsequent orbital overlap required for efficient electron transfer. Lower Fe^{II} sorption densities are also consistent with lack of Fe^{II} oligomerization that, in view

of the results of the present study, could explain the lower U^{VI} – Fe^{II} redox reactivity in natural materials. Alternatively, if conductivity through the oxide lattice between spatially separated U and Fe adsorbates controls the redox process, then direct Fe^{II} – Fe^{II} contact is not necessary for a two-electron transfer, and reactivity enhancement in pure-phase oxide systems comes by virtue of Fe and U atoms being adsorbed to the same crystallite. In the case of natural systems containing several phases, U^{VI} may be sorbed predominantly to one phase, whereas Fe^{II} may predominantly sorb to another, precluding lattice electron transfer between the redox centers. More detailed understanding of the relative importance of differences in electron conductivity vs. Fe^{II} surface coordination/speciation will be required to precisely define the controls on abiotic Fe^{II} -catalyzed U^{VI} reduction in soils and sediments.

5. CONCLUSIONS

Using a combination of pH titrations, uptake measurements, and XAFS spectroscopy, we were able to relate the Fe^{II} – U^{VI} redox reactivity in a carboxyl-surface environment to the molecular structure of the Fe and U species present in the system. Results show that aqueous and carboxyl-adsorbed Fe^{II} do not reduce carboxyl-adsorbed U^{VI} over at least 4 months. In contrast, complete, rapid reduction of U^{VI} to U^{IV} occurs under slightly higher pH conditions that favor Fe^{II} oligomerization. Because hydroxylation of the surface-adsorbed Fe^{II} species was excluded by the large-surface-area experiments as the reason for increased reactivity at higher pH, the latter was attributed to a facilitated two-electron transfer through the bonds of the Fe^{II} oligomer. Based on these results, we propose an Fe^{II} – U^{VI} redox mechanism that can explain the kinetic limitation of the homogeneous reaction, as well as the commonly observed high reactivity when an Fe^{III} oxide surface or structural Fe^{II} is present. The kinetic limitation in the case of monomeric Fe^{II} is attributed to formation of an unstable U^V – Fe^{III} intermediate complex that is not efficiently reduced by other Fe^{II} atoms in solution before it returns to the original Fe^{II} and U^{VI} species. The enhanced reactivity of oxide-adsorbed or structural Fe^{II} toward U^{VI} reduction is attributed to the ability of non-local Fe^{II} atoms to efficiently provide a second electron to an adsorbed U^V intermediate at the oxide surface through the bonds of the crystal. The ability of U^{VI} to obtain two electrons during a single complexation reaction may be an important, yet largely unconsidered, control on U^{VI} reduction.

Characterization of the Fe and U species in the system led to several unexpected results. U^{VI} appears to adsorb to the carboxyl surface at lower pH than the pH range where significant deprotonation of the surface occurs. At circumneutral pH, U^{VI} remains completely adsorbed to the carboxyl surface, whereas bulk stability constants predict predominance of hydrolysis oligomers in the system. These results suggest a significant electrostatic or steric component in the U-surface carboxyl binding energy and underscore the general need for careful characterization of the surface species. The observed inner-sphere

adsorption of Fe^{II} to the carboxyl surface should cause increased reactivity of Fe^{II} , which was not observed with U^{VI} as the oxidant. Without the knowledge of Fe^{II} oligomerization at pH 8.4, the increased Fe^{II} – U^{VI} redox reactivity relative to pH 7.5 might normally be attributed to hydroxylation of the surface Fe^{II} species. However, the absence of U^{VI} reduction in the pH 8.4 high-surface-area system shows that hydroxylation of monomeric surface Fe^{II} species is not responsible for U^{VI} reduction in the pH 8.4 low-surface-area system.

Our study discerns some of the controls on U^{VI} reduction by Fe^{II} in a defined laboratory system. Although this system includes only a subset of all components present in natural environments, the factors considered in our study are expected to be significant in influencing the environmental fate of U. The presence of Fe^{II} in anoxic subsurface systems and its influence on contaminant transformations is well established. The carboxyl ligands, present as a surface in our system, are also present in nature in the form of humic acids, extracellular polymeric substances, and bacterial surfaces. Uranium in the environment will likely interact with Fe^{II} and carboxyl ligands in the subsurface, directly affecting U transport. The two-electron U^{VI} reduction mechanism inferred in our study is likely to be relevant to all forms of Fe^{II} present in environmental systems, such as Fe^{II} adsorbed to clays, Mn/Fe oxides, and bacteria, or structural Fe^{II} in clays, green rusts, and magnetite.

ACKNOWLEDGMENTS

We thank S. Traina at University of California-Merced for suggestions that greatly improved the manuscript. We also thank G. Zlateva for providing the TEM images; S. Kelly, B. Ravel, and the MRCAT staff for assistance in collecting the XAFS data; K. Haugen for editorial help. The constructive comments of three reviewers and the associate editor are also appreciated. Funding for this work was provided by the U.S. Department of Energy, Office of Science, Office of Biological and Environmental Research, Environmental Remediation Science Program (contract W-31-109-Eng-38), and the Environmental Molecular Science Institute at University of Notre Dame (funded by NSF Grant EAR-0221966). Work at the MR CAT beamline was supported by DOE under contract DE-FG02-94-ER45525 and the member institutions. Use of the APS was supported by the DOE Office of Science, Office of Basic Energy Sciences, under contract W-31-109-Eng-38.

APPENDIX A. SUPPLEMENTARY DATA

Detailed methods and materials section. Supplemental figures and tables. Supplementary data associated with this article can be found, in the online version, at [doi:10.1016/j.gca.2007.01.025](https://doi.org/10.1016/j.gca.2007.01.025).

REFERENCES

- Arden T. V. (1950) The solubility products of ferrous and ferrosic hydroxides. *J. Chem. Soc.*, 882–885.
- Batson V. L., Bertsch P. M., and Herbert B. E. (1996) Transport of anthropogenic uranium from sediments to surface waters

- during episodic storm events. *J. Environ. Qual.* **25**(5), 1129–1137.
- Becker U., Rosso K. M., and Hochella M. F. (2001) The proximity effect on semiconducting mineral surfaces: A new aspect of mineral surface reactivity and surface complexation theory? *Geochim. Cosmochim. Acta* **65**(16), 2641–2649.
- Bell P. E., Mills A. L., and Herman J. S. (1987) Biogeochemical conditions favoring magnetite formation during anaerobic iron reduction. *Appl. Environ. Microbiol.* **53**(11), 2610–2616.
- Beveridge T. J., and Murray R. G. E. (1980) Sites of metal deposition in the cell wall of *Bacillus subtilis*. *J. Bacteriol.* **141**(2), 876–887.
- Blake R. L., Hessevick R. E., Zoltai T., and Finger L. W. (1966) Refinement of the hematite structure. *Am. Mineral.* **51**, 123–129.
- Boyanov M. I. (2003) XAFS studies of metal-ligand interactions at organic surfaces and in solution. Ph.D. dissertation. Univ. of Notre Dame, IN.
- Boyanov M. I., Kelly S. D., Kemner K. M., Bunker B. A., Fein J. B., and Fowle D. A. (2003) Adsorption of cadmium to *Bacillus subtilis* bacterial cell walls: a pH-dependent X-ray absorption fine structure spectroscopy study. *Geochim. Cosmochim. Acta* **67**(18), 3299–3311.
- Buerge I. J., and Hug S. J. (1998) Influence of organic ligands on chromium(VI) reduction by iron(II). *Environ. Sci. Technol.* **32**(14), 2092–2099.
- Buerge I. J., and Hug S. J. (1999) Influence of mineral surfaces on chromium(VI) reduction by iron(II). *Environ. Sci. Technol.* **33**(23), 4285–4291.
- Chaudhuri S. K., Lack J. G., and Coates J. D. (2001) Biogenic magnetite formation through anaerobic biooxidation of Fe(II). *Appl. Environ. Microbiol.* **67**(6), 2844–2848.
- Christensen A. N., Lehmann M. S., and Convert P. (1982) Deuteration of crystalline hydroxides - hydrogen-bonds of gamma-AlOO(H,D) and gamma-FeOO(H,D). *Acta Chem. Scand.* **36**(4), 303–308.
- Cornell R. M., and Schwertman U. (1996) *The iron oxides: Properties, reactions, occurrences and uses*. Wiley, New York, pp. 340–343.
- Docrat T. I., Mosselmans J. F. W., Charnock J. M., Whiteley M. W., Collison D., Livens F. R., Jones C., and Edmiston M. J. (1999) X-ray absorption spectroscopy of tricarbonatodioxouranate(V), [UO₂(CO₃)(3)](5-), in aqueous solution. *Inorg. Chem.* **38**(8), 1879–1882.
- Doelsch E., Rose J., Mason A., Bottero J. Y., Nahon D., and Bertsch P. M. (2002) Hydrolysis of iron(II) chloride under anoxic conditions and influence of SiO₄ ligands. *Langmuir* **18**(11), 4292–4299.
- Ekstrom A. (1974) Kinetics and mechanisms of the disproportionation of uranium(V). *Inorg. Chem.* **13**(9), 2237–2241.
- Elsner M., Schwarzenbach R. P., and Haderlein S. B. (2004) Reactivity of Fe(II)-bearing minerals toward reductive transformation of organic contaminants. *Environ. Sci. Technol.* **38**(3), 799–807.
- Fein J. B., Daughney C. J., Yee N., and Davis T. A. (1997) A chemical equilibrium model for metal adsorption onto bacterial surfaces. *Geochim. Cosmochim. Acta* **61**(16), 3319–3328.
- Finneran K. T., Anderson R. T., Nevin K. P., and Lovley D. R. (2002) Potential for bioremediation of uranium-contaminated aquifers with microbial U(VI) reduction. *Soil. Sediment. Contam.* **11**(3), 339–357.
- Fischer A. (2003) Competitive coordination of the uranyl ion by perchlorate and water - the crystal structures of UO₂(ClO₄)₂·3H₂O and UO₂(ClO₄)₂·5H₂O and a redetermination of UO₂(ClO₄)₂·7H₂O. *Z. Anorg. Allg. Chem.* **629**(6), 1012–1016.
- Forsyth J. B., Hedley I. G., and Johnson C. E. (1968) The magnetic structure and hyperfine field of goethite (alpha-FeOOH). *J. Phys. C: Solid State Phys.* **1**(1), 179–188.
- Fredrickson J. K., Zachara J. M., Kennedy D. W., Dong H. L., Onstott T. C., Hinman N. W., and Li S. M. (1998) Biogenic iron mineralization accompanying the dissimilatory reduction of hydrous ferric oxide by a groundwater bacterium. *Geochim. Cosmochim. Acta* **62**(19–20), 3239–3257.
- Fredrickson J. K., Zachara J. M., Kennedy D. W., Duff M. C., Gorby Y. A., Li S. M. W., and Krupka K. M. (2000) Reduction of U(VI) in goethite (alpha-FeOOH) suspensions by a dissimilatory metal-reducing bacterium. *Geochim. Cosmochim. Acta* **64**(18), 3085–3098.
- Gorby Y. A., and Lovley D. R. (1992) Enzymatic uranium precipitation. *Environ. Sci. Technol.* **26**(1), 205–207.
- Grenthe I., Fuger J., Konings R. J. M., Lemire R. J., Muller A. B., Nguyen-Trung C., Wanner, H. (1992) Chemical thermodynamics of uranium. North-Holland, Amsterdam.
- Haim A. (1983) Mechanisms of electron-transfer reactions - the bridged activated complex. *Prog. Inorg. Chem.* **30**, 273–357.
- Haskel D., Islam Z., Lang J., Kmety C., Srajer G., Pokhodnya K. J., Epstein A. J., and Miller J. S. (2004) Local structural order in the disordered vanadium tetracyanoethylene room-temperature molecule-based magnet. *Phys. Rev. B* **70**(5). Art. No. 054422.
- Hudson E. A., Rehr J. J., and Bucher J. J. (1995) Multiple-scattering calculations of the uranium L(3)-edge X-ray absorption near-edge structure. *Phys. Rev. B* **52**(19), 13815–13826.
- Ilton E. S., Haiduc A., Moses C. O., Heald S. M., Elbert D. C., and Veblen D. R. (2004) Heterogeneous reduction of uranyl by micas: crystal chemical and solution controls. *Geochim. Cosmochim. Acta* **68**(11), 2417–2435.
- Ilton E. S., Haiduc A., Cahill C. L., and Felmy A. R. (2005) Mica surfaces stabilize pentavalent uranium. *Inorg. Chem.* **44**(9), 2986–2988.
- Jeon B. H., Dempsey B. A., Royer R. A., and Burgos W. D. (2004) Low-temperature oxygen trap for maintaining strict anoxic conditions. *J. Environ. Eng.-ASCE* **130**(11), 1407–1410.
- Jeon B. H., Dempsey B. A., Burgos W. D., Barnett M. O., and Roden E. E. (2005) Chemical reduction of U(VI) by Fe(II) at the solid-water interface using natural and synthetic Fe(III) oxides. *Environ. Sci. Technol.* **39**(15), 5642–5649.
- Kelly S. D., Kemner K. M., Fein J. B., Fowle D. A., Boyanov M. I., Bunker B. A., and Yee N. (2002) X-ray absorption fine structure determination of pH-dependent U-bacterial cell wall interactions. *Geochim. Cosmochim. Acta* **66**(22), 3855–3871.
- Kostka J. E., and Nealson K. H. (1995) Dissolution and reduction of magnetite by bacteria. *Environ. Sci. Technol.* **29**(10), 2535–2540.
- Kubatko K. A. H., and Burns P. C. (2004) The crystal structure of a novel uranyl tricarbonate, K₂Ca₃[(UO₂)(CO₃)₃]₂(H₂O)₆. *Can. Mineral.* **42**, 997–1003.
- Landa E. R., and Gray J. R. (1995) U.S. Geological Survey - research on the environmental fate of uranium mining and milling wastes. *Environ. Geol.* **26**(1), 19–31.
- Langmuir D. (1978) Uranium solution-mineral equilibria at low temperatures with applications to sedimentary ore deposits. *Geochim. Cosmochim. Acta* **42**(6), 547–569.
- Leussing D. L., and Kolthoff I. M. (1953) The solubility product of ferrous hydroxide and the ionization of the aquo-ferrous ion. *J. Am. Chem. Soc.* **75**(10), 2476–2479.
- Liger E., Charlet L., and Van Cappellen P. (1999) Surface catalysis of uranium(VI) reduction by iron(II). *Geochim. Cosmochim. Acta* **63**(19–20), 2939–2955.

- Lovley D. R., and Phillips E. J. P. (1992a) Bioremediation of uranium contamination with enzymatic uranium reduction. *Environ. Sci. Technol.* **26**(11), 2228–2234.
- Lovley D. R., and Phillips E. J. P. (1992b) Reduction of uranium by *Desulfovibrio desulfuricans*. *Appl. Environ. Microbiol.* **58**(3), 850–856.
- Lovley D. R., Stolz J. F., Nord G. L., and Phillips E. J. P. (1987) Anaerobic production of magnetite by a dissimilatory iron-reducing microorganism. *Nature* **330**(6145), 252–254.
- Lutz H. D., Moller H., and Schmidt M. (1994) Lattice vibration spectra. 82. Brucite-type hydroxides $M(OH)_2$ ($M = Ca, Mn, Co, Fe, Cd$). IR and Raman spectra, neutron diffraction of $Fe(OH)_2$. *J. Mol. Struct.* **328**, 121–132.
- Martell A. E., Smith R. M., Motekaitis R. J. (2001) NIST critically selected stability constants of metal complexes. U.S. Department of Commerce, National Institute of Standards and Technology.
- Morosin B. (1978) Hydrogen uranyl phosphate tetrahydrate, a hydrogen-ion solid electrolyte. *Acta Crystallogr. Sect. B-Struct. Commun.* **34**(DEC), 3732–3734.
- O'Loughlin E. J., Kelly S. D., Cook R. E., Csencsits R., and Kemner K. M. (2003) Reduction of uranium(VI) by mixed iron(II)/iron(III) hydroxide (green rust): formation of UO_2 nanoparticles. *Environ. Sci. Technol.* **37**(4), 721–727.
- Renshaw J. C., Butchins L. J. C., Livens F. R., May I., Charnock J. M., and Lloyd J. R. (2005) Bioreduction of uranium: environmental implications of a pentavalent intermediate. *Environ. Sci. Technol.* **39**(15), 5657–5660.
- Riley R. G., Zachara J. M., Wobber F. J. (1992) Chemical contaminants on DOE lands and selection of contaminant mixtures for subsurface science research. DOE/ER-0547T.U.S. Department of Energy.
- Schwarzenbach R. P., Angst W., Holliger C., Hug S. J., and Klausen J. (1997) Reductive transformations of anthropogenic chemicals in natural and technical systems. *Chimia* **51**(12), 908–914.
- Scott T. B., Allen G. C., Heard P. J., and Randell M. G. (2005) Reduction of U(VI) to U(IV) on the surface of magnetite. *Geochim. Cosmochim. Acta* **69**(24), 5639–5646.
- Segre C. U., Leyarovska N. E., Chapman L. D., Lavender W. W., Plag P. W., King A. S., Kropf A. J., Bunker B. A., Kemner K. M., Dutta P., Duran R. S., and Kaduk J. (2000) The MRCAT insertion device beamline at the Advanced Photon Source. In *Synchrotron Radiation Instrumentation: Eleventh U.S. National Conference* Vol. CP521, (ed. P. Pianetta). American Institute of Physics, New York, pp. 419–422.
- Sørensen J. (1982) Reduction of ferric iron in anaerobic, marine sediment and interaction with reduction of nitrate and sulfate. *Appl. Environ. Microbiol.* **43**(2), 319–324.
- Sposito G. (2004) *The surface chemistry of natural particles*. Oxford University Press, New York.
- Strathmann T. J., and Stone A. T. (2002) Reduction of oxamyl and related pesticides by Fe-II: influence of organic ligands and natural organic matter. *Environ. Sci. Technol.* **36**(23), 5172–5183.
- Strathmann T. J., and Stone A. T. (2003) Mineral surface catalysis of reactions between Fe-II and oxime carbamate pesticides. *Geochim. Cosmochim. Acta* **67**(15), 2775–2791.
- Stumm W. (1992) *Chemistry of the solid-water interface*. Wiley-Interscience, New York.
- Stumm W., and Sulzberger B. (1992) The cycling of iron in natural environments - considerations based on laboratory studies of heterogeneous redox processes. *Geochim. Cosmochim. Acta* **56**(8), 3233–3257.
- Templeton D. H., Zalkin A., Ruben H., and Templeton L. K. (1985) Redetermination and absolute configuration of sodium uranyl(VI) triacetate. *Acta Crystallogr. Sect. C-Cryst. Struct. Commun.* **41**(OCT), 1439–1441.
- Wechsler B. A., Lindsley D. H., and Prewitt C. T. (1984) Crystal structure and cation distribution in titanomagnetites ($Fe_{3-x}Ti_xO_4$). *Am. Mineral.* **69**(7–8), 754–770.
- Wehrli B., Sulzberger B., and Stumm W. (1989) Redox processes catalyzed by hydrous oxide surfaces. *Chem. Geol.* **78**(3–4), 167–179.
- Wersin P., Hochella M. F., Persson P., Redden G., Leckie J. O., and Harris D. W. (1994) Interaction between aqueous uranium(VI) and sulfide minerals - spectroscopic evidence for sorption and reduction. *Geochim. Cosmochim. Acta* **58**(13), 2829–2843.
- Williams A. G. B., and Scherer M. M. (2004) Spectroscopic evidence for Fe(II)–Fe(III) electron transfer at the iron oxide-water interface. *Environ. Sci. Technol.* **38**(18), 4782–4790.
- Wyckoff R. W. G. (1960) *Crystal structures*. Interscience, New York.

Associate editor: Liane G. Benning

A pH-Dependent X-Ray Absorption Spectroscopy Study of U Adsorption to Bacterial Cell Walls

B. Ravel*, S. D. Kelly*, D. Gorman-Lewis[†], M. I. Boyanov*, J. B. Fein[†] and K. M. Kemner*

*Biosciences Division, Argonne National Laboratory, Argonne, IL 60439, USA

[†]Dept. of Civil Engineering and Geological Sciences, University of Notre Dame, Notre Dame, IN 46556, USA

Abstract. Metal mobility in subsurface water systems involves the complex interaction of the metal, the fluid, and the mineral surfaces over which the fluid flows. This mobility is further influenced by metal adsorption onto bacteria and other biomass in the subsurface. To better understand the mechanism of this adsorption as well as its dependence on the chemical composition of the fluid, we have performed a series of metal adsorption experiments of aqueous uranyl (UO_2)²⁺ to the gram-positive bacterium *B. subtilis* in the presence and absence of carbonate along with X-ray Absorption Spectroscopy (XAS) to determine the binding structures at the cell surface. In this paper we demonstrate an approach to the XAS data analysis which allows us to measure the partitioning of the adsorption of uranium to hydroxyl, carboxyl/carbonato, and phosphoryl active sites at the cell surface.

Keywords: uranium adsorption, EXAFS

PACS: 78.70.Dm, 61.10.Ht

The failure of storage facilities containing the contaminated product of industrial, power generation, and weapons production activities has released large quantities of U and other waste products into subsurface environments, threatening water systems used for a wide variety of human activities. Accurate prediction of the fate and transport of U and other waste metals through complex, heterogeneous subsurface systems is essential for the management of waste repositories and connected water systems. [1]

The fate and transport of metals in the subsurface involves their interactions with the surrounding fluid, with the mineral surfaces over which that fluid passes, and with the biomass (such as microbial communities) present in the subsurface. The cell walls of the microbial communities present in well-populated, subsurface systems can represent a significant fraction of the total surface area exposed to the groundwater. The study of U adsorption onto bacteria, particularly at circumneutral pH conditions where U speciation is particularly complex, is ongoing.

This work involves *B. subtilis*, a common groundwater bacterium. *B. subtilis* was cultured and prepared following the procedure of Fein et al. [2, 3], including a sequence of growth, rinsing, and centrifugation. From this wet mass, solutions with known bacterial concentrations were brought to equilibrium with a U-bearing electrolyte solution. One series of samples was maintained in a closed atmosphere with CO_2 excluded. Another series was exposed to the atmosphere (and thus in equilibrium with atmospheric CO_2). A final series was open to atmo-

sphere and reacted with a Ca-bearing electrolyte.

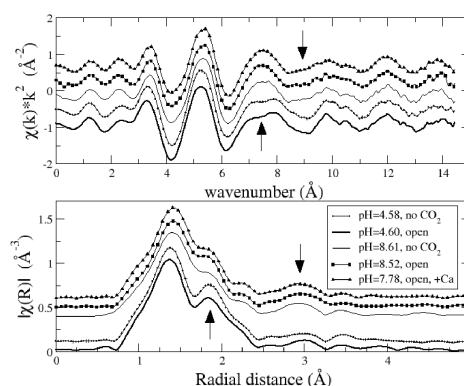


FIGURE 1. The data measured on the five samples. The arrows indicate the regions in k and R which distinguish the two groups of data, as described in the text.

U adsorption to the biomass was measured as a function of pH and modeled [3] as electrostatic interactions between the charged bacterial surface and the aqueous ion using FITEQL. [4] This model identifies multiple binding sites. From previous X-ray absorption spectroscopy (XAS) work [5, 6], these sites were associated with phosphoryl and carboxyl active sites on the cell wall.

From the samples in the U adsorption studies of reference [3], five were selected for XAS measurements. Two samples at pH 4.58 and 8.61 were selected from the closed series of adsorption experiments. Two more at pH

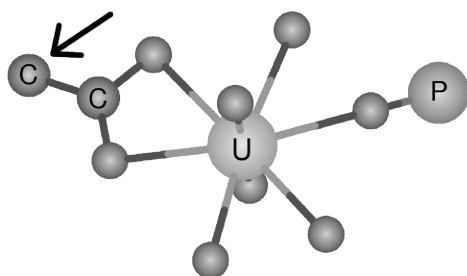


FIGURE 2. Schematic model of the structure about the U atom in this fitting model, showing an example of the phosphoryl and carboxyl ligands in the equatorial plane. The two very short axial oxygen atoms are shown extending into and out of the page. The atom marked with an arrow would be an oxygen in the case of a carbonato complex.

4.60 and 8.52 were chosen from the series in equilibrium with the atmospheric CO_2 . One sample at $\text{pH}=7.78$ was taken from the series with added Ca. The paste from the centrifuged samples, with approximately 400 ppm U on the biomass, was placed in sample containers and sealed from contact with the air by kapton film. They were measured in transmission at the MRCAT [7] beamline at the Advanced Photon Source. These data, shown in Figure 1, are more sensitive to pH than to the presence of CO_2 or Ca. The arrows in the figure indicate the distinctive regions in k and R distinguishing the low pH data from the high.

CONSTRAINTS AND RESTRAINTS

Adsorption experiments like those described in references [2] and [3] are significant in the study of the uranium/bacterium interaction. However they cannot uniquely identify the adsorption complex nor can they directly determine how much of the adsorption is due to each complex. XAS provides a direct measure of the average structural environment around the uranium atoms, thus nicely compliments the adsorption measurements.

As in reference [5], we expect the uranium to be bound to phosphoryl and carboxyl ligands and with bare oxygen atoms (which could be associated with a hydration shell or with a hydroxyl ligands, which are probably impossible to distinguish in our measurements). In our analysis of the extended x-ray-absorption fine-structure (EXAFS) data, we want to allow for the partitioning of the U absorber onto each of these ligands. In the most simple-minded approach to EXAFS data analysis, the parameters of the EXAFS equation — N , S_0^2 , E_0 , ΔR , and σ^2 — are the variables of the fit. Floating N and ΔR independently for each kind of scatterer would introduce a statistically insupportable number of parameters into the

TABLE 1. (top) Partitioning of equatorial oxygens among the ligands considered in this fitting model. (bottom) Distances to the various scatterers.

pH	CO_2	Phosphryl	Carboxyl	Bare O
4.60	yes	2.13(17)	1.18(78)	2.69(79)
4.58	no	2.36(17)	1.19(84)	2.45(86)
7.78	yes	3.50(19)	0.96(86)	1.54(88)
8.61	no	3.78(25)	1.78(1.24)	0.44(1.26)
8.52	yes	3.44(19)	0.59(82)	1.96(83)

O	R (Å)	other	R (Å)
axial	1.772(4)	P	3.578(16)
short	2.270(9)	C	2.931(36)
long	2.424(8)	Na	4.014(28)

fit. Instead, we use the capability of IFEFFIT [8, 9] to describe abstract structural models through the use of constraints and restraints on the parameters refined in the fit.

Constraint An assertion about the value of a fitting parameter or a fixed relation between two or more parameters used in the fit.

Restraint An expression placing a soft limit on the range of values available to one or more fitting parameters. The restraint is added in quadrature to the χ^2 fitting metric.

Uranyl phosphate and uranyl carbonate standards were calculated using FEFF6 [10], following the approach of reference [5]. Uranyl species commonly have two axial O atoms at about 1.78 Å and a number of equatorial oxygen atoms. When the number of equatorial O atoms was allowed to float, it consistently refined to 6 (within uncertainty). For the fits reported here, the number was fixed to 6. Those six atoms were then partitioned among the various ligand types.

This guided our approach to modeling these data. Because phosphorous coordinates to U via a monodentate O bridge with a U–O distance of ~ 2.28 Å, the number of phosphorous scatterers is constrained to equal the number of short equatorial oxygen atoms. Carbon — either as a carboxyl ligand or an inorganic carbonato complex — coordinates U via longer, bidentate O bridge with U–O distance of ~ 2.43 Å, hence the number of carbon scatterers is restrained not to exceed half the number of long equatorial oxygen atoms. Any long equatorial oxygens in excess of twice the number of carbon scatterers are interpreted as bare oxygen atoms. Both the phosphoryl and carboxyl ligands contribute nearly collinear multiple scattering paths whose numbers are constrained by the numbers of single scattering paths. The remainder of the parameters used in the fit used typical constraints. For example, the the axial oxygens were constrained to have the same ΔR and σ^2 regardless of equatorial lig-

ation. As another example, the data did not support independent measurements of σ^2 for the short and long equatorial oxygen atoms, so all equatorial oxygen paths were constrained to have the same σ^2 in the fit. A complete description of the fitting model will be provided in an upcoming publication. The result of this fitting model is shown in Figure 3 for the pH=8.52 sample exposed to atmosphere. The other fits were of comparable quality.

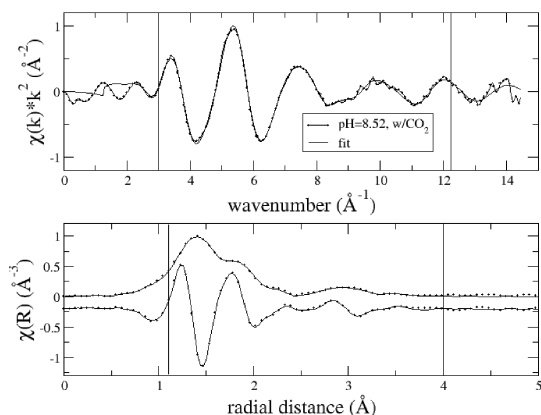


FIGURE 3. Fit to the sample of U adsorbed to *B. subtilis* at pH=8.52 and exposed to atmosphere. The vertical lines indicate the Fourier transform range in k and the fitting range in R . The bottom panel shows the magnitude of $\chi(R)$ along with the real part displaced vertically for clarity.

U ADSORPTION TO *B. SUBTILIS*

These EXAFS results fit well within the context of the adsorption results of reference [3]. As with the earlier EXAFS results [5], we see a decrease in binding to phosphoryl sites with increasing pH. The adsorption results are consistent with the formation of a uranyl carbonate complex on the cell wall at higher pH. In principle, an EXAFS measurement can distinguish between the organic carboxyl ligand and the inorganic carbonate complex. From the perspective of the U absorber, the difference between these two species is the distance between the U absorber and the atom marked by the arrow in Fig. 2. A carbonate has the same bidentate oxygen bridge between the U and C atoms, however the C atom at about 4.35 Å is replaced by an O atom at about 4.20 Å. Whether these data can distinguish between the two species, given the paucity of spectral weight beyond 3.5 Å in these data and the relative weakness of O and C as a scatterer, is a matter of further investigation.

There is one discrepancy between our results shown in Table 1 and the thermodynamic modeling of reference [3]. In that reference, the addition of calcium to the U-*B. subtilis* parent solution resulted in the adsorption data that could only be modeled by the addition of a

calcium uranyl carbonate surface complex. Our fit to the pH=7.78 data containing both CO₂ and added Ca is not consistent with the presence of a Ca scatterer. Rather, to obtain fits of the quality shown in Figure 3, we added a Na scatterer at about 4 Å — the approximate position expected for a Ca scatterer in calcium uranyl carbonate. Work is ongoing to resolve this issue.

ACKNOWLEDGMENTS

Much of this work was supported by the Environmental Remediation Science Program, Office of Biological and Environmental Research, Office of Science, U.S. Department of Energy. Use of the Advanced Photon Source was supported by the U. S. Department of Energy, Office of Science, Office of Basic Energy Sciences, under Contract No. W-31-109-ENG-38. The Materials Research Collaborative Access Team (MRCAT) operations are supported by DOE and the MRCAT member institutions. Additional support by the National Science Foundation through an Environmental Molecular Science Foundation grant (EAR02-21966).

REFERENCES

1. A NABIR Primer, Bioremediation of Metals and Radionuclides: What it is and how it works, Tech. Rep. second edition, Office of Biological and Environmental Research, Office of Science, U.S. Department of Energy (2003).
2. J. Fein, C. Daugheny, N. Yee, and T. Davis, *Geochim. Cosmochim. Acta* **61**, 3319–3328 (1997).
3. D. Gorman-Lewis, P. Elias, and J. Fein, *Environ. Sci. Technol.* **39**, 4906–4912 (2005).
4. A. Herbelin, and J. Westall, Fiteql 4.0: a computer program for determination of chemical equilibrium constants from experimental data, Tech. Rep. 99-01, Department of Chemistry, Oregon State University, Corvallis OR (1999).
5. S. Kelly, K. Kemner, J. Fein, D. Fowle, M. Boyanov, B. Bunker, and N. Yee, *Geochim. Cosmochim. Acta* **66**, 3875–3891 (2002).
6. M. Boyanov, S. Kelly, K. Kemner, B. Bunker, J. Fein, and D. Fowle, *Geochim. Cosmochim. Acta* **67**, 3299–3311 (2003).
7. C. Segre, N. Leyarovska, L. Chapman, W. Lavender, P. Plag, A. King, A. Kropf, B. Bunker, K. Kemner, P. Dutta, R. Duran, and J. Kaduk, “The MRCAT insertion device beamline at the Advanced Photon Source,” in *Synchrotron Radiation Instrumentation: Eleventh U.S. Conference*, 2000, vol. CP521, pp. 419–422.
8. M. Newville, *J. Synchrotron Radiat.* **8**, 322–324 (2001).
9. B. Ravel, and M. Newville, *J. Synchrotron Radiat.* **12**, 537–541 (2005).
10. S. I. Zabinsky, J. J. Rehr, A. Ankudinov, R. C. Albers, and M. J. Eller, *Phys. Rev. B* **52**, 2995–3009 (1995).

XAFS and X-Ray and Electron Microscopy Investigations of Radionuclide Transformations at the Mineral-Microbe Interface

¹Ken Kemner, ¹Ed O'Loughlin, ¹Shelly Kelly, ¹Bruce Ravel, ¹Maxim Boyanov, ¹Deirdre Sholto-Douglas, ²Barry Lai, ³Russ Cook, ⁴Everett Carpenter, ⁵Vince Harris, ⁶Ken Neelson

(1) Biosciences Division, Argonne National Laboratory, Argonne, Illinois 60439, (2) Advanced Photon Source, Argonne National Laboratory, Argonne, Illinois 60439, (3) Electron Microscopy Center, Argonne National Laboratory, Argonne, Illinois 60439, (4) Virginia Commonwealth University, Richmond, Virginia 23284, (5) Northeastern University, Boston, Massachusetts 02115, (6) University of Southern California, Los Angeles, California 90007

Abstract. The microenvironment at and adjacent to surfaces of actively metabolizing cells, whether in a planktonic state or adhered to mineral surfaces, can be significantly different from the bulk environment. Microbial polymers (polysaccharides, DNA, RNA, and proteins), whether attached to or released from the cell, can contribute to the development of steep chemical gradients over very short distances. It is currently difficult to predict the behavior of contaminant radionuclides and metals in such microenvironments, because the chemistry there has been difficult or impossible to define. The behavior of contaminants in such microenvironments can ultimately affect their macroscopic fates. We have successfully performed a series of U L_{III} edge x-ray absorption fine structure (XAFS) spectroscopy, hard x-ray fluorescence (XRF) microprobe (150 nm resolution), and electron microscopy (EM) measurements on lepidocrocite thin films (~1 micron thickness) deposited on kapton films that have been inoculated with the dissimilatory metal reducing bacterium *Shewanella oneidensis* MR-1 and exposed to 0.05 mM uranyl acetate under anoxic conditions. Similarly, we have performed a series of U L_{III} edge EXAFS measurements on lepidocrocite powders exposed to 0.05 mM uranyl acetate and exopolymeric components harvested from *S. oneidensis* MR-1 grown under aerobic conditions. These results demonstrate the utility of combining bulk XAFS with x-ray and electron microscopies.

Keywords: XAFS, uranium, x-ray microscopy, biogeochemistry

PACS: 91.62.+g

INTRODUCTION

Uranium exists in most oxidizing environments as U(VI) in the uranyl ion (UO₂²⁺), which is generally water soluble. An exception, uranyl phosphate, is typically highly insoluble. Uranium is also often found as U(IV) in highly insoluble uraninite (UO₂) in reducing environments such as groundwater. Microorganisms can affect the mobility of uranium and other metals via electron transfer reactions resulting from microbial respiration. They can also affect the mobility of uranium via production of a variety of exopolymeric substances (EPS). Although EPSs may remain attached to the cell membrane (capsular material), many are freely released from the bacteria. Because they typically have a net negative

charge, exuded EPS can travel relatively unimpeded through porous media in which many mineral surfaces are negatively charged. However, some functional groups associated with EPS can also dissolve mineral surfaces, complex cations, and reincorporate the ions into solution. These processes affect the chemistry of elements that are constituents of or are sorbed to the solid phase. In addition to affecting the bioavailability of contaminant elements, the presence or absence of EPS can affect the bioavailability of macro- and micronutrients, an influence ultimately manifested in changes in the metabolic state of a microbial species.

The interactions of metal contaminants with geosurfaces and with EPS have been studied, but very little work has been done to *directly* probe the interaction of a contaminant metal with the microbe-geosurface interface. A better understanding of this

CP882, X-ray Absorption Fine Structure—XAFS13

edited by B. Hedman and P. Pianetta

© 2007 American Institute of Physics 978-0-7354-0384-0/07/\$23.00

ternary interaction will provide the information needed for more realistic models of the transport of metal and radionuclide contaminants through natural soils.

We are using x-ray absorption fine structure (XAFS) spectroscopy, x-ray fluorescence (XRF) microscopy (150 nm spatial resolution), and scanning electron microscopy (SEM) to directly probe the interactions between uranium, *Shewanella oneidensis* MR-1 (a dissimilatory metal reducing bacterium), the exopolymeric material (EPS) produced by the cell, and iron (hydr)oxides. Investigations have been performed to investigate the local chemical environment of uranium exposed to bulk lepidocrocite powders and EPS components produced under aerobic conditions. Additional studies have been made on thin films of lepidocrocite, colonized with monolayers of bacteria, and exposed to 0.05 mM uranyl acetate under anoxic conditions.

INVESTIGATIONS OF THE ROLE OF EPS ON U-IRON (HYDR)OXIDE INTERACTIONS UNDER AEROBIC CONDITIONS

We have performed U L_{III} edge XAFS investigations at the MRCAT [1] insertion device beam line at the Advanced Photon Source (APS) on bulk samples containing either lepidocrocite or ferrihydrite powders and U (1E-4 M) in solutions of either minimal salts bacterial growth media or EPS (i.e., the filtrate passing through a 0.2 micron filter after the onset of stationary phase growth) to directly probe the interactions between U, EPS from aerobically grown *S. oneidensis* MR-1, and iron (hydr)oxides. Measurements were made with an ion chamber filled with Ar gas at atmospheric pressure in the fluorescence mode and utilized a harmonic rejection mirror. Results from U L_{III}-edge XAFS measurements of EPS identify P backscattering atoms around U, consistent with the presence of carboxyl and phosphoryl functional groups in the EPS (figure 1). XAFS measurements of the bulk lepidocrocite in the presence of aerobically grown EPS or growth media indicate less interaction in the solid phase between U and lepidocrocite than between U and phosphates. Further analyses of these data are consistent with some precipitation of hydrous uranyl phosphate. In contrast, XAFS measurements of bulk ferrihydrite in the presence of aerobically produced EPS indicate more U-Fe correlations in the higher coordination shells around U than with phosphoryl functional groups associated with the EPS. These XAFS results indicate that the ability of EPS to complex uranium is dependent on the iron (hydr)oxide mineral surfaces that are present in the system.

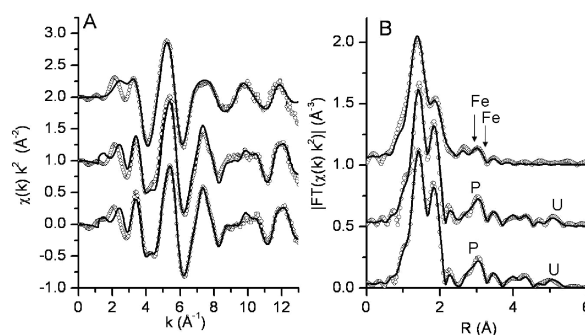


FIGURE 1. U L_{III}-edge $\chi(k)k^2$ and Fourier transformed data of U + ferrihydrite + EPS (top), U + lepidocrocite + EPS (middle), and U + EPS (bottom). See text for further details.

INVESTIGATIONS OF URANIUM-LEPIDOCROCITE-*S. oneidensis* MR-1 INTERACTIONS UNDER ANOXIC CONDITIONS

The combination of the high brilliance of the APS synchrotron and the use of high-resolution zone plates [2] for focusing improves x-ray microimaging experiments of mineral-microbe-metal systems substantially [3]. We have used scanning electron microscopy, XRF microscopy (at the XOR 2ID-D microbe beam line at the APS), and bulk XAFS (at the MRCAT 10ID beam line at the APS) to investigate the interactions between U, *S. oneidensis* MR-1, and amorphous lepidocrocite thin films under anoxic conditions. (figure 2) Results from these studies demonstrate the ability of XRF microscopy to identify the location of U, relative to cells adhered to Fe (hydr)oxide thin films, and the ability of scanning electron microscopy (SEM) to image EPS in close association with cells adhered to the films. XRF microscopy results for samples incubated for one day indicate that U is associated with the bacteria and adjacent extracellular material. XRF microscopy results for samples incubated for three days indicate that U is dispersed throughout the biofilm and coincident with the location of EPS and biomineralization products. Results from U L_{III}-edge XANES measurements of these films indicate that the U is not reduced after three days of incubation. Possible explanations for the lack of discernable reduction of U include (1) a lag in anaerobic respiration of the *S. oneidensis* MR-1, (2) reoxidation of the U by the predominantly ferric (hydr)oxide film, and (3) binding of the U(VI) by EPS with chemical and physical hindering of the bioreduction process. We have observed a similar lag in reduction of Fe in

fine-particle lepidocrocite. In addition, past investigations showed that poorly crystalline ferrihydrite strongly inhibited bioreduction and reoxidized U(IV) [4]. To address this issue, we have begun investigating longer incubation times, the use of different bacterial strains (*S. putrefaciens* CN32, *Geobacter* spp., and *Anaeromyxobacter* spp.), and alternative iron (hydr)oxide thin films for these experiments.

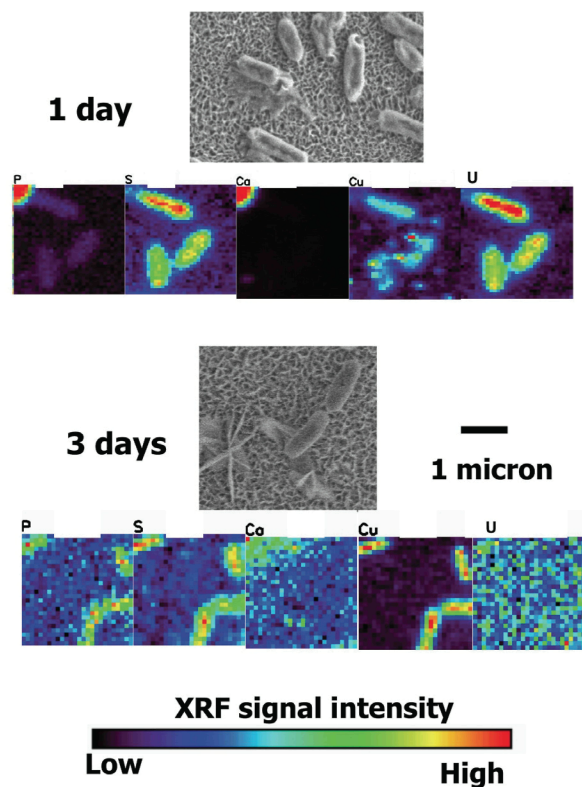


FIGURE 2. Scanning electron microscopy and XRF microscopy results of 1 day and 3 day incubations of *S. oneidensis* MR-1 deposited on lepidocrocite thin films deposited on kapton.

SUMMARY

We have performed a number of x-ray-based and electron-based interrogations of mineral-metal-microbe-EPS interactions. Results indicate that integration of the strengths of each probe, relative to each other (i.e., better spatial resolution for EM, better elemental sensitivity for XRF microscopy, and better chemical sensitivity for XAFS), provide a powerful means to better understand chemical microenvironments that are critical for understanding biogeochemical transformations of contaminant metals and radionuclides.

ACKNOWLEDGMENTS

This work was supported by the Environmental Remediation Science Program, Office of Biological and Environmental Research, Office of Science, U.S. Department of Energy (DOE), under contract W-31-109-Eng-38. Work at the Advanced Photon Source is supported by the DOE Office of Science, Office of Basic Energy Sciences. The Materials Research collaborative Access Team (MRCAT) operations are supported by DOE and the MRCAT member institutions.

REFERENCES

1. C. Segre, N. Leyarovska, L. Chapman, W. Lavender, P. Plag, A. King, A. Kropf, B. Bunker, K. Kemner, P. Dutta, R. Duran, and J. Kaduk, "The MRCAT insertion device beamline at the Advance Photon Source," in Synchrotron Radiation Instrumentation: eleventh U.S. conference, 2000, vol. CP521, pp. 419-422.
2. B. Lai, W. Yun, D. G. Legnini, D. Xiao, J. Chrzas, P. J. Viccaro, V. White, S. Vajjkar, D. Denton, and F. Cerrina, *Appl. Phys. Lett.* **61** 1877-1879 (1992).
3. K. M. Kemner, S. D. Kelly, B. Lai, J. Maser, E. J. O'Loughlin, D. Sholto-Douglas, Z. Cai, M. A. Schneegurt, C. F. Kulpa, and K. H. Nealson, *Science* **306** 686-687 (2004).
4. B. Wielinga, B. C. Bostick, C. M. Hansel, R. F. Rosenzweig, S. Fendorf, *Env. Sci. Tech.* **34**, 2190-2195 (2000).

Comparison of Cd Binding Mechanisms by Gram-Positive, Gram-Negative and Consortia of Bacteria Using XAFS

Bhoopesh Mishra¹, Jeremy B. Fein², Maxim I. Boyanov³, Shelly D. Kelly³,
Kenneth M. Kemner³ and Bruce A. Bunker¹

¹Department of Physics, University of Notre Dame, Notre Dame, IN 46556 USA

²Department of Civil Engineering and Geological Sciences, University of Notre Dame, Notre Dame, IN 46556 USA

³Biological Sciences, Argonne National Laboratory, Argonne, IL 60439 USA

Abstract. A quantitative comparison of the Cd binding mechanism to Gram-positive (*Bacillus subtilis*) and Gram-negative bacteria (*Shewanella oneidensis*) is presented. At pH 6.0, EXAFS data for the Gram-positive bacteria were modeled using carboxyl and phosphoryl sites only. However, additional sulfide sites were required to model the spectrum from the Gram-negative bacteria under similar experimental conditions. Cd binding to a bacterial consortium at the same pH value, sampled from natural river water, was modeled using the models developed for the individual Gram-positive and Gram-negative bacterial strains.

Keywords: XAFS, Cd, bacteria, Gram positive, Gram negative, consortium, adsorption X-ray absorption spectroscopy: EXAFS, NEXAFS, XANES

PACS: 61.10.Ht

INTRODUCTION

Adsorption onto bacterial surfaces can control the speciation and distribution of contaminants in many aquatic and near-surface systems. Accurate models that describe bacteria-metal interactions are critical to understanding the behavior of heavy metal contaminants and the development of contaminant remediation strategies. An obstacle in modeling realistic systems is that a given bacteria-bearing natural system can contain many different bacterial species. However, recent studies have shown that individual pure strains of Gram-positive and Gram-negative bacteria and their artificial mixtures exhibit broadly similar adsorptive behavior [1, 2, 3]. Similarly, Borrok *et al.* found that consortia of bacteria grown from a range of uncontaminated soil and water environments exhibit roughly similar affinities for protons and Cd [4]. In this study, XAFS has been used to compare the Cd binding mechanism of a Gram-positive bacterium (*Bacillus subtilis*) with a Gram-negative bacterium (*Shewanella oneidensis*) at pH 6.0. Further, the Cd binding mechanism of an uncontaminated river water bacterial consortium has been compared with the two pure bacterial strains under similar experimental condition. DGGE analysis of the river water consortium sample shows the

presence of at least six different bacterial species [4]. Our study will help to resolve whether binding sites determined for single species systems are responsible for adsorption in more complex natural bacterial assemblages.

METHODS

The river water sample that was used in this study was collected from the St. Joseph River in South Bend, IN, USA. *Bacillus subtilis*, *Shewanella oneidensis* and the bacterial consortium were harvested from the TSB growth media by centrifugation, transferred to test tubes, and washed five times in 0.1M NaClO₄. In each Cd adsorption experiment, 10g/L of bacterial wet weight was suspended in a pH-neutralized stock solution of 0.1 mol/L NaClO₄ and 30 ppm Cd. After adjustment of the pH, and an additional 2 h of reaction time on a rotating rack, the final pH of each vessel was measured. The individual vessels were then centrifuged. The filtered supernatant was analyzed for Cd using an inductively coupled plasma-atomic emission spectroscopy technique with matrix-matched standards. The biomass pellet formed at the base of each vessel after centrifugation was loaded into slotted Plexiglas holders and covered with Kapton film for XAFS measurements.

CP882, X-ray Absorption Fine Structure—XAFS13

edited by B. Hedman and P. Pianetta

© 2007 American Institute of Physics 978-0-7354-0384-0/07/\$23.00

Powder and aqueous Cd standards were used to determine the XAFS signature of carboxyl, phosphoryl, sulfide and sulfate binding environments. CdS and CdSO₄ powder standards were prepared from commercially available chemicals (Sigma-Aldrich), after grinding and sieving (~ 400 mesh). The aqueous Cd standards include hydrated Cd, Cd acetate and Cd phosphate solutions. All Cd standards were prepared from 1000 ppm Cd perchlorate stock solution. pH of the solution standards were adjusted such that complexation of Cd to the ligands was expected from solution speciation calculations.

XAFS measurements of Cd K edge (26711 eV) were performed at the MRCAT sector 10-ID beamline [5] at the Advanced Photon Source at Argonne National Laboratory. The energy of the incident X-rays was scanned by using a Si(111) reflection plane of a cryogenically-cooled double-crystal monochromator. The beamline was optimized at the 3rd harmonic of the undulator. The undulator was tapered by approximately 3.5 keV to reduce the variation in the incident intensity to less than 15% over the scanned energy range. Higher harmonics were rejected using a Pt-coated mirror. The incident ion chamber was filled with 100% Nitrogen. The transmitted and reference ion chambers were filled with 100% Ar. The fluorescence detector in the Stern-Heald geometry [6] was filled with Kr gas, and Pd filter of three absorption lengths was used to reduce the background signal. The incident X-ray beam profile was 1 mm square. Linearity tests [7] indicated less than 0.1% nonlinearity for a 50% decrease in incident X-ray intensity. The scans were aligned by the simultaneously collected Cd foil data. The first inflection point was set at 26711 eV.

Quick scans (continuous scanning of the monochromator with signal sampled every 0.5 eV in the entire scanning range) were used with an integration time of 0.1 second per point. About 50 consecutive scans of each sample were averaged, and resulting data from all the samples were normalized and background subtracted using ATHENA [8].

The data were analyzed using codes from the UWXAFS package [9]. Data range used for Fourier transforming the k space data was 2.3 – 9.8 Å⁻¹. A Hanning window function was used with a δk of 1.0 Å⁻¹. The Gram-positive, Gram-negative, and river water consortium samples were first fit individually at k weights 1, 2, and 3, and then a simultaneous fitting of these three samples was done. Only four SS paths, Cd-O, Cd-C, Cd-P, and Cd-S were used to fit the biomass samples. These paths were first used to fit hydrated Cd, Cd acetate, Cd phosphate and Cd sulfide to calibrate the theory (not shown). A shell-by-shell fitting approach was used, in which significantly smaller χ_v^2 and R factor values were used as the

criteria for the goodness of fit. The fitting range for all the data sets were set to 1.2 – 3.4 Å. In the simultaneous fit of all three samples, the Debye-Waller factors were set to the optimized values in the fits of the individual samples.

RESULTS AND DISCUSSION

The experimental $k^2\chi$ data for the three samples are shown in Fig. 1. Corresponding magnitude of the Fourier transform and the fits are shown in Fig. 2. The differences between these three spectra are more clearly seen in the real part of the FT, shown in Fig. 3.

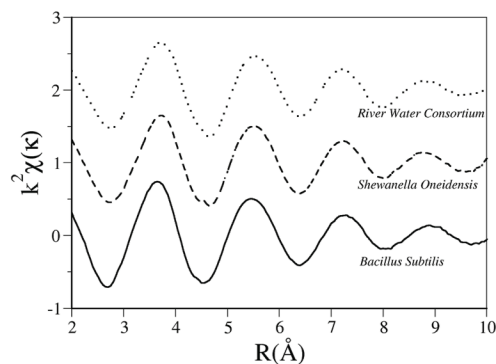


FIGURE 1. $k^2\chi$ data of the Gram positive, Gram negative and river water consortium of bacteria at pH 6.0.

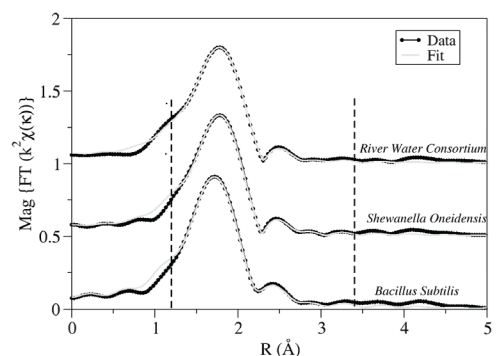


FIGURE 2. Data and Fit for the magnitude of the Fourier transform of the Gram positive, Gram negative and bacterial consortium at pH 6.0.

The Gram positive bacterial sample (*B. subtilis*) was fit using carboxyl and phosphoryl sites, consistent with previous results [10]. An attempt was made to refine a sulfide site to that data, but the fit produced a coordination number of only 0.08 ± 0.05 sulfur atoms. Conversely, the Gram negative bacterial sample *Shewanella oneidensis* could not be modeled using carboxyl and phosphoryl sites alone. Adding a sulfide site to the model significantly improved the fit, reducing χ_v^2 from 110 to 35. Data from the river water consortium sample was successfully fit using the same

paths used for the two pure bacterial strains, producing the parameters in Table 1 and a χ^2 value of 30.

Figure 4 makes it clear that the Cd-S path has significant contribution in the EXAFS signal of the Gram-negative bacteria and the river water consortium. The fitting details are shown in Table 1.

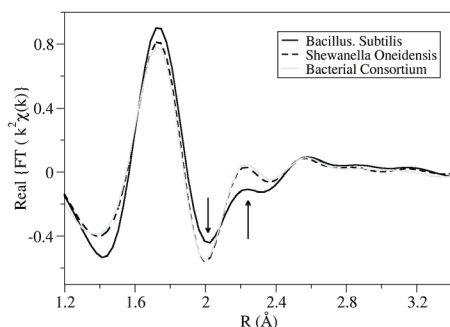


FIGURE 3. Comparing the real part of the FT of *Bacillus subtilis*, *Shewanella oneidensis* and the river water consortium. It can be clearly seen that *B. subtilis* data is significantly different around 2.2 Å, while *Shewanella oneidensis* and the river water consortium are similar.

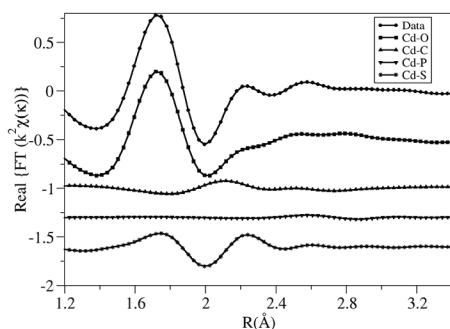


FIGURE 4. Real part of the FT data of the river water consortium and contribution of the four paths (Cd-O, Cd-C, Cd-P, and Cd-S) in fitting this data. Notice the relatively strong sulfide contribution.

TABLE 1. XAFS Fitting Parameters

Sample/Path	N	R(Å)	σ^2 (Å ⁻²) $\times 10^{-3}$
Cd/<i>B. subtilis</i>			
Cd-O	4.78 ± 0.12	2.29 ± 0.01	9.00
Cd-C	0.89 ± 0.46	2.70 ± 0.03	12.00
Cd-P	0.82 ± 0.32	3.38 ± 0.05	15.00
Cd-S	0.08 ± 0.05	2.53 ± 0.02	9.00
Cd/<i>Shewanella</i>			
	N	R(Å)	σ^2 (Å ⁻²) $\times 10^{-3}$
Cd-O	3.72 ± 0.22	2.29 ± 0.01	9.00
Cd-C	1.30 ± 0.56	2.70 ± 0.03	12.00
Cd-P	0.58 ± 0.30	3.38 ± 0.05	15.00
Cd-S	0.90 ± 0.16	2.53 ± 0.02	9.00
Cd/Consortium			
	N	R(Å)	σ^2 (Å ⁻²) $\times 10^{-3}$
Cd-O	3.33 ± 0.25	2.29 ± 0.01	9.00
Cd-C	0.91 ± 0.49	2.70 ± 0.03	12.00
Cd-P	0.65 ± 0.30	3.36 ± 0.05	15.00
Cd-S	1.14 ± 0.10	2.53 ± 0.02	9.00

In summary, this study demonstrates that Cd adsorption to Gram-positive bacteria is different than

Gram-negative bacteria under similar experimental conditions. While Gram-positive bacteria could be modeled using carboxyl and phosphoryl sites only, an additional, sulfide site was required for modeling the Gram-negative bacteria. We also demonstrate that a natural consortium of bacteria sampled from uncontaminated river water, containing at least six different bacterial species, can be modeled using the models developed for the individual Gram-positive and Gram-negative bacterial strains. The XAFS data from the bacterial consortium were similar to that of the Gram-negative bacteria. The possibility of this consortium being dominated Gram-negative bacteria cannot be ruled out. Nevertheless, it can be inferred from our results that Cd adsorption to bacterial consortia could be modeled using models developed for individual bacterial strains. However, this study needs to be extended to a range of pH values and Cd loadings on several Gram-positive, Gram-negative, and bacterial consortium for more reliable interpretation of our results.

ACKNOWLEDGMENTS

B.M. thanks the Bayer Corporation and the Environmental Molecular Science Institute (EMSI) at University of Notre Dame for fellowship support. Help in sample preparation from Jennifer Szymanowski, and beamline setup help from the staff of MRCAT are greatly appreciated. This work was supported by the funding provided by the National Science Foundation through an EMSI grant (EAR02-21966) to the University of Notre Dame. MRCAT is supported by the member institutions. The APS was supported by the U.S. Department of Energy, Office of Science and Office of Basic Energy Sciences.

REFERENCES

1. C. J. Daughney, *et al.*, *Chemical Geology* **144**, 161 (1998).
2. N. Yee and J. Fein, *Geochimica et Cosmochimica Acta* **65**, 2037 (2001).
3. N. Yee and J. B. Fein, *Geomicrobiology Journal* **20**, 43 (2003).
4. D. Borrok, *et al.*, *Geochimica et Cosmochimica Acta* **68**, 3231 (2004).
5. C. U. Segre *et al.*, 521 (American Institute of Physics, New York, 2000), p. 419-422.
6. E. A. Stern and S. M. Heald, *Handbook of Synchrotron Radiation*, North-Holland, Amsterdam, 1983).
7. K. M. Kemner *et al.*, *Phys. Rev. B* **50**, 14327 (1994).
8. B. Ravel, *Journal of Synchrotron Radiation* **8**, 314 (2001).
9. E. A. Stern *et al.*, *Physica B* **209**, 117 (1995).
10. M. I. Boyanov *et al.*, *Geochimica et Cosmochimica Acta* **67**, 3299 (2003).

Mixed-Valence Cytoplasmic Iron Granules Are Linked to Anaerobic Respiration^{∇†}

S. Glasauer,^{1*} S. Langley,² M. Boyanov,³ B. Lai,³ K. Kemner,³ and T. J. Beveridge⁴

Department of Land Resource Science, University of Guelph, Guelph, Ontario N1G 2W1, Canada¹; Department of Earth Sciences, University of Ottawa, Ottawa, Ontario K1N 6N5, Canada²; Argonne National Laboratory, Argonne, Illinois 60439³; and Department of Molecular and Cellular Biology, University of Guelph, Guelph, Ontario N1G 2W1, Canada⁴

Received 28 June 2006/Accepted 18 November 2006

Intracellular granules containing ferric and ferrous iron formed in *Shewanella putrefaciens* CN32 during dissimilatory reduction of solid-phase ferric iron. It is the first in situ detection at high resolution (150 nm) of a mixed-valence metal particle residing within a prokaryotic cell. The relationship of the internal particles to Fe(III) reduction may indicate a respiratory role.

Iron biominerals that develop within living cells are unusual and far less common than extracellular precipitates, which form copiously during the dissimilatory reduction (DR) of Fe(III) compounds (3, 7, 12). Previously we have observed intracellular iron particles forming during DR by *Shewanella putrefaciens* CN32, a gram-negative facultative anaerobe (6). One possibility is that the particles serve a respiratory role, perhaps as a reservoir of oxidant as is known for certain *Thioplaca* spp., freshwater and marine bacteria that use nitrate stored in internal vacuoles to oxidize sulfide (9). The presence of mixed-valence states of Fe in the granules and their disappearance under complete reducing conditions lend further support.

It has not been possible to isolate and purify the intracellular particles because fine-grained extracellular Fe minerals contaminate the growth medium as well as the cell surface. The small size of the internal particles, their intracellular location, and their instability during exposure to a focused electron beam necessitate an in situ, nondestructive spectroscopic approach that can establish the chemical composition, including Fe valence states, at extremely high spatial and chemical resolution. For this, we applied high-energy X-ray microscopy, which combines a spatial resolution of 150 nm with high elemental sensitivity (higher than 1×10^4 atoms within a spot size of 150 nm) (1). X-ray fluorescence (XRF) in concert with X-ray absorption near-edge spectroscopy (XANES) is a recent application of established methods that can achieve the high resolution necessary to articulate chemical information contained in metals associated with bacterial cells (10).

In our study, CN32 was grown to mid- to late exponential growth phase in a defined medium (DM) consisting of mineral salts, phosphate, PIPES [piperazine-*N,N'*-bis(2-ethanesulfonic acid)], and lactate (as an electron donor) under aerobic conditions (6). The cells were then washed, gassed with H₂-Ar

(4:96), and grown in DM to which enough sterile hydrous ferric oxide (HFO) suspension was added as the electron acceptor to produce 4 to 8 mM Fe under strict anaerobic conditions at 22°C (6). Soluble ferric and ferrous iron treatments were included for comparison to treatments with solid ferric iron. Bacteria were inoculated into anaerobic DM containing either 30 mM ferric citrate or 10 mM fumarate and 4 mM FeCl₂.

The internal biomineralization products formed during the dissimilatory reduction of Fe(III) by CN32 were investigated in individual cells by XRF microscopy and micro-X-ray absorption spectroscopy (1) (see the supplemental material).

Cells began to exhibit the intracellular granules (Fig. 1) around 3 days after inoculation under anaerobic conditions with HFO as the electron acceptor, as reported previously (6). A combination of electron microscopy and light microscopy allowed discrete regions of selected cells (those containing Fe particles) to be accurately positioned in the X-ray beam. X-ray fluorescence elemental maps were first obtained, followed immediately by XANES spectra at the Fe K-edge at several positions on and within each bacterium. Spectra were compared to Fe mineral standards with Fe valence states from +2 to +3.

XRF spectra showed that bacteria contained typical cellular elements (Fig. 2). P, Ca, Cl, and S were universal and independent of culture conditions. Differences in distribution between elements could not be correlated with variations exhibited by other elements and were not large enough to exclude possible artifacts due to differences in cell thickness in the region. Potassium was often low or undetectable; however, elevated K was correlated with a high P signal, suggesting potassium phosphate or polyphosphate (not shown). High signals for Fe corresponded to the locations of internal precipitates.

XANES analyses of (i) intracellular granules formed during reduction of HFO, (ii) regions of the bacteria without granules, and (iii) extracellular mineral precipitates provide information on Fe valence state (Fig. 3). This was estimated based on linear calibration obtained by considering the edge position of Fe²⁺, magnetite, and Fe³⁺ spectra at 92% of the absorption edge step. Results indicate that the Fe valence states at precipitate-free and precipitate-rich regions of the cell are 2.2 and 2.5, respectively. This places the Fe valence of the granules as more reduced than

* Corresponding author. Mailing address: Department of Land Resource Science, University of Guelph, Guelph, Ontario N1G 2W1, Canada. Phone: (519) 824-4120. Fax: (519) 824-5730. E-mail: glasauer@uoguelph.ca.

† Supplemental material for this article may be found at <http://aem.asm.org/>.

∇ Published ahead of print on 1 December 2006.

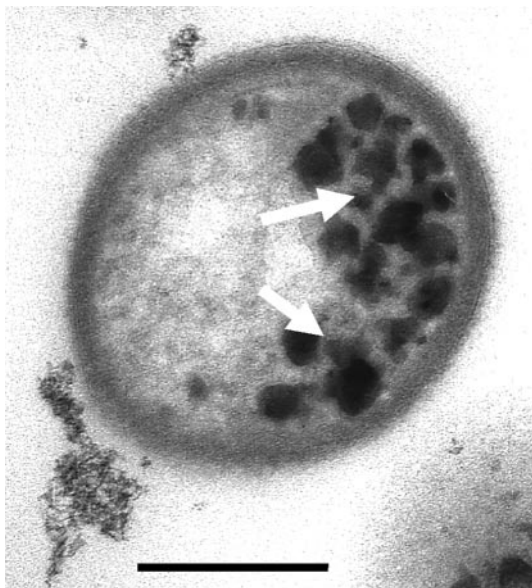


FIG. 1. Transmission electron microscopy image of *S. putrefaciens* CN32 cell in cross section, showing intracellular granules of iron oxide (arrows) formed adjacent to the cytoplasmic membrane during anaerobic dissimilatory iron reduction. Bar, 250 nm.

that of magnetite, or Fe_3O_4 (average valence of 2.66), and more oxidized than that of green rust, or $[\text{Fe}(\text{II})_{(1-x)}\text{Fe}(\text{III})_x(\text{OH})_2]^{x+}$, where x is the ratio $\text{Fe}(\text{III})/\text{Fe}_{\text{total}}$ (average valence of 2.25 to 2.33) (4, 14). The average valence state of the extracellular Fe minerals is consistent with that of magnetite and likely results from reduction of the HFO-associated $\text{Fe}(\text{III})$ by the bacteria during anaerobic respiration (7, 12).

Similar analyses of CN32 cultures exposed to $\text{Fe}(\text{III})$ -citrate or fumarate- Fe^{2+} yielded similar valence state results for the intracellular particles; however, due to the lower average concentration of the precipitates (six granules) formed in these treatments, the results are more uncertain. Exposure of dried CN32 cells on electron microscopy grids exposed to air did not appear to change the distribution of Fe valence states either for the granules or for the cell-associated Fe. This is likely due to stabilization by associated anions (e.g., phosphate or organic molecules) (2) and showed the inherent stability of the granules.

Knowing the oxidation state of the granules allows us to propose a mechanism for their formation. The evidence at this point is consistent with uptake of Fe^{2+} during $\text{Fe}(\text{III})$ respiration, followed by segregation and concentration of the Fe within the cytoplasm at the plasma membrane, with which the granules appear to be intimately associated (Fig. 1). Displacement of granules into the cytoplasm accommodates new granule formation on the membrane. This is supported by observations showing that when few granules have developed they are adjacent to the plasma membrane. A higher proportion is

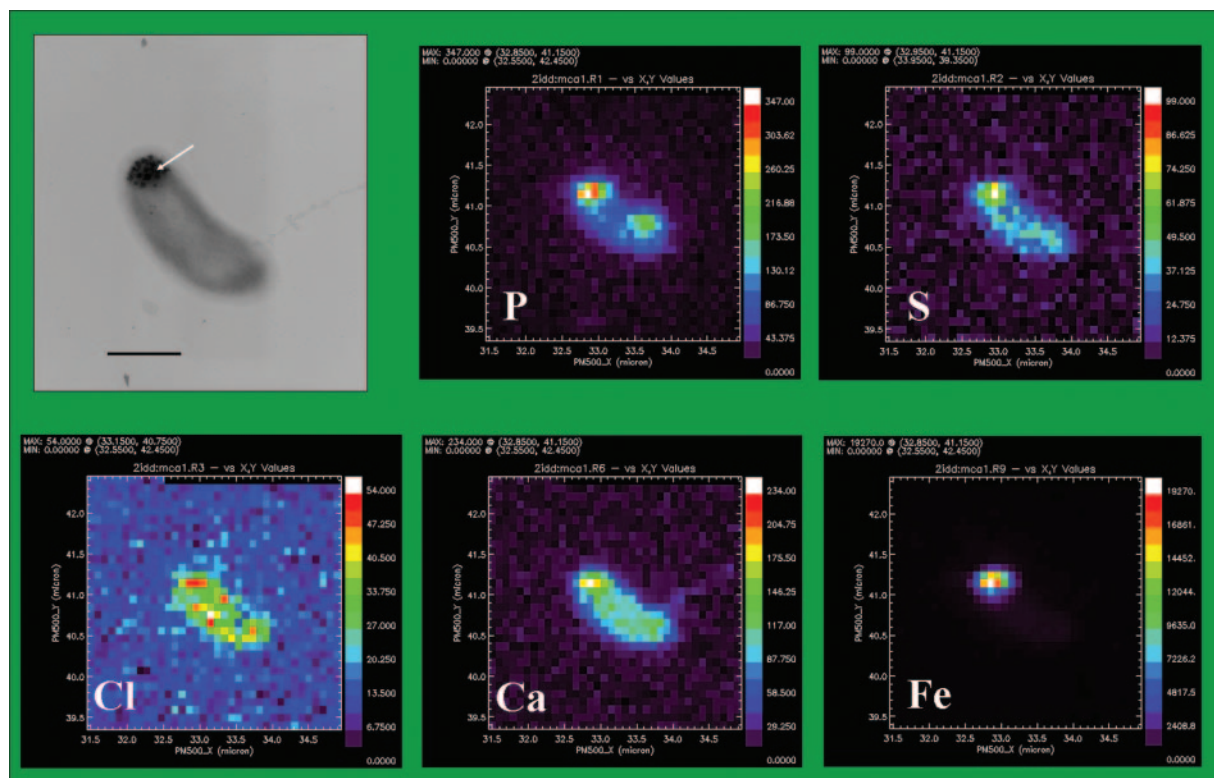


FIG. 2. X-ray spectromicroscopy analyses of *S. putrefaciens* CN32. (Top left panel) Transmission electron microscopy image showing a whole mount of a single CN32 cell with cytoplasmic inclusions (arrow) formed during dissimilatory reduction of hydrous ferric oxide. Bar, 500 nm. (Other panels) X-ray fluorescence spectra of bacterium shown in top left panel for P, S, Cl, Ca, and Fe.

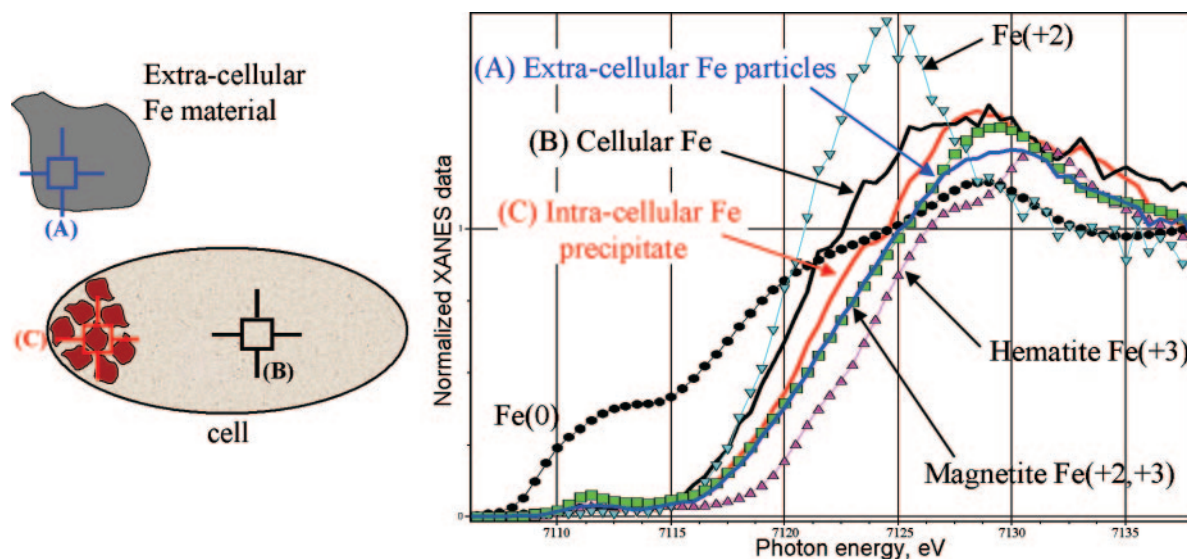


FIG. 3. XANES analyses of (A) extracellular Fe-rich material (blue), (B) regions of the cell without granules (black), and (C) intracellular granules formed during ferrihydrite reduction (red) (drawing not to scale). The calibration standard for Fe(III) was hematite (Fe_2O_3) (magenta triangles), that for Fe(II) and Fe(III) was magnetite (Fe_3O_4) (green squares), and that for Fe(II) was FeCl_2 (light-blue inverted triangles).

located further from the membrane within the cytoplasm when there are more granules. Granules are preferentially located at the ends or poles of the cell under these conditions. The polar location supports specific iron uptake sites at the ends of the cell or rapid segregation to the ends. It is probable that once the poles are exposed to a region of high Fe(III) concentration, DR can result in Fe at sufficient concentrations to trigger uptake; the poles appear to be particularly attractive to Fe oxides (8). Partial oxidation is anticipated to take place after the Fe^{2+} is moved across the membrane. There is previous evidence for a membrane surrounding each granule (6). Most biological membranes possess proteins having oxidation/reduction power, and it is possible that the membrane controls electron flow to Fe atoms within the granules. This is supported by observations that the granules disappear from the cells once the HFO external electron acceptor is exhausted.

To date, we have observed only the particles within CN32, although many species and strains of *Shewanella* are capable of DR. We have also tested *S. oneidensis*, *S. algae*, *S. baltica*, and *Shewanella* sp. strain MR-4, all of which exhibited higher rates of Fe(III) reduction and lower long-term survivability than CN32 when HFO served as the electron acceptor. These strains did not develop the Fe particles. Strain CN32 is a terrestrial bacterium, whereas most isolates are derived from marine systems (15); this may account for a divergence from many of its sister isolates. The presence of unique membrane-bound cytochromes, believed essential for respiration of solid-phase Fe (13), may help to explain the formation of the internal particles during metal respiration. It is unlikely that the cells develop the granules to moderate toxicity effects at high Fe concentrations, which is supported by the observation that fewer granules are actually formed at the higher Fe concentrations of the Fe(III)-citrate treatments.

The fact that the inclusion Fe is intermediate in valency between that of green rust and that of magnetite may be explained by (i) mixed Fe mineral phases, e.g., magnetite and

green-rust domains within the particles (5), or (ii) cation-excess magnetite, which has an $\text{Fe}^{2+}/\text{Fe}_{\text{total}}$ ratio of 0.5 to 0.6 (11). Green rust is a highly reactive reductant in soils and converts to magnetite (4); it is typically unstable under oxic conditions. Vivianite, or $\text{Fe}_3(\text{PO}_4)_2 \cdot \text{H}_2\text{O}$, cannot be excluded; however, the chemical-state information for the granules as well as their homogeneous size and morphology strongly suggests an Fe(II)/Fe(III) phase.

The regulatory mechanisms for attachment of *Shewanella* to Fe oxides, dissimilatory Fe reduction, and Fe compartmentalization have been little studied. There is recent evidence that their pathways are interrelated through the ferric uptake regulator modulon *fur* (16). The scarcity of readily available iron in most natural systems is reflected in the abundance of mechanisms for Fe sequestration by cells (17). Little is known, however, about Fe uptake under conditions of Fe sufficiency, which necessarily must typify the anaerobic environments where dissimilatory Fe reduction occurs. The fact that the granules form best when solid Fe is reduced suggests a unique mechanism closely linked to dissimilatory reduction.

At this point, the most promising routes for future investigations are chemostat culture experiments to optimize conditions for granule formation and molecular genetic studies to articulate mechanisms of Fe uptake and control by *Shewanella*. We aim to investigate a range of *Shewanella* spp. under optimized growth conditions to determine the extent to which the intracellular Fe granules may contribute to Fe cycling in subsurface environments.

We thank S. Vogt and S. Kelly for assistance in using XRF analysis software which they developed, and we thank K. Neilson for his advice.

Partial support was provided to M.B. by the Environmental Molecular Science Institute at the University of Notre Dame. This work is supported by grants to S.G. from the Natural Science and Engineering Research Council of Canada and to T.J.B. and K.K. from the Natural and Accelerated Bioremediation (NABIR) Research Program, Office

of Biological and Environmental Research, Office of Science, U.S. Department of Energy (DOE). Additional support was provided to K.K. by the Office of Science, DOE, Early Career Scientist and Engineering Award, and to T.J.B. through the U.S. DOE-NABIR Grand Challenge program administered through the Pacific Northwest National Laboratory in Richland, WA.

Electron microscopy was performed in the Guelph Regional Integrated Imaging Facility (GRIIF), which was partially funded through a Natural Science and Engineering Research Council of Canada Major Facilities Access (NSERC-MFA) grant to T.J.B. Research at the XOR Sector 2 and the Advanced Photon Source (APS) was supported by the Office of Basic Energy Sciences, Office of Science, DOE, under contract W-31-109-Eng-38.

REFERENCES

- Cai, Z., B. Lai, W. Yun, P. P. Ilinski, D. G. Legnini, J. Maser, and W. Rodrigues. 2000. Hard X-ray scanning microprobe for fluorescence imaging and microdiffraction at the advanced photon source, p. 472–477. In W. Meyer-Ilse, T. Warwick, and D. Attwood (ed.), X-ray microscopy. Proceedings of the 6th International Conference. American Institute of Physics, New York, NY.
- Cornell, R. M., and U. Schwertmann. 2003. The iron oxides: structure, properties, reactions, occurrence and uses, 2nd ed. Wiley-VCH, Weinheim, Germany.
- Fredrickson, J. K., J. M. Zachara, D. W. Kennedy, H. Dong, T. C. Onstott, N. W. Hinman, and S. Li. 1998. Biogenic iron mineralization accompanying the dissimilatory reduction of hydrous ferric oxide by a groundwater bacterium. *Geochim. Cosmochim. Acta* **62**:3239–3257.
- Génin, J.-M. R., P. Refait, L. Simon, and S. H. Drissi. 1998. Preparation and Eh-pH diagrams of Fe(II)-Fe(III) green rust compounds; hyperfine interaction characteristics and stoichiometry of hydroxyl-chloride, -sulfate and -carbonate. *Hyperfine Interact.* **111**:313–318.
- Génin, J.-M. R., P. Refait, G. Bourrié, M. Abdelmoula, and F. Trolard. 2001. Structure and stability of the Fe(II)-Fe(III) green rust fougérite mineral and its potential for reducing pollutants in soil solutions. *Appl. Geochem.* **16**: 559–570.
- Glasauer, S., S. Langley, and T. J. Beveridge. 2002. Intracellular iron minerals in a dissimilatory iron-reducing bacterium. *Science* **295**:117–119.
- Glasauer, S., P. G. Weidler, S. Langley, and T. J. Beveridge. 2003. Controls on Fe reduction and mineral formation by a subsurface bacterium. *Geochim. Cosmochim. Acta* **67**:1277–1288.
- Grantham, M. C., P. M. Dove, and T. J. DiChristina. 1997. Microbially catalyzed dissolution of iron and aluminum oxyhydroxide mineral surface coatings. *Geochim. Cosmochim. Acta* **61**:4467–4477.
- Jørgensen, B. B., and V. A. Gallardo. 1999. Thioplaca spp.: filamentous sulfur bacteria with nitrate vacuoles. *FEMS Microbiol. Ecol.* **28**:301–313.
- Kemner, K. M., S. D. Kelly, B. Lai, J. Maser, E. J. O'Laughlin, D. Sholto-Douglas, Z. H. Cai, M. A. Schneegurt, C. F. Kulpa, and K. H. Nealson. 2004. Elemental and redox analysis of single bacterial cells by X-ray microbeam analysis. *Science* **306**:686–687.
- Kukkadapu, R. K., J. M. Zachara, J. K. Fredrickson, D. W. Kennedy, A. C. Dohnalkova, and D. E. McCready. 2005. Ferrous hydroxy carbonate is a stable transformation product of biogenic magnetite. *Am. Mineral.* **90**:510–515.
- Lovley, D. R., J. F. Stolz, G. L. Nord, Jr., and E. J. P. Philips. 1987. Anaerobic production of magnetite by a dissimilatory iron-reducing microorganism. *Nature* **330**:252–254.
- Myers, J. M., and C. R. Myers. 1998. Isolation and sequence of omcA, a gene encoding a decaheme outer membrane cytochrome c of *Shewanella putrefaciens* MR-1, and detection of omcA homologs in other strains of *S. putrefaciens*. *Biochim. Biophys. Acta* **1373**:237–251.
- Sparks, N. H. C., S. Mann, D. A. Bazylinski, D. R. Lovley, H. W. Jannasch, and R. B. Frankel. 1990. Structure and morphology of magnetite anaerobically produced by a marine magnetotactic bacterium and a dissimilatory iron-reducing bacterium. *Earth Planet. Sci. Lett.* **98**:14–22.
- Venkateswaran, K., D. P. Moser, M. E. Dolhopf, D. P. Lies, D. A. Saffarini, B. J. MacGregor, D. B. Ringelberg, D. C. White, M. Nishijima, H. Sano, J. Burghardt, E. Stackbrandt, and K. H. Nealson. 1999. Polyphasic taxonomy of the genus *Shewanella* and description of *Shewanella oneidensis* sp. nov. *Int. J. Syst. Bacteriol.* **49**:705–724.
- Wan, X.-F., N. C. VerBerkmoes, L. A. McCue, D. Stanek, H. Connelly, L. J. Hauser, L. Y. Wu, X. D. Liu, T. F. Yan, A. Leaphart, R. L. Hettich, J. Z. Zhou, and D. K. Thompson. 2004. Transcriptomic and proteomic characterization of the Fur regulon in the metal-reducing bacterium *Shewanella oneidensis*. *J. Bacteriol.* **186**:8385–8400.
- Wandersman, C., and P. Delepelaire. 2004. Bacterial iron sources: from siderophores to hemophores. *Annu. Rev. Microbiol.* **58**:611–647.

c-Type Cytochrome-Dependent Formation of U(IV) Nanoparticles by *Shewanella oneidensis*

Matthew J. Marshall¹, Alexander S. Beliaev^{1*}, Alice C. Dohnalkova¹, David W. Kennedy¹, Liang Shi¹, Zheming Wang², Maxim I. Boyanov³, Barry Lai⁴, Kenneth M. Kemner³, Jeffrey S. McLean¹, Samantha B. Reed¹, David E. Culley¹, Vanessa L. Bailey¹, Cody J. Simonson¹, Daad A. Saffarini⁵, Margaret F. Romine¹, John M. Zachara², James K. Fredrickson^{1*}

1 Biological Sciences Division, Pacific Northwest National Laboratory, Richland, Washington, United States of America, **2** Chemical Sciences Division, Pacific Northwest National Laboratory, Richland, Washington, United States of America, **3** Biosciences Division, Argonne National Laboratory, Argonne, Illinois, United States of America, **4** Advanced Photon Source, Argonne National Laboratory, Argonne, Illinois, United States of America, **5** Department of Biological Sciences, University of Wisconsin, Milwaukee, Wisconsin, United States of America

Modern approaches for bioremediation of radionuclide contaminated environments are based on the ability of microorganisms to effectively catalyze changes in the oxidation states of metals that in turn influence their solubility. Although microbial metal reduction has been identified as an effective means for immobilizing highly-soluble uranium(VI) complexes in situ, the biomolecular mechanisms of U(VI) reduction are not well understood. Here, we show that c-type cytochromes of a dissimilatory metal-reducing bacterium, *Shewanella oneidensis* MR-1, are essential for the reduction of U(VI) and formation of extracellular UO₂ nanoparticles. In particular, the outer membrane (OM) decaheme cytochrome MtrC (metal reduction), previously implicated in Mn(IV) and Fe(III) reduction, directly transferred electrons to U(VI). Additionally, deletions of *mtrC* and/or *omcA* significantly affected the in vivo U(VI) reduction rate relative to wild-type MR-1. Similar to the wild-type, the mutants accumulated UO₂ nanoparticles extracellularly to high densities in association with an extracellular polymeric substance (EPS). In wild-type cells, this UO₂-EPS matrix exhibited glycocalyx-like properties and contained multiple elements of the OM, polysaccharide, and heme-containing proteins. Using a novel combination of methods including synchrotron-based X-ray fluorescence microscopy and high-resolution immune-electron microscopy, we demonstrate a close association of the extracellular UO₂ nanoparticles with MtrC and OmcA (outer membrane cytochrome). This is the first study to our knowledge to directly localize the OM-associated cytochromes with EPS, which contains biogenic UO₂ nanoparticles. In the environment, such association of UO₂ nanoparticles with biopolymers may exert a strong influence on subsequent behavior including susceptibility to oxidation by O₂ or transport in soils and sediments.

Citation: Marshall MJ, Beliaev AS, Dohnalkova AC, Kennedy DW, Shi L, et al. (2006) c-Type cytochrome-dependent formation of U(IV) nanoparticles by *Shewanella oneidensis*. PLoS Biol 4(8): e268. DOI: 10.1371/journal.pbio.0040268

Introduction

Dissimilatory metal-reducing bacteria (DMRB) constitute a phylogenetically diverse group that spans from hyperthermophilic Archaea to anaerobic Proteobacteria [1,2]. Among those, species of the *Geobacter* and *Shewanella* genera are the most intensively studied metal-reducers, whose hallmark feature is a remarkable respiratory versatility [1,2]. Under anaerobic conditions, these organisms reduce a variety of organic and inorganic substrates, including fumarate, nitrate, nitrite, and thiosulfate as well as various polyvalent metal ions either as soluble complexes or associated with solid phase minerals. These metals include cobalt, vanadium, chromium, uranium, technetium, plutonium, iron, and manganese [2–6].

The ability to utilize such a wide array of electron acceptors is largely due to the diversified respiratory network found in *Shewanella oneidensis* MR-1, in which the c-type cytochromes constitute the integral part of the terminal reductase complexes. Analysis of the genome sequence of *S. oneidensis* MR-1 indicated that this organism contains 42 putative c-type cytochrome genes including many multi-heme-containing proteins [7]. In gram-negative bacteria, the terminal reductases, including c-type cytochromes, are typically located in the cytoplasmic membrane or the periplasm [8]. An unusual feature of organisms like *Shewanella* and *Geobacter* that allows these species to access insoluble metal electron acceptors is

the production of high-molecular-weight c-type cytochromes reported to be in association with the outer membrane (OM) [9–14]. Cell fractionation of *S. oneidensis* MR-1 grown under anaerobic conditions demonstrated that approximately 80% of the membrane-bound c-type cytochromes were associated with OM cell fractions [13]. Subsequent mutagenesis studies in MR-1 have identified a cluster of three metal reduction-specific genes, *mtrC* (locus tag: SO1778), *mtrA* (SO1777), and *mtrB* (SO1776), encoding a putative OM decaheme c-type cytochrome, a periplasmic decaheme c-type cytochrome, and

Academic Editor: Naomi Ward, The Institute for Genomic Research, United States of America

Received: February 8, 2006; **Accepted:** June 12, 2006; **Published:** August 8, 2006

DOI: 10.1371/journal.pbio.0040268

Copyright: © 2006 Marshall et al. This is an open-access article distributed under the terms of the Creative Commons Attribution License, which permits unrestricted use, distribution, and reproduction in any medium, provided the original author and source are credited.

Abbreviations: DAB, diamino benzidine; DMRB, dissimilatory metal-reducing bacteria; EPS, extracellular polymeric substance; HRSEM, high-resolution scanning electron microscopy; OM, outer membrane; OMC, outer membrane cytochrome; TEM, transmission electron microscope; U, uranium; UO₂, uraninite; XRF, X-ray fluorescence

* To whom correspondence should be addressed. E-mail: jim.fredrickson@pnl.gov (JKF); alex.believ@pnl.gov (ASB)

an OM protein of unknown function, respectively [8,15]. Further analysis of *S. oneidensis* MR-1 genome has revealed the presence of three other clusters similar to *mtrAB* and three genes homologous to *mtrC* [10]. One of these genes encodes a decaheme *c*-type cytochrome, designated OmcA (SO1779), which was subsequently isolated and sequenced [16]. Both MtrC and OmcA have been shown to be exposed on the outer face of the OM [17], allowing them to contact extracellular soluble and insoluble electron acceptors.

Among many metal and radionuclide contaminants, uranium (U) is one of the primary concerns at U.S. Department of Energy sites because it typically exists as a soluble U(VI) carbonate complex in oxidized, circumneutral pH groundwater. However, U(VI) is readily reduced by DMRB under anoxic conditions resulting in the precipitation of uraninite (UO₂) [18,19]. The rapid rate of U(VI) reduction by DMRB [20] and the relatively low solubility of U(IV) make bioreduction an attractive remedy for removing soluble U(VI) from contaminated groundwater [21–23]. We have previously demonstrated the reduction and extracellular accumulation of UO₂ precipitates at the OM surface and within the periplasmic space of *S. putrefaciens* strain CN32 [5,24,25]. These observations suggest that the outer membrane cytochromes may, at least partially, be involved in UO₂ formation. To better understand the role of *S. oneidensis* MR-1 outer membrane cytochromes (OMCs) in U(VI) reduction, we evaluated a mutant lacking all functionally active *c*-type cytochromes and constructed several mutants with targeted deletions of specific OMCs to evaluate their potential for extracellular reduction of U(VI). We compared the reduction kinetics of the cytochrome mutants with wild-type MR-1 resting cells and observed the differences in subcellular localizations of the UO₂ nanoparticles in mutant strains after U(VI) reduction. Additionally, we used a novel combination of imaging and co-localization techniques to gain a better understanding of the organized extracellular UO₂ nanoparticles and to gain insight into their biogenesis.

Results

Role of *c*-Type Cytochromes in Uranium Reduction

To investigate the importance of *c*-type cytochromes in U(VI) reduction, we used an *S. oneidensis* MR-1 mutant lacking the ability to covalently incorporate heme into nascent apocytochromes (CcmC⁻) [26]. The CcmC⁻ mutant was unable to reduce U(VI), present as uranyl carbonate complexes [27,28], to U(IV) over a 48-h period, while wild-type MR-1 completely reduced 250 μM U(VI) ($p < 0.005$) under identical conditions (Figure 1). To further investigate the involvement of *c*-type cytochromes in U(VI) reduction, a series of OMC in-frame deletion mutants lacking either *mtrC*, *omcA*, *mtrF*, or both *mtrC* and *omcA* genes were constructed and verified by immunoblot analysis with specific sera (Figure S1). In resting-cell reduction assays, the wild-type reduced U(VI) within 24 h, whereas MtrC⁻, OmcA⁻, and MtrC⁻/OmcA⁻ mutants reduced U(VI) at a slower rate, requiring 48 h to reduce approximately 200 μM U(VI) to U(IV) ($p = 0.001$) (Figure 1). In contrast, U(VI) reduction rates displayed by the MtrF⁻ mutant were not significantly affected and were more similar to the wild-type than to the MtrC⁻, OmcA⁻, and MtrC⁻/OmcA⁻ mutants. While in-frame deletions of single or multiple OMCs slowed reduction rates, none of the mutants

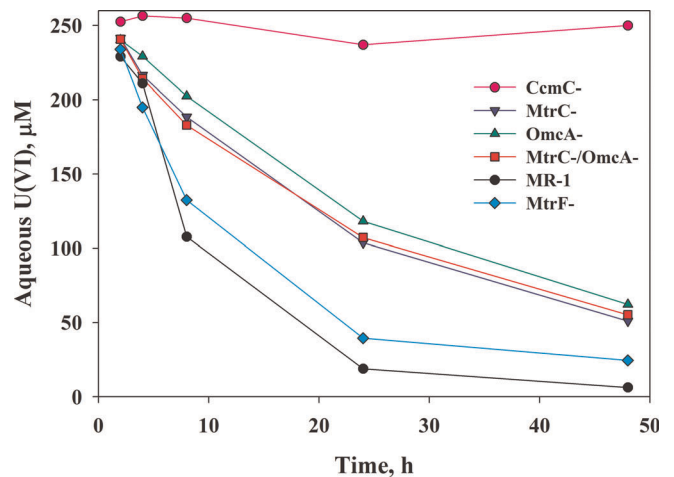


Figure 1. U(VI) Reduction Kinetics by *S. oneidensis* MR-1 and Cytochrome Mutant Cells

The reduction of 250 μM U(VI) was determined for MR-1, a mutant lacking all *c*-type cytochromes (CcmC⁻), single cytochrome deletion mutants (MtrC⁻, OmcA⁻, or MtrF⁻), and a double cytochrome deletion mutant (MtrC⁻/OmcA⁻). Lines represent the mean data from representative experiments.

DOI: 10.1371/journal.pbio.0040268.g001

tested abolished the ability to reduce U(VI) as was seen with the CcmC⁻ mutant.

The *in vitro* ability of purified OMCs to transfer electrons to U(VI) was tested and compared with the ability to reduce Fe(III)-NTA. Both reduced MtrC or OmcA were oxidized by Fe(III)-NTA within 2.5 s of exposure and both reactions were biphasic and followed first-order kinetics. Although purified MtrC was also oxidized by uranyl citrate ($K_{obs1} = 0.039 \pm 0.001$ and $K_{obs2} = 0.008 \pm 0.001$) (Figure S2), the biphasic reaction was not completed within 40 s and the reaction rate was more than 100 times slower than that of Fe(III)-NTA ($K_{obs1} = 4.1 \pm 0.13$ and $K_{obs2} = 1.13 \pm 0.43$). In contrast, reduced OmcA had no detectable electron transfer activity ($< 0.5\%$) when reacted with uranyl citrate but was completely oxidized by Fe(III)-NTA ($K_{obs1} = 2.96 \pm 0.28$ and $K_{obs2} = 0.9 \pm 0.09$). When equal amounts of OmcA and MtrC were combined, their electron transfer activity with uranyl citrate was similar to that observed with MtrC alone (unpublished data).

Inactivation of OM *c*-Type Cytochromes Affects the Localization of UO₂ Nanoparticles in *S. oneidensis* MR-1

The subcellular localization of UO₂ in wild-type MR-1 and the OMC deletion mutants was determined by transmission electron microscope (TEM) analysis of samples collected 24 h after the addition of U(VI) and lactate (Figure 2). Thin sections of MR-1 revealed that UO₂ was predominantly accumulated in cell suspensions as 1- to 5-nm particles (Figures 2A, 2B, and S3). These UO₂ nanoparticles were present primarily in one of three forms: densely packed particles in association with an extracellular polymeric substance (UO₂-EPS) (Figure 2A, arrow), loosely packed aggregates of particles not in association with EPS but external to cells (Figure 2A and 2B, extracellular aggregates of lower contrast), or, to a lesser degree, localized within the cell periplasm (Figure S3). The electron-dense material observed in all samples, regardless of location or association, consisted of U nanoparticles with selected area diffraction

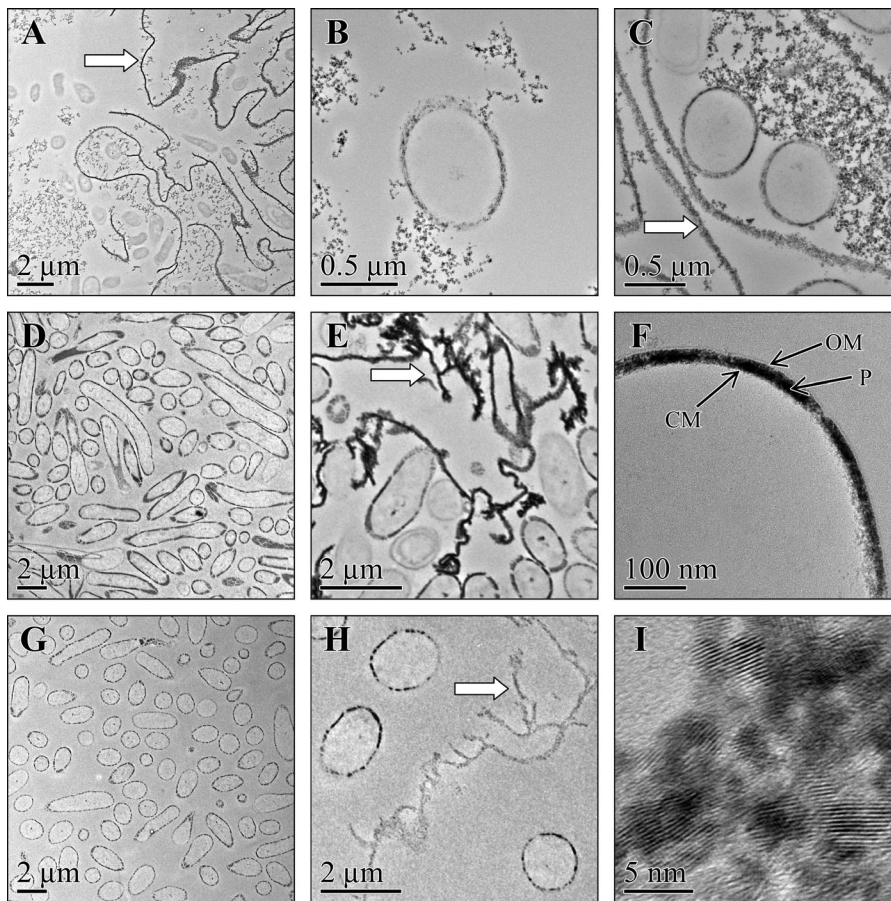


Figure 2. UO_2 Localization in *S. oneidensis* MR-1 Wild-type and Cytochrome-Deficient Mutants

TEM images prepared from cell suspensions incubated with $250 \mu\text{M}$ uranyl acetate and 10 mM lactate for 24 h. The localization of UO_2 by MR-1 (A, B) was compared to OmcA^- (C), MtrC^- (D–F), and $\text{MtrC}^-/\text{OmcA}^-$ (G, H). High-resolution image of extracellular UO_2 nanoparticles showing d-lines values consistent to previous patterns of biogenic and synthetic UO_2 (I). The UO_2 -EPS is designated by the arrows. Locations of the cell membrane (CM), periplasm (P), and outer membrane (OM) are shown.

DOI: 10.1371/journal.pbio.0040268.g002

patterns consistent with those reported for synthetic and biogenic UO_2 (Figures 2I and S4). Similar to the wild-type, the OmcA^- mutant localized UO_2 nanoparticles in the periplasm as well as extracellularly in association with organized EPS structures and random patches of less densely arranged aggregates (Figure 2C). In contrast to the wild-type, the accumulation of UO_2 in the MtrC^- or $\text{MtrC}^-/\text{OmcA}^-$ mutants was predominantly periplasmic and, to a much lesser degree, extracellular in association with the EPS (Figure 2D–2H). The loosely arranged aggregates of UO_2 were absent in both the MtrC^- and $\text{MtrC}^-/\text{OmcA}^-$ mutants (Figure 2D and 2E). Although all three of the OMC deletion mutants exhibited UO_2 nanoparticles in association with EPS, there were distinct differences in the abundance, distribution, and density of the particles localized on the UO_2 -EPS, with the exception of OmcA^- , which was comparable to the wild-type. The MtrC^- mutant UO_2 -EPS features were much less evident relative to the wild-type but, when observed, were associated with densely packed UO_2 particles arranged in short branches. The UO_2 -EPS features from OmcA^- most closely resembled the wild-type in abundance, density of particles, and the branching. The $\text{MtrC}^-/\text{OmcA}^-$ mutant exhibited the lowest abundance and density of UO_2 -EPS, although the

morphology and branching pattern were similar to those of wild-type and OmcA^- strains.

UO_2 -EPS Features Are Co-localized with Fe and P

To obtain a better understanding of the features associated with UO_2 , the following samples analyzed by TEM were subjected to X-ray fluorescence (XRF) microscopy characterization: MR-1 cells, extracellular UO_2 precipitates associated with EPS in MR-1 samples, and diffuse extracellular UO_2 precipitates in MR-1 samples. False-color images of the P, U, and Fe fluorescence intensity for each sample type were aligned with the corresponding TEM image (Figure 3A–3C), and relative area concentrations of these elements in each location were calculated (Figure S5). The shapes observed in the U fluorescence maps clearly corresponded to the morphology observed by TEM, with the highest concentration of P and Fe in MR-1 cells, and was consistent with other studies [29]. This was most evident in the UO_2 -EPS, where a high resolution scan (6-fold longer) of U, Fe, and P concentrations illustrated the spatial co-localization of these elements (Figure 3D). The detection of both P and Fe in the UO_2 -EPS provided additional evidence for the bacterial origin of these structures, while the P and Fe distributions

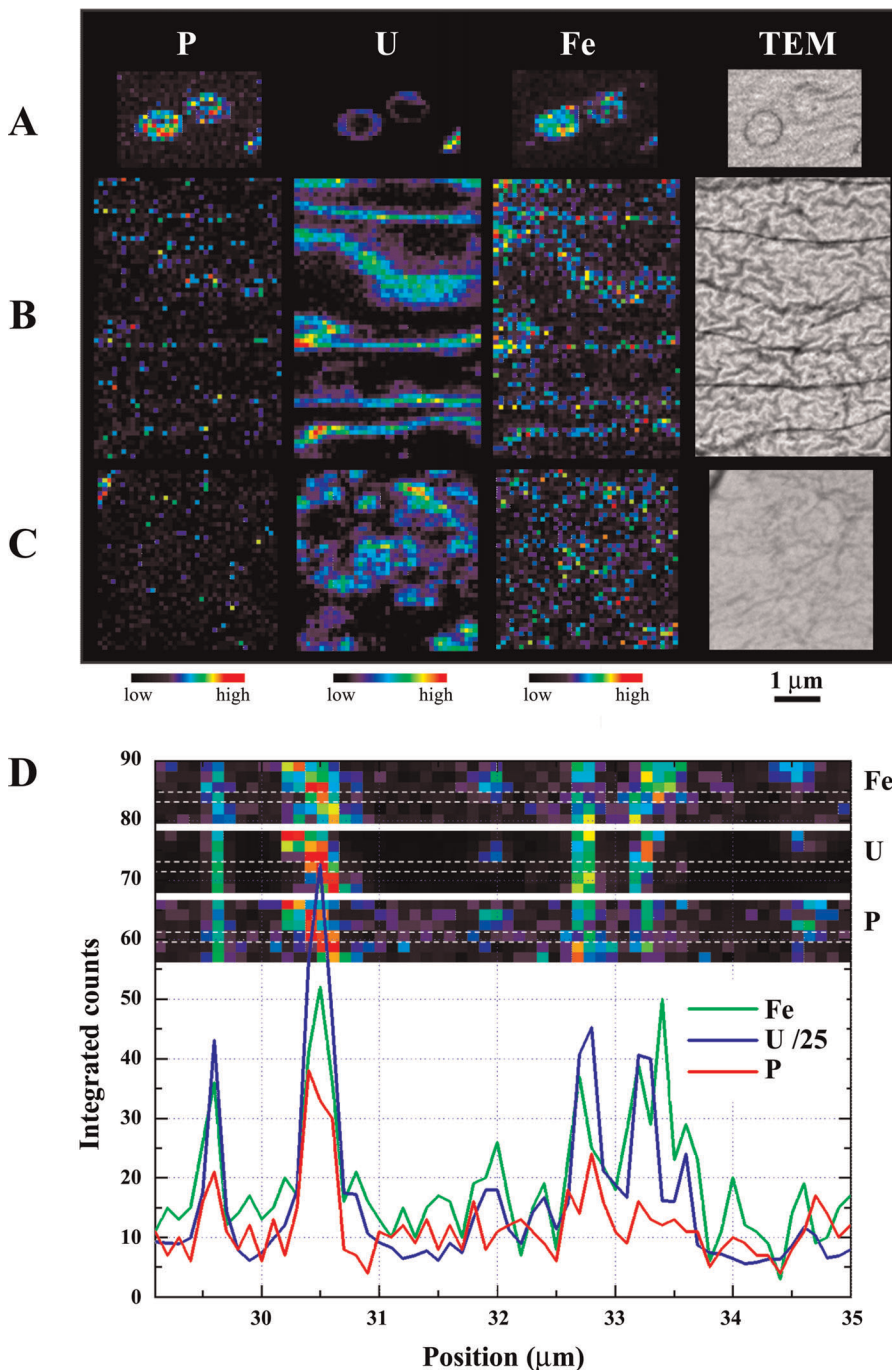


Figure 3. Synchrotron XRF Microscopy of the Elemental Concentration Gradients in Association with *S. oneidensis* MR-1 Cells

False-color micro-XRF maps of qualitative spatial distributions and concentration gradients of P, U, and Fe in and around MR-1 cells. Cells are shown after incubation with 250 μM U(VI) for 24 h in standard assay conditions (A). The extracellular UO₂ precipitates associated with EPS (B) and diffuse extracellular UO₂ nanoparticles (C) observed in MR-1 samples were also evaluated for elemental composition. The scanned regions are represented with each corresponding thin-section TEM image. (D) The UO₂-EPS features seen in (B) were scanned vertically six times longer per point, and the pixel intensity (identified between the dashed lines) was plotted for each element. Although this image is of a smaller area and has a smaller number of features in its field of view, the increased measurement time provides more robust statistics and further supports co-localization of the elements. DOI: 10.1371/journal.pbio.0040268.g003

found within the diffuse UO₂ aggregates appeared more or less randomly.

Heme staining was used to ascertain that the Fe signal in the UO₂-EPS detected by XRF was indicative of heme-containing metalloprotein(s). MR-1 cells incubated in the presence of U(VI) showed heme-bound peroxidase activity

which was uniformly distributed throughout the UO₂-EPS (Figure 4A). Moreover, when a similarly prepared sample was reacted with diaminobenzidine (DAB) but not developed with H₂O₂, the UO₂ nanoparticles were observed in the EPS material, but heme-bound peroxidase activity was not detected (Figure 4B). Together, this suggested that heme-

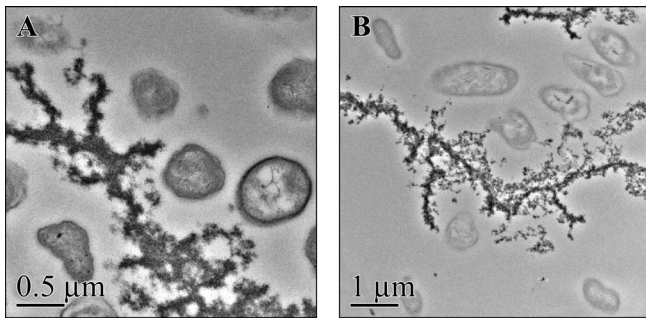


Figure 4. Heme Staining of Extracellular Cytochromes from *S. oneidensis* MR-1

TEM images of thin sections of MR-1 incubated for 24 h with 100 μM U(VI) and stained for the presence of heme. Samples were incubated with DAB and developed with H_2O_2 (A) or with DAB but not developed with H_2O_2 (B) prior to embedding. Heme-containing proteins detected in (A) were shown in close association with the undeveloped UO_2 -EPS seen in (B).

DOI: 10.1371/journal.pbio.0040268.g004

containing proteins were in close association with the UO_2 -EPS. It is of interest to note that the H_2O_2 used to develop the DAB stain caused partial oxidation of UO_2 ; however, the localization of the heme-containing proteins and the UO_2 -EPS was still apparent.

Using high-resolution immune-TEM, the localization of the OMCs in relation to the extracellular UO_2 matrix was investigated (Figure 5). Polyclonal antibodies which were produced toward unique surface-exposed domains of OmcA and MtrC revealed that these proteins were in close proximity with the cell-free UO_2 -EPS matrix (Figure 5B and 5D) and were rarely observed in association with cell surfaces (Figure 5A). MtrC and OmcA were consistently co-localized with each other and the UO_2 nanoparticles. Samples not receiving

MtrC- or OmcA-specific antibody did not reveal any labeling by colloidal gold of either the extracellular matrix or the cell surface (Figure 5F). Interestingly, immune-TEM revealed the close association of the integral OM protein MtrB with extracellular UO_2 -EPS matrix (Figure 5E). MtrB was also densely distributed over exposed regions of the MR-1 cell surface.

The UO_2 -EPS Is a Complex Glycocalyx-Like Structure

To further investigate the structure of UO_2 -EPS matrix, resting cells of *S. oneidensis* MR-1 were incubated in the presence of 250 μM U(VI) without shaking to minimize shear forces. The UO_2 -EPS visualized by whole-mount TEM appeared around many cells (Figure 6A) and also contained features which we attribute to the dehydration and collapse of an extracellular matrix similar to that observed using conventional fixation methods [30]. The use of cryo-HRSEM to preserve the complex three-dimensional structure eliminated the dehydration artifact observed in fixed U(VI)-reducing cultures. When samples were grown anaerobically in defined medium and prepared for cryo-HRSEM, the EPS matrix appeared as an intricate three-dimensional structure encompassing multiple cells. The visualization of single MR-1 cells demonstrated the delicate morphology of this material (Figure 6B and 6C). This demonstrated that the EPS was not only associated with resting cell suspension incubated with lactate and U but was produced under growth conditions.

Furthermore, insight into the composition of the extracellular matrix was gained using electrostatic charge determination, glycoconjugate-specific staining, and glycocalyx fixation techniques. In the absence of UO_2 , either positively or negatively charged particles were used to probe the charge characteristics of the extracellular material. Cationic nanogold particles were bound to small patches near the cell surface and to the EPS matrix (Figure 6D). Binding of anionic

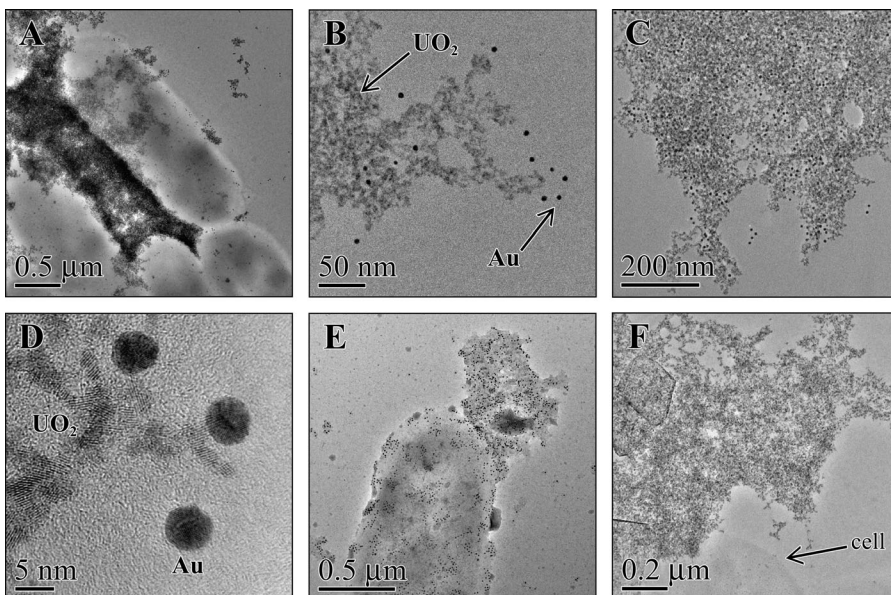


Figure 5. Immune-Localization of MtrC, OmcA, and MtrB with Extracellular UO_2 from *S. oneidensis* MR-1

Whole-mount TEM images of MR-1 incubated with 100 μM U(VI) for 24 h and reacted with specific antibodies to MtrC (A, B), OmcA (C, D), or MtrB (E). High-resolution image of nanocrystalline UO_2 associated with the extracellular matrix and the 5-nm particles of colloidal gold (Au) (B, D). Extracellular matrix and cell labeled with colloidal gold in the absence of specific antibody (F).

DOI: 10.1371/journal.pbio.0040268.g005

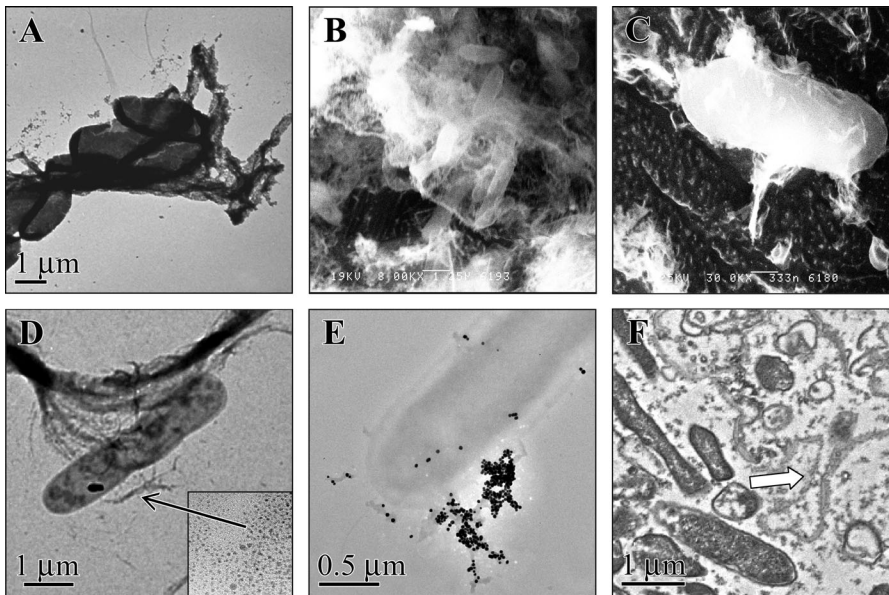


Figure 6. Extracellular Structure of *S. oneidensis* MR-1

Whole mounts of MR-1 incubated with 250 μM U(VI) for 24 h prior to visualization by TEM (A) or incubated in defined media and visualized by cryo-HRSEM (B, C). Whole-mount TEM of cells incubated with 1 mM fumarate added as the electron acceptor in place of U(VI) and reacted with positive charged colloidal nanogold particles (D) to help determine surface charge of the EPS matrix or the glycoconjugate-specific lectin, ConA, complexed with 40-nm particles of colloidal gold (E). High-resolution image of 1.4-nm gold nanoparticles (D inset). Thin-section TEM images of MR-1 incubated for 24 h with 1 mM fumarate prior to ruthenium red staining to visualize extracellular EPS (F). The ruthenium red-EPS is designated by the arrow. DOI: 10.1371/journal.pbio.0040268.g006

nanogold particles was not observed in similarly prepared samples. The glycoconjugate component of the extracellular EPS matrix was visualized using a lectin-colloidal gold complex. These samples showed an amorphous EPS matrix that was densely labeled with the gold (Figure 6E). These structures were similar to the extracellular UO_2 -EPS matrix observed during immune-TEM analysis of MtrC and OmcA. The glycoconjugate affinity was rarely observed in association with cell surfaces. These findings indicated that the UO_2 -EPS matrix also contained a significant glycoconjugate fraction.

Ruthenium red-lysine fixation was chosen as both a fixative and a stain to provide added stability and contrast to elaborate extracellular structures surrounding wild-type MR-1 cells grown in the absence of UO_2 . Ultrastructural analysis of samples fixed with this technique displayed an extended EPS that appeared electron dense due to the interaction with the ruthenium red (Figures 6F and S6). No staining with osmium tetroxide, uranyl acetate, or lead citrate was required to visualize these features. These extracellular structures were morphologically identical to the heme-containing EPS with a high density of associated UO_2 particles observed after U(VI) reduction by MR-1.

Discussion

The widespread distribution, metabolic versatility, and ability to respire metals as terminal electron acceptors underscore the important ecological role of *Shewanella* species in metal cycling in natural environments and their potential importance in controlling reductive transformation processes and metal mobility in contaminated groundwater. Earlier studies using *Shewanella* sp., *Geobacter* sp., and *Desulfovibrio* sp. demonstrated both extracellular and/or

periplasmic accumulation of reduced UO_2 particles and suggested that this process has important implications for the immobilization of U [5,18,25,31–33]. Previous investigations, however, did not identify the mediators of U(VI) reduction or the genesis of materials associated with the extracellular UO_2 . To address these questions, we used a novel combination of genetic, immunological, and microscopic analyses including targeted gene deletion, high-resolution microscopy, synchrotron-based XRF microscopy, heme staining of noncellular structures intricately associated with UO_2 , and visualization of the metal oxide-cytochrome interaction by high resolution immune-localization.

In this study, we established that MtrC, a decaheme *c*-type cytochrome previously reported to be involved in Fe(III) and Mn(IV) reduction [8,26], is responsible for at least a portion of the total extracellular U(VI) reductase activity in *S. oneidensis* MR-1. We found that deletions of *mtrC* or both *mtrC* and *omcA* genes significantly slowed the rate of reduction of U(VI) and affected the distribution and density of the U(IV) particles localized on the extracellular features. Our findings are in agreement with a recent report [34] that the absence of MtrC did not abolish but significantly decreased the reduction of U(VI) in MR-1. Interestingly, the deletion of another OM decaheme *c*-type cytochrome, *mtrF*, had little impact on the rate of U(VI) reduction. Although the amino acid homology of MtrF with MtrC (approximately 38%) suggested a similar function, to date there have been no reports of the involvement of MtrF in electron transfer to metals. Using in vitro electron transfer assays with recombinant cytochromes exhibiting Fe(III)-reductase activity, we demonstrated that MtrC, but not OmcA, can function as a terminal reductase of uranium. The in vivo experiments suggest that OmcA affected the rate of U(VI) reduction

similar to MtrC and thus was important for U(VI) reduction and electron transfer. Since the *in vitro* mixture of MtrC and OmcA did not enhance electron transfer rates, the native system may also require additional, as-of-yet-undetermined protein(s).

Moreover, we demonstrated that a mutant of *S. oneidensis* MR-1 deficient in cytochrome *c* maturation is unable to reduce soluble U(VI) carbonate complexes, indicating that functional *c*-type cytochromes are essential for U(VI) reduction and that MR-1 lacks a secondary independent U(VI) reductase system. Although this observation does not unequivocally rule out the involvement of specific redox enzymes in U reduction, we believe that reductive precipitation of U(IV) in *S. oneidensis* MR-1 is a process driven by low-potential periplasmic or OM-associated *c*-type cytochromes. Given the large number of predicted periplasmic and cytoplasmic membrane *c*-type cytochromes in the MR-1 genome [7] coupled with their typical lack of specificity in regards to electron transfer to metal ions, it seems likely that many of these low-potential *c*-type cytochromes may be capable of transferring electrons to U(VI) within the periplasm. We hypothesize that a complex network of *c*-type cytochromes with some functional redundancy, including MtrC, other OMCs, as well as periplasmic cytochromes, can function as uranyl reductases and influence the localization of both periplasmic and extracellular UO₂ nanoparticles in resting cell suspensions of *S. oneidensis* MR-1. The involvement of a redundant network of both OM and periplasmic cytochromes for U(VI) reduction has not previously been reported for *Shewanella* or other U(VI)-reducing bacteria. Biochemical studies suggest that low-molecular-mass *c*₃ or *c*₇ cytochromes located in the periplasm are important electron carriers in U(VI) reduction by *Desulfovibrio* sp. and *Geobacter* sp., respectively [11,35]. Interestingly, Lloyd et al. found that the periplasmic *c*₇ cytochrome PpcA, produced by *Geobacter sulfurreducens*, was not the sole U(VI) reductase [11] but also reported that the surface OMCs are not involved in U(VI) reduction [31]. Clearly, further studies will be required to fully understand the complete electron transfer pathways involved in microbial U(VI) reduction.

The combination of high-resolution imaging, XRF microscopy, and immune-localization analyses used in this study support the biological origin of the EPS material containing dense accumulations of UO₂ nanoparticles. We established that the extracellular U(IV) nanoparticles are in close association with the MtrC and OmcA decaheme *c*-type cytochromes which are present within the EPS. While the direct involvement of MtrC in U(VI) reduction is not surprising, this is the first report of extracellular localization of a decaheme cytochrome in direct association with UO₂ nanoparticles. It has recently been reported that MtrC and OmcA form a functional high-affinity complex *in vivo* [36]. This finding would explain the co-localization of MtrC and OmcA in direct association with the UO₂ nanoparticles, although the latter had very little effect on the localization of UO₂ nanoparticles and was unable to function as a terminal reductase of U(VI) citrate *in vitro*.

Significantly, the presence of an integral OM protein (MtrB) within the UO₂-EPS matrix as well as on the cell surface of MR-1 suggests that the extracellular material may be comprised, at least in part, of OM or an OM-derived material. MtrB has previously been shown to have epitopes

exposed on the outside surface of the *S. oneidensis* MR-1 OM and has not been found in soluble cell extracts [17]. Together, this evidence suggests the existence of an OM-like EPS produced by MR-1 associated with high-molecular decaheme *c*-type cytochromes which promote the formation of biogenic UO₂ nanoparticles.

In some gram-negative bacteria, such as *Pseudomonas putida* G7, EPS has been shown to have a significant metal-binding capacity [30]. Since our findings suggested that the matrix was negatively charged, we hypothesized that electrostatic interactions may have been involved in the formation of the UO₂-EPS structures in *S. oneidensis* MR-1. Olsson et al. [37], reported that the surface charge of UO₂ (pH of point of zero charge = 5.0 to 5.5) at similar pH conditions would also be negative and thus electrostatic interactions may not be responsible for binding of the biogenic UO₂ nanoparticles. However, these same authors note that the oxidation of the UO₂ surface can lead to higher point of zero charge values, and such effects cannot be excluded here. Given the complexity of the extracellular matrix including the *c*-type cytochromes OmcA and MtrC, other undetermined factors may also attribute to the strong interaction of the matrix with the UO₂. These interactions could be advantageous to maintaining nanoparticle stability because the individual fine-grained UO₂ particles observed in this study were of a size (1 to 5 nm) that would be subject to rapid reoxidation by O₂ [38] or colloidal transport. The apparently close, interactive molecular association of the nanoparticulate UO_{2(s)} with these complex biopolymers in the environment could influence (e.g., slow) the oxidation rate of U(IV) and prevent the mobilization of the small precipitates as dispersed colloids in pore or groundwater. Collectively, our results imply that the environmental behavior of the biogenic UO_{2(s)} will be strongly influenced by this unusual structural association.

Recent microarray expression studies have shown that approximately 7% of all MR-1 genes upregulated under U(VI)-reducing conditions encode proteins involved in membrane/periplasmic stress response [34]. Unlike chromium(VI), there does not appear to be a U(VI)-specific detoxification system in MR-1 [34]. This finding could possibly explain the formation of the UO₂-EPS as a turnover mechanism to rid cells of UO₂. While the detailed composition and genesis of the material associated with the UO₂-EPS remain undetermined, the presence of the lipoproteins MtrC and OmcA, integral OM protein, and the glycoconjugate component together suggests that multiple elements of the OM and polysaccharide are key components of these structures. The formation of the UO₂-EPS matrix observed in our study may represent an important mechanism by which *Shewanella* is able to rid the cell periplasm and surface of the UO₂ nanoparticles that are clearly generated from more than one *c*-type cytochrome. Alternatively, the EPS produced by *Shewanella* may be an extension of the OM-bound electron transport chain that is directly involved in extracellular U(VI) to UO₂ nanoparticle formation that remains in association with EPS [33,39–41].

Although its exact function remains to be determined, production of EPS by *S. oneidensis* MR-1 does not appear to be required for U(VI) reduction since OMC mutants that produce little UO₂-EPS are capable of reducing U(VI). Studies are under way to isolate mutants with reduced or

abolished ability to produce EPS and to characterize their impact on U(VI) reduction and localization as well as to determine whether extracellular UO₂ nanoparticles observed in association with other U(VI)-reducing bacteria are similarly associated with EPS [18,31–33].

This report is the first to confirm the role of *c*-type cytochromes in the reduction of U(VI) in *S. oneidensis* MR-1 and, more specifically, directly link OM-associated *c*-type cytochromes with U(VI) reduction and localization outside the cell. Furthermore, we conclusively show the intimate association of these high-molecular cytochromes with extracellular biogenically reduced UO₂. While the exact function(s) of this novel cytochrome-UO₂ association remains unclear, this co-localization could have important implications for understanding long-term fate of biogenic UO₂ in subsurface environments.

Materials and Methods

Chemicals and media. All chemicals used in this study were purchased from Sigma Chemical Co. (St. Louis, Missouri, United States) unless otherwise noted. Growth media were purchased from BD Diagnostics (Sparks, Maryland, United States).

Generation of cytochrome deletion mutants. *S. oneidensis* MR-1 mutants lacking selected OMC genes were constructed using two-step homologous recombination with a suicide plasmid encoding flanking DNA sequence with a modification of previously described methods [42,43]. The detailed procedures outlining mutant construction and the primers, plasmids, and strains used in this study are described in detail in Protocol S1 and Tables S1 and S2.

U(VI) reduction and localization assay conditions. The kinetics of aqueous U(VI) reduction and localization in wild-type MR-1 and mutant cells were determined in a standard resting cell assay. Tryptic soy broth–dextrose cultures (100 ml) were grown for 16 h (30 °C) at 100 rpm and harvested by centrifugation (5,000 × *g*, 5 min). Cells were washed once in equal volume of 30 mM sodium bicarbonate buffer (pH 7.0, 4 °C), pelleted, and standardized by suspending all treatments in the fresh buffer at a concentration of 2 × 10⁹ cells/ml prior to being purged for approximately 10 min with mixed gas (N₂/CO₂ 80:20). U(VI) reduction assays contained a final concentration of 250 μM U(VI) as uranyl acetate and 10 mM sodium lactate in 30 mM sodium bicarbonate purged with O₂-free mixed gas and sealed with thick butyl rubber stoppers. Kinetic studies were initiated by the addition of 1 ml of standardized cells to the assay tubes followed by horizontal incubation at 30 °C with slow gyratory shaking (25 rpm) resulting in a final assay density of 2 × 10⁸ cells/ml. The amount of soluble U(VI) remaining in filtrates (less than 0.2-μm pore size) from all samples was analyzed at multiple time points using a kinetic phosphorescence analyzer (KPA-10; Chemchek Instruments, Richland, Washington, United States) as previously described [44]. Metal reduction curves were compared using nonparametric procedures, specifically the Wilcoxon signed-rank test. These tests were conducted using Systat 10 (SPSS Inc, Chicago, Illinois, United States) and were considered significant at *p* < 0.01; specific values of *P* are reported where relevant.

Reductase activity of recombinant cytochromes. The recombinant *c*-type cytochromes, OmcA and MtrC, were expressed and purified as described previously [36]. Proteins were prepared at a concentration of 10 μM (100 μM heme) in buffer containing 100 mM HEPES buffer (pH 7.5), 50 mM NaCl, 10% glycerol, and 1% (w/v) of *n*-octyl-β-D-glucopyranoside and purged with O₂-free N₂ gas. The reaction of recombinant cytochrome (rMtrC, rOmcA, or rMtrC and rOmcA), reduced by titrating with dithionite, with U(VI) was initiated by the addition of equal volumes of cytochrome with 300 μM U(VI) in 5 mM sodium citrate buffer in an anoxic atmosphere. Oxidation of heme was monitored using a Hi-Tech SFA-20 stopped-flow system with a 1-cm pathlength cell integrated with a Hewlett-Packard 8543 diode-array spectrophotometer capable of following reaction kinetics at multiple wavelengths. To access the activity of the purified cytochromes used for U(VI) experiments, the reaction of dithionite-reduced cytochrome with an equal volume of 300 μM Fe(III)-NTA in 100 mM HEPES buffer (pH 7.5) was also monitored. The reaction between reduced cytochrome and either U(VI) or Fe(III)-NTA was analyzed using protocols detailed by Dobbin et al. [45].

Production of antibodies. Affinity-purified antibodies toward

predicted hydrophilic and surface-exposed regions of MtrC, OmcA, and MtrB were designed and produced commercially (Biosynthesis, Lewisville, Texas, United States) (Table S3). The peptide sequences selected for antibody production were confirmed for antigenic uniqueness using BLASTP analysis against all MR-1 proteins. Affinity purified antibodies, from 0.4 to 0.7 mg/ml stocks solutions, were tested for specificity using immunoblots of MR-1 and mutant cells as described in Protocol S1.

TEM. Cells were prepared for TEM of plastic sections in an anaerobic glove bag (Ar/H₂, 95:5) using anoxic solutions. Three milliliters of cell suspension incubated for 24 h with U was centrifuged (2,300 × *g*, 5 min), and the cell pellet was fixed in 2.5% glutaraldehyde (Electron Microscopy Sciences [EMS], Fort Washington, Pennsylvania, United States) prior to dehydration in an ascending series of ethanol and infiltration in LR White embedding resin (EMS) and cured at 60 °C. Blocks were sectioned anaerobically to 70 nm with a Diatome 45-degree diamond knife using an Ultracut UCT ultramicrotome (Leica, Bannockburn, Illinois, United States) and mounted on 200 mesh copper grids with formvar support film coated with carbon. Unstained sections were examined at 200 kV using JEOL 2010 high-resolution TEM equipped with LaB₆ filament with a resolution of 1.9 Å. Images were digitally collected and analyzed using DigitalMicrograph software (Gatan Inc, Pleasanton, California, United States). The elemental composition of precipitates was determined using electron dispersive spectroscopy (Oxford Instruments, Fremont, California, United States) equipped with SiLi detector and analyzed with ISIS software. Selected area diffraction patterns were evaluated using the Desktop Microscopist software (Lacuna Laboratories, Tempe, Arizona, United States).

Cryo-high-resolution scanning electron microscopy. Samples of wild-type MR-1 were grown anaerobically with fumarate in modified basal minimal medium (pH 7.5) [46] without agitation and prepared for cryo-high-resolution scanning electron microscopy (HRSEM) as described by Apkarian et al. [47]. Bacterial cell suspension was frozen in high-pressure freezer (Bal-Tec), transferred onto a cryostage (Oxford CT-3500), and sputtered with chromium. Samples were examined at in-lens cryo-HRSEM (DS-130F) at 25 kV at –150 °C. Imaging was done with minimal dwell time to eliminate the beam damage, resulting in images of fully hydrated, unfixed specimens immersed in featureless amorphous ice.

Characterization of extracellular matrix by TEM. For immunolocalizations, cells were prepared as described above except that a final concentration of 100 μM U(VI) was used. After 24-h incubation, cells were briefly fixed in 2% paraformaldehyde (EMS) and 0.1% glutaraldehyde. Following fixation, whole mounts were prepared by placing 10 μl on formvar/copper grids and the liquid removed by wicking. Whole mount TEM grids were also prepared in a similar manner on unfixed cells incubated with 250 μM U(VI) without shaking. Immune-localization samples were blocked in PBS (10 mM sodium phosphate [pH 7.2] and 140 mM sodium chloride) containing 2% BSA (PBS/BSA). Antibodies (diluted 1:2 in PBS/BSA) were reacted for 30 min with the samples followed by five PBS washes before incubation with the 5-nm gold secondary antibody (diluted 1:5 in PBS/BSA). Samples were washed five times in PBS and fixed with 2.5% glutaraldehyde followed by two water rinses. Antibody specificity was verified in all localization studies by reacting similarly prepared grids with colloidal gold detection antibody in the absence of specific antibody and by using naive sera as controls.

The detection of heme by TEM was performed using 3,3'-DAB (EMS) [48]. Cells were collected by centrifugation and fixed for plastic embedding as described above. The fixative was replaced by three washes in 100 mM sodium cacodylate buffer (EMS) followed by three incubations (two 15-min and one 10-min) in cacodylate buffer containing fresh DAB. The heme stain was developed by the addition of 600 μl of fresh DAB solution and 30 μl of 3% H₂O₂. Control samples received fresh DAB solution without 3% H₂O₂. The reaction was stopped by washing three times in cacodylate buffer before embedding.

The extracellular matrix was investigated in the absence of U by labeling with charged nanogold particles, glycoconjugate visualization, or ruthenium red staining. Cells were prepared as described above except that 1 mM fumarate was added as the electron acceptor in place of U(VI). To determine the surface charge of the extracellular material, whole mounts were prepared for TEM and reacted with either positive or negative charged nanogold particles (1.4 nm) (Nanoprobe, Yaphank, New York, United States). Grids were labeled for 1 min with nanogold particles diluted 1:5 in cacodylate buffer followed by one rinse in cacodylate buffer and two water rinses. For glycoconjugate visualization, samples were reacted with a lectin, concanavalin A, conjugated with 40-nm gold beads (EY

Laboratories, Inc, San Mateo, California, United States) diluted 1:5 in cacodylate buffer for 2 min. Samples were rinsed twice in cacodylate buffer followed by two water rinses. To visualize delicate extracellular structures such as a glycocalyx, a ruthenium red-lysine fixation was chosen [49]. An equal volume of 2× stain cocktail (60 mM lysine, 4% paraformaldehyde, 5% glutaraldehyde, 0.15% ruthenium red, and 200 mM cacodylate buffer) was added to each sample and gently mixed by inversion. After 15 min, cells were collected by centrifugation at $2,300 \times g$ for 30 s. Cells were washed three times in 100 mM cacodylate buffer followed by dehydration and embedding as described above.

Synchrotron XRF analysis. Synchrotron-based XRF microscopy analysis [29] was performed using the 2IDD beam line [50] at the Advanced Photon Source (Argonne, Illinois, United States). The steps involved in beam-line calibration, generation of two-dimensional elemental maps, and XRF spectrum analysis are described in Protocol S1.

Supporting Information

Figure S1. Immunoblot Analysis of the MtrC/OmcA Cytochromes in *S. oneidensis* MR-1 and Cytochrome Mutants

Immunoblot analysis of 10 µg of total protein from overnight cultures of MR-1 (lanes 1), MtrC⁻ (lanes 2), OmcA⁻ (lanes 3), and MtrC⁻/OmcA⁻ (lanes 4) resolved by SDS-PAGE and developed with specific antibodies toward MtrC (A) or OmcA (B).

Found at DOI: 10.1371/journal.pbio.0040268.sg001 (2.0 MB TIF).

Figure S2. Oxidation Rates of Reduced MtrC by Uranium Citrate

The oxidation of dithionite-reduced 10 µM MtrC in HEPES buffer (pH 7.5) was calculated when mixed with 300 µM U(VI) in sodium citrate buffer. The oxidation of heme was monitored in an anoxic atmosphere.

Found at DOI: 10.1371/journal.pbio.0040268.sg002 (1.2 MB TIF).

Figure S3. UO₂ Localization in *S. oneidensis* MR-1 Cells

TEM micrographs prepared from cell suspensions incubated with 250 µM uranyl acetate and 10 mM lactate for 24 h. The localization of the UO₂-EPS in close association with MR-1 cells (A–C). High-resolution images of cells illustrate the localization of UO₂ relative to the outer and cell membranes of intact cells (C–F). The UO₂-EPS is designated by the arrows. Locations of the cell membrane (CM), periplasm (P), and OM are shown.

Found at DOI: 10.1371/journal.pbio.0040268.sg003 (7.0 MB TIF).

Figure S4. TEM-Coupled Analysis of Extracellular UO₂ Nanoparticles

Nanocrystalline UO₂ material was evaluated by selected area electron diffraction (A) and electron dispersive spectrometry (B).

Found at DOI: 10.1371/journal.pbio.0040268.sg004 (6.3 MB TIF).

Figure S5. Quantification of the Elemental Area Concentrations within Structures Studied by XRF Analysis

The counts under the peaks of each element in the background-subtracted spectra were used to determine area concentrations of Fe (A) and P (B) in each object of interest. Volume concentrations (ppm) were obtained by assuming a uniform 110 nm thickness of the slices, density of 1.0 g/cm³, uniform coverage of material within the dimension of the X-ray probe, and a uniform distribution along the

sample thickness. Error bars in the final concentrations account only for sample-to-sample variability in the final concentrations.

Found at DOI: 10.1371/journal.pbio.0040268.sg005 (582 KB TIF).

Figure S6. Ruthenium Red Staining of Extracellular Structures from *S. oneidensis* MR-1

Thin section TEM images of MR-1 incubated for 24 h with 1 mM fumarate prior to ruthenium red staining to visualize extracellular structures. The ruthenium red-associated EPS is designated by the arrows.

Found at DOI: 10.1371/journal.pbio.0040268.sg006 (3.4 MB TIF).

Protocol S1. Supporting Methods

Found at DOI: 10.1371/journal.pbio.0040268.sd001 (44 KB DOC).

Table S1. Bacterial Strains and Plasmids Used for This Study

Found at DOI: 10.1371/journal.pbio.0040268.st001 (26 KB DOC).

Table S2. Primers Used to Create the In-frame Mutants in This Study

Found at DOI: 10.1371/journal.pbio.0040268.st002 (19 KB DOC).

Table S3. Peptide Sequences Used to Produce Specific Antisera

Found at DOI: 10.1371/journal.pbio.0040268.st003 (27 KB DOC).

Accession Numbers

The GenBank (<http://www.ncbi.nlm.nih.gov/Genbank>) accession numbers for the protein sequences described in this paper are found are MtrC (gi|24373344), OmcA (gi|24373345), and MtrF (gi|24373346).

Acknowledgments

A portion of the research was performed as part of an EMSL Scientific Grand Challenge project at the W. R. Wiley Environmental Molecular Sciences Laboratory, a national scientific user facility sponsored by OBER and located at Pacific Northwest National Laboratory (PNNL). PNNL is operated for the DOE by Battelle Memorial Institute under contract DE-AC05-76RL01830. Work at the Advanced Photon Source is supported by the DOE Office of Science, Office of Basic Energy Sciences. General user support for the XRF microprobe work was also provided by the DOE's Environmental Remediation Sciences division. Cryo-HRSEM was performed at Emory University with expertise provided by Dr. Robert Apkarian. We would also like to thank Dr. Ray Wildung for his careful review of the manuscript and Tara Hoyem for her assistance in the preparation and submission of the manuscript.

Author contributions. MJM, ASB, KMK, JKF, and JMZ conceived and designed the experiments. MJM, ACD, DWK, LS, ZW, MIB, BL, KMK, JSM, SBR, DEC, and CJS performed the experiments. MJM, ASB, KMK, VLB, JKF, and JMZ analyzed the data. DAS and MFR contributed reagents/materials/analysis tools. MJM, ASB, JKF, and JMZ wrote the paper.

Funding. This research was supported by the United States Department of Energy (DOE), Office of Biological and Environmental Research (OBER), Environmental Remediation Sciences Program (ERSP), and Genomics: Genomes to Life Programs.

Competing interests. The authors have declared that no competing interests exist.

References

- Lovley DR, Holmes DE, Nevin KP (2004) Dissimilatory Fe(III) and Mn(IV) reduction. *Adv Microb Physiol* 49: 219–286.
- Nealson KH, Saffarini D (1994) Iron and manganese in anaerobic respiration: Environmental significance, physiology, and regulation. *Annu Rev Microbiol* 48: 311–343.
- Rusin PA, Quintana L, Brainard JR, Strietelmeier BA, Tait CD, et al. (1994) Solubilization of plutonium hydrous oxide by iron-reducing bacteria. *Environ Sci Technol* 28: 1686–1690.
- Carpentier W, Sandra K, De Smet I, Brige A, De Smet L, et al. (2003) Microbial reduction and precipitation of vanadium by *Shewanella oneidensis*. *Appl Environ Microbiol* 69: 3636–3639.
- Liu C, Gorby YA, Zachara JM, Fredrickson JK, Brown CF (2002) Reduction kinetics of Fe(III), Co(III), U(VI), Cr(VI), and Tc(VII) in cultures of dissimilatory metal-reducing bacteria. *Biotechnol Bioeng* 80: 637–649.
- Myers CR, Nealson KH (1988) Bacterial manganese reduction and growth

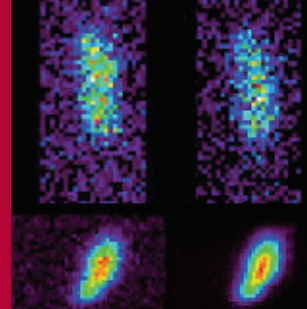
with manganese oxide as the sole electron acceptor. *Science* 240: 1319–1321.

- Meyer TE, Tsapin AI, Vandenberghe I, de Smet L, Frishman D, et al. (2004) Identification of 42 possible cytochrome *c* genes in the *Shewanella oneidensis* genome and characterization of six soluble cytochromes. *Omic* 8: 57–77.
- Beliaev AS, Saffarini DA, McLaughlin JL, Hunnicutt D (2001) MtrC, an outer membrane decahaem *c* cytochrome required for metal reduction in *Shewanella putrefaciens* MR-1. *Mol Microbiol* 39: 722–730.
- Gaspard S, Vazquez F, Holliger C (1998) Localization and solubilization of the iron(III) reductase of *Geobacter sulfurreducens*. *Appl Environ Microbiol* 64: 3188–3194.
- Heidelberg JF, Paulsen IT, Nelson KE, Gaidos EJ, Nelson WC, et al. (2002) Genome sequence of the dissimilatory metal ion-reducing bacterium *Shewanella oneidensis*. *Nat Biotechnol* 20: 1118–1123.
- Lloyd JR, Leang C, Hodges Myerson AL, Coppi MV, Cuifio S, et al. (2003) Biochemical and genetic characterization of PpcA, a periplasmic *c*-type cytochrome in *Geobacter sulfurreducens*. *Biochem J* 369: 153–161.

12. Methe BA, Nelson KE, Eisen JA, Paulsen IT, Nelson W, et al. (2003) Genome of *Geobacter sulfurreducens*: Metal reduction in subsurface environments. *Science* 302: 1967–1969.
13. Myers CR, Myers JM (1992) Localization of cytochromes to the outer membrane of anaerobically grown *Shewanella putrefaciens* MR-1. *J Bacteriol* 174: 3429–3438.
14. Myers CR, Myers JM (1997) Outer membrane cytochromes of *Shewanella putrefaciens* MR-1: Spectral analysis, and purification of the 83-kDa *c*-type cytochrome. *Biochim Biophys Acta* 1326: 307–318.
15. Beliaev AS, Saffarini DA (1998) *Shewanella putrefaciens mtrB* encodes an outer membrane protein required for Fe(III) and Mn(IV) reduction. *J Bacteriol* 180: 6292–6297.
16. Myers JM, Myers CR (1998) Isolation and sequence of *omcA*, a gene encoding a decaheme outer membrane cytochrome *c* of *Shewanella putrefaciens* MR-1, and detection of *omcA* homologs in other strains of *S. putrefaciens*. *Biochim Biophys Acta* 1373: 237–251.
17. Myers CR, Myers JM (2003) Cell surface exposure of the outer membrane cytochromes of *Shewanella oneidensis* MR-1. *Lett Appl Microbiol* 37: 254–258.
18. Gorby YA, Lovley DR (1992) Enzymatic uranium precipitation. *Environ Sci Technol* 26: 205–207.
19. Lovley DR, Phillips EJP, Gorby YA, Landa ER (1991) Microbial reduction of uranium. *Nature* 350: 413–416.
20. Truex MJ, Peyton BM, Valentine NB, Gorby YA (1997) Kinetics of U(VI) reduction by a dissimilatory Fe(III)-reducing bacterium under non-growth conditions. *Biotechnol Bioeng* 55: 490–496.
21. Lovley DR, Phillips EJP (1992) Bioremediation of uranium contamination with enzymatic uranium reduction. *Environ Sci Technol* 26: 2228–2234.
22. Abdelouas A, Lu YM, Lutze W, Nuttall HE (1998) Reduction of U(VI) to U(IV) by indigenous bacteria in contaminated ground water. *J Contam Hydrol* 35: 217–233.
23. Anderson RT, Vrionis HA, Ortiz-Bernad I, Resch CT, Long PE, et al. (2003) Stimulating the *in situ* activity of *Geobacter* species to remove uranium from the groundwater of a uranium-contaminated aquifer. *Appl Environ Microbiol* 69: 5884–5891.
24. Fredrickson JK, Zachara JM, Kennedy DW, Liu C, Duff MC, et al. (2002) Influence of Mn oxides on the reduction of uranium(VI) by the metal-reducing bacterium *Shewanella putrefaciens*. *Geochim Cosmochim Acta* 66: 3247–3262.
25. Liu C, Zachara JM, Fredrickson JK, Kennedy DW, Dohnalkova A (2002) Modeling the inhibition of the bacterial reduction of U(VI) by beta-MnO_{2(s)}. *Environ Sci Technol* 36: 1452–1459.
26. Bouhenni R, Gehrke A, Saffarini D (2005) Identification of genes involved in cytochrome *c* biogenesis in *Shewanella oneidensis*, using a modified mariner transposon. *Appl Environ Microbiol* 71: 4935–4937.
27. Fredrickson JK, Zachara JM, Kennedy DW, Duff MC, Gorby YA, et al. (2000) Reduction of U(VI) in goethite (α -FeOOH) suspensions by a dissimilatory metal-reducing bacterium. *Geochim Cosmochim Acta* 64: 3085–3098.
28. Wang Z, Zachara JM, Yantasee W, Gassman PL, Liu C, et al. (2004) Cryogenic laser induced fluorescence characterization of U(VI) in Hanford Vadose Zone pore waters. *Environ Sci Technol* 38: 5591–5597.
29. Kemner KM, Kelly SD, Lai B, Maser J, O'Loughlin E J, et al. (2004) Elemental and redox analysis of single bacterial cells by x-ray microbeam analysis. *Science* 306: 686–687.
30. Kachlany SC, Lavery SB, Kim JS, Reuhs BL, Lion LW, et al. (2001) Structure and carbohydrate analysis of the exopolysaccharide capsule of *Pseudomonas putida* G7. *Environ Microbiol* 3: 774–784.
31. Lloyd JR, Chesnes J, Glasauer S, Bunker DJ, Livens FR, et al. (2002) Reduction of actinides and fission products by Fe(III)-reducing bacteria. *Geomicrobiology J* 19: 103–120.
32. Lovley DR, Phillips EJP (1992) Reduction of uranium by *Desulfovibrio desulfuricans*. *Appl Environ Microbiol* 58: 850–856.
33. Payne RB, Casalot L, Rivere T, Terry JH, Larsen L, et al. (2004) Interaction between uranium and the cytochrome *c3* of *Desulfovibrio desulfuricans* strain G20. *Arch Microbiol* 181: 398–406.
34. Bencheikh-Latmani R, Williams SM, Hauke L, Criddle CS, Wu L, et al. (2005) Global transcriptional profiling of *Shewanella oneidensis* MR-1 during Cr(VI) and U(VI) reduction. *Appl Environ Microbiol* 71: 7453–7460.
35. Lovley DR, Widman PK, Woodward JC, Phillips EJP (1993) Reduction of uranium by cytochrome *c3* of *Desulfovibrio vulgaris*. *Appl Environ Microbiol* 59: 3572–3576.
36. Shi L, Chen B, Wang Z, Elias DA, Mayer U, et al. (2006) Isolation of high-affinity functional protein complex between OmcA and MtrC: Two outer membrane decaheme *c*-type cytochromes of *Shewanella oneidensis* MR-1. *J Bacteriol* 188: 4705–4714.
37. Olsson M, Jakobsson AM, Albinsson Y (2002) Surface charge densities of two actinide(IV) oxides: UO₂ and ThO₂. *J Colloid Interface Sci* 256: 256–261.
38. Suzuki Y, Kelly SD, Kemner KM, Banfield JF (2002) Nanometre-size products of uranium bioreduction. *Nature* 419: 134.
39. Nevin KP, Lovley DR (2002) Mechanisms for accessing insoluble Fe(III) oxide during dissimilatory Fe(III) reduction by *Geothrix fermentans*. *Appl Environ Microbiol* 68: 2294–2299.
40. Newman DK, Kolter R (2000) A role for excreted quinones in extracellular electron transfer. *Nature* 405: 94–97.
41. Seeliger S, Cord-Ruwisch R, Schink B (1998) A periplasmic and extracellular *c*-type cytochrome of *Geobacter sulfurreducens* acts as a ferric iron reductase and as an electron carrier to other acceptors or to partner bacteria. *J Bacteriol* 180: 3686–3691.
42. Wan XF, Verberkmoes NC, McCue LA, Stanek D, Connelly H, et al. (2004) Transcriptomic and proteomic characterization of the Fur regulon in the metal-reducing bacterium *Shewanella oneidensis*. *J Bacteriol* 186: 8385–8400.
43. Link AJ, Phillips D, Church GM (1997) Methods for generating precise deletions and insertions in the genome of wild-type *Escherichia coli*: Application to open reading frame characterization. *J Bacteriol* 179: 6228–6237.
44. Fredrickson JK, Kostandarites HM, Li SW, Plymale AE, Daly MJ (2000) Reduction of Fe(III), Cr(VI), U(VI), and Tc(VII) by *Deinococcus radiodurans* R1. *Appl Environ Microbiol* 66: 2006–2011.
45. Dobbin PS, Butt JN, Powell AK, Reid GA, Richardson DJ (1999) Characterization of a flavocytochrome that is induced during the anaerobic respiration of Fe³⁺ by *Shewanella frigidimarina* NCIMB400. *Biochem J* 342: 439–448.
46. Beliaev AS, Klingeman DM, Klappenbach JA, Wu L, Romine MF, et al. (2005) Global transcriptome analysis of *Shewanella oneidensis* MR-1 exposed to different terminal electron acceptors. *J Bacteriol* 187: 7138–7145.
47. Apkarian RP, Caran KL, Robinson KA (1999) Topographic imaging of chromium-coated frozen-hydrated cell and macromolecular complexes by in-lens field emission scanning electron microscopy. *Microsc Microanal* 5: 197–207.
48. Thomas PE, Ryan D, Levin W (1976) An improved staining procedure for the detection of the peroxidase activity of cytochrome P-450 on sodium dodecyl sulfate polyacrylamide gels. *Anal Biochem* 75: 168–176.
49. Fassel TA, Edmiston CE (2000) Evaluating adherent bacteria and biofilm using electron microscopy. In: An YH, Friedman RJ, editors. *Handbook of Bacterial Adhesion: Principles, Methods, and Applications*. Totowa (New Jersey): Humana Press. pp. 235–248.
50. Cai Z, Lai B, Yun W, Ilinski P, Legnini D, et al. (2000) A hard X-ray scanning microprobe for fluorescence imaging and microdiffraction at the advanced photon source. In: Meyer-Ilse W, Warwick T, Attwood D, editors. *Proceedings of the Sixth International Conference on X-ray Microscopy*, American Institute of Physics, Melville, NY, pp. 472–477.

Synchrotron X-ray Investigations of Mineral–Microbe–Metal Interactions

Kenneth M. Kemner, Edward J. O’Loughlin, Shelly D. Kelly, and Maxim I. Boyanov¹



Interactions between microbes and minerals can play an important role in metal transformations (i.e. changes to an element’s valence state, coordination chemistry, or both), which can ultimately affect that element’s mobility. Mineralogy affects microbial metabolism and ecology in a system; microbes, in turn, can affect the system’s mineralogy. Increasingly, synchrotron-based X-ray experiments are in routine use for determining an element’s valence state and coordination chemistry, as well as for examining the role of microbes in metal transformations.

KEYWORDS: X-ray, XAFS, X-ray microscopy, geomicrobiology, biogeochemistry

INTRODUCTION

More than 4000 mineral species have been identified, and the advent of molecular biology has revealed that Earth is populated by far more species of microbes than there are types of minerals (Skinner 1997). Archaea and Bacteria are the two prokaryotic domains of microscopic life that influence metal transformations in the environment (Woese 1987; Banfield and Nealson 1997). The most important properties of prokaryotes with regard to metal transformations are their size (typically approximately 0.5–5 microns) and the versatility of their metabolism. Prokaryotes can use a wide variety of electron donors. For respiration, they exploit many different electron acceptors besides O₂, including redox-reactive soluble ions and minerals. Often, the reactions involved in bacterial respiration result in the transfer of electrons (and thus the transformation of an element to a different valence state) or in alteration of an element’s local chemical environment. All of these changes can have profound effects on the element’s mobility through the lithosphere. Researchers are continually finding, in a remarkable array of environments, new microbial species capitalizing on chemical disequilibria in which enzymes catalyze otherwise slow reactions. Typically, cell densities of 10⁶–10⁹ cells per gram occur in soils and in the deeper subsurface (Barns and Nierzwicki-Bauer 1997). Their large cell densities, high surface-to-volume ratios, and versatile catalytic capabilities enable microbes to play major roles in metal transformations in subsurface and aquatic environments.

Many of the most pertinent questions regarding biogeochemical processes at microbe–mineral interfaces involve understanding which chemical reactions a microbe uses to gain energy, and the mechanisms by which it does this. The reactions often result in the transfer of electrons between living and nonliving entities. Synchrotron-based X-ray investigations of biogeochemical systems can identify the changes in an element’s valence state and chemical speciation, which often result from microbially mediated electron transfer. These are powerful approaches for studying samples in their natural, often hydrated, states.

The double-headed arrows in FIGURE 1 represent some of the biogeochemical interactions near the mineral–microbe interface that are responsible for metal transformations. Extracellular organic material commonly found in soils and aquifers consists of a vast array of particulate and dissolved organic matter. These include humic substances, low-molecular-weight organic acids and carbohydrates,

and a variety of microbially produced outer cellular polymeric substances (which include polysaccharides, DNA, RNA, and proteins) that may be attached to or exuded from the cell. These materials can interact with mineral surfaces and metals and can serve as a carbon source or electron shuttle for respiring microbes. Many prokaryotes can use soluble redox-active metal ions as electron acceptors for respiration, thus directly affecting the transformation of the metal. Biomineralization products (either associated with the mineral or bacterial surface or existing as a physically separate entity) can also affect metal transformations. Finally, in some instances, metal ions can be assimilated into the cell for use in metabolic processes. To date, the chemical interactions occurring at mineral–metal–microbe interfaces and the feedback-like responses between living and nonliving entities are poorly understood. However, such knowledge is imperative for addressing many issues related to global warming, carbon sequestration, and environmental cleanup, as well as most questions related to biogeochemical cycling of elements, to name just a few topics.

An ideal approach for investigating metal transformations at the mineral–microbe interface would employ a non-destructive, noninvasive method that could probe these

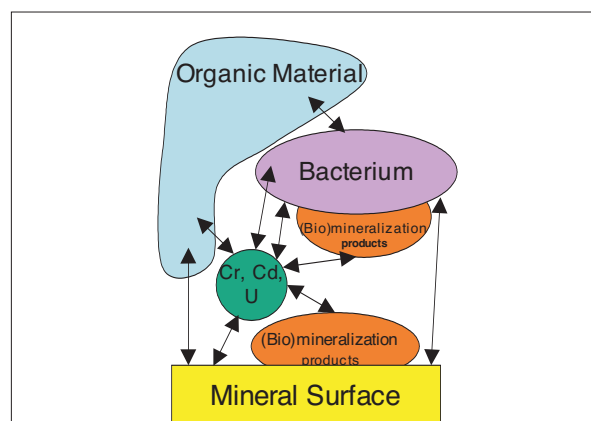


FIGURE 1 General types of chemical and physical interactions responsible for metal transformations at mineral–microbe–metal interfaces.

¹ Environmental Research Division, Argonne National Laboratory
9700 South Cass Avenue, Argonne, IL 60439-4843, USA
Corresponding author: kemner@anl.gov

transformations directly. Synchrotron-based X-ray absorption spectroscopy is such a method. In particular, the X-ray absorption fine-structure (XAFS) spectroscopy (Koningsberger and Prins 1988) techniques yield chemical and structural information for specific elements in a variety of unmodified—even hydrated—samples, including whole soils. The information provided by XAFS includes an element's oxidation state and coordination chemistry (in the form of the average number, distance, and atomic species of elements surrounding the element of interest).

Besides illustrating the complexity of mineral-microbe interactions and their role in metal transformations, FIGURE 1 also illustrates the spatial heterogeneities (less than a few microns) at the mineral-microbe interface. In some instances, to elucidate the interactions occurring at the mineral-microbe interface, the dimensions of the X-ray probe must be adjusted to place the vast majority of the X-rays in strategic positions relative to that interface. Recent advances in synchrotron-based X-ray imaging have led to the development of a class of techniques that address these requirements, where the electron beam of an energy-dispersive X-ray microanalysis experiment is replaced by an apertured or focused X-ray beam from a synchrotron source (Sutton et al. 1993; Kirz et al. 1995; Schulze and Bertsch 1995; Kemner et al. 2004). X-ray imaging microscopy is performed by focusing or aperturing the incident X-ray beam to a small spot and recording an image point by point by scanning the sample in the two dimensions perpendicular to the X-ray beam. At each point in the image, the energy-resolved X-ray fluorescence (XRF) spectrum is monitored. Selecting and plotting the intensity of the XRF of the element of interest yields an element-specific image of the sample. Currently, spatial resolutions of approximately 1 micron can be achieved with Kirkpatrick-Baez focusing optics (Eng et al. 1998). However, the use of high-resolution zone plates (Lai et al. 1992) has improved the spatial resolution of hard X-ray microimaging experiments to better than 100 nm. These techniques also can be combined with X-ray absorption spectroscopy techniques for "spectroscopic imaging," providing additional spatially resolved information in the form of an element's valence state and local chemical environment.

Numerous reviews have addressed the study of mineral-microbe interactions (i.e. geomicrobiology or biogeochemistry) (Beveridge 1988; Banfield and Nealson 1997; Fein 2000; Warren and Haack 2001) and the use of synchrotron radiation in environmental science (Schulze and Bertsch 1995; Brown et al. 2004). The present article briefly summarizes the use of synchrotron-based XAFS and X-ray microscopy by our group to investigate biogeochemical transformations of metal ions. These examples are by no means representative of the breadth of work performed by many other scientists in this field. Rather, they illustrate the types of information that can be generated by synchrotron-based techniques applied to biogeochemical systems. We recommend browsing the abbreviated list of references in this review for more examples of synchrotron-based experiments aimed at a better understanding of metal transformations at the mineral-microbe interface.

Below are three examples of ways our group has used synchrotron-based approaches to elucidate mineral-microbe-metal interactions and the effects of these interactions on the valence state and chemical speciation of contaminant elements. These examples progress toward increasing complexity, moving from metal-microbe interactions, to biomineral-metal interactions, to microbe-mineral-metal interactions.

XAFS INVESTIGATIONS OF INTERACTIONS BETWEEN CADMIUM-URANIUM AND THE MICROBIAL CELL WALL

Like previous studies of minerals, acid-base titrations and metal-uptake studies have shown that bacteria have reactive surfaces that can bind many metals (Beveridge and Murray 1980; Fein et al. 1997) and affect mass transport in aqueous systems. Developing models for contaminant transport in the environment necessitates detailed understanding of the contaminant's solution chemistry in a complex system of adsorbents. To address this need, surface complexation modeling approaches are currently being used to understand metal solution chemistry in the presence of bacteria (Koretsky 2000; Warren and Haack 2001).

Previous surface complexation modeling of the uptake of cadmium and uranium (a contaminant metal and radionuclide found at many contaminated sites) by *Bacillus subtilis* (a model microorganism found in many natural environments) biomass indicates that (1) at pH 1.5–3.0, uranium binds to protonated phosphoryl groups, but there is no cadmium uptake; (2) at pH 3.0–5.0, both uranium and cadmium bind to carboxyl groups; and (3) at higher pH, cadmium binds consecutively to deprotonated phosphoryl and hydroxyl sites (Fein et al. 1997; Fowle et al. 2000). Reactions are identified on the basis of the cell's elemental composition and the similarity of the deprotonation constants to those for aqueous acids.

To verify the surface complexation model and provide information for its refinement, we directly determined the average local atomic environment of uranium and cadmium bound to bacteria by making uranium L₃-edge and cadmium K-edge fluorescence XAFS measurements of wet, homogeneous *B. subtilis* biomass harvested at several pH values (Kelly et al. 2002; Boyanov et al. 2003). As in most of our work, we constructed theoretical XAFS models by using the program FEFF7 (Zabinski et al. 1995). Our theoretical models were based on the crystal structures of uranyl or cadmium acetate and phosphate. Structural XAFS parameters determined for the data are the number of carbon and phosphorus atoms surrounding the cadmium or uranium atoms, the distances between the cadmium and uranium and carbon and phosphorus atoms, and the relative mean square displacement about these average atomic distances. Additional details of the analysis of the XAFS data are provided elsewhere (Kelly et al. 2002; Boyanov et al. 2003).

FIGURE 2 shows the imaginary part of the Fourier transform of the cadmium K-edge XAFS data from solution standards, with a representative cadmium-biomass spectrum. The imaginary part of a Fourier transform of XAFS data can be thought of as illustrating a convoluted radial distribution function, where the location of the increased amplitude of the oscillation corresponds to the approximate radial distance between the atomic species that absorbs the X-ray and the atoms surrounding the absorbing species. The signals from carbon and phosphorus atoms are easily distinguished, as marked on the spectra. The carbon and phosphorus regions of the spectra for the pH-dependent cadmium-biomass spectra (not shown here) indicate a decrease in the phosphorus signal and an increase in the carbon signal with increasing pH.

The uranium XAFS results (Kelly et al. 2002) indicate that at extremely low pH (1.67), the uranyl ion (UO₂²⁺) binds exclusively to phosphoryl functional groups, forming a monodentate inner-sphere complex¹. With increasing pH (3.22 and 4.80), UO₂²⁺ binds increasingly to carboxyl

1 EDITORS' NOTE: terms such as functional group and inner-sphere complex are defined in the article by Sparks in this issue.

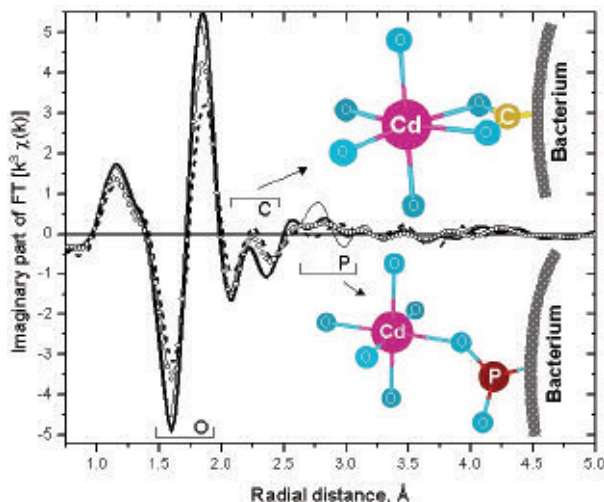


FIGURE 2 Imaginary part of Fourier-transformed XAFS data for Cd bound to the bacterial cell wall at pH 5.9 (circles). Data are compared to standards of hydrated (thick solid line), acetate-bound (broken line), and phosphate-bound (thin solid line) Cd in solution. The contributions to the XAFS spectrum from the C and P atoms in the corresponding ligand are noted.

functional groups, forming a bidentate inner-sphere complex. The cadmium XAFS results (Boyanov et al. 2003) indicate that at pH 3.0–5.0, phosphoryl groups are primarily responsible for the uptake of cadmium, while the additional sorption capacity at pH 5.0–7.5 is due to carboxyl binding. The onset of another binding mechanism observed at pH 7.8 was tentatively ascribed to further deprotonation of phosphoryl sites. The cadmium–phosphorus structural parameters are indicative of inner-sphere, monodentate binding to a singly deprotonated phosphoryl group, while cadmium–carbon structural parameters show inner-sphere, bidentate chelation in the cadmium–carboxyl complex. Results for simulations with the model developed to describe the chemical interactions between cadmium and the carboxyl and phosphoryl functional groups associated with the bacterial cell wall are shown as insets to FIGURE 2.

We identified the reactions responsible for cadmium and uranium uptake by *B. subtilis* by using XAFS to determine the local environment of the adsorbed uranium and cadmium. Our data in general corroborate results from surface complexation models; however, some details of the binding, such as ligand numbers, distances, and binding mode, can be observed only by XAFS. This information can be used in molecular calculations to independently constrain the stability constants used in surface complexation modeling. Taken together, bulk adsorption measurements, XAFS experiments, and *ab initio* calculations represent a powerful approach for determining and modeling metal speciation in metal–microbe–water systems.

XAFS INVESTIGATIONS OF URANIUM REDUCTION BY GREEN RUST

Although many microorganisms directly reduce a range of organic and inorganic contaminants, many elements are also reduced by reductants formed directly or indirectly by the metabolic processes of anaerobically respiring cells, particularly dissimilatory iron-reducing bacteria (DIRB) and sulfate-reducing bacteria. The DIRB are a diverse group of microorganisms that couple the oxidation of organic compounds or hydrogen to ferric ion (Fe^{3+}) reduction. The reduction of Fe^{3+} by DIRB typically results in the formation of a suite of ferrous (Fe^{2+}) species, including soluble Fe^{2+} complexes; Fe^{2+} surface complexes with organic and inorganic solid phases; and a host of Fe^{2+} -bearing minerals

including magnetite, siderite, vivianite, and green rust (Lovley et al. 1987; Fredrickson et al. 1998; Ona-Nguema et al. 2002).

Green rusts are mixed ferrous and ferric hydroxides that have brucite-like layered structures consisting of alternating positively charged hydroxide layers and hydrated anion layers. Recent research showed that green rusts can reduce a number of organic and inorganic contaminants. These results suggest that green rusts may be highly reactive reductants in suboxic environments.

Besides demonstrating direct microbial reduction of U^{6+} by indigenous microorganisms isolated from sediments collected from an abandoned uranium mine (Suzuki et al. 2002), we recently reported the reduction of U^{6+} to U^{4+} by green rust (O’Loughlin et al. 2003). In both instances, the resulting solid phase was identified as nanoparticulate uraninite (UO_2). Analysis by uranium L_3 -edge X-ray absorption near-edge spectroscopy (XANES) (Koningsberger and Prins 1988) of aqueous green rust suspensions spiked with uranyl (U^{6+}) showed that U^{6+} was stoichiometrically reduced to U^{4+} by green rust. Extended XAFS data for the U^{6+} reduced by green rust indicated the formation of a UO_2 phase. Fitting of data from the green rust samples to a theoretical model based on the crystal structure of UO_2 (see FIGURE 3) indicated that the number of nearest-neighbor uranium atoms decreased from 12 for the standard UO_2 structure to 5.4 for the uranium–green rust sample. With an assumed 4 near-neighbor uranium atoms per uranium atom on the surface of UO_2 , the best-fit value for the average number of uranium atoms indicated the presence of UO_2 particles with an average diameter of 1.7 ± 0.6 nm (O’Loughlin et al. 2003). A schematic representing the uraninite nanoparticles identified in these experiments is shown as an inset to FIGURE 3.

The formation of biogenic green rusts by DIRB provides a means of coupling the redox cycling of iron to contaminant reduction in subsurface environments. Our results clearly indicate that U^{6+} (as soluble uranyl ion) is readily reduced by green rust to U^{4+} in the form of relatively insoluble UO_2 nanoparticles. This suggests that the presence of green rusts in the subsurface has significant effect on the mobility of uranium, particularly under iron-reducing conditions.

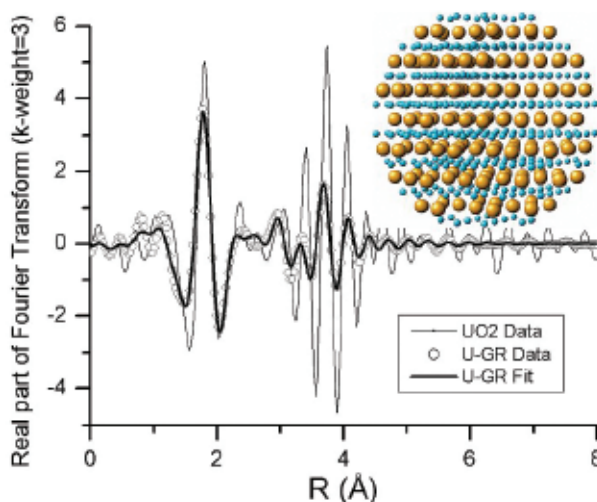


FIGURE 3 Real part of the Fourier transform of uranium L_3 -edge XAFS data collected for a uraninite (UO_2) standard, a sample of green rust to which U^{6+} was added, and the fit to the green rust data. The data indicate the reduction of U^{6+} to U^{4+} , consistent with a UO_2 phase. Inspection of the data at 3–5 Å reveals a smaller uranium backscattering signal for the green rust sample than for the UO_2 standard, implying the formation of nanocrystalline uraninite. A model depicting the proposed uraninite nanoparticle is shown as an inset.

In addition, because these tiny particles can still be transported in an aqueous environment, precipitation of uranium as insoluble uraninite cannot be presumed to immobilize the metal. Thus, investigation of the transport of nanoparticles is currently a very important research area. Uranium XAFS studies of these systems can provide critical information concerning physical and chemical characteristics of these particles.

X-RAY MICROSCOPY ELEMENTAL AND REDOX ANALYSIS OF CHROMIUM INTERACTIONS WITH SINGLE BACTERIAL CELLS

Attachment of prokaryotic cells to surfaces often leads to major changes in metabolism and resistance to elevated concentrations of metals (Costerton et al. 1987). In addition, in many natural environments, bacteria exist predominantly in surface-adhered (biofilm) states rather than in free-floating (planktonic) states. Thus, understanding metal transformations at microbial interfaces and the role of microbes in transformations of metals in natural environments requires observation of the surface-adhered microbes. In one approach, X-ray surface-scattering techniques have been combined with X-ray absorption spectroscopy techniques to investigate selenium and lead speciation in biofilms (Templeton et al. 2001, 2003). In an alternative approach (Kemner et al. 2004), we used high-energy XRF microscopy to examine elemental compositions of single hydrated bacterial cells in both surface-adhered and planktonic states. We have also combined XAFS techniques with XRF microscopy approaches (XRF microspectroscopy) to determine the redox state and location of chromium relative to single surface-adhered and planktonic cells.

Results from XRF microscopy imaging experiments, depicted in FIGURE 4, demonstrate that the spatial distributions of many elemental macronutrients required for cell growth (phosphorus, sulfur, chlorine, potassium, and calcium) can enable imaging of single bacterial cells with resolution of approximately 100 nm (Kemner et al. 2004). We also observed changes in cell morphology and elemental concentrations in single cells attached to a solid substrate. Upon exposure to elevated concentrations of Cr^{6+} , we observed interactions between the cell surface and the chromium for the planktonic cells, but no interactions for the surface-adhered cells. In addition, XRF-microscopy analyses of macronutrient concentrations in the cells were consistent with death of the planktonic cells but not the surface-adhered cells. Finally, to determine the spatial distribution of the redox states of chromium in these systems at a number of locations relative to the cell, we measured XANES at the chromium K-edge with the X-ray microbeam (spatial resolution of approximately 100 nm) (Koningsberger and Prins 1988). Comparison of the chromium XANES spectra from these samples with spectra for standards indicated reduced chromium complexed to a phosphoryl functional group in contact with the cell surface of the planktonic cells but not in contact with the cell surface of the surface-adhered cells. Copious amounts of extracellular polysaccharides (EPS) and reducing end sugars residing within EPS are often observed to be produced in conjunction with the adhesion of cells to surfaces. Our results suggest that the EPS and reducing sugars impart to surface-adhered cells a tolerance to Cr^{6+} and the ability to reduce and immobilize the metal outside the cell. Similarly, the absence of these products around the planktonic cells renders them susceptible to the strong oxidizing power of the Cr^{6+} . The result is ruptured cell membranes and cell death upon exposure to Cr^{6+} .

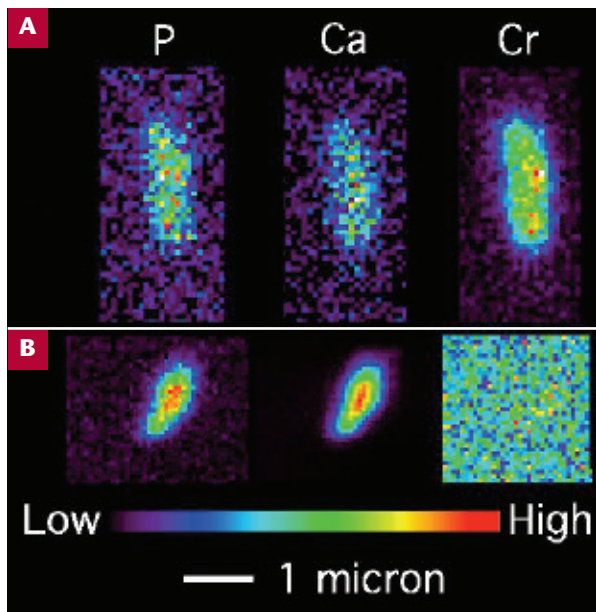


FIGURE 4 False-color micro-XRF maps of the qualitative distribution and concentration gradients of phosphorus, calcium, and chromium in and around (A) planktonic and (B) surface-adhered *Pseudomonas fluorescens* microbes harvested after exposure to potassium dichromate (Cr^{6+}) solution (1000 ppm) for 6 h.

This was one of the first studies of its kind at this spatial resolution; clearly, the use of XRF microscopy and microspectroscopy holds great promise for investigating a cell's metabolic state. Future studies of this type should also provide insight into biomineralization processes (i.e. the formation of minerals within and near microbes), another forefront research topic in the study of mineral-microbe interactions.

SUMMARY

The importance of microbes and microbe-mineral interactions in metal transformations is increasingly recognized. With newly developed synchrotron-based X-ray sources, our ability to characterize the chemical states of dilute elements in a variety of systems is enhanced. The studies presented here provide new insights concerning (1) chemical interactions between cell surfaces and metals, (2) the formation and chemistry of nanoparticles, and (3) changes in a cell's resistance to heavy metals upon attachment to surfaces. None of these new insights were possible solely with classical macroscale techniques. Synchrotron capabilities hold great promise for more sophisticated studies and increased understanding of metal transformations at mineral-microbe interfaces, as well as progression toward investigation of mineral-microbe interfaces in natural samples.

ACKNOWLEDGMENTS

Much of the work reported here was supported by the Natural and Accelerated Bioremediation Research Program, Office of Biological and Environmental Research, Office of Science, US Department of Energy (DOE). Additional support for KMK was provided by the DOE Office of Science Early Career Scientist and Engineer Award. Additional support for MIB was provided by the Environmental Molecular Science Institute at the University of Notre Dame. Work at the MRCAT and the Advanced Photon Source was supported by the DOE Office of Science, Office of Basic Energy Sciences. ■■

REFERENCES

- Banfield JF, Nealson KH (eds) (1997) *Geomicrobiology: Interactions Between Microbes and Minerals*. Reviews in Mineralogy 35, Mineralogical Society of America, Washington, DC, 448 pp
- Barns SM, Nierzwicki-Bauer S (1997) Microbial diversity in modern subsurface, ocean, surface environments. In: Banfield JF, Nealson KH (eds) *Geomicrobiology: Interactions Between Microbes and Minerals*, Reviews in Mineralogy 35, Mineralogical Society of America, Washington, DC, pp. 35-79
- Beveridge TJ (1988) The bacterial surface: general considerations towards design and function. *Canadian Journal of Microbiology* 34: 363-372
- Beveridge TJ, Murray RGE (1980) Sites of metal deposition in the cell wall of *Bacillus subtilis*. *Journal of Bacteriology* 141: 876-887
- Boyanov MI, Kelly SD, Kemner KM, Bunker BA, Fein JB, Fowle DA (2003) Adsorption of cadmium to *Bacillus subtilis* bacterial cell walls: a pH-dependent X-ray absorption fine structure spectroscopy study. *Geochimica et Cosmochimica Acta* 67: 3299-3311
- Brown Jr GE, Sutton SR, Bargar JR, Shuh DK, Bassett WA, Bertsch PM, Bisognano J, Bleam WF, Clark DL, De Stasio G, Fendorf SE, Fenter PA, Fontes E, Hormes J, Kemner KM, Myneni SCB, O'Day PA, Pecher KH, Reeder RJ, Roy A, Traina SJ, Wilson CS, and Zachara JM (2004) *Molecular environmental science: an assessment of research accomplishments, available synchrotron radiation facilities, and needs*. Stanford Linear Accelerator Center, Stanford
- Costerton JW, Cheng K-J, Geesey GG, Ladd TI, Nickel JC, Dasgupta M, and Marrie TJ (1987) Bacterial biofilms in nature and disease. *Annual Reviews of Microbiology* 41: 435-464
- Eng PJ, Neville M, Rivers ML, Sutton SR (1998) Dynamically figured Kirkpatrick Baez X-ray micro-focusing optics. In: McNulty (ed) *X-ray microfocusing: applications and technique*, SPIE Proceeding 3449: 145-146
- Fein JB (2000) Quantifying the effects of bacteria on adsorption reactions in water-rock systems. *Chemical Geology* 169: 265-280
- Fein JB, Daughney CJ, Yee N, Davis TA (1997) A chemical equilibrium model for metal adsorption onto bacterial surfaces. *Geochimica et Cosmochimica Acta* 61: 3319-3328
- Fowle DA, Fein JB, Martin AM (2000) Experimental study of uranyl adsorption onto *Bacillus subtilis*. *Environmental Science & Technology* 34: 3737-3741
- Fredrickson JK, Zachara JM, Kennedy DW, Dong H, Onstott TC, Hinman NW, Li S-M (1998) Biogenic iron mineralization accompanying the dissimilatory reduction of hydrous ferric oxide by a groundwater bacterium. *Geochimica et Cosmochimica Acta* 62: 3239-3257
- Kelly SD, Kemner KM, Fein JB, Fowle DA, Boyanov MI, Bunker BA, Yee N (2002) X-ray absorption fine structure determination of pH-dependent U-bacterial cell wall interactions. *Geochimica et Cosmochimica Acta* 66: 3855-3871
- Kemner KM, Kelly SD, Lai B, Maser J, O'Loughlin EJ, Sholto-Douglas D, Cai Z, Schneegurt MA, Kulpa CF, Nealson KH (2004) Elemental and redox analysis of single bacterial cells by X-ray microbeam analysis. *Science* 306: 686-687
- Kirz J, Jacobsen C, Howells M (1995) Soft X-ray microscopes and their biological applications. *Quarterly Reviews of Biophysics* 28: 33-130
- Koningsberger DC, Prins R (eds) (1988) *X-ray Absorption: Principles, Applications, and Techniques of EXAFS, SEXAFS and XANES*. John Wiley and Sons, New York
- Koretsky C (2000) The significance of surface complexation reactions in hydrologic systems: a geochemist's perspective. *Journal of Hydrology* 230: 127-171
- Lai B, Yun W, Legnini DG, Xiao D, Chrzas J, Viccaro PJ, White V, Bajikar S, Denton D, Cerrina F (1992) Hard X-ray phase zone plate fabricated by lithographic techniques. *Applied Physics Letters* 61: 1877-1879
- Lovley DR, Stolz JF, Nord Jr GL, Phillips EJP (1987) Anaerobic production of magnetite by a dissimilatory iron-reducing microorganism. *Nature* 330: 252-254
- O'Loughlin EJ, Kelly SD, Cook RE, Csencsits R, Kemner KM (2003) Reduction of uranium(VI) by mixed iron(II)/iron(III) hydroxide (green rust): formation of UO₂ nanoparticles. *Environmental Science & Technology* 37: 721-727
- Ona-Nguema G, Abdelmoula M, Jorand F, Benali O, Géhin A, Block J-C, Génin J-MR (2002) Iron(II,III) hydroxycarbonate green rust formation and stabilization from lepidocrocite bioreduction. *Environmental Science & Technology* 36: 16-20
- Schulze DG, Bertsch PM (1995) Synchrotron X-ray techniques in soil, plant, and environmental research. *Advances in Agronomy* 55: 1-67
- Skinner CH (1997) in *Geomicrobiology: Interactions Between Microbes and Minerals*. Reviews in Mineralogy 35: Mineralogical Society of America, Washington, DC (*Note: Skinner provided the Preface to the book*).
- Sutton SR, Jones KW, Gordon B, Rivers ML, Bajt S, Smith JV (1993) Reduced chromium in olivine grains from lunar basalt 15555: X-ray Absorption Near Edge Structure (XANES). *Geochimica et Cosmochimica Acta* 57: 461-468
- Suzuki Y, Kelly SD, Kemner KM, Banfield JF (2002) Nanometre-size products of uranium bioreduction. *Nature* 419: 134
- Templeton AS, Trainor TP, Traina SJ, Spormann AM, Brown Jr GE (2001) Pb(II) distribution at biofilm-metal oxide interfaces. *Proceedings of the National Academy of Sciences* 98: 11897-11902
- Templeton AS, Trainor TP, Spormann AM, Brown Jr GE (2003) Selenium speciation and partitioning within *Burkholderia cepacia* biofilms formed on α -Al₂O₃ surfaces. *Geochimica et Cosmochimica Acta* 67: 3547-3557
- Warren LA, Haack EA (2001) Biogeochemical controls on metal behaviour in freshwater environments. *Earth-Science Reviews* 54: 261-320
- Woese CR (1987) Bacterial evolution. *Microbiological Reviews* 51: 221-271
- Zabinski SI, Rehr JJ, Ankudinov AL, Albers RC, Eller MJ (1995) Multiple-scattering calculations of X-ray absorption spectra. *Physical Review B* 52: 2995-3009 ■

FRANKLIN & STERLING HILL— The World's Most Magnificent Mineral Deposits by Dr. Pete J. Dunn – Smithsonian Institution

It has finally arrived: the 2004 revised HARDCOVER edition of Dr. Dunn's monumental work on the Franklin and Sterling Hill deposits. Over 750 pages in two volumes, handsomely bound in royal blue buckram, oversewn, with acid-free endpapers and gold-stamped on spine and cover, this set is a comprehensive treatment of the mineralogy and history of this prolific and complex deposit! Over 900 b/w illustrations and photographs fill this careful, descriptive, precise work that meticulously documents the diverse mineralogy of this famous NJ locality. Every scientific library, serious collector and bibliophile should own this set, and we are the exclusive distributor for this limited printing. The two volume set is 195.00 plus 15.00 s/h in the USA;

Canadian and overseas customers: please inquire for shipping costs.

Excalibur Mineral Corporation ~ 1000 North Division Street ~ Peekskill, NY 10566 USA

Local Structure around Cr³⁺ Ions in Dilute Acetate and Perchlorate Aqueous SolutionsMaxim I. Boyanov^{*,†,‡} Kenneth M. Kemner[†], Tomohiro Shibata[‡], and Bruce A. Bunker[‡]*Environmental Research, Argonne National Laboratory, Argonne, Illinois 60439, and Department of Physics, University of Notre Dame, Notre Dame, Indiana 46556**Received: February 6, 2004; In Final Form: April 7, 2004*

The hydration structure and aqueous acetate complexation of Cr³⁺ ions were studied by X-ray absorption fine structure (XAFS) spectroscopy as a function of pH, concentration, acetate:Cr ratio, and age of the solution. In the perchlorate solutions, we found an octahedral hydration shell around the Cr³⁺ ion at 1.96 Å, confirming previous results through an independent analysis. Distinct Cr–Cr correlation was observed in the Cr acetate solutions, indicating that acetate groups bridge between the metal ions in a polymer structure. Modeling of the data confirmed a cyclic trichromium complex in acetate solutions. Similar spectral features in the Fourier transform were observed at 3.0–3.5 Å for both hydrated and polynuclear Cr. Comparison of the spectral content of such features in the two different cases showed that the origin of the 3.0–3.5 Å structure is multiple scattering within the first O shell alone. Thus, no spectral contribution could be attributed to the outer hydration molecules in data for hydrated Cr³⁺. We also report on differences in first-shell O backscattering (or possible spectral contributions from H atoms) in the aqueous solutions relative to the crystal oxide, determined by systematic analysis of a Cr₂O₃ standard.

Introduction

In many areas of science, it is necessary to model the properties of aqueous solutions. Continuum models were found insufficient in that respect,¹ pointing to the importance of the hydration structure studies carried out for many elements during the last three decades.^{2,3} Understanding aqueous metal adsorption to mineral and biological surfaces also requires structural information, as the process is determined by the solvated ion's form, size, and availability in solution, as well as by the geometry of the complex it forms with surface functional groups.

The structure of hydrated Cr³⁺ has been investigated previously by X-ray and neutron techniques.^{4–16} An octahedral hydration sphere was determined, with a Cr–O distance of 1.97–1.98 Å.^{4–7} Because of the unusually long residence time of Cr inner hydration molecules (~10⁶ s),¹⁷ an outer hydration sphere distinct from bulk water can be formed. Evidence for this has been provided by scattering,^{4,8–10} vibration spectroscopy,¹¹ NMR,¹² and transport studies.¹³ More recently, the structure of dilute Cr solutions (as low as 0.005 M) has been investigated by X-ray absorption fine structure (XAFS) spectroscopy and contributions from second-hydration-shell molecules were reported in the spectra.^{5,14–16}

Metal–acetate complexation in solution has been studied previously by Fourier transform infrared (FT-IR) spectroscopy.¹⁸ The technique correlates shifts in the carboxylate stretching frequencies with the binding mode in known crystalline compounds^{19,20} and applies this dependence to solution complexes. On this basis, the aqueous metal–acetate chelation types for several ions were classified in four main groups: ionic, monodentate, bidentate, and bridging-bidentate (Figure 1). Aqueous Cr³⁺ acetate, detailed in a separate study,²¹ showed

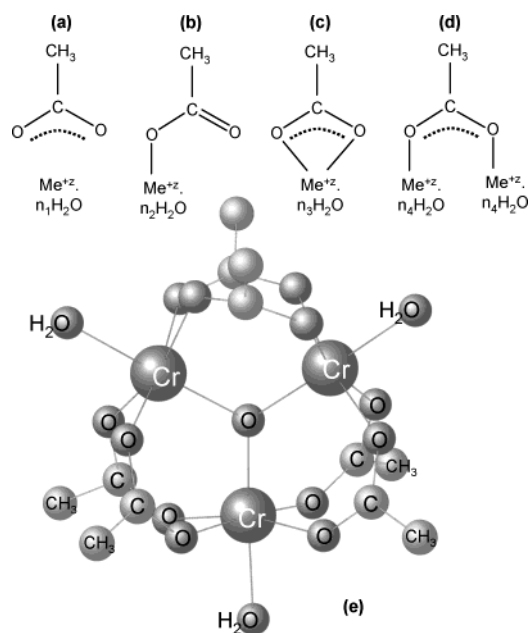


Figure 1. (a–d) Binding modes of an acetate group to a hydrated metal ion. (a) ionic, (b) monodentate, (c) bidentate, (d) bridging; dotted lines indicate the distributed electron density of the acetate group. (e) Structure of the trichromium acetate complex (bridging mode). Based on data from Chang et al.²²

dependence of the spectra on pH, acetate:metal ratio, and age of the solution. The speciation diagram derived suggests that below pH 5.4 the dominant species is a cyclic Cr trimer, Cr₃O-(Ac)₆, in which acetate groups are in a bridging configuration between Cr³⁺ ions (Figure 1e).

As part of our efforts to understand metal adsorption to carboxyl-rich bacterial surfaces, we began an XAFS study of metal–acetate complexes in aqueous solution.²³ In the present work, we investigate the hydration and acetate complexation of Cr³⁺ in 0.03–0.3 M aqueous solutions. The aim is to confirm

* To whom correspondence should be addressed. Current address: Argonne National Laboratory, Argonne, IL 60439; e-mail: mboyanov@nd.edu.

[†] Argonne National Laboratory.

[‡] University of Notre Dame.

TABLE 1: Sample Identification Names and Composition

sample	[Cr ³⁺] (M/l)	[CH ₃ COO ⁻] (M/l)	pH	aged (h)
CrClO4-02-22	0.2	0.0	2.2	96
CrClO4-01-25	0.1	0.0	2.5	96
CrClO4-005-22	0.05	0.0	2.2	96
CrAc1-01-41	0.1	0.1	4.1	96
CrAc3-03-62	0.3	0.9	6.2	96
CrAc3-03-42	0.3	0.9	4.2	96
CrAc3-01-68	0.1	0.3	6.8	96
CrAc3-01-42	0.1	0.3	4.2	96
CrAc3-01-420	0.1	0.3	4.2	1
CrAc10-01-35	0.1	1.0	3.5	96
CrAc10-003-35	0.03	0.3	3.5	96
CrAc100-01-28	0.1	10.0	2.8	96

structural results found in previous work for the first hydration sphere and to determine the precise origin of XAFS features seen at larger distance in the Fourier transform of hydrated Cr spectra. On the basis of knowledge obtained for hydrated Cr, changes resulting from increased acetate availability in solution are examined to determine the mechanism of acetate–Cr complexation. Previous reports suggested polymerization of Cr when sufficient acetate was present in solution. We attempted to confirm the metal–metal correlation and study the structure of the polymer complex as a function of pH, concentration, acetate:Cr ratio, and age of the solution.

Experiment

Solutions were prepared by dissolving commercial Cr perchlorate and Cr acetate salts (Sigma-Aldrich and Alfa-Aesar, used without further purification) in distilled deionized water (18 MΩ). Three Cr(ClO₄)₃ solutions (0.05, 0.1, and 0.2 M) were used to study hydrated Cr³⁺ ions. A series of aqueous Cr acetate solutions with different acetate:Cr ratios and concentrations was used to observe the shift in equilibrium between hydrated and acetate-complexed ions toward the complexed species. The names, concentration, acetate:Cr ratio, and pH of the samples are given in Table 1. The water was boiled for at least 20 min to remove CO₂. Acetate overloading was achieved by adding acetic acid, and the pH was adjusted when necessary with NaOH.

The Cr K-edge XAFS experiments were carried out at the Materials Research Collaborative Access Team (MRCAT) beamline²⁴ of the Advanced Photon Source. The beamline undulator was tapered, and the incident energy was scanned by using the Si(111) reflection of the double-crystal monochromator in quick-scanning mode (approximately 3 min per scan for the extended region and 1 min per scan for the near-edge region). Harmonic rejection was achieved by reflection from a Rh-coated mirror. The beam was defined as 0.7 mm by 0.7 mm. Linearity tests²⁵ indicated less than 0.3% nonlinearity at 50% beam attenuation for the experimental setup and all samples. The beam intensity varied by less than 40%, approximately monotonically, over the energy range of the collected data. The solutions were kept in drilled Plexiglas slides sealed with Kapton film windows during the measurements. Spectra were recorded in fluorescence mode. Energy calibration was continuously monitored during data collection by using a Cr₂O₃ standard placed above the beam and in front of the defining slits.²⁶

Standard data analysis procedures were followed.²⁷ Raw data from the beamline were aligned on the energy axis by the reference data; background was subtracted by using AUTOBK.²⁸ Different background removal parameters were compared to identify the most consistent procedure. Model calculations were obtained with FEFF8,^{29,30} (The Cr–O and Cr–Cr backscattering

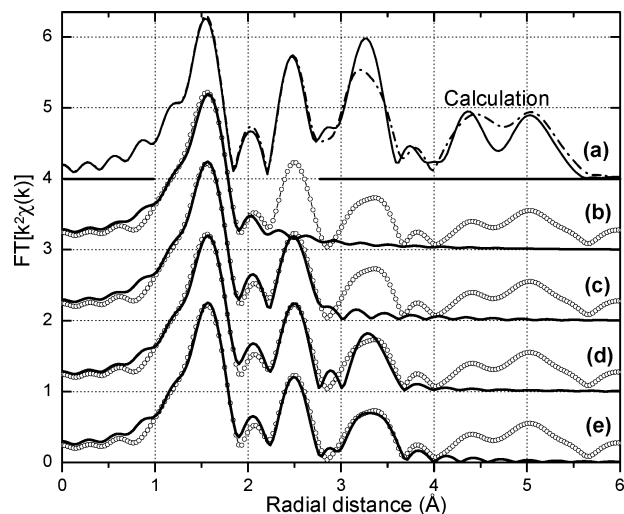


Figure 2. Comparisons of theoretical spectra (a) and modeling of Cr₂O₃ experimental data (b–e). Transform and fit parameters of the k^2 -weighted data are $\Delta k = 2.8\text{--}13.5 \text{ \AA}^{-1}$ and $\Delta R = 1.0\text{--}4.0 \text{ \AA}$. Shown are experimental data (symbols) and fit (lines). (a) Comparison of theoretical calculations when only SS paths are used (solid) and when MS paths are included (broken). (b) Fit with O near neighbors only. (c) Fit with O, Cr1 shells. (d) Fit with O, Cr1, Cr2 shells. (e) Fit with O, Cr1, and Cr2 shells, plus MS paths.

amplitudes were calibrated with the Cr₂O₃ standard.) Data were modeled by using the FEFFIT program.³¹

Results and Discussion

Cr₂O₃ Standard. Data from the Cr₂O₃ standard were used to relate features in the extended XAFS (EXAFS) spectrum of a Cr oxide compound to its known structure. The EXAFS method in X-ray spectroscopy uses the electron wave of an ejected photoelectron to probe the surroundings of the emitting atom. Electron scattering is treated in EXAFS theory by summing contributions from “scattering paths” that the electron wave can take before it returns to the central atom to interfere with itself.²⁷ Besides single reflections from neighbor atoms (single scattering, or SS), several scattering events can occur before the electron returns to the emitting atom (multiple scattering, or MS). The contribution of MS paths is usually negligible relative to that of SS paths, but when atoms are aligned their electron scattering ability is enhanced, and corresponding MS features appear in the spectrum. The importance of such collinear MS paths is illustrated in Figure 2a, in which Fourier transforms (FTs) of EXAFS calculations for Cr₂O₃ are compared, with and without consideration of MS paths. Differences are observed in the region 2.8–4.0 Å, where MS paths due to the octahedral O first shell contribute. Some calculated SS and MS paths might not contribute in a real sample because of loss of coherence due to thermal and structural disorder. The contribution of each path is weighed by a Debye–Waller type factor, $\exp[-2k^2\sigma^2]$, where σ is the rms deviation in path length for each path, and k is the electron wave vector.²⁷

The theoretical Cr₂O₃ spectrum was calculated using the published Cr₂O₃ structure.³² The following paths were necessary to fit the experimental spectrum: SS from the octahedral O first shell; SS from four Cr atoms, each sharing either two or three O atoms with the central Cr atom; SS from nine Cr atoms (sharing one O atom with the central Cr atom) at two different distances; MS within the first O shell. The sequential inclusion of these shells in the fit and the resulting parameters are shown in Figure 2 and Table 2. Constraints on the fit parameters resulted from initial systematic testing of unconstrained shells

TABLE 2: Results from Modeling Cr₂O₃, Cr-perchlorate (CrClO₄-01-22), and Cr-acetate (CrAc100-01-28) Data^a

sample	figure	shell	<i>N</i>	<i>R</i> (Å)	σ^2 (10 ⁻³ Å ²)	ΔE_0 (eV)	<i>R</i> -factor	χ^2_ν	ν
Cr ₂ O ₃ ^b	2b	O1	2 × 3 ^c	1.98 ^c	2.0 ± 1.4	6.9 ± 2.9	0.22	1126	19
Cr ₂ O ₃ ^b	2c	O1	2 × 3 ^c	1.98 ^c	1.9 ± 0.9	7.1 ± 1.4	0.09	511	17
		Cr1	1	2.65	2.7 ± 1.1	3.2 ± 3.1			
		Cr1	3	2.89	2.7 ± 1.1	3.2 ± 3.1			
Cr ₂ O ₃ ^b	2d	O1	2 × 3 ^c	1.98 ^c	2.0 ± 0.6	7.1 ± 0.8	0.03	177	16
		Cr1	1	2.65	3.1 ± 0.7	5.6 ± 1.1			
		Cr1	3	2.89	3.1 ± 0.7	5.6 ± 1.1			
		Cr2	3	3.43	3.9 ± 0.8	5.6 ± 1.1			
		Cr2	6	3.65	3.9 ± 0.8	5.6 ± 1.1			
Cr ₂ O ₃ ^{b,d}	2e	O1	2 × 3 ^c	1.98 ^c	2.0 ± 0.4	7.2 ± 0.5	0.016	94	16
		Cr1	1	2.65	3.1 ± 0.5	5.0 ± 0.8			
		Cr1	3	2.89	3.1 ± 0.5	5.0 ± 0.8			
		Cr2	3	3.43	3.6 ± 0.5	5.0 ± 0.8			
		Cr2	6	3.65	3.6 ± 0.5	5.0 ± 0.8			
CrClO ₄ -01-22	3a	O1	6.1 ± 0.5	1.96 ± 0.01	0.6 ± 1.0	1.6 ± 1.1	0.041	256	17
CrClO ₄ -01-22	3b	O1	5.8 ± 0.3	1.96 ± 0.01	0.2 ± 0.6	1.8 ± 0.6	0.020	91	14
		O2	13.7 ± 6.3	4.01 ± 0.03	20.9 ± 13.7	1.8 ± 0.6			
CrClO ₄ -01-22	3a	O1	6.0 ± 0.4	1.96 ± 0.01	0.5 ± 0.7	1.2 ± 0.6	0.023	112	16
		MS ^d	0.64 ± 0.11						
CrClO ₄ -01-22	3a	O1	7.0 ± 0.4	1.96 ± 0.01	1.5 ± 0.6	0.7 ± 0.6	0.011	57	14
		H	2 × N _{O1}	1.96 ± 0.01	3.4 ± 3.2	0.7 ± 0.6			
		MS ^d	0.67 ± 0.09						
CrAc100-01-28 ^e	7a	O1	5.9 ± 0.6	1.98 ± 0.01	2.2 ± 1.0	5.5 ± 1.5	0.019	206	10
		Cr	2.8 ± 1.2	3.30 ± 0.03	5.2 ± 3.5	-1.6 ± 3.7			
CrAc100-01-28 ^f	7b	O1	5.7 ± 0.4	1.96 ± 0.01	1.9 ± 1.0	1.4 ± 1.0	0.042	405	13
		Cr	18.9 ± 7.4	3.43 ± 0.04	30.7 ± 8.3	7.7 ± 1.7			
CrAc100-01-28 ^g	7c	O1	5.8 ± 0.5	1.96 ± 0.01	2.2 ± 1.1	0.4 ± 0.9	0.031	363	12
		MS ^d	0.64 ± 0.18						
		Cr	3.2 ± 1.8	3.32 ± 0.05	7.3 ± 5.4	0.6 ± 4.8			
CrAc100-01-28 ^h	7d	O1	5.8 ± 0.4	1.96 ± 0.01	2.2 ± 1.0	0.3 ± 0.8	0.030	350	14
		MS ^d	0.66 ± 0.17						
		Cr	2.6 ± 0.6	3.31 ± 0.02	5.2	0.3 ± 0.8			

^a *N*, *R*, σ^2 , and ΔE_0 are the parameters used to calculate the EXAFS contribution from the corresponding shell. Parameters for which deviations are not given are kept constant in the fits. Graphic fit results are shown in the corresponding figures. *R*-factor and χ^2_ν are statistical parameters, and ν values are the degrees of freedom in the fit. ^b An expansion parameter α is used to vary the path length on the basis of the crystallographic distance: $R = R_0(1 + \alpha)$. Values for α were in the range (0.001–0.003). The amplitude factor S_0^2 was 0.69 ± 0.09 for the fit with O1 + Cr1 shells and was fixed to that value in all other fits. ^c Two separate shells at crystallographic distances of 1.96 and 2.01 Å were used in the fit. The quoted distance is the average. ^d Fit with first-shell MS included. All MS parameters were constrained to O1 shell SS parameters. If *N* is provided for an MS path, it represents an amplitude scaling factor. Explanations are given in the text. ^e $\Delta k = 3.8$ –12.5 Å⁻¹. ^f $\Delta k = 2.5$ –12.5 Å⁻¹. ^g $\Delta k = 2.5$ –12.5 Å⁻¹, including MS from O1 shell. ^h $\Delta k = 2.5$ –12.5 Å⁻¹, MS from O1 shell, constrained.

in isolated parts of the spectrum. A single lattice expansion variable was applied for all distances. The MS parameters were constrained to those of the first shell, under the assumption of uncorrelated atom movements.³³ The paths that were found necessary to fit the data represent the local crystallographic environment of the Cr atom, except for all O atoms that are outside the near-neighbor “O1” shell. The lack of signal from these O atoms is probably due to the expected large Debye–Waller (DW or σ^2) factor of these paths resulting from lattice vibrations in room-temperature measurements. Unlike the outer-shell O atoms, all detected Cr atoms share one to three first-shell “O1” atoms with the central Cr atom. The better-defined Cr–Cr distance, together with the generally larger backscattering amplitude of heavier atoms, results in detectable Cr contributions in the spectrum. The inclusion of MS from the first O shell significantly improved the fit quality at 2.8–4.0 Å. This observation demonstrates that first-shell MS can be significant in experimental data of octahedrally coordinated Cr.

Cr Perchlorate Solutions. The perchlorate anion is a weakly binding ligand, and no complexation with the Cr³⁺ ion is expected.³⁴ To test this expectation and to look for fluorescence self-absorption effects, the spectra at three Cr(ClO₄)₃ concentrations (0.05–0.2 M) were compared. No differences were observed, suggesting that the perchlorate anion is not bound to the metal in this concentration range. A 4% reduction in the nearest FT peak amplitude was observed in the 0.2 M sample relative to the 0.05 and 0.1 M samples. We conclude that even

if self-absorption effects are present at 0.2 M Cr concentration, they are within the approximately 10% uncertainty in EXAFS first-shell amplitudes.

The FT of data from the 0.1 M Cr perchlorate solution are shown in Figure 3. The main peak at 1.5 Å was modeled by a single shell of O atoms. The resulting parameters are shown in Table 2. We observed an octahedral hydration sphere at 1.96 ± 0.01 Å, with very little disorder ($\sigma^2 = 0.0006$ Å²). The sixfold coordination was not assumed in our model but was rather obtained as a result of the fit. The small disorder is indicative of the strong interaction between the Cr³⁺ ion and the water molecules, consistent with the long residence time obtained by NMR.¹⁷ The distance and coordination numbers determined by XAFS are consistent with the octahedral shell at 1.97–1.98 Å determined by X-ray and neutron scattering and by other XAFS studies.^{2,15,16} The distance is also in excellent agreement with electronic structure calculations (optimized Cr–H₂O distance of 1.965 Å).³⁵ Differences between experiment and model spectra observed at about 2.0 Å in the FT (Figure 3) can also be seen in modeling of the Cr₂O₃ standard (Figure 2). These differences could be attributed to systematic error in the Cr–O backscattering calculation, but they appear more pronounced in modeling of solution data. Addition of the H atoms from hydration water molecules significantly improved the fit (Figure 3d, Table 2), but the obtained distance of 2.30 Å was quite different from the 2.60 Å determined for the Cr–H correlation by neutron scattering.⁴ The reason for the discrepancy could

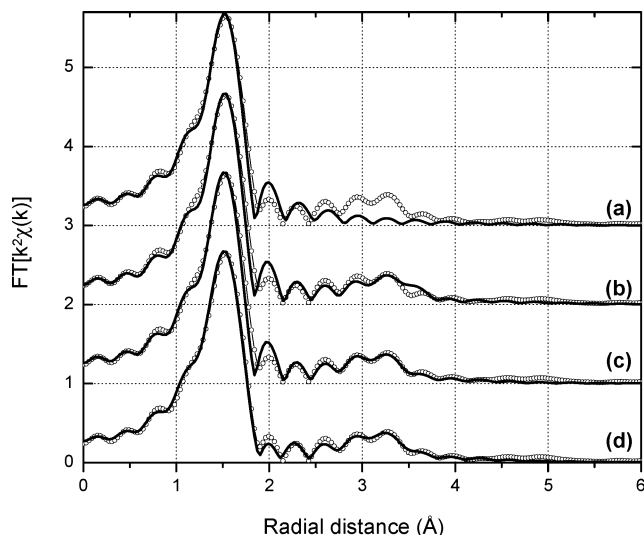


Figure 3. Fourier transforms of k^2 -weighted data (circles) and fits (line) for the 0.1 M $\text{Cr}(\text{ClO}_4)_3$ solution. Transform and fit parameters are $\Delta k = 2.5\text{--}12.5 \text{ \AA}^{-1}$ and $\Delta R = 1.0\text{--}4.0 \text{ \AA}$. Fits: (a) nearest-neighbor O1 shell only. (b) O1 and SS paths from O2 shell. (c) O1 and MS paths from O1 shell. (d) O1, H, and MS paths from O1 shell.

be inaccurate calibration of phase shifts for electron backscattering from the H atoms in the calculation. Modeling of the H shell also slightly affects O1 shell parameters (although within their uncertainties) and will need additional careful consideration. A future study will examine these differences, as a similar effect was observed in Cd perchlorate solutions.³⁶ Alternatively, electron backscattering from the O atoms could be slightly different in an aqueous environment than in a crystal oxide. (This alternative is supported by the fact that comparable differences between experiment and model at this distance are observed in modeling Cr acetate solutions, in which only one water molecule is present in the local environment. See Figure 7b–d.) Because the differences are localized in the Fourier transform and are of relatively small magnitude, they do not interfere with contributions at distances larger than about 2.2 Å. Thus, the conclusions presented below are not affected.

That a defined second hydration sphere is formed around Cr^{3+} was determined previously.^{4,8,9,12,13,15,16} Perhaps the most convincing structural evidence is provided by neutron scattering, through analysis of both the Cr–O and Cr–H correlations in a double-difference isotopic substitution method.⁴ In these studies, a second hydration shell is observed at a distance of about 4 Å, with a coordination number between 15 and 18. The ability of EXAFS to detect this shell in Cr solutions was examined in a series of studies,^{14–16} by careful analysis of the structure observed at about 3.2 Å in the FT. The conclusion was that SS from a second hydration sphere is an important spectral contribution but that first-shell MS paths are also necessary to fit the data accurately. In later work, the role of second-shell SS in the high- R features was determined to be smaller than the effect of first-shell MS but still large enough to be detected and analyzed.^{35,37,38} Other researchers have dismissed contributions of the second hydration shell in the EXAFS of aqueous ions on the basis of large disorder in the second hydration shell.^{39,40} The apparent controversy and difficulty in interpretation arises because the distance to the second hydration molecules in Cr^{3+} is twice that to the first, so first-shell collinear MS contributions overlap second-shell SS ones in the FT.

Our data confirm the presence of FT structure at 3.2 Å in the spectra of all Cr perchlorate solutions (Figure 3). This structure becomes almost extinct when the lower FT limit is

changed from 2.5 to 3.8 Å^{-1} , as seen previously.¹⁵ We were able to model this part of the spectrum both by using SS from an outer O shell (Figure 3b, Table 2) and by using only MS within the tightly bound first hydration sphere (Figure 3c, Table 2). The MS model seems to fit the data better in the region at 3.0–3.7 Å. Additional support for an MS interpretation comes from our inability to observe SS from any O atoms other than the near-neighbor ones in the Cr_2O_3 powder standard. However, our fit results do not indicate that the MS model is statistically different from the second hydration SS model. Sakane et al.¹⁶ compared the SS, MS, and a combination of the two models in fitting this part of a hydrated Cr^{3+} spectrum. An inherent limitation in MS modeling is the necessity to constrain the large number of variables. Employing the chosen constraints for the MS path parameters and the number of second-hydration-shell molecules, the authors concluded that a combined SS and MS model produced a superior fit than each model alone. We limited our analysis to testing either SS or MS contributions. In our MS model, the distance and the DW factors were constrained to the first-shell SS parameters in a way that ignores correlated atom motion.³³ The shape and phase of the features at 3.0–3.5 Å were reproduced correctly, but an amplitude variable for only MS contributions had to be introduced to fit the amplitude. The fit value of this variable (0.64 ± 0.11) shows that the actual amplitude of the MS features is about 35% smaller than predicted from the number of first coordination sphere molecules. Assuming for a moment that MS is the main contribution in this part of the spectrum, the origin of this amplitude reduction could be an overestimated electron mean free path in the XAFS calculation, correlated vibrations of first-shell water molecules (such as a “breathing” mode of opposite molecules, resulting in a different DW factor for MS paths), deviations from the 180° O1–Cr–O1 angle used in calculating the MS paths, or an unknown combination of these. An alternative explanation for the amplitude could be the presence of out-of-phase second-shell SS contributions, destructively interfering with the MS contribution and reducing the amplitude.

The limitations of MS modeling and the lack of information to account for the amplitude factors discussed above precluded a reliable SS versus MS analysis of this part of the spectrum. Recent studies employing ab initio electron structure calculations and molecular dynamics simulations have made significant progress in constraining the MS parameters in aqueous Cr^{3+} and determining the relative importance of SS and MS paths. On the basis of the adopted model, the contribution of second-shell SS is limited to about one-third of the total amplitude.^{35,37,38} We present here an alternative approach for determining a contribution of SS paths from an outer hydration shell. Because the structure at 3.0–3.5 Å is, in general, a linear superposition of SS and MS paths, a reduction in the amplitude of each component should result in change of the overall amplitude. The amplitude parameters that are specific to a molecular configuration are the coordination number and the DW factor. One can thus anticipate a change in the overall amplitude when the number of second-hydration-shell molecules is reduced or when their disorder is increased. This can be the result, for instance, of an interfering anion in the second shell. The approach then is to fit accurately the observed structure at 3.0–3.5 Å in the experimental Cr perchlorate spectrum regardless of the SS or MS origin of the features, and look for amplitude differences in a case where the second hydration shell is disturbed.

Such a case is provided by the Cr acetate aqueous complex. As will be shown in the analysis for Cr acetate solutions, the

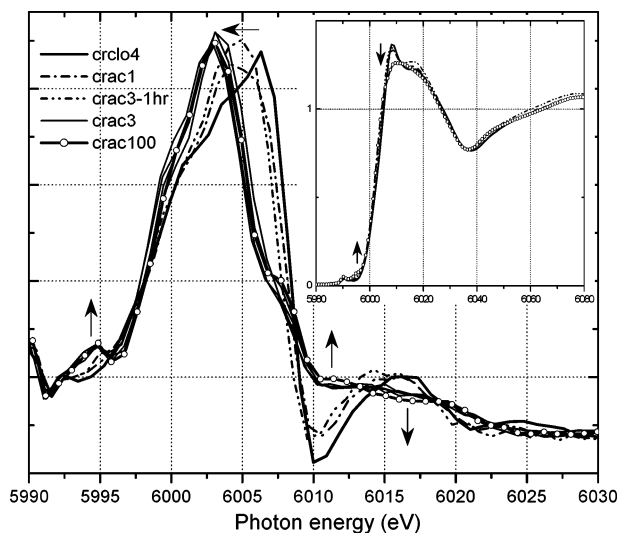


Figure 4. Derivative of normalized near-edge spectra (XANES) for 0.1 M Cr perchlorate (heavy line) and Cr acetate solutions. The broken lines show spectra for freshly prepared acetate:Cr = 3 and aged acetate:Cr = 1 solutions. The multiple thin lines show similar spectra for all aged acetate:Cr = 3 solutions. Symbols show the spectrum for sample CrAc100-01-28. Arrows indicate the effect of increased acetate binding relative to the hydrated Cr spectrum. Inset: normalized XANES.

SS or MS features at 3.0–3.5 Å in the Cr perchlorate spectrum are present with the *same amplitude* in spectra for solutions having the trichromium acetate structure (Figure 1e). The number of second hydration molecules around each Cr atom should be reduced in the acetate solutions because of spatial considerations. In addition, the acetate groups in the structure of Figure 1e are likely to significantly broaden the distribution of Cr–H₂O_{II} distances. Charge compensation by the acetate groups will also reduce the polarizing ability of the Cr³⁺ ion, diminishing the strength of the interactions and further broadening the distribution. The result of any of the above would be reduced or null amplitude of contributions assigned to second-shell hydration molecules. It is difficult to estimate the amount of the reduction, but the presented arguments indicate that it is likely to be significant. Assuming complete absence of second-shell SS in the Cr acetate spectra and using the 35% estimate for the SS relative contribution,^{35,37,38} we obtain a maximum possible amplitude change of 35%. We did not observe any amplitude change in the Cr acetate samples, suggesting that the 3.0–3.5 Å structure in the Cr perchlorate spectra is due to MS. This conclusion is supported by the fact that the Cr first-shell environment in the Cr acetate complex is similar to that of hydrated Cr³⁺ ions, leading to the same MS contributions in the spectra.

Chromium Acetate Solutions. Figure 4 shows the derivative of near-edge (XANES) spectra for the Cr perchlorate solution and several acetate solutions. Significant differences relative to the hydrated Cr spectrum are observed with increasing fraction of acetate-bound Cr³⁺ ions in solution. When the acetate solutions are not aged or the acetate:Cr ratio is less than 3, the spectra are intermediate between hydrated and acetate-bound. Spectra cross at isosbestic points, indicating transition of equilibrium between only two distinct species.

The XANES part of the spectrum is sensitive to changes in the local potential at the Cr atom site.²⁷ The magnitude of change between the XANES of hydrated and acetate-bound Cr is larger than that seen for metals that form mononuclear acetate complexes, such as Cu²⁺, Cd²⁺, and Pb²⁺.²³ This observation suggests that the local potential is modified because of atoms

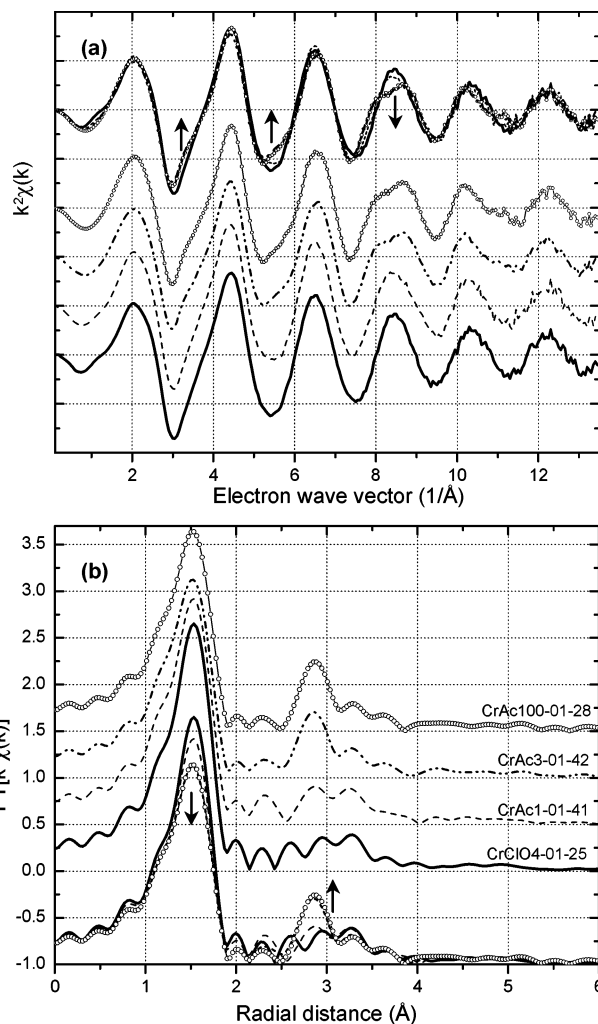


Figure 5. (a) k^2 -weighted $\chi(k)$ from 0.1 M Cr perchlorate and aged Cr acetate solutions of different acetate:Cr ratios. (b) FT of data in (a), $\Delta k = 2.5$ – 12.5 \AA^{-1} . Spectra are shifted vertically for clarity and are shown together at bottom of graph. The same line convention is used in a and b. Crac10 data (not shown) are the same as crac3/crac100 data. Arrows point at trends concurrent with Cr–acetate binding.

more polarizing than O or C in the local Cr environment, and is thus consistent with a polynuclear Cr structure.

Qualitative EXAFS Analysis. As mentioned in the Introduction, a series of 0.1 M Cr acetate solutions has been studied extensively by using FT-IR, NMR, and mass spectrometry.²¹ The spectra show dependence on the pH and acetate:Cr ratio of the solution. Evolution in the spectra can be seen during the first 70 h. The speciation diagram derived from the results of all methods shows that when the pH is in the range 4.0–5.5 and the acetate:Cr ratio is 3 or higher, the cyclic Cr acetate trimer (Figure 1e) is the predominant species in solution. Above pH 5.5, substitution of OH groups for bridging acetate groups is proposed, leading to the formation of a linear chromium triacetate chain (Figure 1B of Tackett²¹). For aged solutions with acetate:Cr ratio = 1, mononuclear bidentate complexes are suggested as the predominant species.

Effect of Age and Acetate:Cr Ratio. Figure 5 shows the XAFS spectra and FTs from aged 0.1 M Cr solutions. Though only two are shown, spectra of all aged samples having acetate:Cr ratio of 3 or higher are similar and display a prominent peak at 2.8 Å, in addition to the high- R features observed in the hydrated Cr spectrum. We attribute the additional peak to Cr–Cr coordination in a trichromium acetate structure, consistent with previous results.²¹ Numerical modeling of the EXAFS confirms

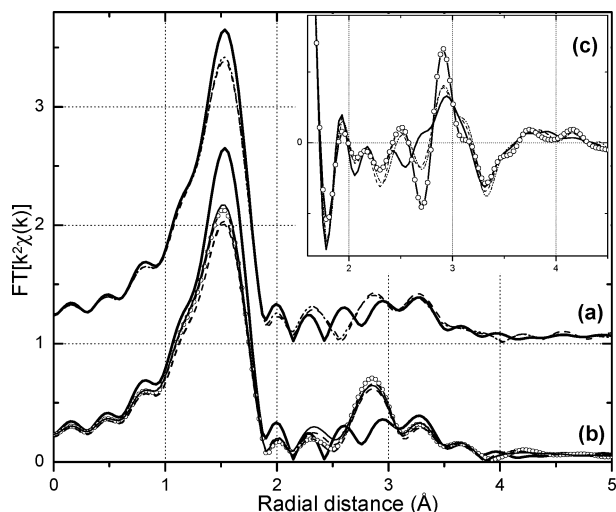


Figure 6. Fourier transforms of $k^2\chi(k)$ data showing the effects of aging, acetate:Cr ratio, and concentration. The hydrated Cr data (heavy line) are shown in all panels for reference. Transform range is $\Delta k = 2.5\text{--}12.5 \text{ \AA}^{-1}$. (a) Fresh acetate:Cr = 3 (dash-dot) and aged acetate:Cr = 1 (dashed) solutions, 0.1 M. (b) Aged acetate:Cr = 3 solutions. Cr concentrations are 0.3 M (broken lines, pH 6.2 and 4.8) and 0.1 M (circles for pH 6.8, thin solid line for pH 4.2). (c) Imaginary part of data in a, together with the aged acetate:Cr = 3 solution of pH 4.2 (circles) from b.

our qualitative assignment (see below). Concurrently with the increase in amplitude of the peak at 2.8 \AA , we observe a small decrease in the nearest-neighbor O peak at 1.5 \AA . The imaginary part of the FT in the region $1.6\text{--}4.5 \text{ \AA}$ is shown in Figure 6. Significant differences in the phase and amplitude of the features are observed only in the region $2.4\text{--}3.2 \text{ \AA}$, where the Cr–Cr interaction contributes.

Spectra taken from a freshly prepared (1-h) acetate:Cr = 3 sample and an aged acetate:Cr = 1 sample are identical (Figure 6a, c). The small changes observed relative to the hydrated Cr spectra resemble the initial formation of the peak at 2.8 \AA in the aged acetate:Cr = 3 sample and can be interpreted as a small fraction of the Cr atoms forming the trichromium complex, while the rest remain hydrated ions. For the fresh acetate:Cr = 3 sample (CrAc3-01-420), this interpretation is consistent with the slow kinetics (on the order of days) of Cr acetate trimer formation.²¹ For the spectrum of the aged acetate:Cr = 1 sample, such interpretation suggests the absence of the mononuclear bidentate binding proposed by Tackett²¹ as predominant under these conditions. This last conclusion is supported by lack of spectral features from the C atom and from MS in the metal–C–CH₃ axis of a bidentate CH₃COO–Me complex (see Figure 1c). Spectra of the bidentate acetate complexes of Cd²⁺(aq) and Pb²⁺(aq) show prominent SS and MS features from C and CH₃ atoms, owing to the well-defined metal–C distance and the metal–C–CH₃ alignment.^{36,41} We also did not observe spectral features from C atoms in the bridging acetate configuration of Cr (Figure 1e). This finding can be rationalized by the rotational degree of freedom of the acetate groups around an axis through the two O atoms in the COO. Large metal–C distance distributions resulting from rotation will destroy the coherence of backscattering coming from C and CH₃ atoms.

Effect of pH. Figure 6b shows spectra from samples at pH 4.2 and 6.8, for two Cr concentrations, 0.1 and 0.3 M. All spectra are identical, except for a small amplitude reduction at higher concentrations attributed to fluorescence self-absorption. This result suggests that the cyclic structure is preserved at pH 6.8. In the proposed linear complex at high pH,²¹ the average Cr–

Cr coordination is reduced by 33% relative to the cyclic structure. The linear structure can also be assumed to be more flexible, resulting in a Cr–Cr distance that is less well defined. Both factors will cause significant amplitude reduction in the FT peak centered at 2.8 \AA . From the lack of such reduction, we conclude that the cyclic structure is retained, although it is possible that OH[−] groups substitute for acetate groups at high pH. Differences between the spectra from all aged Cr acetate solutions with acetate:Cr ratios of 3 or more are negligible in the pH range 2.8–6.8. This is an indication that no substantial change in structure occurs because of possible hydrolysis. Although hydrolysis constants⁴² suggest the formation of a Cr₃(OH)₄³⁺ polymer in the absence of acetate, the FT-IR spectroscopy data clearly indicate that the acetate groups are bound to the Cr³⁺ ion.²¹ The FAB mass spectrometry and ion exchange results in the same study are also consistent with the mass and +1 charge of a Cr₃OAc₆ complex.

Effect of Concentration. As mentioned earlier, we found no difference in local structure for aged acetate:Cr = 3 solutions of 0.1 and 0.3 M Cr concentrations. A dilute 0.03 M sample (CrAc10-003-35) yielded data of lower quality but showed no significant difference from the 0.1 M sample (CrAc10-01-35).

Qualitative Conclusions. The qualitative EXAFS analysis showed that over a wide range of experimental conditions the only structure observed by XAFS was a Cr acetate polymer. The conditions included samples ranging in Cr concentration from 0.03 to 0.3 M and pH changes from 2.8 to 6.8 (above and below which a structural transition has been suggested²¹). When the solution had not aged or only one acetate group was available per Cr³⁺ ion, the local Cr environment consisted predominantly of hydration molecules. Spectra cross at isosbestic points (Figure 6c), indicating a linear combination of only two local environments around Cr: hydrated and acetate-bound species. We thus modeled only the end members of the series: a Cr perchlorate (CrClO₄-01-25, see above) sample and a Cr acetate (CrAc100-01-28) sample, representative of the hydrated and acetate-bound species, respectively.

EXAFS Modeling. Data from sample CrAc100-01-28 were fitted in *R*-space simultaneously at three FT k -weightings (FT- $[k^n\chi(k)]$, $n = 1, 2, 3$).⁴³ This approach to the fitting takes advantage of the differences in the backscattering amplitude of heavier (e.g., Cr) and lighter (e.g., O, C) atoms, without overemphasizing any one of them as could happen in single k -weighting fits. It can also enable further decoupling of the correlations between the XAFS coordination number and DW factor parameters for individual backscattering shells.

As an initial step, the data were fitted with the lower FT range limit set to 3.8 \AA^{-1} . This was done to filter out the low- k contribution mentioned in the analysis of the hydrated Cr samples, which appears as structure around 3.2 \AA in the FT. The O and Cr shells appear well resolved in the FT, and modeling them as such produced an excellent fit (Figure 7a and Table 2). The Cr–O distance is close to that obtained for the hydrated Cr sample. The Cr–O DW factor is very small, indicating strong binding. Its slightly larger value than that of the hydrated sample most likely results from the three different types of O atoms present in the octahedral coordination around Cr (i.e., four O atoms from the bridging acetate groups, one central O atom, and one water molecule). Though it is surprising that different types of O atoms in a shell would not cause more disorder, the Cr³⁺ ions seem to have very strong, similar interactions with water molecules, with atomic O, or with O atoms in the carboxyl group. The Cr–Cr distance obtained from fits of the XAFS data is consistent with the 3.28 \AA determined

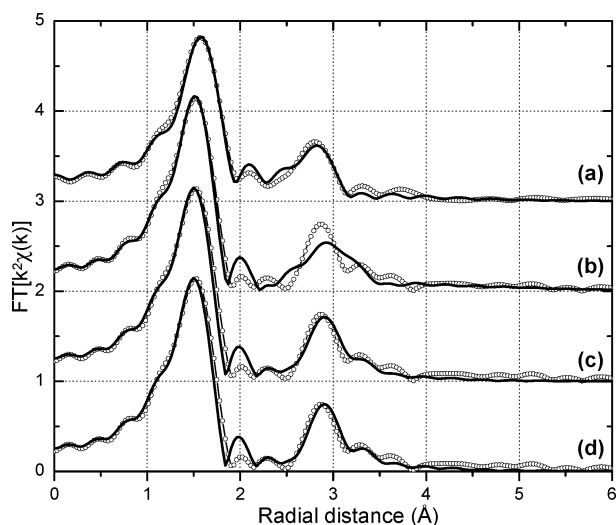


Figure 7. Fourier transforms of $k^2\chi(k)$ data (circles) and fits (line) for the CrAc100-01-28 solution. Transform and fit parameters are $\Delta k = 2.5-12.5 \text{ \AA}^{-1}$ (except for a, where $\Delta k = 3.8-12.5 \text{ \AA}^{-1}$) and $\Delta R = 1.0-4.0 \text{ \AA}$. Fits: (a) O and Cr shells. (b) O and Cr shells. (c) O and Cr shells, with MS paths from O shell, unconstrained. (d) O and Cr shells, with MS paths from O shell, constrained as explained in text.

in crystalline $6\text{H}_2\text{O}\cdot[\text{OCr}_3(\text{CH}_3\text{COO})_6\cdot 3\text{H}_2\text{O}]^+\text{Cl}^-$.^{22,44} The Cr–Cr coordination number (2.8 ± 1.2) is larger than but consistent with the 2.0 expected for the trichromium acetate structure. The reason for the larger coordination number could be correlation of this variable with the DW factor because of the limited data range, resulting also in the large error bars on the parameters. The Cr atoms in the acetate structure are at similar distances and in similar binding geometries (sharing one O atom) as the Cr2 atoms in Cr_2O_3 (Table 2). If the Cr–Cr DW factor in the fits of the Cr acetate data is set to the value obtained for Cr2 atoms in the Cr_2O_3 fits, we obtain a coordination number of 2.2, closer to the theoretical 2.0 for a trichromium acetate complex. Overall, with these two shells the data are fitted well at all three k -weightings, and the major contributions in the XAFS spectrum of this sample are determined.

When the lower FT limit is set to 2.5 \AA^{-1} , the quality of the fit around 2.8 \AA in R -space is degraded, and fit parameters become unrealistic (Figure 7b, Table 2). A Cr shell alone is insufficient to fit the data. A closer analysis of the imaginary part of the FT (Figure 6c) reveals that the acetate spectrum is almost identical to the perchlorate spectrum outside the range $2.5-3.1 \text{ \AA}$. The features in that region show that with increasing acetate binding, an increasing contribution is added to a constant “baseline”. As argued in the Cr perchlorate analysis, either a second-hydration-shell SS path or first-shell MS paths can be used to fit the “baseline” part of the data equally well. We chose to include first-shell MS paths in the analysis of the acetate solution, in addition to the Cr contribution. The MS paths were constrained to the first O shell SS parameters, and a scaling variable was used as in the Cr perchlorate analysis. Results of this model are shown in Figure 7c and Table 2. The Cr and MS contributions overlap in R -space, resulting in large correlations between dependent variables (typically $R - \Delta E_0$ and $N - \sigma^2$). On the basis of the results of this “unconstrained” fit, all ΔE_0 variables were constrained to be equal, and the DW factor for the Cr shell was set to the one obtained when the MS contributions were filtered out (i.e., 0.0052 \AA^2). Results of this final model are given in Figure 7d and Table 2.

The refined parameters obtained from the constrained model allow us to make two observations. First, we recovered structural information for the Cr shell obtained when the “second

hydration/multiple scattering” shell signal was filtered out. Despite the overlap in R -space of the MS and Cr shell contributions, the fact that the imaginary part of one is rapidly oscillating, whereas the other varies slowly and over a wider R -range, allows differentiation between the two and makes extraction of the quantitative information possible. Each Cr atom has 2.6 ± 0.6 Cr neighbors, supporting the cyclic Cr polymer structure in solution. (When the DW factor was set to the value obtained for Cr2 atoms in the Cr_2O_3 fits, as justified earlier, we obtained a coordination number of 2.2.) The latter is further supported by the relatively small DW factor for a second-shell Cr–Cr interaction; a linear arrangement would allow more flexibility than a cyclic one. Second, the scaling factor obtained for first-shell MS contributions is the same as that obtained in fitting of the high- R region of the hydrated Cr sample with the same paths. This means that the “second hydration shell/multiple scattering” contribution has the same amplitude in both the hydrated Cr sample and the Cr acetate trimer. Considering the quite different structures in the two cases, a reduction or complete absence of the contribution by the second hydration shell is expected in the Cr acetate solutions versus the hydrated Cr solutions. This expectation follows from the fact that the space around each Cr atom lying on the inside of the trimer structure is inaccessible to outside water molecules (Figure 1e). The $\text{Cr}_3\text{O}(\text{Ac})_6$ structure is also likely to increase the disorder in an outer hydration shell around each Cr, further reducing the amplitude. We observe no change of this signal in the Cr acetate spectra relative to the hydrated Cr spectra. Therefore, these features must be due to MS within the first coordination sphere of the Cr atom. This conclusion is strengthened by the similar parameters for the first O shell obtained in fitting of both the hydrated Cr and the Cr acetate solution data. The octahedral first-shell environment in both samples is likely to produce similar MS effects. The possibility of contributions from the acetate groups compensating the lack of second-hydration-shell contributions in Cr acetate spectra can be dismissed on the basis of the lack of features from C atoms discussed earlier in the qualitative analysis.

Summary

The distinct Cr–Cr interaction in the XAFS spectra indicates that a Cr polymer structure is the dominant species in aqueous acetate solutions with acetate:Cr ratios of 3 or higher. The spectra are unchanged when pH is varied in the range 2.8–6.8 or the Cr concentration is changed from 0.03 to 0.3 M. Only a small fraction of the Cr³⁺ ions are complexed when solutions are not aged sufficiently or when only one acetate group per Cr³⁺ ion is available. In the latter case, we did not observe the mononuclear bidentate binding suggested in previous studies. Modeling of the data corroborates previous findings that Cr forms a $\text{Cr}_3\text{O}(\text{Ac})_6$ cyclic polymer in acetate solutions. The similarity of spectra regardless of pH indicates preservation of the cyclic complex and lack of structural transition to a linear Cr polymer with increased pH. However, substitution of OH[−] for acetate groups in the cyclic structure with increased pH could not be ruled out. Incorporation of MS contributions because of the first Cr–O shell enabled an accurate fit of hydrated Cr data at a distance of $3.0-3.5 \text{ \AA}$ in the FT. In modeling data from Cr acetate solutions, the same contributions needed to be included with the same amplitude. This allowed us to clarify the origins of the features at $3.0-3.5 \text{ \AA}$ and attribute them entirely to MS in the first shell. Therefore, backscattering from the outer water molecules in the Cr³⁺ hydration structure could not be identified in the EXAFS spectrum.

This and other studies show that XAFS is a sensitive technique for investigating metal hydration and complexation structures at environmentally relevant concentrations. Such information can help in studies of the binding of dilute aqueous Cr to carboxyl ligands (e.g., in cell walls, Langmuir monolayers, micelles, and cell exudates), as well as in investigations of metal-metal interactions and polymerization in solution. Formation of the Cr acetate polymer can be a factor in Cr transport when dissolved acetate groups are present, as it can significantly affect reactivity and partitioning.

Acknowledgment. M.B. acknowledges support from the Environmental Molecular Science Institute at University of Notre Dame (funded by NSF grant EAR-0221966), the United States Department of Energy, and the Bayer Corporation through a fellowship in environmental science. Help in beamline setup from the staff of MRCAT is greatly appreciated, as is use of the laboratory of J. Fein. We would like to thank M. Duncan for the editorial handling and the reviewers for their comments. This work was supported in part by National Science Foundation grant EAR-0207169 and EAR-9905704, and the U.S. Department of Energy, Office of Science, Office of Biological and Environmental Research, Natural and Accelerated Bioremediation program. MRCAT is supported by the U.S. Department of Energy under Contract DE-FG02-94-ER45525 and the member institutions. Use of the Advanced Photon Source was supported by the U.S. Department of Energy, Office of Science, Office of Basic Energy Sciences, under Contract W-31-109-Eng-38.

References and Notes

- Ohtaki, H. Structure and dynamics of solutions. In *Structure and dynamics of solutions*; Ohtaki, H., Yamatera, H., Eds.; Elsevier: Amsterdam, 1992; Chapter 2.
- Ohtaki, H.; Radnai, T. *Chem. Rev.* **1993**, *93*, 1157.
- Marcus, Y. *Chem. Rev.* **1988**, *88*, 1475.
- Broadbent, R. D.; Neilson, G. W.; Sandstrom, M. *J. Phys.: Condens. Matter* **1992**, *4*, 639.
- Lindqvist-Reis, P.; Munoz-Paez, A.; Diaz-Moreno, S.; Pattanaik, S.; Persson, I.; Sandstrom, M. *Inorg. Chem.* **1998**, *37*, 6675.
- Magini, M. *J. Chem. Phys.* **1980**, *73*, 2499.
- Caminiti, R.; Licheri, G.; Piccaluga, G.; Pinna, G. *Chem. Phys.* **1977**, *19*, 371.
- Read, M. C.; Sandstrom, M. *Acta Chem. Scand.* **1992**, *46*, 1177.
- Caminiti, R.; Licheri, G.; Piccaluga, G.; Pinna, G. *J. Chem. Phys.* **1978**, *69*, 1.
- Bol, W.; Welzen, T. *Chem. Phys. Lett.* **1977**, *49*, 189.
- Bergstrom, P. A.; Lindgren, J.; Read, M.; Sandstrom, M. *J. Phys. Chem.* **1991**, *95*, 7650.
- Bleuzen, A.; Foglia, F.; Furet, E.; Helm, L.; Merbach, A. E.; Weber, J. *J. Am. Chem. Soc.* **1996**, *118*, 12777.
- Easteal, A. J.; Mills, R.; Woolf, L. A. *J. Phys. Chem.* **1989**, *93*, 4968.
- Diaz-Moreno, S.; Munoz-Paez, A.; Martinez, J. M.; Pappalardo, R. R.; Marcos, E. S. *J. Am. Chem. Soc.* **1996**, *118*, 12654.
- Munoz-Paez, A.; Pappalardo, R. R.; Marcos, E. S. *J. Am. Chem. Soc.* **1995**, *117*, 11710.
- Sakane, H.; Munoz-Paez, A.; Diaz-Moreno, S.; Martinez, J. M.; Pappalardo, R. R.; Marcos, E. S. *J. Am. Chem. Soc.* **1998**, *120*, 10397.
- Cusanelli, A.; Frey, U.; Richens, D. T.; Merbach, A. E. *J. Am. Chem. Soc.* **1996**, *118*, 5265.
- Tackett, J. E. *Appl. Spectrosc.* **1989**, *43*, 483.
- Deacon, G. B.; Phillips, R. J. *Coord. Chem. Rev.* **1980**, *33*, 227.
- Nakamoto, K. *Infrared and Raman spectra of inorganic and organic coordination compounds*, 4th ed.; Wiley: New York, 1986.
- Tackett, J. E. *Appl. Spectrosc.* **1989**, *43*, 490.
- Chang, S. C.; Jeffrey, G. A. *Acta Crystallogr., Sect. B* **1970**, *B26*, 673.
- Boyanov, M. I.; Shibata, T.; Kelly, S. D.; Kemner, K. M.; Bunker, B. A. Spectral features in the XAFS of aqueous metal-acetate complexes. Presented at the XAFS 12 conference in Malmo, Sweden, May 2003; Abstract A7400, p 169.
- Segre, C. U.; Leyarowska, N. E.; Chapman, L. D.; Lavender, W. M.; Plag, P. W.; King, A. S.; Kropf, A. J.; Bunker, B. A.; Kemner, K. M.; Dutta, P.; Duran, R. S.; Kaduk, J. The MRCAT insertion device beamline at the Advanced Photon Source. In *Synchrotron Radiation Instrumentation: Eleventh U.S. National Conference*; Pianetta, P., Ed.; American Institute of Physics: New York, 2000; Vol. CP521, p 419.
- Kemner, K. M.; Kropf, J.; Bunker, B. A. *Rev. Sci. Instrum.* **1994**, *65*, 3667.
- Cross, J. O.; Frenkel, A. I. *Rev. Sci. Instrum.* **1999**, *70*, 38.
- Koningsberger, D. C.; Prins, R. *X-ray Absorption: Principles, Applications, Techniques of EXAFS, SEXAFS, and XANES*; Wiley: New York, 1988.
- Newville, M.; Livins, P.; Yacoby, Y.; Rehr, J. J.; Stern, E. A. *Phys. Rev. B* **1993**, *47*, 14126.
- Ankudinov, A. L.; Ravel, B.; Rehr, J. J.; Conradson, S. D. *Phys. Rev. B* **1998**, *58*, 7565.
- Ravel, B. *J. Synchrotr. Radiat.* **2001**, *8*, 314.
- Newville, M.; Ravel, B.; Haskel, D.; Rehr, J. J.; Stern, E. A.; Yacoby, Y. *Physica B* **1995**, *208-209*, 154.
- Wyckoff, R. W. G. *Crystal Structures*; John Wiley & Sons: New York, 1964; Vol. 2.
- Haskel, D. Local Structural Studies of Oriented High-Temperature Superconducting Cuprates by Polarized XAFS Spectroscopy. Ph.D. Dissertation, University of Washington, 1998; p 256.
- Martell, A. E.; Smith, R. M. *Critical Stability Constants*; Plenum Press: New York, 1974; Vol. 1-5.
- Campbell, L.; Rehr, J. J.; Schenter, G. K.; McCarthy, M. I.; Dixon, D. J. *Synchrotr. Radiat.* **1999**, *6*, 310.
- Boyanov, M. I.; Kelly, S. D.; Kemner, K. M.; Bunker, B. A.; Fein, J. B.; Fowle, D. A. *Geochim. Cosmochim. Acta* **2003**, *67*, 3299.
- Merkling, P. J.; Munoz-Paez, A.; Marcos, E. S. *J. Am. Chem. Soc.* **2002**, *124*, 10911.
- Merkling, P. J.; Munoz-Paez, A.; Martinez, J. M.; Pappalardo, R. R.; Marcos, E. S. *Phys. Rev. B* **2001**, *6401*.
- Filipponi, A.; Dangelo, P.; Pavel, N. V.; Diccico, A. *Chem. Phys. Lett.* **1994**, *225*, 150.
- Benfatto, M.; Natoli, C. R.; Bianconi, A.; Garcia, J.; Marcelli, A.; Fanfoni, M.; Davoli, I. *Phys. Rev. B* **1986**, *34*, 5774.
- Boyanov, M. I.; Kmetko, J.; Shibata, T.; Datta, A.; Dutta, P.; Bunker, B. A. *J. Phys. Chem. B* **2003**, *107*, 9780.
- Baes, C. F.; Mesmer, R. E. *Hydrolysis of Cations*; Wiley: New York, 1973.
- Kelly, S. D.; Kemner, K. M.; Fein, J. B.; Fowle, D. A.; Boyanov, M. I.; Bunker, B. A.; Yee, N. *Geochim. Cosmochim. Acta* **2002**, *66*, 3855.
- Figgis, B. N.; Robertson, G. B. *Nature (London)* **1965**, *205*, 694.

Mechanism of Pb Adsorption to Fatty Acid Langmuir Monolayers Studied by X-ray Absorption Fine Structure Spectroscopy

Maxim I. Boyanov,^{*,†,‡} Jan Kmetko,^{§,||} Tomohiro Shibata,[†] Alokmay Datta,^{§,⊥} Pulak Dutta,[§] and Bruce A. Bunker[†]

Department of Physics, University of Notre Dame, Notre Dame, Indiana 46556, and Department of Physics and Astronomy, Northwestern University, Evanston, Illinois 60208

Received: January 22, 2003; In Final Form: June 11, 2003

The local atomic environment of lead (Pb) adsorbed to a $\text{CH}_3(\text{CH}_2)_{19}\text{COOH}$ Langmuir monolayer was investigated in situ using grazing-incidence X-ray absorption fine structure (GI-XAFS) spectroscopy at the Pb L_{III} edge. Measurements were performed at pH 6.5 of the 10^{-5} M PbCl_2 solution subphase, a condition under which grazing incidence diffraction (GID) revealed a large-area commensurate superstructure underneath the close-packed organic monolayer. The XAFS results indicate covalent binding of the Pb cations to the carboxyl headgroups, and the observed Pb–Pb coordination suggests that the metal is adsorbed as a hydrolysis polymer, rather than as individual Pb^{2+} ions. The data are consistent with a bidentate chelating mechanism and a one Pb atom to one carboxyl headgroup binding stoichiometry. We discuss how this adsorption model can explain the peculiarities observed with Pb in previous metal–Langmuir monolayer studies. A systematic study of lead perchlorate and lead acetate aqueous solutions is presented and used in the analysis. XAFS multiple scattering effects from alignment of the Pb–C–C atoms in the lead acetate solutions are reported.

1. Introduction

Langmuir monolayers of carboxylic acids spread on aqueous solutions have been the object of intense investigation in the past decades.¹ Interest is driven by the desire for fundamental understanding of the interactions, as well as by the technological promise of transferred (“Langmuir–Blodgett” or LB) films.² Langmuir systems are also studied as templates for oriented growth of crystals and as a model for the nucleation phase of biomineralization.^{3,4} Previous work shows that monolayers formed over dilute metal solutions have properties quite different from those formed over pure water. The “compressed” phase is attained even at large areas per molecule, and the viscoelastic response, surface potential, refractive index, and layer transferability to solid substrates are affected appreciably by the subphase metal.^{5–10} Infrared spectroscopy results suggest that the carboxyl headgroups become deprotonated and complexed as pH increases.^{11,12} More recently, synchrotron grazing incidence diffraction (GID) experiments determined precise in-plane lattice parameters, chain tilt, and the layer thickness of the acid monolayer, for various aqueous metals, concentrations, and pH.^{13–18} The existence of thin commensurate superstructures for some of the metals is also revealed. Attempts to correlate the lattice parameters with the cationic radii or Pauling electronegativity have not been successful.¹⁸ Anomalous diffraction and X-ray reflectivity data suggest that Pb and Cd adsorb as hydrolysis products rather than as individual cations.^{15,17} Among the metals studied in the above works, Pb can be singled out as

having the greatest influence on the monolayer by compressing it the most,⁵ producing the greatest surface potential and refractive index change,^{5,6,8} the largest surface loss tangent,⁸ and the largest area superlattice.¹⁷ These effects are observed at the lowest subphase pH and metal concentration for Pb.

The existing literature suggests that models in which individual cations interact with the amphiphiles may be inadequate in explaining the superstructures and the monolayer properties mentioned above. Questions remain as to what the structure of the adsorbed complex is, the nature of the adsorbent–headgroup interactions (ionic, covalent, or mixed), and the adsorbent: headgroup stoichiometry. These are all essential parameters in thermodynamic^{19,20} and electrochemical^{21,22} theories that model the experimental data. Most studies conclude subphase metal adsorption on the basis of circumstantial data, and there are few direct in situ confirmations that the divalent ion (and not, for instance, precipitates or the pH-controlling agent) is condensed at the interface and influencing the monolayer ordering.^{23,24} Aqueous Pb, in particular, seems to have a very specific effect when compared to other divalent metals.

We report here the results from grazing incidence XAFS (X-ray absorption fine structure) experiments on a monolayer of heneicosanoic acid ($\text{CH}_3(\text{CH}_2)_{19}\text{COOH}$) spread over an aqueous PbCl_2 solution. This study extends previous GID work on the same system.¹⁷ New structural and chemical information about the adsorbed Pb atoms is presented. On the basis of the XAFS data, an adsorption model of a hydrolysis trimer in which each Pb atom is bound to one carboxyl headgroup is proposed. The role of this model in explaining the results of previous Langmuir monolayer studies with Pb is discussed.

2. Experimental Procedures

2.1. Experimental Setup.

XAFS experiments were carried out at the Materials Research Collaborative Access Team

* Corresponding author. E-mail: mboyanov@nd.edu.

† University of Notre Dame.

‡ Present Address: Argonne National Laboratory, Argonne, IL 60439.

§ Northwestern University.

|| Present address: Department of Physics, Cornell University, Ithaca, NY 14853.

⊥ Present address: Saha Institute of Nuclear Physics, Calcutta 700064, India.

(MRCAT) beamline of the Advanced Photon Source. The beamline is equipped with a tunable undulator and a cryogenic double-crystal Si (111) monochromator.²⁵ A rhodium-coated mirror was used for harmonic rejection. The incident X-ray beam was defined to a vertical thickness of 0.1 mm and a 20 mm horizontal width. The Langmuir samples were studied in a total external reflection configuration, with the incidence angle set at 0.065°, slightly below the calculated critical angle of an air–water interface (0.09° at 13.6 keV photon energy). The calculated penetration depth of the evanescent wave is about 90 Å. The effect of the Pb atoms in the Stern and diffuse layers underneath the 30 Å acid monolayer on the optical properties is assumed negligible. The Pb L_{III} edge XAFS data were collected in fluorescence mode, using a sealed Stern–Heald type detector²⁶ filled with Kr and placed on the side of the aqueous surface (perpendicular to the beam). The continuous-scanning mode of the monochromator was used which reduces the radiation exposure during a single scan (ca. 3 min/EXAFS scan, 1 min/XANES scan). Before the XAFS experiments, GID data were collected from the Pb–Langmuir monolayer system to verify that the monolayer structure is the same as the one observed in previous GID experiments.¹⁷ The stability of the film to radiation damage was determined by observing the changes in the GID pattern with irradiation time. The diffraction pattern was unchanged for 40 min at the intensity used, after which gradual deterioration of the superlattice peaks began. Fresh samples were thus prepared every 35 min of measurements, after careful cleaning of the trough with hexane and water, and following an identical preparation procedure. The scans were aligned by the simultaneously collected Pb foil data; the first inflection point of the absorption edge was set at 13035 eV. The derivative of the individual reference channel scans were repeatable within less than 1 eV in the XANES area. The maximum scatter between the individual scans of the monolayer sample was 2–3 eV due to the lower signal-to-noise ratio. Because the Pb–Langmuir data are produced by averaging about 35 scans, a conservative energy resolution estimate for the final data set is 1 eV. Data from consecutive scans of each sample were averaged, and the resulting data from all identical Pb–Langmuir samples were normalized and averaged. The edge energies for the samples were chosen at the inflection point, and background was subtracted using the AUTOBK program.²⁷

2.2. Sample Preparation. The Langmuir monolayer preparation is outlined in a previous paper.¹⁷ Briefly, heneicosanoic acid dissolved in chloroform was spread by gently dropping it with a syringe over the solution subphase. After evaporation of the chloroform, the monolayer was compressed with a Teflon barrier until a slight increase in the surface pressure was observed. The Langmuir trough that was used is described in detail elsewhere;²⁸ it is an enclosed system with Kapton windows for the incident, scattered, and fluorescence X-rays, with gas lines to maintain slight overpressure of He gas and a liquid circulator to maintain the sample temperature at 9 °C. The pH of the 10^{−5} M PbCl₂ subphase solution was raised to 6.5 by adding NaOH solution in 5 μL aliquots to the 300 mL solution. A single stock solution for the subphase was used throughout the study.

Powder and aqueous Pb standards were used for comparison and theory calibration in the analysis. The PbO₂ powder standard was prepared from commercially available chemicals (Sigma-Aldrich), after grinding and sieving (−400 mesh). The phase purity was checked by powder X-ray diffraction before mounting on Kapton tape. The spectrum was measured at ~10 K. We were unable to obtain commercial red (tetragonal) PbO in

the pure crystallographic phase, so we have used an XAFS spectrum of that material from the XAFS Spectra Library at SSRL.²⁹ The aqueous standards were prepared with distilled deionized water (resistivity 18 MΩ cm) and analytical grade chemicals (Sigma-Aldrich) without further purification. To avoid the formation of carbonate aqua complexes and precipitates, the water was boiled to remove dissolved CO₂. All further preparation, pH adjustment, and sample mounting was carried out in an Ar-purged glovebox. The solution sample holders were sealed Plexiglas slides with Kapton film windows for transmission measurements. The samples and identification names (in quotation marks) are as follows: as a standard for hydrated Pb cation (“Pb(aq)”), a 0.2 M solution of Pb(ClO₄)₂ at pH 2.5 (unadjusted) was used; as a standard for Pb hydrolysis complex (“[Pb₄(OH)₄]⁴⁺”), a 0.2 M solution of Pb(ClO₄)₂ at pH 6.1 (adjusted with NaOH) was prepared; as standards for aqueous Pb bound to a carboxyl group in solution, several solutions of Pb(CH₃COO)₂·3H₂O with different amounts of NH₄(CH₃COO) added were prepared. The NH₄(CH₃COO) was added to overload the solution with carboxyl anions, thus gradually shifting the equilibrium between hydrated lead and lead bound to carboxyl groups toward the bound species. Because XAFS measures the average local environment of all Pb atoms, it is necessary that the standards contain predominantly one species to obtain a representative spectrum for that environment. The Pb:carboxyl groups ratios and Pb concentrations are as follows: “PbAc-1”, 1:2 (no additional acetate added), 0.2 M; “PbAc-2”, 1:10, 0.1 M; “PbAc-3”, 1:10, 0.2 M; “PbAc-4”, 1:~100, 0.1 M. Speciation of Pb in the solution standards was calculated using published hydrolysis and stability constants.^{30,31}

3. XAFS Theory and Data Reduction

Extended X-ray absorption fine structure (EXAFS) spectroscopy uses the small periodic variations in the absorption coefficient above the absorption edge energy of an element to extract information about the local environment of that atom. There are complete references on the subject.^{32,33} Only a short description of this theory is given here.

The EXAFS of a powder-like sample with Gaussian disorder can be derived as follows:³³

$$\chi(k) = \sum_i \frac{(N_i S_0^2) F_i(k)}{k R_i^2} \exp\left(-2k^2 \sigma_i^2 - \frac{2R_i}{\lambda(k)}\right) \times \sin(2R_i k + \delta_i(k)) \quad (1)$$

The sum is taken over all distinguishable single and multiple scattering paths that the ejected photoelectron wave traverses in the material before it returns to the absorber atom. Here k is the electron wave vector, $k \propto \sqrt{\hbar\omega - E_0}$, E_0 is the edge energy and $\hbar\omega$ is the incident photon energy, N_i is the multiplicity of the path (coordination number in the case of single scattering), S_0^2 is the constant passive electron reduction factor, R_i is the half path length (interatomic distance in the case of single scattering), σ_i^2 is the relative mean square displacement of the path length (EXAFS Debye–Waller factor, which differs from the X-ray diffraction Debye–Waller factor), $F_i(k)$ and $\delta_i(k)$ are the effective scattering amplitude and phase shift of the scattered electron, respectively, and $\lambda(k)$ is the mean free path of the photoelectron. An energy origin shift variable ΔE_0 is added when fitting, $k \rightarrow \sqrt{k^2 - (2m\Delta E_0/\hbar^2)}$, to account for differences in the calculated and measured edge energies. As can be seen, $\chi(k)$ is a superposition of sinusoidal waves in k -space with

frequency related to the length of the scattering path. Data are usually weighed by k^n ($n = 1-3$) to emphasize different parts of the spectrum. A Fourier transform (FT) of $k^n\chi(k)$ results in peaks at close to the half path length distance that appear similar to a radial distribution function, but peak positions are shifted to smaller R values due to $\delta_i(k)$. In cases of destructive interference between neighboring shells, a peak may not be observed even though an atom is present. The contribution from multiple scattering paths can be neglected in most room temperature measurements because of thermal motion, except when the scattering atoms are aligned in a straight line (focusing multiple scattering). In the real or imaginary part of the FT the contributions corresponding to the different scattering atoms combine linearly to produce the observed features, so comparison to spectra of standards in which the features are assigned can reveal the presence of a certain atom in the unknown sample. The final structural parameters are obtained from fits of the real and imaginary parts of FT[$k^n\chi(k)$], using model scattering amplitudes and phase shifts.

In current EXAFS analysis, $F_i(k)$ and $\delta_i(k)$ are calculated ab initio for a cluster of atoms and then calibrated by using appropriate standards with known structure. The calibrated $F_i(k)$ and $\delta_i(k)$ are then used in a fitting procedure where the structural parameters N_i , R_i , and σ_i^2 are varied until a best fit to the experimental data is achieved. The ATOMS,³⁴ FEFF8,³⁵ and FEFFIT³⁶ programs were used in this work. Simultaneous multiple k -weighting (k^1 , k^2 , and k^3) R -space fits of each spectrum were performed, which reduces the possibility of obtaining erroneous parameters due to correlations at any single k -weighting. The fit quality is characterized by two parameters: the XAFS reliability factor R , which measures the sum-of-squares difference between data and fit normalized to the experimental data, and the reduced factor χ_r^2 , which also takes into account the number of variables and noise in the data. R values of a few percent or less and a fit that visually follows the main features of the data are generally considered acceptable in XAFS analysis.³⁷ The χ_r^2 should theoretically be close to 1 for a good fit.³⁸ In practice, it is always close to several tens or hundreds in XAFS fitting, even for a visually good fit of data from a known system. A detailed discussion on the origin of this and how it is handled to determine accurately the fitting parameter uncertainties is given in the FEFFIT documentation. Even though larger than 1, χ_r^2 can be used for comparison between different fitting scenarios—if the χ_r^2 reduction observed by adding a new shell or new fitting parameters is statistically significant, then the extra flexibility introduced in the fit is considered justified by the data.

When the incoming photon has energy slightly larger than the binding energy, the absorption probability is determined by the absorbing atom's density of states near the Fermi energy. Thus, the near-edge (XANES) region of the spectrum is sensitive to the valence state, bond type, bond orientation, and symmetry. Rigorous treatment to extract that information from XANES spectra is not currently possible, but comparisons with the spectra of model compounds can reveal details about the atom's bond geometry.

4. Experimental Results

4.1. Powder and Solution XAFS Standards. Fit results from the PbO and PbO₂ standards are listed in Table 1. These standards have relatively simple local structures for Pb²⁺ and Pb⁴⁺ charge states, respectively, and were used to test the ability of FEFF8 to model a known system. The EXAFS was calculated from the known crystal structures^{39,40} using single scattering

Pb–O and Pb–Pb paths, where the distances of the shells were not varied independently, but a single linear lattice expansion parameter was applied to all. The fit (not shown) reproduced the spectral features in the entire fit range (1.0–4.2 Å) for both samples. The S_0^2 factors obtained for Pb²⁺ (PbO) and Pb⁴⁺ (PbO₂) at room temperature were 0.71(5) and 0.81(6), respectively. The S_0^2 was set to 0.71 in the analysis of all Pb²⁺ samples with an oxygen first shell environment.

Data from the solution standards are presented on Figure 1. A notable observation in the acetate spectra is that they all cross at the same points (isosbestic points) when overlaid together with the hydrated Pb standard. This indicates that there are only two distinct Pb species (hydrated and bound to acetate), and that only the ratio of one to the other is changing with acetate overloading. The sample most overloaded with acetate anions, PbAc-4, is thus considered to be representative of most Pb ions bound to acetate and is used to obtain structural information for the Pb–acetate aqua complex. Fit results are shown in Figure 2 and Table 1. The immediate Pb environment is fit well by an O and C shell from the bound acetate group. The obtained 4 O atoms in the first shell and 2 C atoms in the second are consistent with a bidentate-chelating binding mechanism (Figure 2a), observed also in crystal Pb acetate⁴¹ and inferred by infrared spectroscopy in solution.⁴² An interesting feature in the magnitude of the FT is the peak at 3.8 Å. It has a large amplitude, which is unlikely for EXAFS from a loosely coordinated second hydration shell in a solution complex. Another possibility is a Pb atom from Pb–Pb interactions. Testing models with an O or Pb shell at this distance does not result in satisfactory fits. The best fit is obtained using focusing multiple scattering (MS) paths from the two C atoms in the acetate group. This is additional evidence for the bidentate mechanism, as the Pb–C1–C2 straight line can only be formed when the Pb atom is bound in the acetate plane with both O atoms. In our final fit, a single distance change and σ^2 variables are used for all MS and C2 paths, and their numbers are constrained to be the same as the number of the carboxyl C1 atoms. The distance between the closer C1 and farther C2 atoms calculated from the fitted Pb–C distances is consistent with the structure of the acetate group in crystalline Pb acetate.⁴¹ The σ^2 values for all Pb–C and Pb–O paths are about the same. The similar disorder is an indication that these atoms behave as a rigid group. All of the above supports a binding mechanism in which the Pb ion is bound by both carboxyl O atoms.

The hydrated sample, Pb(aq), shows a broad asymmetric peak in the FT, which is shifted to higher distance relative to the acetate spectra (Figure 2). The main peak is fit with an O shell from hydration water at ca. 2.6 Å (Table 1). The addition of a second, closer O shell at 2.15 Å, improves the fit at the left shoulder of the main peak. This Pb–O distance is the same as in PbO₂ and is at the lower end of the range of Pb–O distances found in Pb(II) oxides, hydroxides, and oxalates.⁴³ The origin of this atom in the solution is unclear—a small amount of Pb may have been complexed due to impurities in the dissolved chemicals or as hydroxide. The presence or absence of this atom in the fit model does not, however, alter appreciably the fit values for the hydration shell at 2.6 Å (Table 1).

The data from the [Pb₄(OH)₄]⁴⁺ hydrolyzed solution standard are modeled on the basis of the crystal structure of Pb₄(OH)₄(NO₃)₄.⁴⁴ A drawing of the [Pb₄(OH)₄]⁴⁺ complex is shown in Figure 2b. It can be described as two interleaved Pb₄ and (OH)₄ tetrahedrons, forming a distorted cubical cage. This structure is preserved in aqueous solutions.⁴⁵ Fitting of the split FT peak between $R = 3$ and 4 Å was indeed most consistent with Pb–

TABLE 1: Numerical Fit Results^a

powders	path	CN	R (Å)	σ^2 (Å ²)	ΔE_0 (eV)	χ^2_ν	R , %
PbO-tetr	Pb–O	4.0	2.30(1)	0.007(1)	0.0(6)	247	1.4
	Pb–Pb	4.0	3.67(1)	0.006(1)	–2.7(7)		
	Pb–Pb	4.0	3.80(1)	0.013(5)	–2.7(7)		
	Pb–Pb	4.0	3.94(1)	0.012(4)	–2.7(7)		
PbO ₂ (10 K)	Pb–O	2.0	2.15(0)	0.002(1)	4.4(6)	1457	2.0
	Pb–O	4.0	2.17(0)	0.001(1)	4.4(6)		
	Pb–Pb	2.0	3.38(0)	0.003(1)	3(1)		
	Pb–Pb	8.0	3.89(0)	0.003(1)	3(1)		
solutions	path	CN	R (Å)	σ^2 (Å ²)	ΔE_0 (eV)	χ^2_ν	R , %
PbAc-4	Pb–O	3.7(2)	2.36(1)	0.011(1)	1.8(5)	139	0.8
	Pb–C1	2.0(2)	2.92(1)	0.009(3)	7.2(5)		
	Pb–C2 ^b	N _{C1}	4.47(2)	0.009(3)	7.2(5)		
	–C1–C2– ^b	2 × N _{C1}	4.47(2)	0.009(3)	7.2(5)		
	–C1–C2–C1– ^b	N _{C1}	4.47(2)	0.009(3)	7.2(5)		
Pb ₄ (OH) ₄ ⁴⁺	Pb–O1	1.3(5)	2.37(1)	0.015(4)	4(3)	92	0.1
	Pb–O2	8(2)	2.72(1)	0.034(2)	2.3(4)		
	third→ ^c		0.009(1)	0.016(1)	–5.1(4)		
Pb ²⁺ (aq) ^d	Pb–Pb	3.0(2)	3.77(1)	0.016(1)	–5.1(4)	302	0.5
	Pb–O2	11.3(4)	2.59(2)	0.030(1)	–0.4(5)		
	third→ ^c		0.002(1)	0.003(2)	0.0(2)		
Pb ²⁺ (aq) ^d	Pb–O1	0.5(2)	2.14(1)	0.003(2)	0.0(2)	73	0.1
	Pb–O2	12.7(5)	2.64(1)	0.029(1)	0.0(2)		
	third→ ^c		0.006(0)				
sample	path	CN	R (Å)	σ^2 (Å ²)	ΔE_0 (eV)	χ^2_ν	R , %
Pb–Langm	C(COO) ^e	0.9(2)	2.91(2)	0.0096	–1.9(9)	17	1.7
	O (hydration)	14(9)	2.70	0.08(3)	–1.9(9)		
	Pb (Pb + OH) ^e	2.8(9)	3.77(4)	0.016	–1.9(9)		

^a Column headers and sample identification names are explained in the theory and experimental sections. CN = coordination number, ΔE_0 is an energy origin shift variable (see the FEFFIT documentation). Error bars are given in parentheses and show standard deviation from the value in the last digit shown (e.g., 0.71(5) = 0.71 ± 0.05). When no error bars are given, the parameter is held fixed to the listed value. The coordination numbers of the powder standards are fixed to those determined in the X-ray diffraction studies. ^b Single and multiple scattering (MS) paths associated with the farther C2 atom in the acetate group. CNs are constrained to be equal to the C1 coordination number. ^c Third cumulant, included in the fit because of the large disorder. ^d Fits with and without the closer O shell are compared to determine its effect on the hydration shell parameters. ^e Only the C and Pb shell fit values are given in the table, the notes in parentheses indicate that these parameters are used to calculate the O and OH shell parameters in the corresponding group (see text).

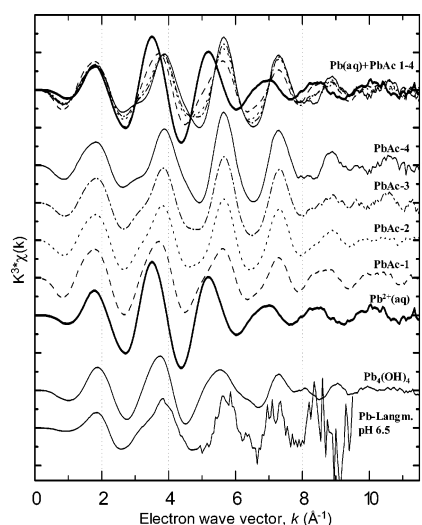


Figure 1. Data from the aqueous standards (Pb²⁺(aq), [Pb₄(OH)₄]⁴⁺, PbAc-*n*) and the Pb–Langmuir monolayer sample. The arrow indicates increasing Pb–acetate binding. The Pb(aq) and all PbAc-*n* data are all overlaid at the top, using the line convention from the individual spectra

Pb coordination, at all k weightings. The obtained coordination number and distances for Pb–Pb (Table 1) are consistent with the crystallographic data⁴⁴ and with previous XAFS studies.^{43,46} The short Pb–O distance is consistent with the bridging Pb–OH bonds in the [Pb₄(OH)₄]⁴⁺ cage, and the disordered O shell at 2.7 Å is attributed to a hydration shell around the aqueous

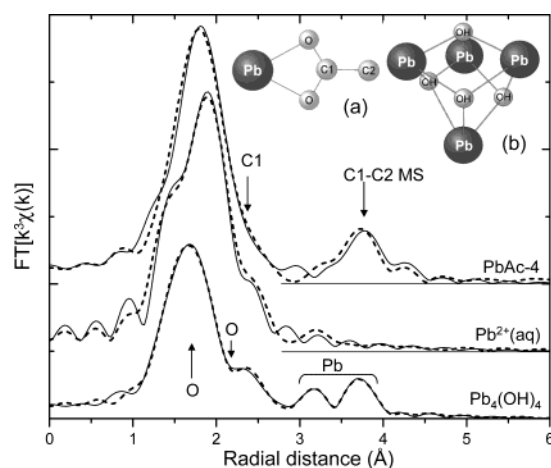


Figure 2. Aqueous Pb standards: Fourier transform ($\Delta k = 2.2–11.0$ Å^{–1}) of $k^3\chi(k)$, of experimental data (dash) and fits (solid line). These standards were considered as models for Pb bound to an acetate group (PbAc-4), hydrated Pb [Pb²⁺(aq)], and hydrolyzed Pb, [Pb₄(OH)₄]⁴⁺. (a) Pb bound bidentate to an acetate group. (b) Structure of the [Pb₄(OH)₄]⁴⁺ complex.

complex. Coordination numbers for the Pb–OH shell (O1 in Table 1) do not correlate well with the number of Pb–OH bonds in the crystal structure. This discrepancy might be caused in part by the correlation between the number and the σ^2 variables, but also by the large disorder in the shell. As discussed in previous XAFS work on model Pb compounds, the detection

of some of the atoms in a shell with large anharmonic thermal motion or large degree of distortion can be complicated or not possible at room temperature.^{43,46,47} The Pb–OH bond lengths in the crystal $[\text{Pb}_4(\text{OH})_4]^{4+}$ groups are in the range $R = 1.97\text{--}2.60$ Å, the average distance being 2.34 ± 0.15 Å. The disorder for the hydration shell is also quite large. Rather than trying to account for every possible disorder or thermal effect, we have used the obtained coordination numbers as parameters fitting well the data from the aqueous standards and quantifying the Pb–OH contribution relative to the better defined Pb–Pb coordination. We can then interpret or scale the coordination numbers of that shell in the fits of the unknown sample relative to the Pb–Pb numbers, provided that the σ^2 values are held fixed to the ones obtained in solution.

In summary, the solution standards provide spectra of Pb^{2+} atoms in several isolated environments that are likely to be present in the sample of interest. EXAFS is sensitive to the average coordination around the absorber atom, so it is important to understand the individual contributions before performing a fit of an unknown sample. Fits of the standards demonstrate the ability of the FEFF8 code to model separately a hydrated Pb ion, Pb bound to an acetate group in solution, and a hydrolysis $[\text{Pb}_4(\text{OH})_4]^{4+}$ product. The fit values place constraints on the EXAFS structural variables, which may become correlated in samples with mixed environment or when the data range is limited.

4.2. Pb–Langmuir Monolayer Sample. 4.2.1 XANES Results. The grazing incidence geometry allows sampling of a thin layer at the air–water interface, corresponding to the evanescent wave penetration depth. X-ray absorption near-edge structure (XANES) scans without the organic monolayer, but with the PbCl_2 subphase solution were performed. There was no observable absorption edge, indicating an undetectable amount of Pb in the sampled thickness. Another control measurement was performed with heneicosanol ($\text{CH}_3(\text{CH}_2)_{20}\text{OH}$) spread over the PbCl_2 solution. Heneicosanol has the same hydrocarbon chain structure but lacks the carboxyl headgroup of heneicosanoic acid ($\text{CH}_3(\text{CH}_2)_{19}\text{COOH}$). Again, no absorption edge was observed. When heneicosanoic acid was spread on the solution, the data showed a clear absorption edge. This result is direct confirmation that there is considerable increase in the Pb concentration at the interface and that the charged headgroup is responsible for the metal condensation. It also shows that the XAFS data are representative of only the atoms condensed in the interfacial region and sampling of the bulk solution is not significant.

Figure 3 compares the normalized XANES data (a) and its energy derivative (b) for the standards and the Pb–Langmuir monolayer sample. Differences are observed between Pb in the +2 and +4 oxidation state. The PbO_2 standard has a pronounced preedge feature corresponding to the 2p–6s electron transition.⁴⁸ This feature is not present or is very small in Pb^{2+} compounds, where the 6s state is unavailable for a dipole transition. The XANES of the Langmuir monolayer sample does not have a preedge feature and the edge shape is very different from that of metallic Pb (not shown). It can be concluded that the oxidation state of the Pb atoms adsorbed at the interface is Pb^{2+} . This is not unexpected; however the XANES data provide unambiguous proof of this fact.

Differences can also be seen between XANES of Pb^{2+} atoms in different local environments. In the $\text{Pb}(\text{aq})$ standard where Pb–O interactions are electrostatic, the XANES has larger

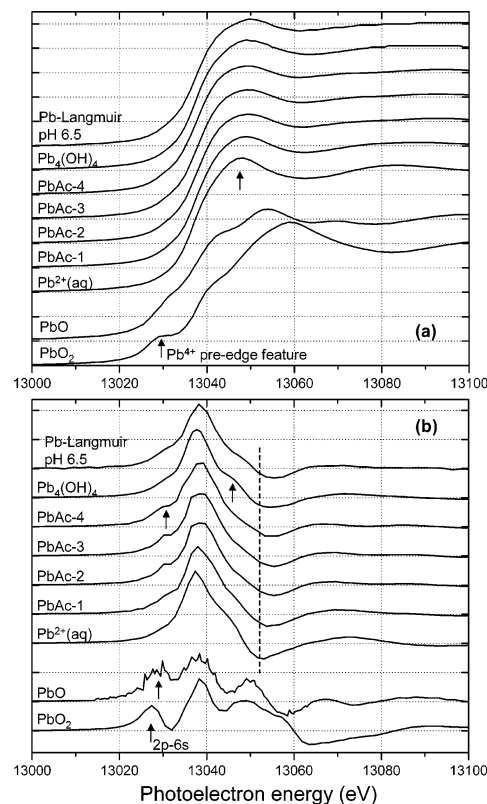


Figure 3. (a) XANES data from the Pb–Langmuir sample compared to the aqueous ($\text{Pb}^{2+}(\text{aq})$, $\text{PbAc-}n$, $[\text{Pb}_4(\text{OH})_4]^{4+}$) and powder (PbO , PbO_2) standards. (b) Energy derivative of the data in (a). The arrows and the dotted line point to features that are discussed in the text.

“white line” amplitude (13048 eV). The first minimum in the XANES derivative (Figure 3b, vertical line at 13052 eV) occurs at energies slightly lower than those of the other Pb standards. Both shoulders of the main peak are featureless. In the acetate solutions, the derivative minimum shifts to higher energies (13055 eV), and a feature appears on the left shoulder of the main derivative peak (13030 eV). Differences similar to those from $\text{Pb}(\text{aq})$ are seen in the $[\text{Pb}_4(\text{OH})_4]^{4+}$ sample as well; however, the feature on the left shoulder is not present and there is a concave down shape (13045 eV) on the right shoulder of the main derivative peak. A comprehensive Pb L_{III} XANES analysis of similar Pb^{2+} standards can be found in Bargar et al.⁴³ The authors use similarities in the XANES such as the dampened “white line” and the shift in the derivative minimum (13052 eV) as evidence of covalent binding in their samples. Furthermore, the small preedge feature in the PbO spectrum is attributed to the pyramidal tetragonal coordination of the Pb atom in this compound, which makes the 2p–6s transition possible by creating 6s vacancies through 6s–6p_z hybridization levels resulting from the C_{4v} symmetry. The $[\text{Pb}_4(\text{OH})_4]^{4+}$ standard that has O in distorted trigonal pyramidal coordination around Pb does not have this feature. It is seen, however, in the $\text{PbAc-}n$ standards, which is another indication of the bidentate binding of two acetate groups, resulting in 4 O atom coordination at the same distance.

The Pb–Langmuir sample data show similarities to the acetate and hydrolyzed Pb species—the derivative minimum is shifted to higher energies and the main peak in the derivative shows features seen in the lead acetate and hydrolyzed lead solutions. This indicates covalent Pb binding at the interface. The absence of the preedge feature is interpreted as a lack of pyramidal O coordination around the bound Pb^{2+} atoms.

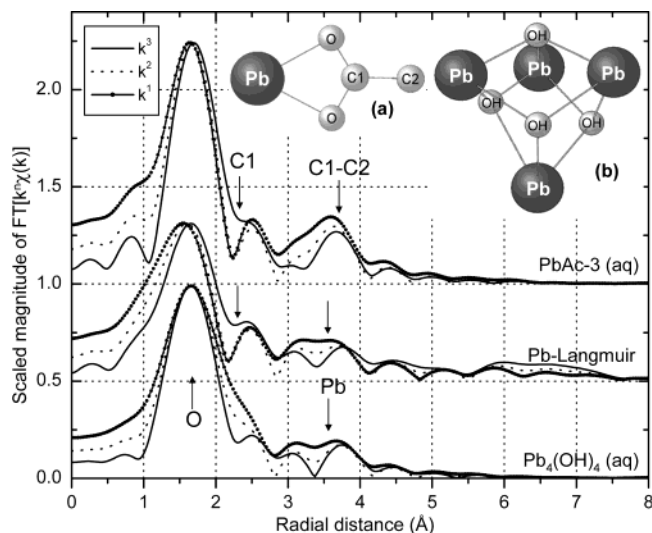


Figure 4. Comparison of the Fourier transforms ($\Delta k = 2.2\text{--}8.0 \text{ \AA}^{-1}$) of $k^n \chi(k)$, $n = 1, 2, 3$, for Pb bound to an acetate group (PbAc-3), Pb adsorbed to the Langmuir monolayer (Pb-Langmuir), and hydrolyzed Pb, $[\text{Pb}_4(\text{OH})_4]^{4+}$. The amplitudes of the transform at k^1 and k^2 weighting are scaled so the main peak is the same height as that of the k^3 -weighted transform for each sample. The k^3 transforms are unadjusted and shifted vertically for clarity. (a) Pb ion bidentate to an acetate group. (b) Structure of the $[\text{Pb}_4(\text{OH})_4]^{4+}$ hydrolysis complex.

4.2.2. EXAFS Analysis and Numerical Fits. The $k^3 \chi(k)$ for the Langmuir monolayer sample is shown on Figure 1. Data are used only up to $k = 8 \text{ \AA}^{-1}$ in the FT, because at higher k values the peak-to-peak variations (noise) are larger than the amplitude of the oscillation. The scaled FT magnitude at three different k weightings for the Pb-Langmuir sample and the PbAc-3 and $[\text{Pb}_4(\text{OH})_4]^{4+}$ solutions is shown on Figure 4. The PbAc-3 is chosen for comparison among the acetate standards because its $k^3 \chi(k)$ shows the greatest similarity to that of the Langmuir sample, particularly at $k = 3\text{--}5 \text{ \AA}^{-1}$ (Figure 1). This is an indication of hydration water around the adsorbed Pb ions, as the PbAc-3 sample is intermediate between the PbAc-4 and Pb(aq) standards. The largest FT peak (due to O backscattering) of the monolayer sample can be seen to shift with k -weighting change, the same way it does in the acetate solution standard. The shift is caused by the interference of the O and C backscattering signals. The features at $R = 2.3 \text{ \AA}$ that are present in both the monolayer sample and acetate standard can also be traced to the C1 atom from the carboxyl group. At larger distances ($3\text{--}4 \text{ \AA}$), the Langmuir sample resembles more closely the $[\text{Pb}_4(\text{OH})_4]^{4+}$ standard—the peak is split and the peak height is smaller than that observed for C-C multiple scattering. The k -weight dependence is similar to the $[\text{Pb}_4(\text{OH})_4]^{4+}$ standard. The imaginary part of the FT (Figure 5) shows similar trends. The C1 atom feature at $R = 2.3 \text{ \AA}$ can be seen to grow with increased carboxyl binding in solution and is also present in the Pb-Langmuir sample. Between $R = 3$ and 4 \AA , the Pb-Langmuir sample is similar in shape to the $[\text{Pb}_4(\text{OH})_4]^{4+}$ standard. Additional arguments against assignment of the $3\text{--}4 \text{ \AA}$ features to linear C1-C2 multiple scattering are the sawtooth-shaped chain structure of the fatty acid⁴⁹ and the fact that the positions of the Pb ions, even though covalently bound to the headgroup at a certain distance, are also influenced by electrostatic interactions in the Stern and diffuse layer.⁵⁰ The Pb-C1-C2 angle, if at all the same for all Pb ions, is likely to be different from 180° in either case. In contrast, both the Pb atom and the acetate group are essentially unconstrained in solution

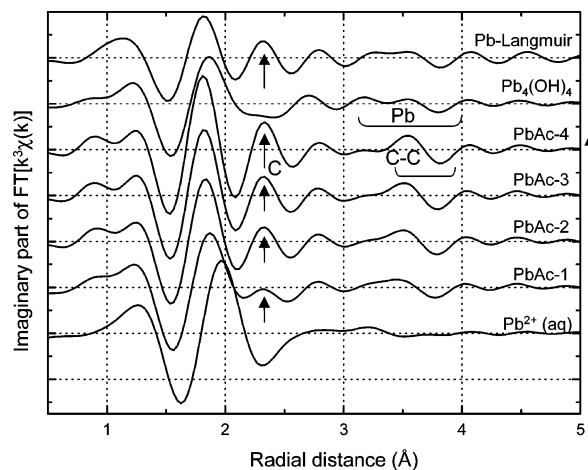


Figure 5. Comparison of the imaginary part of the FT for the Pb-Langmuir sample and the aqueous standards (Pb(aq), PbAc- n , and $[\text{Pb}_4(\text{OH})_4]^{4+}$). The contributions from the different shells in the standards is shown. The arrow to the right of the figure points to increasing proportion of acetate-bound Pb in the PbAc- n samples.

and a planar bidentate acetate complex with Pb-C1-C2 alignment is expected.

Two qualitative conclusions can be drawn from the observations in the FT: the immediate Pb^{2+} environment suggests carboxyl binding, and the features between 3 and 4 \AA suggest the presence of Pb-Pb interactions. Theoretical modeling of the data is necessary to ascertain the qualitative findings. Standard EXAFS shell-by-shell fitting, however, is not well suited in this case. The short data range causes the contributions from the different shells to overlap in the FT, which produces correlations in the fitting parameters. This is further complicated by the mixed carboxyl-hydrolysis Pb environment suggested by the qualitative analysis. To deal with these complications, we adopt an approach in which contributions from entire entities (rather than individual coordination shells) are included in the fit. For instance, if a Pb-Pb interaction from a $[\text{Pb}_4(\text{OH})_4]^{4+}$ entity is included, the Pb-OH interaction must also be included in the appropriate proportion, at the appropriate distance, and with the appropriate disorder; similarly, adding a Pb-C interaction from COO binding should be accompanied by appropriate constraints on the O shell. The coordination numbers of the entire entities are then varied in the unknown sample. Such an approach is in essence a linear combination of known spectra and rests on the assumption that the Pb-acetate and Pb-Pb interactions in solution are similar to the metal-headgroup and Pb-Pb interactions at the interface. We test this assumption by allowing the distances of the characteristic atoms in each entity to vary, as a different binding mechanism is likely to produce different bond lengths. The best fit model consists of the O and C1 shells from a carboxyl group, O1 and Pb shells from the $[\text{Pb}_4(\text{OH})_4]^{4+}$ standard, and a hydration water O2 shell. In the carboxyl group paths, the number of O atoms is constrained to be twice the number of C atoms (bidentate binding is assumed, as suggested by the solution standards and infrared studies on a Pb-Langmuir monolayer¹¹). The Pb-C and Pb-O distances are allowed to vary but the relative O-C distance is fixed. In the $[\text{Pb}_4(\text{OH})_4]^{4+}$ paths, the number of Pb-OH interactions is constrained to be in the same proportion to Pb-Pb interactions as in the solution fit; however, the Pb-Pb coordination number is varied. A single distance change variable scaled to the distance from the absorbing Pb atom is applied for both. In the hydration O shell, the coordination number,

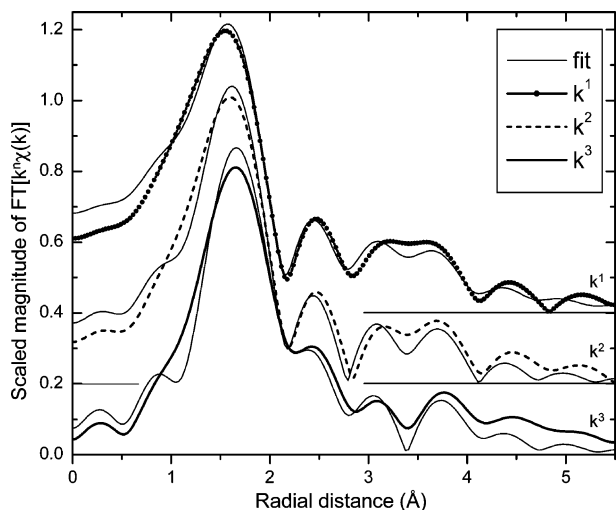


Figure 6. Fit results for the Pb–Langmuir monolayer sample. The amplitude at k^1 and k^2 weightings is scaled so that the main peak amplitudes are equal to that of the k^3 -weighted transform. Spectra are shifted vertically for clarity. The fit parameters are $\Delta k = 2.2\text{--}8.0 \text{ \AA}^{-1}$, $\Delta R = 1.0\text{--}4.0 \text{ \AA}$.

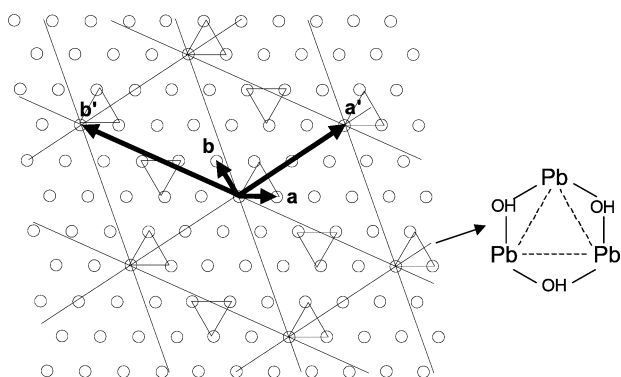


Figure 7. Schematic drawing of the proposed adsorption mechanism, viewed from under the organic monolayer. The circles represent the carboxyl headgroups and the triangles represent the proposed $[\text{Pb}_3(\text{OH})_3]^{3+}$ structure pictured on the right. The unit vectors are \mathbf{a} and \mathbf{b} for the organic lattice, and \mathbf{a}' and \mathbf{b}' for the superlattice. Each Pb atom binds covalently one carboxyl headgroup.

distance change, σ^2 , and third cumulant parameters are all varied. In all paths of the model, the ΔE_0 and σ^2 values (except σ^2 of the hydration shell) are set to the ones obtained in the fits of the corresponding solutions. A uniform energy origin shift variable is added to all ΔE_0 's.

Results from the fits are shown in Figure 6. The fit line reproduces the data features at all three of the k weightings used in the simultaneous fits. Fit parameters are listed in Table 1. The values for the distance of the C and Pb atoms are in good agreement with those found in the solution standards. The Pb coordination is 0.9 ± 0.2 carboxyl groups and 2.8 ± 0.9 Pb neighbors. These results are consistent with the adsorption of either a Pb_3 triangle by itself, or of the Pb_3 triangle that is one face of the Pb_4 tetrahedron in the $[\text{Pb}_4(\text{OH})_4]^{4+}$ hydrolysis complex (Figure 4b). In the case of a Pb_3 adsorbent, each two Pb atoms are most likely bridged by an OH group on the side opposite the monolayer, resulting in a $[\text{Pb}_3(\text{OH})_3]^{3+}$ complex (Figure 7). The C coordination number is consistent with one Pb ion binding one carboxyl group. The 1:1 stoichiometry is also supported by the XANES results—in the bidentate mode considered here, binding to two headgroups would result in tetragonal coordination and a preedge XANES feature. Such a feature, however, is not observed.

On Figure 7 we present a possible arrangement of a Pb_3 triangle relative to the monolayer lattice that is consistent with the fit results. Each Pb atom in the triangle vertices is covalently bound to one carboxyl headgroup, resulting in 0.75 or 1.0 average coordination (for an adsorbed Pb_4 tetrahedron or Pb_3 triangle, respectively), consistent with the fitted 0.9 ± 0.2 carboxyl groups per Pb atom. The distances between the headgroups in the monolayer¹⁷ are close to the Pb–Pb distance and allow such a configuration. Without having definitive proof for it, we propose two Pb_3 or Pb_4 clusters per unit cell of the superlattice, so better headgroup charge compensation and space filling can be achieved. The Pb clusters are likely to electrostatically repel each other, so the arrangement of Figure 7 allows for “vertex” interactions between Pb_3 triangles when they are close and “side” interactions when they are farther apart. Further experiments and calculations should provide more insight into the number and arrangement of these hydrolysis complexes.

The use of spherically averaged EXAFS in the analysis of the planar Pb–Langmuir sample requires justification. Because the Langmuir monolayer is a two-dimensional powder in the plane of the solution surface,¹ it has axial symmetry about the vertical direction (z). The incident X-ray beam is linearly polarized in the horizontal plane, so electron backscattering from atoms coordinating Pb in this plane will be enhanced relative to those that are out-of-plane. Exact treatment for an L_{III} edge is complicated⁵¹ and requires information about the angle of the Pb–carboxyl bond and of the Pb_3 plane, which are not known. Any polarization dependence will be observed as changes in the coordination numbers obtained in the fits. To determine the maximum possible effect, FEFF8 calculations for different orientations of the Pb–carboxyl and Pb–Pb bonds were performed. Circular averaging in the interface plane (xy) was done to account for the axial symmetry. Results are shown on Figure 8 for the limiting cases in the orientation. The spherically averaged spectrum can be reproduced by scaling the limiting cases up or down by no more than 20%. This limits to $\sim 20\%$ the maximum error in coordination numbers that could be introduced by using spherically averaged EXAFS. We estimate the uncertainty to be even lower, because the dimensions of the carboxyl lattice and Pb–Pb distance imply an intermediate angle between 0 and 90 deg for the Pb–carboxyl bond. Assuming that the Pb atoms lie in a horizontal plane and accounting for polarization will reduce the Pb–Pb coordination number in the fits closer to 2.0, making the proposed Pb_3 model even more consistent with the data. Taken at its largest value, the 20% uncertainty in coordination numbers is smaller than the ca. 30% error bars obtained in the fits. An exact treatment with known bond angles will therefore not change the presented conclusions, even if feasible.

4.2.3 Discussion of the Proposed Model in the Context of Previous Studies. As mentioned in the Introduction, Pb is known to affect the monolayer quite differently from otherwise similar divalent metals. Specifically, only Pb compresses the monolayer at pH as low as 4.0.⁵ This is inconsistent with the ionization constants of carboxyl acids and with bulk Pb^{2+} –carboxyl stability constants³¹ and can be explained by an adsorbed Pb hydrolysis complex in the following manner: when the monolayer is spread, the charged surface attracts the positive ions in the solution (Pb^{2+} and H^+) and produces a higher local Pb concentration close to the surface. This creates favorable conditions for the polymerization into hydrolysis complexes. The resulting +4 charges are more strongly attracted to the surface than H^+ , effectively raising the local pH. The hydrolysis complexes are then able to bind to the deprotonated headgroups

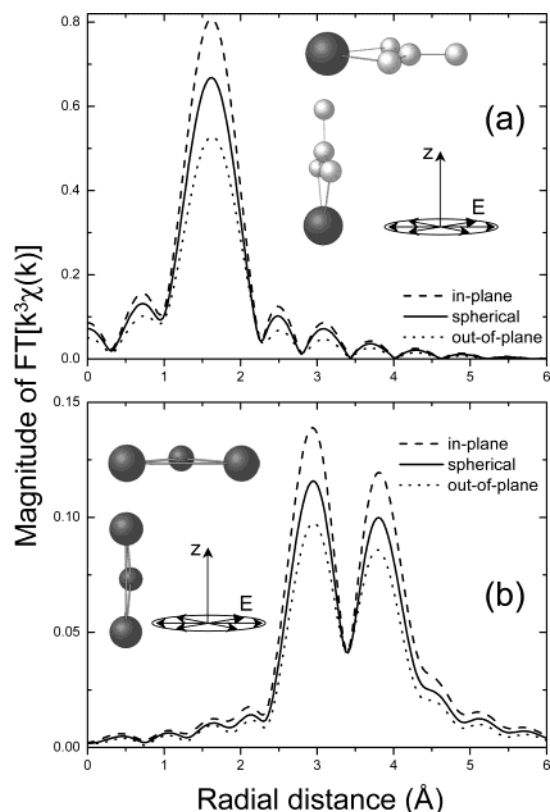


Figure 8. Polarization dependence of simulated Pb-carboxyl (a) and Pb triangle (b) data. The structural parameters (N , R , σ^2) obtained in the Pb-Langmuir fit are used in the simulation and the data are Fourier transformed over the same FT range ($k^3\chi(k)$, $\Delta k = 2.2-8.0 \text{ \AA}^{-1}$). In-/out-of-plane indicates the electric vector being in/out of the plane of the structure, top/bottom drawing in each subfigure, correspondingly. Spherical indicates spherical averaging of the EXAFS. The circular electric polarization indicates the in-plane powder averaging of the data.

and compress the monolayer. Studies on Tb^{3+} show that the adsorption step occurs at lower pH, supporting the described mechanism for ions of larger charge.⁵²

The experiments of Yazdaniyan et al.⁵ find that the surface potential change caused by Pb saturates at much lower concentrations than Ba, Ca, Mg, Co, and Cd (Figure 5 in Yazdaniyan et al.⁵). This can also be explained better by a hydrolysis complex of higher charge. It is likely that the monolayer is able to attract more of the larger charge complex than the hydrated +2 cations through stronger Coulomb interaction, and the necessary amount for surface site saturation is extracted from the solution even at very low subphase concentrations.

The surface rheological properties are also affected the strongest by Pb, resulting in a film having the highest surface loss tangent ("stiffness") among Ba, Ca, Mg, Co, and Cd.⁸ This supports the proposed model, as more energy is required to break the Pb-Pb or Pb-OH-Pb bonds in a Pb_3 triangle, than if single cations compress the monolayer by electrostatic attraction between the headgroups. The formation of "lines" of these complexes along the superlattice directions may also increase the stiffness of the monolayer.

The large area of the supercell ($14 \times$ the headgroup unit cell area) found for Pb in the GID experiments¹⁷ is also better explained by a large adsorption complex—such relatively long-range modulations are less likely to be caused by individual cation interactions. For comparison, Mn^{2+} , Mg^{2+} , and Cd^{2+} , which do not hydrolyze as easily, form a 1×2 , 2×2 , and 2×3 superlattices, respectively.^{15,18}

5. Conclusions

Grazing-incidence XAFS spectroscopy can give new insight on the binding mechanism of adsorbed metals underneath Langmuir monolayers. The experimental geometry allows selective sampling of the interfacial region and enhances the signal-to-background ratio, so that spectra from a metal monolayer can be obtained. Our experiments prove directly that the charged carboxyl headgroups cause the Pb ions to segregate in the interfacial region and that their oxidation state is Pb^{2+} . Furthermore, comparisons with spectra taken from aqueous standards indicate that the adsorbed Pb is covalently bound to the carboxyl headgroups. Pb-Pb coordination at the interface is observed. Modeling of the data determines 0.9 ± 0.2 carboxyl groups and 2.8 ± 0.9 Pb neighbors in the average local environment of each Pb atom. On the basis of these results, we propose a binding mechanism for Pb as a polynuclear hydrolysis complex, rather than as individual ions. The numerical results are consistent with an adsorbed Pb triangle parallel to the interface, in a 1:1 metal:carboxyl binding stoichiometry. We discuss this possible structure in the context of previous studies on Langmuir monolayers and describe how it can explain the peculiarities observed with Pb in them. So far, infrared absorption spectroscopy studies on metal-Langmuir systems have been concentrating on the carboxyl modes, whereas Raman modes observed in $[\text{Pb}_4(\text{OH})_4]^{4+}$ solutions standards have not been looked for. Further vibration spectroscopy studies can help elucidate the character of the Pb-Pb interactions observed by XAFS.

Acknowledgment. M.B. thanks the Bayer Corp. for its support through the Bayer Predoctoral Fellowship. Beamline setup help from the staff of MRCAT is greatly appreciated. We thank J. Fein for use of his laboratory for some of the sample preparations. This work is supported in part by the National Science Foundation through Grant NSF-EAR99-05704. MRCAT is supported by the U.S. Department of Energy under Contract DE-FG02-94-ER45525 and the member institutions. Use of the Advanced Photon Source was supported by the U.S. Department of Energy, under Contract No. W-31-109-Eng-38.

Supporting Information Available: Color versions of Figures 2, 4, 7, and 8. This material is available free of charge via the Internet at <http://pubs.acs.org>.

References and Notes

- (1) Kaganer, V. M.; Mohwald, H.; Dutta, P. *Rev. Mod. Phys.* **1999**, *71*, 779.
- (2) Roberts, G. G. *Adv. Phys.* **1985**, *34*, 475.
- (3) Rapaport, H.; Kuzmenko, I.; Berfeld, M.; Kjaer, K.; Als-Nielsen, J.; Popovitz-Biro, R.; Weissbuch, I.; Lahav, M.; Leiserowitz, L. *J. Phys. Chem. B* **2000**, *104*, 1399.
- (4) Mann, S.; Archibald, D. D.; Didymus, J. M.; Douglas, T.; Heywood, B. R.; Meldrum, F. C.; Reeves, N. J. *Science* **1993**, *261*, 1286.
- (5) Yazdaniyan, M.; Yu, H.; Zograf, G. *Langmuir* **1990**, *6*, 1093.
- (6) Kim, M. W.; Sauer, B. B.; Yu, H.; Yazdaniyan, M.; Zograf, G. *Langmuir* **1990**, *6*, 236.
- (7) Bettarini, S.; Bonosi, F.; Gabrielli, G.; Martini, G. *Langmuir* **1991**, *7*, 1082.
- (8) Yazdaniyan, M.; Yu, H.; Zograf, G.; Kim, M. W. *Langmuir* **1992**, *8*, 630.
- (9) Zasadzinski, J. A.; Viswanathan, R.; Madsen, L.; Garnæs, J.; Schwartz, D. K. *Science* **1994**, *263*, 1726.
- (10) Ghaskadvi, R. S.; Carr, S.; Dennin, M. *J. Chem. Phys.* **1999**, *111*, 3675.
- (11) Gericke, A.; Huhnerfuss, H. *Thin Solid Films* **1994**, *245*, 74.
- (12) Simon-Kutscher, J.; Gericke, A.; Huhnerfuss, H. *Langmuir* **1996**, *12*, 1027.

- (13) Dutta, P.; Peng, J. B.; Lin, B.; Ketterson, J. B.; Prakash, M.; Georgopoulos, P.; Ehrlich, S. *Phys. Rev. Lett.* **1987**, *58*, 2228.
- (14) Leveiller, F.; Jacquemain, D.; Lahav, M.; Leiserowitz, L.; Deutsch, M.; Kjaer, K.; Alsnielsen, J. *Science* **1991**, *252*, 1532.
- (15) Leveiller, F.; Bohm, C.; Jacquemain, D.; Mohwald, H.; Leiserowitz, L.; Kjaer, K.; Alsnielsen, J. *Langmuir* **1994**, *10*, 819.
- (16) Datta, A.; Kmetko, J.; Yu, C. J.; Richter, A. G.; Chung, K. S.; Bai, J. M.; Dutta, P. *J. Phys. Chem. B* **2000**, *104*, 5797.
- (17) Kmetko, J.; Datta, A.; Evmenenko, G.; Durbin, M. K.; Richter, A. G.; Dutta, P. *Langmuir* **2001**, *17*, 4697.
- (18) Kmetko, J.; Datta, A.; Evmenenko, G.; Dutta, P. *J. Phys. Chem. B* **2001**, *105*, 10818.
- (19) Yamauchi, A.; Matsubara, A.; Kimizuka, H.; Abood, L. G. *Biochim. Biophys. Acta* **1968**, *150*, 181.
- (20) Petrov, J. G.; Kuleff, I.; Platikanov, D. *J. Colloid Interface Sci.* **1982**, *88*, 29.
- (21) Bloch, J. M.; Yun, W. B. *Phys. Rev. A* **1990**, *41*, 844.
- (22) Pezron, E.; Claesson, P. M.; Berg, J. M.; Vollhardt, D. *J. Colloid Interface Sci.* **1990**, *138*, 245.
- (23) Bloch, J. M.; Yun, W. B.; Yang, X.; Ramanathan, M.; Montano, P. A.; Capasso, C. *Phys. Rev. Lett.* **1988**, *61*, 2941.
- (24) Watanabe, I.; Tanida, H.; Kawachi, S. *J. Am. Chem. Soc.* **1997**, *119*, 12018.
- (25) Segre, C. U.; Leyarovska, N. E.; Chapman, L. D.; Lavender, W. M.; Plag, P. W.; King, A. S.; Kropf, A. J.; Bunker, B. A.; Kemner, K. M.; Dutta, P.; Duran, R. S.; Kaduk, J. The MRCAT insertion device beamline at the Advanced Photon Source. In *Synchrotron Radiation Instrumentation: Eleventh U.S. National Conference*; Pianetta, P., Ed.; American Institute of Physics: New York, 2000; Vol. CP521, p 419.
- (26) Stern, E. A.; Heald, S. M. *Rev. Sci. Instrum.* **1979**, *50*, 1579.
- (27) Newville, M.; Livins, P.; Yacoby, Y.; Rehr, J. J.; Stern, E. A. *Phys. Rev. B* **1993**, *47*, 14126.
- (28) Barton, S. W.; Thomas, B. N.; Flom, E. B.; Rice, S. A.; Lin, B.; Peng, J. B.; Ketterson, J. B.; Dutta, P. *J. Chem. Phys.* **1988**, *89*, 2257.
- (29) <http://www.ssrsl.slac.stanford.edu/mes/spectra/index.html>.
- (30) Baes, C. F.; Mesmer, R. E. *Hydrolysis of Cations*; Wiley: New York, 1973.
- (31) Martell, A. E.; Smith, R. M. *Critical Stability Constants*; Plenum Press: New York, 1974; Vols. 1–5.
- (32) Stern, E. A.; Heald, S. M. Basic principles and applications of EXAFS. In *Handbook of Synchrotron Radiation*; Koch, E. E., Ed.; North-Holland: New York, 1983; p 995.
- (33) Koningsberger, D. C.; Prins, R. *X-ray Absorption: Principles, Applications, Techniques of EXAFS, SEXAFS, and XANES*; Wiley: New York, 1988.
- (34) Ravel, B. *J. Synchrotron Radiat.* **2001**, *8*, 314.
- (35) Ankudinov, A. L.; Ravel, B.; Rehr, J. J.; Conradson, S. D. *Phys. Rev. B* **1998**, *58*, 7565.
- (36) Newville, M. FEFFIT: Using FEFF to Model XAFS data. In *FEFFIT Program Documentation*, 1998.
- (37) http://ixs.iit.edu/subcommittee_reports/sc/err-rep.pdf. Error Reporting Recommendations: A Report of the Standards and Criteria Committee; International XAFS Society, 2000.
- (38) Bevington, P. R. *Data reduction and error analysis for the physical sciences*; McGraw-Hill: New York, 1992; p 190.
- (39) Leciejewicz, J. *Acta Crystallogr.* **1961**, *14*, 1304.
- (40) D'Antonio, P.; Santoro, A. *Acta Crystallogr. Sect. B—Struct. Sci.* **1980**, *36*, 2394.
- (41) Rajaram, R. K.; Rao, J. K. M. *Z. Kristallogr.* **1982**, *160*, 225.
- (42) Tackett, J. E. *Appl. Spectrosc.* **1989**, *43*, 483.
- (43) Bargar, J. R.; Brown, G. E.; Parks, G. A. *Geochim. Cosmochim. Acta* **1997**, *61*, 2617.
- (44) Grimes, S. M.; Johnston, S. R.; Abrahams, I. *J. Chem. Soc., Dalton Trans.* **1995**, 2081.
- (45) Maroni, V. A.; Spiro, T. G. *J. Am. Chem. Soc.* **1967**, *89*, 45.
- (46) Strawn, D. G.; Sparks, D. L. *J. Colloid Interface Sci.* **1999**, *216*, 257.
- (47) Manceau, A.; Boisset, M. C.; Sarret, G.; Hazemann, R. L.; Mench, M.; Cambier, P.; Prost, R. *Environ. Sci. Technol.* **1996**, *30*, 1540.
- (48) Rao, K. J.; Wong, J. *J. Chem. Phys.* **1984**, *81*, 4832.
- (49) Small, D. M. *The physical chemistry of lipids: from alkanes to phospholipids*; Plenum Press: New York, 1986; Vol. 4.
- (50) Adamson, A. W.; Gast, A. P. *Physical chemistry of surfaces*; Wiley: New York, 1997.
- (51) Stohr, J.; Jaeger, R. *Phys. Rev. B* **1983**, *27*, 5146.
- (52) Linden, D. J. M.; Peltonen, J. P. K.; Rosenholm, J. B. *Langmuir* **1994**, *10*, 1592.



doi:10.1016/S0016-7037(00)01343-1

Adsorption of cadmium to *Bacillus subtilis* bacterial cell walls: A pH-dependent X-ray absorption fine structure spectroscopy study

M. I. BOYANOV,^{1,*} S. D. KELLY,² K. M. KEMNER,² B. A. BUNKER,¹ J. B. FEIN,³ and D. A. FOWLE^{3,†}¹Department of Physics, University of Notre Dame, Notre Dame, IN 46556, USA²Environmental Research Division, Argonne National Laboratory, Argonne, IL 60439, USA³Department of Civil Engineering and Geological Sciences, University of Notre Dame, Notre Dame, IN 46556, USA

(Received May 1, 2002; accepted in revised form October 22, 2002)

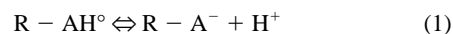
Abstract—The local atomic environment of Cd bound to the cell wall of the gram-positive bacterium *Bacillus subtilis* was determined by X-ray absorption fine structure (XAFS) spectroscopy. Samples were prepared at six pH values in the range 3.4 to 7.8, and the bacterial functional groups responsible for the adsorption were identified under each condition. Under the experimental Cd and bacterial concentrations, the spectroscopy results indicate that Cd binds predominantly to phosphoryl ligands below pH 4.4, whereas at higher pH, adsorption to carboxyl groups becomes increasingly important. At pH 7.8, we observe the activation of an additional binding site, which we tentatively ascribe to a phosphoryl site with smaller Cd-P distance than the one that is active at lower pH conditions. XAFS spectra of several cadmium acetate, phosphate, and perchlorate solutions were measured and used as standards for fingerprinting, as well as to assess the ability of FEFF8 and FEFFIT to model carboxyl, phosphoryl, and hydration environments, respectively. The results of this XAFS study in general corroborate existing surface complexation models; however, some binding mechanism details could only be detected with the XAFS technique. Copyright © 2003 Elsevier Ltd

1. INTRODUCTION

Discerning the chemical controls on metal transport in the environment is a prerequisite for understanding the fate of contaminants as well as for designing effective and efficient remediation strategies. Aqueous metal cations are exposed to mineral and biologic surfaces that affect their mobility in the subsurface; therefore, interaction with both must be well understood. Studies of metal adsorption onto mineral surfaces have been conducted for a wide variety of aqueous metals and environmentally important minerals. X-ray absorption spectroscopy has provided information about the mineral surfaces, binding sites, and the surface complexation reactions that occur at the mineral–water interface (Brown, 1990; Spadini et al., 1994; Sery et al., 1996; Venema et al., 1996; Farquhar et al., 1997; O’Day et al., 1998; Collins et al., 1999; O’Day, 1999; Randall et al., 1999). Substantially less is known about the mechanisms of biosorption. (For recent reviews, see Fein, 2000; Warren and Haack, 2001). Laboratory and field studies have demonstrated that bacterial cell walls efficiently adsorb a variety of aqueous metal cations (Beveridge and Murray, 1976, 1980; Beveridge and Koval, 1981; Crist et al., 1981; Harvey and Leckie, 1985; Goncalves et al., 1987; Konhauser et al., 1993). Therefore, it is likely that bacterial adsorption reactions can significantly affect metal contaminant transport and distribution in aqueous systems. A large portion of the bacterial adsorption data has been modeled by using a bulk partitioning approach, wherein a bulk partition coefficient is determined for the bacterial species of interest under fixed experimental conditions. This approach does not require a detailed understanding of the surfaces or of the adsorption mechanisms involved,

but the applicability of the derived coefficient is limited to the conditions at which it was determined. Partition coefficients vary significantly as a function of pH, fluid composition, bacterial concentration, etc. (Bethke and Brady, 2000; Koretsky, 2000). Conversely, surface complexation models, which apply the formalism of aqueous ion association reactions to solute adsorption onto surfaces, are more flexible. Equilibrium constants can be determined for environmentally important adsorption reactions that are isolated in the laboratory. These constants can then be combined with other individually determined constants into a computational geochemical model of a complex system that has not been studied in the laboratory. Although in some cases workable surface complexation models can be obtained without exact assignment of the surface sites, the accuracy of these models increases with more precise identification of the adsorption mechanisms.

Fein et al. (1997) used a surface complexation approach to model metal adsorption onto the cell walls of *Bacillus subtilis*, an aerobic gram-positive bacterium. They employed acid/base titrations to determine acidity constants and site concentrations for the major surface functional groups, and they used bulk metal adsorption experiments to determine site-specific thermodynamic stability constants for the different surface complexes involved in metal adsorption. The acidity of the functional groups was modeled according to the following reaction stoichiometry:



Here, R denotes the bacterium to which each functional group type, A, is attached. The equilibrium between protonated and deprotonated sites is quantified with the corresponding equilibrium constant:

$$K_A = [R - A^{-}]a_{H^{+}} \exp(\Delta Z F \Psi / RT) / [R - AH^{\circ}] \quad (2)$$

Here, the brackets represent concentration in moles of sites per

* Author to whom correspondence should be addressed (mboyanov@nd.edu).

† Present address: University of Windsor, Windsor, ON N9B, Canada.

Table 1. Compositions of the aqueous solution standards (mol L⁻¹).

Sample description	Cd	CH ₃ COO ^a / PO ₄ ^b	H ₂ O	NH ₄ ⁺ / H ^b	^c N _{bound}
Cd(ClO ₄) ₂	— ^d	—	—	—	0.00
Cd:PO ₄ = 1:5	1.00	5.00 ^b	41.68	13.0 ^b	0.95 ^e
Cd:PO ₄ = 1:100	0.10	10.00 ^b	28.50	9.93 ^b	—
Cd:CH ₃ COO = 1:10	0.05	0.50 ^a	53.74	0.40 ^a	1.35 ^f
Cd:CH ₃ COO = 1:2	2.00	4.00 ^a	43.56	0.00 ^a	1.70 ^g
Cd:CH ₃ COO = 1:4	1.00	4.00 ^a	46.05	2.00 ^a	2.60 ^g
Cd:CH ₃ COO = 1:100	0.05	5.00 ^a	37.42	4.90 ^a	2.90 ^h

^a For the acetate solutions.

^b For phosphate solutions.

^c N_{bound} is the calculated average number of ligands attached to the cadmium ion using equilibrium calculations.

^d Samples with 0.05, 0.1, 0.15, and 0.2 M Cd were measured and found to be identical.

^e As calculated by Caminiti (1982).

^f Calculated with stability constants from Sillen and Martell (1971).

^g As calculated by Caminiti et al. (1984a).

^h Calculated with stability constants from Caminiti et al. (1984a).

kilogram of solution, and a represents the aqueous activity. ΔZ is the change in the charge of the surface species in the reaction; Ψ is the electric potential associated with the bacterial surface; T is absolute temperature, and F and R are Faraday's and the gas constants, respectively. Similar reactions can be used to model aqueous metal adsorption. Fein et al. (1997) reported that three types of binding sites, with pK_A (negative logarithm of K_A) values of 4.8, 6.9, and 9.4, were necessary to yield a satisfactory fit to the titration data for *B. subtilis*. They ascribed these values to carboxyl, phosphoryl, and hydroxyl functional groups, respectively, on the basis of known deprotonation constants for aqueous organic acids. It was also demonstrated that successful modeling of Cd adsorption data requires a model that accounts for binding to two different types of surface sites in the 2.0 to 8.0 pH range. These conclusions were based only on the titration studies and the pH dependence of the Cd adsorption, and not on a direct structural investigation. Martinez and Ferris (2001) invoke three binding sites for Cd on *B. subtilis*, under similar experimental conditions to those studied by Fein et al. (1997), to account for their ion selective electrode measurements of Cd⁺² concentrations.

The objective of this X-ray absorption fine structure (XAFS) study is to determine directly the local environment of Cd adsorbed to *B. subtilis* cell walls as a function of pH. XAFS spectroscopy has the ability to determine atom types and numbers in the near vicinity of the atom whose absorption spectrum is being measured, as well as the distance of these atoms from the absorber. The main advantages of XAFS that make it one of the few structural methods applicable to natural and hydrated samples are as follows: the technique has elemental selectivity by tuning to the absorption edge of interest; no long-range (crystalline) order in the sample is required; and measurements are performed on the "as prepared" samples (i.e., no drying or ultrahigh vacuum environment is necessary). The local structural information obtained from those measurements and from spectra of appropriately chosen, well-characterized standards enable identification and quantification of the functional groups responsible for the bacterial surface complexation, thereby

providing a rigorous test of the adsorption model. XAFS has been used previously to address metal speciation in lichens (Sarret et al., 1998a) and whole cells of microbes (Panak et al., 2000, 2002; Hennig et al., 2001; Webb et al., 2001), and to determine the binding mechanism in isolated fungal cell walls (Sarret et al., 1998b). The method has been applied to metal speciation in root and plant biomass (Salt et al., 1995, 1997; Kramer et al., 1996; Sarret et al., 2001) and humic substances (Xia et al., 1997a,b, 1998, 1999). The current study isolates and identifies the binding mechanism of Cd to the bacterial cell wall over a range of pH values. To our knowledge, the only similar study on bacteria to date is of uranyl adsorption onto *B. subtilis* at low pH (Kelly et al., 2001b).

2. MATERIALS AND METHODS

Detailed preparation and characterization procedures for *B. subtilis* cells can be found elsewhere (Fein et al., 1997, 2001). Cells were harvested during stationary growth phase, and were washed first in 0.1 mol/L NaClO₄ electrolyte, followed by a rinse with 0.03 mol/L HNO₃, and five rinses in fresh 0.1 mol/L NaClO₄ electrolyte. Washed bacteria were suspended in 0.1 mol/L NaClO₄ electrolyte to form a parent solution of 10 g (wet weight) bacteria L⁻¹. Six samples were prepared, into which appropriate amounts of dissolved metal were added from an aqueous 1000 ppm Cd standard to attain a final Cd concentration of 30 ppm. The pH was adjusted with 1.0 N NaOH or HNO₃. After the samples were allowed to equilibrate, the final pH was recorded, with final pH values being 3.4, 4.4, 5.5, 5.9, 6.4, and 7.8. Formation of Cd hydrolysis complexes is negligible in this pH range (Baes and Mesmer, 1973). The solutions were centrifuged, the supernatant was removed, and the resulting homogenous pastes were loaded into slotted Plexiglas holders and covered with Kapton film.

The XAFS spectrum taken from a sample reflects the average local environment of all probed atoms in it. To be able to separate, identify, and quantify the binding mechanism of Cd in the multiple binding-site case of the biomass requires a clear understanding of the isolated contributions in the spectra from all potential ligands. Gram-positive bacteria, such as the species used in this study, possess a cell wall constructed of a polymer network of macromolecules such as peptidoglycan and teichoic acid. These molecules are rich in carboxylate, phosphoryl, hydroxyl (or phenolic), and amino functional groups (Beveridge and Murray, 1980). We examined a series of cadmium acetate and cadmium phosphate aqueous solutions as possible end-member analogues to the likely important binding sites on the bacterial cell wall, and we tested the ability of FEFF8 (Ankudinov et al., 1998) to model the observed binding in each case. Although we recognize that interactions of Cd with the cell-wall functional groups may differ from the interactions with similar aqueous anions, it is likely that near-neighbor and next-near-neighbor electrostatic and/or covalent interactions will be quite similar, provided that the structures of the functional groups is similar. Several of the solution compositions were chosen to match the compositions of samples that were previously characterized by X-ray scattering. For hydrated Cd, four cadmium perchlorate solutions of different concentrations were prepared; for Cd bound to carboxyl functional groups, four cadmium acetate aqueous solutions of dif-

Table 2. Fit results from the perchlorate and phosphate aqueous solutions

Shell	N	R(Å)	$\sigma^2(10^{-3} \text{ \AA}^2)$	$\Delta E_0(\text{eV})$
Cd(ClO ₄) ₂				
O →	6.0 ± 0.2	2.27 ± 0.01	8.7 ± 0.5	-1.8 ± 0.4
H →	2 × N _O	2.93 ± 0.05	14 ± 5	-1.8 ± 0.4
Cd:PO ₄ = 1:5				
O →	5.9 ± 0.2	2.26 ± 0.01	9.4 ± 0.5	-4.0 ± 0.4
H →	2 × (N _O - N _P)	2.95 ± 0.05	13 ± 8	-4.0 ± 0.4
P →	1.0 ± 0.4	3.41 ± 0.03	14 (±5) ^a	-4.0 ± 0.4
Cd:PO ₄ = 1:100				
O →	5.9 ± 0.2	2.26 ± 0.01	9.5 ± 0.5	-3.3 ± 0.4
H →	2 × (N _O - N _P)	2.96 ± 0.05	13 ± 8	-3.3 ± 0.4
P →	1.5 ± 0.3	3.42 ± 0.02	14 (±5) ^a	-3.3 ± 0.4

^a σ^2 factor held fixed to the best-fit value in a simultaneous fit of the two phosphate solution standards and the pH 3.4 sample.

ferent concentrations and different Cd:acetate ratios were prepared; and for Cd bound to a phosphoryl ligand, two cadmium phosphate aqueous solutions of different concentrations and Cd:phosphate ratios were prepared. The exact compositions are given in Table 1. Reference to works reporting studies of some of the solutions by X-ray scattering and nuclear magnetic resonance is also summarized in Table 1. All of the solutions were prepared by dissolving the appropriate amount of salt (reagent quality from Alfa Aesar) in reverse-osmosis ultrapure water (18 MΩ) and diluting the solution to a known volume. To shift the equilibrium toward complexed Cd ions, phosphoric acid was added to the Cd phosphate solutions and ammonium acetate was added to the Cd acetate solutions without pH adjustment. Cd K-edge XAFS spectra were taken from all samples at the Materials Research Collaborative Access Team (MRCAT) undulator beamline at the Advanced Photon Source, Argonne National Laboratory (Segre et al., 2000). The incident energy was scanned by using the Si(111) reflection of the double-crystal monochromator in quick-scanning mode, with the beamline undulator tapered approximately 2 keV on the third harmonic. Harmonic rejection was achieved by reflection from a Pt mirror. Beam size was adjusted to approximately 0.7 by 0.7 mm. The incident beam intensity, monitored with an ion chamber filled with nitrogen, did not change by more than 15% over the scan range. Linearity tests (Kemner et al., 1994) indicated less than 0.3% nonlinearity for the experimental setup with 50% beam attenuation.

The biomass sample spectra were measured in fluorescence mode with a Stern-Heald type detector (Stern and Heald, 1979) filled with Kr gas. To minimize radiation exposure and to test for repeatability of the scans, data were taken on each sample from four to six different incident beam positions. A total of 12 to 30 extended XAFS (EXAFS) scans (depending on Cd concentration in the sample) were collected and averaged. In addition, quick X-ray absorption near-edge scans lasting 1 to 2 min each were collected at the beginning on each sample to check for the possibility of radiation damage. No changes were observed on this time scale.

The solution standards were measured in transmission mode. A potential problem with solution measurements is that the formation of bubbles during intense X-ray exposure adds to the experimental noise. In these measurements, the intensity of the X-ray beam was reduced slightly until no bubble formation was observed. Six scans at three different beam positions were

taken for each sample and averaged. In all measurements, a Cd foil was used to calibrate monochromator energy.

The EXAFS spectroscopy technique uses the small periodic variations in the absorption coefficient above the absorption edge energy of an element of interest to extract information about the local environment of that atom. There are complete references on the subject such as Koningsberger and Prins (1988) and Stern and Heald (1983). Only a short description of this theory is given here.

The EXAFS of a powderlike sample with Gaussian disorder can be derived as follows (Koningsberger and Prins, 1988):

$$\chi(k) = \sum_i \frac{(N_i S_0^2) F_i(k)}{k(R_i + \Delta R_i)^2} \exp\left(-2k^2\sigma^2 - \frac{2(R_i + \Delta R_i)}{\lambda(k)}\right) \sin(2k(R_i + \Delta R_i) + \delta_i(k)) \quad (3)$$

The sum is taken over the scattering paths that the ejected electron wave traverses in the material before it returns to the absorber atom. Here k is the electron wave vector,

$$k = \sqrt{2m(\hbar\omega - E_0)/\hbar^2}, \quad (4)$$

where E_0 is the edge energy and $\hbar\omega$ is the incident photon energy; N_i is the multiplicity of the path; S_0^2 is the constant passive electron reduction factor; R_i is the half-path length; ΔR_i is a shift in distance; σ_i^2 is the relative mean square displacement of length of the path (EXAFS Debye-Waller factor, which differs from the X-ray diffraction Debye-Waller factor); $F_i(k)$ and $\delta_i(k)$ are the effective scattering amplitude and phase shift of the scattered electron, respectively; and $\lambda(k)$ is the mean free path of the photoelectron. Thus, $\chi(k)$ is a superposition of sinusoidal waves in k -space with frequency related to the length of the path, and a Fourier transform (FT) of XAFS data results in peaks at close to the half path-length distance. The contribution from multiple scattering paths can be neglected in most room temperature measurements because of disorder and thermal motion. For the remaining single-scattering events the half-path length is equal to the distance of the scattering atoms from the absorber; thus, $|\text{FT } k''\chi(k)|$ may look like a radial distribution function, but distances will be shifted slightly to smaller R values because of the electron phase shift $\delta_i(k)$. The amplitudes of these peaks will depend in part on N_i and σ_i^2 , the number of atoms and the disorder in the shells for a single-scattering path, but they can also be influenced by constructive

or destructive interference of signals from neighboring shells. By comparing $|\text{FT } k''\chi(k)|$ of similar samples and observing a peak's amplitude increase or decrease, one can, in general, make qualitative conclusions about the numbers or disorder of the atoms at the corresponding distance. The real or imaginary part of the FT may also be compared, keeping in mind that contributions corresponding to the different scattering atoms combine linearly to produce the observed features. The final structural parameters are obtained from fits of the real and imaginary parts of $\text{FT}[k''\chi(k)]$ by using model-scattering amplitudes and phase shifts.

In current EXAFS analysis, the electron effective scattering amplitude $F_i(k)$ and phase shift $\delta_i(k)$ are calculated *ab initio* for a cluster of atoms and then calibrated by using appropriate standards with known structure. The calibrated $F_i(k)$ and $\delta_i(k)$ are then used in a fitting routine where the structural parameters N_i , ΔR_i , and σ_i^2 are varied until a best fit to the experimental data are achieved. The UWXAFS suite of programs (Stern et al., 1995), including ATOMS (Ravel, 2001), FEFF8 (Ankudinov et al., 1998), and FEFFIT (Newville et al., 1995), was used in this work. The known crystallographic structures of cadmium acetate dihydrate (Harrison and Trotter, 1972) and cadmium phosphate (Averbuch-Pouchot et al., 1973; Bigi et al., 1986) were used as a basis for calculating backscattering amplitudes and phase shifts by using FEFF8, for clusters similar to those found in the aqueous solutions of cadmium perchlorate (Ohtaki et al., 1974), cadmium acetate (Caminiti et al., 1984a), and cadmium phosphate (Caminiti, 1982). FEFFIT was used to find the structural parameters that fit the observed spectrum best. The goodness of fit is characterized by two parameters: the XAFS reliability factor R , which measures how close the fit is to the experimental data, and the reduced χ^2 factor χ_r^2 , which takes into account the number of floating parameters and noise in the data. A comparison of these values for different fitting scenarios allows for an evaluation of the validity of one fitting model over another. More information is given in the FEFFIT documentation (Newville et al., 1995).

The raw data scans were aligned by the reference foil data and averaged. The edge energies for the samples were chosen at the inflection point of the absorption edges, and background was removed by using standard procedures with AUTOBK (Newville et al., 1993).

3. RESULTS AND DISCUSSION

3.1. Solution Standards

A series of cadmium perchlorate solutions was studied to gain an understanding of the EXAFS data from a hydrated Cd ion. Previous X-ray scattering studies of similar samples identified an octahedral hydration shell around the Cd ion (Ohtaki et al., 1974; Caminiti et al., 1984b; Marcus, 1988; Ohtaki and Radnai, 1993). No perchlorate-Cd ion interactions were expected in the samples, because perchlorate is typically a weakly binding ion. Indeed, no change in the EXAFS was observed with concentration changes in the range 0.05 to 2.0 mol/L. The data were successfully fitted with a hydration sphere of six water molecules. The final fit values and paths used are in Table 2. The empirical S_0^2 value for this solution and powder CdO was found to be 1.03 ± 0.05 ; this value was fixed in all subsequent fits.

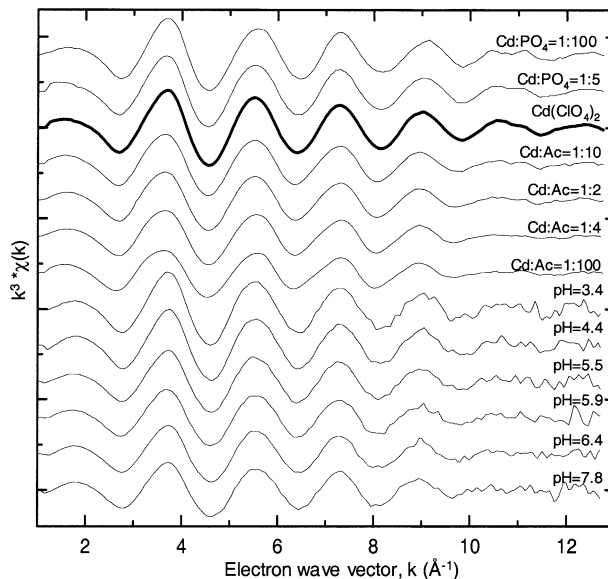


Fig. 1. k^3 -weighted $\chi(k)$ data for the solution standards and biomass samples.

The data obtained for the solution standards are shown in Figure 1. Calculations based on published stability constants (Sillen and Martell, 1964, 1971) and measured for samples $\text{Cd}:\text{CH}_3\text{COO} = 1:2$ and $1:4$ (Caminiti et al., 1984a), indicate that Cd is complexed in the studied solutions. The calculated numbers of bound ligands are listed in Table 1. The results from the aqueous Cd studies suggested that complexation to a phosphate or carboxyl group involves substitution of one or more of the waters of hydration with the binding oxygen atom or atoms. Such inner-sphere complexation has been observed in X-ray scattering works on these and similar solutions (Caminiti and Johansson, 1981; Caminiti, 1982; Caminiti et al., 1984a,b). An increase in the disorder of the first hydration sphere, distance change, or a decrease in hydration number, are all possible results from complexation. This would affect the amplitude or position of the FT peak corresponding to that shell in the XAFS data, as discussed above. In addition, contribution from C or P atoms of bound carboxyl and phosphate groups, respectively, should be observed.

Figure 2 shows the magnitude of the transform, $|\text{FT } k^3\chi(k)|$, and, for a smaller distance range the imaginary part, $\text{Im}[\text{FT } k^3\chi(k)]$, of the perchlorate and two phosphate solutions. The spectra for the phosphate solutions are similar to the hydrated cadmium spectrum. A slight decrease in first-shell amplitude is observed, along with an increasing feature at 2.85 \AA with the increase of phosphate:Cd ratio. The phosphate solution data were fitted with single scattering paths from a hydration shell at 2.3 \AA and a P shell at 3.5 \AA , and simultaneous data set and multiple k -weight fits were performed. Numerical results are in Table 2, and the quality of the fits is illustrated in Figure 3.

The attachment of a phosphate group preserves the number of oxygen atoms in the first coordination shell, but it increases the disorder slightly, as is seen by the increase in the O-shell σ^2 value. The number of P atoms is increased with increasing phosphate:Cd ratio, indicating that more Cd atoms are bound to

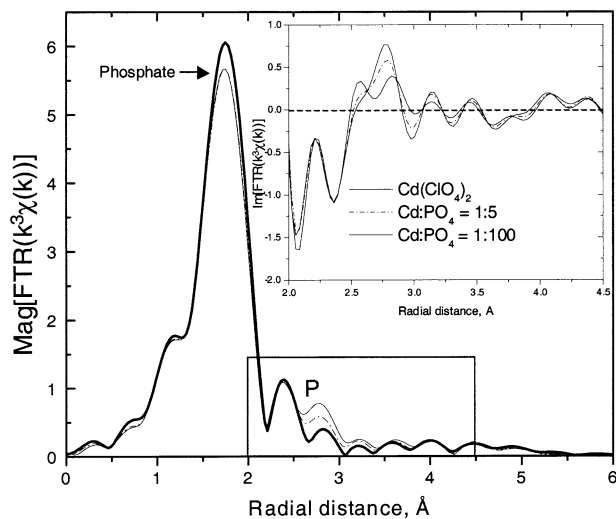


Fig. 2. Magnitude and imaginary part of $\text{FT}[k^3\chi(k)]$ of the data for the Cd perchlorate and two Cd phosphate solutions. The contribution to the EXAFS signal from the P atom in the region 2.5 to 3.3 Å is noted.

phosphate groups. Complexation constants are not available in the literature, so we could not compare the obtained coordination numbers. X-ray scattering studies on a solution identical to our Cd:PO₄ = 1:5 (Caminiti, 1982) determine a Cd-P distance of 3.5 Å and a Cd-P coordination of 0.95, which are close to the values we find in the fits. On the basis of the pH 0.7 to 1.0 of the solution and the H₃PO₄ and H₂PO₄⁻ free radicals present at this pH, Caminiti (1982) suggests that the complexed species are Cd(H₂O)_{6-x}(OPO₃H₂)_x^{+2-x}. The Cd-P distance in crystal Cd(H₂PO₄)₂ · H₂O is also 3.5 Å (Averbuch-Pouchot et al., 1973). Thus, it is likely that Cd is bound to a diprotic phosphate group (H₂PO₄⁻) in these solutions; however, lack of Cd-phosphate stability constants precludes exact speciation and the other possibilities cannot be excluded.

Figure 4 shows the magnitude $|\text{FT } k^3\chi(k)|$ and, for a smaller

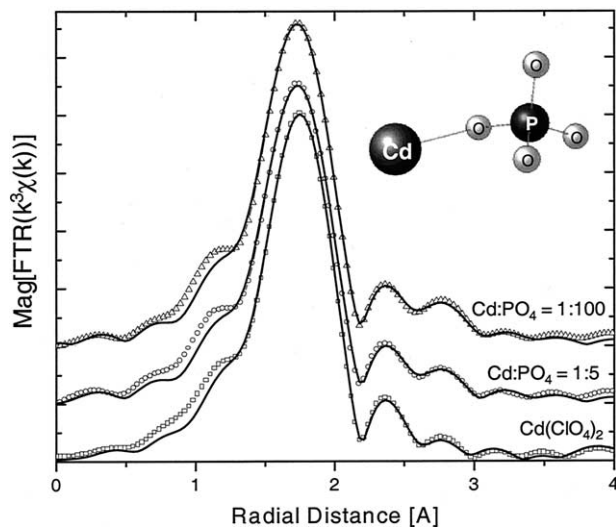


Fig. 3. Data (symbols) and fit (line) for the cadmium perchlorate and phosphate solutions.

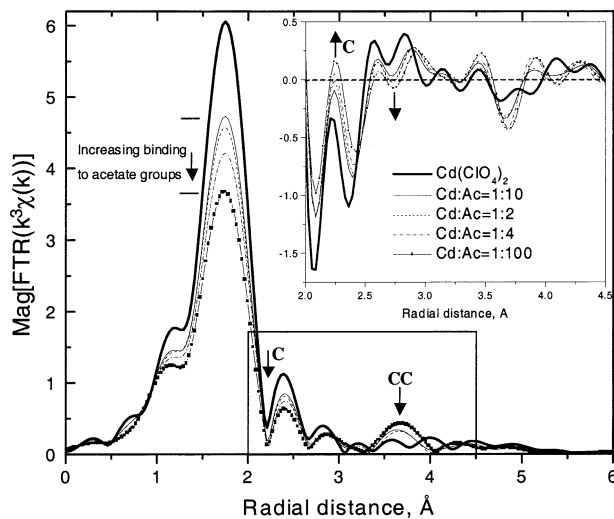


Fig. 4. Magnitude and imaginary part of $\text{FT}[k^3\chi(k)]$ of the data for the Cd perchlorate and four Cd acetate solutions.

distance range, the imaginary part $\text{Im}[\text{FT } k^3\chi(k)]$, of the perchlorate and the four acetate solutions. A large reduction in first-shell amplitude relative to that of the hydrated Cd sample and a decreasing peak height at 2.3 Å of $|\text{FT } k^3\chi(k)|$ occurs with increasing acetate:Cd ratio. Qualitative observation of $\text{Im}[\text{FT } k^3\chi(k)]$ in the range 2.2 to 3.0 Å also reveals a feature that becomes more pronounced with increasing acetate:Cd ratio. The acetate solution data were fitted with single-scattering paths from a hydration shell at 2.3 Å and a C shell at 2.7 Å, and simultaneous, multiple k-weight fits were performed. The large decrease in the main peak amplitude is caused by the destructive interference between the contribution from the hydration shell and that of the C atom in the carboxyl group. Increased amplitude in the acetate samples relative to the hydrated Cd and the phosphate solutions is also noticeable in the range 3.5 to 4.0 Å. The data in this region of the FT were successfully modeled with collinear multiple scattering from the second, farther C atom in the acetate molecule, with the number of paths constrained to the number of closer C atoms. We do not observe that feature in the biomass spectra. Numerical results are in Table 3, and the quality of the fits is illustrated in Figure 5.

Complexation of a Cd atom by acetate molecules decreases the hydration number from 6 to 5 and increases the disorder slightly, as seen by the increase in the O-shell σ^2 value. The C-shell distance we obtain is close to the 2.8 Å determined in crystal Cd(CH₃COO)₂ · 0.3H₂O (Harrison and Trotter, 1972) and in X-ray scattering studies on solutions with Cd:acetate = 2:4 and Cd:acetate = 1:4 (Caminiti et al., 1984a). The C-shell σ^2 parameter in each of the acetate solutions standards, even though it was unconstrained, converged to similar values, justifying the use of a single σ^2 for a Cd-C interaction, regardless of the number of Cd bound. These results indicate that a Cd-C distance of approximately 2.7 Å is characteristic of an acetate group bound to hydrated Cd.

In summary, the solution standards data provide a qualitative and quantitative understanding of the isolated contribution in the EXAFS spectrum of hydrated Cd, aqueous Cd bound to a carboxyl group, and aqueous Cd bound to a phosphate group.

Table 3. Fit results for the cadmium acetate aqueous solutions.^a

Shell	N	R(Å)	$\sigma^2(10^{-3} \text{ \AA}^2)$	$\Delta E_0(\text{eV})$
Cd:Ac = 1:10				
O →	5.9 ± 0.3	2.29 ± 0.01	10.7 ± 0.8	-1.9 ± 0.3
H ^b →	$2 \times (N_{\text{O}} - 2^{\text{c}} \times N_{\text{C}})$	3.01 ± 0.05	15 ± 10	-1.9 ± 0.3
C →	1.4^{d}	2.67 ± 0.03	12 ± 5	-1.9 ± 0.3
CC ^e →	N_{C} or $2 \times N_{\text{C}}$	4.24 ± 0.02	14 ± 3	-1.9 ± 0.3
Cd:Ac = 1:2				
O →	5.9 ± 0.2	2.29 ± 0.01	11.2 ± 0.4	-1.9 ± 0.3
H ^b →	$2 \times (N_{\text{O}} - 2^{\text{c}} \times N_{\text{C}})$	3.01 ± 0.06	22 ± 10	-1.9 ± 0.3
C →	1.7^{d}	2.67 ± 0.01	10 ± 1	-1.9 ± 0.3
CC ^e →	N_{C} or $2 \times N_{\text{C}}$	4.24 ± 0.02	19 ± 2	-1.9 ± 0.3
Cd:Ac = 1:4				
O →	5.5 ± 0.3	2.30 ± 0.01	11.1 ± 0.7	-0.4 ± 0.3
C →	2.6^{d}	2.69 ± 0.01	14 ± 2	-0.4 ± 0.3
CC ^e →	N_{C} or $2 \times N_{\text{C}}$	4.27 ± 0.02	20 ± 3	-0.4 ± 0.3
Cd:Ac = 1:100				
O →	5.1 ± 0.3	2.30 ± 0.01	11.8 ± 0.8	-1.0 ± 0.3
C →	2.9^{d}	2.70 ± 0.01	14 ± 2	-1.0 ± 0.3
CC ^e →	N_{C} or $2 \times N_{\text{C}}$	4.29 ± 0.03	20 ± 3	-1.0 ± 0.3

^a Samples are ordered top to bottom by increasing carboxyl binding.

^b H contribution is not included in the last samples Cd:acetate = 1:4 and 1:100, because it does not contribute significantly to the fit.

^c Bidentate binding is assumed, whereby the acetate binds with both oxygen atoms, removing two water molecules.

^d Constrained to values in Table 1.

^e The number of collinear multiple scattering paths is either N_{C} or $2 \times N_{\text{C}}$, depending on the degeneracy of the path.

These models of isolated contributions are used in interpreting the data for the biomass.

3.2. Cd Bound to Biomass: Qualitative Analysis

The edge-step height in fluorescence XAFS spectra is proportional to the total concentration of the element present in the beam, provided that the matrix in which it is embedded and other experimental parameters (e.g., sample geometry, sample thickness, beamline and detector settings) remain unchanged. This feature of XAFS allows comparison of the Cd adsorption

in samples of different pH values. Figure 6 shows the edge-step heights as a function of pH. These data show that the Cd concentration in the samples increases with pH, approximately five-fold over the range studied. Comparisons to the edge step heights obtained from solutions of known concentration indicate that Cd concentration is in the mM L^{-1} range. The trend is in general agreement with the model of Fein et al. (1997), although the method used here is less accurate. The biomass concentration in the centrifuged sample paste is not known, and the extent of adsorption should be determined as Cd concentration relative to that of the biomass. All samples were centrifuged the same way so the final biomass concentrations in the

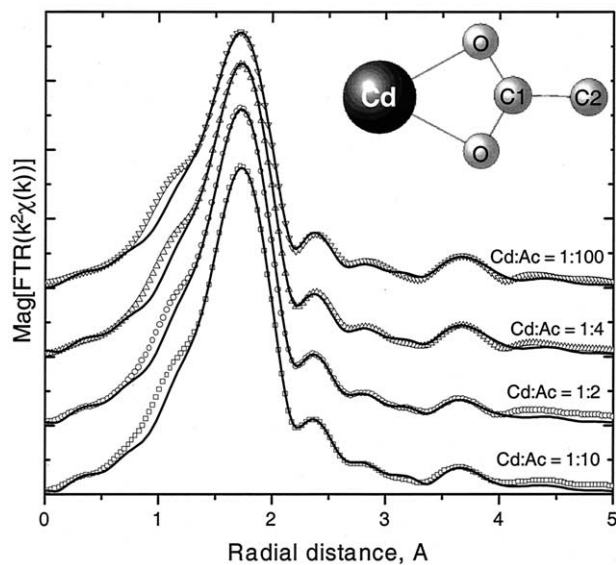


Fig. 5. Data (symbols) and fits (line) for the cadmium acetate solutions.

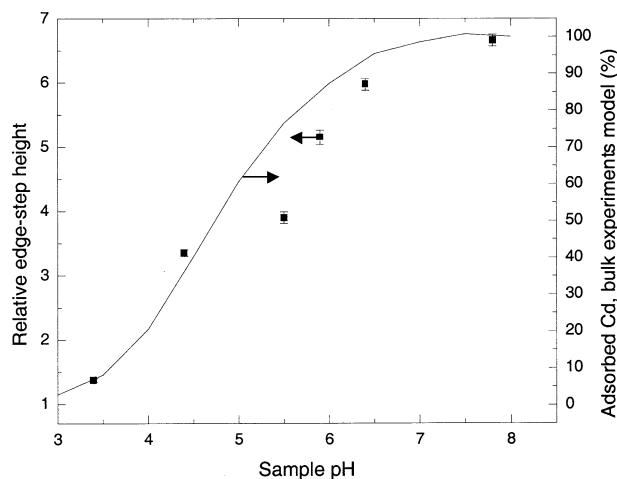


Fig. 6. (square) Edge-step height vs. pH for the biomass samples; (line) normalized bulk adsorption for the current experimental conditions, based on the model in the experiments of Fein et al. (1997). Error bars show the standard deviation of the measurements at four to six beam positions on the samples.

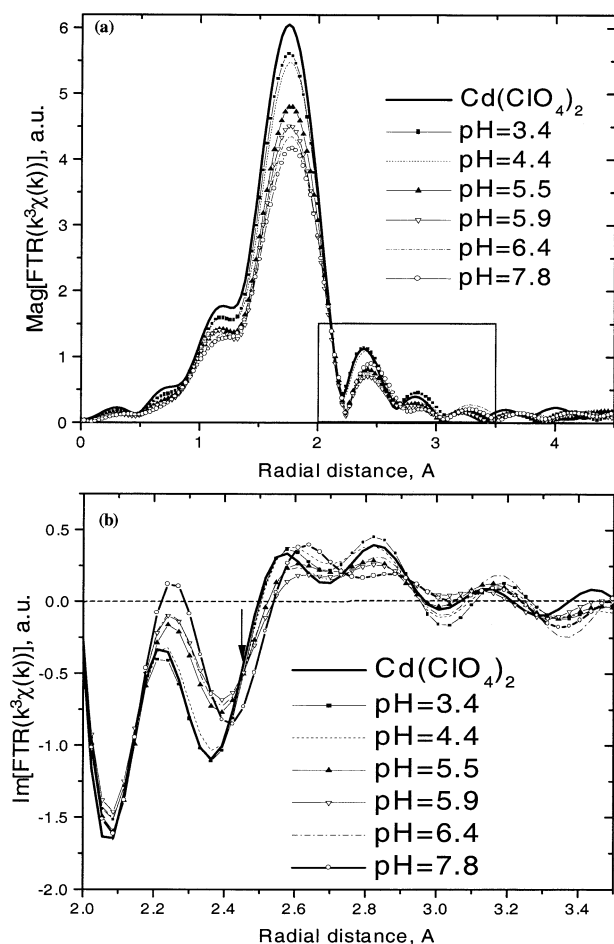


Fig. 7. FT of $[k^3\chi(k)]$ data for all biomass samples (pH 3.4, 4.4, 5.5, 5.9, 6.4, and 7.8). The hydrated cadmium spectrum is included for reference. (a) Magnitude. (b) Imaginary part in the rectangular region shown in (a)

samples are most likely identical; however, differences could in principle be present. In the bulk adsorption experiments where the metal concentration in the supernatants is measured, the control of the initial Cd and biomass concentrations in the suspension is sufficient to determine the amount of Cd adsorbed to the biomass.

The data quality for the biomass samples is illustrated in Figure 1, and Figure 7 shows (a) $|FT k^3\chi(k)|$ and (b) $Im[FT k^3\chi(k)]$ in which the fine differences are observed. The spectrum of the hydrated Cd is also included for reference. Qualitative observation of Figure 7a indicates increasing pH is accompanied by a decrease in amplitude of the first peak, at 1.5 to 2.0 Å in the FT. Spectra for the pH 3.4 and 4.4 samples are quite similar, indicating similar local Cd environments. Compared with the hydrated Cd spectrum, these spectra have smaller first-peak amplitudes and slightly increased amplitudes at 2.8 Å. Similar features are observed for the phosphate solution standards (Fig. 2). This evidence strongly suggests phosphoryl binding in the pH 3.4 and 4.4 samples. Results of the fitting procedure are discussed in the next section.

The next sample in the pH series, at pH 5.5, has a significantly reduced first FT peak amplitude (1.5 to 2.0 Å). Figure 7b

indicates larger amplitude at 2.3 Å than in the spectra for hydrated Cd and lower-pH samples. Features are similar to those of the C contribution in the acetate solution spectra (Fig. 4), suggesting that carboxyl binding is significant in controlling Cd adsorption in this sample. Moreover, features become more pronounced at pH 5.9 and 6.4, indicative of increased relative amounts of Cd atoms binding to the carboxyl site. No peaks corresponding to C-C multiple scattering are observed in the biomass spectra, suggesting that the Cd atom, the carboxyl C, and the atom to which this C is attached are not collinear.

The sample at pH 7.8 has a smaller first-peak amplitude than the other biomass samples, and the peak is slightly shifted to higher distance (Fig. 7a). The amplitude of the peak at 2.3 to 2.6 Å is increased relative to that of the mid-pH samples. In the imaginary part of the FT (Fig. 7b), the feature at 2.2 to 2.5 Å has larger amplitude, and its peak-to-peak difference is increased. This was not observed in the mid-pH samples. Finally, all lower-pH samples intersect at the same point (arrow at c.a. 2.5 Å), whereas a shift toward a larger distance is observed for pH 7.8. We hypothesize that a contribution from another atom (i.e., binding site) at this distance is mixing with the effect of the carboxyl site already present. The titration data in Fein et al. (1997) and the deprotonation constants of phosphoric acid (Martell and Smith, 1974) suggest that a candidate for a binding site at this pH would be a doubly deprotonated phosphoryl site, HPO_4^{2-} , later modeled with a short-distance P shell labeled P_H . No standard for qualitative comparison could be found.

3.3. Cd Bound to Biomass: Fitting Results and Discussion

On the basis of the qualitative results in the previous section, the following models were used to fit the data from the biomass samples: a hydrated Cd, Cd bound to a carboxyl group, and Cd bound to a phosphoryl ligand, similar to those used in the solution standards fit. Linear combinations of these models were used to represent a mixed binding-site environment.

In all fits, a hydration shell model was first attempted, followed by the addition of a P and/or C shells. Visual improvement of the fit (i.e., elimination of particular misfit in $Im[FT k^3\chi(k)]$ by addition of the shell) and a significant reduction in the \mathcal{R} -factor and χ_r^2 were considered grounds for including the shell in the fit model. For each sample, simultaneous fits of the data were performed at k-weightings of 1, 2, and 3. This was done to reduce the possibility that correlations in the fitting parameters would compensate for a misfit at any single k-weighting and thus increased confidence in the fit model. Because coordination numbers and σ^2 factors are generally correlated when the EXAFS signal is small and the data range is short, a further check of the correctness of the model was a correspondence of obtained σ^2 values with the values in the solution standards or with samples where the Cd local environment is predominantly of one type. Simultaneous fitting of data sets from similar samples was also used to reduce correlations and place common constraints on parameters (e.g., distances and E_0).

The lowest-pH sample, pH 3.4, was successfully fitted with the phosphoryl ligand model, the same model that was fitted to the phosphate solution standards. Fits with a hydration shell model without a phosphoryl ligand (P shell) resulted in a χ_r^2 value ~ 2 times larger, and a significant visual misfit was

Table 4. Fit results for the cadmium biomass pH 3.4 sample.

Shell	N	R(Å)	$\sigma^2(10^{-3} \text{ \AA}^2)$	$\Delta E_0(\text{eV})$
O \rightarrow	5.8 ± 0.2	2.27 ± 0.01	9.3 ± 0.4	-2.2 ± 0.3
H \rightarrow	$2 \times (N_O - N_P)$	2.91 ± 0.03	11 ± 5	-2.2 ± 0.3
P \rightarrow	0.8 ± 0.3	3.43 ± 0.03	$14 (\pm 5)^a$	-2.2 ± 0.3

^a σ^2 factor held fixed to the best-fit value in a simultaneous fit of the two phosphate solution standards and the pH 3.4 sample.

present in the region of the P atom, at all three k-weightings. This result excludes the possibility that the Cd left in the sample after centrifugation was predominantly aqueous. We also tested a carboxyl model with a C atom at the distance in the carboxyl ligand. When allowed to vary, the coordination number of such C atoms minimized to zero. Results for the phosphoryl ligand fit are shown in Table 4 and Figure 8. To deal with the correlation between the coordination number and the σ^2 of the P shell, simultaneous fitting of these data and the data from the phosphate solutions was performed, with the σ^2 parameter varying, but equal for all three. Similar values were obtained when all three data sets were fitted independently. By use of this constraint, a common binding mechanism in our solution standards and the biomass is implicitly assumed. This is reasonable if each Cd atom is attached to one biomass ligand. This optimum σ^2 was then used and fixed in the individual data set fits. The final fitting results (Table 4) are similar to those for the phosphate solution standards (Table 2).

The number of P atoms that we calculate to be bound to each Cd atom, 0.8 ± 0.3 , supports a metal:ligand stoichiometry of 1:1. Therefore, we conclude that aqueous Cd at pH 3.4 is adsorbed to *B. subtilis* at just one binding site, with structure analogous to the Cd-phosphate solution species. As mentioned before, the speciation of the phosphate solutions could not be determined unequivocally, but a $\text{Cd}(\text{H}_2\text{O})_{6-x}(\text{OPO}_3\text{H}_2)_x^{+2-x}$

species is suggested. The ionization constants (Martell and Smith, 1974) of phosphoric acid, $\text{p}K_A=2.1$ and $\text{p}K_A=7.2$, for removal of one and two hydrogen atoms, respectively, make a diprotic phosphoryl ligand a likely candidate. Recent results on adsorption of a uranyl cation to the same bacterium (Kelly et al., 2001a) also showed that protonated phosphoryl ligands are responsible for the metal complexation at very low pH; that study demonstrated that uranyl adsorption is due to purely phosphoryl binding at pH 1.7, with an increasing carboxyl component to the adsorption in pH 3.2 and pH 4.8 samples.

For our pH 4.4, 5.5, 5.9, and 6.4 biomass samples, the qualitative results indicate an increasing contribution from a carboxyl binding site. This contribution to the EXAFS signal was modeled by addition of a C shell to the pH 3.4 model. For these fits, we assumed that each Cd ion is adsorbed to only one type of ligand (carboxyl or phosphoryl) and that increasing the pH does not change the binding mechanism. Any changes in it (e.g., from monodentate to bidentate or bridged species), would lead to different metal–ligand geometry and should be observed at least as a significant change in distance of the corresponding atom (C, P, etc.). Under these assumptions, parameters of the P shell were held fixed (except for the distance) to the parameters determined in the pH 3.4 fit, and the P-shell contribution at higher pH was weighed by a fraction variable, x_p . The C-shell contribution was weighed by the remainder, $x_c = 1 - x_p$. Correlations caused by the short data range ($k = 2.6$ to 10.3 \AA^{-1}) precluded accurate determination of the coordination number and σ^2 value for this shell from fitting. Fits with the coordination number of C atoms constrained to one and two resulted in overlapping error bars for the fraction parameter x_p . Therefore, the question of Cd:carboxyl stoichiometry cannot be addressed with these data. Fein et al. (1997) obtained better fits to their bulk adsorption data by using a 1:1 metal:ligand stoichiometry when compared with a 1:2 stoichiometry. In the EXAFS fits, we have used this constraint and the number of C atoms in the shell was set to 1.0. Fitting results with a varying C-shell σ^2 parameter are shown in the top half of Table 5. The C-shell σ^2 values for samples at pH 5.5 and 5.9 are similar to those obtained in the standard solutions fits. The results for samples at pH 3.4 and 4.4 are also consistent with the solution standards; however, the amplitude of the C signal is very small, and error bars are correspondingly large. The sample at pH 6.4 displays a sharp drop in C-shell σ^2 value and the fit is of lower quality. This observation becomes more pronounced in the pH 7.8 sample, where this model proves insufficient to fit the data (see below). Thus, the fits at pH 5.5 and 5.9 are assumed to be representative of Cd predominantly bound to a carboxyl biomass ligand, whereas results for the pH 6.4 and 7.8 samples indicate an increase in importance of another binding site. Under our assumption that the carboxyl binding mechanism does not change with pH, the C-shell σ^2 parameter was constrained to the average value found in the samples at pH 5.5 and 5.9, and this constrained model was used to repeat the fitting. This was done to reduce the coordination number– σ^2 correlations (and consequently, error bars) and to make possible a comparison between samples at different pH values in terms of the actual content of the carboxyl and phosphoryl signals. Results for these fits are shown in the bottom part of Table 5, and the quality of the fit is illustrated in Figure 8.

The sample at pH 7.8 is significantly different, as seen from

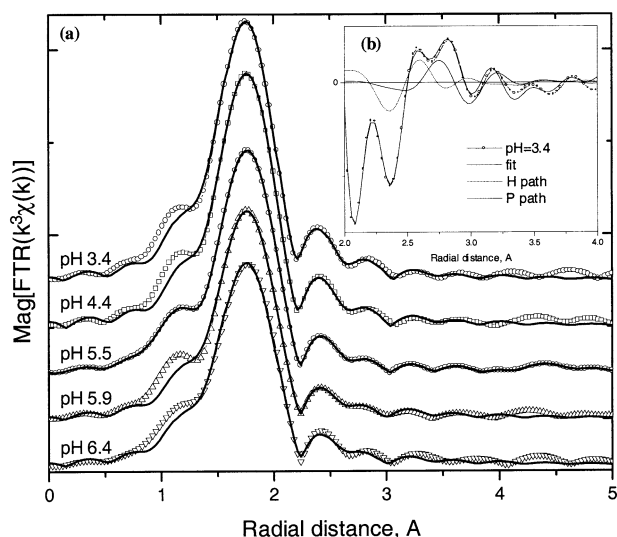


Fig. 8. (a) Magnitude of $\text{FT}[k^3\chi(k)]$ fits of the pH 3.4, 4.4, 5.5, 5.9, and 6.4 samples. (b) The imaginary part of the pH 3.4 data and fit in the region 2 to 4 Å, showing the contribution from the P atom and lack of significant overlap with the hydration water H atom paths.

Table 5. Fit results for the cadmium biomass samples data, pH 3.4 to pH 6.4.

Fitting parameter ^a	pH = 3.4	pH = 4.4	pH = 5.5	pH = 5.9	pH = 6.4
Floating C shell ^b					
ΔE_0	-2.2 ± 0.6	-1.2 ± 0.5	-1.3 ± 0.5	-1.3 ± 0.5	-1.8 ± 0.8
N_O	5.8 ± 0.2	5.6 ± 0.2	5.2 ± 0.2	4.8 ± 0.2	5.0 ± 0.2
R_O	2.27 ± 0.01	2.28 ± 0.01	2.28 ± 0.01	2.28 ± 0.01	2.27 ± 0.01
σ_O	9.4 ± 0.7	9.2 ± 0.8	9.6 ± 0.6	9.5 ± 0.7	10.6 ± 0.9
R_H	2.91 ± 0.04	2.94 ± 0.04	2.96 ± 0.06	3.00 ± 0.07	2.89 ± 0.07
x_P	0.95 ± 0.25	0.72 ± 0.23	0.32 ± 0.18	0.17 ± 0.19	0.39 ± 0.28
R_P	3.43 ± 0.03	3.43 ± 0.04	3.41 ± 0.08	3.41 ± 0.19	3.45 ± 0.08
R_C	2.71 ± 0.27	2.70 ± 0.13	2.78 ± 0.04	2.76 ± 0.04	2.76 ± 0.03
σ_C	0 ± 65	10 ± 23	11 ± 11	16 ± 11	1 ± 7
Constrained C shell ^b					
ΔE_0	-2.2 ± 0.4	-1.1 ± 0.5	-1.3 ± 0.3	-1.4 ± 0.4	-1.3 ± 0.6
N_O	5.8 ± 0.2	5.6 ± 0.2	5.1 ± 0.1	4.9 ± 0.1	4.8 ± 0.2
R_O	2.27 ± 0.01	2.28 ± 0.01	2.28 ± 0.01	2.28 ± 0.01	2.28 ± 0.01
σ_O	9.4 ± 0.5	9.1 ± 0.6	9.5 ± 0.4	9.6 ± 0.5	10.0 ± 0.7
R_H	2.91 ± 0.03	2.94 ± 0.03	2.97 ± 0.03	2.99 ± 0.04	2.97 ± 0.05
x_P	0.95 ± 0.19	0.71 ± 0.20	0.31 ± 0.15	0.17 ± 0.15	0.25 ± 0.22
R_P	3.43 ± 0.03	3.43 ± 0.03	3.40 ± 0.07	3.44 ± 0.13	3.42 ± 0.13
R_C	2.75 ± 0.81	2.69 ± 0.13	2.78 ± 0.04	2.76 ± 0.03	2.77 ± 0.05
χ^2_v	36	61	56	13	97
R factor %	0.07	0.07	0.06	0.09	0.22

^a Units are eV for ΔE , Å for R, and 10^{-3}Å^2 for σ^2 .

^b Fits with varying and constrained σ^2 for the C shell are compared to show that fixing σ^2 does not alter the fit values, but reduces the error bars significantly. $\sigma_C^2 = 0.0135 \text{Å}^2$ for the constrained fits, as explained in the text.

the qualitative observation of the data. The constrained model used for the lower-pH samples does not adequately fit the pH 7.8 data (Fig. 9) and Table 6, model O+H+C-P). The largest misfit is in the range 2.2 to 3.0 Å. As a starting point, attempts were made to model the data by a hydration shell (O+H), with C or P shells added at the misfit distance. To distinguish this closer P atom from the one in the lower-pH model, it is labeled P_{7.8}. Either a C or P_{7.8} shell could separately fit the data, but the

numerical results are not realistic and χ^2_v is about two times larger than for the best fit obtained. In the C-shell fit (Table 6, O+H+C), the C-shell σ^2 value obtained was 0. No such value is seen in the standard solutions or lower-pH samples, and no abrupt change in the carboxyl mechanism of binding is expected for this small change in pH. For the P_{7.8}-shell fit (Table 6, O+H+P_{7.8}), the σ^2 value obtained was also 0. We could not find a standard to compare this value, but the obtained P_{7.8} number (0.3 ± 0.1) is too small to attribute Cd binding solely to a short-distance phosphoryl ligand. Cd-Cd interactions, as a result of possible polynuclear complex formation or precipitation at this pH, were also considered. The data are inconsistent with Cd-Cd interactions. We conclude that a model consisting of a hydration shell, and a C, P_{7.8}, or Cd shells by themselves is not supported by the data.

Adding the P_{7.8} shell to the O+H+C-P model used in the lower-pH samples provides the best fit to the pH 7.8 data, with χ^2_v and R factor less than half of those for all other fits (Table 6, model O+H+C-P+P_{7.8}). The fit model consists of a hydration shell and a linear combination of a C, P, and P_{7.8} shells, weighed so their total contribution adds up to 1. The parameters for the C and P shells were constrained in the same way as for the lower-pH samples, described above. The parameters for the P_{7.8} shell were allowed to vary freely. The 0.2 coordination number obtained for that shell is interpreted as the Cd being coordinated to one P_{7.8} atom at that binding site, and the site accounting for ~20% of all Cd atoms. The P-shell contribution was weighed by the x_p fraction variable used in the lower pH fits, and the C-shell contribution is weighed by the remainder, $1 - x_p - N_{P_{7.8}}$. Results of the fit are shown in Figure 9c and Table 6 (model O+H+C-P+P_{7.8}). The fit fraction values for each binding site are as follows: P-shell: 0.33 ± 0.17 ; C-shell: 0.46 ± 0.19 ; P_{7.8}-shell: 0.21 ± 0.07 .

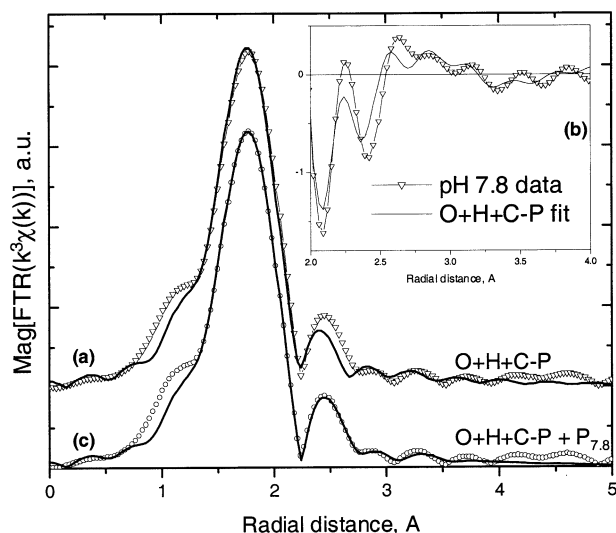


Fig. 9. Magnitude (a) and imaginary part (b) of FT [$k^3\chi(k)$] (triangles) and fit (line) for the pH 7.8 sample, with the model used to fit the low- and mid-pH samples (O+H+C-P). The misfit is clearly seen. (c) Data (circles) and best fit (line) of the pH 7.8 sample, using the constrained O+H+C-P model with an added P_{7.8} shell. Numerical results are in Table 6.

Table 6. Comparison of the fit results for the pH 7.8 sample using different fit models.

Fit model	^a Ligand atom, L	N _L	R _L (Å)	σ_L^2 (10 ⁻³ Å ²)	^b N _H	^c X _p	χ _v ²	R (%)
O+H+ C-P	—	—	—	—	—	0.03 ± 0.36	129	0.44
O+H+ C	C	0.8 ± 0.9	2.75 ± 0.02	0 ± 9	6 ± 6	—	46	0.11
O+H+ P _{7.8}	P _{7.8}	0.26 ± 0.13	2.90 ± 0.02	0 ± 4	0 ± 4	—	50	0.14
O+H+ C-P + P _{7.8}	P _{7.8}	0.21 ± 0.07	2.90 ± 0.01	0 ± 3	0 ± 2	0.33 ± 0.17	21	0.07

^a This column lists the atom for which information is given in the N_L, R_L, and σ_L columns.

^b The number of atoms in the H shell is varied while the distance and σ² factor are held fixed.

^c Contribution from the fixed-parameter P shell is weighted by x_p, as in the lower-pH samples fit.

The choice of the shorter distance P_{7.8} shell to compensate the misfit at pH 7.8 requires some justification. In principle, any of the known cell-wall ligands in *B. subtilis* (amino, carboxyl, phosphoryl, hydroxyl) (Beveridge and Murray, 1980) could be responsible for the new binding in the pH 7.8 sample. As mentioned above, the pK_A value for the second deprotonation constant of phosphoric acid is 7.2, making the phosphoryl ligand a likely candidate. Even though XAFS cannot distinguish between atoms at the same distance that have small differences in atomic number (e.g., C/N/O or P/S), it is able to distinguish between atoms in different rows of the periodic table, and the P_{7.8} shell provides a good fit. The C atom does not provide a good fit, which also makes a N-based ligand unlikely. A further constraint on the type of atom is the bond length. On the basis of a tetrahedral PO₄ group of side 2.56 Å and a Cd-O bond length of 2.3 Å, we calculate the maximum Cd-P bond length to be 2.8 Å when both O atoms bind (bidentate) the Cd in the Cd-O-O-P plane. This is close to the determined Cd-P_{7.8} bond length by EXAFS. The small difference could be attributed to a stretched POO< ligand, and/or an increased Cd-O bond length in the bidentate mode. The small σ² value is additional evidence for this tight-binding mode. Similarities between the XAFS backscattering functions (F(k)) for P and S mentioned above, as well as structural similarities between PO₄ and SO₄ moieties, do not allow the XAFS technique to exclude the possibility of a SO₄-type functional group participating in the Cd sorption in addition to, or in place of, the PO₄ functional group model proposed here. However, the cell wall of *B. subtilis* is rich in phosphoryl binding sites, and no S-based analog sites have been identified (Beveridge and Murray, 1980).

Figure 10 shows the relative concentrations of the three different Cd-bacterial surface species that are responsible for the pH dependence of Cd adsorption, according to the proposed EXAFS model. The total concentration of adsorbed Cd is normalized to the extent of adsorption observed at pH 7.8 for comparison purposes. At pH 3.4, Cd-phosphoryl binding dominates the adsorption behavior. Carboxyl ligands account for the majority of the adsorption in the range pH 5.0 to pH 7.8, with the same type of Cd-phosphoryl binding remaining significant throughout this pH range. At pH 7.8, a third binding site becomes available, which accounts for ~20% of the total Cd adsorbed and which is consistent with a shorter distance P bond, possibly from deprotonated phosphoryl sites on the bacterial cell wall similar to HPO₄⁻² groups.

This speciation model is in general agreement with the surface complexation model proposed by Fein et al. (1997);

however, a number of differences exist. Most of the binding in this model and that of Fein et al. (1997) is caused by Cd attachment to deprotonated carboxyl or phosphoryl functional groups, with carboxyl binding increasing in importance from pH 3.4 to 5.9 and short distance (deprotonated) phosphoryl binding becoming important under higher pH conditions. However, the model of Fein et al. (1997) suggests that, under the experimental conditions of this study, attachment of Cd to deprotonated phosphoryl sites should dominate the binding environment of Cd above pH 5.5, and that virtually no Cd-phosphoryl interaction should occur under low pH conditions.

The discrepancy between the extent of deprotonated phosphoryl binding predicted by the model of Fein et al. (1997) compared with our EXAFS data can be ascribed to the relatively large uncertainty associated with the stability constant for Cd-phosphoryl binding reported by Fein et al. (1997). The EXAFS data suggest that the stability constant is significantly lower than the value reported by Fein et al. (1997), with the short Cd-P binding only becoming evident in the pH 7.8 sample. Refinements of Cd-phosphoryl stability constants will be included in a future investigation of metal-phosphoryl binding onto the cell wall of *B. subtilis*.

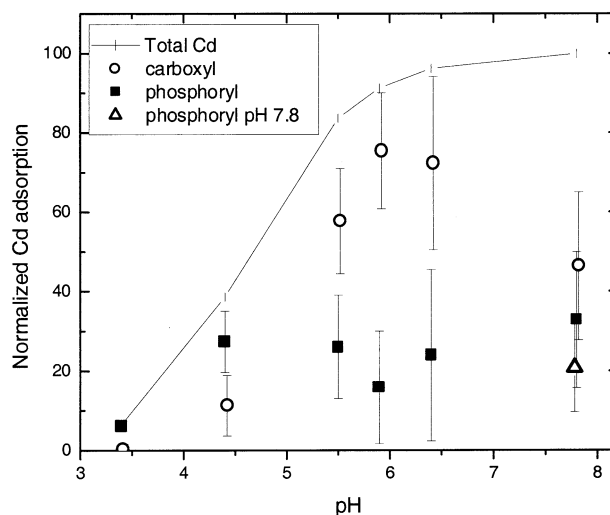


Fig. 10. (solid line) Total Cd adsorption to the biomass according to the model of Fein et al. (1997); (symbols) Cd bound to the different binding sites as a function of pH within the proposed EXAFS model. The data are normalized to the Cd concentration at pH 7.8. Error bars include EXAFS fitting uncertainties and bulk adsorption deviations, added in quadrature.

Fein et al. (1997) modeled the phosphoryl functional group as a site that undergoes a single deprotonation reaction, so that the stoichiometry can be represented as $R\text{-POH}^{\circ}$ or $R\text{-PO}^{-}$. In this model, metal attachment only occurs onto the deprotonated species. However, the EXAFS data from this study, along with that of Kelly et al. (2001b) for uranyl-bacteria adsorption, suggest that the phosphoryl site may be more complicated. This study suggests that its chemical behavior is closer to that of aqueous phosphoric acid, with multiple deprotonations possible, and with more than one surface species interacting with adsorbing metal cations. Because little adsorption occurs under low pH conditions in the Cd system, the bulk adsorption data of Fein et al. (1997) could be successfully fitted by ignoring the interactions between Cd and the less-deprotonated phosphoryl site or sites. However, the binding is detectable in the Cd and U EXAFS data, as well as in uranyl bulk adsorption data (Fowle and Fein, 2000). Because of the small amount of adsorption that occurs under these lower pH conditions in the Cd system, such binding could not be detected by using the less sensitive approach of bulk adsorption measurements.

According to the model of Fein et al. (1997), the speciation of the phosphoryl sites remains unchanged between pH 3.4 and 4.4, so the observed increase in adsorption over this pH range could not be ascribed to a corresponding increase in deprotonated phosphoryl sites. The EXAFS data indicate that the low pH binding of Cd is predominantly due to phosphoryl binding. Therefore, this study suggests that the model of Fein et al. (1997) is incomplete, and that another acidity constant for the phosphoryl site exists below the pH range studied by Fein et al. (1997).

4. CONCLUSIONS

Qualitative analysis of the data for the solution standards gives insight into the isolated contributions to the EXAFS from a hydrated Cd ion, a Cd ion bound to a carboxyl group, and a Cd ion bound to a phosphate group. Fits of these standards demonstrate that the ab initio code FEFF8 can model such environments and that the fits place constraints on the correlated structural parameters. On the basis of the analysis of these well-defined standards, we have identified the local environment of Cd adsorbed onto the cell wall of *B. subtilis* and have determined how that environment changes as a function of pH. Very little Cd adsorption to biomass was observed at pH 3.4, and the similarity of the biomass EXAFS data to the phosphate solution standard indicates that Cd is complexed predominantly to groups with similar structure to the aqueous phosphate molecule. As pH increases, a dramatic increase in the amount of Cd bound to the biomass is observed, and the features corresponding to carboxyl binding become more pronounced in the FT. This observation indicates increasing importance of carboxyl binding with increasing pH. Quantitative modeling of the data confirms the qualitative interpretation that binding changes with increasing pH from predominantly phosphoryl to predominantly carboxyl. This analysis also yields quantitative estimates of the Cd:ligand ratios for each ligand, up to pH 6.4.

The spectrum for the biomass sample at pH 7.8 shows a significantly different binding environment compared with that seen for the lower pH samples. Binding to phosphoryl and carboxyl sites cannot account for the EXAFS spectrum ob-

served for the pH 7.8 sample, and binding to a third ligand type must be invoked. This third site is consistent with another type of phosphoryl group, one having a shorter Cd-P distance than that observed for the phosphoryl site present under lower pH conditions. We propose that this third site represents a further deprotonated phosphoryl group, with the shorter Cd-P distance resulting from the bidentate binding to this more electronegative phosphoryl site. The cell-wall structure of *B. subtilis*, the deprotonation constants of phosphoric acid, and the bacterial surface titration data are consistent with the proposed speciation, although an S-bearing ligand cannot be excluded on the basis of the EXAFS data alone.

This study not only provides a detailed understanding of Cd binding to a common type of bacterial surface, but it also illustrates that EXAFS spectroscopy is ideally suited to complement bulk adsorption measurements in constructing quantitative models of adsorption of metals onto bacteria. XAFS provides detailed information concerning the binding environment of the metal of interest, whereas bulk adsorption measurements can be used to constrain the values of the thermodynamic stability constants for the important metal-bacterial surface complexes. Taken together, bulk adsorption measurements and XAFS experiments represent a powerful approach for determining and modeling metal speciation and distribution in microbe-water-mineral systems.

Acknowledgments—M.B. thanks the Bayer Corporation for its support through the Bayer Predoctoral Fellowship in Environmental Science. Beamline setup help from the staff of MRCAT is greatly appreciated. We thank associate editor David J. Wesolowski and three anonymous reviewers for comments that significantly improved the manuscript. This work was supported in part by NSF grant EAR99-05704 and the U.S. Department of Energy, Office of Science, Office of Biologic and Environmental Research, NABIR program. MR-CAT is supported by the U.S. Department of Energy under contract DE-FG02-94-ER45525 and the member institutions. Use of the Advanced Photon Source was supported by the U.S. Department of Energy under contract W-31-109-Eng-38.

Associate editor: D. Wesolowski

REFERENCES

- Ankudinov A. L., Ravel B., Rehr J. J., and Conradson S. D. (1998) Real-space multiple-scattering calculation and interpretation of X-ray absorption near-edge structure. *Phys. Rev. B* **58**, 7565–7576.
- Averbuch-Pouchot M. T., Durif A., Guitel J. C., Tordjman I., and Laugt M. (1973) Crystal structure of $\text{Cd}(\text{H}_2\text{PO}_4)_2 \cdot \text{H}_2\text{O}$. *Bull. Soc. Fr. Mineral. Cristallogr.* **96**, 278–280.
- Baes C. F. and Mesmer R. E. (1973) *Hydrolysis of Cations*. Wiley.
- Bethke C. M. and Brady P. V. (2000) How the K-d approach undermines ground water cleanup. *Ground Water* **38**, 435–443.
- Beveridge T. J. and Murray R. G. E. (1976) Uptake and retention of metals by cell-walls of *Bacillus subtilis*. *J. Bacteriol.* **127**, 1502–1518.
- Beveridge T. J. and Murray R. G. E. (1980) Sites of metal deposition in the cell wall of *Bacillus subtilis*. *J. Bacteriol.* **141**, 876–887.
- Beveridge T. J. and Koval S. F. (1981) Binding of metals to cell envelopes of *Escherichia coli* K-12. *Appl. Environ. Microbiol.* **42**, 325–335.
- Bigi A., Foresti E. B., Gazzano M., Ripamonti A., and Roveri N. (1986) Cadmium-substituted tricalcium phosphate and crystal structure refinement of beta'-tricalcium phosphate. *J. Chem. Res* **5**(S), 170–171.
- Brown G. E. (1990) Spectroscopic studies of chemisorption reaction mechanisms at oxide-water interfaces. In *Mineral-Water Interaction Geochemistry*, Vol. 23 (eds. M. F. Hochella and A. F. White), pp.

- 309–363. Reviews in Mineralogy. Mineralogical Society of America.
- Caminiti R. (1982) Nickel and cadmium phosphates in aqueous solution—Cation-anion complex formation and phosphate-H₂O interactions. *J. Chem. Phys.* **77**, 5682–5686.
- Caminiti R. and Johansson G. (1981) On the structures of cadmium sulfate complexes in aqueous solutions. *Acta Chem. Scand., Ser. A* **35**, 373–381.
- Caminiti R., Cucca P., Monduzzi M., Saba G., and Crisponi G. (1984a) Divalent metal–acetate complexes in concentrated aqueous solutions—An X-ray diffraction and NMR spectroscopy study. *J. Chem. Phys.* **81**, 543–551.
- Caminiti R., Cucca P., and Radnai T. (1984b) Investigation on the structure of cadmium nitrate aqueous solutions by X-ray diffraction and Raman spectroscopy. *J. Phys. Chem.* **88**, 2382–2386.
- Collins C. R., Ragnarsdottir K. V., and Sherman D. M. (1999) Effect of inorganic and organic ligands on the mechanism of cadmium sorption to goethite. *Geochim. Cosmochim. Acta* **63**, 2989–3002.
- Crist R. H., Oberholser K., Shank N., and Nguyen M. (1981) Nature of bonding between metallic ions and algal cell-walls. *Environ. Sci. Technol.* **15**, 1212–1217.
- Farquhar M. L., Vaughan D. J., Hughes C. R., Charnock J. M., and England K. E. R. (1997) Experimental studies of the interaction of aqueous metal cations with mineral substrates: Lead, cadmium, and copper with perthitic feldspar, muscovite, and biotite. *Geochim. Cosmochim. Acta* **61**, 3051–3064.
- Fein J. B. (2000) Quantifying the effects of bacteria on adsorption reactions in water-rock systems. *Chem. Geol.* **169**, 265–280.
- Fein J. B., Daughney C. J., Yee N., and Davis T. A. (1997) A chemical equilibrium model for metal adsorption onto bacterial surfaces. *Geochim. Cosmochim. Acta* **61**, 3319–3328.
- Fein J. B., Martin A. M., and Wightman P. G. (2001) Metal adsorption onto bacterial surfaces: Development of a predictive approach. *Geochim. Cosmochim. Acta* **65**, 4267–4273.
- Fowle D. A. and Fein J. B. (2000) Experimental measurements of the reversibility of metal–bacteria adsorption reactions. *Chem. Geol.* **168**, 27–36.
- Goncalves M. D. S., Sigg L., Reutlinger M., and Stumm W. (1987) Metal–ion binding by biological surfaces—Voltammetric assessment in the presence of bacteria. *Sci. Total Environ.* **60**, 105–119.
- Harrison W. Trotter J. (1972) Crystal and molecular structure of cadmium diacetate dihydrate. *J. Chem. Soc. Dalton Trans.* 956–960.
- Harvey R. W. and Leckie J. O. (1985) Sorption of lead onto two gram-negative marine bacteria in seawater. *Mar. Chem.* **15**, 333–344.
- Hennig C., Panak P. J., Reich T., Rosberg A., Raff J., Selenska-Pobell S., Matz W., Bucher J. J., Bernhard G., and Nitsche H. (2001) EXAFS investigation of uranium(VI) complexes formed at *Bacillus cereus* and *Bacillus sphaericus* surfaces. *Radiochim. Acta* **89**, 625–631.
- Kelly S. D., Boyanov M. I., Bunker B. A., Fein J. B., Fowle D. A., Yee N., and Kemner K. M. (2001a) XAFS determination of the bacterial cell wall functional groups responsible for complexation of Cd and U as a function of pH. *J. Synchrotron Radiat.* **8**, 946–948.
- Kelly S. D., Kemner K. M., Fein J. B., Fowle D. A., Boyanov M. I., Bunker B. A., and Yee N. (2002) X-ray absorption fine structure determination of pH-dependent U–bacterial cell wall interactions. *Geochim. Cosmochim. Acta* **66**(2), 3855–3871.
- Kemner K. M., Kropf J., and Bunker B. A. (1994) A low-temperature total electron yield detector for X-ray absorption fine-structure spectra. *Rev. Sci. Instrum.* **65**, 3667–3669.
- Konhauser K. O., Fyfe W. S., Ferris F. G., and Beveridge T. J. (1993) Metal sorption and mineral precipitation by bacteria in two Amazonian river systems—Rio-Solimoes and Rio-Negro, Brazil. *Geology* **21**, 1103–1106.
- Koningsberger D. C. and Prins R. (1988) *X-ray Absorption: Principles, Applications, Techniques of EXAFS, SEXAFS, and XANES*. Wiley.
- Koretsky C. (2000) The significance of surface complexation reactions in hydrologic systems: A geochemist's perspective. *J. Hydrol.* **230**, 127–171.
- Kramer U., Cotter–Howells J. D., Charnock J. M., Baker A. J. M., and Smith J. A. C. (1996) Free histidine as a metal chelator in plants that accumulate nickel. *Nature* **379**(6566), 635–638.
- Marcus Y. (1988) Ionic radii in aqueous solutions. *Chem. Rev.* **88**, 1475–1498.
- Martell A. E. and Smith R. M. (1974) *Critical Stability Constants*. Plenum Press.
- Martinez R. E. and Ferris F. G. (2001) Chemical equilibrium modeling: Techniques for the analysis of high-resolution bacterial metal sorption data. *J. Colloid Interface Sci.* **243**, 73–80.
- Newville M., Livins P., Yacoby Y., Rehr J. J., and Stern E. A. (1993) Near-edge X-ray absorption fine structure of Pb—A comparison of theory and experiment. *Phys. Rev. B* **47**, 14126–14131.
- Newville M., Ravel B., Haskel D., Rehr J. J., Stern E. A., and Yacoby Y. (1995) Analysis of multiple-scattering XAFS data using theoretical standards. *Physica B* **208–209**, 154–156.
- O'Day P. A. (1999) Molecular environmental geochemistry. *Rev. Geophys.* **37**, 249–274.
- O'Day P. A., Carroll S. A., and Waychunas G. A. (1998) Rock-water interactions controlling zinc, cadmium, and lead concentrations in surface waters and sediments, US Tri-State Mining District. I. Molecular identification using X-ray absorption spectroscopy. *Environ. Sci. Technol.* **32**, 943–955.
- Ohtaki H., Maeda M., and Ito S. (1974) X-ray diffraction studies of aqueous solutions of cadmium perchlorate and sodium tetraiodocadmate. *Bull. Chem. Soc. Jpn.* **47**, 2217–2221.
- Ohtaki H. and Radnai T. (1993) Structure and dynamics of hydrated ions. *Chem. Rev.* **93**, 1157–1204.
- Panak P. J., Raff J., Selenska-Pobell S., Geipel G., Bernhard G., and Nitsche H. (2000) Complex formation of U(VI) with *Bacillus* isolates from a uranium mining waste pile. *Radiochim. Acta* **88**, 71–76.
- Panak P. J., Booth C. H., Caulder D. L., Bucher J. J., Shuh D. K., and Nitsche H. (2002) X-ray absorption fine structure spectroscopy of plutonium complexes with *Bacillus sphaericus*. *Radiochim. Acta* **90**, 315–321.
- Randall S. R., Sherman D. M., Ragnarsdottir K. V., and Collins C. R. (1999) The mechanism of cadmium surface complexation on iron oxyhydroxide minerals. *Geochim. Cosmochim. Acta* **63**, 2971–2987.
- Ravel B. (2001) ATOMS: Crystallography for the X-ray absorption spectroscopist. *J. Synchrotron Radiat.* **8**, 314–316.
- Salt D. E., Prince R. C., Pickering I. J., and Raskin I. (1995) Mechanisms of cadmium mobility and accumulation in Indian mustard. *Plant Physiol.* **109**, 1427–1433.
- Salt D. E., Pickering I. J., Prince R. C., Gleba D., Dushenkov S., Smith R. D., and Raskin I. (1997) Metal accumulation by aquacultured seedlings of Indian mustard. *Environ. Sci. Technol.* **31**, 1636–1644.
- Sarret G., Manceau A., Cuny D., Van Haluwyn C., Deruelle S., Hazemann J. L., Soldo Y., Eybert-Berard L., and Menthonnex J. J. (1998a) Mechanisms of lichen resistance to metallic pollution. *Environ. Sci. Technol.* **32**, 3325–3330.
- Sarret G., Manceau A., Spadini L., Roux J. C., Hazemann J. L., Soldo Y., Eybert-Berard L., and Menthonnex J. J. (1998b) Structural determination of Zn and Pb binding sites in *Penicillium chrysogenum* cell walls by EXAFS spectroscopy. *Environ. Sci. Technol.* **32**, 1648–1655.
- Sarret G., Vangronsveld J., Manceau A., Musso M., D'Haen J., Menthonnex J. J., and Hazemann J. L. (2001) Accumulation forms of Zn and Pb in *Phaseolus vulgaris* in the presence and absence of EDTA. *Environ. Sci. Technol.* **35**, 2854–2859.
- Segre C. U., Leyarovska N. E., Chapman L. D., Lavender W. M., Plag P. W., King A. S., Kropf A. J., Bunker B. A., Kemner K. M., Dutta P., Duran R. S., and Kaduk J. (2000) The MRCAT insertion device beamline at the Advanced Photon Source. In *Synchrotron Radiation Instrumentation: Eleventh U.S. National Conference* (ed. P. Pianetta), pp. 419–422. CP521. American Institute of Physics.
- Sery A., Manceau A., and Greaves G. N. (1996) Chemical state of Cd in apatite phosphate ores as determined by EXAFS spectroscopy. *Am. Miner.* **81**, 864–873.
- Sillen L. D. and Martell A. E. (1964) *Stability Constants*. Special Publication No. 17. Chemical Society, London.
- Sillen L. D. and Martell A. E. (1971) *Stability Constants*. Supplement No. 1, Special Publication No. 25. Chemical Society, London.
- Spadini L., Manceau A., Schindler P. W., and Charlet L. (1994) Structure and stability of Cd²⁺ surface complexes on ferric oxides. I. Results from EXAFS spectroscopy. *J. Colloid Interface Sci.* **168**, 73–86.

- Stern E. A. and Heald S. M. (1979) X-ray filter assembly for fluorescence measurements of X-ray absorption fine structure. *Rev. Sci. Instrum.* **50**, 1579–1582.
- Stern E. A. and Heald S. M. (1983) Basic principles and applications of EXAFS. In *Handbook of Synchrotron Radiation* (ed. E. E. Koch), pp. 995–1014. Elsevier.
- Stern E. A., Newville M., Ravel B., Yacoby Y., and Haskel D. (1995) The UWXAFS analysis package—philosophy and details. *Physica B* **209**, 117–120.
- Venema P., Hiemstra T., and van Riemsdijk W. H. (1996) Multisite adsorption of cadmium on goethite. *J. Colloid Interface Sci.* **183**, 515–527.
- Warren L. A. and Haack E. A. (2001) Biogeochemical controls on metal behaviour in freshwater environments. *Earth-Sci. Rev.* **54**, 261–320.
- Webb S. M., Gaillard J. F., Jackson B. E., and Stahl D. A. (2001) An EXAFS study of zinc coordination in microbial cells. *J. Synchrot. Radiat.* **8**, 943–945.
- Xia K., Bleam W., and Helmke P. A. (1997a) Studies of the nature of binding sites of first row transition elements bound to aquatic and soil humic substances using X-ray absorption spectroscopy. *Geochim. Cosmochim. Acta* **61**, 2223–2235.
- Xia K., Bleam W., and Helmke P. A. (1997b) Studies of the nature of Cu^{2+} and Pb^{2+} binding sites in soil humic substances using X-ray absorption spectroscopy. *Geochim. Cosmochim. Acta* **61**, 2211–2221.
- Xia K., Weesner F., Bleam W. F., Bloom P. R., Skyllberg U. L., and Helmke P. A. (1998) XANES studies of oxidation states of sulfur in aquatic and soil humic substances. *Soil Sci. Soc. Am. J.* **62**, 1240–1246.
- Xia K., Skyllberg U. L., Bleam W. F., Bloom P. R., Nater E. A., and Helmke P. A. (1999) X-ray absorption spectroscopic evidence for the complexation of Hg(II) by reduced sulfur in soil humic substances. *Environ. Sci. Technol.* **33**, 257–261.

XAFS determination of the bacterial cell wall functional groups responsible for complexation of Cd and U as a function of pH

S. D. Kelly,^a M. I. Boyanov,^b B. A. Bunker,^b J. B. Fein,^b D. A. Fowle,^{b,c} N. Yee^b and K. M. Kemner^a

^aArgonne National Laboratory, Argonne, IL, 60439, USA, ^bUniversity of Notre Dame, Notre Dame, IN, 46556, USA, and ^cpresent address: University of Windsor, Windsor, ON N9B 3P4, Canada

Bacteria, which are ubiquitous in near-surface geologic systems, can affect the distribution and fate of metals in these systems through adsorption reactions between the metals and bacterial cell walls. Recently, Fein *et al.* (1997) developed a chemical equilibrium approach to quantify metal adsorption onto cell walls, treating the sorption as a surface complexation phenomenon. However, such models are based on circumstantial bulk adsorption evidence only, and the nature and mechanism of metal binding to cell walls for each metal system have not been determined spectroscopically. The results of XAFS measurements at the Cd K-edge and U L3-edge on *Bacillus subtilis* exposed to these elements show that, at low pH, U binds to phosphoryl groups while Cd binds to carboxyl functional groups.

Keywords: Environmental science; biogeochemistry; microbiology; uranium; cadmium.

1. Introduction

Bacteria, which are ubiquitous in near-surface geologic systems, can affect the distribution and fate of metals in these systems through adsorption reactions between the metals and bacterial cell walls. Many studies have addressed relative binding capacities of metals to cell walls (Ribbe, 1997). Recently, Fein *et al.* (1997) developed a chemical equilibrium approach to quantify metal adsorption onto Gram positive cell walls, treating the sorption as a surface complexation phenomenon. The authors used acid/base titrations to determine acidity constants for the important surface functional groups, and they used metal adsorption experiments to yield site-specific stability constants for the metal-bacteria surface complexes. This approach implies that different functional group types have different pH ranges in which they deprotonate and adsorb metals from solution. Fein *et al.* (1997) observed negligible Cd adsorption under low-pH conditions, with adsorption increasing with increasing pH above approximately pH 3.0 as the surface functional groups successively deprotonated. Fowle *et al.* (2000) observed a similar pH dependence for UO_2^{+2} adsorption onto the same bacteria, but they also observed significant uranyl adsorption even under low-pH conditions. Fowle *et al.* (2000) ascribed the low-pH adsorption to an interaction between the uranyl cation and a neutrally charged phosphoryl group on the cell wall. However, all of these models are based on circumstantial bulk adsorption evidence only, and the nature and mechanism of metal binding to the cell walls for each metal system has not been determined. X-ray

absorption fine structure (XAFS) measurements at the complexed metal absorption edge can distinguish between the different functional groups proposed to be important in metal uptake, thereby proving or disproving the proposed surface complexation models.

2. Methods

Samples of Cd and U adsorbed to cultures of *B. subtilis* were prepared by exposing aqueous Cd and U solutions to a known concentration of biomass, so that the ratio of metal to cell surface area remained constant. To probe pH-dependent changes in the adsorption mechanism, samples were prepared as a function of pH, from pH 1 to 5 for the U biomass samples and from pH 2.5 to 10 for the Cd biomass samples. Only the lowest-pH samples are discussed here. Sample preparation details are described elsewhere (Fowle & Fein, 2000). The biomass solution was centrifuged, and fluorescence XAFS measurements were made on the wet homogeneous paste. All XAFS measurements were made at the Materials Research Collaborative Access Team (MR-CAT) sector 10-ID beamline at the Advanced Photon Source (Segre *et al.*, 2000).

The beamline optics and setup parameters for the Cd K-edge measurements were as follows: The Si(333) reflection of the double-crystal monochromator running on the fifth harmonic of the beamline undulator was used. The fundamental energy was blocked with a 3-mm-thick, 30-adsorption-lengths aluminum plate. Higher harmonics were rejected by using a Pt mirror at approximately 1.9 mrad relative to the incident beam direction. The fluorescence data were taken by using a fluorescence detector filled with Kr gas. The incident and transmitted x-ray ion chambers were filled with nitrogen and a 1:1 mixture of nitrogen:argon gas, respectively.

For the U L3-edge measurements, the Si(111) reflection of the double-crystal monochromator running on the third harmonic of the beamline undulator was used. Higher harmonics were rejected by using a Rh mirror. The fluorescence detector was filled with argon gas, and the incident and transmitted ion chambers were both filled with nitrogen gas.

For both the U and Cd measurements, the undulator was tapered approximately 2 keV to reduce the variation in the incident intensity to about 15% over the scanned energy range. Linearity tests (Kemner *et al.*, 1994) indicated less than 0.3% nonlinearity for a 50% decrease in incident intensity. To minimize radiation exposure, the X-ray beam was reduced to 0.7 mm square, and the data were collected by using slew scanning mode. Data were collected at six sample locations, with 2 to 5 scans at each. Slew scanning mode allows data collection in the X-ray absorption near edge structure (XANES) region or extended X-ray absorption fine structure (EXAFS) region in approximately one minute. Measuring several spectra at each location allows for the determination of radiation-induced chemical effects at the one-minute time scale. No change in the XANES or EXAFS spectra was found for any of the samples.

The theoretical $\chi(k)$ was constructed by using the program FEFF7 (Zabinsky *et al.*, 1995). The data were analyzed with codes from the UWXAFS package (Stern *et al.*, 1995). The error analysis and the goodness-of-fit parameters were calculated by the fitting routine FEFFIT (Newville, 1994). Listed with the fit results are the XAFS reliability factor \mathcal{R} and the reduced-chi-squared value χ^2_ν (Newville, 1994). Quoted errors in the fitted variables include systematic contributions introduced from measurement, theory, and analysis (Stern *et al.*, 1995).

The U L3 XAFS measurements were taken in fluorescence and transmission modes. Two EXAFS measurements were taken at

three different spots for a total of six measurements. The background was removed by using the AUTOBK program (Newville *et al.*, 1993). The resulting six chi data sets were averaged. The average $\chi(k)$ data is shown in Fig. 1a.

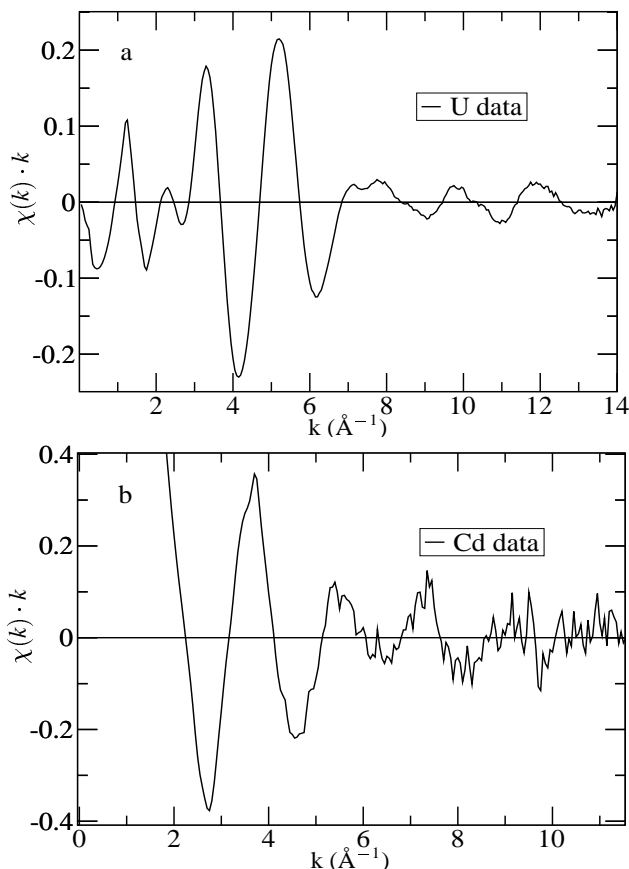


Figure 1
Average $\chi(k) \cdot k$ data for the biomass samples (a) U data at pH 1.67 (b) Cd data at pH 3.5.

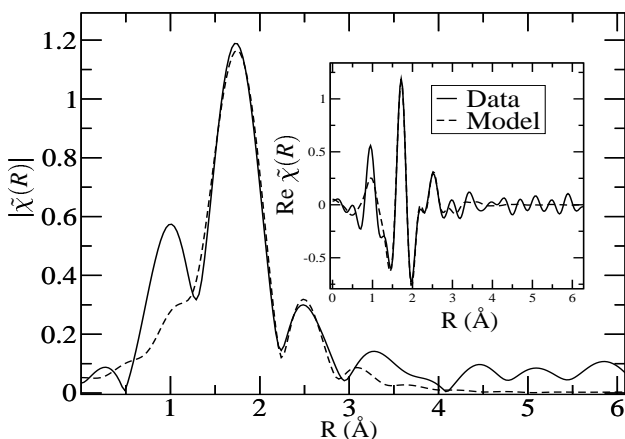


Figure 2
The magnitude, $|\tilde{\chi}(R)|$, and real part, $\text{Re } \tilde{\chi}(R)$ (inset), of the Fourier transform of the $\chi(k) \cdot k$ best-fit model and data from the Cd-biomass sample at pH 3.5. The data range $\Delta k = [3 : 9.25] \text{ \AA}^{-1}$ was used in the Fourier transform.

Five successive Cd EXAFS fluorescence measurements were made at 5 different locations on the biomass samples, for a total of 25 measurements. The $5 \mu(\text{E}) \cdot x$ data sets taken at each spot were averaged before the background was removed. The 5 resulting $\chi(k)$ data sets were averaged. The average $\chi(k)$ is shown in Fig. 1b. The relative concentration of U absorbed to the biomass was approximately 50 times greater than that of Cd; therefore the U signal was much cleaner, and fewer averaged data sets were required.

Several Cd-acetate solutions with different concentrations of Cd were also measured in fluorescence and transmission modes. Comparison of the XAFS fluorescence and transmitted signals showed that a Cd concentration of 80 mM resulted in a 17% reduction in the fluorescence signal. The amount of Cd in each biomass sample was estimated by comparing the step height of the fluorescence signal from the biomass to that of the solution standards. To determine the fluorescence corrections (Pfalzer *et al.*, 1999), the transmission $\chi(k)$ value was divided by the fluorescence $\chi(k)$ value for each concentration of the Cd-acetate solution.

An initial step in the analysis is determination of the value for S_0^2 , the passive electron amplitude reduction factor. Both S_0^2 and σ_i^2 affect the XAFS amplitude and are highly correlated. Because of the different k dependencies of these terms, multiple k -weighted fitting of the data was used to break their correlation (Kelly *et al.*, to be published).

Table 1

Best-fit values for the Cd-biomass data at pH 3.5, with goodness-of-fit parameters. The subscript c indicates that the parameter was determined in the fit but was constrained as explained in the text. The model names P, C, and H stand for phosphoryl, carboxyl, and hydroxyl, respectively. The χ^2_ν values for the models are 13, 11, and 12, respectively.

Model	Path	N_{degen}	R (Å)	$\sigma^2 (10^{-3} \text{ \AA}^2)$	\mathcal{R}
P	Cd→O	6.1 ± 1.1	2.27 ± 0.01	6 ± 2	0.032
	Cd→P	1.0 ± 1.0	3.34 ± 0.08	6_c	
C	Cd→O	5.8 ± 1.0	2.28 ± 0.01	5 ± 2	0.028
	Cd→C	3.0 ± 1.6	3.13 ± 0.06	5_c	
H	Cd→O	6.8 ± 1.1	2.28 ± 0.02	7 ± 2	0.047

3. Results and Discussion

For both the Cd and U data, three models were needed to describe binding to hydroxyl, phosphoryl, and carboxyl functional groups. Theoretical models for cadmium acetate dihydrate (Harrison & Trotter, 1972), cadmium phosphate (Bigi *et al.*, 1986), sodium uranyl triacetate (Templeton *et al.*, 1985), hydrogen uranyl phosphate tetrahydrate (Morosin, 1978) were generated by FEFF7. The difference in data due to the different binding models will be in the second shell, where we expect to find a signal from a P, C, or H for the phosphoryl, carboxyl, or hydroxyl functional group. For the hydroxyl binding mechanism, the signal is expected to be similar to that for hydrated U/Cd. The U/Cd hydroxide was simulated by taking the paths from the first oxygen shell surrounding the U/Cd in previous structures. Several solution standards of hydrated U/Cd, U/Cd-acetate, and U/Cd-phosphate were measured to simulate the hydroxyl, carboxyl, and phosphoryl binding in the biomass samples.

For the Cd-acetate and Cd-phosphate solution standards, a two-shell (O and then P/C) fit was sufficient to distinguish acetate from phosphate. In these models, σ^2 was constrained for both shells (O and P/C) to the same value. This constraint reduced the χ^2_ν significantly (by a factor of 30). Both the Cd-acetate and Cd-phosphate

models, along with a single O shell model (to represent a Cd-hydroxyl) were applied to the Cd-biomass data at pH 3.5. The results are in Table 1. The Cd-phosphate model gives a degeneracy of the P shell that is consistent with zero, indicating that the P shell is not significantly improving the fit quality. The larger \mathcal{R} value of 0.047 (Newville, 1994) for the Cd-hydroxyl model indicates that it is not optimal for the data. The Cd-acetate model gives the best fit with reasonable fit parameters. The data and the best-fit model are shown in Fig. 2.

First a model for a hydrated uranyl standard was developed, and the values were used as input parameters in FEFF7 to create a theoretical fit for a hydrated uranyl. This model was then used to generate a fit to the experimental data for the U-biomass sample. The best-fit values for the fits to the U-biomass sample and the hydrated uranyl sample are similar, giving confidence in this model for the biomass sample. However, careful consideration of the data between 2.5 and 3.8 Å indicates the presence of an additional atom(s) surrounding the U atoms in the biomass sample.

Table 2

Models considered for the data in the region at 2.5–4.0 Å in the U-biomass $|\tilde{\chi}(R)|$ data, listed in order of increasing χ^2_{ν} . S.S. and M.S. stand for single- and multiple-scattering paths, respectively. Initial path lengths of 2.6 and 2.9 Å were used for the short and long paths, respectively.

Model Name	Path description	\mathcal{R}	χ^2_{ν}	ν
<i>fit-mPP</i>	M.S. O-P and S.S. long P	0.08	13	7
<i>fit-PP</i>	S.S. short P and long P	0.05	16	6
<i>fit-PO</i>	S.S. short P and long O	0.13	28	6
<i>fit-mPC</i>	M.S. O-P and S.S. long C	0.11	32	6
<i>fit-OP</i>	S.S. short O and long P	0.19	36	6
<i>fit-mP</i>	M.S. O-P	0.20	46	9
<i>fit-P2</i>	S.S. long P	0.22	50	9
<i>fit-P1</i>	S.S. short P	0.31	82	9
<i>fit-CC</i>	S.S. short C and long C	0.29	100	5

Table 3

Best-fit values for the U-biomass samples at pH 1.67. These fits had 22.6 independent points in the data and 15 variables. $E_0 = 4.4 \pm 1.1$.

Path	N_{degen}	R (Å)	$\sigma^2 (10^{-3} \text{Å}^2)$
U→Oax	2.0	1.777 ± 0.006	1.2 ± 0.3
U→Oeq	6.3 ± 0.5	2.387 ± 0.009	9.1 ± 1.3
U→Oax1→U→Oax1	2.0	3.553 ± 0.011	2.5 ± 0.7
U→Oax1→Oax2→U	2.0	3.553 ± 0.011	2.5 ± 0.7
U→Oax1→U→Oax2→U	2.0	3.553 ± 0.011	2.5 ± 0.7
U→P1	1.0 ± 0.8	3.628 ± 0.038	5.7 ± 5.0
U→P2	1.9 ± 1.3	3.904 ± 0.027	5.7 ± 5.0

With the hydrated uranyl model held constant, this region (2.5 to 3.8 Å) was modeled with several different combinations of single- and multiple-scattering C, O, and, P shells. The different models and the goodness-of-fit values for these models are in Table 2. Two statistically equivalent best-fit models are at the top of Table 2. One consists of two single-scattering U→P paths, and the other consists of all the multiple-scattering U→Oeq→P paths and a single-scattering U→P path. Both models are consistent with two phosphate binding sites. Finally, the U-biomass data were fitted over the entire R-space range (1 to 3.8 Å) by using the paths from the hydrated uranyl model and the two single-scattering U→P paths. The best-fit values to these data are in Table 3. The quality of the fit to the data is illustrated in Fig. 3.

In summary, XAFS can be used to distinguish hydroxyl, carboxyl, and phosphoryl bonding to metals in biomass. These preliminary results at the lowest pH are consistent with the surface complexation models proposed by Fein *et al.* (1997) and Fowle *et al.*

(2000). We plan to use this technique to investigate pH-dependent sorption to cell walls.

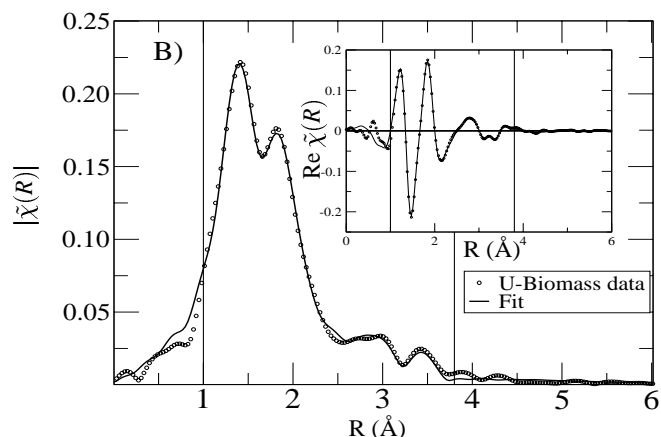


Figure 3

The magnitude, $|\tilde{\chi}(R)|$, and real part, $\text{Re } \tilde{\chi}(R)$ (inset), of the Fourier transform of the $\chi(k) \cdot k$ best-fit model, with data from the U-biomass sample at pH 1.67. The data range $\Delta k = [2.5 : 13.5] \text{Å}^{-1}$ was used in the Fourier transform.

Support for SDK and KMK was provided by the U.S. Department of Energy (DOE), Office of Science, Office of Biological and Environmental Research, NABIR Program, and use of the MR-CAT sector of the APS was supported by the DOE Office of Basic Energy Sciences, both under contract W-31-109-Eng-38. Other support was provided by National Science Foundation grant EAR-9905704 and by the donors of the Petroleum Research Fund, administered by the American Chemical Society.

References

- Bigi, A., Foresti, E., Gazzano, M., Ripamonti, A. & Roveri, N. (1986). *J. Chem. Research*, **35**, 170.
- Fein, J. B., Daughney, C. J., Yee, N. & Davis, T. A. (1997). *Geochim. Cosmochim. Acta*, **61**(16), 3319.
- Fowle, D. A. & Fein, J. B. (2000). *Chemical Geology*, **168**, 27–36.
- Fowle, D. A., Fein, J. B. & Martin, A. M. (2000). *Environ. Sci. Technol.*, **34**(17), 3737–3741.
- Harrison, W. & Trotter, J. (1972). *Chem. Soc. Dalton Trans.* 956.
- Kelly, S. D., Ingalls, R. & Stern, E. A. (to be published). *Phys. Rev. B*.
- Kemner, K. M., Kropf, J. & Bunker, B. A. (1994). *Rev. Sci. Instrum.*, **65**, 3667–3669.
- Morosin, B. (1978). *Acta Crystallography*, **B34**, 3732–3834.
- Newville, M., (1994). FEFFIT: Using FEFF to model XAFS in R-space. unpublished. This documentation is part of the UWXAFS3.0 package.
- Newville, M., Liviņš, P., Yacoby, Y., Rehr, J. J. & Stern, E. A. (1993). *Phys. Rev. B*, **47**(21), 14126–14131.
- Pfalzer, P., Urbach, J. P., Klemm, M., & Horn, S. (1999). *Phys. Rev. B*, **60**(13), 9335.
- Ribbe, P. (ed.) (1997). *Geomicrobiology: Interactions between Microbes and Minerals*, vol. 35 of *Reviews in Mineralogy*, chap. 5. Washington, D.C.: Mineralogical Society of America.
- Segre, C. U., Leyarovska, N. E., Chapman, L. D., Lavender, W. M., Plag, P. W., King, A. S., Kropf, A. J., Bunker, B. A., Kemner, K. M., Dutta, P., Duran, R. S. & Kaduk, J. (2000). In *Synchrotron Radiation Instrumentation: Eleventh U.S. National Conference*, edited by P. Pianetta, *et al.*, vol. CP521, pp. 419–422. New York: American Institute of Physics.
- Stern, E. A., Newville, M., Ravel, B., Yacoby, Y. & Haskel, D. (1995). *Physica B*, **208&209**, 117–120.
- Templeton, D., Zalkin, A., Ruben, H., & Templeton, L. (1985). *Acta Crystallography*, **C41**, 1439–1441.
- Zabinsky, S. I., Rehr, J. J., Ankudinov, A., Albers, R. C. & Eller, M. J. (1995). *Phys. Rev. B*, **52**(4), 2995–3009.

Nonmetabolic Reduction of Cr(VI) by Bacterial Surfaces Under Nutrient-Absent Conditions

JEREMY B. FEIN
DAVID A. FOWLE
JOSHUA CAHILL

University of Notre Dame
Civil Engineering and Geological Sciences
Notre Dame, Indiana, USA

KEN KEMNER

Argonne National Laboratory
Environmental Sciences Division
Argonne, Illinois, USA

MAXIM BOYANOV
BRUCE BUNKER

University of Notre Dame
Department of Physics
Notre Dame, Indiana, USA

*We have measured the ability of nonmetabolizing cells of the bacterial species *Bacillus subtilis*, *Sporosarcina ureae*, and *Shewanella putrefaciens* to reduce aqueous Cr(VI) to Cr(III) in the absence of externally supplied electron donors. Each species can remove significant amounts of Cr(VI) from solution, and the Cr(VI) reduction rate is strongly dependent on solution pH. The fastest reduction rates occur under acidic conditions, with decreasing rates with increasing pH. XANES data demonstrate that Cr(VI) reduction to Cr(III) occurs within the experimental systems. Control experiments indicate that the Cr removal is not a purely adsorptive process. Reduction appears to occur at the cell wall, and is not coupled to the oxidation of bacterial organic exudates. Detailed kinetic data suggest that the reduction involves at least a two-stage process, involving an initial rapid removal mechanism followed by a slower process that follows first-order reaction kinetics. Due to the prevalence of nonmetabolizing cells and cell wall fragments in soils and deeper geologic environments, our results suggest that the observed nonmetabolic*

Received 4 January 2001; accepted 29 May 2001.

Acknowledgment is made to the donors of the Petroleum Research Fund, administered by the American Chemical Society, for partial support of this research. The research was also supported by NSF grant EAR-9905704. Use of the MR-CAT sector and the Advanced Photon Source was supported by the U.S. Department of Energy, Basic Energy Science, Office of Science, under Contract No. W-31-109-Eng-38. Support for KMK was provided by the U.S. Department of Energy's Office of Biological and Environmental Research NABIR program and Argonne National Laboratory LDRD funds. The comments made by two anonymous journal reviewers were helpful and are appreciated.

Address correspondence to Dr. Jeremy Fein, Civil Engineering & Geological Sciences, 156 Fitzpatrick Hall, University of Notre Dame, Notre Dame, IN 46556, USA. E-mail: fein.1@nd.edu

reduction of Cr(VI) to Cr(III) may significantly affect the environmental distribution of Cr in bacteria-bearing systems.

Keywords bacteria, chromium, kinetics, reduction, X-ray absorption spectroscopy

Introduction

The fate of chromium in the environment is strongly dependent on its valence state. Under oxidizing conditions, chromium exists as Cr(VI), and is readily bioavailable due to the high solubility of Cr(VI)-bearing minerals. Cr(VI) is present in oxidizing solutions primarily as the aqueous species CrO_4^{-2} or as HCrO_4^- , depending on pH. Conversely, Cr(III) minerals are extremely insoluble under near-neutral pH conditions, and therefore, when chromium is present as Cr(III), its availability to organisms is limited. Interactions between bacteria and chromium can alter the valence state and speciation of chromium in the subsurface (e.g., Bopp and Ehrlich 1988), and hence can control the fate of chromium in the environment. Therefore, in order to understand the response of natural systems to chromium contamination and in order to design bioremediation strategies for such contaminated systems, it is imperative to understand each of the important bacterial mechanisms that affect chromium distribution.

Virtually all previous experimental studies of bacterial Cr(VI) reduction focused on enzymatic Cr(VI) reduction to Cr(III) as a product of metabolic activity, using large excess concentrations of electron donors in the experimental systems (e.g., Bopp and Ehrlich 1988; Wang et al. 1989; DeLeo and Ehrlich 1994; Shen and Wang 1994; Wang and Xiao 1995; Wang and Shen 1997; Philip et al. 1998; Tebo and Obraztsova 1998; Kashefi and Lovley 2000). These studies indicate that Cr(VI)-reducing bacteria can utilize a range of organic compounds as electron donors in the Cr(VI) reduction reaction. However, this range is, in general, limited to natural aliphatics, typically low molecular weight amino acids, carbohydrates, and fatty acids (Wang and Shen 1995). H_2 and other reducing agents such as benzoate have also been used to induce bacterial reduction of Cr(VI) (Wang and Xiao 1995; Kashefi and Lovley 2000). Metabolic enzymatic Cr(VI) reduction has been observed both in the presence and absence of O_2 (e.g., Bopp and Ehrlich 1988; Shen and Wang 1994), and Cr(VI) reduction rates are strongly dependent on pH (Wang et al. 1989; Shen and Wang 1994; Wang and Xiao 1995; Philip et al. 1998), temperature, and electron donor and Cr(VI) concentrations (Wang and Xiao 1995). The optimum pH conditions for metabolic enzymatic Cr(VI) reduction by bacteria appears to be close to pH 7. Reduction rates decrease significantly at both higher and lower pH conditions, with little or no metabolic enzymatic Cr(VI) reduction occurring under acidic conditions.

High rates of bacterial metabolism and Cr(VI) reduction can be induced for engineered bioremediation approaches through the introduction of high concentrations of electron donors in the system of interest, and similar conditions can be found in some geologic settings. However, in general bacteria exist in the subsurface under nutrient-poor conditions (Ehrlich 1996). Mineral surfaces and organic compounds can both catalyze Cr(VI) reduction (e.g., Cainelli and Cardillo 1984; Deng and Stone 1996a, 1996b), so it is possible that bacterial surfaces can induce Cr(VI) reduction in and of themselves, independent of active bacterial metabolism and in the absence of high concentrations of electron donors. If such nonmetabolic, nutrient-absent Cr(VI) reduction occurs, then it could be an important reductive pathway in nonengineered geologic systems.

Some experimental studies have examined the Cr(VI) reduction capabilities of resting cells, killed cells, cell extracts, or cells in the absence of electron donors. These studies constrain the conditions under which nonmetabolic Cr(VI) reduction by bacteria occurs;

however, all of these studies have been conducted under pH 7 conditions. Although metabolic enzymatic Cr(VI) reduction is well documented, there are few controlled studies examining nonmetabolizing cells under conditions in which external electron donors are absent. Bopp and Ehrlich (1988) found that resting *Pseudomonas fluorescens* LB300 cells would not reduce Cr(VI) without added glucose. Similar results were noted for *Escherichia coli* ATCC 33456 and *Bacillus coagulans* by Shen and Wang (1994) and by Philip et al. (1998), respectively, who observed no Cr(VI) reduction by resting cells in the absence of an external electron donor. Killed cells of *Escherichia coli* ATCC 33456 and *Pseudomonas fluorescens* LB300 also did not cause Cr(VI) reduction, even in the presence of external electron donors (Shen and Wang 1994; Wang and Shen 1997). A number of studies have examined the Cr(VI) reduction capabilities of cell extracts. In general, the soluble enzymes within these extracts appear to be responsible for Cr(VI) reduction, and most of these appear to require external electron donors for reduction to occur (e.g., Bopp and Ehrlich 1988; Shen and Wang 1994). However, Horitsu et al. (1987) and Philip et al. (1998) report Cr(VI) reduction by cell extracts in the absence of added electron donors.

In this study, we measure the Cr(VI) reduction capabilities of three bacterial species in the absence of external electron donors. The experiments utilize both resting state cells as well as Cs-irradiated cells to isolate nonmetabolic reduction pathways. The objective of this study is to determine if such a nonmetabolic, nutrient-absent reductive pathway exists involving bacterial cell walls, and if so to quantify the kinetics of, and controls on, the dominant reduction reaction.

Materials and Methods

Bacterial Strains and Culture Conditions

We investigated the Cr(VI) reduction capabilities of the bacterial strains *Shewanella putrefaciens*, *Sporosarcina ureae*, and *Bacillus subtilis*. *S. putrefaciens* was obtained from K. H. Nealson (California Institute of Technology); *S. ureae* was obtained from C. F. Kulpa, Jr. (University of Notre Dame); *B. subtilis* was the same strain used by our research group previously, and was originally obtained from T. J. Beveridge, University of Guelph. Each strain was grown aerobically in trypticase soy broth with 0.5% yeast extract. We washed the bacterial cells using a procedure similar to one employed previously by our group (e.g., Fein et al. 1997; Fein and Delea 1999; Fowle and Fein 1999), except we omitted the EDTA soak step. The cells were washed twice in 0.1 M NaClO₄, soaked in 0.03 M HNO₃ for 1 h, and rinsed five times in 0.1 M NaClO₄. The wash procedure ensures that the cell walls are free of components of the growth medium prior to experimentation. Prior to the experiments, cells were centrifuged at 10,000 g for 60 min and weighed. In this study, bacterial concentrations are reported using this wet weight, which is 9.9 ± 1.1 times more than the weight of fully dried cells (Fein and Delea 1999); 1.0 gm bacteria/L (wet weight) corresponds to approximately 8×10^5 cells/mL.

Cr(VI) Removal Experiments

Cr(VI) removal from solution was measured using batch experiments in which the initial concentration of Cr was 5.0 ppm, and the bacterial concentration was 12.0 gm/L. Two experiments (one at pH 3.0 and one at pH 7.0) were conducted using *B. subtilis*, with 3.3 ppm Cr and 1.2 gm bacteria/L. The suspended bacteria were in a resting viable, but nongrowth state. No external electron donors or carbon sources were included in the experimental

systems. Ionic strength was held constant through the use of 0.1 M NaClO₄, and pH was adjusted and maintained using the addition of small volumes of 1.0 M NaOH or 70% HNO₃. All solutions were prepared with deionized 18 MΩ H₂O and reagent grade chemicals. The starting Cr(VI) solutions were prepared from 1,000 ppm Cr (K₂CrO_{4(aq)}) atomic absorption aqueous standards. After suspension of the bacteria in the Cr-bearing electrolyte solution, the solution pH was adjusted, and samples were taken periodically for up to 200 h. Experiments were conducted in the pH range of 2.0 to 9.0. Samples were extracted after thorough mixing of the experimental systems to ensure that the bacterial concentration did not change during the course of the experiment. This was tested by determining the weight of the bacteria relative to the total sample weight for each sample. Samples were centrifuged and filtered through 0.45-μm nylon filters, and solutions were analyzed for aqueous Cr concentration using inductively coupled plasma atomic emission spectroscopy (ICP-AES) with matrix-matched Cr standards. Analytical uncertainties for the ICP-AES measurements were approximately ±2% or better.

XANES Experiments

The fate of the Cr that was removed from solution during the experiments was investigated using X-ray absorption near-edge structure (XANES) spectroscopy (Koningsberger and Prins 1988; Schulze and Bertsch 1995). Three duplicate Cr(VI) removal experiments were conducted as described above using *Bacillus subtilis* exposed to a 100-ppm aqueous Cr(VI) solution with 5.0 gm bacteria/L at pH 3.0. The biomass was collected by centrifugation at 10,000 g for 10 min, and the XANES signature of the biomass sample was compared to those of a Cr(VI) aqueous solution and a Cr(III)-phosphate powder to quantify the relative proportion of Cr(VI):Cr(III) present in the biomass sample.

The element specificity of the XANES technique makes it particularly valuable for studying dilute (concentrations > 10 ppm), multielement, and disordered chemical systems such as the Cr-microbe cell wall system. The determination of Cr speciation in the biomass using the XANES technique is facilitated by the large differences between the near-edge spectra of Cr(VI) and Cr(III) (Manceau and Charlet 1992; Bajt et al. 1993). In particular, Cr(VI) has an extremely large, sharp pre-edge feature that is totally absent in Cr(III). Thus, the deconvolution of the observed XANES spectra by using spectra of known Cr(III) and Cr(VI) standards is relatively straightforward. With this approach, a quantitative determination of the Cr(VI) or Cr(III) fraction of the total Cr in the sample is quite feasible.

The Cr XANES measurements presented here were made at the Materials Research Collaborative Access Team (MR-CAT) sector 10 of the Advanced Photon Source. All samples were at ambient room temperature during the XAFS measurements. Measurements of the biomass and dilute standards were made in the fluorescence mode. Concentrated samples were measured in the transmission mode. In order to reduce the effects of any radiation-induced valence changes in the Cr, three sequential XAFS measurements were made in the quick-XAFS mode (90 s/XANES scan) on two biomass samples. No significant change in Cr(III)/Cr(VI) ratio was observed for these experiments, indicating that radiation-induced reduction of the Cr in these samples did not appreciably effect these results.

Control Experiments

A number of experiments were conducted as controls. Bacteria-free systems that were otherwise identical to those described previously were sampled to test for abiotic Cr(VI) removal from solution, both under pH 2.0 and pH 5.0 conditions. The role of bacterial

exudates (defined as any organic molecule being emitted from the cell or released due to lysis) was determined for both *S. putrefaciens* and *B. subtilis* by suspending both types of bacteria (separately) in electrolyte for 24 h prior to experimentation. These suspended bacteria were removed from solution via centrifugation. Cr(VI) was added to the supernatant to achieve a concentration of 5.0 ppm, and the separated bacteria were resuspended in a different 5.0 ppm Cr(VI) electrolyte solution. Both of these systems were then sampled periodically over 24 h and tested for Cr removal from solution.

The reversibility of the Cr removal reactions was tested for *B. subtilis* by initially exposing the bacteria to a 5.0 ppm Cr(VI) solution at pH 2.25 for either a short duration (3.25 h) or a long duration (20.75 h). The pH of both systems was then increased first to 3.0 and sampled for approximately 20 h, and then further increased to pH 5.9 (for the short initial exposure system) or 5.2 (for the long initial exposure system) and sampled for another 24 h.

Although no external electron donor or carbon source was included in any experiment or control, it is possible that the cells utilized internal energy supplies for metabolism to some extent. To determine the role of this potential metabolic activity, we conducted Cr(VI) reduction measurements identical to those described before, only using cells that were made metabolically inactive by exposure to gamma radiation from a Cs source for 1.5 h at 35,000 rads/h. Heat or chemical treatments to stop bacterial metabolic activity can cause significant alterations to the cell wall structure. Urrutia Mera et al. (1992) have demonstrated that this irradiation procedure is sufficient to kill over 90% of the cells, with minimal disturbance to the cell wall structure or integrity. Our irradiation control experiments were conducted at pH 3.2 in 0.1 M NaClO₄. Two sets of experiments were run: one with irradiated cells under these conditions, and one with nonirradiated cells. Both batches of cells had undergone the same growth and wash procedures prior to experimentation, and both sets of experiments were conducted under identical pH and ionic strength conditions.

Results and Discussion

Bacteria-free control experiment samples (results not depicted) exhibited no significant change in the aqueous Cr concentration, either at pH 2.0 or at pH 5.0, indicating that abiotic Cr(VI) reduction and/or adsorption onto the experimental apparatuses were negligible. The influence of pH on Cr removal from solution after 4 h of contact between aqueous Cr and *B. subtilis* is depicted in Figure 1. Bacterial removal of Cr from solution is strongly pH dependent, but with a radically different pH behavior than has been observed for metabolically driven enzymatic Cr(VI) reduction in the presence of high concentrations of electron donors. In our experiments, Cr removal is greatest under acidic conditions, with decreasing extents of removal with increasing pH. At pH 7 (the pH at which metabolic Cr(VI) reduction peaks in efficiency) and above, little Cr is removed from solution in our experimental systems.

The reversibility control experiments (results shown in Figure 2) demonstrate that once Cr is removed from solution, increasing the solution pH does not cause reversal of the removal reaction. The extent of initial Cr removal from solution at pH 2.25 depends on the duration of the experiment, with 35% of the Cr removed after 3.25 h, and over 60% removed after 20.75 h. Adjustment of the pH up to 3.0 did not cause reversal to occur, but rather additional Cr was removed as the experiments progressed. Similar results were observed for the second pH adjustment from 3.0 to pH values greater than 5.0. This type of behavior contrasts with that observed for cation or anion adsorption and desorption onto bacterial cell walls, which is rapid and fully reversible with changes in pH (Daughney and Fein 1998; Fein et al. 1999; Fowle and Fein 2000). These results indicate that the Cr removal is not purely an adsorption process.

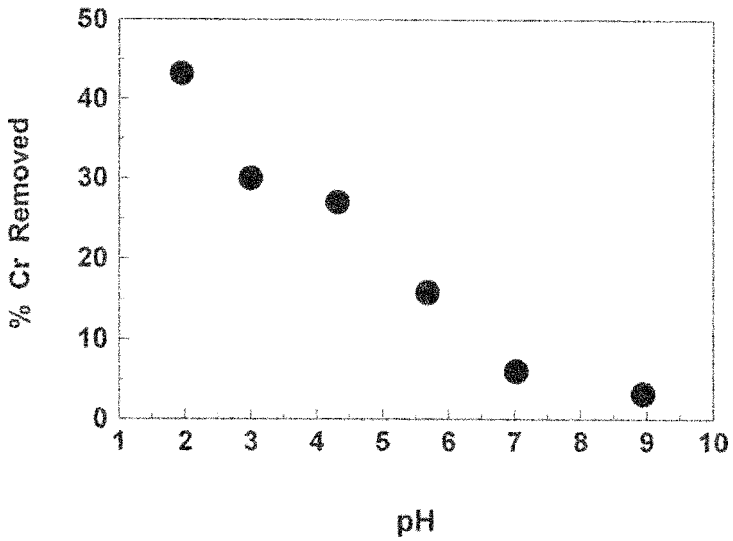


FIGURE 1 Percent of Cr removed from solution after 4 h of exposure to *Bacillus subtilis* suspensions (12 gm bacteria/L; 5 ppm Cr in starting solution) in 0.1 M NaClO₄ as a function of pH.

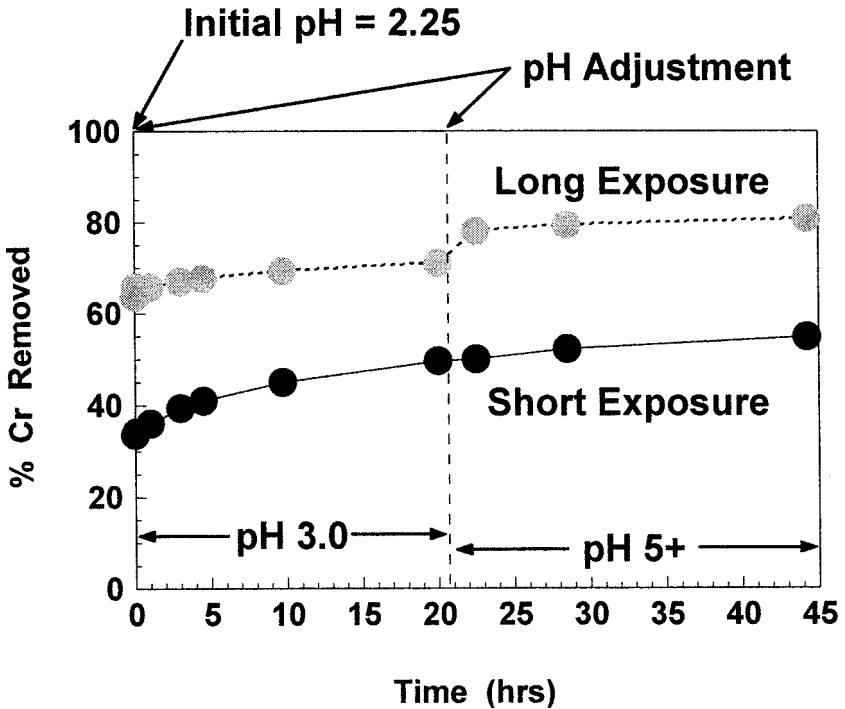


FIGURE 2 Results from reversibility experiments depicted in terms of percent Cr removed from solution as a function of time since first pH adjustment. Initially, 12 gm *Bacillus subtilis*/L were placed in contact with 5 ppm Cr in 0.1 M NaClO₄ at pH 2.25 for either 20.75 h (long exposure) or 3.25 h (short exposure). pH was then adjusted to 3.0. After approximately 21 h, pH was adjusted upward again to values over 5.2.

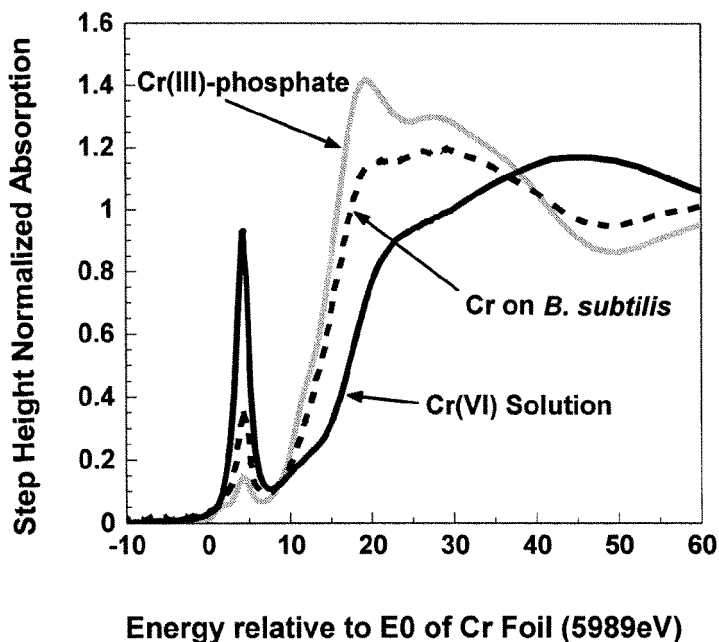


FIGURE 3 XANES data depicting Cr in a Cr(VI) aqueous solution; in a Cr(III)-phosphate powder; and from a *Bacillus subtilis* sample, exposed to 100 ppm aqueous Cr(VI) solution with 5.0 gm bacteria/L at pH 3.0.

XANES spectroscopy yields information concerning the valence state of the Cr once it is removed from solution. Figure 3 depicts Cr XANES data for one of the Cr-*B. subtilis* samples (pH = 3) and two reference standards: an aqueous Cr(VI) solution and a Cr(III)-phosphate solid. Note that Figure 3 shows step height normalized absorption, so the relative heights of the three curves are not functions of Cr concentration in each sample. Also note that each of the three duplicate biomass experiments yielded virtually identical data curves (other two not shown). A comparison of the XANES intensity from the Cr-*B. subtilis* sample to the standards at ~ 4 eV (Figure 3) indicates that $74 \pm 10\%$ of the Cr on the bacteria is Cr(III). These data are consistent with one of two scenarios. Either the Cr, which was initially Cr(VI) at the beginning of the experiment, adsorbed onto the bacterial surface and then was reduced to Cr(III), causing Cr precipitation and irreversible removal of Cr from solution, or the Cr was reduced in solution and precipitated and/or adsorbed onto the cell wall surface.

To distinguish between these two possibilities, we conducted controls to determine whether bacterial exudates were causing Cr(VI) reduction independent of the bacterial cells (Figure 4). After allowing both *S. putrefaciens* and *B. subtilis* to be suspended in electrolyte solution for 24 h (separately), the bacteria were separated from the electrolyte by centrifugation and filtration. Figure 4 demonstrates that these bacteria-free solutions exhibited no ability to reduce Cr(VI) under pH 3.0 conditions. The figure also shows the Cr concentrations of the pH 3.0 solutions into which the filtered bacteria were resuspended. These systems exhibited immediate and continual Cr removal from solution, demonstrating that bacterial exudates, if present, were not causing Cr removal via reduction to Cr(III), and that the presence of the bacterial cells is a requirement for Cr removal from solution. The fact that less than 100% of the biomass-associated Cr is Cr(III) is also consistent with a reduction process that occurs only on the cell wall (or within the cell) after adsorption or uptake of Cr(VI).

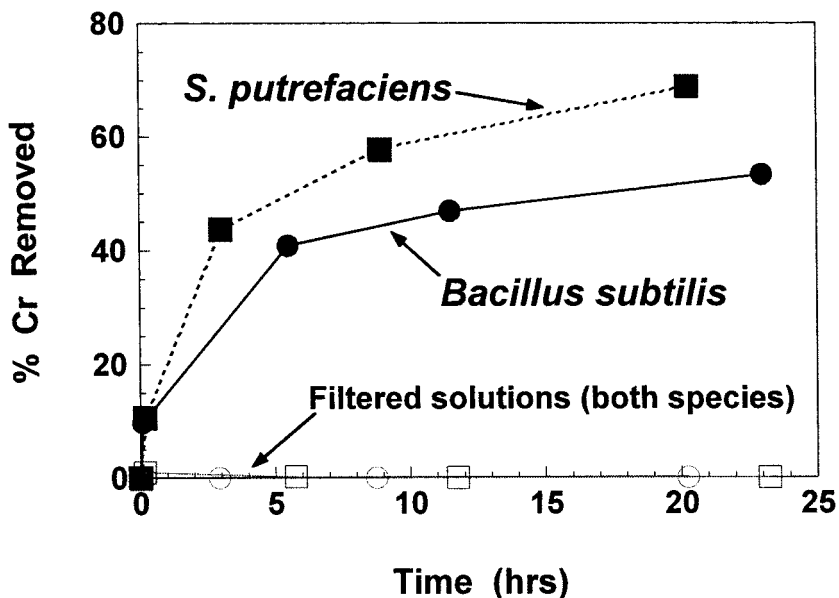


FIGURE 4 Exudate Cr(VI) reduction experimental results, for two types of systems: bacteria-free pH 3.0 solutions that had been in contact with either *Bacillus subtilis* or *Shewanella putrefaciens* for 24 h (filtered solutions); and the filtered bacteria from these systems, resuspended in pH 3.0 solutions.

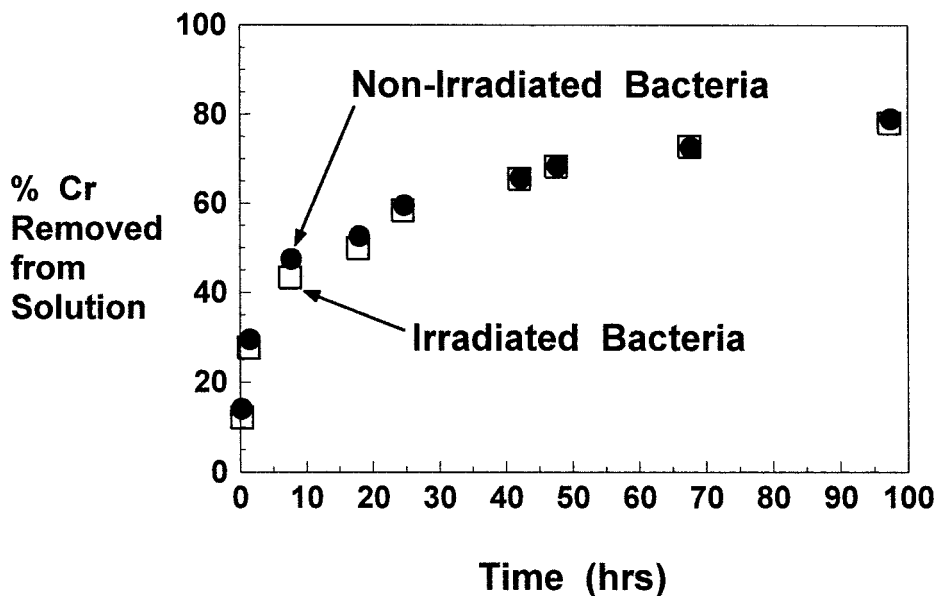


FIGURE 5 Effect of irradiation on Cr(VI) reduction. Circles are samples from a system containing nonirradiated *Bacillus subtilis*; open squares are from a system containing irradiated *Bacillus subtilis*. Both sets of experiments conducted at pH 3.0, with 5.0 ppm Cr(VI) in the starting solution, with 20 gm bacteria/L in 0.1 M NaClO₄.

The role of bacterial metabolism in our experimental systems was tested by conducting Cr(VI) reduction experiments with Cs-irradiated bacteria and with nonirradiated cells, with all other conditions identical. Figure 5 shows these experimental results, indicating that there is no significant difference between the two runs in terms of the rate or extent of Cr(VI) removal from solution. Because the irradiation inactivates most, if not all, metabolic activity of the bacteria in the experimental system, yet leaves the cell walls intact, these experiments strongly suggest that the Cr(VI) reduction that we observe under the experimental conditions is not dependent on cell metabolism, and that the previous experimental results were not caused by metabolic processes. It is likely that some component of the cell wall serves as the electron donor for the reduction-oxidation reaction, and that proximity between the cell wall and aqueous Cr(VI) is required for reduction to occur. The reversibility experiments indicate that adsorption alone cannot explain the observed Cr removal, and it is likely that Cr(VI) reduction on the bacterial surface is the rate-controlling step.

The pH data indicate that the reduction rate is strongly pH dependent, and we have determined the pH dependence of the reaction kinetics. Figure 6 depicts Cr removal from solution as a function of time, and indicates that under most pH conditions studied, the experimental systems did not reach equilibrium. In each system, there was a period of relatively rapid Cr removal that lasted for approximately 20 h, followed by a period of slower, but steady Cr removal. Figure 7 illustrates the time dependence of the Cr concentration in solution. The early rapid removal is nonlinear on this graph, but the second slower removal phase exhibits the linear removal that is indicative of first-order reaction kinetics. It is possible that the two-step kinetics results from two processes that together act to remove Cr from solution: a rapid adsorption step followed by a slower reduction step. It is impossible to ascertain from our data whether the Cr is within the cells or on the cell surface when reduction occurs. However, the experiments conducted using the Cs-irradiated cells (which cannot actively transport Cr through the cell wall via metabolic pathways) suggest that reduction is a surface phenomenon.

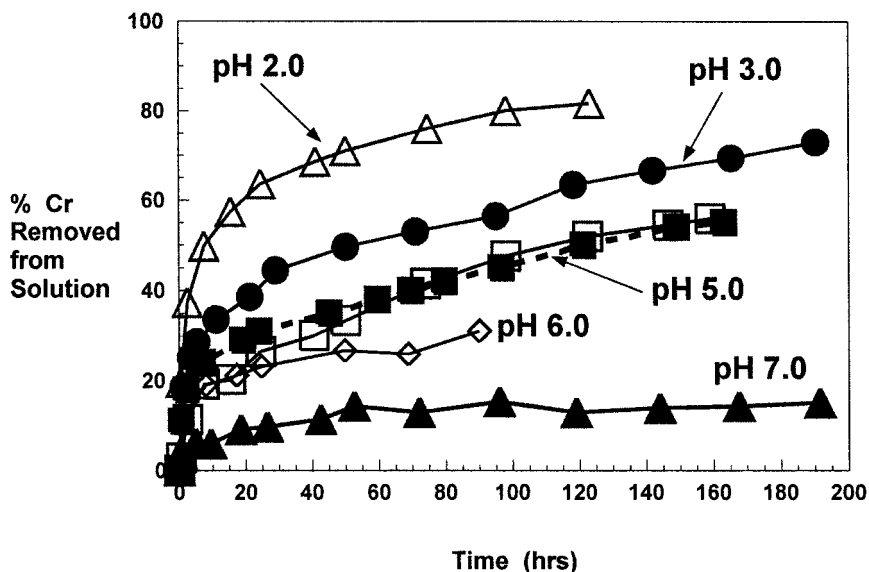


FIGURE 6 Kinetic data from pH 2.0 (open triangles), 3.0 (circles), 5.0 (2 replicate experiments - squares), 6.0 (diamonds), and 7.0 (filled triangles) experiments. All experiments conducted with 12 gm *Bacillus subtilis*/L, with 5.0 ppm Cr(VI) in the starting solution of 0.1 M NaClO₄.

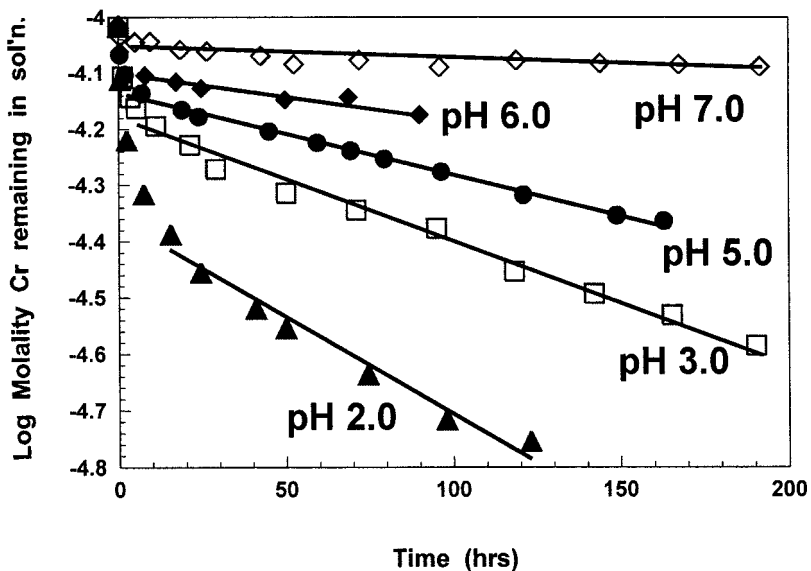


FIGURE 7 Kinetic data from Figure 6, depicted in terms of log molality Cr remaining in solution as a function of time. Linear segments exhibit periods when systems display first-order Cr(VI) reduction kinetics.

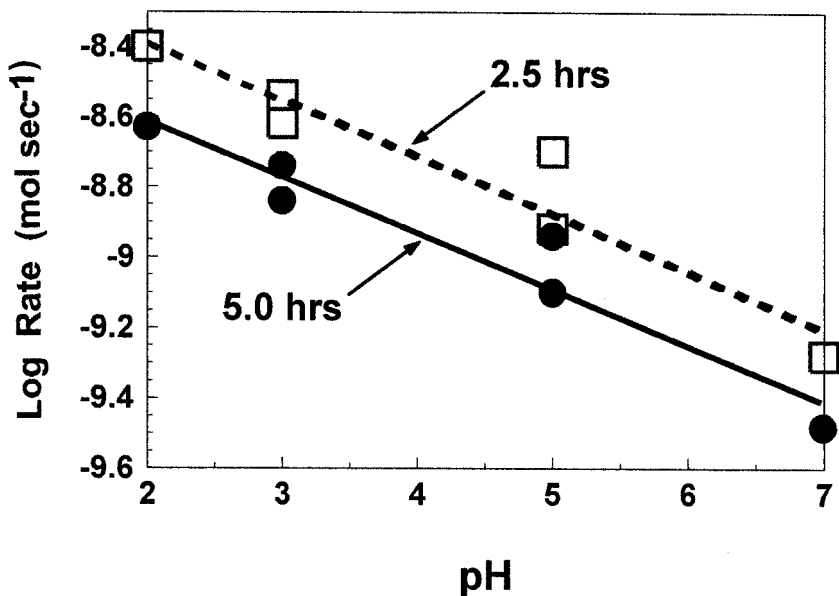


FIGURE 8 Cr(VI) reduction rates depicted in terms of log of molality of Cr removed from solution per second as a function of pH. Data shown for 2.5 (squares) and 5.0 h from beginning of experiments. pH 3.0 and 5.0 experiments were conducted in replicate. pH 6.0 data not shown due to lack of samples during the first 5 h of exposure.

The pH control on the extent of Cr removal from solution observed in Figure 1 is clearly a kinetic effect, with the removal rate highest under low pH conditions, decreasing with increasing pH. This behavior is in contrast to the pH dependence of Cr(VI) reduction by metabolic enzymatic reactions, which is most rapid at pH 7, with slower reduction rates observed at both higher and lower pH values (Wang et al. 1989; Shen and Wang 1994; Wang and Xiao 1995; Philip et al. 1998). The pH control on Cr(VI) reduction observed here is similar for both the early phase, rapid reduction observed within the first 20 h of each experiment, and for the first-order kinetics reduction observed after that. Figure 8 depicts the 2.5- and 5.0-h reduction rates as a function of solution pH. Figure 9 shows the rate constants for the first-order reactions, also as a function of solution pH. Each figure demonstrates that the primary control on the reduction rate is solution pH, with reduction accelerated under acidic conditions.

It is likely that the surface speciation of the cell wall functional groups controls the reaction rate. The bacterial cell wall becomes progressively more negatively charged with increasing pH due to successive deprotonation of functional groups such as carboxyl and phosphoryl (Fein et al. 1997). Because Cr(VI) is present in solution as an anionic species, there should be an increasing electrostatic repulsion between the Cr and the bacterial cell wall with increasing solution pH, slowing the reduction reaction significantly. These experimental results also suggest that proximity between aqueous Cr and the bacterial cell wall is required for Cr(VI) reduction reactions to proceed.

Figure 10 compares the reduction kinetics of *B. subtilis* with those of *S. putrefaciens* and *S. ureae*. Each experiment was conducted with the same concentration of bacteria by weight, under identical pH and ionic strength conditions, yet the *S. putrefaciens* and *S. ureae* experiments exhibit significantly faster and more extensive Cr(VI) removal from solution. It is interesting to note that most of the difference in extent of reaction is due to the more rapid early phase kinetics associated with the *S. putrefaciens* and *S. ureae* systems. Although we have few samples taken during the slower first-order reaction kinetics phase

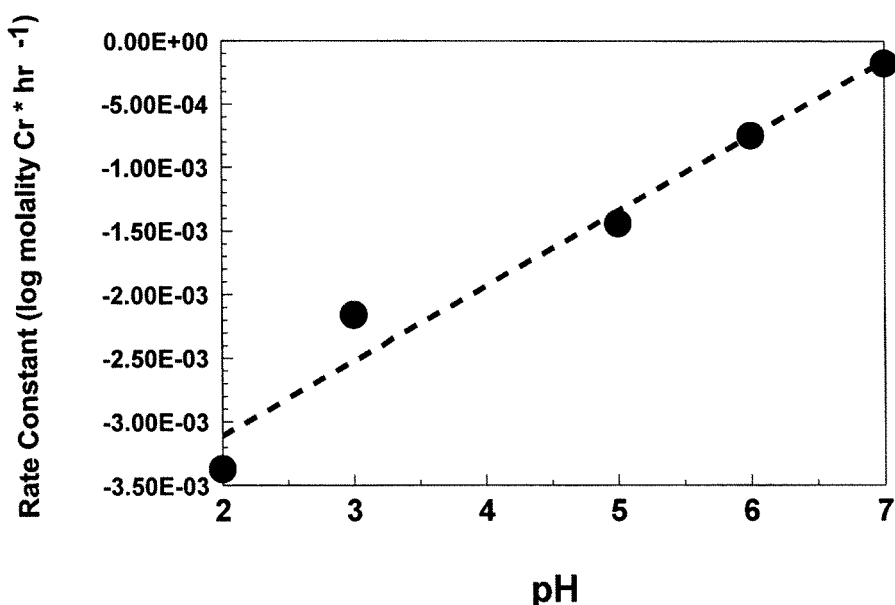


FIGURE 9 First-order rate constants (from linear portions of curves shown in Figure 7) as a function of solution pH. Experimental conditions described previously (see Figure 6).

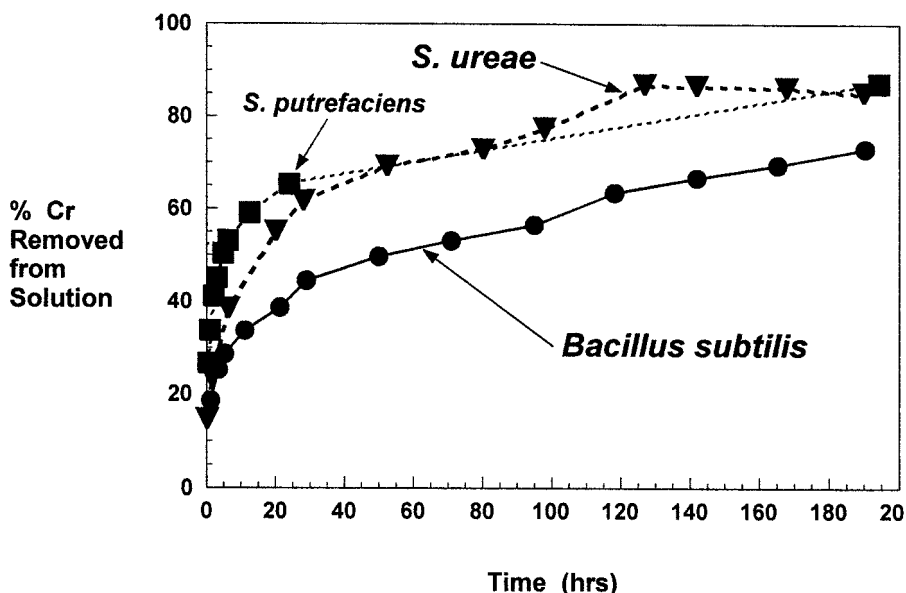


FIGURE 10 Comparison of Cr(VI) reduction kinetic data for systems containing *Bacillus subtilis* (circles), *Sporosarcina ureae* (triangles), and *Shewanella putrefaciens* (squares). All experiments conducted at pH 3.0, with 12 gm bacteria/L, with 5.0 ppm Cr(VI) in the starting solution of 0.1 M NaClO₄.

for *S. putrefaciens*, the data suggest that the rates during this second phase are similar between the three bacteria-bearing systems.

The experiments conducted with only 1.2 gm *B. subtilis*/L exhibit much slower removal rates of Cr from solution, yet the pH dependence appears to remain intact under conditions of lower bacterial concentration (Figure 11). For *B. subtilis*, we have data at two bacterial concentrations at both pH 3.0 and pH 7.0, and we use these data to calculate the mass-normalized Cr removal rates. We calculate an average rate for each experiment, using data corresponding to samples taken after 80 h, when rates appear to become steady. The mass-normalized rates from each bacterial concentration are approximately the same after 80 h for a given experimental pH. For the pH 3.0 experiments, the 12 gm *B. subtilis*/L and the 1.2 gm *B. subtilis*/L experiments yield an average rate of $10^{-7.50 \pm 0.25}$ mol Cr removed \cdot (gm bacteria/L)⁻¹ \cdot (h)⁻¹, with the uncertainty representing the 2 sigma error. For the pH 7.0 experiments, the 12 gm *B. subtilis*/L and the 1.2 gm *B. subtilis*/L experiments yield an average rate of $10^{-8.05 \pm 0.25}$ mol Cr removed \cdot (gm bacteria/L)⁻¹ \cdot (h)⁻¹.

The relative constancy of the mass-normalized removal rate for a given pH permits extrapolation of these data to environmentally relevant systems. For example, Cr contamination concentrations in groundwater on U.S. Department of Energy sites range from 0.42 to 9,010 μ g/L (Riley et al. 1992). Typical bacterial concentrations in soil range from 10⁶ to 10⁹ cells/gm soil (Barns and Nierzwicki-Bauer 1997), and a 2.5 gm/L bacterial suspension has approximately 10¹⁰ cells/mL. Using a value of 10⁷ cells/gm soil, and a soil porosity of 50%, yields an average concentration of 0.1 gm bacteria/L of groundwater. For this bacterial abundance in a groundwater system with a Cr concentration of 0.1 mg/L, the pH 7 mass-normalized reduction rate expression can be used to determine the length of time for reduction of all Cr(VI). Under these reasonably realistic conditions for a contaminated near-surface system, we calculate that nonmetabolic bacterial cell wall reduction of Cr(VI) will be complete in 2,160 h. The time for complete removal would be significantly less for

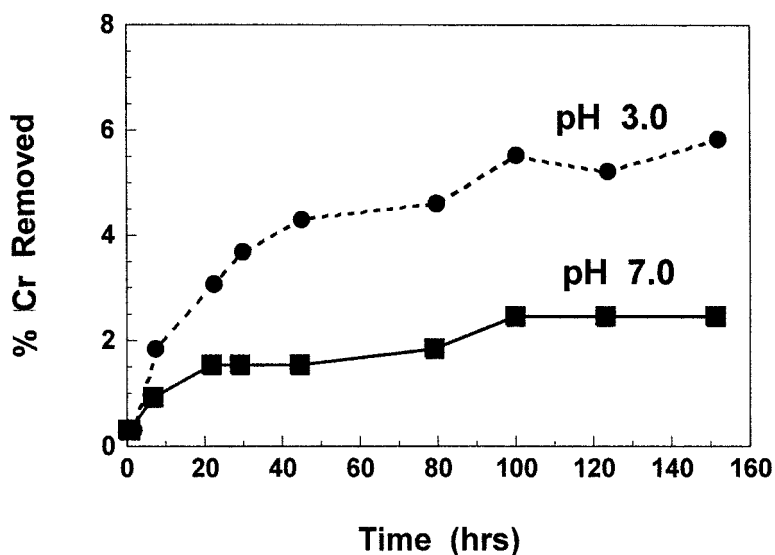


FIGURE 11 Kinetic data from pH 3.0 (circles) and pH 7.0 (squares) experiments. Both sets of experiments conducted with 1.2 gm *Bacillus subtilis*L, with 3.3 ppm Cr(VI) in the starting solution of 0.1 M NaClO₄.

lower pH conditions, and/or for higher bacterial concentrations. These calculations suggest that nonmetabolic bacterial cell wall reduction of Cr(VI) can significantly affect the fate of Cr under realistic environmental conditions.

The nonmetabolic Cr(VI) reduction observed in this study in the absence of externally added electron donors is likely a result of the oxidation of organic molecules within the cell wall, possibly the Cr-reducing enzymes responsible for metabolic enzymatic Cr(VI) reduction or cell wall cytochromes, which have large reduction potentials. Cr can serve as a strong oxidant for a wide range of organic molecules (e.g., Cainelli and Cardillo 1984), and these reactions typically are most rapid under acidic conditions. Our experiments suggest that in the absence of abundant external electron donors, there are molecules within the cell wall matrix that serve as electron donors for Cr(VI) reduction to Cr(III). This process is likely to be environmentally significant because under natural conditions most bacteria in the subsurface exist in nutrient-poor or -absent conditions. Our research indicates that Cr(VI) reduction can occur even under such conditions. In fact, under conditions of low metabolic activity, the nonmetabolic process may control the speciation, and hence the fate, of Cr in geologic environments.

References

- Bajt S, Clark SB, Sutton SR, Rivers ML, Smith JV. 1993. Synchrotron x-ray microprobe determination of chromate content using x-ray absorption near-edge structure. *Anal Chem* 65:1800-1804.
- Barns SM, Nierzwicki-Bauer SA. 1997. Microbial diversity in ocean, surface and subsurface environments. In: Banfield JF, Nealson KH, editors. *Geomicrobiology: interactions between microbes and minerals. Reviews in mineralogy*, vol 35. Washington, DC: Mineralogical Society of America. p 35-79.
- Bopp LH, Ehrlich HL. 1988. Chromate resistance and reduction in *Pseudomonas fluorescens* strain LB300. *Arch Microbiol* 150:426-431.
- Cainelli G, Cardillo G. 1984. *Chromium oxidations in organic chemistry*. Springer-Verlag: Berlin. 264 p.

- Daughney CJ, Fein JB. 1998. Sorption of 2,4,6-trichlorophenol by *Bacillus subtilis*. Environ Sci Technol 32:749–752.
- DeLeo PC, Ehrlich HL. 1994. Reduction of hexavalent chromium by *Pseudomonas fluorescens* LB300 in batch and continuous cultures. Appl Microbiol Biotechnol 40:756–759.
- Deng B, Stone AT. 1996a. Surface-catalyzed chromium(VI) reduction: the TiO₂-Cr^{VI}-mandelic acid system. Environ Sci Technol 30:463–472.
- Deng B, Stone AT. 1996b. Surface-catalyzed chromium(VI) reduction: reactivity comparisons of different organic reductants and different oxide surfaces. Environ Sci Technol 30:2484–2494.
- Ehrlich HL. 1996. Geomicrobiology, 3rd edition. New York: Marcel Dekker. 719 p.
- Fein JB, Boily J-F, Güçlü K, Kaulbach E. 1999. Experimental study of humic acid adsorption onto bacteria and Al-oxide mineral surfaces. Chem Geol 162:33–45.
- Fein JB, Daughney CJ, Yee N, Davis T. 1997. A chemical equilibrium model for metal adsorption onto bacterial surfaces. Geochim Cosmochim Acta 61:3319–3328.
- Fein JB, Delea DE. 1999. Experimental study of the effect of EDTA on Cd adsorption by *Bacillus subtilis*: a test of the chemical equilibrium approach. Chem Geol 161:375–383.
- Fowle DA, Fein JB. 1999. Competitive adsorption of metals onto bacterial surfaces: application of a surface complexation approach. Geochim Cosmochim Acta 63:3059–3067.
- Fowle DA, Fein JB. 2000. Experimental measurements of the reversibility of metal-bacteria adsorption reactions. Chem Geol 168:27–36.
- Horitsu H, Futo S, Miyazawa Y, Ogai S, Kawai K. 1987. Enzymatic reduction of hexavalent chromium by hexavalent chromium tolerant *Pseudomonas ambigua* G-1. Agri Biol Chem 51:2417–2420.
- Kashefi K, Lovley DR. 2000. Reduction of Fe(III), Mn(IV), and toxic metals at 100°C by *Pyrobaculum islandicum*. Appl Environ Microbiol 66:1050–1056.
- Koningsberger DC, Prins R. 1988. X-ray absorption: principles, applications, techniques of EXAFS, SEXAFS, and XANES. New York: Wiley. 673 p.
- Manceau A, Charlet L. 1992. X-ray absorption spectroscopic study of the sorption of Cr(III) at the oxide water interface. 1. Molecular mechanism of Cr(III) oxidation on Mn oxides. J Coll Inter Sci 148:425–442.
- Philip L, Iyengar L, Venkobachar C. 1998. Cr(VI) reduction by *Bacillus coagulans* isolated from contaminated soils. J Environ Eng 124:1165–1170.
- Riley RG, Zachara JM, Wobber FJ. 1992. Chemical contaminants on DOE lands and selection of contaminant mixtures for subsurface science research. Report ER-0547T, Washington, DC: U.S. Department of Energy.
- Schulze DG, Bertsch PM. 1995. Synchrotron X-ray techniques in soil, plant, and environmental research. Adv Agron 55:1–66.
- Shen H, Wang Y-T. 1994. Biological reduction of chromium by *E. coli*. J Environ Eng 120:560–572.
- Tebo BM, Obraztsova AY. 1998. Sulfate-reducing bacterium grows with Cr(VI), U(VI), Mn(IV), and Fe(III) as electron acceptors. FEMS Microbiol Lett 162:193–198.
- Urrutia Mera M, Kemper M, Doyle R, Beveridge TJ. 1992. The membrane-induced proton motive force influences the metal binding ability of *Bacillus subtilis* cell walls. Appl Environ Microbiol 58:3837–3844.
- Wang P-C, Mori T, Komori K, Sasatsu M, Toda K, Ohtake H. 1989. Isolation and characterization of an *Enterobacter cloacae* strain that reduces hexavalent chromium under anaerobic conditions. Appl Environ Microbiol 55:1665–1669.
- Wang Y-T, Shen H. 1995. Bacterial reduction of hexavalent chromium. J Indus Microbiol 14:159–163.
- Wang Y-T, Shen H. 1997. Modelling Cr(VI) reduction by pure bacterial cultures. Water Res 31:727–732.
- Wang Y-T, Xiao C. 1995. Factors affecting hexavalent chromium reduction in pure cultures of bacteria. Water Res 29:2467–2474.



PII S0016-7037(02)00947-X

X-ray absorption fine structure determination of pH-dependent U-bacterial cell wall interactions

S. D. KELLY,¹ K. M. KEMNER,^{1,*} J. B. FEIN,² D. A. FOWLE,^{2,†} M. I. BOYANOV,^{1,2} B. A. BUNKER,² and N. YEE¹¹Argonne National Laboratory, Argonne, IL60439, USA²University of Notre Dame, Civil Engineering and Geological Sciences, Notre Dame, IN46556, USA

(Received September 21, 2001; accepted in revised form April 23, 2002)

Abstract—X-ray absorption fine structure (XAFS) measurements was used at the U L3-edge to directly determine the pH dependence of the cell wall functional groups responsible for the absorption of aqueous UO_2^{2+} to *Bacillus subtilis* from pH 1.67 to 4.80. Surface complexation modeling can be used to predict metal distributions in water–rock systems, and it has been used to quantify bacterial adsorption of metal cations. However, successful application of these models requires a detailed knowledge not only of the type of bacterial surface site involved in metal adsorption/desorption, but also of the binding geometry. Previous acid-base titrations of *B. subtilis* cells suggested that three surface functional group types are important on the cell wall; these groups have been postulated to correspond to carboxyl, phosphoryl, and hydroxyl sites. When the U(VI) adsorption to *B. subtilis* is measured, observed is a significant pH-independent absorption at low pH values (<3.0), ascribed to an interaction between the uranyl cation and a neutrally charged phosphoryl group on the cell wall. The present study provides independent quantitative constraints on the types of sites involved in uranyl binding to *B. subtilis* from pH 1.67 to 4.80. The XAFS results indicate that at extremely low pH (pH 1.67) UO_2^{2+} binds exclusively to phosphoryl functional groups on the cell wall, with an average distance between the U atom and the P atom of 3.64 ± 0.01 Å. This U-P distance indicates an inner-sphere complex with an oxygen atom shared between the UO_2^{2+} and the phosphoryl ligand. The P signal at extremely low pH value is consistent with the UO_2^{2+} binding to a protonated phosphoryl group, as previously ascribed. With increasing pH (3.22 and 4.80), UO_2^{2+} binds increasingly to bacterial surface carboxyl functional groups, with an average distance between the U atom and the C atom of 2.89 ± 0.02 Å. This U-C distance indicates an inner-sphere complex with two oxygen atoms shared between the UO_2^{2+} and the carboxyl ligand. The results of this XAFS study confirm the uranyl-bacterial surface speciation model. Copyright © 2002 Elsevier Science Ltd

1. INTRODUCTION

Laboratory and field studies have demonstrated that bacterial cell walls efficiently adsorb a variety of aqueous metal cations (Beveridge and Murray, 1976; Gonçalves et al., 1987; Harvey and Leckie, 1985; Konhauser et al., 1993). Therefore, because bacteria are abundant in near-surface geologic systems, bacterial adsorption reactions can significantly affect metal mobilities in aqueous systems (Harvey et al., 1982; Ledin et al., 1999). The extent of adsorption of aqueous metals onto bacterial surfaces can vary markedly with changing conditions such as pH, ionic strength, and fluid composition (Ferris et al., 1989; Fein et al., 1997; Daughney et al., 1998; Fein and Delea, 1999; Fowle and Fein, 1999; Small et al., 1999, 2001). The effects of these changing conditions on adsorption/desorption reactions can be quantified by using one of two different approaches: partitioning relationships or surface complexation models. A number of studies have used partitioning approaches to model metal adsorption onto bacteria (Ferris et al., 1989; Mullen et al., 1989; Small et al., 1999, 2001; Beolchini et al., 2001). In view of the complexities associated with natural systems, partitioning adsorption models are relatively simple to apply because they do not require a detailed understanding of the nature of the

surfaces or adsorption mechanisms involved. That is, the extent of adsorption can be measured directly on a sample of material from the field, and a bulk partition coefficient can be determined that describes the distribution of the species of interest between the bacterial surface and the other phase or phases of interest. However, partition coefficient values under conditions not studied in the laboratory cannot be estimated theoretically from a set of measured partition coefficient values. Partition coefficient models cannot predict the distribution of metals in systems not previously studied.

Surface complexation models, which apply the formalism of aqueous ion association reactions to solute adsorption reactions with surfaces, require a detailed understanding not only of the surfaces involved, but also of the adsorption/desorption mechanisms. A surface complexation model treats the adsorbed metal as another metal species whose stability can be quantified with an equilibrium constant. By knowing all of the important reactions that exist in a system (and their stoichiometries), as well as the values of their equilibrium constants, the distribution of metals between various reservoirs (in aqueous solution, on mineral surfaces, on bacterial surfaces) can be explicitly calculated. The equilibrium constants that describe the extent of adsorption in surface complexation models are invariant with respect to most of the parameters affecting partition coefficients (Bethke and Brady, 2000; Koretsky, 2000).

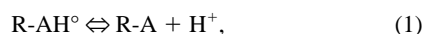
The surface complexation approach can be used to quantify bacterial adsorption of metal cations (Plette et al., 1995; Fein et

* Author to whom correspondence should be addressed (skelly@anl.gov).

† Present address: University of Windsor, Great Lakes Institute for Environment Research, Windsor, ON N9B 3P4.

al., 1997; He and Tebo, 1998; Fowle et al., 2000). For example, Fein et al. (1997) used acid-base titrations of *Bacillus subtilis* suspensions to determine acidity constants for the important surface functional groups and metal adsorption experiments to yield site-specific stability constants for the metal-bacterial surface complexes. However, these and subsequent batch adsorption experiments provide only circumstantial evidence regarding the mechanism of adsorption (or the stoichiometry of the adsorption reaction). Clearly, successful application of a surface complexation approach to quantifying bacterial adsorption of aqueous metal cations requires a detailed understanding of the binding mechanism. That information can be provided directly by using X-ray absorption fine structure (XAFS) spectroscopy.

Gram-positive cell walls are constructed of linear polymers of peptidoglycan covalently linked together around the cell membrane. The peptidoglycan forms a single giant macromolecule (~25 nm thick) rich in carboxyl and hydroxyl functional groups. The gram-positive cell wall is also composed of secondary polymers (e.g., teichoic acid) having phosphoryl functional groups (Beveridge and Murray, 1976, 1980). Numerous studies have shown that bacterial surfaces display pH-dependent charging and acid-base characteristics (Harden and Harris, 1953; Plette et al., 1995; Fein et al., 1997; Cox et al., 1999). These surface characteristics are controlled by the proton-active functional groups found on the cell wall. The surface complexation approach employed by Fein et al. (1997) models the acidity of these surface functional groups by using the equilibrium equation



where R denotes the bacterium to which each functional group type, A, is attached. The distribution of protonated and deprotonated sites can be quantified with the corresponding mass action equation

$$K_a = [\text{R-A}][\text{H}^{+}]/[\text{R-AH}^{\circ}]. \quad (2)$$

Here, $[\text{R-A}^{-}]$ and $[\text{R-AH}^{\circ}]$ represent the concentration of deprotonated and protonated surface species, respectively, and $[\text{H}^{+}]$ represents the activity of protons in solution. The notation pK_a represents the negative logarithm of the value of the equilibrium constant, K_a , for reaction 1. The data of Fein et al. (1997), Daughney et al. (1998), and Yee and Fein (2001) demonstrate that models involving three distinct types of surface organic acid functional groups (each with its own discrete pK_a value) provide an excellent fit to the observed protonation/deprotonation behavior of a wide range of bacterial species. Fein et al. (1997) reported pK_a values of 4.82, 6.9, and 9.4 for *B. subtilis* and postulated that the active surface functional groups correspond to carboxyl, phosphoryl, and hydroxyl groups, respectively. Cox et al. (1999) reported five pK_a values, ranging from 5.2 to 10.0. The spectroscopic data described in this study are independent of these bacterial surface charging models and can be used to provide some constraints on the bacterial surface functional groups responsible for binding under the experimental conditions.

Fein et al. (1997) observed negligible Cd, Cu, and Pb adsorption to *B. subtilis* under low-pH conditions, with adsorption increasing with increasing pH above approximately pH 3.0 as

the surface functional groups are successively deprotonated. Fowle et al. (2000) observed similar pH dependence for UO_2^{+2} adsorption to the same bacteria, along with significant uranyl adsorption even under low-pH conditions. The low-pH adsorption was ascribed to an interaction between the uranyl cation and a neutrally charged phosphoryl group on the cell wall. However, all of these models are based only on bulk adsorption data, and the nature and mechanism of metal binding to the cell walls have not been determined. XAFS measurements at the complexed metal absorption edge can distinguish between the different functional groups proposed to be important in metal uptake, thereby providing additional independent constraints on the stoichiometry of the adsorption reactions.

A number of U XAFS studies have investigated the interactions between U(VI) and solutions (Allen et al., 1995, 1996, 1997; Thompson et al., 1995, 1997; Docrat et al., 1999; Hay et al., 2000); sediments, soils, and soil constituents (Dent et al., 1992; Morris et al., 1996; Reich et al., 1996; Sturchio et al., 1998; Barger et al., 2000; Duff et al., 2000; Reeder et al., 2000); fungal biomass (Sarret et al., 1998); halophilic bacteria (Francis et al., 1998); and the gram-positive bacterium *B. subtilis* (Hennig et al., 2000). Other studies have used indirect methods, such as spectrophotometric and potentiometric measurements, to investigate the interaction between U and other heavy metals with *Zoogloea ramigera* biomass (Norber and Persson, 1984). However, to our knowledge, no systematic study of the pH-dependent sorption of U to bacterial cell membranes has been undertaken.

2. METHODS

2.1. Experimental Procedures

Suspensions of *B. subtilis* in 0.1 mol/L NaClO_4 were exposed to aqueous U solutions and allowed to equilibrate for 2 h, as determined sufficient by Fowle et al. (2000), under three different pH conditions. Samples U11, U12, and U13 contained 83 μm of U(VI) and 1.5 g (wet weight) of bacteria per liter at pH values of 1.67, 3.22, and 4.80, respectively. Samples Uh1, Uh2, and Uh3, respectively, contained 210 μm of U(VI) and 1.5 g (wet weight) of bacteria per liter at the same pH values. Biomass and sample preparation details were identical to those employed by Fowle et al. (2000). The pH values studied here cover the range examined by those authors. These samples therefore enable the use of XAFS for the determination of the different metal binding mechanisms that are responsible for the adsorption behavior observed by Fowle et al. (2000) over this pH range. After equilibration between the uranyl-bearing aqueous solution and the biomass, each experimental system was centrifuged at 10,000 g for 60 min, and the supernatant was removed. Fluorescence U $L_{3\text{-edge}}$ XAFS measurements were made on the wet, homogeneous biomass. The XAFS measurements were performed at the MRCAT sector 10-ID beamline (Segre et al., 2000) at the Advanced Photon Source.

The beamline optics and setup parameters for the U $L_{3\text{-edge}}$ XAFS measurements were as follows. The undulator was tapered by approximately 2 keV to reduce the variation in the incident intensity to less than 15% over the scanned energy range. The energy of the incident X-rays was scanned by using the Si(111) reflection of the double-crystal monochromator

running on the third harmonic of the beamline undulator. Higher harmonics were rejected with a Rh mirror. The incident and transmitted X-ray ion chambers were both filled with nitrogen gas. The fluorescence detector in the Stern-Heald geometry (Stern and Heald, 1983) was filled with Ar gas, and a Sr filter of three absorption lengths was used to reduce the background signal. The incident X-ray beam profile was 0.7 mm square. Linearity tests (Kemner et al., 1994) indicated less than 0.3% nonlinearity for a 50% decrease in incident X-ray intensity.

The results from the analysis of several solution standards are the foundation for the analysis of the U biomass data. The uranyl cations in the standards and the uranyl adsorbed to the biomass are likely to have similar local U atomic structure. From each standard, we gain well-characterized, isolated information of the interaction of uranyl with water, acetate, and phosphate groups. The hydrated uranyl standard provides a baseline view of the uranyl cation, and the acetate and phosphate standards represent the carboxyl and phosphoryl functional groups, respectively, in the biomass samples. This information is combined to constrain a model of the binding mechanism or mechanisms that control uranyl adsorption to biomass. In each model tested, we consider the uranyl bound to any combination of atoms (C, P, and/or H) in the second coordination shell, because of the attachment to different cell wall functional groups. Additionally, data from the standards were analyzed to assess the ability of FEFF7 (Zabinsky et al., 1995), a theoretical XAFS modeling code, to accurately model the uranyl cation's local chemical environment.

The aqueous uranyl standards include hydrated uranyl, uranyl acetate, and uranyl phosphate solutions. All uranyl standards were prepared by using a 1000-ppm uranyl nitrate stock solution. The hydrated uranyl sample (U-H₂O) was prepared by diluting the stock solution with deionized water. The standard had a final solution pH of 0.96. The uranyl acetate standard (U-C) was prepared by adding glacial acetic acid to the uranyl stock solution to achieve an acetate:U ratio of 100:1, then adjusting the final pH to 4.4 with NaOH. The uranyl phosphate standard (U-P) was prepared by adding concentrated phosphoric acid to the uranyl stock solution to achieve a phosphate:U ratio of 100:1, with a final pH of 1.5. The final U concentrations are ~2.9 and 3.4 mM for the U-P and U-C samples. Aqueous species calculations by FITEQL (Westall, 1982) in conjunction with the thermodynamic data of Grenthe et al. (1992) and Smith et al. (1997) for the U-C and U-P standard solutions indicate 11% UO₂(Ac), 42% UO₂(Ac)₂, 46% UO₂(Ac)₃, and 1% other species for the U-C standard and 46% UO₂(H₂PO₄), 48% UO₂(H₂PO₄)₂ and 6% other species for the U-P standard. These percentages indicate that the average number of near-neighbor C and P atoms to the uranyl in the U-C and U-P standards are ~2.33 and ~1.42, respectively. The X-ray absorption near-edge structure (XANES) standards include powder uraninite (UO₂) and γ -UO₃ purchased from Alfa Aesar, diluted approximately 1 to 100 in SiO₂ and measured in fluorescence mode. X-ray diffraction measurements indicate that the purity levels of the crystal phases of the XANES standards are ~95% uraninite (UO₂) for the U(IV) standard and ~95% γ -UO₃ for the U(VI) standard.

2.2. XAFS Analysis

2.2.1. XANES

Two energy scans were collected at three different locations on the sample to reduce radiation exposure. The sample was exposed for approximately 1 min for each of the scans at each location. Measuring two spectra at each location enabled determination of radiation-induced chemical effects at the 1-min timescale. No time-dependent change in the data was observed for any of the samples.

XANES is useful in determining the average valence state of U adsorbed to the biomass samples. The energy position of the edge step is directly related to the valence state of the uranium. Therefore, careful monitoring of the monochromator energy is paramount for making these comparisons. We used the transmission XAFS signal of a Y-foil as described elsewhere (Cross and Frenkel, 1998), as a reference for accurately aligning the edge energy positions of U(IV) (UO₂) and U(VI) (UO₃) powder standards, along with the U biomass data. The edge positions for the U(IV) and U(VI) standards differed by approximately 4.3 eV, as determined by the energy value at half the step height of the normalized data. For the 0.7-mm vertical beam size used in these experiments, the line width of the monochromator at 17 keV is ~4.0 eV. Additionally, the step accuracy of the monochromator at 17 keV is ± 0.13 eV (A. J. Kropf, private communication). For our experiments, the limiting factor in determining the valence state of the U in the biomass sample is purity of the XANES standards. A generous estimation of the uncertainty in the U valence state determination is $\pm 10\%$.

2.2.2. Extended XAFS

Detailed discussions of extended XAFS (EXAFS) theory can be found elsewhere (Stern and Heald, 1983). Here we give an overview of EXAFS spectroscopy and its role in determining the average atomic environment of the U atoms in these samples. The EXAFS signal for a particular element in a sample is the oscillatory part of the X-ray absorption coefficient above the adsorption edge of that element and can be written as the sum of the contributions from each path (*i*) of the photoelectron, generated by the absorption of an X-ray by the atom, as it scatters from the atoms surrounding the U atoms. It is useful to group the paths by symmetry by multiplying the individual contributions to the EXAFS signal by the degeneracy of each path N_{degen} . For the special case of a single-scattering event, N_{degen} represents the number of atoms in a shell about the U atoms.

The theoretical EXAFS models are constructed by the program FEFF7 (Zabinsky et al., 1995) on the basis of the crystal structure of uranyl acetate (Templeton et al., 1985) and hydrogen uranyl phosphate tetrahydrate (Morosin, 1978). Overlapping muffin-tin spheres were used in the FEFF7 calculation as reported previously (Hudson et al., 1995). FEFF7 calculates the values for $F_i(k)$, $\delta_i(k)$, and $\lambda(k)$, which are the effective scattering amplitude, the effective scattering phase shift, and the mean free path of the photoelectron, respectively. These variables depend on *k*, the photoelectron wave number, and are related to energy of the photoelectron (*E*) through the relationship $k^2 = 2m(E - E_0)/\hbar$. Here, *m* is the mass of an electron, E_0

Table 1. Fit range, ΔR ; data range, Δk ; number of independent points in the fit, N_{idp} ; number of variables determined in the fit, N_{var} ; degrees of freedom in the fit, ν ; reduced-chi-squared value, χ_{γ}^2 ; and r factor, R .^a

Sample	Model	ΔR (Å)	Δk (Å ⁻¹)	N_{idp}	N_{var}	ν	χ_{γ}^2	R %
U-H ₂ O	Hydrated	[1.0–3.2]	[2.0–10.7]	14	7	7	10	0.5
U-C	Acetate	[1.0–4.2]	[2.5–11.7]	20	14	6	9	0.5
U-P	Phosphate	[1.1–4.0]	[2.8–14.0]	22	13	9	8	1.6
Uh1, Uh2, Uh3	Biomass	[1.0–3.8]	[2.0–13.5]	20	9	11	33	0.9
U11, U12, U13	Biomass	[1.0–3.8]	[2.0–13.5]	20	9	11	37	0.6

^a Data were processed with k weight = 1, 2, and 3 in the Fourier transform. Full width of the Hanning window sill, $dk = 1 \text{ \AA}^{-1}$.

is the Fermi energy, and \hbar is Plank's constant. The structural EXAFS parameters that are often determined by a fit to data are N_{degen} (degeneracy of the path), ΔR_i (change in the half-path length), σ_i^2 (relative mean square displacement about the equilibrium path length), S_0^2 (passive electron reduction factor), and ΔE_0^1 (energy shift of the photoelectron). The parameters determined in the fits to the data are discussed in more detail in the following sections. The value for the EXAFS parameter S_0^2 was found to converge to 1.0 ± 0.10 for all U L3-EXAFS standard and biomass data. Therefore, S_0^2 was held to that value for all models.

Fits to the EXAFS data are made in R-space and obtained by taking the Fourier transform (FT) of $\chi(k)$. Because the EXAFS signal depends on $\sin[2kR_i + \delta_i(k)]$, a maximum in $|\text{FT } \chi(R)|$ amplitude occurs at positions close to the half-path length, R_i . In this work, we refer to the crystallographic positions of the atoms in terms of their actual distance in Å from the U atoms and their contribution to the Fourier transform of the data in terms of the distance in Å uncorrected for the photoelectron phase shift, $\delta_i(k)$. For example, a crystallographic position resulting in a U→O path of 2.3 Å will have a maximum contribution to the Fourier transform of the data at approximately 1.9 Å. (For a more detailed discussion of the photoelectron phase shift, see Stern and Heald, 1983.)

The data were analyzed by the codes from the UWXAFS package (Stern et al., 1995). These programs include AUTOBK (Newville et al., 1993) to remove the background, FEFFIT (Newville et al., 1995) to fit the theoretical model to the EXAFS data, and FEFF7 (Zabinsky et al., 1995) to create the theoretical model. The data sets were aligned and the backgrounds were removed by the AUTOBK program. The input parameter to AUTOBK that determines the maximum frequency of the background R_{bkg} was set to 0.8 Å. Two EXAFS measurements were taken at three different spots, for a total of six measurements. The resulting six $\chi(k)$ data sets were averaged. FEFFIT can also adjust the background in the fit and report the correlation between the background and the structural-fit parameters. We found that this correlation was always less than 60%, indicating that the background was not significantly affecting the structural-fit parameters. The fits were performed in R-space obtained by taking the Fourier transform of the $\chi(k)$ data. The data and fit ranges, along with the goodness-of-fit parameters, are listed in Table 1.

The definitions of the goodness-of-fit values for EXAFS data analysis are not standardized, and therefore they are given here. The goodness-of-fit values are the EXAFS reliability factor, R , and the reduced χ^2 value, χ_{γ}^2 . Here, γ is the number of degrees of freedom in the fit, given by the number of independent

points, N_{idp} , in the fit, minus the number of parameters determined in the fit (Stern, 1993).

The value for χ_{γ}^2 is normalized by the uncertainty in the measurement and has both statistical and systematic contributions. The contribution to the uncertainty from statistical noise can be obtained by measuring the fluctuations in R-space between 15 and 25 Å. If the uncertainties are purely random with no systematic error, the χ_{γ}^2 value is expected to be close to one. Typically, however, the χ_{γ}^2 value is much larger. This could indicate either an incorrect model or dominance of systematic errors. To identify the sources of uncertainties, an EXAFS reliability factor, R , is calculated. The reliability factor is the sum of the differences between the model value and data squared, divided by the sum of the squares of the data. Good fits occur for R values of a few percent. With such values of R , the large value for χ_{γ}^2 can confidently be attributed to systematic errors. The quoted uncertainties in fitted parameters are multiplied by χ_{γ}^2 to correct for an underestimation of the uncertainties in the value for χ_{γ}^2 .

3. RESULTS

3.1. XANES

An example of the aligned and normalized absorption data from the standards and U biomass at pH = 1.67 is shown in Figure 1. The data clearly indicate that the U(VI) added to the biomass solution was not reduced to U(IV) by either the bacterial biomass or X-ray radiation, because the edge position is

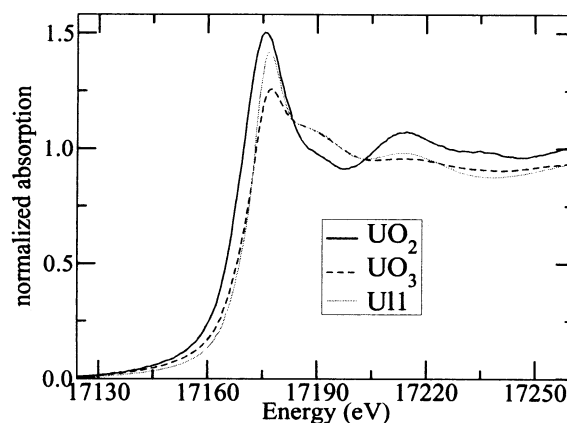


Fig. 1. Normalized adsorption data for U(VI) and U(IV) standards UO_3 and UO_2 , respectively, and U11 data.

Table 2. Description of the paths included in the models followed by their parameterization in terms of the XAFS parameters determined in the fit to the uranyl standards.

Path ^a	R (Å) ^b	N _{degen} ^c	Amp ^d (%)	N _{degen}	ΔR _i	σ ²	ΔE _{0i}
U→Oax	1.76	1	100	2	ΔR ₁	σ ₁ ²	ΔE ₀₁
U→Oeq	2.45	1	100	N ₂	ΔR ₂	σ ₂ ²	ΔE ₀₂
U→Oeq ^e	2.33	1	100	N ₃	ΔR ₃	σ ₂ ²	ΔE ₀₂
U→C1 ^f	2.85	3	53	N ₄	ΔR ₄	σ ₄ ²	ΔE ₀₃
U→Oeq→C1 ^f	3.29	12	30	4 × N ₄	ΔR ₅	σ ₅ ²	0.5 × ΔE ₀₂ + 0.5 × ΔE ₀₃
U→Oax1→U→Oax1	3.52	2	20	2	2 × ΔR ₁	2 × σ ₁ ²	ΔE ₀₁
U→Oax1→Oax2	3.52	2	17	2	2 × ΔR ₁	2 × σ ₁ ²	ΔE ₀₁
U→Oax2→U→Oax1	3.52	2	28	2	2 × ΔR ₁	2 × σ ₁ ²	ΔE ₀₁
U→p ^e	3.60	4	32	N ₆	ΔR ₆	σ ₆ ²	ΔE ₀₂
U→Oeq→P ^e	3.72	8	26	2 × N ₆	ΔR ₆	σ ₆ ²	ΔE ₀₂
U→C2 ^f	4.35	3	13	N ₄	ΔR ₇	σ ₇ ²	ΔE ₀₃
U→C1→C2 ^f	4.35	6	33	2 × N ₄	ΔR ₇	σ ₇ ²	ΔE ₀₃
U→C1→C2→C1 ^f	4.35	6	20	N ₄	ΔR ₇	σ ₇ ²	ΔE ₀₃

^a Atom types in the scattering path.

^b Initial path length from the theoretical models.

^c Degeneracy from the theoretical models.

^d Amplitude ratio relative to the first path, with assumed degeneracy calculated by FEFF7.

^e Additional paths for the uranyl phosphate standard.

^f Additional paths for the uranyl acetate standard.

consistent with the U(VI) standard and not the U(IV) standard. The U XANES data from these experiments indicate a single U(VI) valence state.

3.2. EXAFS

Each of the reference compounds is closely related to the others and to the U biomass data. The signal from uranyl is expected to be a part of the signal in each of the other data sets. Therefore, the hydrated uranyl model is used as a starting point for each of the other models.

3.2.1. Hydrated uranyl

All scattering paths used and parameters determined in the fit of the hydrated uranyl (U-H₂O) data are listed in Table 2, with the parameters constrained in the fit written in terms of the constraining relationship. This best-fit model for the hydrated uranyl sample consists of two axial oxygen (Oax) atoms and approximately six equatorial oxygen (Oeq) atoms (Table 2), Figure 2 shows the structure of the uranyl moiety, a uranium atom with two closely bound Oax atoms, and approximately six Oeq atoms, which would be the O atoms from the waters of hydration for the hydrated uranyl standard. The acetate/phosphate group also shown in Figure 2 is for the other uranyl aqueous standards. Other studies of crystalline uranyl compounds have reported a split Oax distance of 0.001 to 0.03 Å (Morosin, 1978; Mercier et al., 1984; Templeton et al., 1985). Therefore, two Oax distances were considered but were found to be unnecessary with the XAFS resolution of 0.14 Å determined from the data range listed in Table 1. Multiple-scattering paths from the Oax atoms were found to contribute significantly in the fit region. This result is due partially to the tight binding of the Oax atoms to the U, as determined by the small σ² value (Table 3) and the linearity of the Oax-U-Oax bond. The data and best-fit model for the hydrated uranyl are shown

in Figure 3a and b. The model follows the data well over the entire fit range of 1.0 to 3.2 Å, including the multiple-scattering region (2.5 to 3.2 Å), whereas the parameterization for the multiple-scattering paths was completely determined from the single-scattering U→Oax path (Table 2). The degeneracy

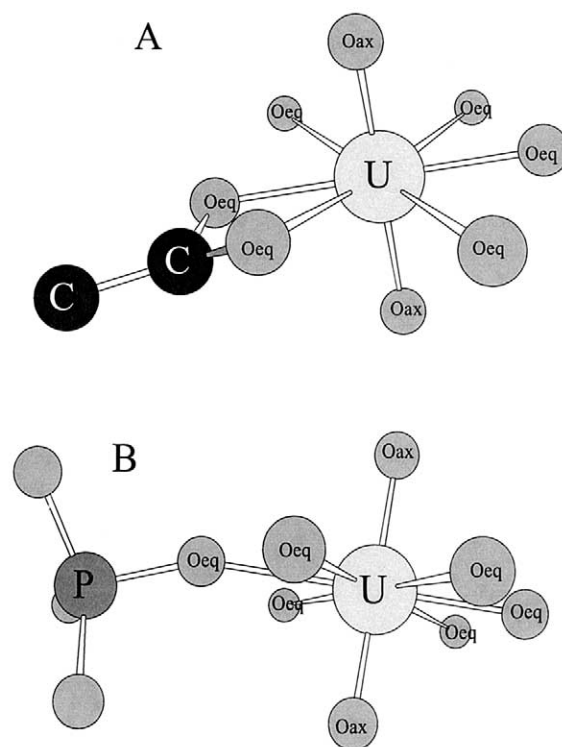


Fig. 2. (A) Bidentate binding of the uranyl to an acetate group. (B) Monodentate binding of the uranyl to a phosphate group.

Table 3. Paths, initial path length (R), and parameters (N_{degen} , ΔR_i , σ_i^2 , ΔE_{0i}) determined in the fit to each series of U biomass data.

Path	R (Å)	N_{degen}	ΔR_i (Å)	σ_i^2 (Å ²)	ΔE_{0i}
U→Oax	1.79	2	ΔR_1	σ_1^2	ΔE_{01}
U→Oeq1	2.28	N_2	ΔR_2	σ_2^2	ΔE_{02}
U→Oeq2	2.49	N_3	ΔR_3	σ_3^2	ΔE_{02}
U→C	2.85	N_4	ΔR_4	σ_4^2	ΔE_{02}
U→Oeq→C	3.29	$4 \times N_4$	ΔR_5	σ_4^2	ΔE_{02}
U→Oax→Oax2	3.58	2	$2 \times \Delta R_1$	$2 \times \sigma_1^2$	ΔE_{01}
U→Oax1→U→Oax2	3.58	2	$2 \times \Delta R_1$	$2 \times \sigma_1^2$	ΔE_{01}
U→Oax2→U→Oax1	3.58	2	$2 \times \Delta R_1$	$2 \times \sigma_1^2$	ΔE_{01}
U→P	3.74	N_6	ΔR_6	σ_6^2	ΔE_{02}
U→Oeq→P	3.82	$2 \times N_6$	ΔR_6	σ_6^2	ΔE_{02}

(N_{degen}) of each multiple-scattering path is two because there are two equivalent paths (i.e., U→Oax1→Oax2 and U→Oax2→Oax1 are equivalent paths).

3.2.2. Aqueous uranyl acetate

All scattering paths used and parameters determined in the fit of the aqueous uranyl acetate complex (U-C) standard are listed in Table 2. The uranyl structure with a single acetate group attached is illustrated in Figure 2A. This best-fit model for the uranyl acetate sample consists of two Oax atoms, approximately six Oeq atoms, approximately three carbon (C1) atoms at 2.89 Å and three more carbon (C2) atoms at 4.37 Å, multiple-scattering from the Oeq atoms to the C1 atoms, multiple-scattering from the Oax atoms, and multiple-scattering between the two nearly linear carbon (C1-C2) atoms. This model is identical to the hydrated uranyl model described above, with the addition of two carbon shells to account for the acetate group attached to the uranyl (Fig. 2A). The importance of the multiple-scattering paths is illustrated by the amplitude ratios in Table 2. If these paths are not included in the model, the χ_γ^2 value increases only slightly because the coordination numbers for the Oeq and C paths increase to unrealistic values to compensate for the loss of amplitude from these important multiple-scattering paths. The data and best-fit model for the aqueous uranyl acetate complex are shown in Figure 3c and d. The model follows the data well over the entire fit range (1.0 to 4.2 Å). The individual contributions for carbon atoms are apparent; the arrows in Figure 3c mark a feature in the uranyl acetate data that is due to the carbon atoms and is not present in the hydrated uranyl data (Fig. 3a).

3.2.3. Aqueous uranyl phosphate

The aqueous uranyl phosphate (U-P) data are shown in Figure 3e and f. The arrows in Figure 3e mark the signals in the Fourier transform due to the phosphorus. Diffraction results (Morosin, 1978; Mercier et al., 1984) for solid uranyl phosphate compounds report U→P distances in the range 3.60 to 3.70 Å. They also report a split in the Oeq shell due to the phosphate. Building on the previously described hydrated uranyl model, we modeled the aqueous uranyl phosphate data with an Oax path, two Oeq paths, multiple-scattering paths from the Oax atoms, a U→P path at approximately 3.6 Å, and a multiple-scattering path U→Oeq→P (Fig. 2B). These paths and their parameterizations are in Table 2. The Oax and corresponding multiple-scattering paths are described in section

3.2.1. The addition of another U→Oeq shell and U→P shell accounts for the phosphate attached to the uranyl. The data and best-fit model are shown in Figure 3e and f. The model follows the data well over the entire fit range (1.1 to 4.0 Å). The arrows in Figure 3e mark the contribution from the P shell that was not needed to describe the hydrated uranyl data (Fig. 3a). The data and fit ranges, along with the goodness-of-fit parameters for this fit, are in Table 1. The significance of the multiple-scattering P paths is illustrated by the amplitude ratios relative to the first oxygen shell (Table 2), and also by the goodness-of-fit values. Including these multiple-scattering paths reduced the χ_γ^2 value by a factor of three.

3.3. U Biomass

The analysis of the hydrated uranyl, aqueous uranyl acetate, and aqueous uranyl phosphate standards described in the previous sections established a qualitative fingerprint for water, acetate, and phosphate groups bound to the uranyl cation. The Fourier transforms of the U biomass data at three different pH values for the lower (U1 series) and higher (Uh series) U concentrations are shown in Figures 4 and 5, respectively. Qualitative observation of these figures indicates that with increasing pH (U11→U12→U13, Uh1→Uh2→Uh3), (1) the signal due to the U→P shell decreases, (2) the signal due to the U→C shell increases, and (3) the signal due to the U→Oeq shell decreases.

The model for the U biomass data combines the paths from the hydrated uranyl, aqueous uranyl acetate, and aqueous uranyl phosphate standards (Table 2). Table 3 summarizes these paths and their parameterization. This model includes two Oax atoms, two shells of equatorial oxygen atoms (Oeq1 and Oeq2), a shell of carbon (C) atoms at approximately 2.85 Å, multiple-scattering paths from the Oeq atoms to the C atom, multiple-scattering paths from the two tightly bound Oax atoms, a shell of phosphorus (P) atoms at approximately 3.74 Å, and multiple-scattering paths from the Oeq atoms to the P atoms. The mean square displacement (σ^2) values for the two Oeq shells were constrained to the same value.

Each data set was tested for the presence of the C and P paths in the fit region (2.0 to 3.8 Å). These tests were performed by fitting each data set with and without the C paths and then again with and without the P paths while simultaneously monitoring the goodness-of-fit parameters. All of the U biomass data needed the contribution from the P paths. For the lowest-pH data, Uh1 and U11, the C path was not needed. The χ_γ^2 value

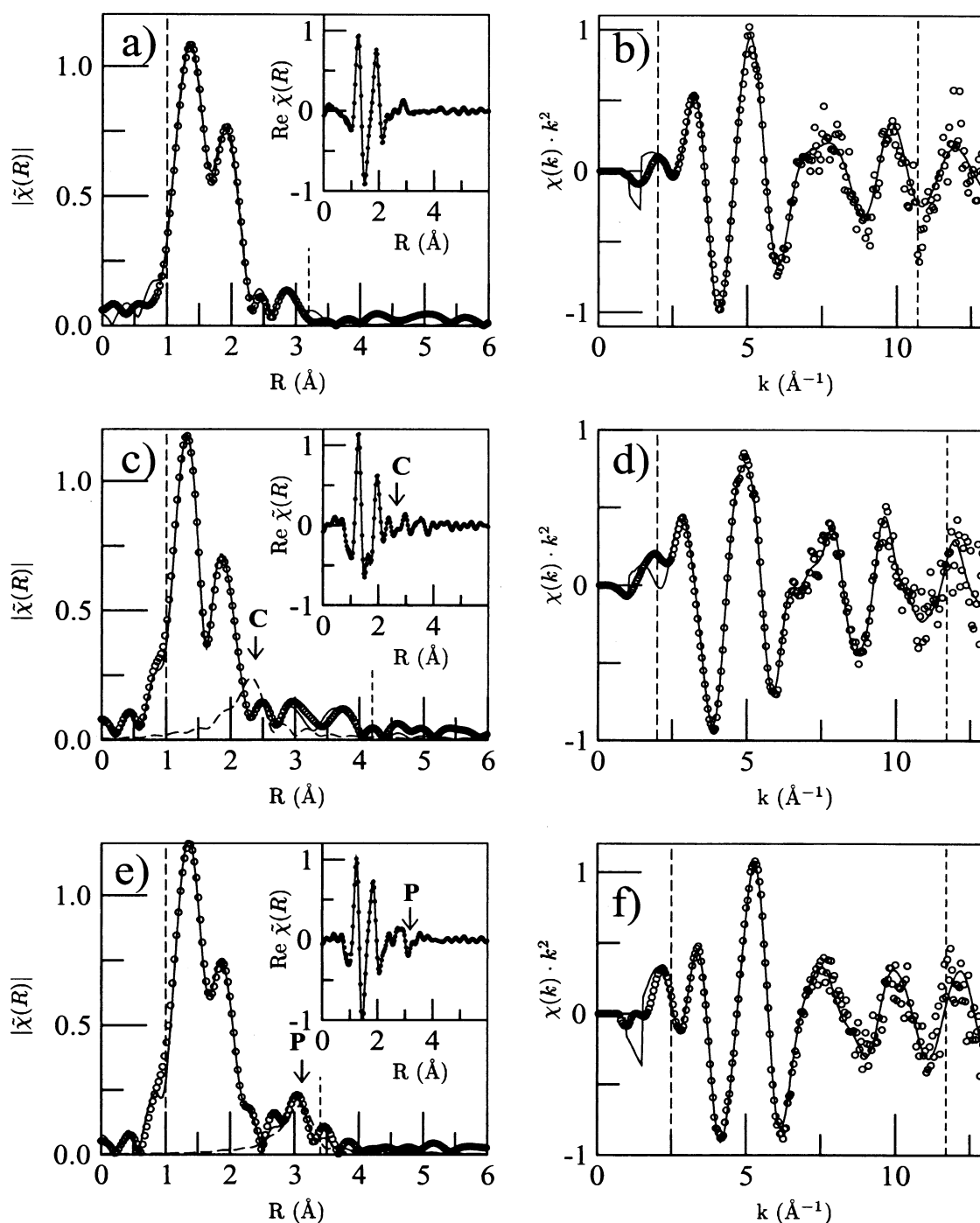


Fig. 3. Data (circles) and best-fit model (line) for the aqueous uranyl standards. (a) Magnitude of Fourier transform, with inset showing real part of Fourier transform for the U-H₂O data. (b) $\chi(k) \times k^2$ for the U-H₂O data. (c) Magnitude of Fourier transform, with inset showing real part of Fourier transform for the U-C data. (d) $\chi(k) \times k^2$ for the U-C data. (e) Magnitude of Fourier transform, with inset showing real part of Fourier transform for the U-P data. (f) $\chi(k) \times k^2$ for the U-P data.

did not change significantly (34 to 29) with a decrease in the degrees of freedom in the fit from 8 to 4 due to the addition of the C paths. Therefore, these paths were not included in the models for lowest-pH data. In contrast, for the higher-pH data, inclusion of the C path was found to be significant, decreasing the χ^2_{ν} value from 58 to 23.

These models were fitted simultaneously to each series of data, U11, U12, and U13 for the low uranyl concentration and Uh1, Uh2, and Uh3 for the high uranyl concentration. The simultaneous fitting was performed in R-space by using k weighting of 1, 2, and 3 for each data set. Therefore, the model was optimized to nine data sets. The data and best-fit model for

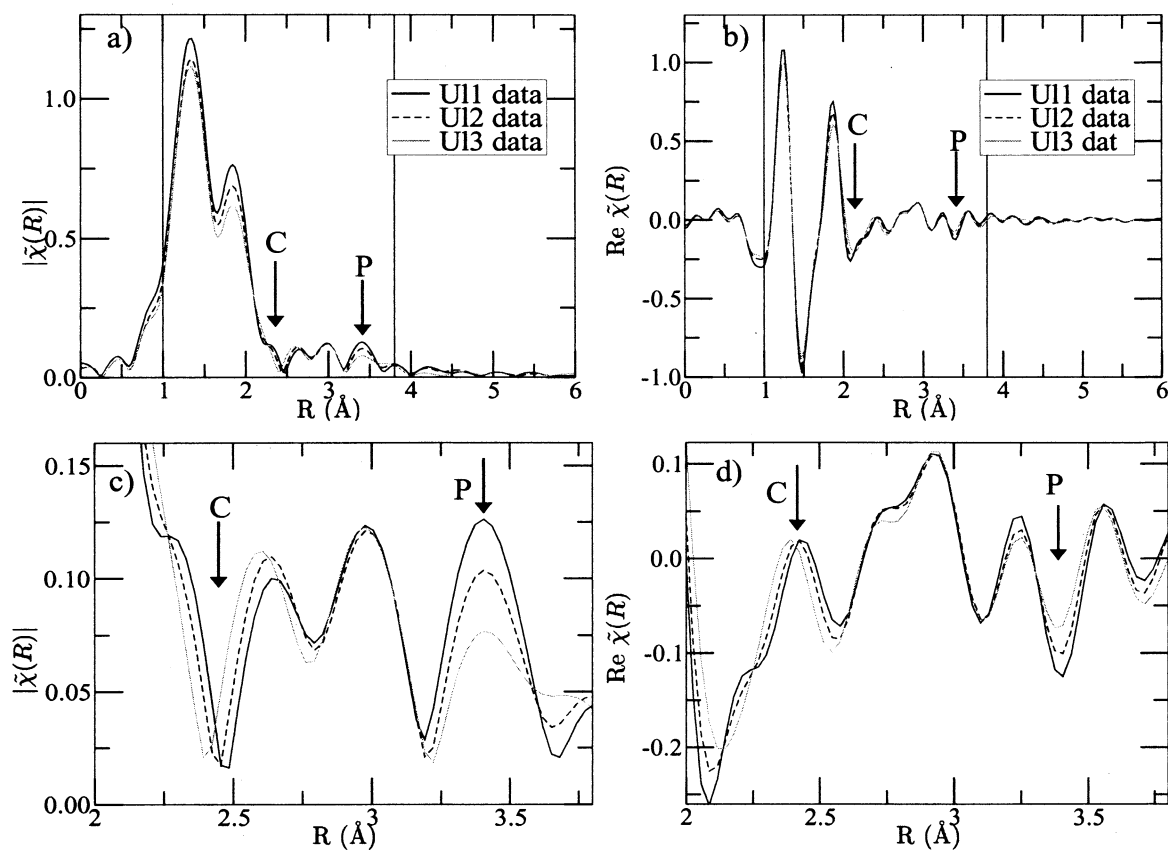


Fig. 4. Comparison of U biomass data U11, U12, and U13. (a) Magnitude of Fourier transform. (b) Real part of Fourier transform. (c) Enlargement of C and P regions in magnitude of Fourier transform. (d) Enlargement of C and P regions in real part of Fourier transform.

the U11 data processed with a k -weighting values of 1, 2, and 3 in the Fourier transform are shown in Figure 6. By use of all three k -weighting values decreases the correlation between the best-fit values for the local atomic uranyl structure, which have different k dependencies. For each series of data, the path length (R_i) values were constrained to a single best-fit value independent of pH. The mean square displacement values were also constrained to a single best-fit value independent of pH, except for the Oeq shell, for which we determined that a pH-dependent σ^2 value was required. The best-fit values for these parameters are listed in Table 4. The data and best-fit model for both the low (U11, U12, and U13) and high (Uh1, Uh2, and Uh3) series, respectively, illustrated with a k weighting of 2 in the Fourier transform, are shown in Figures 7 and 8. The model is in agreement with the data over the entire fit range (1.1 to 3.8 Å) for each pH value.

4. DISCUSSION

4.1. Aqueous Uranyl Standards

4.1.1. Hydrated uranyl

Our XAFS results for the aqueous hydrated uranyl standard are listed in Table 5. The Fourier transform of the data and best-fit model are shown in Figure 3. Our XAFS result for the

Oax distance (1.78 ± 0.01 Å) is similar to the distance reported for other aqueous (1.70 to 1.81 Å) (Antonio et al., 2001) and solid (1.75 to 1.79 Å) (Morosin, 1978; Mercier et al., 1984; Templeton et al., 1985) uranyl compounds. Our XAFS result for the U→Oax σ^2 -value (0.002 ± 0.001 Å²) is similar to values (0.002 to 0.005 Å²) for other aqueous complexes (Allen et al., 1997) and solid (Barger et al., 2000) uranyl compounds. For the uranium to Oeq atoms (U→Oeq), we found a number, distance, and σ^2 value of 6.0 ± 0.4 , 2.42 ± 0.01 Å, and 0.009 ± 0.001 Å², respectively. These values are similar to the number of equatorial waters (4 to 6) (Allen et al., 1997; Thompson et al., 1997; Antonio et al., 2001); the U→Oeq bond lengths (2.41 to 2.43 Å) (Mercier et al., 1984; Allen et al., 1997); and the σ^2 values (0.007 Å²) (Allen et al., 1997) reported previously for U→Oeq of a hydrated uranyl.

4.1.2. Aqueous uranyl acetate

Our XAFS results for the aqueous uranyl acetate standard are in Table 5. The Fourier transform of the data and best-fit model are shown in Figure 3. Our XAFS results for the U→Oax path in the aqueous uranyl acetate standard (bond length 1.78 ± 0.01 Å and mean square displacement 0.001 ± 0.001 Å²) are the same, within the experimental uncertainties, as for the

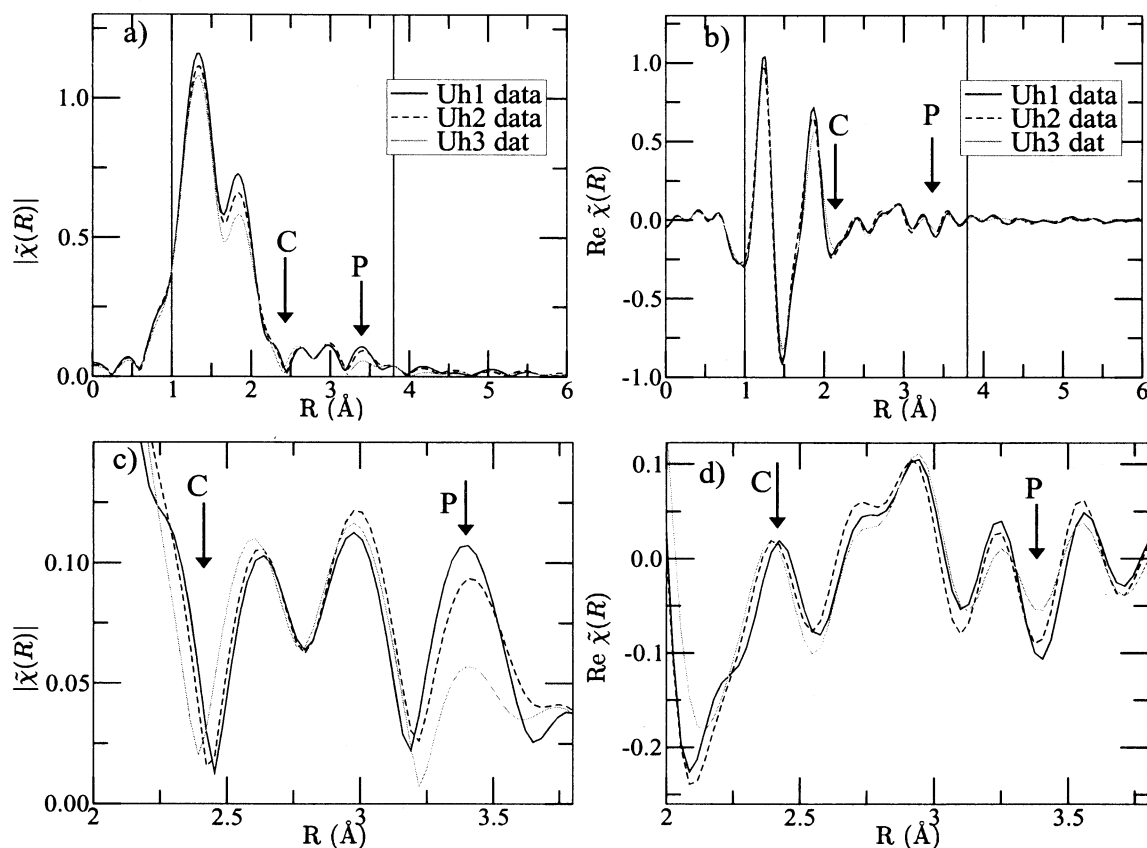


Fig. 5. Comparison of U biomass data Uh1, Uh2, and Uh3. (a) Magnitude of Fourier transform. (b) Real part of Fourier transform. (c) Enlargement of C and P regions in magnitude of Fourier transform. (d) Enlargement of C and P regions in real part of Fourier transform.

hydrated uranyl standard discussed in section 4.1.1. Within the experimental uncertainties, the best-fit values for the $U \rightarrow O_{eq}$ path for the number of O_{eq} atoms (6.0 ± 1.2) and the mean square displacement value ($0.009 \pm 0.002 \text{ \AA}^2$) are the same as the results for the hydrated uranyl standard results discussed in section 4.1.1. The $U-O_{eq}$ bond length has increased from $2.42 \pm 0.01 \text{ \AA}$ for the hydrated uranyl to $2.47 \pm 0.02 \text{ \AA}$ for the aqueous uranyl acetate complex. This bond length ($2.47 \pm 0.02 \text{ \AA}$) compares well with the $U-O_{eq}$ bond length (2.46 \AA) (Allen et al., 1995; Reich et al., 1996) for aqueous $[(UO_2)_3(CO_3)_6]^{6-}$, in which all of the uranyl equatorial oxygen atoms are part of a bidentate carbonate. It is also within the range (2.41 to 2.47 \AA) of bond lengths reported for several types of solid $U-O_{eq}-C$ compounds (Allen et al., 1995; Templeton et al., 1985; Barger et al., 2000). Our XAFS result for the number of carbon (C1) atoms is 3.0 ± 1.5 , indicating that each O_{eq} atom is associated with a carboxyl group (Fig. 2A). The parameterizations listed in Table 2 show that the number of O_{eq} and C1 have not been constrained. On the basis of calculations for aqueous species (section 2.1) the average number of C1 atoms (2.33) is consistent with our XAFS results (3.0 ± 1.5). Our best-fit value for the $U \rightarrow C$ distance ($2.90 \pm 0.02 \text{ \AA}$) and our σ^2 value ($0.003 \pm 0.004 \text{ \AA}^2$) are similar to the values (2.90 \AA and 0.004 \AA^2) (Allen et al., 1995) for aqueous $[(UO_2)_3(CO_3)_6]^{6-}$. Our $U \rightarrow C$ distance ($2.90 \pm 0.02 \text{ \AA}$) is also similar to the previously

reported distances (2.86 to 2.94 \AA) for several chelating (bidentate) solid uranyl-carbon complexes (Howatson et al., 1975; Allen et al., 1995; Barger et al., 2000). Bridging (monodentate) acetate $U \rightarrow C$ distances are longer at 3.98 \AA (Howatson et al., 1975).

4.1.3. Aqueous uranyl phosphate

Our XAFS results for the aqueous uranyl phosphate standard are in Table 5. The Fourier transform of the data and best-fit model are shown in Figure 3. The best-fit values for the two O_{ax} atoms are consistent with those found for the hydrated uranyl standard discussed previously. Our XAFS result for the short O_{eq1} distance of $2.32 \pm 0.02 \text{ \AA}$ compare well with the values (2.31 to 2.35 \AA) reported from diffraction measurements of crystalline structures (Morosin, 1978; Mercier et al., 1984), indicating that we have correctly assigned them to the phosphate groups. Our XAFS results for the longer O_{eq} distance of $2.47 \pm 0.03 \text{ \AA}$ compares well with previously reported values for a hydrated O_{eq} distance (Mercier et al., 1984; Antonio et al., 2001). The σ^2 value for the $U \rightarrow O_{eq}$ path ($0.002 \pm 0.002 \text{ \AA}^2$) is less than the value for the hydrated equatorial uranyl and aqueous uranyl acetate models ($0.009 \pm 0.001 \text{ \AA}^2$). This decrease is due to the removal of a structural σ^2 component included in the single O_{eq} shell model. Constraining our σ^2

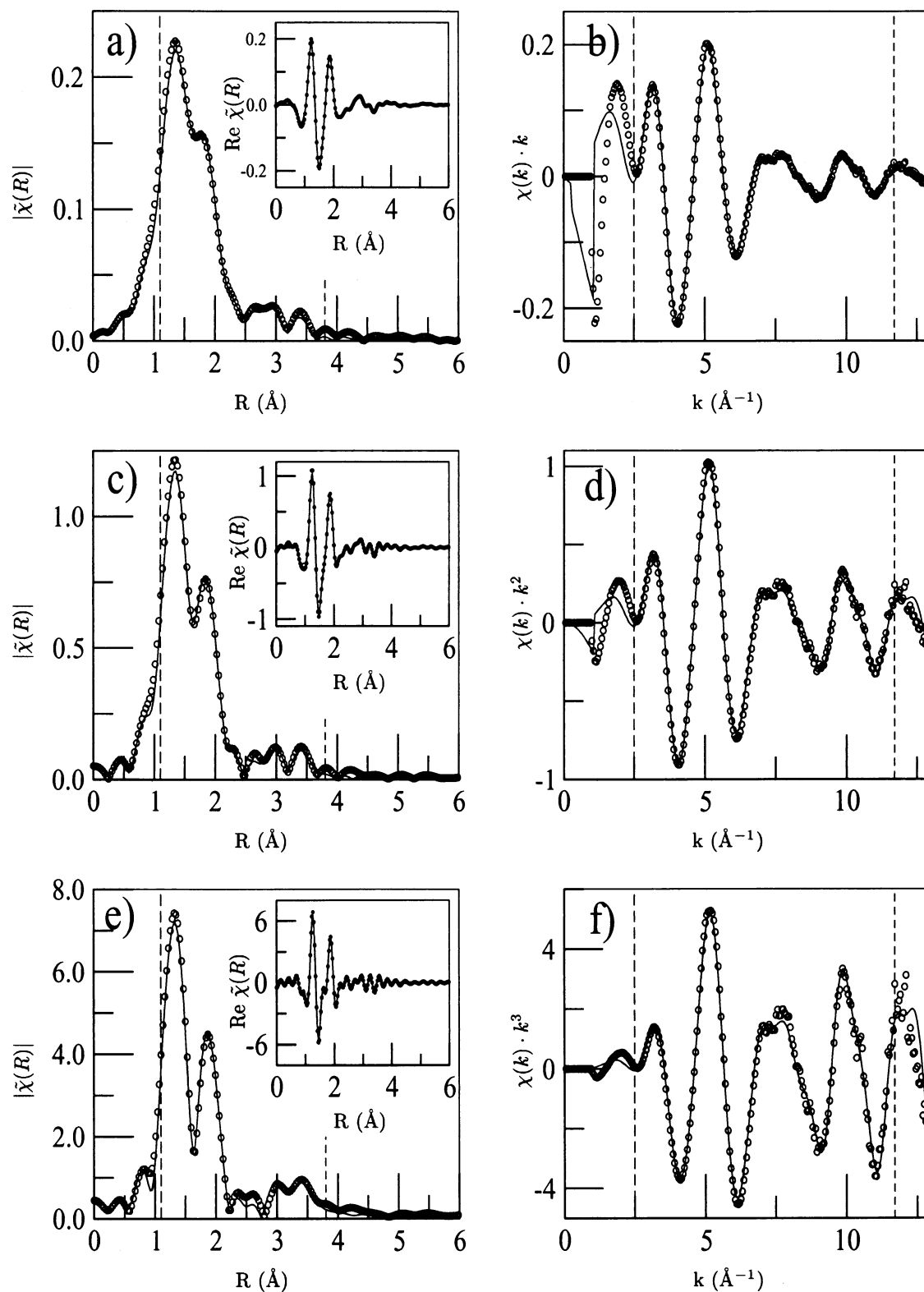


Fig. 6. Data (circles) and best-fit model (line) for U biomass data, U11. (a) Magnitude of Fourier transform, with real part of Fourier transform processed with a k weighting of 1 (inset). (b) $\chi(k) \times k^1$. (c) Magnitude of Fourier transform, with real part of Fourier transform processed with a k weighting of 2 (inset). (d) $\chi(k) \times k^2$. (e) Magnitude of Fourier transform, with real part of Fourier transform processed with a k weighting of 3 (inset). (f) $\chi(k) \times k^3$.

Table 4. Best-fit values for the pH-independent parameters for local structure about uranium sorbed to biomass.

Path	N_{degen}	R (Å)	σ^2 (10^{-3} Å ²)	E_0 (eV)
			UI1, UI2, UI3	
U→Oax	2.0 ^a	1.77 ± 0.01	2 ± 1	0.2 ± 0.9
U→Oeq1	N ₂	2.33 ± 0.02	4, 7, 10 ± 3	4.4 ± 1.1
U→Oeq2	N ₃	2.45 ± 0.02	4, 7, 10 ± 3	4.4 ± 1.1
U→C	N ₄	2.89 ± 0.02	1 ± 5	4.4 ± 1.1
U→Oeq→C	4 × N ₄	3.32 ± 0.02	1 ± 5	4.4 ± 1.1
U→Oax1→U→Oax1	2.0 ^a	3.53 ± 0.01	3 ± 1	0.2 ± 0.9
U→Oax1→Oax2	2.0 ^a	3.53 ± 0.01	3 ± 1	0.2 ± 0.9
U→Oax1→U→Oax2	2.0 ^a	3.53 ± 0.01	3 ± 1	0.2 ± 0.9
U→P	N ₆	3.64 ± 0.01	3 ± 3	4.4 ± 1.1
U→Oeq1→P	2 × N ₆	3.78 ± 0.01	3 ± 3	4.4 ± 1.1
			Uh1, Uh2, Uh3	
U→Oax	2.0 ^a	1.76 ± 0.01	2 ± 1	1.0 ± 0.7
U→Oeq1	N ₂	2.32 ± 0.02	4, 6, 9 ± 2	5.2 ± 0.9
U→Oeq2	N ₃	2.45 ± 0.02	4, 6, 9 ± 2	5.2 ± 0.9
U→C	N ₄	2.89 ± 0.02	2 ± 4	5.2 ± 0.9
U→Oeq→C	4 × N ₄	3.33 ± 0.02	2 ± 4	5.2 ± 0.9
U→Oax1→U→Oax1	2.0 ^a	3.53 ± 0.01	4 ± 1	1.0 ± 0.7
U→Oax1→Oax2	2.0 ^a	3.53 ± 0.01	4 ± 1	1.0 ± 0.7
U→Oax1→U→Oax2	2.0 ^a	3.53 ± 0.01	4 ± 1	1.0 ± 0.7
U→P	N ₆	3.64 ± 0.01	2 ± 3	5.2 ± 0.9
U→Oeq1→P	2 × N ₆	3.77 ± 0.01	2 ± 3	5.2 ± 0.9

^a Values without uncertainties were held constant during the fit.

values to 0.01 Å², as has been done in earlier work (Barger et al., 2000), results in an overestimation of the number of Oeq atoms in our system. For our XAFS data, the amount of overestimation corresponds to ~40% for Oeq shells. On the basis of calculations for aqueous species (see section 2.1), the average number of P atoms (1.42) is consistent with our XAFS results (1.0 ± 0.8). The P distance of 3.64 ± 0.04 Å, consistent with the range of previously reported values (3.60 to 3.70 Å) (Morosin, 1978; Mercier et al., 1984) for solid inorganic compounds, indicates monodentate phosphate binding (Fig. 2B).

4.2. U Biomass

In most cases, the best-fit values for both the UI and Uh series are consistent with each other. Therefore, only the values for the Uh series are quoted in the text. If differences were significant, both results are discussed. Our XAFS result (Table 4) for the Oax distance (1.76 ± 0.01 Å) is similar to the distance found for the uranyl standards (1.77 to 1.78 ± 0.01 Å). The short equatorial oxygen (U-Oeq1) bond length (2.32 ± 0.02 Å) is the same as the distance found for the aqueous uranyl phosphate standard (2.32 ± 0.02 Å) and is within the range of previously reported values for the oxygen atom of the phosphate bound to a uranyl (2.24 to 2.35 Å) (Morosin, 1978; Mercier et al., 1984). The longer equatorial oxygen (U-Oeq2) bond length (2.45 ± 0.02 Å) is consistent with the distance found for the aqueous uranyl phosphate standard (2.47 ± 0.03 Å) and similar to previously reported values for the oxygen atom of the carboxyl or water bound to a uranyl (2.41 to 2.51 Å) (Howatson et al., 1975; Allen et al., 1995; Barger et al., 2000). The best-fit value for the U→C path length ($r = 2.89 \pm 0.02$ Å) is consistent with the aqueous uranyl acetate standard (2.90 ± 0.02 Å) and similar to previously reported values for acetate bound to uranyl. The phosphorus (P) distance (3.64 ± 0.01 Å) is the same as that found for the aqueous uranyl

phosphate standard (3.64 ± 0.01 Å) and within the range of previously reported values for a phosphate bound to a uranyl in a crystal structure (3.60 to 3.70 Å) (Morosin, 1978; Mercier et al., 1984).

Our XAFS result (Table 4) for the U→Oax σ^2 -value (0.002 ± 0.001 Å²) is consistent with the value found for the uranyl standards (0.001 to 0.002 ± 0.001 Å²). These values compare well with reported values discussed in section 3.2.1. The σ^2 values for the equatorial oxygen shells increase with pH (0.004, 0.006, 0.009 ± 0.002 Å²) and are consistent with the range of values for the aqueous uranyl standards (0.002 to 0.009 ± 0.002 Å²). The best-fit value for the U→C mean square displacement ($\sigma^2 = 0.002 \pm 0.004$ Å²) is similar to the value for the aqueous uranyl acetate standard (0.003 ± 0.004 Å²). The σ^2 value for the U→P paths (0.002 ± 0.003 Å²) is similar to the value for the aqueous uranyl phosphate standard (0.008 ± 0.005 Å²).

The pH dependence for the number of equatorial oxygen, carbon, and phosphorus atoms is summarized in Table 6. The number of P atoms decreases slightly as the pH increases. The high correlations in the numbers of P and C atoms, the values for their distances from the uranyl, and their mean-square displacement values make the uncertainties in the numbers of P and C atoms large. For the high uranyl:biomass ratio, the number of phosphoryl bonds (P atoms) decreases from 1.9 ± 0.9 to 0.8 ± 0.5 as the pH increases from 1.67 to 4.80. The results are similar for the low uranyl:biomass ratio. For the high uranyl:biomass ratio, the number of carboxyl bonds (carbon atoms) is consistent with zero at pH 1.67, and the number increases to nonzero values (0.5 ± 0.4 and 1.0 ± 0.7) at the higher pH values (3.22 and 4.80, respectively). The results are similar for the low uranium:biomass ratio.

On the basis of previous studies, a uranyl to carbon distance of approximately 2.90 Å indicates a bidentate carboxyl bond

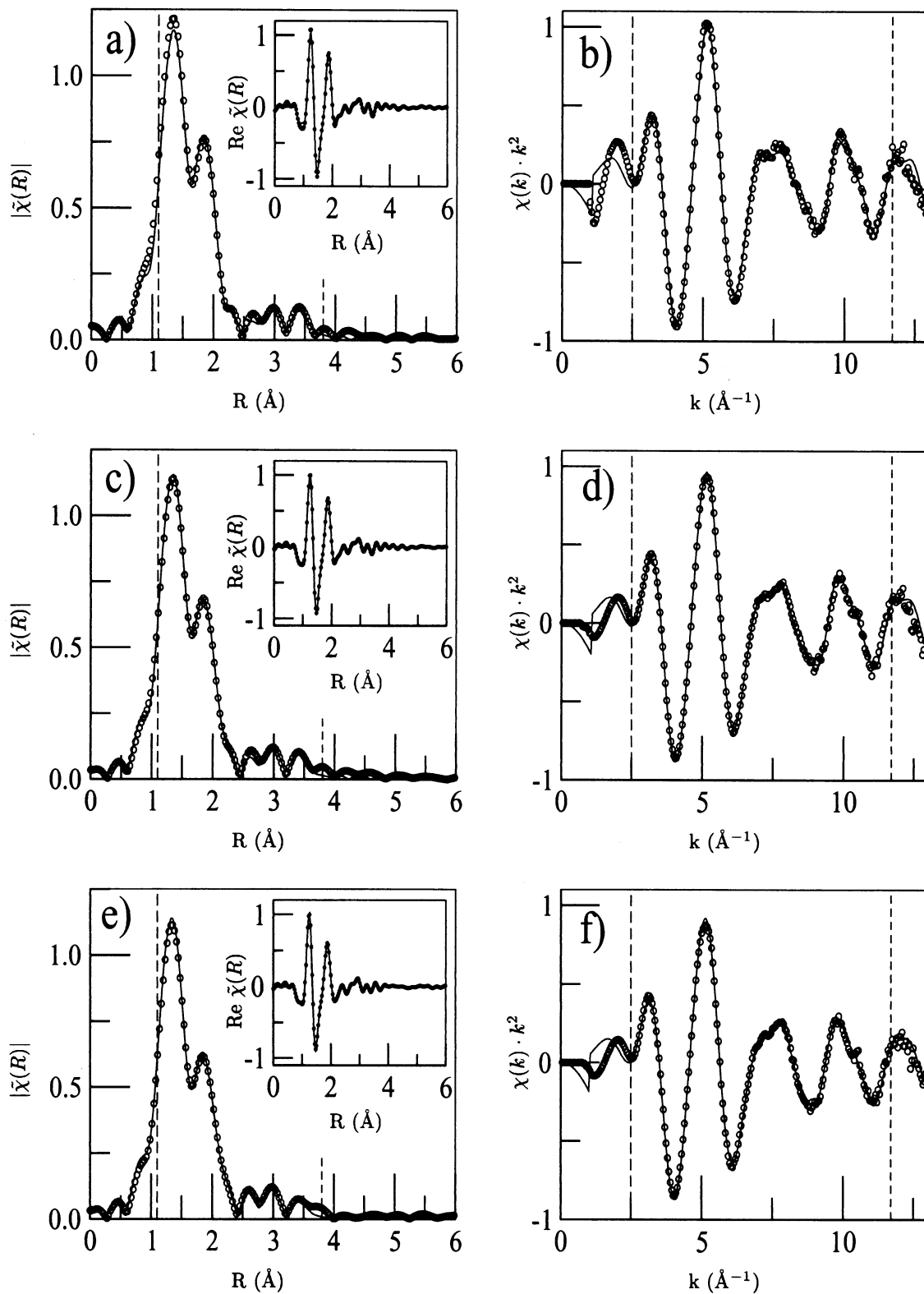


Fig. 7. Data (circles) and best-fit model (line) for U biomass data, U11, U12, and U13. (a) Magnitude of Fourier transform, with real part of Fourier transform of U11 (inset). (b) $\chi(k) \times k^2$ of U11. (c) Magnitude of Fourier transform, with real part of Fourier transform of U12 (inset). (d) $\chi(k) \times k^2$ of U12. (e) Magnitude of Fourier transform, with real part of Fourier transform of U13 (inset). (f) $\chi(k) \times k^2$ of U13.

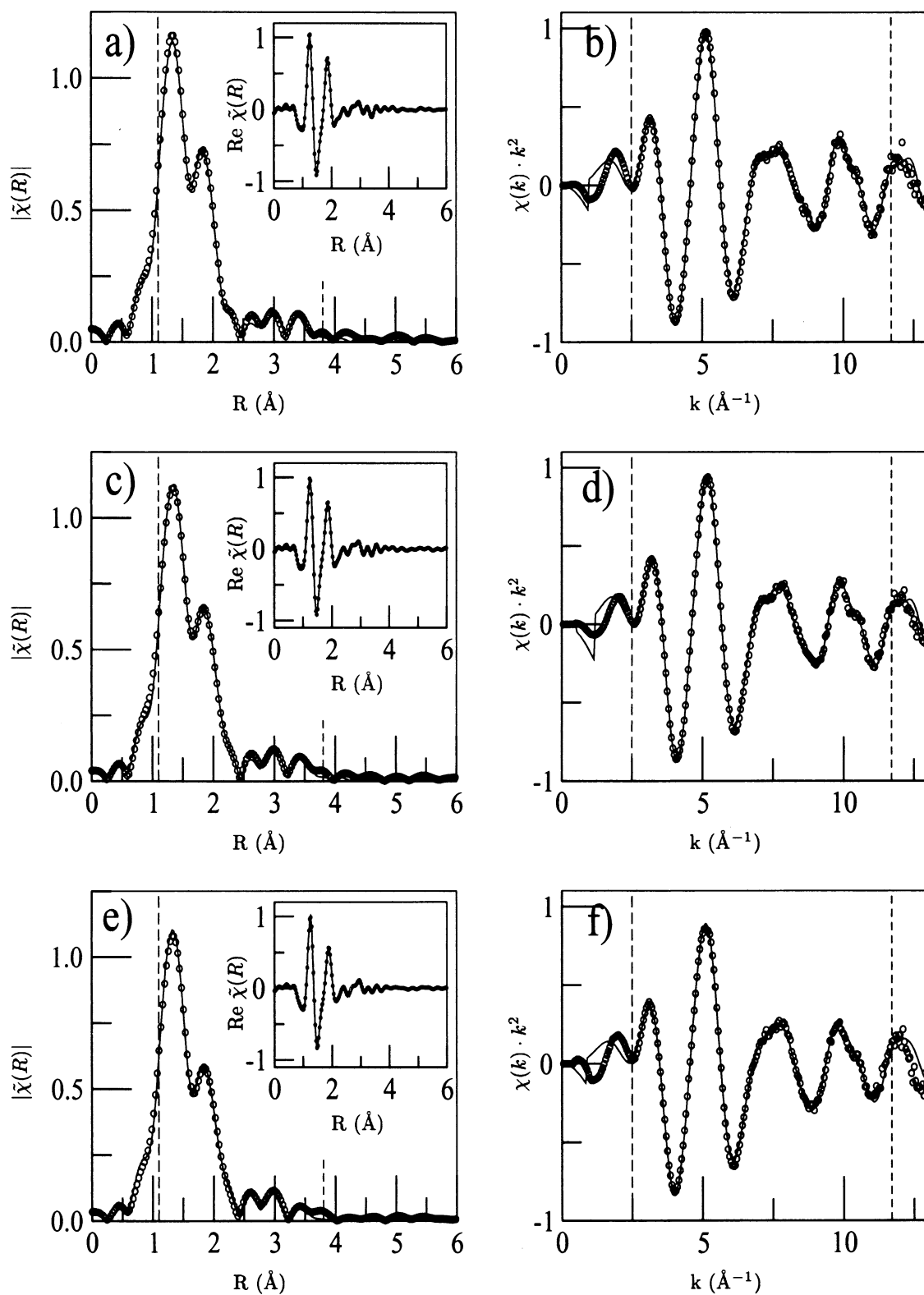


Fig. 8. Data (circles) and best-fit model (line) for U biomass data, Uh1, Uh2, and Uh3. (a) Magnitude of Fourier transform, with real part of Fourier transform of Uh1 (inset). (b) $\chi(k) \times k^2$ of Uh1. (c) Magnitude of Fourier transform, with real part of Fourier transform of Uh2 (inset). (d) $\chi(k) \times k^2$ of Uh2. (e) Magnitude of Fourier transform, with real part of Fourier transform of Uh3 (inset). (f) $\chi(k) \times k^2$ of Uh3.

Table 5. Best-fit values for hydrated uranyl (U-H₂O), uranyl acetate (U-C), and uranyl phosphate (U-P) standards.^a

Path	N _{degen}	R (Å)	σ^2 (10 ⁻³ Å ²)	E ₀ (eV)
U-H ₂ O				
U→Oax	2.0 ^b	1.78 ± 0.01	2 ± 1	4.1 ± 0.9
U→Oeq	6.0 ± 0.4	2.42 ± 0.01	9 ± 1	7.6 ± 0.7
U→Oax1→U→Oax1	2.0 ^b	3.56 ± 0.01	3 ± 1	4.1 ± 0.9
U→Oax1→Oax2	2.0 ^b	3.56 ± 0.01	3 ± 1	4.1 ± 0.9
U→Oax1→U→Oax2	2.0 ^b	3.56 ± 0.01	3 ± 1	4.1 ± 0.9
U-C				
U→Oax	2.0 ^b	1.78 ± 0.01	1 ± 1	-1.6 ± 1.4
U→Oeq	6.8 ± 1.2	2.47 ± 0.02	9 ± 2	3.8 ± 1.2
U→C1	3.0 ± 1.5	2.90 ± 0.02	3 ± 4	5.1 ± 1.5
U→Oeq→C1	12.0 ± 6.0	3.26 ± 0.06	3 ± 4	4.5 ± 1.0
U→Oax1→U→Oax1	2.0 ^b	3.56 ± 0.01	2 ± 1	-1.6 ± 1.4
U→Oax1→Oax2	2.0 ^b	3.56 ± 0.01	2 ± 1	-1.6 ± 1.4
U→Oax1→U→Oax2→U	2.0 ^b	3.56 ± 0.01	2 ± 1	-1.6 ± 1.4
U→C2	3.0 ± 1.5	4.37 ± 0.05	5 ± 5	5.1 ± 1.5
U→C1→C2	6.0 ± 1.5	4.37 ± 0.05	5 ± 5	5.1 ± 1.5
U-P				
U→Oax	2.0 ^b	1.77 ± 0.01	1 ± 1	3.7 ± 1.3
U→Oeq1	2.9 ± 0.6	2.32 ± 0.02	2 ± 2	9.0 ± 1.0
U→Oeq2	2.4 ± 0.4	2.47 ± 0.03	2 ± 2	9.0 ± 1.0
U→Oax1→Oax2	2.0 ^b	3.53 ± 0.02	1 ± 1	3.7 ± 1.3
U→Oax1→U→Oax2	2.0 ^b	3.53 ± 0.02	1 ± 1	3.7 ± 1.3
U→Oax1→U→Oax1	2.0 ^b	3.53 ± 0.02	1 ± 1	3.7 ± 1.3
U→P	1.0 ± 0.8	3.64 ± 0.04	8 ± 5	9.0 ± 1.0
U→Oeq1→P	2.0 ± 1.6	3.76 ± 0.04	8 ± 5	9.0 ± 1.0

^a S₀² was found to converge to 1.0 ± 0.10 for all U L3 XAFS measurements.

^b Values without uncertainties were not determined in the fit but were held at the given value.

(Howatson et al., 1975; Templeton et al., 1985). In this study, bidentate refers to an inner-sphere complex where two oxygen atoms of a single carboxyl functional group are shared with the uranyl, rather than oxygen atoms of two carboxyl groups (Fig. 2A). Therefore, there should be at least two longer equatorial oxygen (Oeq2) bonds for every carbon atom, and there could be more Oeq2 atoms because of water bound to the uranyl. As Table 6 shows, the best-fit value for number of Oeq2 atoms (2.4 to 2.7 to 3.3) is more than twice number of C atoms (0 to 0.5 to 1.0) for the high uranyl:biomass ratio. Again the results are similar for the low uranyl:biomass ratio.

The amount of uranium that is adsorbed to the biomass is not

constant with pH. At low pH, all cell wall functional groups are protonated, and therefore less adsorption occurs. As the functional groups become deprotonated with increasing pH, the electronegativity of the cell wall increases, causing adsorption to increase. This trend is important in interpreting the average numbers of phosphoryl and carboxyl ligands attached to the uranyl. At pH 1.67, we observe only phosphoryl binding. With increasing pH above 1.67, we detect not only the onset of carboxyl binding, but also an increase in the total number of uranyl atoms bound to the cell walls. The slight decrease in the number of phosphoryl groups bound to the uranyl atom with increasing pH could be due to two factors: (1) the uranyl is

Table 6. The pH dependence for the number of Oeq1, Oeq2, C, and P atoms and their distance from the uranium atom.

Atom type	R (Å)	No. of neighboring atoms		
		U11 (pH = 1.67)	U12 (pH = 3.22)	U13 (pH = 4.80)
Oax	1.77 ± 0.01	2.0 ^a	2.0 ^a	2.0 ^a
Oeq1	2.33 ± 0.03	3.1 ± 0.8	3.1 ± 0.9	2.9 ± 0.8
Oeq2	2.45 ± 0.03	2.3 ± 0.7	2.7 ± 0.8	3.3 ± 1.0
C	2.89 ± 0.02	~0 ^b	0.4 ± 0.4	0.9 ± 0.7
P	3.64 ± 0.01	2.4 ± 1.3	1.9 ± 1.1	1.3 ± 0.8
		Uh1 (pH = 1.67)	Uh2 (pH = 3.22)	Uh3 (pH = 4.80)
Oax	1.76 ± 0.01	2.0 ^a	2.0 ^a	2.0 ^a
Oeq1	2.32 ± 0.02	2.9 ± 0.5	2.8 ± 0.5	2.8 ± 0.5
Oeq2	2.45 ± 0.02	2.4 ± 0.4	2.7 ± 0.4	3.3 ± 0.6
C	2.89 ± 0.02	~0 ^b	0.5 ± 0.4	1.0 ± 0.7
P	3.64 ± 0.01	1.9 ± 0.9	1.7 ± 0.8	0.8 ± 0.5

^a The number of Oax atoms was held at 2.0.

^b The carbon atom was not included in the fit for the lowest-pH data.

preferentially adsorbed to the carboxyl ligand relative to the protonated phosphoryl site (so that as the carboxyl becomes deprotonated, carboxyl binding replaces phosphoryl binding to some extent with increasing pH) and/or (2) the number of uranyl atoms bound to the phosphoryl group is constant, and additional uranium is bound to the carboxyl group. Both of these situations would result in a decrease in the average number of phosphoryl groups bound to the uranyl atom, and they cannot be distinguished on the basis of the XAFS data alone.

Fowle et al. (2000) measured the extent of uranyl adsorption to suspensions of *B. subtilis* in 0.1 mol/L NaClO₄ as a function of pH. They observed significant amounts of uranyl adsorption below pH 2.5, with no pH dependence for this adsorption at least down to pH 1.5. This extent of pH-independent bacterial adsorption at low pH was not observed for any other aqueous cations studied (Fein et al., 1997). Above pH 2.5, Fowle et al. (2000) observed an increase in the extent of adsorption with increasing pH, behavior typical of other cations in this pH range. On the basis of these indirect observations, Fowle et al. (2000) postulated that the low-pH adsorption was caused by uranyl binding with protonated phosphoryl groups on the cell wall, whereas the behavior at higher pH was caused by uranyl binding with bacterial carboxyl groups. Thermodynamic stability constants were determined for each type of bacterial surface complex. The pH-independent adsorption behavior would be expected at low pH, because the concentration of protonated phosphoryl sites does not change markedly until the pH approaches the pK_a of the phosphoryl sites (6.9). Carboxyl sites, with a pK_a of 4.8, deprotonate at lower pH, and therefore uranyl binding to these sites increases with increasing pH above pH 2.5.

The XAFS data from this study are completely independent from the adsorption data set of Fowle et al. (2000), yet they offer identical conclusions regarding the nature of uranyl binding to the cell wall of *B. subtilis*. The XAFS data demonstrate that low-pH binding is caused by a phosphoryl site, and increased binding to carboxyl sites is observed as an increase in adsorption with increasing pH above pH 2.5. Fein et al. (1997) identified the cell wall sites with a pK_a value of 4.8 as being carboxyl, entirely on the basis of similar typical pK_a values of carboxyl functional groups for aqueous organic acid molecules. This study provides direct confirmation of the importance of carboxyl binding sites in this pH range. This study also demonstrates the power of incorporating spectroscopic measurements with bulk adsorption measurements to yield both detailed constraints on the nature and stoichiometry of the important binding reactions and thermodynamic properties of surface species.

5. CONCLUSIONS

The uranium L3-edge XANES measurements of the U biomass data and U(IV) and U(VI) standards clearly indicate that U(VI) added to biomass samples was not reduced by either the bacteria or radiation exposure during XAFS measurements. The uranium L3-edge XAFS data give information about the average local atomic environment of the U atoms in the biomass samples. The Fourier transforms of the XAFS data at three different pH values (1.67, 3.22, and 4.80) and two dif-

ferent U:bacteria concentration ratios show changes in the uranyl local atomic environment due to different percentages of phosphoryl and/or carboxyl groups bound to the uranyl ion. At the lowest pH value (1.67) and at both U:bacteria ratios (U11 and Uh1), the XAFS data indicate uranyl binding to a phosphoryl functional group, with an average distance between the uranium atom and the phosphorus atom of approximately 3.6 Å. This distance is indicative of an inner-sphere complex with one oxygen atom shared between the uranyl and the phosphoryl ligand (Fig. 2B). No carboxyl-uranyl bonds are needed to model the XAFS data accurately for the low-pH samples (U11 and Uh1). Our detection limit for the number of carbon atoms is 0.2 because of interference in the data from equatorial oxygen atoms. Therefore, we cannot completely rule out the possibility of a small carboxyl component at pH 1.67. At the higher pH values (3.22 and 4.80), inclusion of C atoms is required to accurately simulate the experimental data (U12, U13, Uh2, and Uh3). The C atom distance of approximately 2.9 Å indicates that the uranyl-carboxyl bond is also the inner-sphere type, with two oxygen atoms shared between the uranyl and the carboxyl ligand (Fig. 2A). These results indicate an increase in the number of carboxyl bonds with increasing pH (Table 6). Our XAFS results are consistent with the surface complexation models proposed by Fein et al. (1997) and Fowle et al. (2000), demonstrating the complementary role XAFS spectroscopy and bulk adsorption measurements can play in determining metal distribution behaviors in the environment.

Acknowledgments—Special appreciation is extended to E. J. O'Loughlin for insightful discussions and assistance with U XAFS data collection and also to P. C. Burns and A. J. Locoek for additional insightful discussions and for the U(VI) and U(IV) standards. N. Leyarovska is acknowledged for her assistance with U XAFS data collection at the MRCAT sector. We thank P. A. O'Day and three anonymous reviewers for their constructive comments. Support for S.D.K. and K.M.K. was provided by the U.S. Department of Energy, Office of Science, Office of Biologic and Environmental Research, NABIR Program. This research was also supported in part by the U.S. National Science Foundation (grant EAR-9905704) and by the Donors of the Petroleum Research Fund, administered by the American Chemical Society. Use of the MR-CAT sector at the Advanced Photon Source (APS) and of the APS was supported by the U.S. Department of Energy, Office of Science, Office of Basic Energy Sciences, under contract W-31-109-ENG-38.

Associate editor: P. A. O'Day

REFERENCES

- Allen P. G., Bucher J. J., Clark D. L., Edelstein N. M., Ekberg S. A., Gohdes J. W., Hudson E. A., Kaltsoyannis N., Lukens W. W., Neu M. P., Palmer P. D., Reich T., Shuh D. K., Tait C. D., and Zwick B. D. (1995) Multinuclear NMR, Raman, EXAFS, and X-ray diffraction studies of uranyl carbonate complexes in near-neutral aqueous solution: X-ray structure of [C(NH₂)₃]₆[(UO₂)₃(CO₃)₆].6.5H₂O. *Inorg. Chem.* **34**, 4797–4807.
- Allen P. G., Shuh D. K., Bucher J. J., Edelstein N. M., Reich T., Denecke M. A., and Nitsche H. (1996) EXAFS determination of uranium structures: The uranyl ion complexed with tartaric, citric, and malic acids. *Inorg. Chem.* **35**, 784–787.
- Allen P. G., Bucher J. J., Sheh D. K., Edelstein N. M., and Reich T. (1997) Investigation of aquo and chloro complexes of UO₂²⁺, NpO₂²⁺, Np⁴⁺, and Pu³⁺ by X-ray absorption fine structure spectroscopy. *Inorg. Chem.* **36**, 4676–4683.

- Antonio M. R., Soderholm L., Williams C. W., Blaudeau J. P., and Bursten B. E. (2001) Neptunium redox speciation. *Radiochim. Acta* **89**, 17–25.
- Barger J. R., Reitmeyer R., Lenhart J. J., and Davis J. A. (2000) Characterization of U(VI)-carbonate ternary complexes on hematite: EXAFS and electrophoretic mobility measurements. *Geochim. Cosmochim. Acta* **64**, 2737–2749.
- Beolchini F., Pagnanelli F., and Veglio F. (2001) Modeling of copper biosorption by *Arthrobacter* sp. in a UF/MF membrane reactor. *Environ. Sci. Technol.* **35**, 3048–3054.
- Bethke C. M. and Brady P. V. (2000) How the K-d approach undermines ground water cleanup. *Ground Water* **38**, 435–443.
- Beveridge T. J. and Murray R. G. E. (1976) Uptake and retention of metals by cell walls of *Bacillus subtilis*. *J. Bacteriol.* **127**, 1502–1518.
- Beveridge T. J. and Murray R. G. E. (1980) Sites of metal deposition in the cell wall of *Bacillus subtilis*. *J. Bacteriol.* **141**, 876–887.
- Cox J. S., Smith D. S., Warren L. A., and Ferris F. G. (1999) Characterizing heterogeneous bacterial surface functional groups using discrete affinity spectra for proton binding. *Environ. Sci. Technol.* **33**, 4514–4521.
- Cross J. L. and Frenkel A. I. (1998) Use of scattered radiation for absolute energy calibration. *Rev. Sci. Instrum.* **70**, 38–40.
- Daughney C. J., Fein J. B., and Yee N. (1998) A comparison of the thermodynamics of metal adsorption onto two gram-positive bacteria. *Chem. Geol.* **144**, 161–176.
- Dent A. J., Ramsay J. D. F., and Swanton S. W. (1992) An EXAFS study of uranyl ion in solution and sorbed onto silica and montmorillonite clay colloids. *J. Colloid Interface Sci.* **150**, 45–60.
- Docrat T. L., Mosselmans J. F. W., Charnock J. M., Whiteley M. W., Collison D., Livens F. R., Jones C., and Edmiston M. J. (1999) X-ray absorption spectroscopy of tricarbonatodioxouranate(V), $[\text{UO}_2(\text{CO}_3)_3]^{5-}$, in aqueous solution. *Inorg. Chem.* **38**, 1879–1882.
- Duff M. C., Morris D. E., Hunter D. B., and Bertsch P. M. (2000) Spectroscopic characterization of uranium in evaporation basin sediments. *Geochim. Cosmochim. Acta* **64**, 1535–1550.
- Fein J. B., Daughney C. J., Yee N., and Davis T. A. (1997) A chemical equilibrium model for metal adsorption onto bacterial surface. *Geochim. Cosmochim. Acta* **61**, 3319–3328.
- Fein J. B. and Delea D. (1999) Experimental study of the effect of EDTA on Cd adsorption by *Bacillus subtilis*. **161**, 375–383.
- Ferris F. G., Schultze S., Witten T. C., Fyfe W. S., and Beveridge T. J. (1989) Metal interactions with microbial biofilms in acidic and neutral pH environments. *Appl. Environ. Microbiol.* **55**, 1249–1257.
- Fowle D. A. and Fein J. B. (1999) Competitive adsorption of metal cations onto two gram positive bacteria: Testing the chemical equilibrium model. *Geochim. Cosmochim. Acta* **63**, 3059–3067.
- Fowle D. A., Fein J. B., and Martin A. M. (2000) Experimental study of uranyl adsorption onto *Bacillus subtilis*. *Environ. Sci. Technol.* **34**, 3737–3741.
- Francis A. J., Gillow J. B., Dodge C. J., Dunn M., Mantione K., Strietelmeier B. A., Pansoy-Hjelvik M. E., and Papenguth H. W. (1998) Role of bacteria as biocolloids in the transport of actinides from a deep underground radioactive waste repository. *Radiochim. Acta* **82**, 347–354.
- Gonçalves M. L. S., Sigg L., Reutlinger M., and Stumm W. (1987) Metal ion binding by biological surfaces: Voltammetric assessment in the presence of bacteria. *Sci. Total Environ.* **60**, 105–119.
- Grenthe I., Fuger J., Konings R. J. M., Lemire R. J., Muler A. B. (1992) *Chemical Thermodynamics of Uranium*. Elsevier.
- Harden V. P. and Harris J. O. (1953) The isoelectric point of bacterial cells. *J. Bacteriol.* **65**, 198–202.
- Harvey R. W. and Leckie J. O. (1985) Sorption of lead onto two gram-negative marine bacteria in seawater. *Mar. Chem.* **15**, 333–344.
- Harvey R. W., Lion L. W., Young L. Y., and Leckie J. O. (1982) Enrichment and association of lead and bacteria at particulate surfaces in a salt-march surface layer. *J. Mar. Res.* **40**, 1201–1211.
- Hay P. J., Martin R. L., and Schreckenbach G. (2000) Theoretical studies of the properties and solution chemistry of AnO_2^{2+} and AnO_2^+ aquo complexes for An = U, Np, and Pu. *J. Phys. Chem. A* **104**, 6259–6270.
- He L. M. and Tebo B. M. (1998) Surface charge properties of and Cu(II) adsorption by spores of the marine *Bacillus* sp. strain SG-1. **64**, 1123–1129.
- Hennig C., Panak P. J., Reich T., Raff J., Selenska-Poball S., Bernhard G., and Nitsche H. (2000) Uranium(VI) complexation by *Bacillus* species isolated from uranium mining waste pile—A comparative EXAFS study. In *Programme and Abstracts of the 2nd Euroconference on Bacteria-Metal/Radionuclide Interaction: Basic Research and Bioremediation*. Rossendorf.
- Howatson J., Grev D. M., and Morosin B. (1975) Crystal and molecular structure of uranyl acetate dihydrate. *J. Inorg. Nucl. Chem.* **37**, 1933–1935.
- Hudson E. A., Rehr J. J., and Bucher J. J. (1995) Multiple-scattering calculations of the uranium L3-edge X-ray-absorption near-edge structure. *Phys. Rev. B* **52**, 13815–3826.
- Kemner K. M., Kropf A. J., and Bunker B. A. (1994) A low-temperature total electron yield detector for X-ray absorption fine structure spectra. *Rev. Sci. Instrum.* **65**, 3667–3669.
- Konhauser K., Fyfe W. S., and Ferris F. G. (1993) Metal sorption and mineral precipitation by bacteria in 2 Amazonian river systems, Rio-Solimoes and Rio-Negro, Brazil. *Geology* **21**, 1103–1106.
- Koretsky C. (2000) The significance of surface complexation reactions in hydrologic systems: A geochemist's perspective. *J. Hydrol.* **230**, 127–171.
- Ledin M., Krantz-Rulcker C., and Allard B. (1999) Microorganisms as metal sorbents: Comparison with other soil constituents in multi-compartment systems. *Soil. Biol. Biochem.* **31**, 1639–1648.
- Mercier R., Pham Thi M., and Colomban P. (1984) Structure, vibrational study and conductivity of the trihydrated uranyl bis(dihydrogenophosphate): $\text{UO}_2(\text{H}_2\text{PO}_4)_2 \cdot 3\text{H}_2\text{O}$. *Solid State Ionics* **15**, 113–126.
- Morosin B. (1978) Hydrogen uranyl phosphate tetrahydrate, a hydrogen ion solid electrolyte. *Acta Cryst.* **B34**, 3732–3734.
- Morris D. E., Allen P. G., Berg J. M., Chisholm-Brause C. J., Conradson S. D., Donohoe R. J., Hess N. J., Musgrave J. A., and Tait C. D. (1996) Speciation of uranium in Fernald soils by molecular spectroscopic methods: Characterization of untreated soils. *Environ. Sci. Technol.* **30**, 2322–2331.
- Mullen M. D., Wolf B. C., Ferris F. G., Beveridge T. J., Flemming C. A., and Bailey G. W. (1989) Bacterial sorption of heavy metals. *Appl. Environ. Microbiol.* **55**, 3300–3306.
- Newville M., Livinš P., Yacoby Y., Rehr J. J., and Stern E. A. (1993) Near-edge X-ray absorption fine structure of Pb: A comparison of theory and experiment. *Phys. Rev. B* **47**, 14126–14131.
- Newville M., Ravel B., Haskel D., and Stern E. A. (1995) Analysis of multiple scattering XAFS data using theoretical standards. *Physica B* **208/209**, 154–156.
- Norber A. B. and Persson H. (1984) Accumulation of heavy-metal ions by *Zoogloea ramigera*. *Biotechnol. Bioengineer.* **26**, 239–246.
- Plette A. C. C., van Riemsdijk W. H., Benedetti M. F., and Van der Wal A. (1995) pH dependent charging behavior of isolated cell walls of a gram-positive soil bacterium. *J. Colloid Interface Sci.* **173**, 354–363.
- Reeder R. J., Nugent M., Lamble G. M., Tait C. D., and Morris D. E. (2000) Uranyl incorporation into calcite and aragonite: XAFS and luminescence studies. *Environ. Sci. Technol.* **34**, 638–644.
- Reich T., Denecke M. A., Pompe S., Bubner M., Heise K.-H., Schmidt M., Brendler V., Baraniak L., Nitsche H., Allen P. G., Bucher J. J., Edelstein N. M., and Shuh D. K. (1996) Characterization of the interaction of uranyl ions with humic acids by X-ray absorption spectroscopy. In *Synchrotron Radiation Techniques in Industrial, Chemical, and Material Science* (ed. D'Amico). Plenum Press.
- Sarret G., Manceau A., Spadini L., Roux J.-C., Hazemann J.-L., Soldo Y., Eybert-Berard L., and Menthonnex J.-J. (1998) Structural determination of Zn and Pb binding sites in *Penicillium chrysogenum* cell walls by EXAFS spectroscopy. *Environ. Sci. Technol.* **32**, 1648–1655.
- Segre C. U., Leyarovska N. E., Chapman L. D., Lavender W. M., Plag P. W., King A. S., Kropf A. J., Bunker B. A., Kemner K. M., Dutta P., Druan R. S., and Kaduk J. (2000) The MRCAT insertion device beamline at the Advanced Photon Source. In: *Synchrotron Radiation Instrumentation: Eleventh U.S. Conference* **CP521**, 419–422.

- Small T., Warren L. A., Roden E., and Ferris F. G. (1999) Sorption of strontium by bacteria, Fe(III) oxide, and bacteria-Fe(III) oxide composites. *Environ. Sci. Technol.* **33**, 4465–4470.
- Small T. D., Warren L. A., and Ferris F. G. (2001) Influence of ionic strength on strontium sorption to bacteria, Fe(III) oxide, and composite bacteria-Fe(III) oxide surfaces. *Appl. Geochem.* **11**, 547–554.
- Smith R. M., Martell A. E., and Motekaitis R. J. (1997) NIST critically selected stability constants of metal complexes database, version 4.0. In: *NIST Standard Reference Database*. Vol. 46. U.S. Department of Commerce.
- Stern E. A. (1993) Number of relevant independent points in X-ray-absorption fine-structure spectra. *Phys. Rev. B* **48**, 9825–9827.
- Stern E. A. and Heald S. M. (1983) Basic principles and applications of EXAFS. In *Handbook of Synchrotron Radiation*, Vol. 10 (ed. E. E. Koch), pp. 995–1014. North-Holland.
- Stern E. A., Newville M., Ravel B., Yacoby Y., and Haskel D. (1995) The UWXAFS analysis package: Philosophy and details. *Physica B* **208–209**, 2995–3009.
- Sturchio N. C., Antonio M. R., Soderholm L., Sutton S. R., and Brannon J. C. (1998) Tetravalent uranium in calcite. *Science* **281**, 971–973.
- Templeton D., Zalkin A., Ruben H., and Templeton L. (1985) Redetermination and absolute configuration of sodium uranyl(VI) triacetate. *Acta Cryst.* **C41**, 1439–1441.
- Thompson H. A., Brown G. E. Jr., and Parks G. A. (1995) Low and ambient temperature XAFS study of U(VI) in solids and aqueous solution. *Physica B* **208/209**, 167–168.
- Thompson H. A., Brown G. E. Jr., and Parks G. A. (1997) XAFS spectroscopic study of uranyl coordination in solids and aqueous solutions. *Am. Mineral.* **82**, 483–496.
- Westall J. C. (1982) FITEQL, A computer program for determination of chemical equilibrium constants from experimental data. Dept. Chem., Oregon St. Univ.
- Yee N. and Fein J. B. (2001) Cd adsorption onto bacterial surfaces: A universal adsorption edge? *Geochim. Cosmochim. Acta* **65**, 2037–2042.
- Zabinsky S. I., Rehr J. J., Ankudinov A., Albers R. C., and Eller M. J. (1995) Multiple-scattering calculations of X-ray-absorption spectra. *Phys. Rev. B* **52**, 2995–3009.

XAFS studies of gold and silver-gold nanoparticles in aqueous solutions

Tomohiro Shibata,^{a,*} Holger Tostmann,^b
Bruce Bunker,^a Arnim Henglein,^c Dan Meisel,^c
Seongkyun Cheong^a and Maxim Boyanov^a

^aDepartment of Physics, University of Notre Dame, Notre Dame IN 46556, USA, ^bDepartment of Chemistry, University of Florida, Gainesville, FL 32611, USA, and ^cDepartment of Chemistry and Radiation Laboratory, University of Notre Dame, Notre Dame IN 46556, USA. E-mail: tshibata@darwin.helios.nd.edu

The x-ray absorption fine structure (XAFS) of colloidal Au and Au/Ag nanoparticles (3.5nm and 20nm mean diameter) in an aqueous solution has been investigated. Size dependent alloying was observed upon deposition of Ag on Au core. Ag forms distinct layers around the 20 nm Au nanoparticles. In contrast, random mixing is found for Ag deposited on 3.5nm Au particles.

Keywords: nanoparticles, XAFS, alloy, gold, silver.

1. Introduction

Metallic nanoparticles in solution have recently gained great interest because of their catalytic (Haruta, 1997, Grunwaldt *et al.*, 1999) and electronic properties (Henglein, 1993; Link & El-Sayed, 1999). The structure of these particles can be investigated by high-resolution transmission electron microscopy (TEM); however, this technique yields no information about the internal structure of nano-composites. Most previous XAFS studies on nanoparticles were performed on particles on solid support. Here we report an XAFS study of nanoparticles suspended in solution. Both, single metal (Au) and core-shell particles (Ag shell on Au core) were studied.

2. Experimental

20nm diameter gold particles of a narrow size distribution (10% standard deviation) were prepared by reducing AuCl_4^- by citrate (Henglein & Meisel, 1998), and 3.5nm diameter particles with a wider size distribution ($\pm 0.5\text{nm}$) via radiolytic reduction of AuCl_4^- . Particles size, morphology, and the size distribution were determined by TEM as described previously (Henglein, 1999). The Ag layer was deposited by adding the desired amount of $\text{Ag}(\text{CN})_2^-$ to the colloidal Au and reducing the Ag complex radiolytically on the surface of the Au particles (Hodak *et al.*, 2000). 1-6 atomic Ag layers were deposited on the 20nm Au particles, and one monolayer on the 3.5nm particles. In order to prevent the nanoparticles from coagulating, the outermost atomic layer necessarily carries some charged species (mostly citrate in this case). However, no effect of the ligand coverage on the XAFS spectra was observed. The concentration of metal particles typically varies around $5 \times 10^{-4}\text{M}$.

These solutions were investigated by fluorescence XAFS at the Au L_3 edge using a conventional Lytle detector at room temperature. Because of the low concentration of the sample, we used a thick x-ray filter (nine absorption lengths at the Au edge) and Soller slits to reduce the scattered background. Because of artifacts from radiolysis bubbles, several scans were taken, changing the liquid or

sample positions and the spectra were averaged. All the measurements were performed at the MRCAT undulator beamline at the Advanced Photon Source. Data analysis was done using FEFFIT (Newville, *et al.*, 1995) and FEFF6.01 (Rehr *et al.*, 1992).

3. Results and Discussion

We measured a Au foil standard as well as pure Au nanoparticles of 20nm and 3.5nm. The Au-Au nearest neighbor distance as obtained from fitting the Au foil data is about 0.02\AA shorter than the bulk crystallographic bond length using XAFS scattering calculations from FEFF6.01. This well-known effect is due to the fact that the near-neighbor Au-Au distribution is slightly asymmetric at room temperature for Au. In this paper, we analyzed the data without including the higher cumulants, instead showing changes in bond length relative to that of the bulk. This is justified as the Debye Waller factor (DWF) observed for these nanoparticles is very close to that of the bulk, showing a similar degree of disorder. Relative to the distance in the Au foil, the Au-Au nearest neighbor distance is shorter by $0.026 \pm 0.01\text{\AA}$ in the 3.5nm Au nanoparticles. On the other hand, the Au-Au bond lengths are about the same in the 20nm pure Au nanoparticles and the Au foil, consistent with previous XAFS measurements (Balerna *et al.*, 1985). The data for the pure 3.5nm Au particles can be fitted with a coordination number (CN) of 10.6 ± 1.2 and the DWF of $(9 \pm 1) \times 10^{-3}\text{\AA}^2$; this is a reasonable reduction of the CN considering the increased number of surface atoms relative to fully coordinated core atoms.

XAFS spectra of Au nanoparticles of 20nm diameter with different degrees of deposition of Ag (molar ratios Au:Ag of (a) 8:1 (b) 4:1 (c) 2:1) were measured. This corresponds to 1.7, 3.3, and 6.2 atomic layers of Ag on a Au core respectively for (a), (b), and (c), assuming that no alloy formation takes place in the core. The XAFS spectra of (a) - (c) look similar to those of the pure Au nanoparticles, indicating that Ag forms layers around the Au core without affecting it. We analyzed the first shell data only even though higher shell features are discernible. To describe the first shell of the 20nm Au/Ag nanoparticles, six parameters have to be determined: the CN, the bond length and the DWF for both the Au-Au and the Au-Ag pairs. However, due to the limited data range, the number of degrees of freedom is limited and not all the parameters can be varied at once. Since the majority of the Au-Au pairs are located in the Au core and the core is essentially unaffected by the Ag deposition, it is reasonable to assume that the bond length and the DWF for the Au-Au pairs are the same for the pure 20nm Au particles and the 20nm Au particles with Ag added. This leaves us with the CN, the bond length and the DWF for the Au-Ag pairs, as well as the CN of Au-Au pairs as variables. This assumption is consistent with the fitting results shown below.

Table 1 shows the fitting results for Au/Ag colloids. N_{tot} is the total CN of the nearest neighbors of the Au, $N_{\text{tot}} = N(\text{Au}) + N(\text{Ag})$; $N(\text{Au})$ and $N(\text{Ag})$ are the CN of Au and Ag around Au; $N(\text{Ag})/N_{\text{tot}}$ is the ratio of Ag to the total number of neighbors around Au; $\Delta R_{\text{Au-Au}}^{\text{Nano}}$ and $\Delta R_{\text{Au-Ag}}^{\text{Nano}}$ are the changes in bond lengths for Au-Au ($R_{\text{Au-Au}}^{\text{Nano}}$) and Au-Ag ($R_{\text{Au-Ag}}^{\text{Nano}}$) relative to that of bulk Au-Au ($R_{\text{Au-Au}}^{\text{Bulk}}$), defined as $\Delta R_{\text{Au-Au}}^{\text{Nano}} = R_{\text{Au-Au}}^{\text{Nano}} - R_{\text{Au-Au}}^{\text{Bulk}}$ and $\Delta R_{\text{Au-Ag}}^{\text{Nano}} = R_{\text{Au-Ag}}^{\text{Nano}} - R_{\text{Au-Au}}^{\text{Bulk}}$ respectively. The DWF for the Au-Ag bond is $(9 \pm 1) \times 10^{-3}\text{\AA}^2$ for (a) - (c). In the series of (a) - (c), a small portion of Ag atoms ($N(\text{Ag})/N_{\text{tot}}$) is observed in the first shell around Au with little sample dependence. The uncertainty is somewhat large, because of parameter correlation, but for all of these samples $N(\text{Ag})/N_{\text{tot}}$ is less than 9% assuming the maximum possible error

Table 1

XAFS parameters for pure Au and Au/Ag nanoparticles. (a), (b), and (c) are Au(20nm)/Ag nanoparticles with Au:Ag=8:1, 4:1, and 2:1 respectively, and (d) is Au(3.5nm)/Ag with Au:Ag=2:1. N_{tot} is the sum of coordination numbers of Au and Ag around Au, and $N(Ag)/N_{tot}$ is the contribution of the Ag neighbors to the Au XAFS scattering path. ΔR_{Au-Au}^{Nano} , and ΔR_{Au-Ag}^{Nano} are the difference in bond length of Au-Au (R_{Au-Au}^{Nano}) and Au-Ag (R_{Au-Ag}^{Nano}) for nanoparticles relative to the fitting value for the bulk (R_{Au-Au}^{Bulk}) defined as $\Delta R_{Au-Au}^{Nano} = R_{Au-Au}^{Nano} - R_{Au-Au}^{Bulk}$, and $\Delta R_{Au-Ag}^{Nano} = R_{Au-Ag}^{Nano} - R_{Au-Ag}^{Bulk}$ respectively and given in Å. The large error bar in ΔR_{Au-Ag}^{Nano} for (a)-(c) is due to the small effect of Ag on the Au XAFS.

Sample	N_{tot}	$N(Ag)/N_{tot}$	ΔR_{Au-Au}^{Nano}	ΔR_{Au-Ag}^{Nano}
Au _{foil}	12 (fix)	0	0 (fix)	–
Au _{20nm}	11.5 ± 1.0	0	-0.01 ± 0.01	–
Au _{3.5nm}	10.6 ± 1.2	0	-0.026 ± 0.01	–
a	11.5 ± 1.2	0.04 ± 0.04	-0.01 (fix)	0.06 ± 0.08
b	11.5 ± 1.2	0.03 ± 0.03	-0.01 (fix)	0.02 ± 0.07
c	12.4 ± 1.2	0.06 ± 0.03	-0.01 (fix)	-0.02 ± 0.04
d	11.6 ± 0.7	0.27 ± 0.05	-0.03 ± 0.01	-0.02 ± 0.02

bar.

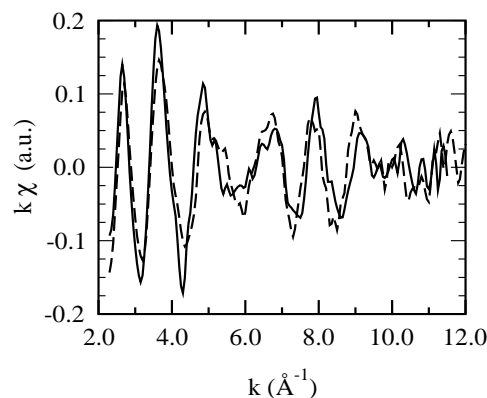
Based on the values given in Table 1, we consider the following models for the internal structure of the Au/Ag nanoparticles with a 20nm Au core: The TEM image shows that the particles are spherical and the size distribution is reasonably uniform (Henglein, 1999). This greatly facilitates the interpretation of XAFS data which average over all particles. First, we consider the formation of Ag layers on the Au core. For simplicity, we assume an FCC (111) lattice on the surface and for the outermost Au atoms, 3 out of the 12 nearest neighbors are replaced by Ag. About 7% of the Au atoms are facing the surface in the case of 20nm Au particles, so only an average 2% contribution of the Ag atoms should be observed independent of the amount of Ag deposition. This is consistent with our experimental finding that the Ag essentially does not affect the Au data. Next we consider complete miscibility within the particle as a whole. This model gives the contribution of Au-Ag scattering of 11, 20, and 33 % respectively for (a), (b), and (c), thus a completely random distribution of Ag within the particle is well outside the experimental error for all three samples (a) - (c). We cannot rule out that some of the Ag alloys with the Au core but at least one complete layer of Ag at the outermost surface layer of the particle has to be assumed in order to explain the data for sample (c).

Now we discuss the sample (d), which is a 3.5nm Au core with Ag added. The amount of Ag is Au:Ag=2:1, which is about one atomic monolayer on the surface of the Au core. Fig.1 shows a distinct difference especially in the phase of the XAFS oscillation for the pure 3.5nm Au particles compared to the 3.5nm Au nanoparticles with Ag added. Fortunately, large differences in the backscattering phase and amplitude for Au-Au and Au-Ag pairs allow for the discrimination between a heterogeneous particle – where the Au is only slightly affected by the presence of Ag layers at the outermost layers – and a random alloy particle – where the Au is surrounded by a significant number of Ag atoms. This feature appears as the double peak in the real space data in Fig.2. The two peaks around 2.4Å and 3.0Å are the first shell data split due to the dip in the backscattering amplitude vs. k for Au. Here we see that the relative intensity of the double peak is markedly changed with Ag deposition. We find that $N(Ag)/N_{tot}$ is 27 ± 5%. In the fitting, the bond length and the DWF for the Au-Au pair are also left as fitting variables, in addition to those used for the 20nm Au/Ag nanoparticles in spite of parameter correlation. We comment that

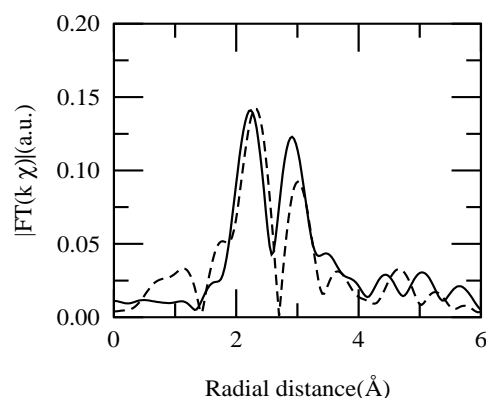
the $N(Ag)/N_{tot}$ has smaller correlation with the DWF than N_{tot} as long as the DWF of Au-Au and Au-Ag pair have a similar value.

Again, we compare our data to the two possible models: First we consider the case of a heterogeneous particle with Ag forming layers around the Au core. Since the 3.5nm particles have about 40% of the Au particles facing the surface, $N(Ag)/N_{tot}$ should be 10%, which is not consistent with the experimental data. Next we consider homogeneous alloying of Au with Ag within the particle: Random alloy formation would result in Ag being 33% of the atoms in the Au nearest neighbor coordination shell, which is consistent with our data. The smaller reduction of N_{tot} for Au/Ag nanoparticles compared with 3.5nm Au nanoparticles can be understood if we consider that only ~ 67% of the surface atoms are Au when a random alloy is formed.

It is important to discuss the effect of the size distribution on the analysis of our data since the 3.5nm particles have a wider size distribution function than the 20nm particles. For a nanoparticle, the ratio of the surface atoms to the inner atoms increases when the size becomes smaller. However, the number of atoms in the particle decreases more rapidly. Therefore, the average ratio of the surface atoms to the inner atoms is mainly determined by the number distribution of the larger particles. Since the distribution obtained


Figure 1

$k\chi$ of 3.5nm Au nanoparticles (dotted line) and Au(3.5nm)/Ag nanoparticles with Ag (Au:Ag=2:1) (solid line) (sample (d)).


Figure 2

Amplitude of Fourier transform of Au nanoparticles(3.5nm) (dotted line) and Au (3.5nm)/Ag nanoparticles (Au:Ag=2:1) (sample (d)) (solid line).

from the TEM image is nearly symmetric, the distribution effect reduces the number of the surface atoms. It should also be stressed that the growth of the radius of the particle is faster for smaller particles and the ratio of Ag/Au deposited should be larger for a smaller Au core. Both of these effects indicate a layered structure would result in less than 10% backscattering from Ag which is clearly inconsistent with our data for 3.5nm nanoparticles. This striking size dependence is under investigation, with studies of a number of different particle sizes and compositions planned.

4. Summary and Conclusions

We successfully measured nano-sized Au and Au/Ag colloidal nanoparticles in a dilute solution using XAFS to study the internal structure of ligand- and support-free nanoparticles. By comparing Ag deposition on differently sized Au cores we conclude:

(i) when Ag is deposited on a 20nm Au core, Ag and Au form an interface with at most several layers of interdiffusion. The data are inconsistent with the formation of a homogeneous Au/Ag alloy.

(ii) when Ag is deposited on a 3.5nm core, Au and Ag form a homogeneous alloy and the data are inconsistent with the layer formation found for the larger nanoparticles.

This striking difference is reproducible and is apparently a size effect. Further studies of the nanocomposites, varying the particle

size, composition, and preparation methods are underway.

This work is supported by the Office of Basic Energy Science of the US Department of Energy (DOE) as contribution NDRL 4262 of the Notre Dame Radiation Laboratory. The MRCAT is supported by the DOE under Contract DE-FG02-94-ER45525 and the member institutions. The Advanced Photon Source is supported by the DOE, under Contract No.W-31-102-Eng-38.

References

- Balerna, A. Bernieri, E. Picozzi, P. Reale, A. Santucci, S. Burattini, E. & Mobilio, S. (1985) *Phys.Rev.B.* **31**, 5058–5065.
- Grunwaldt, J.D. Kiener, C. Wogerbauer, C. & Baiker, A. (1999). *J.Catal.* **181**, 223–232.
- Haruta, M. (1997). *Catal.Today* **36**,153–166.
- Henglein, A. (1993). *J.Phys.Chem.* **97**,5457–5471.
- Henglein, A. & Meisel, D. (1998). *Langmuir* **14**,7392–7396.
- Henglein, A. (1999). *Langmuir* **15**,6738–6744.
- Hodak, J.H. Henglein, A. Giersig, M. & Hartland, G.V. (2000). *J.Phys.Chem. B* **112**,5942–5947.
- Link, S & El-Sayed, M.A. (1999). *J.Phys.Chem.B.* **103**,8410–8426.
- Mulvaney, P. Giersig, M. & Henglein, A. (1993). *J.Phys.Chem.* **97**,7061–7064.
- Newville, M. Ravel, B. Haskel, D. Stern, E. & Yacoby, Y. (1995). *Physica B* **208&209**, 154–156.
- Rehr, J. Albers, R.C. & Zabinski, S. (1992). *Phys.Rev.Lett.* **69**,3397–3400.

Analytical determination of the optical constants of a substrate in the presence of a covering layer by use of ellipsometric data

S. C. Russev

Department of Solid State Physics, Faculty of Physics, University of Sofia, 5 James Bourchier Boulevard, Sofia 1164, Bulgaria

M. I. Boyanov

Department of Physics, University of Notre Dame, Notre Dame, Indiana 46556

J.-P. Drolet

Scientech R&D Inc., 2200 Sidbec Sud, Suite 203, Trois-Rivières-Ouest, Québec, Canada G8Z 4H1

R. M. Leblanc

Department of Chemistry, University of Miami, Coral Gables, Florida 33124

Received August 26, 1998; accepted December 8, 1998; revised manuscript received January 19, 1999

An analytical solution for the determination of the substrate refractive index of a single-layered system from ellipsometric measurements is presented. It is shown that the above ellipsometric inverse problem is reduced to the finding of the roots of a third-degree polynomial. A unique approximate solution in the case of a thin covering layer is also presented. © 1999 Optical Society of America [S0740-3232(99)00106-4]

OCIS codes: 120.2130, 100.3190, 160.4760.

1. INTRODUCTION

It is well known that ellipsometry is very sensitive to the surface structure of a sample. This sensitivity is exploited in a wide variety of ellipsometry applications in physics, chemistry, and biology. The experimental determination of optical constants of bulk material in a broad spectral range is another application of ellipsometry. A generally complex parameter, refractive index, can be extracted from a single-wavelength ellipsometric measurement, in contrast to the methods that use the Kramers–Kronig relation, which requires reflectivity measurements in a very broad (theoretically infinite) spectral range. Thus the ellipsometric method is potentially more powerful and free of errors.

Usually the simplest possible ambient–substrate model is used to obtain the substrate refractive index from measured ellipsometric data. Special precautions are needed to ensure that the model is as close as possible to the real sample; i.e., the sample surface must be smooth and free of contaminants such as oxides. Nevertheless, the real sample is not fully described by this simple model, and some errors are introduced by neglecting the inevitably present surface layer. The so called pseudodielectric function instead of the real one is obtained in the above case. The question of finding the substrate refractive index in the presence of a covering layer (or layers) arises from this problem.

In this paper we show that the above inversion task

leads to the cubic equation for the bulk dielectric function, thus making the solution analytical. The initial assumption in the above solution is that all the parameters of the covering structure are known. Although such a formulation of the problem may seem rather artificial and rarely applicable in practice, we think that the solution given is interesting for several reasons:

1. This solution adds another analytical inversion to the small list of ellipsometric tasks that have known analytical solutions. To our knowledge, these solutions are as follows: (a) finding the substrate refractive index for a two-phase system,¹ (b) finding the layer thickness for a single-layer system,¹ (c) generalization of case (b) to the multilayer system,² and (d) finding the real refractive index and the thickness of an embedded layer in a symmetrical system.^{3–5} These four solutions lead to polynomials of degree 3 or less and are therefore analytical. To this list we may also add solutions that are not analytical but are polynomial (of degree greater than 4), thus reducing the general iterative inversion to the simpler task of finding the roots of a real polynomial: (e) finding the real refractive index and the thickness of a single-layer system for a nonabsorbing⁶ and an absorbing⁷ system, and (f) finding two thicknesses in an arbitrary multilayer system.⁸ The new analytical solution presented here is part of this polynomial-solutions group of polynomial degree 3.

2. In some cases the parameters of the covering layer

(or layers) may be found from measurements at a single wavelength (using, for example, multiangle ellipsometry). This information can then be applied in the present solution to find the refractive index of the substrate as a function of the wavelength from spectroscopic ellipsometry measurements. An example is the determination of the Si refractive index in a broad spectral range, where the covering layer is always present. Then the initially determined parameters of the covering layer can be used. The properties of the intermediate layer between the Si and the SiO₂ layers is the subject of intensive study; see Refs. 9 and 10 and references therein. This intermediate layer is usually treated as a mixture of Si and SiO₂. With Bruggeman's theory, the composition of this layer is found to be Si_{0.8}(SiO₂)_{0.2} of thickness 0.7 nm (Ref. 10). With this information, one can find the substrate Si refractive index more precisely from ellipsometric experimental data at any wavelength, using the solution presented here.

3. Even in the case in which the covering structure parameters are not exactly known, some reasonable assumptions can usually be made. Then the solution presented here can be used to estimate the expected errors introduced by this covering structure if the pseudodielectric function is determined. These errors may vary with wavelength and may become significant in certain spectral ranges. The errors largely affect the extinction coefficient, which is often overestimated by a factor of 2 to 10.^{11,12} Analytical solution may reduce these large errors and is a fast and effective way to assign the error limits to the pseudodielectric function as determined from the spectroscopic ellipsometry data.

4. The present solution can be used in the more complex task of searching more than two parameters (for example, using multiple-angle ellipsometry data). In this situation a minimization procedure is usually used. If part of the unknown parameters of the system are the substrate parameters, then the presented analytical solution can be used to reduce the minimization space dimension by two.

5. An analytical solution gives insight into the complexity of the ellipsometric inversion task. In minimization procedures the number of possible absolute minimums is usually unknown (in addition to the possible local minimums). This leads to the requirement that for achieving convergence, the starting point must be close to the actual solution.¹ Analytical solutions give the number of all possible mathematical absolute minimums. For example, if the substrate refractive index is added as an unknown to the other unknown parameters of the system in the minimization procedure, it will triple the absolute minimums.

It should be noted that the analytical solution of the present problem in the approximation for the nonabsorbing thin layer (layer thickness/wavelength $\ll 1$) is given in Ref. 13. Here we consider the general case of finding the substrate refractive index in the presence of the generally absorbing layer with arbitrary thickness. An approximate solution for the substrate refractive index in the presence of a covering layer for small layer thickness is then derived from the exact polynomial solution, which

includes only the pseudorefractive index (zero approximation) and the layer parameters, to give the corrected substrate refractive index. The result coincides with that given by Aspnes,¹⁴ but here we emphasize the parameters of the substrate rather than of the overlayer.

2. DETERMINATION OF THE SUBSTRATE REFRACTIVE INDEX FOR THE SINGLE-LAYER SYSTEM

Let us consider an ambient-layer-substrate system described by the ambient refractive index n_0 , layer refractive index n_1 , layer thickness d_1 , and unknown substrate refractive index n_2 . Parameters n_0 , n_1 , and d_1 are assumed known. All the refractive indices may be generally complex. The ellipsometric ratio ρ for this system is¹

$$\rho = R_p/R_s. \quad (1)$$

The generalized Fresnel coefficients R_p and R_s for a one-layer system are

$$R_p = \frac{r_{01p} + r_{12p}X}{1 + r_{01p}r_{12p}X}, \quad (2a)$$

$$R_s = \frac{r_{01s} + r_{12s}X}{1 + r_{01s}r_{12s}X}, \quad (2b)$$

where r_{ijp} and r_{ijs} ($ij = 01, 12$) are the Fresnel coefficients for the p and s polarizations, respectively, for the corresponding boundaries:

$$r_{01p} = \frac{n_1 \cos \phi_0 - n_0 \cos \phi_1}{n_1 \cos \phi_0 + n_0 \cos \phi_1}, \quad (3a)$$

$$r_{01s} = \frac{n_0 \cos \phi_0 - n_1 \cos \phi_1}{n_0 \cos \phi_0 + n_1 \cos \phi_1}, \quad (3b)$$

$$r_{12p} = \frac{n_2 \cos \phi_1 - n_1 \cos \phi_2}{n_2 \cos \phi_1 + n_1 \cos \phi_2}, \quad (3c)$$

$$r_{12s} = \frac{n_1 \cos \phi_1 - n_2 \cos \phi_2}{n_1 \cos \phi_1 + n_2 \cos \phi_2}, \quad (3d)$$

and

$$X = \exp\left(-i4\pi \frac{d_1}{\lambda} n_1 \cos \phi_1\right). \quad (4)$$

All the angles are connected through Snell's law:

$$n_0 \sin \phi_0 = n_1 \sin \phi_1 = n_2 \sin \phi_2. \quad (5)$$

The unknown substrate refractive index n_2 is present in both r_{12p} and r_{12s} . The procedure below will reduce the number of the parameters that contain the unknown n_2 from two to only one parameter. Let us use instead of the Fresnel coefficients for the 1-2 boundary the ellipsometric ratio ρ_{12} for this boundary:

$$\rho_{12} = r_{12p}/r_{12s}. \quad (6)$$

The unknown refractive index n_2 can be expressed through ρ_{12} (Ref. 1):

$$n_2 = n_1 \sin \phi_1 \left[1 + \left(\frac{1 - \rho_{12}}{1 + \rho_{12}} \right)^2 \tan^2 \phi_1 \right]^{1/2}. \quad (7)$$

Thus, if we can find ρ_{12} analytically, we can find n_2 by using Eq. (7). For this we need to express both r_{12p} and r_{12s} through ρ_{12} . From Eq. (6) and Snell's law [Eq. (5)] it is straightforward to obtain

$$n_2 \cos \phi_2 = n_1 \frac{\sin^2 \phi_1}{\cos \phi_1} \frac{1 - \rho_{12}}{1 + \rho_{12}}. \quad (8)$$

Now if we substitute Eq. (8) into Eq. (3d), after some algebra r_{12s} can be expressed through ρ_{12} in the following way:

$$r_{12s} = \frac{\rho_{12} + \cos 2\phi_1}{1 + \rho_{12} \cos 2\phi_1}. \quad (9)$$

When we use Eq. (6), r_{12p} is also expressed with ρ_{12} :

$$r_{12p} = \rho_{12} \frac{\rho_{12} + \cos 2\phi_1}{1 + \rho_{12} \cos 2\phi_1}. \quad (10)$$

Now we can substitute Eqs. (9) and (10) into Eqs. (1)–(3). This leads to the cubic equation for ρ_{12} , the only term now containing the unknown n_2 :

$$a\rho_{12}^3 + b\rho_{12}^2 + c\rho_{12} + d = 0. \quad (11)$$

The coefficients a , b , c , and d depend only on the known layer parameters

$$\begin{aligned} a &= (z_2 X + c_1 z_1) X, \\ b &= 2c_1 z_2 X^2 + (c_1^2 z_1 + c_1 z_4 + z_1) X + c_1^2 z_3, \\ c &= c_1^2 z_2 X^2 + (c_1^2 z_4 + c_1 z_1 + z_4) X + 2c_1 z_3, \\ d &= c_1 z_4 X + z_3, \end{aligned} \quad (12)$$

where

$$\begin{aligned} z_1 &= 1 - \rho r_{01p} r_{01s}, \\ z_2 &= r_{01s} - \rho r_{01p}, \\ z_3 &= r_{01p} - \rho r_{01s}, \\ z_4 &= r_{01p} r_{01s} - \rho, \end{aligned} \quad (13)$$

$$c_1 = \cos 2\phi_1 = 1 - 2(n_0/n_1)^2 \sin^2 \phi_0, \quad (14)$$

ρ is the measured ellipsometric ratio, and X is given by Eq. (4). The substrate refractive index n_2 can then be found by replacement of the roots of polynomial (11) into Eq. (7).

The above solution can be reformulated with use of Eq. (7) through the normalized admittance

$$u_{2s} = \frac{n_2 \cos \phi_2}{n_0} = (n_2^2/n_0^2 - \sin^2 \phi_0)^{1/2} \quad (15)$$

as unknown. Here we give only the final result, avoiding discussion of the long but straightforward transformations.

If we denote the following coefficients

$$\begin{aligned} p &= n_0^2 [(r_{01p} + X)(1 - r_{01s} X) - \rho(r_{01s} - X) \\ &\quad \times (1 + r_{01p} X)], \\ q &= n_0 u_{1s} [(r_{01p} + X)(1 + r_{01s} X) - \rho(r_{01s} + X) \\ &\quad \times (1 + r_{01p} X)], \\ r &= n_0^2 [(r_{01p} - X)(1 + r_{01s} X) - \rho(r_{01s} + X) \\ &\quad \times (1 - r_{01p} X)], \\ s &= n_0 u_{1p} [(r_{01p} - X)(1 - r_{01s} X) - \rho(r_{01s} - X) \\ &\quad \times (1 - r_{01p} X)], \end{aligned} \quad (16)$$

where

$$\begin{aligned} u_{1s} &= n_1 \cos \phi_1, \\ u_{1p} &= n_1 / \cos \phi_1, \end{aligned} \quad (17)$$

then the unknown u_{2s} satisfies the cubic equation again:

$$p u_{2s}^3 + (q + s) u_{2s}^2 + (r + p \sin^2 \phi_0) u_{2s} + q \sin^2 \phi_0 = 0. \quad (18)$$

The roots of polynomial (18) can be used to compute the unknown refractive index n_2 as follows from Eq. (15):

$$n_2 = n_0 (u_{2s} + \sin^2 \phi_0)^{1/2}. \quad (19)$$

A cubic equation for the substrate dielectric function ϵ_2

$$e_3 \epsilon_2^3 + e_2 \epsilon_2^2 + e_1 \epsilon_2 + e_0 = 0, \quad (20)$$

where

$$\epsilon_2 = n_2^2/n_0^2, \quad (21)$$

can be achieved by use of Eqs. (18), (19), and (21). The coefficients of polynomial (20) are expressed through coefficients (16) as follows:

$$\begin{aligned} e_3 &= p^2, \\ e_2 &= 2pr - p^2 \sin^2 \phi_0 - (q + s)^2, \\ e_1 &= r^2 - 2[pr - s(q + s)] \sin^2 \phi_0, \\ e_0 &= -(r^2 + s^2 \sin^2 \phi_0) \sin^2 \phi_0. \end{aligned} \quad (22)$$

In practice, the above form of the inversion task is more useful because the variable of polynomial (20) does not depend on the angle of incidence as in the other two formulations, Eqs. (11) and (18); it gives the substrate dielectric function directly. This is a useful property in multiangle ellipsometry data treatment when the substrate refractive index is unknown. Measuring at different incidence angles will give different coefficients (22), but one of the roots of the so formed polynomials (20) must be stable.

It should be noted that polynomials (11), (18), and (20) are equivalent in that they give the same final result for the computed substrate refractive index. In the most general case, they have three complex roots that yield six complex values for n_2 . Physically meaningful roots are those having a positive real part and a negative imaginary part, at most three physically acceptable values for n_2 . In the case of a nonabsorbing substrate, roots with small positive k should also be considered, because owing to experimental and round-off errors there might be a small positive imaginary part. In the case in which,

among three mathematical solutions more than one solution is physically acceptable, the true root of the measured system is easily chosen from measurements at different angles of incidence.

3. DETERMINATION OF THE SUBSTRATE REFRACTIVE INDEX IN THE PRESENCE OF AN ULTRATHIN LAYER

Here we consider the case in which the thickness of the covering layer satisfies the condition

$$d_1/\lambda \ll 1. \quad (23)$$

Let us first consider the approximate solution for the polynomial roots when the polynomial coefficients change slightly. Let $P_n(x)$ denote a polynomial of the n th degree of x with coefficients a_k ($k = 0..n$). We assume that the exact solution x_0 for $P_n(x) = 0$ is known. If the polynomial coefficients are changed by δa_k , then the root x_0 will change by δx , where¹⁵

$$\delta x = -\sum_{k=0}^n \delta a_k x_0^k / P'(x_0). \quad (24)$$

Let us consider polynomial (20), $P_3(\epsilon_2)$, with coefficients given by Eqs. (22). The root ϵ_{20} of this polynomial for a bare surface ($d_1 = 0$) is known¹:

$$\epsilon_{20} = n_0^2 \sin^2 \phi_0 \left[1 + \left(\frac{1 - \rho}{1 + \rho} \right)^2 \tan^2 \phi_0 \right]. \quad (25)$$

Equation (24), when the change is due to the change of the layer thickness from 0 to d_1 , will now read

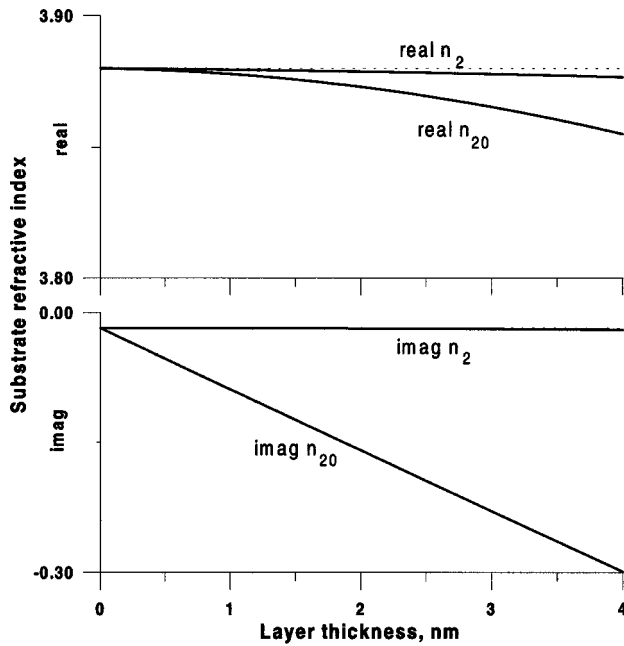


Fig. 1. Real and imaginary parts of the substrate refractive index for the air-SiO₂ ($n = 1.46$)-Si ($n = 3.88 - i*0.018$) system as computed by using the zero approximation with Eq. (28) (n_{20} , layer presence neglected), and the first approximation n_2 with Eq. (27). The ellipsometric data are simulated for an angle of incidence of 70° and wavelength 632.8 nm. The dashed curve represents exact values.

$$\delta \epsilon_{20} = -d_1 \left(\sum_{k=0}^3 \epsilon_{20}^k \frac{\partial \epsilon_k}{\partial d_1} \Big|_{d_1=0} \right) / \left(\frac{\partial P_3}{\partial d_1} \Big|_{d_1=0, \epsilon=\epsilon_{20}} \right). \quad (26)$$

After some algebra, Eq. (26) can be simplified, and the final result for the substrate refractive index is

$$n_2 = n_{20} \left[1 + 2\pi i \frac{d_1}{\lambda} (n_{20}^2 - n_0^2 \sin^2 \phi_0)^{1/2} \times \frac{(n_1^2 - n_0^2)(n_1^2 - n_{20}^2)}{n_1^2(n_0^2 - n_{20}^2)} \right], \quad (27)$$

where

$$n_{20} = \sqrt{\epsilon_{20}} = n_0 \sin \phi_0 \left[1 + \left(\frac{1 - \rho}{1 + \rho} \right)^2 \tan^2 \phi_0 \right]^{1/2} \quad (28)$$

is the zero approximation for the substrate refractive index.

A comparison between the results with zero approximation (28) and approximation (27) for the air-SiO₂-Si system is given in Fig. 1. There is a large error (especially in the imaginary part) in the substrate refractive index if the layer presence is neglected by using Eq. (28). Equation (27) gives better results and is useful and accurate for layer thicknesses up to several nanometers. For thicker layers the exact solutions, which are given in Section 2, should be used.

4. CONCLUSION

An analytical solution to calculate the substrate refractive index in the presence of an arbitrary uniform covering layer from a single ellipsometric measurement was presented. It was shown that the inverse ellipsometric problem in this case can be reduced to find the roots of a third-degree polynomial. For a thin covering layer, the approximate formula for a pseudodielectric function correction that takes into account the layer presence was presented.

REFERENCES

1. R. M. A. Azzam and N. M. Bashara, *Ellipsometry and Polarized Light* (North-Holland, Amsterdam, 1977).
2. S. C. Russev and D. D. Georgieva, "Analytical solution of another ellipsometric inverse problem," *J. Mod. Opt.* **38**, 1217-1222 (1991).
3. R. M. A. Azzam, "Ellipsometry of unsupported and embedded thin films," *J. Phys. (France)* **C10**, 67-70 (1983).
4. R. M. A. Azzam, "Transmission ellipsometry on transparent unbacked or embedded thin films with application to soap films in air," *Appl. Opt.* **30**, 2801-2806 (1991).
5. J. Lekner, "Analytic inversion of ellipsometric data for an unsupported nonabsorbing uniform layer," *J. Opt. Soc. Am. A* **7**, 1875-1877 (1990).
6. J. Lekner, "Inversion of reflection ellipsometric data," *Appl. Opt.* **33**, 5159-5165 (1994).
7. J. P. Drolet, S. C. Russev, M. I. Boyanov, and R. M. Leblanc, "Polynomial inversion of the single transparent layer problem in ellipsometry," *J. Opt. Soc. Am. A* **11**, 3284-3292 (1994).
8. S. C. Russev, I. Mircheva, J.-P. Drolet, D. Ducharme, and R. M. Leblanc, "Polynomial solution for two thicknesses of a multilayer system from a single ellipsometric measurement," *J. Opt. Soc. Am. A* **13**, 152-157 (1996).

9. I. Ohlidal and F. Lukes, "Analysis of semiconductor surfaces with very thin native oxide layers by combined immersion and multiple angle of incidence ellipsometry," *Appl. Surf. Sci.* **5**, 259–273 (1989).
10. F. Lukes, "Ellipsometry of silicon with natural surface film at 632.8 nm," *Phys. Status Solidi A* **93**, 223–230 (1986).
11. J. P. Moy, "Immersion ellipsometry," *Appl. Opt.* **20**, 3821–3822 (1986).
12. H. R. Philipp, "Influence of oxide layers on the determination of optical properties of silicon," *J. Appl. Phys.* **43**, 2835–2839 (1972).
13. A. F. Antippa, R. M. Leblanc, and D. Ducharme, "Multiple-wavelength ellipsometry in thin uniaxial nonabsorbing films," *J. Appl. Phys.* **43**, 2835–2839 (1972).
14. D. E. Aspnes, "Optical properties of thin films," *Thin Solid Films* **89**, 249–262 (1982).
15. W. S. Dorn and D. D. McCracken, *Numerical Methods with FORTRAN IV: Case Studies* (Wiley, New York, 1972).

Polynomial inversion of the single transparent layer problem in ellipsometry

Jean-Pierre Drolet

Centre de Recherche en Photobiophysique, Université du Québec à Trois-Rivières, Trois-Rivières, Québec G9A 5H7, Canada

Stoyan C. Russev and Maxim I. Boyanov

Department of Solid State Physics, Faculty of Physics, University of Sofia, 5 James Bourchier Avenue, Sofia 1126, Bulgaria

Roger M. Leblanc

Department of Chemistry, University of Miami, Coral Gables, Florida 33124

Received March 15, 1994; revised manuscript received June 24, 1994; accepted June 29, 1994

It is shown that for a uniform transparent layer over a substrate the layer dielectric constant satisfies a fifth-degree polynomial. The problem of extracting the layer index and thickness from the ellipsometric measurement is then reduced to finding the roots of this polynomial. The coefficients of this polynomial are determined by the angle of incidence, the real incident-medium index, the complex substrate index, and the measured complex ellipsometric ratio ρ . This approach to the problem gives directly all the possible physical solutions without the need for initial guesses or ranges. Special cases are examined. Numerical analysis and error analysis are provided for the case of a silicon oxide layer over silicon.

Key words: ellipsometry, single-layer system, thickness, refractive index, solution.

1. INTRODUCTION

The complex ellipsometric ratio $\rho = (\tan \Psi)\exp(i\Delta)$ is obtained experimentally with the measurement of the two angles Δ and Ψ . For a given model of the system under investigation it is in principle possible, from these two angles, to find two unknown parameters of the system. When the physical systems are modeled by two or more isotropic media having planar interfaces, the analytical inversion (calculation of the unknown in closed-form expression) is possible in only a few cases:

(1) Two-phase system with unknown complex refractive index of one phase.¹ The inversion is complete in the sense that two unknowns are computed from two measured parameters.

(2) Three-phase system (ambient layer substrate) with unknown thickness of the layer.¹ Inversion is incomplete; only one parameter is computed from two measured.

(3) Multilayer system with unknown thickness of any one layer.² This is a generalization of case (2), and the inversion is also incomplete.

(4) Multilayer system with unknown complex refractive index of the substrate.³ Complete inversion.

(5) Symmetric system of one layer of unknown thickness and real refractive index embedded in two identical phases having a real index.⁴ Complete inversion.

In all cases listed above, all parameters of the system

are defined except those stated as unknown, and the analytical result is based on a single measurement of Δ and Ψ . Thus the list does not include cases of possible analytical inversion when, for example, along with reflection ellipsometry, information from transmission ellipsometry is available.⁵⁻⁷ We can also cite the paper of Dagman,⁸ who achieved analytical inversion to solve for the thickness and the complex index of an absorbing layer from four measurements (two angles of incidence in two different incident media).

In all other cases in which analytical inversion is not (yet) possible, we must rely on iterative numerical procedures for solving transcendental equations. These numerical procedures are useful in determining layer refractive index and thickness requirements and relationships for prespecified systems such as ideal polarizers, ideal phase retarders, and polarization-independent systems.^{9,10} However, numerical procedures have problems of their own. First, the convergence may be slow or may not even be achieved. It depends strongly on the initial guesses for the unknown parameters. Second, there is usually more than one mathematical or physical solution for a given measurement on the system (i.e., many systems can yield to the same Δ and Ψ). One must know all the physically acceptable solutions to be able to discriminate (for example, with a second measurement at another angle of incidence) the solution corresponding to the system under investigation. With the use of numerical procedures it is difficult to find all solutions to a given problem or to know in advance the number of solutions to look for, because that number can be different from one

system to another. Consequently, there is no guarantee that all solutions are found.

In this paper we consider the ellipsometric inversion problem for one nonabsorbing layer with unknown thickness and refractive index over an arbitrary substrate. Many numerical solutions to the above model have been proposed.¹¹⁻¹⁷ We suggest a new approach to this problem, using the fact that the solution can be separated into two steps: the first step is to solve an equation that depends only on the refractive index, and the second step is to calculate the thickness from this refractive index. We show that this equation for the refractive index, which is complicated at first sight, can be reduced to a fifth-degree polynomial for the relative dielectric constant. Although the inversion is not fully analytical (at least one root must be found by iteration), it is direct and complete in the sense that it permits one to know, from the maximum of five different roots for the polynomial, which solutions are good and which are to be rejected. Thus our proposal overcomes the problems stated above for numerical procedures.

2. DERIVATION OF THE FIFTH-DEGREE POLYNOMIAL

The ellipsometric ratio ρ measured for a layer having a thickness d and a refractive index n_1 between an incident medium of index n_0 and a substrate of index n_2 is given by

$$\rho = \frac{(Xrp_{12} + rp_{01})(Xrs_{12}rs_{01} + 1)}{(Xrp_{12}rp_{01} + 1)(Xrs_{12} + rs_{01})}, \quad (1)$$

$$X = \exp\left[-\frac{4\pi i(\cos \phi_1)d n_1}{\lambda}\right], \quad (2)$$

$$rp_{01} = \frac{-n_0 \cos \phi_1 + n_1 \cos \phi}{n_0 \cos \phi_1 + n_1 \cos \phi}, \quad (3)$$

$$rp_{12} = \frac{-n_1 \cos \phi_2 + n_2 \cos \phi_1}{n_1 \cos \phi_2 + n_2 \cos \phi_1}, \quad (4)$$

$$rs_{01} = \frac{-n_1 \cos \phi_1 + n_0 \cos \phi}{n_1 \cos \phi_1 + n_0 \cos \phi}, \quad (5)$$

$$rs_{12} = \frac{-n_2 \cos \phi_2 + n_1 \cos \phi_1}{n_2 \cos \phi_2 + n_1 \cos \phi_1}, \quad (6)$$

$$\cos \phi_j = \frac{[n_j^2 - n_0^2(\sin \phi)^2]^{1/2}}{n_j}, \quad (7)$$

where rp_{ij} and rs_{ij} are the Fresnel reflection coefficients for the ij th interface and the measurement is made with incident light of wavelength λ at an angle of incidence ϕ . The problem is to compute the unknowns n_1 and d for the layer when all the other parameters are known. If the relative index $n = n_1/n_0$ is real, the complex Eq. (1) can be solved for the index and the thickness of the layer with a single measurement of ρ . The usual procedure for computing the unknown uses numerical inversion of a nonlinear problem. In what follows we show that, in the case in which n is real, the solution is achieved by determination of the roots of a fifth-degree polynomial. In some of the steps this derivation requires the manipulation of many hundreds of terms and would not be possible without the assistance of a symbolic algebra software. We

used Theorist, from Prescience Corporation (939 Howard Street, No. 306, San Francisco, California) running on a Macintosh IIsi.

The first step is to obtain an equation dependent on only the relative index. Equation (1) can be recast as a polynomial in X :

$$aX^2 + bX + c = 0, \quad (8)$$

where the coefficients are

$$a = (-rs_{01} + rp_{01}\rho)rp_{12}rs_{12}, \quad (9)$$

$$b = rp_{12} - rp_{01}rs_{12}rs_{01} + \rho(rs_{12} + rp_{12}rp_{01}rs_{01}), \quad (10)$$

$$c = -rp_{01} + rs_{01}\rho. \quad (11)$$

We use the fact that $X^\dagger = 1/X$ when the relative index $n = n_1/n_0$ is real, and then the complex conjugate of Eq. (8) leads to

$$c^\dagger X^2 + b^\dagger X + a^\dagger = 0. \quad (12)$$

The elimination of X^2 in Eqs. (8) and (12) gives an expression for X that is free of radicals:

$$X = \frac{aa^\dagger - cc^\dagger}{-ab^\dagger + bc^\dagger}. \quad (13)$$

It is important to emphasize the fact that Eq. (13) gives a unique solution for X , instead of two solutions if one solves Eq. (8) with the usual expressions for the roots of the quadratic equations. Equation (13) is not widely used, even though it permits reduction of the numerical task by a factor of 2 through the elimination of the false root of X at the beginning.

Using again $X^\dagger = 1/X$, we obtain an equation [Eq. (14a) below] that depends on only the relative index n and is independent of the thickness d . This equation must be solved for n :

$$(-ab^\dagger + bc^\dagger)^\dagger(-ab^\dagger + bc^\dagger) - (aa^\dagger - cc^\dagger)^2 = 0, \quad (14a)$$

or

$$-|a|^4 + |a|^2|b|^2 - |c|^4 + 2|a|^2|c|^2 + |b|^2|c|^2 - ac(b^\dagger)^2 - b^2a^\dagger c^\dagger = 0. \quad (14b)$$

Up to now we have followed the derivation of Eqs. (14) given in Ref. 18. In the present form of Eqs. (14) with a , b , and c given by Eqs. (9), (10), and (11), respectively, the unknown n is included in the four reflection coefficients rs_{01} , rp_{01} , rs_{12} , and rp_{12} . To our knowledge, an explicit expression for n with the use of Eqs. (14) has never been published. This can be achieved if we make the following substitutions to express Eqs. (14) in terms of only one real unknown t :

$$t = \frac{n_1 \cos \phi_1}{n_0 \cos \phi}, \quad (15)$$

$$x = -\tan \phi \tan \phi_2, \quad (16)$$

$$y = \frac{n_2 \cos \phi_2}{n_0 \cos \phi}, \quad (17)$$

$$z = \frac{\rho - 1}{\rho + 1}. \quad (18)$$

In the system to be solved we have one real unknown n_1 and five independent known parameters (one for the

angle of incidence ϕ , two for the complex substrate index n_2 , and two for the complex ellipsometric ratio ρ). Using the substitutions (15)–(18), we have one real unknown t and six parameters (real and imaginary part of complex x , y , and z). But x and y are linked through the relation $xy = x^\dagger y^\dagger = \tan^2 \phi$, so there are still five independent parameters in Eqs. (14).

With these definitions, the Fresnel coefficients and ρ become

$$r_{p01} = \frac{(t-1)(t-xy)}{(t+1)(t+xy)}, \tag{19}$$

$$r_{p12} = -\frac{(t+x)(t+y)}{(t-x)(t-y)}, \tag{20}$$

$$r_{s01} = -\frac{t-1}{t+1}, \tag{21}$$

$$r_{s12} = \frac{t+y}{t-y}, \tag{22}$$

$$\rho = \frac{z-1}{z+1}, \tag{23}$$

and the coefficients a , b , and c of Eqs. (14) can be written as

$$a = -(t+1)(t-1)(t+x)(t+y)^2(t+xzy)C, \tag{24}$$

$$b = 2(t+y)(t-y)[t^4 + (2xy + x^2zy + 2xz + 1)t^2 + x^2zy]C, \tag{25}$$

$$c = -(t+1)(t-1)(t-x)(t-y)^2(t-xzy)C, \tag{26}$$

$$C = \frac{\rho + 1}{(t+1)^2(t-x)(t-y)^2(t+xy)}, \tag{27}$$

where C is a common factor that can be eliminated from Eqs. (14). After the cancellation of C each term of the expanded form of Eq. (14b) yields a polynomial of degree 24. This degree is rather high for one to expect any useful analytical result, but, fortunately, because of the sign symmetry between a and c , many simplifications occur.

After substitution of Eqs. (24)–(26) into Eqs. (14), we can cancel the common factor $(t-1)^2(t+1)^2$ reducing the degree by 4, so the equations then become

$$(-b_1 a_1^\dagger + c_1 b_1^\dagger)(-b_1 a_1^\dagger + c_1 b_1^\dagger)^\dagger - (a_1 a_1^\dagger - c_1 c_1^\dagger)^2 (t^2 - 1)^2 = 0, \tag{28}$$

where the coefficients are defined as

$$a_1 = -(t+x)(t+y)^2(t+xzy), \tag{29}$$

$$b_1 = 2(t+y)(t-y)[t^4 + (2xy + x^2zy + 2xz + 1)t^2 + x^2zy], \tag{30}$$

$$c_1 = -(t-x)(t-y)^2(t-xzy). \tag{31}$$

We can now proceed to the expansion of the terms in Eq. (28) to obtain gradually the coefficients of the expanded polynomial and show step by step how the degree of the polynomial is reduced. We have then

$$a_1 = -t^4 - \alpha_3 t^3 - \alpha_2 t^2 - \alpha_1 t - \alpha_0, \tag{32}$$

$$b_1 = 2(t^6 + \alpha_4 t^4 + \alpha_5 t^2 - \alpha_0), \tag{33}$$

$$c_1 = -t^4 + \alpha_3 t^3 - \alpha_2 t^2 + \alpha_1 t - \alpha_0, \tag{34}$$

where the coefficients α are defined as

$$\alpha_0 = x^2 y^3 z,$$

$$\alpha_1 = xy^2 + xy^3 z + 2x^2 y^2 z,$$

$$\alpha_2 = y^2 + 2xy + 2xy^2 z + x^2 yz,$$

$$\alpha_3 = x + 2y + xyz,$$

$$\alpha_4 = -y^2 + 2xy + 2xz + x^2 yz + 1,$$

$$\alpha_5 = -2xy^3 - y^2 - x^2 y^3 z - 2xy^2 z + x^2 yz. \tag{35}$$

The symmetry between a_1 and c_1 cancels the even powers of t when the difference of their squared modulus is expanded. The eighth power of t vanishes, and so does the constant term. We are left with

$$a_1 a_1^\dagger - c_1 c_1^\dagger = 2(g_6 t^6 + g_4 t^4 + g_2 t^2 + g_0)t. \tag{36}$$

The remaining g coefficients are all real:

$$g_0 = \alpha_0 \alpha_1^\dagger + \alpha_1 \alpha_0^\dagger,$$

$$g_2 = \alpha_0 \alpha_3^\dagger + \alpha_1 \alpha_2^\dagger + \alpha_2 \alpha_1^\dagger + \alpha_3 \alpha_0^\dagger,$$

$$g_4 = \alpha_1 + \alpha_2 \alpha_3^\dagger + \alpha_3 \alpha_2^\dagger + \alpha_1^\dagger,$$

$$g_6 = \alpha_3 + \alpha_3^\dagger. \tag{37}$$

Squaring both sides of Eq. (36) leads to terms with only even powers of t , and multiplication by $(t^2 - 1)^2$ gives an even polynomial of degree 18 with real coefficients.

In the expansion of $c_1^\dagger b_1 - a_1 b_1^\dagger$ the same cancellation of the highest and lowest powers occurs. The remaining coefficients are alternately real and imaginary, and it is important to note that the constant term and the eighth-degree coefficient are the same as in Eq. (36):

$$c_1^\dagger b_1 - a_1 b_1^\dagger = 2(g_6 t^8 + f_7 i t^7 + f_6 t^6 + f_5 i t^5 + f_4 t^4 + f_3 i t^3 + f_2 t^2 + f_1 i t - g_0)t, \tag{38}$$

where the f coefficients are all real and defined by

$$f_1 = (-\alpha_0 \alpha_5^\dagger - \alpha_0 \alpha_2^\dagger + \alpha_5 \alpha_0^\dagger + \alpha_2 \alpha_0^\dagger)i,$$

$$f_2 = \alpha_1 \alpha_5^\dagger - \alpha_0 \alpha_3^\dagger + \alpha_5 \alpha_1^\dagger - \alpha_3 \alpha_0^\dagger,$$

$$f_3 = (-\alpha_0 - \alpha_2 \alpha_5^\dagger - \alpha_0 \alpha_4^\dagger + \alpha_5 \alpha_2^\dagger + \alpha_4 \alpha_0^\dagger + \alpha_0^\dagger)i,$$

$$f_4 = \alpha_3 \alpha_5^\dagger + \alpha_1 \alpha_4^\dagger + \alpha_5 \alpha_3^\dagger + \alpha_4 \alpha_1^\dagger,$$

$$f_5 = (\alpha_5 - \alpha_0 - \alpha_5^\dagger - \alpha_2 \alpha_4^\dagger + \alpha_4 \alpha_2^\dagger + \alpha_0^\dagger)i,$$

$$f_6 = \alpha_1 + \alpha_3 \alpha_4^\dagger + \alpha_4 \alpha_3^\dagger + \alpha_1^\dagger,$$

$$f_7 = (\alpha_4 - \alpha_2 - \alpha_4^\dagger + \alpha_2^\dagger)i. \tag{39}$$

When Eq. (38) is multiplied by its conjugate, the alternation of real and imaginary coefficients makes the odd powers of t cancel each other and leads to another polynomial of degree 18 with real coefficients. Further, the two polynomials [Eq. (36) squared and Eq. (38) multiplied by its complex conjugate] have a common factor of $4t^2$ that reduces the degree from 18 to 16 after cancellation. Having only even powers of t , we now substitute a new

variable, $s = t^2$, and the degree of polynomials is now 8 in s , defined as

$$s = \frac{n_1^2(\cos \phi_1)^2}{n_0^2(\cos \phi)^2} \text{ or } s = (xy + 1)\epsilon - xy \quad (40a)$$

or

$$\epsilon = s(\cos \phi)^2 + (\sin \phi)^2, \quad (40b)$$

where $\epsilon = (n_1/n_0)^2$ is the relative dielectric constant and $xy \equiv \tan^2 \phi$. Since the two polynomials have the same coefficients for the highest and lowest powers of s , their difference leads to a seventh-degree polynomial with no constant term, that is, a sixth-degree polynomial after cancellation of the trivial zero root. The polynomial is now reduced to

$$j_6s^6 + j_5s^5 + j_4s^4 + j_3s^3 + j_2s^2 + j_1s + j_0 = 0, \quad (41)$$

where the j 's are real and related to the f 's and the g 's by

$$\begin{aligned} j_0 &= f_1^2 + 2g_0^2 - 2f_2g_0 - 2g_2g_0, \\ j_1 &= f_2^2 + 2f_3f_1 - g_2^2 - g_0^2 - 2f_4g_0 - 2g_4g_0 + 4g_2g_0, \\ j_2 &= f_3^2 + 2f_4f_2 + 2f_5f_1 + 2g_2^2 - 2g_4g_2 - 2f_6g_0 \\ &\quad - 2g_6g_0 + 4g_4g_0 - 2g_2g_0, \\ j_3 &= f_4^2 + 2f_5f_3 + 2f_6f_2 + 2f_7f_1 - g_4^2 - g_2^2 - 2g_6g_2 \\ &\quad + 4g_4g_2 + 2g_6g_0 - 2g_4g_0, \\ j_4 &= f_5^2 + 2f_6f_4 + 2f_7f_3 + 2f_2g_6 + 2g_4^2 - 2g_6g_4 \\ &\quad + 4g_6g_2 - 2g_4g_2 - 2g_6g_0, \\ j_5 &= f_6^2 + 2f_7f_5 - g_6^2 + 2f_4g_6 - g_4^2 + 4g_6g_4 - 2g_6g_2, \\ j_6 &= f_7^2 + 2g_6^2 + 2f_6g_6 - 2g_6g_4. \end{aligned} \quad (42)$$

We may want to express the polynomial with the physical variable ϵ instead of s , using Eq. (41). This yields a polynomial of ϵ with the constant term

$$j_6x^6y^6 - j_5x^5y^5 + j_4x^4y^4 - j_3x^3y^3 + j_2x^2y^2 - j_1xy + j_0, \quad (43)$$

which is Eq. (41) with $s = -xy$. One can prove analytically that this term is always zero. In order to do so, one must express the j 's directly in terms of x , y , and z [using the substitution sets (35), (37), and (39) and replacing them in expression (43)]. The operation gives an expression with 2047 terms that finally cancel to zero. The trivial zero root can then be removed from the polynomial, and we finally obtain a fifth-degree polynomial for the relative dielectric constant:

$$k_5\epsilon^5 + k_4\epsilon^4 + k_3\epsilon^3 + k_2\epsilon^2 + k_1\epsilon + k_0 = 0, \quad (44)$$

where

$$\begin{aligned} k_0 &= j_1 - 6j_6x^5y^5 + 5j_5x^4y^4 - 4j_4x^3y^3 + 3j_3x^2y^2 \\ &\quad - 2j_2xy, \\ k_1 &= (j_2 + 15j_6x^4y^4 - 10j_5x^3y^3 + 6j_4x^2y^2 \\ &\quad - 3j_3xy)(xy + 1), \\ k_2 &= (j_3 - 20j_6x^3y^3 + 10j_5x^2y^2 - 4j_4xy)(xy + 1)^2, \\ k_3 &= (j_4 + 15j_6x^2y^2 - 5j_5xy)(xy + 1)^3, \\ k_4 &= (j_5 - 6j_6xy)(xy + 1)^4, \\ k_5 &= (xy + 1)^5j_6. \end{aligned} \quad (45)$$

The polynomial of Eq. (44) has real coefficients and thus has one, three, or five real roots. Only the real roots satisfying $\epsilon \geq \sin^2 \phi$ lead to $XX^\dagger = 1$, while all the other roots are inconsistent with the initial restriction to the derivation of the polynomial. When $\epsilon < \sin^2 \phi$, internal reflection for the layer occurs, this case is treated separately in Section 3.

For each valid root we obtain the thickness by isolating d in Eq. (2):

$$d = \left(\frac{1}{4} \frac{\lambda}{\pi(\cos \phi_1)n_1} \right) i \ln X + \frac{1}{2} \frac{m\lambda}{(\cos \phi_1)n_1}. \quad (46)$$

The thickness is known only to an integral multiple of $\lambda/2(\cos \phi_1)n_1$, a value that changes the optical path length of light in the layer by one wavelength, and m stands for any integer that makes the thickness positive and physically reasonable. To calculate X , one could use Eqs. (9)–(11) and compute the reflection coefficients. But if we develop the right-hand side of Eq. (13) with the given substitutions, we can express X with coefficients that are already computed:

$$X = \frac{g_6t^8 + f_6t^6 + f_4t^4 + f_2t^2 - g_0 - i(f_7t^6 + f_5t^4 + f_3t^2 + f_1)t}{(t^2 - 1)(g_6t^6 + g_4t^4 + g_2t^2 + g_0)}. \quad (47)$$

The quantity $i \ln X$ in Eq. (46) is the phase of X with the sign reversed. If one wants to compute the phase using the real form $\arctan[(\text{Im } X)/(\text{Re } X)]$, Eq. (47) can easily be used because the real and imaginary parts are already separated (the only complex term in the equation is i). One must take care to choose the right quadrant for the phase, according to the signs of the real and imaginary parts of X .

The factor $(1 + xy)^n$ could be excluded from k_n and the polynomial solved for $(1 + xy)\epsilon$, but numerically the k 's are more balanced when they are computed with Eqs. (45). The numerical computation of the polynomial coefficients is straightforward with the use of Eqs. (15)–(18), (35), (37), (40), (42), and (45). Algorithms that find the real roots of a real-coefficient polynomial are fast, accurate, well documented, and available in many computer languages, so this approach to the problem gives directly and easily all the possible physical solutions.

The preceding derivation may seem complicated, but it consists solely of the explicit expansion of products and sums of polynomials. We give here a summary of the method.

For the quadratic equation in X to have a root with unit modulus imposes a condition over the coefficients a , b , and c . This condition is stated in Eq. (14a). Once the common factor C (in fact, $|C|^4$) is canceled from this equation, it becomes a polynomial in t . Moreover, one can see by examination that any real root common to coefficients a and c is a double root of this polynomial. This permits us to remove the common term $(t - 1)^2(t + 1)^2$ and yields Eq. (29). Expansion of the polynomial, which needs only multiplication and addition of numeric coefficients, leads to a fifth-degree polynomial for the layer dielectric constant ϵ . The algorithm that computes the solutions thus involves the following steps:

- (1) Compute complex x , y , and z from n_0 , n_2 , ϕ , and measured ρ [Eqs. (16)–(18)].
- (2) Compute complex α 's from x , y , and z [Eqs. (35)].
- (3) Compute real g 's from the α 's [Eqs. 37].
- (4) Compute real f 's from the α 's [Eqs. (39)].
- (5) Compute real j 's from the f 's and the g 's [Eqs. (42)].
- (6) Compute real k 's from the j 's [Eqs. (45)].
- (7) Find the roots of the polynomial [Eq. (44)].
- (8) For each valid root $\epsilon > 0$:
 - (8.1) Compute index $n_1 = +n_0\sqrt{\epsilon}$ and t [Eq. (15)].
 - (8.2) Compute X [Eq. (47)].
 - (8.3) Compute thickness d [Eq. (46)].

The only iterative step is step (7), which finds the roots of the polynomial. First, one real root must be found by iteration. Second, the four other roots are computed with the use of the standard analytical solution for the fourth-degree equation obtained after the extraction of the first root from the polynomial.

3. SPECIAL CASES

Reflection for Angles Greater Than the Critical Angle of the Layer

When the index of the layer is lower than the index of the incident medium, $\cos \phi_1$ is then a pure imaginary number for angles of incidence greater than the critical angle of the layer, $\phi_c = \arcsin n$, or, equivalently, when $\epsilon < \sin^2 \phi$ (total internal reflection does not occur here because of the finite thickness of the layer). In this situation X no longer has modulus 1 but becomes real, in contradiction with the initial assumption for the derivation of the polynomial. We can make a similar derivation for this case. When X is real, the complex conjugate of Eq. (8) is

$$X^2 a^\dagger + X b^\dagger + c^\dagger = 0, \quad (48)$$

and cancellation of X^2 in Eqs. (8) and (48) leads to a solution for X :

$$X = \frac{c^\dagger a - c a^\dagger}{b a^\dagger - a b^\dagger}. \quad (49)$$

The condition for Eq. (8) to have a real root then becomes

$$(c^\dagger b - c b^\dagger)(-b a^\dagger + a b^\dagger) - (c^\dagger a - c a^\dagger)^2 = 0. \quad (50)$$

From Eq. (50) we can derive a polynomial for ϵ in the same way that we did for Eq. (14) and have an expression for X in Eq. (49). When we do so, it appears that the equations are exactly the same in both cases. Consequently, in any case we must solve a unique polynomial for ϵ and calculate X according to Eq. (49) even if $\epsilon < \sin^2 \phi$. Effectively, it can easily be checked that X is real in Eq. (47) when t is pure imaginary. The thickness when $\epsilon < \sin^2 \phi$ is still calculated with Eq. (46), but m must then be zero because there is no periodicity anymore. In the peculiar case in which ϵ is exactly $\sin^2 \phi$ one must take the limit $t \rightarrow 0$ in order to calculate the thickness.

Total Internal Reflection for the Substrate

When the substrate index is real and the angle of incidence is greater than its critical angle, all the incident light is totally reflected by the substrate and then Ψ is always 45° . Information for the layer is then given by only one experimental parameter, Δ , so one cannot expect to solve the equations for both thickness and index. In this case all the coefficients of the polynomial vanish and thus any ϵ is a zero of the polynomial. Equation (46) gives then for every value of the index the thickness that is consistent with the experimental Δ .

Layer Embedded in Two Identical Phases with a Real Index

This peculiar system has an analytical solution⁴ (ϵ must satisfy a cubic equation), and it is interesting to compare the two solutions. In this case all the polynomial coefficients vanish when they are calculated with Eqs. (45). The reason is that the coefficients have a common factor $(y^2 - 1)$ when the substrate index is real, and y is -1 if the substrate and the incident medium have the same index. Once this common factor is canceled, we are able to find five solutions for ϵ , but the system is known to have a maximum of three solutions for the cubic equation. One can identify the two roots in excess by dividing the fifth-degree polynomial by the cubic equation whose coefficients are given by Eq. (12) in Ref. 4 (translated into our notation and taking into account the different sign conventions in the two papers). The two polynomials divide exactly, indicating that they have three common roots (those of the cubic equation); thus our polynomial derived for the general case includes the solutions for this special case. The result of the division is a quadratic equation in ϵ . The roots in excess are the roots of this quadratic equation. One root is always $\epsilon = 1$ (no layer), and the other is real and depends on the angle of incidence (through x) and on the layer (through z). This second root is

$$\epsilon = \frac{(zx + z^\dagger x + 2zz^\dagger x + z + z^\dagger + 2)x}{zx^2 + z^\dagger x^2 - 2zz^\dagger x^2 - 3zx - 3z^\dagger x + 2x - 4} \quad (51)$$

and cannot possibly be consistent with $XX^\dagger = 1$, but this statement requires further analysis.

4. NUMERICAL ANALYSIS

The polynomial method can be restricted to a search of a single root of the polynomial, given an initial value for the index. When doing so, we have found that it is more

Table 1. Comparative Results for Different Inversion Methods: Solution for Silicon Oxide Layer over Silicon Substrate^a

Method	Polynomial	Yoriume (Ref. 13)	Reinberg (Ref. 15)
Index	1.5115	1.5114	1.5110
Thickness (nm)	14.46	14.46	14.46
Computation time (ms)	7.5	16.8	9.9
Accuracy (digits)	13	6	5

^aBased on measured $\Psi = 14.27^\circ$, measured $\Delta = 137.45^\circ$, angle of incidence of 70.0° , wavelength of 546.1 nm, ambient index of 1.00, and substrate index of $4.08 - 0.028i$.

Table 2. Five Polynomial Solutions for the Same Measurement

Solution	Layer Index	Layer Thickness (nm)
1	1.5115	$14.46 + 230.64m$
2	0.5936	-3.89
3	$0.0761i$	$7.44 - 14.48i$
4	$3.5039 - 1.1015i$	$28.90 - 14.36i$
5	$3.5039 + 1.1015i$	$28.90 + 14.36i$

efficient to avoid the computation of the k coefficients and to solve directly the sixth-degree equation for s [Eq. (41)]. This gives a common base with which one can compare the efficiency of the polynomial method with that of other numerical methods. We have implemented the polynomial method, along with Yoriume's¹³ and Reinberg's¹⁵ methods, in Pascal, using double precision for all numbers. The programs were run on an IBM PS/2 30 286 computer with a coprocessor. We took one of the examples given in Yoriume's paper¹³ for a layer of silicon oxide over silicon. The three methods started the search with an initial index of 1.4 and an increment of 0.1. Comparative results are shown in Table 1. The polynomial method is superior both in execution time and in accuracy. The accuracy is the accuracy of the inversion procedure itself, independent of measurement errors. It is defined as the number of digits of agreement of Δ and Ψ computed from the solution with the values given as input. The influence of the measurement errors on the solution is the subject of Section 5. With a smaller convergence criterion Yoriume's method can be as accurate as the polynomial method; the computation time increases then to 22.8 ms. The solutions for all possible real indices and thicknesses from the fifth-degree polynomial for ϵ were computed in 12 ms. Results for the same example are shown in Table 2. The complex solutions 3–5 are easily discarded. Solution 2 is mathematically valid and gives back the measured Δ and Ψ when ρ is computed with an index of 0.5936 and a thickness of -3.89 nm. But this solution is not correct for two physical reasons: the index is too low relative to air, and the thickness is negative (m must be zero for this case, where $\epsilon < \sin^2 \phi$). Solution 1 is then the only reasonable decision for this measurement.

When we used the polynomial method to invert computer-generated data, it did not show significant error or convergence problems even for extreme cases, where $d/\lambda = 10^{-6}$ or $\phi = 0.01^\circ$ or 89.99° . The silicon substrate system was solved for a large set (many 10^6) of random

values of Ψ and Δ within their full respective ranges, and the inversion method proved to be accurate for most cases. However, for some values of the ellipsometric angles, the polynomial shows some difficulties commonly encountered in root solving, e.g., when $k_5 \approx 0$ and when two roots are nearly degenerate. The polynomial root-solving procedure must handle these special cases. For every (Ψ, Δ) pair tested, at least one solution was found with an index greater than unity.

5. ERROR PROPAGATION ANALYSIS

One can use the polynomial method to study the effect of measurement errors on the solutions. Figure 1 shows the domain of solutions if an error of $\pm 0.05^\circ$ is included in the Ψ and Δ measurements for the silicon-silicon oxide system of Section 4. The solution for the index is 1.512 ± 0.044 , and that for the thickness is 14.51 ± 0.52 nm. The system is more sensitive to errors in Ψ than in Δ for this angle of incidence.

We simulated the silicon-silicon oxide system ($n_1 = 1.5115$ and $d = 14.46$ nm) for a wide range of angles of incidence to see the behavior of the solutions. The system has only two real roots from 0° to 90° , and, as one would expect, the true solution is stable over this range. The second real root has no physical meaning but is also very stable, the index varying slowly from 0.581 near 0° to 0.595 near 90° . The critical angle for this root is approximately 36° ; above this angle the corresponding thickness is negative from -3.75 nm to -3.92 nm at 90° . Below the critical angle the thickness is large and positive, growing from 466 nm near 0° to an infinite value as the critical angle is approached.

As in Ref. 4, Figs. 2 and 3 show the results of the inversion process on index and thickness, given a uniform spread of error of $\pm 0.1^\circ$ in Ψ and $\pm 0.2^\circ$ in Δ about their calculated values, with the same system parameters. The roots with real indices and positive thicknesses are shown. One can observe the following features:

- (1) There is an angle of incidence with minimum error near 77° .
- (2) Below 50° , positive thicknesses become possible for the low-index root.

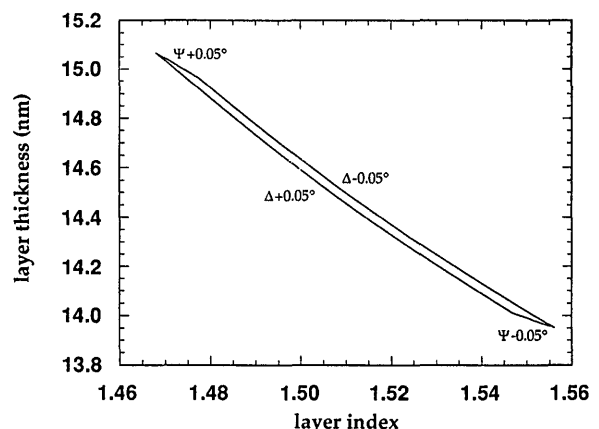


Fig. 1. Domain of possible solutions for the layer index and thickness when the polynomial is solved with experimental errors of $\pm 0.05^\circ$ in Ψ and Δ .

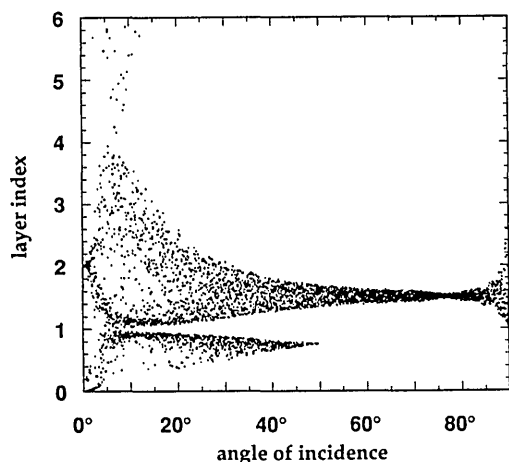


Fig. 2. Scatter in index values produced from the roots of the polynomial when random errors are introduced in the simulated ellipsometric data. The errors are uniformly distributed within $\pm 0.1^\circ$ in Ψ and $\pm 0.2^\circ$ in Δ .

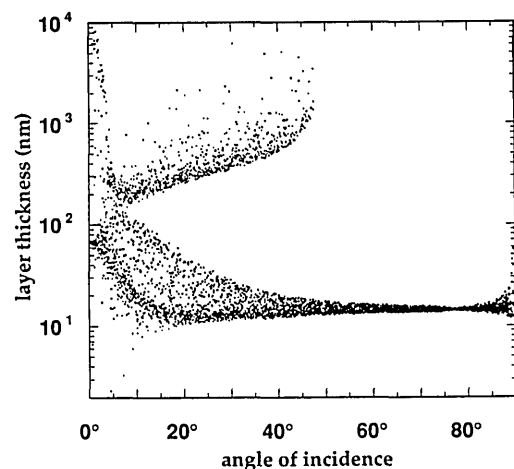


Fig. 3. Scatter in thickness values related to the indices of Fig. 2.

(3) The large spread of thicknesses requires a logarithmic scale for Fig. 3. Large values for thickness are associated with the low-index root and are due to a large layer period.

(4) Below 15° , a third real root appears (points with index larger than 4 in Fig. 2) with high index and low thickness. The index domain of this root extends to infinity.

(5) For low angles of incidence and a uniform spread of errors the spread of solutions is not uniform, as indicated by the nonuniform point density of Figs. 2 and 3.

One final comment concerns the resolution: it becomes poor for low angles of incidence, as the different root domains merge together into a single large error domain.

6. CONCLUSION

The above analysis illustrates how easy it is to find and identify all the possible (n, d) solution pairs from a given ellipsometric measurement over a single transparent layer system. The computation is very fast and can be used in real-time control applications. Moreover,

the choice of the correct solution is clear enough to be easily programmed.

Iterative methods achieve convergence to a solution when they find an index and a thickness that produce a (Δ, Ψ) pair that falls into the provided error range for experimental ellipsometric angles. There is thus a source of error inherent in the inversion procedure. An advantage of the present method is that it inverts the equations with almost as many digits as the computer can hold: the computed n and d give back accurately the Δ and Ψ given as input. Consequently, the inversion procedure is now a negligible source of error and facilitates the analysis of errors of experimental sources.

The only iterative (nonanalytical) task left in the solution of the single transparent layer system is the computation of the first root of the fifth-degree polynomial; once this first root is known, the remaining four roots are found by standard analytical techniques for the biquadratic equation. All these advantages make the method efficient for solving this problem of general interest in ellipsometry.

ACKNOWLEDGMENTS

One author (S. C. Russev) gratefully acknowledges the Natural Sciences and Engineering Research Council of Canada for its support. The authors express appreciation to Daniel Ducharme for his helpful revision of the manuscript.

REFERENCES

1. R. M. A. Azzam and N. M. Bashara, *Ellipsometry and Polarized Light* (North-Holland, Amsterdam, 1977), Chap. 4.
2. S. C. Russev and D. D. Georgieva, "Analytical solution of another ellipsometric inverse problem," *J. Mod. Opt.* **38**, 1217–1222 (1991).
3. Information available on request from S. C. Russev and M. I. Boyanov at the address on the title page of the present paper.
4. J. Lekner, "Analytic inversion of ellipsometric data for an unsupported nonabsorbing uniform layer," *J. Opt. Soc. Am. A* **7**, 1875–1877 (1990).
5. R. M. A. Azzam, "Simple and direct determination of complex refractive index and thickness of unsupported or embedded thin films by combined reflection and transmission ellipsometry at 45° angle of incidence," *J. Opt. Soc. Am.* **73**, 1080–1082 (1983).
6. R. M. A. Azzam, "Ellipsometry of unsupported and embedded thin films," *J. Phys. (Paris)* **C10**, 67–70 (1983).
7. R. M. A. Azzam, "Transmission ellipsometry on transparent unbacked or embedded thin films with application to soap films in air," *Appl. Opt.* **30**, 2801–2806 (1991).
8. E. E. Dagman, "Analytical solution of the inverse ellipsometry problem in the modeling of a single-layer reflecting system," *Opt. Spectrosc. (USSR)* **62**, 500–503 (1987).
9. R. M. A. Azzam and B. E. Perilloux, "Constraint on the optical constants of a film-substrate system for operation as an external-reflection retarder at a given angle of incidence," *Appl. Opt.* **24**, 1171–1179 (1985).
10. R. M. A. Azzam and B. E. Perilloux, "Equalization of the complex reflection coefficients for the parallel and perpendicular polarizations of an absorbing substrate coated by a transparent thin film," *Opt. Acta* **32**, 767–777 (1985).
11. V. Krisdhasima, J. McGuire, and R. Sproull, "A one-film-model ellipsometry program for the simultaneous calculation of protein film thickness and refractive index," *Surf. Interface Anal.* **18**, 453–456 (1992).
12. F. K. Urban III, "Ellipsometry algorithm for absorbing films," *Appl. Opt.* **32**, 2339–2344 (1993).

13. Y. Yoriome, "Method for numerical inversion of the ellipsometry equation for transparent films," *J. Opt. Soc. Am.* **73**, 888–891 (1983).
14. O. Hunderi, "New method for accurate determination of optical constants," *Appl. Opt.* **11**, 1572–1578 (1972).
15. A. R. Reinberg, "Ellipsometer data analysis with a small programmable desk calculator," *Appl. Opt.* **11**, 1273–1274 (1972).
16. T. Yamaguchi and H. Takahashi, "Ellipsometric method for separate measurement of n and d of a transparent film," *Appl. Opt.* **14**, 2010–2015 (1975).
17. F. L. McCrackin, E. Passaglia, R. R. Stromberg, and H. L. Steinberg, "Measurement of the thickness and refractive index of very thin films and the optical properties of surfaces by ellipsometry," *J. Res. Nat. Bur. Stand. Sect. A* **67**, 363–377 (1963).
18. M. C. Dorf and J. Lekner, "Reflection and transmission ellipsometry of a uniform layer," *J. Opt. Soc. Am. A* **4**, 2096–2100 (1987).